



New study of afterglow light curves in gamma ray bursts

by

Roberta Del Vecchio

Astronomical Observatory of the Jagiellonian University
ul. Orla 171, 30-244, Kraków

Supervisor:

Prof. M. Ostrowski

Co-supervisor:

Dr. M.G. Dainotti

A thesis submitted to the Faculty of Physics, Astronomy and Applied
Computer Science of the Jagiellonian University
for the degree of Doctor of Philosophy in Astronomy.

Oświadczenie

Ja niżej podpisana Roberta Del Vecchio (nr indeksu: 1098475) doktorantka Wydziału Fizyki, Astronomii i Informatyki Stosowanej Uniwersytetu Jagiellońskiego oświadczam, że przedłożona przeze mnie rozprawa doktorska pt. "New study of afterglow light curves in gamma ray bursts" jest oryginalna i przedstawia wyniki badań wykonanych przeze mnie osobiście, pod kierunkiem prof. dr hab. Michała Ostrowskiego i dr Marii Giovanny Dainotti. Pracę napisałam samodzielnie. Oświadczam, że moja rozprawa doktorska została opracowana zgodnie z Ustawą o prawie autorskim i prawach pokrewnych z dnia 4 lutego 1994 r. (Dziennik Ustaw 1994 nr 24 poz. 83 wraz z późniejszymi zmianami). Jestem świadom, że niezgodność niniejszego oświadczenia z prawdą ujawniona w dowolnym czasie, niezależnie od skutków prawnych wynikających z ww. ustawy, może spowodować unieważnienie stopnia nabytego na podstawie tej rozprawy.

Kraków, dnia

Podpis doktorantki

Contents

Acknowledgements	xi
Abstract	xii
Streszczenie	xiv
1 Introduction	1
1.1 The phenomenology of the GRBs	4
1.1.1 The prompt emission	5
1.1.2 The afterglow emission	7
1.1.3 The broadband spectrum	8
1.1.4 The observational classification: long, short, the intermediate class and the ultra-long GRBs	9
1.1.5 The hardness ratio: GRB, X-ray Rich and X-ray flashes	11
1.2 The phenomenological Willingale model	13
1.2.1 The functional form of the X-rays decays	13
1.3 The past and current missions observing GRBs	16
1.4 The SNe historical background	20
1.4.1 Classification of the SNe	21
2 GRB models	22
2.1 The Compactness problem	22
2.2 The jet opening angle	24
2.3 The fireball model	26
2.3.1 Energy conversion	27
2.3.2 Light curves within the fireball model	28
2.4 Central engine models	30
2.4.1 Long GRB models	30
2.4.2 Short GRB models	34
2.5 Additional Models	36
2.6 The SNe Ib/c models	39
3 The GRB correlations among prompt parameters	44
3.1 Why Standard candles and sirens are important for cosmology?	44
3.2 Notations, nomenclature and abbreviations	46
3.3 The GRB correlations among prompt parameters	51

3.3.1	The $L_{\text{peak}} - \tau_{\text{lag}}$ correlation	51
3.3.2	The $L_{\text{peak}} - V$ correlation	55
3.3.3	The $L_{\text{iso}} - \tau_{\text{RT}}$ correlation and its physical interpretation	57
3.3.4	The $\Gamma_0 - E_{\text{prompt}}$ and $\Gamma_0 - L_{\text{iso}}$ correlations and their physical interpretation	59
3.3.5	Correlations between the energetics and the peak energy	61
3.3.6	Correlations between the luminosity and the peak energy	71
3.3.7	Comparisons between $E_{\text{peak}} - E_{\text{iso}}$ and $L_{\text{peak}} - E_{\text{peak}}$ correlation	76
3.3.8	The $L_{X,p} - T_{X,p}^*$ correlation and its physical interpretation	78
3.3.9	The $L_{X,f} - T_{X,f}$ correlation and its physical interpretation	80
3.3.10	Redshift estimator for correlations among prompt parameters	82
3.3.11	Applications to cosmology of GRB correlations among prompt parameters	84
3.3.12	Statistical approaches related to SNe Ia Cosmology	89
4	Correlations among afterglow and prompt-afterglow parameters	93
4.1	The correlations among afterglow parameters	93
4.1.1	The LT correlation ($L_{X,a} - T_{X,a}^*$)	93
4.1.2	The unified $L_{X,a} - T_{X,a}^*$ and $L_{O,a} - T_{O,a}^*$ correlations	103
4.1.3	The $L_{O,200s} - \alpha_{O,>200s}$ correlation and its physical interpretation	106
4.2	Correlations among prompt-afterglow parameters	109
4.2.1	The $E_{X,\text{afterglow}} - E_{\gamma,\text{prompt}}$ correlation and its physical interpretation	109
4.2.2	The $L_{X,\text{afterglow}} - E_{\gamma,\text{prompt}}$ correlation and its physical interpretation	113
4.2.3	The $L_{X,a} - L_{O,a}$ correlation and its physical interpretation	119
4.2.4	The $L_{X,a} - L_{\text{iso}}$ correlation	121
4.2.5	The $L_{X,a} - L_{X,\text{peak}}$ correlation	123
4.2.6	The $L_{O,\text{peak}}^F - T_{O,\text{peak}}^{*F}$ correlation and its physical interpretation	127
4.3	Selection Effects	130
4.3.1	Redshift induced correlations	130
4.3.2	Redshift induced correlations through Efron and Petrosian method	132
4.3.3	Evaluation of the intrinsic slope	136
4.3.4	Selection effects for the optical and X-ray luminosities	137
4.3.5	Selection effects in the $L_{O,200s} - \alpha_{O,>200s}$ correlation	138
4.4	Redshift Estimator	138
4.5	Cosmology	141
4.5.1	The problem of the calibration	141
4.5.2	Applications of GRB afterglow correlations	143
5	Selection Effects in Gamma Ray Burst Correlations: Consequences on the Ratio between Gamma Ray Burst and Star Formation Rates	150
5.1	Preface	150
5.2	Main Analysis	150

5.3	Results	154
6	Study of the decaying part of the X-ray afterglow	156
6.1	Preface	156
6.2	Introduction	157
6.3	Data Sample	158
6.4	Analysis of the afterglow decay light curves	159
6.5	Final discussion and Conclusions	166
6.5.1	Theoretical models	167
6.5.2	GRB standardization	168
7	Summary and final remarks	169
Bibliography		171
A	Fits of the decay indices $\alpha_{X,a}$ for the GRB afterglow light curves	222
A.1	The fitted values	222
A.2	Illustrations of performed fits	227
B	The Swift mission	314
C	Published papers used in this work	319

List of Figures

1.1.1 An example of a GRB light curve: GRB 080430.	5
1.1.2 Samples of prompt emission light curves observed by Swift.	6
1.1.3 Examples of GRB afterglow light curves with X-ray flares.	8
1.1.4 An example of a spectrum of GRB 050319 taken from the Swift XRT repository and a model of broadband GRB spectra	9
1.1.5 Histogram of the duration of 1234 GRBs observed by BATSE as shown in the BATSE 4B Catalogue.	10
1.1.6 The hardness-duration correlation for BATSE GRBs.	12
1.2.1 The two components of the Willingale model	14
1.2.2 Examples of the fit with the Willingale model	15
1.3.1 The distribution of the GRBs detected by BATSE.	17
2.2.1 Sketch of the jet opening angle, its relation with the emitting source of the progenitor, and the Γ factor.	25
2.3.1 Sketch of the fireball model.	27
2.4.1 A representation of the GRB accretion model.	31
2.4.2 Sketch of the collapsar model summarizing the main phases from the progenitor star until the collapse.	32
2.4.3 A sketch of the magnetar model.	34
2.5.1 GRB model for a jet observed off-axis.	37
2.5.2 GRB afterglow light curve flux F_ν in the GRB photosphere and external shock model in four emission frequencies.	39
2.6.1 A sketch summarizing the SNe types.	41
2.6.2 Energy of the explosion versus envelope masses and nickel masses for seven SNe Ib/c and 16 SNe II.	42
3.1.1 Distance indicators used in astronomy.	46
3.3.1 The $L_{\text{peak}} - \tau_{\text{lag}}^*$ and $\log L_{\text{peak}} \sim 2.53 \log(1+z) - 0.282 \log \tau_{\text{lag}}$ correlations.	52
3.3.2 The $\log L_{\text{peak}} - \log V$ correlation.	56
3.3.3 The $\log L_{\text{iso}} - \log \tau_{\text{RT}}^*$ correlation.	58
3.3.4 The $\log \Gamma_0 - \log E_{\text{prompt}}$ and $\log \Gamma_0 - \log L_{\text{iso}}$ correlations.	60
3.3.5 Peak energies versus intensity with displayed error bars for five GRB sets.	61
3.3.6 The E_{peak} versus S_{tot} and E_{peak} versus F_{peak} distributions.	62
3.3.7 The $E_{\text{peak}} - E_{\text{iso}}$ correlation.	64
3.3.8 The $E_{\text{peak}}^* - E_\gamma$ correlation and rest-frame distribution of the Ghirlanda correlation.	71

3.3.9 Fit of the $\log E_{\text{peak}} - \log L_{\text{iso}}$ correlation.	72
3.3.10 The $E_{\text{peak}}^* - L_{\text{iso}}$ correlation for GRBs 990123 and 990510.	73
3.3.11 The $\log L_{\text{peak}} - \log E_{\text{peak}}$ correlation.	74
3.3.12 The $\log L_{X,p} - \log T_{X,p}^*$ correlation.	79
3.3.13 The $L_{X,f} - T_{X,f}^*$ and $L_{X,f} - E_{\text{peak}}$ distributions.	81
3.3.14 The distribution of z through the $\log L_{\text{peak}} - \log E_{\text{peak}}$ correlation.	83
3.3.15 Contours of Ω_M and Ω_Λ from the $E_{\text{peak}} - E_\gamma$ correlation.	85
3.3.16 Contours for Ω_M and Ω_Λ .	87
3.3.17 Maximum likelihood $\Delta\chi^2$ contours.	88
3.3.18 Contours at 68% CL in the $\Omega_M - \Omega_\Lambda$ space.	89
4.1.1 The LT correlation.	94
4.1.2 The flux versus time and $\log L_{X,a} - \log F_{X,a}$ distributions.	95
4.1.3 Light curves for the accretion model and total accretion mass for the afterglow phase.	99
4.1.4 Light curves for the magnetar model and distribution of B and P.	99
4.1.5 Light curves in the optical and X-ray ranges in the case of wind (left panel) and ISM (right panel) external media.	101
4.1.6 Light curves in optical and X-ray wavelengths before and after the injection break and the $F_{X,a} - T_{X,a}$ correlation slope versus the electron distribution index for the FS and the RS.	102
4.1.7 Simulated slopes of the X-ray and optical LT correlations for 1000 thin shell samples considering the FS or the RS scenario.	102
4.1.8 The optical and X-ray light curves for the GRB data set and the $T_{O,\text{peak}}^* - L_{O,\text{peak}}$ correlation.	104
4.1.9 The $L_{O,a}^S - T_{O,a}^{S,*}$ correlation and the distributions of $L_{O,a}^S$ and $T_{O,a}^S$ for the whole GRB sample.	104
4.1.10 Light curves in the optical range and the $\log L_{O,200s} - \alpha_{O,>200s}$ correlation.	107
4.1.11 The $\alpha_{O,>200s} - \alpha_{X,>200s}$ and $\alpha_{O,>200s} - \beta_{O,>200s}$ correlations.	108
4.2.1 The fluences, the $\log E_{X,\text{afterglow}} - \log E_{\gamma,\text{prompt}}$ and the $\log E_{X,\text{plateau}} - \log E_{\gamma,\text{prompt}}$ correlations.	110
4.2.2 The $E_{O,\text{afterglow}} - E_{\gamma,\text{prompt}}$ and the $E_{k,\text{aft}} - E_{\gamma,\text{prompt}}$ correlations.	111
4.2.3 The X-ray fluence versus prompt fluence, the XRT fluence–BAT fluence, and the $\log E_{X,\text{afterglow}} - \log E_{\gamma,\text{prompt}}$ correlations.	112
4.2.4 The $F_{X,11} - S_{\gamma,\text{prompt}}$ correlation.	113
4.2.5 The $F_{O,11} - S_{\gamma,\text{prompt}}$, the $F_{X,11} - S_{\gamma,\text{prompt}}$, the $L_{O,11} - E_{\gamma,\text{prompt}}$ and the $L_{X,11} - E_{\gamma,\text{prompt}}$ correlations.	115
4.2.6 The $E_{\gamma,\text{prompt}} - F_{O,a}$ and the $L_{X,1d} - E_{\gamma,\text{prompt}}$ correlations.	116
4.2.7 The $L_{X,10} - E_{\gamma,\text{prompt}}$ and the $L_{O,\text{peak}} - E_{\gamma,\text{prompt}}$ correlations.	116
4.2.8 The $F_{O,1d} - E_{\gamma,\text{prompt}}$, the $L_{X,11} - E_{\gamma,\text{prompt}}$ and the $L_{O,7} - E_{\gamma,\text{prompt}}$ correlations.	117
4.2.9 The $\log L_{O,200s} - \log E_{\gamma,\text{prompt}}$ and the $\log L_{X,200s} - \log E_{\gamma,\text{prompt}}$ correlations.	117
4.2.10 The $\log F_{O,11} - \log F_{X,11}$ correlation.	120
4.2.11 The $L_{O,7} - L_{X,11}$ and the $\log L_{X,200s} - \log L_{O,200s}$ correlations.	120
4.2.12 The $\log < L_{\text{iso}} >_{45} - \log L_{X,a}$, the correlation coefficients versus $u = \sigma_E$ for a few correlations, and the $L_{X,a} - L_{\text{iso}}$ correlation.	121

4.2.13 The log $L_{X,a}$ -log $L_{X,peak}$ and log $F_{X,a}$ – log $F_{X,peak}$ correlations.	123
4.2.14 The log L – log T^* and the log E – log T^* correlations for all the pulses in the prompt and afterglow phases.	124
4.2.15 Distribution of the ratio of the BAT to XRT fluxes for a set of Swift GRBs.	127
4.2.16 The log w^F -log $T_{O,peak}^F$ correlation with the best fit line.	128
4.2.17 The log $L_{O,peak}^F$ -log $T_{O,peak}^{*F}$ correlation with optical and X-ray flares.	129
4.3.1 The LT correlation with the data set split in the three redshift ranges and LT correlation for 101 GRBs split into five redshift groups.	131
4.3.2 The slope b as a function of the average value of the redshift ranges and b as a function of z .	132
4.3.3 The log $L_{X,a} - z$ and the log $L_{X,peak} - z$ distributions.	133
4.3.4 The $\tau - k_{L_{X,a}}$ and the $\tau - k_{L_{X,peak}}$ distributions.	134
4.3.5 The log $T_{X,a}^* - z$ and the log $T_{X,prompt}^* - z$ distributions.	135
4.3.6 The observed and rest-frame T_{90} versus the redshift.	135
4.3.7 The $\tau - k_{T_{X,a}^*}$ and the $\tau - k_{T_{X,prompt}^*}$ distributions.	136
4.3.8 The $\tau - b_{int}$ and the $r - b_{int}$ distributions for the log $L_{X,a} - \log L_{X,peak}$ correlation.	137
4.4.1 The $z_{obs} - z_{est}$ correlation for the sample split in three σ_E intervals.	140
4.5.1 The $(N, \Delta z)$ space with the distribution of $\log P$.	142
4.5.2 The likelihood functions $\mathcal{L}(b, \sigma_{int})$ and $\mathcal{L}(\Omega_M, h)$ for the Full data set and the High Luminosity data set.	147
4.5.3 HD for SNe Ia and GRBs.	148
4.5.4 $w(z > 1)$ solutions computed through synthetic GRB data sets obtained for $w(z) = -1$	148
5.2.1 GRBs rate density using the method by Li (2008) and the observed GRBs rate density obtained by the linear efficiency functions and the polynomial efficiency function.	152
5.2.2 Examples of the efficiency function for the linear case versus the times, τ , of the GRBs in the data sample and for the fourth order polynomial case.	153
6.3.1 Comparison of the derived indices $\alpha_{X,a}$ and α_W .	160
6.4.1 Distribution of log $L_{X,a}$ versus $\alpha_{X,a}$ for the long GRBs+XRFs subsample.	160
6.4.2 Normalized cumulative distribution functions versus $\alpha_{X,a}$ for the analysed GRBs.	161
6.4.3 GRB distributions of $\alpha_{X,a}$ for the analysed subsamples.	162
6.4.4 Distribution of the long GRBs+XRFs subsample on the $(\log L_{X,a}, \log T_{X,a}^*)$ plane.	163
6.4.5 Normalized cumulative distributions function versus $\log(L_{X,a}/L_{LT})$ for the analysed GRBs.	164
6.4.6 Distributions of $\log(L_{X,a}/L_{LT})$ for the long GRBs+XRFs subsamples.	165
6.4.7 Distribution of the long GRBs+XRFs subsample on the $(\alpha_{X,a}, \log(L_{X,a}/L_{LT}))$ plane.	165
6.4.8 The results of the Monte Carlo simulations for the long subsample.	166
A.2.1 - A.2.172 Fits of the X-ray GRB light curves.	227
B.1.1 A drawing of the Swift satellite.	314

B.1.2 Plot displaying the BAT instrument from the Swift website.	315
B.1.3 Plot displaying the XRT instrument from the Swift website.	316
B.1.4 Plot displaying the UVOT instrument from the Swift website.	316

List of Tables

3.1	Table with abbreviations.	50
4.1	Summary of the LT correlation.	96
4.2	Summary of the unified $L_{X,a}$ - $T_{X,a}^*$ and $L_{O,a}$ - $T_{O,a}^*$ correlations.	105
4.3	Summary of the $L_{O,200s}$ - $\alpha_{O,>200s}$ correlation.	108
4.4	Summary of the $E_{X,afterglow}$ - $E_{\gamma,prompt}$ correlation.	112
4.5	Summary of the $L_{X,afterglow}$ - $E_{\gamma,prompt}$ correlation.	118
4.6	Summary of the $L_{X,a}$ - $L_{O,a}$ correlation.	121
4.7	Summary of the correlations among prompt and prompt-afterglow parameters.	122
4.8	Summary of the $L_{O,peak}^F$ - $T_{O,peak}^{*F}$ correlation.	129
4.9	Calibration results for GRBs split in three equally populated redshift bins.	131
5.1	Slope a and zero point b of the fitted vs. input parameters for both the best fit and median values.	154
5.2	Same as Table 5.1.	155
A.1a	Table describing the results of the afterglow decay index fit.	222
A.1b	Continuation of Table A.1a.	223
A.1c	Continuation of Table A.1a.	224
A.1d	Continuation of Table A.1a.	225
A.1e	Continuation of Table A.1a.	226
A.1f	Continuation of Table A.1a.	227
B.1	Technical specifications of the BAT instrument on board of Swift satellite.	317
B.2	Technical specifications of the XRT instrument on board of Swift satellite.	317
B.3	Technical specifications of the UVOT instrument on board of Swift satellite.	318

Acknowledgements

I want to thank my supervisor, Prof. Michał Ostrowski, and my co-supervisor, Dr. Maria Giovanna Dainotti, for all the knowledge and the professional experience they transmitted to me during my PhD studies, and I am grateful to Dr. Mariusz Tarnopolski for his valuable comments and remarks on this manuscript.

Of course presenting this thesis, which I consider an important achievement in my life, would not have been possible without the presence of my dear Pasquale, my parents, Giuseppe and Mariangela, and my sister Francesca. For this reason huge thanks go to them.

Finally, I am deeply grateful to those people that for all these years shared their lives with me at the Astronomical Observatory of the Jagiellonian University: Natalia, Arti and Dorota.

Even if good and bad moments were coming and going, these people enriched a lot this period of my life.

The work presented here made extensive use of data supplied by the UK Swift Science Data Centre at the University of Leicester. In addition, I want to thank Dr. Samantha Oates for providing me with the GRB optical data, even if not used for the work presented here. This work was supported by the Polish National Science Centre through the grant DEC-2012/04/A/ST9/00083.

Abstract

The main aim of this thesis is to study the afterglow phase in the gamma-ray burst (GRB) light curves to better understand the physics and the radiation processes driving these phenomena, and to eventually use this knowledge in search for a method to turn GRBs into cosmological standard candles. In the proceedings a sample of 176 GRB light curves in the X-ray energy band, taken from the Swift catalogue, is analysed. The GRB physical parameters, like emitted energy, luminosity, temporal decay index, spectral index, and so forth, of the afterglow phase were investigated. In particular, the correlations among these parameters were studied, as the well known correlation between the luminosity at the end of the plateau phase, $L_{X,a}$, and the end time of the plateau phase itself, $T_{X,a}^*$ (Dainotti et al. 2008, hereafter LT correlation). In the investigation of these correlations the selection effects influencing the measurements were studied and published in the paper Dainotti, Del Vecchio, Nagataki, and Capozziello (2015b). As a result of further analysis, a correlation between the temporal decay index, $\alpha_{X,a}$, and the relative luminosity, $\log(L_{X,a}/L_{\text{LT}})$ (the ratio of $L_{X,a}$ to the value of the luminosity of the LT correlation best fit line at the same time), is discovered and a systematic effect on the LT correlation depending on $\alpha_{X,a}$ is revealed. A novelty of the presented analysis comes from the performed systematic study – using a large data sample – of the X-ray afterglow light curve decaying phase and the discovery of a new correlation between the light curve decay speed and the characteristic afterglow luminosity (Del Vecchio, Dainotti & Ostrowski, ApJ, 828, 36 (2016)). The study of this correlation is useful in investigation of the nature and the properties of the GRB surrounding medium, which on the other hand can play an important role in shaping the GRB emission. Also, a method for correcting the afterglow luminosity applying measurements of the afterglow power-law decay index was developed and tested within an assumed simple model. Unfortunately, the method resembling the one by Phillips (1993) for supernovae (SNe) Ia, has a limited effect in GRB standardization attempt due to largely scattered data.

This thesis is organised as follows: in the Introduction (Chapter 1) a phenomenological overview of GRBs and the missions involved in their observations are described. In Chapter 2 the compactness problem and the main GRB models are introduced. Chapter 3, following the paper Dainotti, Del Vecchio, and Tarnopolski (2018), is dedicated to the discussion of the correlations between GRB prompt phase parameters, while Chapter 4, following the paper Dainotti and Del Vecchio (2017), describes the correlations among afterglow phase parameters, as well as those among the prompt phase and the afterglow phase parameters. In Chapter 5 the work Dainotti, Del Vecchio, Nagataki, and Capozziello (2015b) studying the selection effects in the GRB correlations is presented. Then, in Chapter 6, the results

of the $\alpha_{X,a}$ analysis in the GRB afterglow phase light curves are presented, following the paper Del Vecchio, Dainotti, and Ostrowski (2016). A final discussion and the conclusions are presented in Chapter 7.

The main text is followed by 3 appendices. Appendix A displays the table with the values of the X-ray light curve $\alpha_{X,a}$ fits and the plots illustrating the fits performed by the thesis author. Appendix B presents in more detail the Swift space mission, the main data source for the GRB studies. Appendix C contains copies of the four published papers of the thesis author whose results are included as parts of the thesis.

Streszczenie

Tematyką niniejszej rozprawy doktorskiej jest badanie fazy poświaty rozbłysków gamma w ich krzywych zmian blasku w celu lepszego zrozumienia procesów fizycznych i radiacyjnych powodujących te zjawiska oraz by użyć tą wiedzę do poszukiwania metody pozwalającej traktować rozbłyski gamma jako świece standardowe. Aby to osiągnąć, zanalizowana została próbka 176 krzywych zmian blasku rozbłysków gamma w zakresie rentgenowskim wziętych z katalogu Swift. Zbadane zostały takie parametry fizyczne fazy poświaty rozbłysków gamma, takie jak: emitowana energia, jasność, indeks czasowego zaniku, indeks widmowy i inne. W szczególności, zbadano korelacje występujące pomiędzy tymi parametrami, jak przykładowo dobrze znana korelacja między jasnością końca płaskiej części fazy poświaty, $L_{X,a}$, a czasem jej trwania, $T_{X,a}^*$ (Dainotti et al. 2008, nazywana tutaj korelacją LT). Podczas studiowania tych korelacji zbadany został efekt selekcji wpływający na pomiary, zaś rezultaty zostały opublikowane w Dainotti, Del Vecchio, Nagataki, and Capozziello (2015b). W wyniku kolejnych analiz odkryta została korelacja między wskaźnikiem czasowego zaniku, $\alpha_{X,a}$, a jasnością względową, $\log(L_{X,a}/L_{LT})$ (stosunkiem $L_{X,a}$ do najlepszego dopasowania wartości jasności korelacji LT w tym samym czasie) a także systematyczny efekt korelacji LT zależący od $\alpha_{X,a}$. Nowym podejściem w prezentowanych analizach jest przeprowadzenie systematycznych badań – użycie dużej próbki danych krzywych zmian blasku w zakresie rentgenowskim fazy zaniku poświaty i odkrycie nowej korelacji między prędkością zaniku krzywej blasku a charakterystyczną jasnością poświaty (Del Vecchio, Dainotti & Ostrowski, ApJ, 828, 36 (2016)). Analizowanie tej korelacji jest użyteczne przy badaniu natury i własności ośrodka otaczającego rozbłyski gamma, które również mogą odgrywać istotną rolę w kształtowaniu się emisji rozbłysków gamma. Dodatkowo, rozwinięto metodę korygowania jasności poświaty przy zastosowaniu pomiarów indeksu potęgowego zaniku i przetestowano ją w ramach założonego prostego modelu. Niestety metoda przypominająca przedstawioną przez Phillips (1993) dla supernowych typu Ia, ma ograniczony wpływ na próbę standaryzacji rozbłysków gamma ze względu na bardzo rozproszone dane.

We wstępie przedstawionej rozprawy doktorskiej (rozdział 1) opisany jest fenomenologiczny przegląd rozbłysków gamma i ich obserwacje. W rozdziale 2 przedstawiony został problem zwartości oraz główne modele rozbłysków gamma. Rozdział 3, oparty na publikacji Dainotti, Del Vecchio, and Tarnopolski (2018), jest poświęcony dyskusji o korelacjach między parametrami pierwotnej emisji rozbłysków gamma, podczas gdy rozdział 4, odnoszący się do publikacji Dainotti and Del Vecchio (2017), opisuje korelacje pomiędzy parametrami fazy poświaty, jak również między parametrami fazy pierwotnej i poświaty. W rozdziale 5 zaprezentowana została praca Dainotti, Del Vecchio, Nagataki, and Capozziello (2015b) badająca

efekty selekcji w korelacjach rozbłysków gamma. Następnie, w rozdziale 6, przedstawione zostały wyniki analiz $\alpha_{X,a}$ w krzywych zmian blasku fazy poświaty na podstawie publikacji Del Vecchio, Dainotti, and Ostrowski (2016). Końcowa dyskusja i wnioski są zaprezentowane w rozdziale 7.

Tekst główny rozprawy uzupełniają trzy aneksy. Pierwszy aneks A zawiera tabelę z wartościami dopasowania $\alpha_{X,a}$ rentgenowskich krzywych zmian blasku oraz wykresy ilustrujące dopasowania przeprowadzone przez autorkę rozprawy. Dodatek B prezentuje szczegóły związane z misją kosmiczną Swift, która jest głównym źródłem danych użytych do badań nad rozbłyskami gamma. Aneks C zawiera kopie czterech publikacji autorki rozprawy, których wyniki są załączone jako części rozprawy.

Introduction

Gamma-ray bursts (GRBs) release in few seconds the same energy that the Sun releases in its entire lifetime, namely their isotropic emission is about $10^{48} - 10^{55}$ erg (see Nakar 2007b; Zhang 2011; Gehrels and Razzaque 2013; Berger 2014b; Kumar and Zhang 2015; Mészáros and Rees 2015). GRBs were discovered by chance by the satellites Vela in late 1960's and scientists immediately realised that they were born outside our galaxy (Klebesadel et al., 1973). The isotropic angular distribution in the sky as well as an intensity distribution deviating from the $-3/2$ power-law (Paczynski, 1991a,b; Meegan et al., 1992; Fishman and Meegan, 1995; Briggs et al., 1996) explained this outcome. The first GRB with measured redshift validated these results. Indeed, this GRB has been found at least at 2.9 Gpc (Metzger et al., 1997) with $0.835 < z \lesssim 2.3$. Mazets et al. (1981) found a bimodal distribution in the duration of GRBs detected by the BATSE (Burst and Transient Source Experiment) instrument (Meegan et al., 1992). After this discovery, GRBs are currently divided into two classes: short (SGRBs) and long GRBs (LGRBs) with durations $T_{90} < 2$ s and $T_{90} > 2$ s, respectively (Kouveliotou et al., 1993). Moreover, Horváth (1998) and Mukherjee et al. (1998) claimed the existence of a third class with intermediate durations. Later, Norris and Bonnell (2006) found a class of SGRBs with extended emission (SEE-GRBs) showing features common between SGRBs and LGRBs, but counter-arguments were recently discussed (Zitouni et al., 2015; Tarnopolski, 2017). For SGRBs, even if initially retained isotropically distributed, it was pointed out that they are anisotropically distributed in the sky, while LGRBs are isotropically distributed (Balazs et al., 1998; Mészáros et al., 2000a,b; Mészáros and Štoček, 2003; Magliocchetti et al., 2003; Bernui et al., 2008; Vavrek et al., 2008; Tarnopolski, 2017). Mészáros et al. (2009) and Mészáros and Rees (2015) investigated the cosmological effects of the anisotropic celestial distribution of SGRBs. Regarding the progenitor of LGRBs and SGRBs two main scenarios are currently plausible: the collapse of a massive star connected to supernovae (SNe) for the first (Hjorth et al., 2003; Malesani et al., 2004; Woosley and Bloom, 2006b; Sparre et al., 2011; Schulze et al., 2014) and the coalescence of binary systems of neutron star–black hole (NS–BH) or NS–NS mergers (Eichler et al., 1989; Paczynski, 1991b; Narayan et al., 1992a; Nakar and Piran, 2005) for the latter. In the latter case no connection to SNe has been claimed (Zhang et al., 2009).

The fireball model (Cavallo and Rees, 1978a; Wijers et al., 1997; Mészáros, 1998, 2006) is

one of the most famous models applied for the description of the GRB emission. In this model an ultra-relativistic and beamed electron/positron/baryon plasma is radiated by a compact central engine either of LGRBs or SGRBs. The prompt emission, which consists of gamma-rays and hard X-rays, is generated from the collisions of blobs within the jet. Instead, the afterglow phase, namely a long broadband radiation (X-ray, optical and radio) following the prompt phase, is created by the impact of the jet with the density medium. In the context of the fireball model different X/Gamma radiation processes are possible, such as the synchrotron, the Inverse Compton, the blackbody radiations, and sometimes a combination of these. Two types of fireball exist: the kinetic energy and the Poynting flux dominated (magnetic field dominated). Recently, Begue & Pe'er (2015) investigated the Poynting flux dominated outflow that undergoes photospheric emission. The processes that characterize the plasma thermalization lose its efficiency at a radius which has been indicated to be beneath the photosphere radius by approximately two orders of magnitude. A combination of the Compton scattering below the photosphere and the conservation of the total number of photons imposes kinetic equilibrium between photons and electrons. Consequently, this gives as outcome an increase of the photon temperature that goes up to 8 MeV, specifically when the decoupling process of the plasma occurs in the photosphere. But, the model parameters do not strongly influence the results even though they are not fixed parameters. Begue & Pe'er (2015) indicated that the expected thermal luminosity, which is a tiny fraction of the total luminosity, could be observed. The magnetization of the outflows is constrained because the predicted peak energy is greater than the observed one that characterizes the majority of the GRBs. Continuing on this research theme, Pe'er (2015) summarizes new ideas, methods and instruments which have revolutionized the way the prompt emission is studied. Particularly, the author explains the latest observational outcomes as well as the up-to-date theoretical interpretation of the same. The time-resolved spectral analysis has been demonstrated as a huge step forward from the observational perspective. This analysis has resulted in the discovery of a distinct high-energy component that leads to the delayed observation of the GeV photons, and strong evidence regarding the occurrence of the thermal component in many bursts. The outcomes led to numerous theoretical efforts that were meant to highlight the physical conditions characterizing the internal regions of the jet that emits the prompt photons and is responsible of the observed different spectral features. The main results of Pe'er (2015)'s review are: a) the clarification of the magnetic fields which determine the GRB spectra and their outflow; b) the comprehension of the process of particle acceleration to higher energies in magnetic reconnection layers as well as shock waves; c) the study of the dissipation of sub-photospheric energy broadening the Planck spectrum; and d) the geometric effects deriving from the aberration of the light.

Difficulties to match the fireball model with observations are found because it is not possible to distinguish among the radiation processes or between these two kinds of fireball (kinetic energy or pointing flux dominated). An additional problem is that a more precise estimate of the jet opening angles and of the jet structure is needed. Additionally, Willingale et al. (2007),

hereafter W07, pointed out some issues in describing the light curves within this model. Indeed, the observed afterglow phase appears in agreement with the model only for $\sim 50\%$ of GRBs. The discrepancy with the standard fireball model came out when Swift satellite was launched in 2004. For a brief summary of the current missions see Section 1.3. A rapid observation of the afterglow phases in several wavelengths was supplied by Swift with better coverage than earlier missions. Swift unveils a more complicated light curve trend (O’Brien et al., 2006; Sakamoto et al., 2007; Zhang et al., 2007b) compared to the previous studies. Nousek et al. (2006) showed that GRBs often follow “canonical” light curves which consists of several segments. The second segment, in the case it is flat, is named plateau phase and can be described as generated from the accretion onto a BH (Cannizzo and Gehrels, 2009; Cannizzo et al., 2011; Kumar et al., 2008), the evolution of a top-heavy jet (Duffell and MacFadyen, 2015), and the delayed injection of rotational energy ($\dot{E}_{rot} \sim 10^{50} - 10^{51}$ erg s $^{-1}$) from a fast rotating magnetar (Usov, 1992; Zhang and Mészáros, 2001; Dall’Osso et al., 2011; Metzger et al., 2011; Rowlinson and O’Brien, 2012; Rowlinson et al., 2014; Rea et al., 2015). Indeed, a new magnetar can be produced through the explosion of a massive star or from the coalescence of two NSs. In Chapter 2 these models are described.

In this framework the analysis of correlations amongst several physical quantities of the prompt and plateau phases is relevant to discriminate among the models presented in the literature. The correction for selection biases of the phenomenological correlations can broad the knowledge of the mechanism responsible for such emissions. The first observation of gravitational waves (GWs), GW150914, was carried out by the Laser Interferometer Gravitational Wave Observatory (LIGO) (Abbott et al., 2016a). It was allegedly produced by the merge of two BHs with masses (in units of solar masses) $36_{-4}^{+5} M_\odot$ and $29_{-4}^{+4} M_\odot$, and represents an extremely relevant discovery. It became even more important due to the analysis by Connaughton et al. (2016) who announced a weak transient emission lasting 1 s and observed by Fermi/GBM (Narayana Bhat et al., 2016) almost in coincidence with the GW150914, named GW150914-GBM. The false alarm probability of this event is 0.0022. Although the directions of this GW and GRB events are compatible, their association is still tentative due to the large errors in their estimated position. In addition, SGRBs seem to be produced by NS–NS or NS–BH mergers, thus this connection is surprising. Besides, any signals of a compatible GRB were discovered neither by INTEGRAL (Savchenko et al., 2016), nor by Swift (Evans et al., 2016). Nevertheless, this discovery has already produced several scenarios to describe how a BH–BH merger can become a GRB: Li et al. (2016) proposed that in a dense medium (see also Loeb 2016) GRBs are created by a BH via accretion of a mass $\simeq 10^{-5} M_\odot$, or, as described by Perna et al. (2016), an SN explosion of a two-high mass, low metallicity stars and the matter emitted can produce an accretion disk and following an SGRB. The observation of an afterglow phase visible months after the GW (Morsony et al., 2016) could help to understand better the connection between GWs and SGRBs. The confirmation of the event was given by the discovery of an X-ray counterpart for the GW170817 (Troja et al., 2017). The X-ray and radio observations suggested an

SGRB viewed off-axis.

1.1 The phenomenology of the GRBs

Despite the fact that a very large variety of GRBs with different features are observed nowadays, the theoretical efforts of the existing models in the literature is devoted to identify common properties of a canonical GRB.

The first GRB peculiarity is their enormous observed fluence (energy flow per unit area), between 10^{-7} and 10^{-5} erg/cm². Usually, the prompt high-energy emission, the main event, is observed in the gamma-rays lasting from fraction of seconds to tens of seconds followed by its counterpart, a long lasting multi-wavelength emission called the afterglow phase. The gamma-ray duration ranges from 10^{-3} to 10^3 s.

The GRB light curve components are visually introduced to make acquainted the reader. In Figure 1.1.1, the light curve of GRB 080430 observed by Swift is shown as a representative example displaying the prompt and the afterglow phases.

Another important feature of GRB light curves is the variability, V , defined in Section 3.2. Recent results about variability are discussed in Golkhou et al. (2014, 2015). In the first paper, the authors constrained the lowest variability timescales of 938 GRBs observed until July 2012, using the Fermi/Gamma Ray Burst Monitor (GBM). It has been shown that the variability timescale in the soft band (or hard X-rays observed by Swift) is two to three times longer than the hardest bands. Taking into account the upper limits and the detections, it has been discovered that less than 10% of the GRBs presented variability timescale less than 2 ms. These particular timescales need the Lorentz factor of the emitting source, Γ , to be ≥ 400 as well as typical emission radii with $R \equiv 10^{14}$ cm for LGRBs and $R \equiv 3 \times 10^{13}$ cm for SGRBs. Golkhou et al. (2015) established the minimum variability timescale that characterizes the light curves of GRBs using Haar wavelets. The employed approach takes the average of GRB data, determining a cumulative measure regarding signal variation whilst maintaining the sensitivity for narrow pulses present in complex time series. The technique is applied to study a huge sample of the GRB light curves observed by Swift. Given the large number of GRBs with known redshift it has been defined a new quantity called the minimum rest-frame variability timescale. They discovered a minimum timescale for LGRBs of 0.5 s, whilst the briefest timescale discovered, implying a compact central engine, is of 10 ms. Further implications on the GRB fireball model are presented together with a correlation between the redshift and minimum timescale that may be partly caused by the redshift evolution.

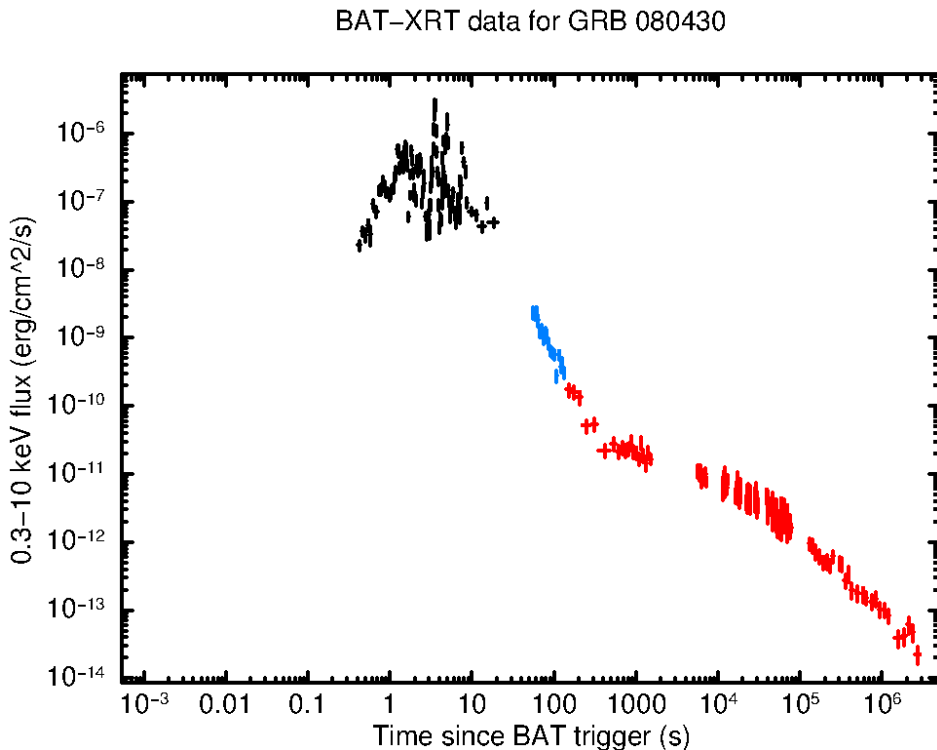


Figure 1.1.1: An example of a GRB light curve: GRB 080430 (from http://www.swift.ac.uk/burst_analyser).

1.1.1 The prompt emission

The prompt emission is the phase in which the gamma-ray instrument detects a signal above the background in a statistical meaningful way (Piran, 2004). Usually, a lower-energy emission (X-ray, optical) occurs simultaneously with the gamma-ray one. Sometimes such X-ray signal results to be more intense than the gamma-ray one: bursts in which this situation occurs are called X-ray Flashes (XRF, Heise et al., 2001), as explained in Section 1.1.5.

The main feature of the prompt emission light curve is the great variety of temporal profiles shown in Figure 1.1.2. Indeed, it is possible to find very simple light curves with a FRED (Fast Rise Exponential Decay) structure or very complex multi-peaked structures on timescales up to $\delta t_a \approx 10$ ms, where δt_a is an observed single pulse width (Piran, 2004).

If one looks at the most complex light curves, they seem to be composed of individual pulses, which are the fundamental elements of the light curve (Piran, 2004). Each pulse is characterized by: **a**) a FRED structure (Norris et al., 1996b), always present also in the simple profiles, **b**) a spectral trend where the peak energy declines as a function of the photon fluence in an exponential way (Norris et al., 1996b), **c**) a low-energy emission delayed compared to the high-energy one (Norris et al., 1996b).

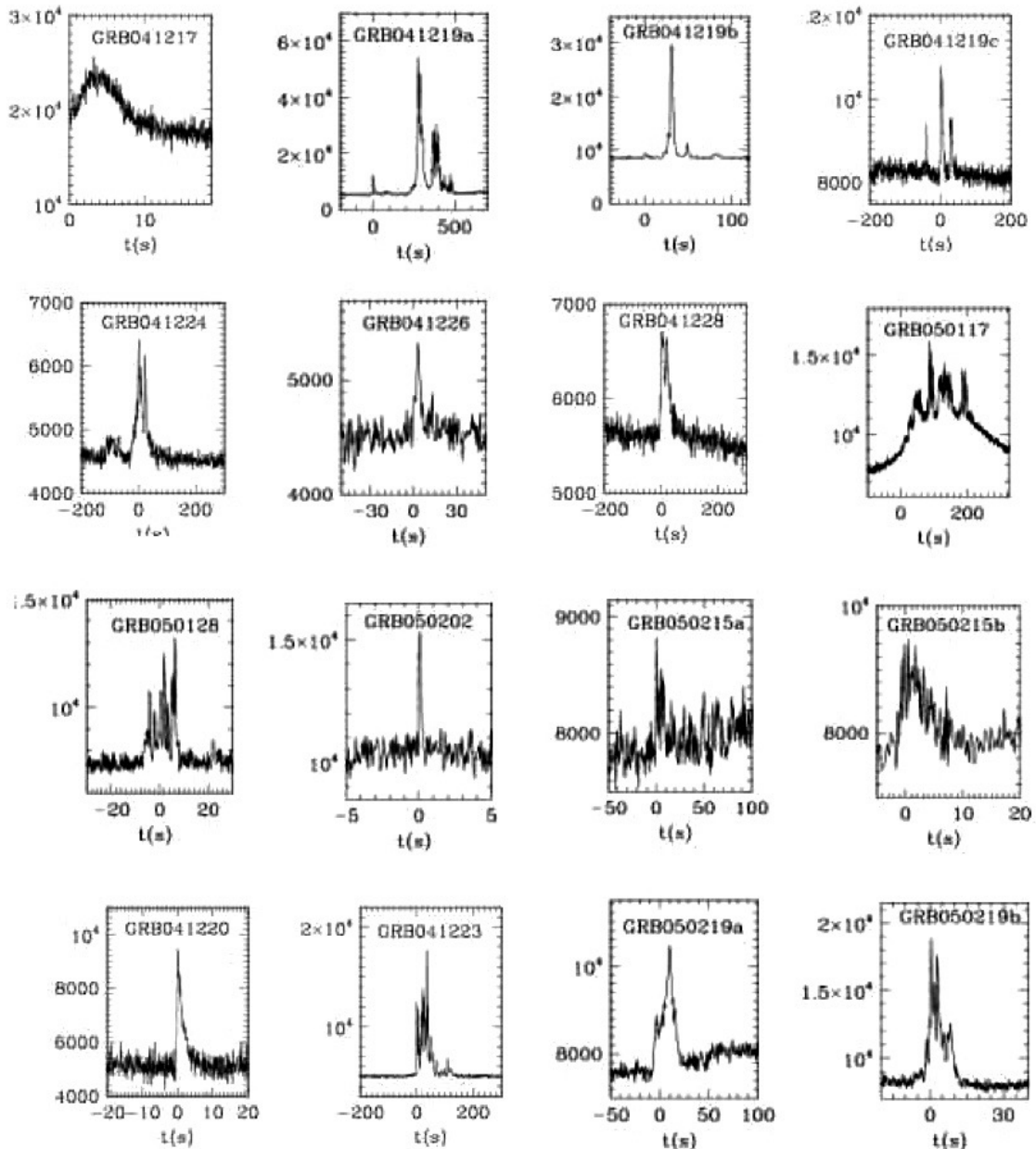


Figure 1.1.2: Samples of prompt emission light curves observed by Swift. (Figure taken from the Swift repository.)

1.1.2 The afterglow emission

After the prompt emission occurrence, the afterglow multi-wavelength emission starts. The overall energy emitted in this stage is generally a few percent of the GRB total energy. The X-ray afterglow phase usually starts from hundreds of seconds to several hours after the prompt emission. In this region the X-ray afterglow fluxes show a phenomenological relation both with the frequency ν and the observed time t (Piro et al., 2000): $f_\nu(t) \propto \nu^{-\beta} t^{-\alpha}$, with $\alpha \sim 1.4$ and $\beta \sim 0.9$.

Together with this X-ray emission, the afterglow phase may also be observed in optical and IR bands. Around one day after the burst, the brightness of the optical afterglow phase is about 19–20 mag. In the beginning, the light curve declines as a power-law, $t^{-\alpha}$ with $\alpha \approx 1.2$, but with large variations around this number. The optical afterglow phases show a behaviour similar to the X-ray one only in some cases, as shown by Nardini et al. (2006).

Many afterglow light curves at later times show a change in the power-law index to a steeper decline with $\alpha \approx 2$. Such a break in the afterglow phase usually is chromatic (dependent on the frequency), but in few cases it has been observed in different energy bands. A classic example of such a situation was seen in GRB 990510. Usually, the break is fitted with a phenomenological formula: $F_\nu(t) = f_*(t/t_*)^{-\alpha_1} \{1 - \exp[-(t/t_*)^{(\alpha_1-\alpha_2)}]\}(t/t_*)^{(\alpha_1-\alpha_2)}$ (Piran, 2004). This break is known as jet break and the time at which such break appears can be applied to calculate the jet opening angle (Rhoads, 1997) or the observing angle of the standard jet model.

With the launch of Swift a new era started for the study of GRBs. Swift's primary goal is not only to detect a large number of GRBs so that a statistical meaningful sample can be achieved, but also to retrieve data in the bands between 0.3 – 10 keV and between 1700 and 6500 Å after the initial few tens of seconds after the trigger. The result is that the afterglow light curve shows a more complex behaviour than the simple power-law decay observed in the pre-Swift era. The up-to-date Swift light curves in X-ray range can be divided in two morphological types (Chincarini et al., 2007): one starting with a very steep light curve decay and the other showing a flat decline. The first class is preferred from the majority of GRBs, displaying a “canonical” behaviour (Nousek et al., 2006; O'Brien et al., 2006; Sakamoto et al., 2007): after the initial steep decay ($F \propto t^{-\alpha_1}$, with $3 \leq \alpha_1 \leq 5$) the light curve presents a flat decaying phase ($F \propto t^{-\alpha_2}$, with $0.5 \leq \alpha_2 \leq 1$) followed by a steeper decay ($F \propto t^{-\alpha_3}$, with $1 \leq \alpha_3 \leq 1.5$), consistent with those seen in previous missions and, in some cases, overlaid X-ray flares. The spectrum, except in few cases, remains constant throughout all these stages of the afterglow phase in the sample used by Nousek et al. (2006). However, spectral evolution of the afterglow is presented later (Evans et al., 2009) when more data became to be a statistical significant sample. It is noteworthy that the final break has been seen only in less than $\sim 10\%$ of the afterglow phases followed by Swift. Even if the last part of the GRB prompt emission seems to be represented by the steep α_1 segment, shown in the canonical behaviour, Liang and Zhang (2005) and Sakamoto et al. (2007) stated that the

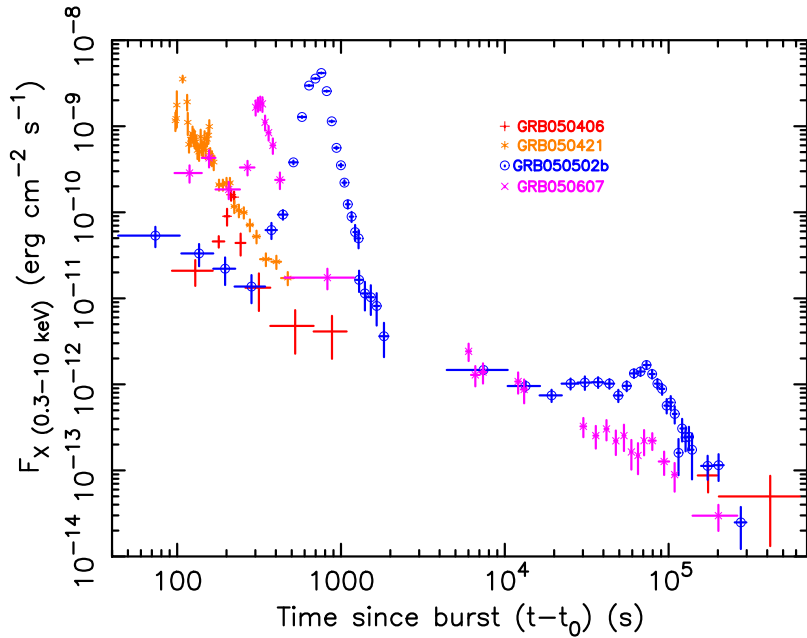


Figure 1.1.3: Examples of GRB afterglow light curves with X-ray flares. (Figure from Nousek et al. (2006). © AAS. Reproduced with permission.)

origin of the transition phase from a shallow α_2 to a steeper α_3 needs further analysis to be fully explained.

In the Swift XRT light curves flares are present (Nousek et al., 2006, see Fig. 1.1.3). In some of them the flux varies on timescales $\delta t_a \ll T_{X,a}$ with a very steep rise and decay. In the case the flare is luminous enough, its spectral index is not in agreement with the power-law behaviour exhibited from the X-ray light curve without the flares.

1.1.3 The broadband spectrum

An important physical characteristic of the GRB phenomenology is the emission energy spectrum (see Fig. 1.1.4). Usually, LGRBs have spectral peak energy around 150 keV, a low energy spectral slope around -1 and a high energy slope around -2 (Band et al., 1993). Instead, SGRBs often have a greater spectral energy peak and a low energy spectral slope around -0.5 . Originally, the GRB spectra had been fitted employing the Band function (Band et al., 1993):

$$N_E(E) = A_{\text{norm}} \times \begin{cases} \left(\frac{E}{100 \text{ keV}}\right)^\alpha \exp\left(-\frac{E}{E_0}\right), & E \leq (\alpha - \beta)E_0 \\ \left[\frac{(\alpha - \beta)E_0}{100 \text{ keV}}\right]^{\alpha - \beta} \left(\frac{E}{100 \text{ keV}}\right)^\beta \exp(\alpha - \beta), & E \geq (\alpha - \beta)E_0 \end{cases} \quad (1.1)$$

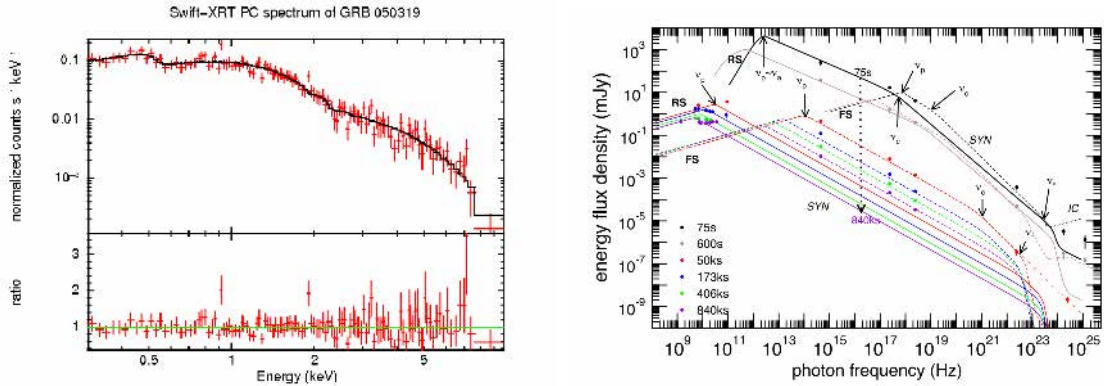


Figure 1.1.4: Left panel: an example of a spectrum of GRB 050319 taken from the Swift XRT repository. Right panel: a model of broadband GRB spectra. Solid lines are for the reverse shock (RS) emission while dashed ones for the forward shock (FS). Data points are provided for different times: 75 s (black), 600 s (pink), 50000 s (red), 173000 s (blue), 406000 s (green), 840000 s (purple). (Figure from Panaiteescu et al. (2013).)

where A_{norm} is the normalization, α and β are the low- and high-energy exponents of the Band function, respectively, E_0 is the spectral break energy, and $N_E(E)$ is the photon flux density computed in photons cm⁻² s⁻¹ keV⁻¹. Nowadays, additional components need to be considered in spectral modelling to describe the thermal radiation from the photosphere: a high energy power-law or exponentially attenuated power-law component (González et al., 2003) and a blackbody or photospheric component (Ryde et al., 2006).

1.1.4 The observational classification: long, short, the intermediate class and the ultra-long GRBs

This section describes more in detail the problem of GRB classification mentioned in the beginning of Chapter 1. LGRBs and SGRBs appear to have very different observational properties beyond the difference in the duration (see Fig. 1.1.5). It was concluded that SGRBs have a harder spectrum than LGRBs, and this enforced the idea that SGRBs were different entity, instead of being, for example, single peaks of LGRBs hidden by noise. From the analysis of the unimodal duration distributions (Horváth, 1998, 2002; Horváth et al., 2008; Horváth, 2009; Huja et al., 2009; Řípa et al., 2009) and the higher dimensional parameter spaces (Mukherjee et al., 1998; Horváth et al., 2006; Řípa et al., 2009; Horváth et al., 2010; Veres et al., 2010; Koen and Bere, 2012) an intermediate class (IC) of GRBs was introduced. This class was later further investigated (Norris and Bonnell, 2006; Levan et al., 2007; Norris et al., 2010). The observed afterglow phases of this intermediate class are characterized by a soft long bump following the prompt emission, and by a temporal evolution at late time analogous to the LGRBs, showing a “canonical” behaviour and, in several cases, the presence of X-ray flares (Barthelmy et al., 2005). These bursts are harder than LGRBs (Amati, 2006).

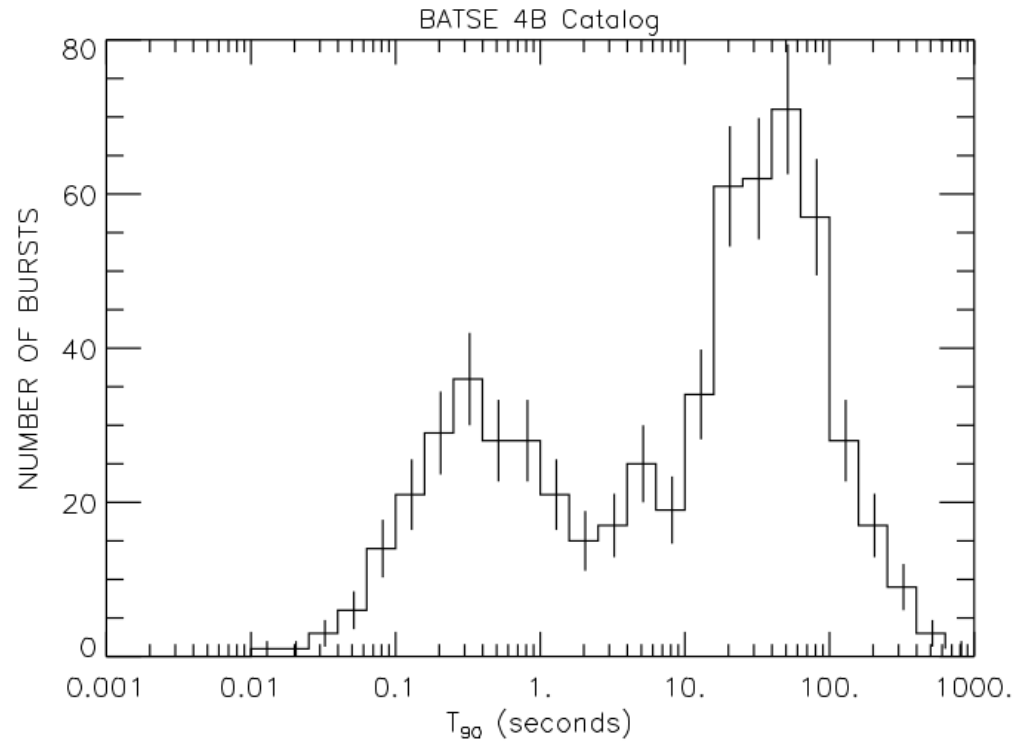


Figure 1.1.5: Histogram of the duration of 1234 GRBs observed by BATSE as shown in the BATSE 4B Catalogue.

Moreover, they appear to be also nearer than what was expected before. Infact, the average redshift is $z \sim 0.4$, much smaller than the average z of the LGRBs detected by Swift, $z \sim 2.3$ (Guetta, 2006) and, therefore, their luminosity is lower and their local rate is higher (Guetta, 2006; Barthelmy et al., 2005; Fox et al., 2005). All these recent observations support the idea that these bursts belong to a different population than the LGRBs (Fox et al., 2005). In particular, it has been supported by Barthelmy et al. (2005) that their association with non-star-forming host galaxies indicates that the collapse of massive star cannot generate these IC GRBs. On the other hand, the similarity of all their properties definitely indicates commonalities among the origins of SGRBs (Fox et al., 2005). Indeed, their origin seems to be consistent with the merging of a compact object binary (Fox et al., 2005), even if the NS–NS binary merger models predict energy injection times much shorter than, for example, the 200 s observed for GRB 050724 (Barthelmy et al., 2005). BH–NS mergers are more promising, but even these models cannot extend the emission beyond a few tens of seconds (Barthelmy et al., 2005). However, with the advent of the GW associated with a SGRB, the NS–NS scenario is confirmed. Virgili et al. (2013), Nakauchi et al. (2013), Stratta et al. (2013), and Levan et al. (2014) claimed that GRBs with $T_{90} > 10000$ s (ULGRBs) are statistically separated from the classic LGRBs, thus they could constitute an additional class.

In previous years, far star-forming galaxies seem to produce LGRBs. Later on, associations with core collapse SNe were pointed out, but not for each LGRB (Fynbo et al., 2006; Della Valle et al., 2006). This indicates the existence of different type of progenitors for LGRBs. The metallicity Z is another characteristic worth considering to study the progenitor system. Woosley and Bloom (2006b) concluded that, in the collapsar model, LGRBs come from massive stars with Z/Z_\odot lower than $\simeq 0.1 - 0.3$. Metal-rich systems are the suitable environment for many GRBs (Perley et al., 2016). Greiner et al. (2015) found that other models than the collapsar one are able to produce LGRBs and they are relevant for GRB studies.

1.1.5 The hardness ratio: GRB, X-ray Rich and X-ray flashes

The hardness ratio is given by the ratio of the flux of the third BATSE channel to the flux of the second BATSE channel (100–300 keV and 50–100 keV respectively, see Figure 1.1.6). Recently, a new phenomenon very similar to GRBs, called X-ray flashes (XRFs), were investigated (Barraud et al., 2003). The only difference with GRBs is that XRF flux has its peak in the X-ray range, and it was firmly indicated that these two phenomena are connected. Strohmayer et al. (1998) pointed out 22 bursts detected by Ginga. Among the bursts detected by Ginga, the spectra of just 36 was found very soft, with duration and spectral form similar to LGRBs, but with lower observed peak energy than BATSE bursts (Kaneko et al., 2007; Sakamoto et al., 2005). Among Wide Field Cameras (WFCs) sources, a group of fast X-ray transients which last less than 10^3 s and not observed by the GBM

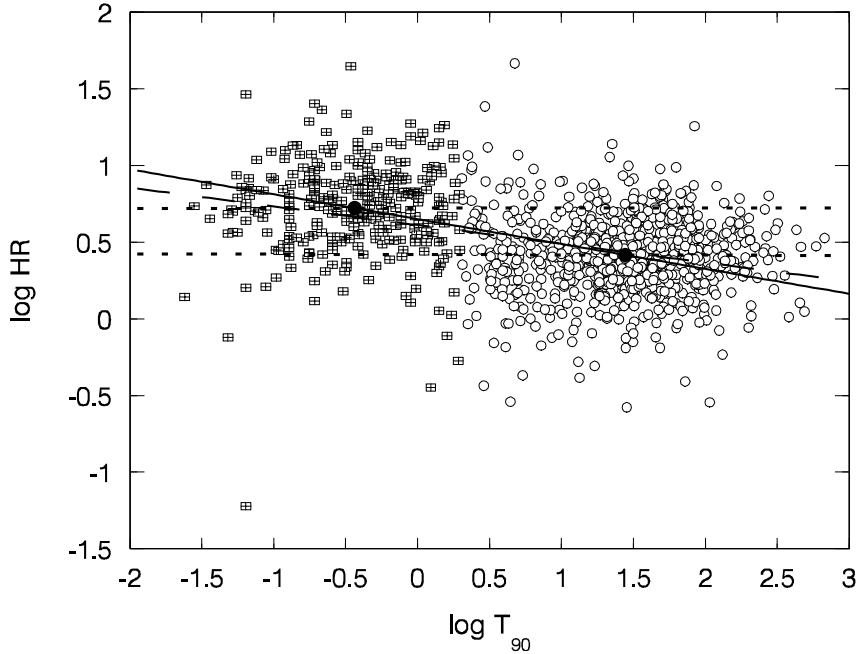


Figure 1.1.6: The hardness-duration correlation for BATSE GRBs. SGRBs (squares) seem to be harder than the LGRBs (circles). The ratio of the flux of the 3rd BATSE channel to the flux of the 2nd BATSE channel (100–300 keV and 50–100 keV, respectively) is called hardness. (Figure from Qin et al. (2000). Copyright @ 2000 Oxford University Press-Journals.)

was pointed out.

From the analysis of LGRBs and XRFs, it was noted that the spectral properties of X-ray afterglow phases for these two classes are compatible, but the temporal features are dissimilar. LGRB afterglow phases present a break at earlier times and with steeper indices than XRF ones; in addition, the XRF afterglow luminosity is lower than that of LGRBs. To conclude, XRFs emit X-ray energy with spatial distribution, spectral and temporal features comparable to LGRBs (Heise et al., 2001; Kippen et al., 2001). The feature discriminating XRFs from GRBs is the prompt emission spectrum, which for XRFs peaks at energies one order of magnitude smaller than the energies for LGRBs. Besides, XRFs have higher fluence between 2 and 30 keV in comparison to the one in the gamma-ray band (30 – 400 keV).

In addition, it was found that the progenitor for these two phenomena may not be the same (Zhang et al., 2004; Stratta et al., 2007; Ruffini et al., 2016). For example, Zhang et al. (2004) claimed that, even if a common jet model is suggested for both these phenomena, this model does not explain breaks in the light curves and the energy of the progenitor. In fact, in this scenario, GRBs require jets with opening angles smaller than 1°, while XRFs are isotropic emissions. Stratta et al. (2007) analysed the spectrum of XRF 040912 founding that it can be classified as a regular soft GRB (with a spectral peak energy smaller than

40 keV). Comparing this XRF with other ones in the literature, they found that most of these XRFs are soft GRBs. Nevertheless, few of them, like XRF 060218 and XRF 020903, showed spectral characteristics different from the other ones. This result indicates a probably separated progenitor type for these phenomena. Later, from their classification, Ruffini et al. (2016) found out that in the case of long bursts, XRFs appear when there is no BH creation. These XRFs have isotropic energy smaller than 10^{52} erg and spectral peak energy in the rest frame tinier than 200 keV. Instead, if a BH is created, these phenomena belong to another class of events with isotropic energy greater than 10^{52} erg and spectral peak energy in the rest frame larger than 200 keV.

The current distinction presented here is helpful for the study of GRB correlations also because they can be modified by employing several GRBs classes (Amati, 2006; Dainotti et al., 2010). Between XRFs and GRBs there is an additional class called X-ray Rich (XRR) characterized by very dim gamma to X-ray fluence in comparison with that of GRBs (D'Alessio and Piro, 2005).

1.2 The phenomenological Willingale model

After the description of the properties of the prompt and afterglow phases, this section describes a phenomenological model introduced by W07 to well characterize the plateau emission.

1.2.1 The functional form of the X-rays decays

W07 studied several X-ray Swift light curves and claimed that they can be fitted with one or two parts described by an exponential decay plus a power-law decaying phase. The first part represents the prompt phase, while the second the afterglow phase. The functional form for both the parts is given:

$$f_i(t) = \begin{cases} F_i e^{\alpha_i(1 - \frac{t}{T_i})} e^{-\frac{t_i}{t}}, & t < T_i, \\ F_i (\frac{t}{T_i})^{-\alpha_i} e^{-\frac{t_i}{t}}, & t \geq T_i. \end{cases} \quad (1.2)$$

where $i = p, a$ where p and a denote the prompt and afterglow phases, respectively. (T_i, F_i) is the point where the exponential phase changes into the power-law decaying phase. α_i defines the temporal decay index of the power-law, while t_i indicates when, in each component, the rise phase starts. The two component model is shown in Figure 1.2.1. W07 fitted the light curves of 107 GRBs (see Fig. 1.2.2) assuming the form $f(t) = f_p(t) + f_a(t)$.

The prompt phase, mostly observed by BAT, takes place at $t < T_{X,p}$ (see Section 3.2 for the definition), while the plateau phase, observed by XRT, at $t < T_{X,a}$. Besides, the growing

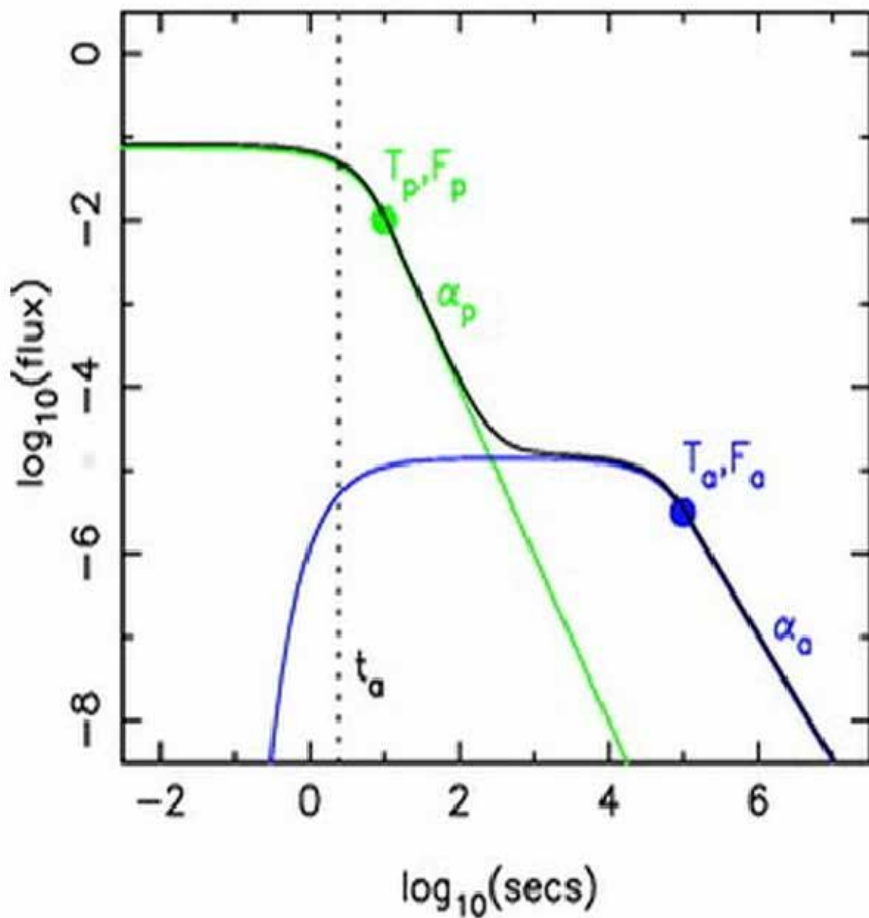


Figure 1.2.1: From W07: the functional form of the X-ray decay. The prompt component (green) has $t_p = 0$. The afterglow component (blue) begins at time t_a . $\log(\text{flux})$ represents the quantity $f_i(t)$ from the Equation 1.2 for the prompt and afterglow components, and $\log(\text{secs})$ indicates the time.

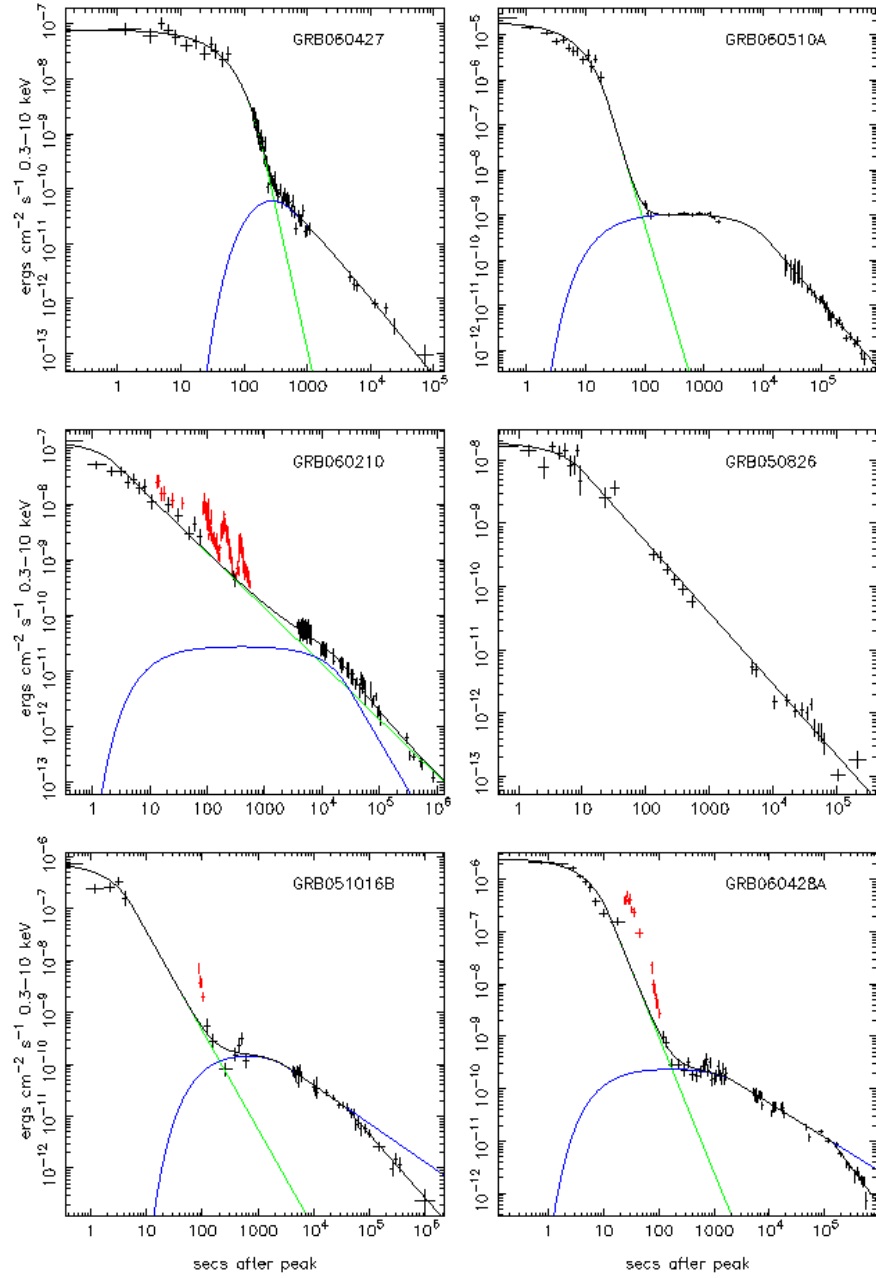


Figure 1.2.2: From W07: several fits to X-ray decay curves. Both prompt and afterglow phases are represented similarly to Figure 1.2.1. Top panels: here it is shown an example of when the afterglow component is dominant at late times. Middle panel left: here it is shown an example of when the afterglow phase displays a bump in the decline, but the prompt phase decay is dominant at late times. Middle panel right: a single power-law fit showing no afterglow phase. Bottom panels: two fits which include a late temporal break. Flares are represented in red colour and were excluded from the fitting.

part of the afterglow phase is not visible because the prompt phase in the beginning is always dominating. Even if bright flares are responsible for only $\sim 10\%$ of the total fluence, they were removed from the W07 fitting procedure.

From the above analysis, W07 derived the distribution of $T_{X,a}$ versus $T_{X,p}$ for those objects with two component fits, pointing out no correlation between these two parameters. Studying the prompt and afterglow fluences, it was retrieved that high prompt fluence implies high afterglow fluence, with large scatter though.

In conclusion, applying the model by W07, the X-ray light curve can be well reproduced and many of the correlations among afterglow parameters are based on this phenomenological model.

1.3 The past and current missions observing GRBs

GRBs were detected by Vela satellites composed of X-ray (working in the 3 – 12 keV energy range) and gamma-ray (in the 150–750 keV range) detectors. Through the investigation of the different arrival times of the GRB emission to each satellite the terrestrial origin of these phenomena was ruled out. At the beginning of the Compton Gamma Ray Observatory mission (CGRO, Meegan et al. 1992) in 1991, a systematic observation of GRBs could begin. The CGRO mission was constituted of four instruments (The Burst and Transient Source Experiment (BATSE), The Oriented Scintillation Spectrometer Experiment, The Compton Telescope and the Energetic Gamma Ray Experiment Telescope) and worked in the range between 30 keV and 30 GeV. With BATSE, it was discovered that GRBs have no preferential direction in the sky (Meegan et al., 1992; Efron and Petrosian, 1995; Tegmark et al., 1996)¹. This space mission was running until the beginning of 2000 and it was one of the most decisive space missions at the time, providing the first survey of the whole sky above 100 MeV, an extensive survey of the Galactic Centre of the Milky Way, and the discovery of the first soft gamma ray repeaters (Bassani et al., 1995). In particular, the CGRO mission followed in detail GRB 990123, one of the most luminous GRBs at that time. From its analysis it was confirmed that GRBs are highly collimated jet phenomena.

Figure 1.3.1 displays the fluence of the GRBs detected by BATSE. The purple points mark the lowest fluence values ($\sim 10^{-7}$ erg cm $^{-2}$), while the red dots denote the highest fluence values reaching $\sim 10^{-4}$ erg cm $^{-2}$.

Later, in 1996, an Italian-Dutch space mission BeppoSAX (Boella et al., 1997) was launched to explore GRBs. In six years of operation, the precision of its observations in the energy range between 0.1 and 300 keV confirmed the extra-galactic origin of GRBs (Costa et al., 1997). BeppoSAX was composed of four X-ray telescopes with two spectrometers (Low Energy Concentrator Spectrometer and Medium Energy Concentrator Spectrometer), the

¹For the most recent works on this topic, see Tarnopolski (2017) and Řípa and Shafieloo (2017).

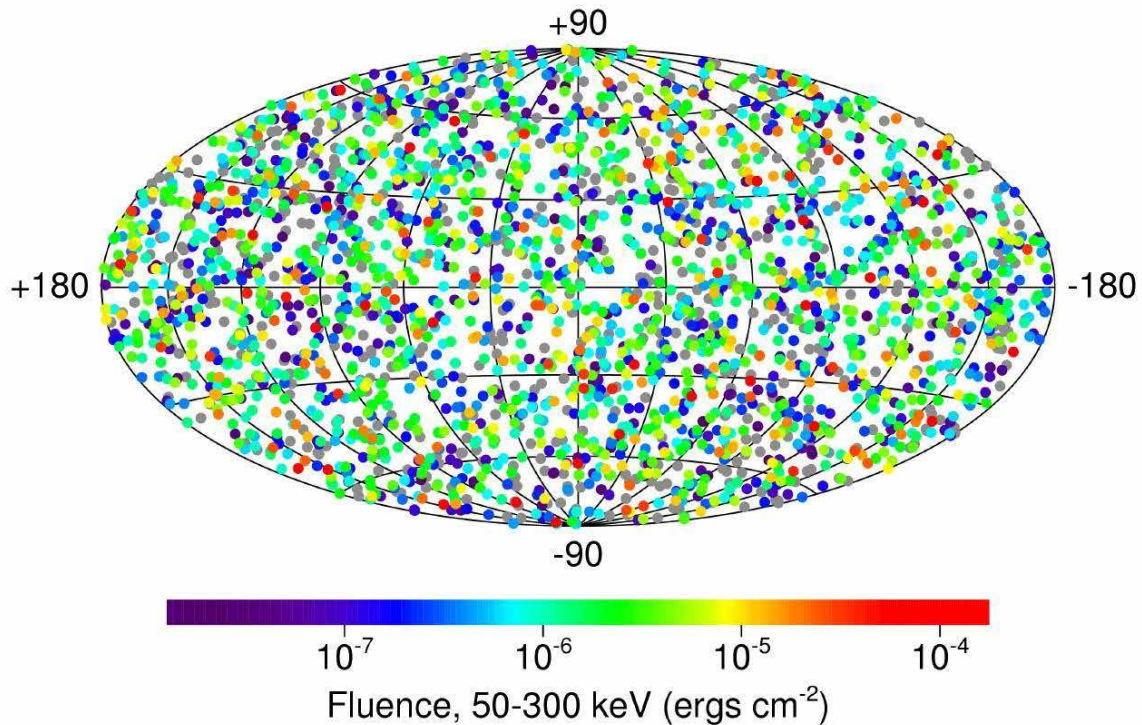


Figure 1.3.1: The distribution of the GRBs detected by BATSE (from <http://www.swift.ac.uk/about/grb.php>). The coloured bar denotes the GRB fluence scale.

High Pressure Gas Scintillator Proportional Counter, the Phoswich Detection System, and the Wide Field Camera. As shown in Sections 1.1.1 and 1.1.2, GRB light curves are composed of the prompt phase followed by a decaying afterglow phase. For the first time in February 1997 the BeppoSAX satellite detected the afterglow phase as a fading X-ray emission related to the GRB 970228 (Costa et al., 1997). It was followed, 20 hours after the GRB, by the optical counterpart detected by the William Herschel Telescope² (Groot et al., 1997).

In 1999 the Chandra X-ray observatory³ was launched and it is still operating. It carries the following instruments: the AXAF Charged Coupled Imaging Spectrometer, the High Resolution Camera, the High Energy Transmission Grating, and the Low Energy Transmission Grating, all working between 0.1 and 10 keV X-ray energy range. With its high resolution, large collecting area, and sensitivity to hard X-ray energy band, Chandra is useful for the analysis of the GRB spectral emission lines (Sako et al., 2005), for the investigation of the nature of GRB host galaxies (Fruchter, 2000) and their star formation regions (Watson et al., 2004). In particular, with the observation of GRB 991216, spectral X-ray emission lines were connected for the first time with a GRB (Piro et al., 2000). This finding is important

²<http://www.ing.iac.es/Astronomy/telescopes/wht/>

³<http://chandra.harvard.edu/about/specs.html>

because it allowed for the first time to estimate the nature of the GRB progenitor in more detail.

Also in 1999, the XMM-Newton space mission⁴ was launched (Jansen et al., 2001) and it is still obtaining important results about X-ray sources, carrying out narrow and broad range spectroscopy, and providing the X-ray and optical (0.1–15 keV and 180–650 nm, respectively) imaging for each object. The main instruments of this mission are: the European Photon Imaging Camera Metal-Oxide-Silicon, the European Photon Imaging Camera-PN, the Reflection Grating Spectrometer, and the Optical Monitor. In particular, it observed GRB 001025A for investigating the so-called dark bursts. These bursts are optically subluminous GRBs with optical-to-X-ray spectral index, $\beta_{OX,a}$, less than 0.5 (Jakobsson et al., 2004). Furthermore, XMM Newton observed GRB 011211 and GRB 030227 for studying the X-ray emission lines (Reeves et al., 2002; Watson et al., 2003), and GRB 030329 for investigating the late afterglow phase (Tiengo et al., 2003).

In 2000, the High Energy Transient Explorer 2 (HETE-2) was launched⁵ (Shirasaki et al., 2003) after the failed launch in 1996 of the first High Energy Transient Explorer. Until the end of the mission in 2008, its main goal was the multi-wavelength investigation of GRBs and the precise detection of their positions with \sim 10 arcseconds accuracy. The mission included two X-ray detectors (Soft X-ray Camera, SXC, and Wide-Field X-ray Monitor, WXM) working in the range 0.5–14 keV and 2–25 keV, respectively, and four gamma-ray detectors (FREGATE) operating in the 6–400 keV energy band. In particular, this mission detected GRB 030329, a reliable proof for the GRBs-SNe connection, and GRB 050709, the first SGRB with an observed optical counterpart. Then, due to the observations of HETE-2, it was found out that some dark GRBs fade in the optical energy band very rapidly, while others are dimmer, but still detectable with large telescopes. In addition, HETE-2 discovered the existence of XRFs (for details see Section 1.1.5), and achieved an arcminute-precise position of GRBs within tens of seconds since the beginning of a GRB.

In 2002, the INTEGRAL space mission was launched (Teegarden and Sturner, 1999) and nowadays it is still operative. Its main result is a sky map in the soft X-ray range (15 keV–10 MeV). INTEGRAL is composed of an imager (IBIS), a spectrometer (SPI), together with X-ray (JEM-X, 3–35 keV) and optical (OMC, 500–850 nm) detectors to provide simultaneous observations in these energy bands. In particular, the INTEGRAL mission investigated GRB 031203, one of the few GRBs connected to SNe at that time, and GRB 041219A, one of the longest and brightest GRBs ever observed at that time (Gotz, 2013).

A major important space mission for investigating GRBs is the Swift satellite (Gehrels et al., 2004), still operating since 2004. It is composed of three instruments: the Burst

⁴<http://sci.esa.int/xmm-newton/>

⁵<http://space.mit.edu/HETE/spacecraft.html>

Alert Telescope, (BAT, 15–150 keV), the X-ray Telescope, (XRT, 0.3–10 keV) and the Ultraviolet/Optical Telescope (UVOT, 170–650 nm). As a result, the Swift space mission detected the furthest GRBs (GRB 090423 at $z = 8.26$ and GRB 090429B at $z = 9.2$) and one of the brightest GRBs ever observed (GRB 130427A, $z = 0.34$ and one-second peak photon flux measured by BAT equal to $331 \text{ ph/cm}^2/\text{s}$). The analysis of the GRB light curves detected by Swift pointed out the complex and often different behaviour of these phenomena (Nousek et al., 2006).

In 2007, the AGILE (Astro-Rivelatore Gamma a Immagini Leggero) mission was launched (Longo et al., 2007) with the main aim of studying the gamma-ray sources in the universe at high energies. In particular, it is investigating Active Galactic Nuclei (AGN), GRBs, X-ray and gamma galactic objects, and diffuse galactic and extra-galactic gamma-ray emissions. AGILE includes a Gamma Ray Imaging Detector (GRID) working from 30 MeV to 50 GeV, a SuperAGILE (SA) hard X-ray monitor operating in the energy range between 18–60 keV, a Mini-Calorimeter (MCAL) running in the interval 350 keV–100 MeV, and an Anti-Coincidence System (AC), consisting of a plastic scintillator, to support the removal of unwanted background events.

Another ongoing mission used for gamma-ray studies of GRBs is the Fermi gamma-ray space observatory launched in 2008 (Carson, 2007). Its aim is to observe the universe in the low and medium gamma-ray energy ranges and it is composed of two instruments: the Large Area Telescope (LAT) for obtaining an all-sky survey investigating the high energy emission between 20 MeV and 300 GeV, and the GBM for analysing GRBs in the energy band between 8 keV and 40 MeV. As a result, Fermi detected the strongest GRB at the time, GRB 080916C, (Abdo et al., 2009b). In parallel to the Swift mission, it detected the even more energetic GRB 130427A⁶ (Liu et al., 2013). GBM was able to localize the SGRB associated with GW170817.

One should also mention the NuSTAR X-ray mission launched in 2012 (Hailey et al., 2010). It works in the energy range between 3 and 79 keV and focuses especially on high energy X-ray spectroscopy of astrophysical sources. It mostly investigates the compact galactic objects radiating in X-ray band and non-thermal radiation in young SN remnants using the excellent technology of solid state cadmium zinc telluride pixel detectors. Actually, NuSTAR observed just a few GRBs with data in other energy ranges also available from other telescopes, like GRB 130427A and GRB 130925A. The wide-range data samples available for these GRBs allowed for their broadband spectral analysis.

Finally, the Indian Astrosat satellite⁷, launched in 2015 (Agrawal, 2005), is one of the most recent space missions capable of multi-wavelength observations. It is composed of The Ultra

⁶<https://www.nasa.gov/topics/universe/features/shocking-burst.html>

⁷<http://astrosat.iucaa.in/>

Violet Imaging Telescope (UVIT), The Soft X-ray imaging Telescope (SXT), The LAXPC Instrument, The Cadmium Zinc Telluride Imager (CZTI), The Scanning Sky Monitor (SSM), and The Charged Particle Monitor (CPM). These instruments cover the emission range from the far ultraviolet (130–180 nm) to the hard X-ray (10–150 keV) energy bands. Even if CZTI is a spectroscopic device, it is employed as a wide angle GRB monitor and it allows for spectro-polarimetric analysis of GRBs in the 100–300 keV band. The study of the polarization of the brightest 11 GRBs observed by CZTI during its first year exhibited the importance of this satellite for the investigation of GRBs.

All the telescopes mentioned above are space missions, but there are also some ground based telescopes important for the study of GRBs. The main ground based telescopes are: the radio telescope Very Large Array (VLA) (Napier et al., 1983), the Gamma Ray Burst Optical/Near-Infrared Detector (GROND) (Greiner et al., 2008) and the optical/infrared telescope Very Large Telescope (VLT) (Dekker et al., 2000).

VLA became operational in 1980, it is composed of 27 independent antennae working in the frequency range 74 MHz – 50 GHz with an angular resolution between 0.04 and 0.2 arcseconds. Its main goal is to investigate galaxies, stars, quasars, pulsars, and GRBs. However, radio observations of GRBs from VLA are mostly used to support optical and X-ray observations from other telescopes.

GROND started its work in 2007 in the optical and near infrared energy bands. It is a detector linked to the MPG/ESO telescope at La Silla Observatory. As its main results, it detected and set the distance to one of the most distant GRBs (GRB 080913, $z = 6.695$), and then it detected GRB 080916C pointing out that this was the most energetic GRB at that time.

VLT observes in the visible and infrared wavelengths and is composed of four independent telescopes (Antu, Kueyen, Melipal, Yepun). It is made of large-field imagers, adaptive optics corrected cameras and spectrographs, high-resolution and multi-object spectrographs, and works in the energy ranges from deep ultraviolet to mid-infrared. It has an angular resolution of 0.001 arcseconds when the four telescopes are working together. As a main result, together with the GROND telescope, VLT enabled to analyse the afterglow phase of the furthest GRB at that time (GRB 080913).

1.4 The SNe historical background

The Novae and SNe have been observed for thousands of years, but their systematic study began in 1885, when Hartwig observed a “Nova” in the center of the Andromeda galaxy. This object had been visible for 18 months. After 4 years it was clear that the object discovered by Hartwig was 1000 times more luminous than a typical Nova. Another similar event was observed in 1895, but we have to wait until 1934 to have a clear distinction between Novae and SNe. From that moment thanks to Zwicky in 22 years 54 SNe were discovered. In 1939

it was evident an apparent uniformity in the intrinsic brightness at the maximum luminosity and after 15 days from the maximum. This circumstance brought to suggest that SNe could be used as distance indicators. But even at that time, the question of the uniformity and homogeneity in the properties presented difficulties, because in 1940 SN 1940c was observed, an event with spectral properties very different from the other SNe already observed. So another distinction was necessary and SNe were classified in type I if they were resembling SN 1937c or type II if they were similar to SN 1940c.

1.4.1 Classification of the SNe

At the beginning of the 1940s' R. Minkowski noted the presence of two main classes of SNe, characterized by the presence or the lack in the spectrum of hydrogen. If these lines were observed, the SNe were called of type I, otherwise SNe of type II. SNe I are observed in every type of galaxies and are referred to as stars of population II, namely old with small values of the mass. This simple classification has been unchanged until the middle of 1980 when it was clear that SNe type I were divided in other two different types, called Ia e Ib (Baade and Zwicky, 1934). Nowadays the classification is based on the properties of the observed spectrum. SNe I lack the hydrogen Balmer series at the maximum luminosity, while SNe II present these lines. SNe type I are further classified in SNe Ia, SNe Ib, SNe Ic if they have lines of silicon ionized (SiII at 615.0 nm), helium lines not ionized (HeI at 587.6 nm) or if they have neither of both features, respectively. SNe type II are classified, instead, in SNe IIP or SNe IIL if the light curve presents a plateau phase or a linear decreasing trend, respectively. This class of SNe presents lines broadened by the high velocity of the ejecta. There are also sometimes SNe with very narrow lines, indicated with SNe IIn where n means narrow. SNe Ia are produced by thermonuclear explosion of white dwarf with prevalence of Si or by accretion in the binary system with a companion star more massive. From a photometric point of view, they present a light curve quite uniform and a correlation between the peak luminosity and the wideness of the light curve, called the Phillips correlation (Phillips, 1993). These properties are used for cosmological purpose. From the moment of the explosion an SN Ia takes 15-20 day to reach the maximum of the luminosity. The dispersion around the maximum is quite small (0.13 mag). After the maximum, the light curve of the SN shows a fast decline (2 – 3 order of magnitude in 30 days) followed by a slow decline in logarithmic scale (0.015 mag for day). SNe Ib are in the early stages similar to SNe Ia: the light curve have the same shape, but the magnitude at the maximum is usually smaller by 1.5 mag. The final stages are different and they do not follow the Phillips law. This is the reason why SNe Ib cannot be used as standard candles as SNe Ia, although recent studies by Cano (2014) showed some pieces of evidence for the use of this type of SNe as standardizable candles.

CHAPTER 2

GRB models

Two GRB progenitors have been preferentially discussed in the literature: explosions of massive stars for LGRBs, as pointed out by MacFadyen and Woosley (1999), and NS–NS or BH–NS coalescence for SGRBs, as stated by Paczynski (1991b). There are several detailed models describing the phenomenon, but available observations are insufficient to constrain these models. In this chapter, the most popular GRB models will be shortly described.

2.1 The Compactness problem

It is known that the GRB is emitted not from the source, where the energy was initially deposited, but from a moving material, which has large Γ . For this reason, the size of the source R_0 is smaller than the size of the emitting region, R_{er} . In fact, assuming that the source is not moving relativistically, the size of the emitting region can be estimated from the timescale of the GRB temporal variability t_{var} through the relation $R_{er} \sim ct_{var}$. Given that some bursts have t_{var} of the order of milliseconds (Piran, 1999), it is found

$$R_{er} \sim 10^7 \text{ cm} \quad (2.1)$$

so $R_0 \leq 10^7$ cm. This gives raise to the so-called compactness problem (Piran, 1999). In fact, the source is very compact having size of typical compact astrophysical objects like NSs or BHs. Therefore, the observed energy implies very large energy density in the sources of GRBs. This leads in turn to the conclusion that the source must be optically thick to pair production via the process $\gamma\gamma \rightarrow e^+e^-$. Let's now consider the GRB with luminosity L_γ and average energy of photons ϵ_γ emitted during the time t_{var} . Then, the entire photons' number, radiated from the source, is

$$N_\gamma = \frac{E_\gamma}{\epsilon_\gamma} = \frac{L_\gamma t_{var}}{\epsilon_\gamma} \sim \frac{L_\gamma R_{er}}{\epsilon_\gamma c}, \quad (2.2)$$

with the light speed c and E_γ the total GRB energy. The optical depth¹ for pair production through the reaction $\gamma\gamma \rightarrow e^+e^-$ is

$$\tau_{\gamma\gamma} \sim n_\gamma \sigma_T R_{er} \sim \frac{3N_\gamma \sigma_T}{4\pi R_{er}^2} \sim \frac{3L_\gamma \sigma_T}{4\pi \epsilon_\gamma c^2 t_{var}}, \quad (2.3)$$

where $\sigma_T = 6.6524 \times 10^{-25}$ cm² is the Thomson's cross-section, and spherical geometry of the source is assumed. Taking typical parameters as $L_\gamma = 10^{52}$ erg/sec, $t_{var} = 1$ ms, and $\epsilon_\gamma = 1$ MeV, it is found

$$\tau_{\gamma\gamma} \sim 10^{15}, \quad (2.4)$$

which means that indeed the source is optically thick. Then, the only radiation one would see is the emission from the photosphere, but the source is so far that nothing would be visible. And in any case a thermal spectrum should be observed. However, special relativistic effects can resolve this difficulty. In fact, if the emitting material moves with ultra-relativistic velocity towards us, then its proper variability timescale is

$$t_{prop,var} \sim \Gamma^2 t_{var}. \quad (2.5)$$

In addition, there are less energetic photons with the factor of $\Gamma^{-2\nu}$, where $\nu \sim 2$ is the high energy photons spectral index, so substituting t_{var} with $t_{prop,var}$ the optical depth becomes

$$\tau_{\gamma\gamma} \sim \frac{3L_\gamma \sigma_T}{4\pi \epsilon_\gamma c^2 t_{var}} \Gamma^{-6}, \quad (2.6)$$

and can be smaller than unity for $\Gamma \geq 100$. Thus, the problem of compactness is solved when $\Gamma \geq 100$. In fact, similar assumptions are the basis of indirect methods allowing estimation of the Lorentz factors of GRBs (Lithwick and Sari, 2001b).

Ultra-relativistic expansion of GRBs is unprecedented in astrophysics. There are indications that relativistic jets in AGN have $\Gamma \sim 2 - 10$, but some GRBs have $\Gamma \sim 300$ and more. There is common consensus that the acceleration required to reach ultra-relativistic velocities comes from the radiation pressure, namely from photons and electron-positron pairs. Therefore, the source expands from a very compact region, almost reaching the speed of light. The bulk of radiation is emitted far from the region of formation of the plasma, when it becomes transparent to photons, trapped initially inside by the huge optical depth. The other side of the compactness problem is that the optical depth must exist in the beginning, when the plasma is just formed. Therefore, intense interactions between electrons, positrons and

¹The optical depth is the measure of how thick a medium is for the radiation travelling through it.

photons take place in the plasma. Even if initially the plasma is composed of only photons, or only pairs, creation or annihilation of pairs soon redistribute energy between particles so that the final state will be a mixture of pairs and photons. The main question arises: what is the initial state, prior to expansion, of electron-positron-photon plasma? Is it in a kind of equilibrium and, if so, is it thermal equilibrium, as expected from the plasma with large optical depth? Usually, when one deals with stationary sources in astrophysics, there is enough time for such equilibrium to be achieved. On the contrary, for GRBs with the timescale of expansion given by $t_{var} = 1$ ms, it is not at all clear, if there is sufficient time for any type of equilibrium to be reached. Regarding this aspect there is still a vivid debate in the literature. Some authors assumed thermal equilibrium as the initial state prior to expansion (Goodman, 1986; Ruffini et al., 1999), while others did not (Cavalo and Rees, 1978b). In fact, the study of the pair plasma equilibrium configurations in detail, performed in Svensson (1982), cannot answer to this question, because essentially non-equilibrium processes have to be taken into account. The prediction of thermal equilibrium has been confirmed by Vereshchagin (2008) giving the final answer to the previous question. In fact, Vereshchagin (2008) performed simulations whose final result is a $t_{thermalizazion} = 10^{-12}$ s so 9 orders of magnitude smaller than ms. With this result it is confirmed that there is more than enough time to reach the thermal equilibrium. This fact, together with energy assumptions, suggests that the origin of GRBs may be the gravitational collapse or mergers of compact objects like BHs, NSs or white dwarfs (Piran, 2004; Mészáros, 2006; Zhang, 2007; Nakar, 2007a).

2.2 The jet opening angle

The explanation of the afterglow phase is more complex in the case in which the relativistic jets are not spherically distributed. The commonly called jet is composed of relativistic matter emitted in a cone with a given opening angle θ_{jet} . Jets were introduced initially to solve the energetics problem. In fact, if the emission is not isotropic, but collimated by a narrow beaming angle (Mao and Yi, 1994), the total energy is reduced. Furthermore, they were also used to make similarities with the extragalactic sources and to explain the break in the phenomenological power-law (Sari et al., 1999). Within the scenario of the jet model, the emitting surface is proportional to Γ until $\Gamma \gg \theta_{jet}^{-1}$. Under this condition, while the plasma expands, Γ decreases and the emitting surface increases. When Γ becomes $\sim 1/\theta_{jet}$ the so-called jet break in the light curve of the GRB afterglow phase can be observed (Rhoads, 1999; Sari et al., 1999). If $\Gamma^{-1} > \theta_{jet}$, the radiation arrives far away from the initial jet causing the detection of a jet break for an observer looking at the original jet. A sketch of the jet opening angle with an on-axis observer, its relation with the emitting source of the progenitor, and the Γ factor is presented in Figure 2.2.1.

An observer off-axis will detect an orphan afterglow, namely an afterglow phase without an

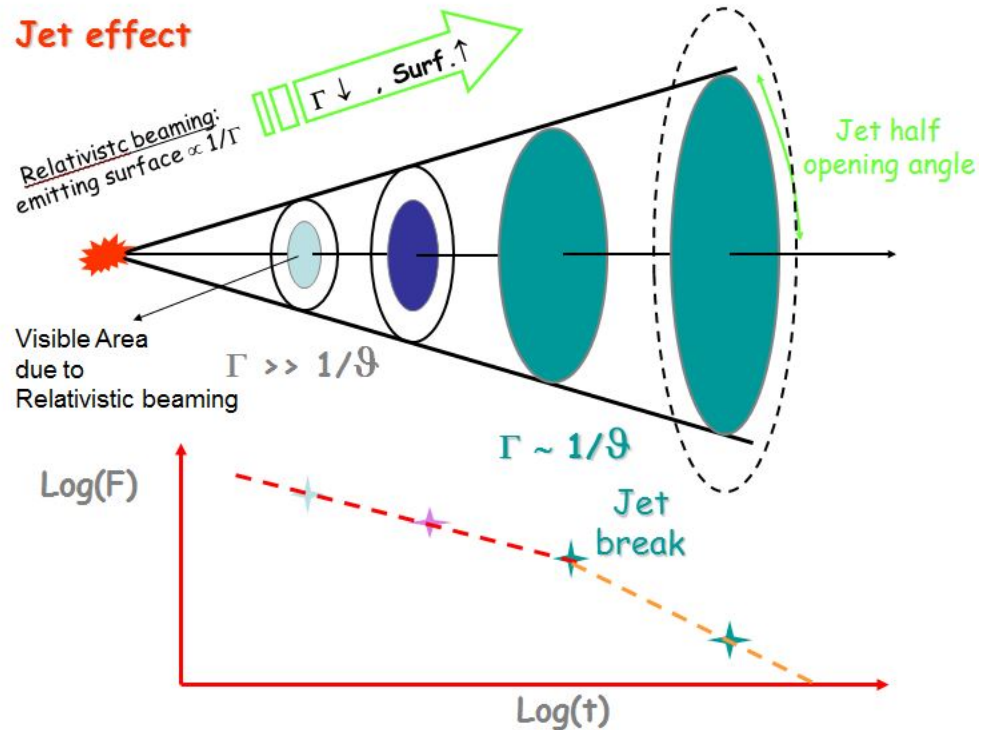


Figure 2.2.1: Sketch of the jet opening angle, its relation with the emitting source of the progenitor, and the Γ factor. Courtesy of Dr. M.G. Dainotti.

earlier GRB. However, there is the observational evidence of jets that exceed 37° as in the case of GRB 060218. These pieces of evidence underline the fact that the fireball model may present problems in explaining these features of the observational data. As presented in Sari et al. (1999) and Frail et al. (2001), the jet opening angle is given by

$$\theta_{\text{jet}} = 0.057 \times \left(\frac{T_{\text{break}}^*}{1 \text{ day}} \right)^{3/8} \times \left(\frac{1+z}{2} \right)^{-3/8} \times \left(\frac{E_{\text{iso}}}{10^{53} \text{ erg}} \right)^{-1/8} \times \left(\frac{\eta}{0.2} \right)^{1/8} \times \left(\frac{n}{0.1 \text{ cm}^{-3}} \right)^{1/8}, \quad (2.7)$$

where T_{break}^* is the jet break (with the * symbol used for rest-frame quantities), z is the GRB redshift, η is the jet efficiency, and n is the external medium density (Frail et al., 2001; Piran, 2004). The mean value of the jet opening angle has been evaluated to be around 10° for the Swift measurements and 7° for the pre-Swift measurements (Le and Dermer, 2007; Goldstein et al., 2016). As shown by Xin et al. (2016) and Troja et al. (2016), the jet opening angle can be an important parameter for defining the afterglow phase.

2.3 The fireball model

The GRB non-thermal observed spectrum indicates that the sources must be optically thin, instead a wide optical depth is found (Piran, 2004). This compactness problem (Ruderman and Cheng, 1988), as already explained in Section 2.1, has been bypassed assuming that the emitting matter moves relativistically towards the observer (Piran, 1999). In this case, in fact, the optical depth decreases by $\Gamma^{(4+2\alpha)}$, with α the high energy spectral index, so when $\Gamma \sim 10^2$ this problem is solved.

The kinetic energy of particles at relativistic energies is the best source for a relativistic jet. Even if some alternative ways for the relativistic jet production are taken into account (Thompson, 1994; Usov, 1994; Smolsky and Usov, 1996; Mészáros and Rees, 1997a; Katz, 1997), nevertheless at a given time power should transform itself into kinetic energy (Piran, 1999).

A model proposed to accelerate particles to relativistic velocities is the fireball model (Goodman, 1986; Paczynski, 1986) (see Figure 2.3.1). A huge amount of gamma-ray photons should be ejected and, thus the creation of e^\pm pairs can generate a thick fireball. A thick plasma with initial energy larger than its rest mass is what defines a fireball (Piran, 1999). Shemi and Piran (1990) and Paczynski (1990) took into account the effect of a baryonic load, showing that the ultimate outcome will be the transfer of all the energy of the fireball to the kinetic energy of the baryons.

In a pure radiation fireball the photons at energy E_1 may come into contact with photons at smaller energy E_2 creating electron-positron pairs through $\gamma\gamma \rightarrow e^+e^-$ if $\sqrt{E_1 E_2} > m_e c^2$. Due to the opacity the radiation remains confined. This plasma is assumed to be a perfect fluid and described by the stress-energy tensor $T^{\mu\nu}$ with pressure p , energy density ϵ and equation of state $p = \epsilon/3$. In addition to radiation and e^\pm pairs, also baryonic matter can be present in the astrophysical fireballs either in the original jet or in the external medium (Piran, 1999). The evolution of the fireball can be affected in two ways by these baryons. The thickness grows due to the electrons bound to this matter, while the accelerated baryons transform the radiation energy in bulk kinetic energy.

The expansion of the plasma is ruled by the relativistic conservation equations of baryon number, energy and momentum

$$(\rho_B U^\mu)_{;\mu} = 0 \quad (2.8)$$

$$(T^{\mu\nu})_{;\nu} = 0, \quad (2.9)$$

where ρ_B is the baryon mass density. The dynamics of the fireball might be split in two stages: the radiation dominated phase and the matter dominated one. During the radiation dominated phase ($\Gamma \ll (\epsilon_0/\rho_{B_0})\Gamma_0$) the conservation equations are reduced to these simple

scaling laws (Piran, 1999):

$$\Gamma \propto r, \quad \rho_B \propto r^{-3}, \quad \epsilon \propto r^{-4}. \quad (2.10)$$

The matter dominated phase, under the same approximation, is characterized by (Piran, 1999):

$$\Gamma \rightarrow const, \quad \rho_B \propto r^{-2}, \quad \epsilon \propto r^{-8/3}. \quad (2.11)$$

During this stage, since $\epsilon \ll \rho_B$, the dynamical effect of the radiation on the motion is not so crucial and thus no relevant radial acceleration is produced. Thus, Γ keeps constant on streamlines. Because each shell moves with a different relativistic velocity, the frozen pulse approximation is no longer valid at some large radius. There is a specific time during the expansion in which the fireball will become optically thin. After this point the radiation and the baryons do not have the same velocity and the radiation pressure becomes negligible. Any remaining radiation will escape freely now and the baryon shells will coast with their own individual velocities.

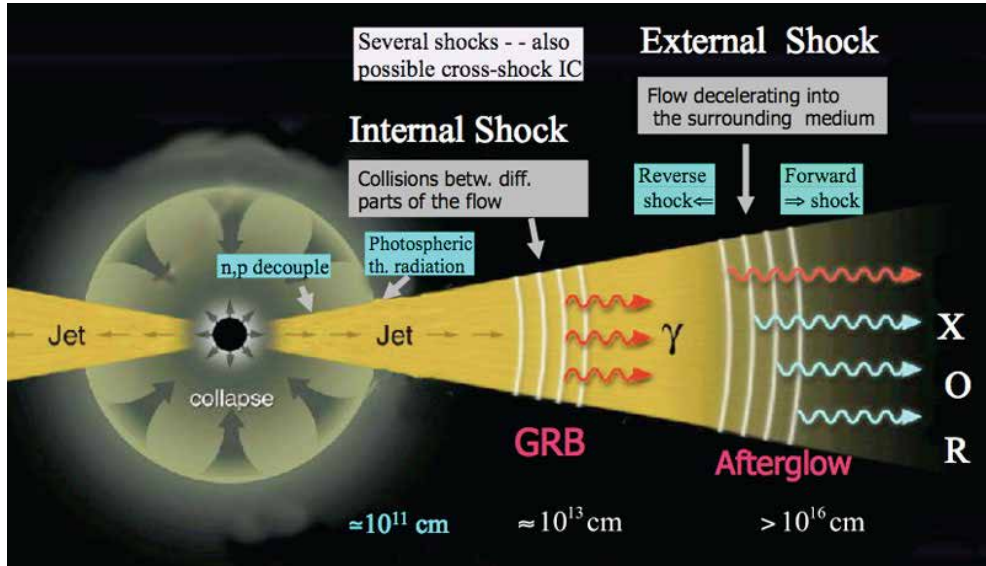


Figure 2.3.1: Sketch of the fireball model. (Figure from Mészáros and Rees (2015). Copyright © 2015 Cambridge University Press.)

2.3.1 Energy conversion

In the standard fireball model the energy transport occurs through the kinetic energy of a shell composed of relativistic particles. The energy transformation can happen in two ways (Piran, 1999): through external shocks (Rees and Meszaros, 1992) or through internal shocks (Rees and Meszaros, 1994).

Internal shocks are believed to describe the observed temporal structure of GRBs (Piran,

1999). Occurring at $\sim 10^{15}$ cm from the progenitor, twenty percent of the jet kinetic energy is transformed into thermal energy (Piran, 1999) and almost fifty percent of the shell's energy (Kobayashi et al., 1997; Katz, 1997) is taken out through internal shocks.

Sari and Piran (1997) claimed that in the case the external medium is interstellar medium (ISM), collisionless shocks occur and the relativistic shell is disperse by external shocks. This implies a further burst which explains the afterglow phase (Piran, 1999). Therefore, the standard fireball model is characterized by an “internal-external” scenario (Sari and Piran, 1997) in which the prompt GRB phase is generated by internal shocks, while the afterglow phase is caused by external shocks.

In the case a cold shell (with internal energy negligible in respect to the rest mass) approaches another cold shell or passes through the cold ISM, two kind of shocks are produced: a shock going forward in the ISM or in the external shell, and a reverse shock (RS) moving backwards in the inner shell. The Lorentz factor Γ and f , which is the ratio between the particle densities, define the structure of the jet.

There are three interesting cases (Piran, 1999):

- Ultra-relativistic shock ($\Gamma \gg 1$ and $f > \Gamma^2$). It occurs at the beginning of an external shock or during the very late propagation of the internal shock, when only one shock is present. Given that in this case the RS is non-relativistic or mildly relativistic (Piran, 1999), this pattern is named Newtonian. It was claimed that the energy conversion happens in the forward shock (FS) (Piran, 1999).
- The density ratio diminishes during the shell diffusion and $f < \Gamma^2$; besides the FS and the RS are relativistic.
- Internal shocks are characterized by $f \approx 1$, namely the density is analogous for both shells, and $\Gamma \sim$ a few units, describing the relative motion of the shells. Both shocks are mildly relativistic and the factor Γ of the two shells affects their power.

2.3.2 Light curves within the fireball model

After having described the theoretical process of the internal shock model that produces the prompt and afterglow phases it is relevant to investigate how the observed behaviour of the GRB light curves has been interpreted (Piran, 1999; Mészáros, 2002; Nakar and Piran, 2002; Piran, 2004).

The prompt phase within the internal shock

According to the fireball model the pulse duration and the time distance between the pulses depend on the same quantity, namely the time interval between the shells emitted by the inner engine.

If two shells separated by a distance L are considered (see e.g. Piran, 2004), the slower outer shell has Lorentz factor $\Gamma_S = \Gamma$, and that one of the inner faster shell is $\Gamma_F = a\Gamma$ ($a > 2$ for an efficient collision). The shells are ejected at t_{a_1} and $t_{a_2} \approx t_{a_1} + L/c$, where t_a is the time measured in the observer frame. Interactions occur at $R_s \approx 2\Gamma^2 L$. In fact, $R_s = c(t_2 - t_1)$ where $t_{a_1} = t_1/2\Gamma^2$ and $t_{a_2} = t_2/2\Gamma^2$ so $R_s = 2\Gamma^2 c(t_{a_2} - t_{a_1}) = 2\Gamma^2 L$. The collision radiates photons arriving to the observer at time:

$$t_{a_0} \approx t_{a_1} + R_s/(2c\Gamma^2) \approx t_{a_1} + L/c \approx t_{a_2}. \quad (2.12)$$

The photons from this pulse and a photon from the inner engine radiated with the second shell would be contemporaneous. This argument has been investigated by various numerical simulations (Kobayashi et al., 1997; Daigne and Mochkovitch, 1998; Panaiteescu et al., 1999), which argue that for internal shocks the light curve reproduces the temporal activity of the central engine.

To determine the time interval Δt_a between the pulses multiple collisions should be taken into account. All combinations of multiple collisions can be divided into three types (Piran, 2004). The angular time without cooling time defines the pulse width: $\delta t_a = R_s/(2c\Gamma_s^2)$ where Γ_s represents the value of the Lorentz factor for the radiating area.

The afterglow phase within the external shocks

In the fireball model, the external medium making slower the relativistic ejecta gives rise to the afterglow phase (Mészáros and Rees, 1997b) and the external shock leads the process (Piran, 1999). In the beginning the emission mechanism is radiative, namely with dissipation of the kinetic energy, while later it is adiabatic and less radiation losses occur (Piran, 2004). Later, when $\Gamma \approx 1.5$ the emission process passes into the Newtonian regime.

The propagation of a relativistic shell into the ISM was developed by Blandford and McKee (1976). An adiabatic ultra-relativistic blast wave with $\Gamma \gg 1$ is explained from this model. For this blast wave, the total energy is proportional to $r^3\Gamma^2$, leading to the scaling law:

$$\Gamma \propto r^{-3/2}. \quad (2.13)$$

Analogously, it is possible to find for a fully radiative regime another scaling law (Blandford and McKee, 1976):

$$\Gamma \propto r^{-3}. \quad (2.14)$$

In the adiabatic model the GRB energy is constant. Although, in the case further slower material is emitted besides the initial matter (Piran, 2004), the energy can vary. When this matter is decelerated by the circumburst matter, the slower material catches up and generates “refreshed shocks” (Rees and Mészáros, 1998; Kumar and Piran, 2000; Sari and

Mészáros, 2000). The extra injection of energy from these “refreshed shocks” modifies the blast wave dynamics (Rees and Mészáros, 1998; Sari and Mészáros, 2000), causing a slower decay in the light curve (Piran, 2004). In addition to the FS going outwards, a RS diffusing into the slower material is produced when this material catches up the faster one (Kumar and Piran, 2000).

2.4 Central engine models

The fireball model is independent of the details of the inner engine that releases the initial energy (Mészáros, 2002). Nevertheless, simple assumptions on the energetics and the timescales lead to the idea that the central engine producing the required energy flow could be an accretion disk. Many frameworks could lead to a BH with a massive accretion disk system. This could include mergers, as NS–NS (Eichler et al., 1989; Narayan et al., 1992a), NS–BH (Paczynski, 1991b) or NS–white dwarf (Fryer et al., 1999b) binary systems, and models founded on “failed supernovae” or collapsars (Woosley, 1993; Paczyński, 1998; MacFadyen and Woosley, 1999). Models for LGRBs include mechanisms like the BH accretion (Page and Thorne, 1974), the rotation of a BH powering the Blandford-Znajek jet generation mechanism (Hartmann and Woosley, 1995), the collapse of a massive star (MacFadyen, 2001), while for SGRBs there are the magnetar model (Usov, 1992), the supranova model (Vietri and Stella, 1998) and the merging neutron stars model (Duncan and Thompson, 1992; Narayan et al., 1992b). Starting with Dall’Osso et al. (2011) the magnetar model began to be used also for explaining LGRBs. These models are shortly described in the following sections.

2.4.1 Long GRB models

Accretion model by Page and Thorne (1974)

In the accretion model by Page and Thorne (1974), the disk sustained by fall-back material from the explosion of a massive stellar progenitor accretes onto a BH involving neutrino cooling (see Fig. 2.4.1). The energy is then released as a GRB jet. Nowadays, this is one of the most validated and widely-used scenarios for the formation of LGRBs (Piran, 2004).

In their work, Page and Thorne (1974) investigated the dynamics of the accretion disk starting from the assumption that the BH is stationary and axially symmetric, and the accretion disk is placed in the equatorial plane of the BH. The energy flux radiated from the surface of the accretion disk is a function of the distance. In addition, Thorne (1974) analysed the evolution of the BH in the context of the accretion model. As a result, he confirmed the high efficiency of the conversion of the accreting mass into energy (30%) and

constrained the value for the ratio of the spin to the BH mass suitable for the model (0.998)².

It is worth mentioning that also a merging system constituted of NS–NS or BH–NS forms a disk accreting finally onto a BH. However, in this case, due to the different physical conditions of the accretion disk, an SGRB will be produced (Narayan et al., 2001).

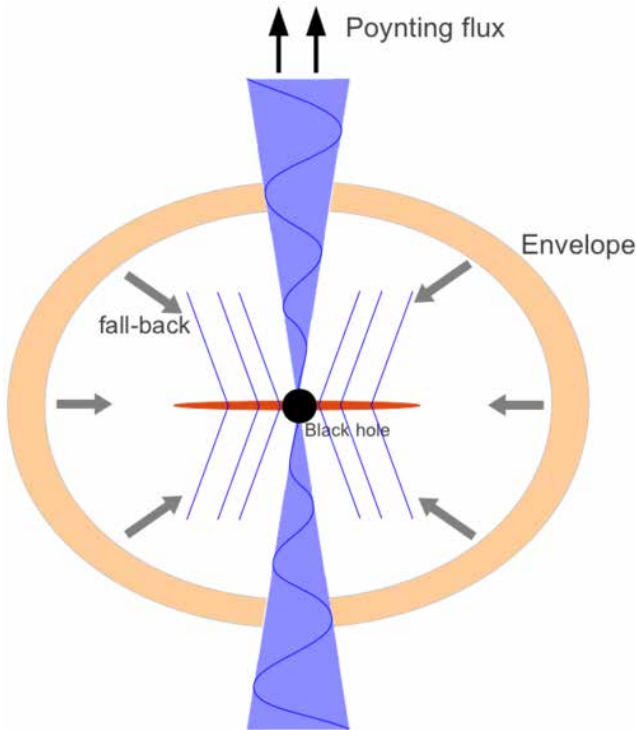


Figure 2.4.1: A representation of the GRB accretion model. (Figure from Wu et al. (2013). © AAS. Reproduced with permission.)

Rotating black hole model

Another model for LGRBs was proposed to be a rotating BH in a strong magnetic field with the rotational (spin) energy extracted by the magnetic field through the Blandford-Znajek mechanism (Blandford and Znajek, 1977). In this case the power can be estimated using the following widely-used formula by Thorne et al. (1986):

$$P \sim 10^{49} \left(\frac{ac}{GM} \right)^2 \times \left(\frac{M}{M_{\odot}} \right)^2 \times \left(\frac{B}{10^{15} \text{ G}} \right)^2 \text{ erg/s}, \quad (2.15)$$

where B is the magnetic field strength, a is the BH spin, M is the BH mass, and M_{\odot} represents the solar mass (1.99×10^{30} kg). This formula allows for estimation of the energy emitted from the BH to compare it with the GRB observations.

Further theoretical results obtained within this model are often in agreement with those

²This value is compatible with the results for a rotating BH (Kerr, 1963; Newman et al., 1965).

described by Hartmann and Woosley (1995) and Hartmann (1996). Indeed, they presented the investigation of the models describing the BH accretion and its jet. They derived the energy rate of the radiation emitted by the accretion process to be $\sim 5 \times 10^{52} \times (10 \dot{M}/M_{\odot} s^{-1})$ erg s $^{-1}$ (with \dot{M} the mass accretion rate), and the angular velocity of the BH to be $\sim 0.1 \times \left(\frac{M_{\text{disk}}}{M_{\odot}}\right) \times \left(\frac{M_{\text{BH}}}{5 M_{\odot}}\right)^{1/2} \times \left(\frac{10^8 \text{ cm}}{b}\right)^{2.5} \text{ s}^{-1}$, with b the distance of the disk from the BH. These values are still the best estimates for these parameters nowadays.

The Collapsar

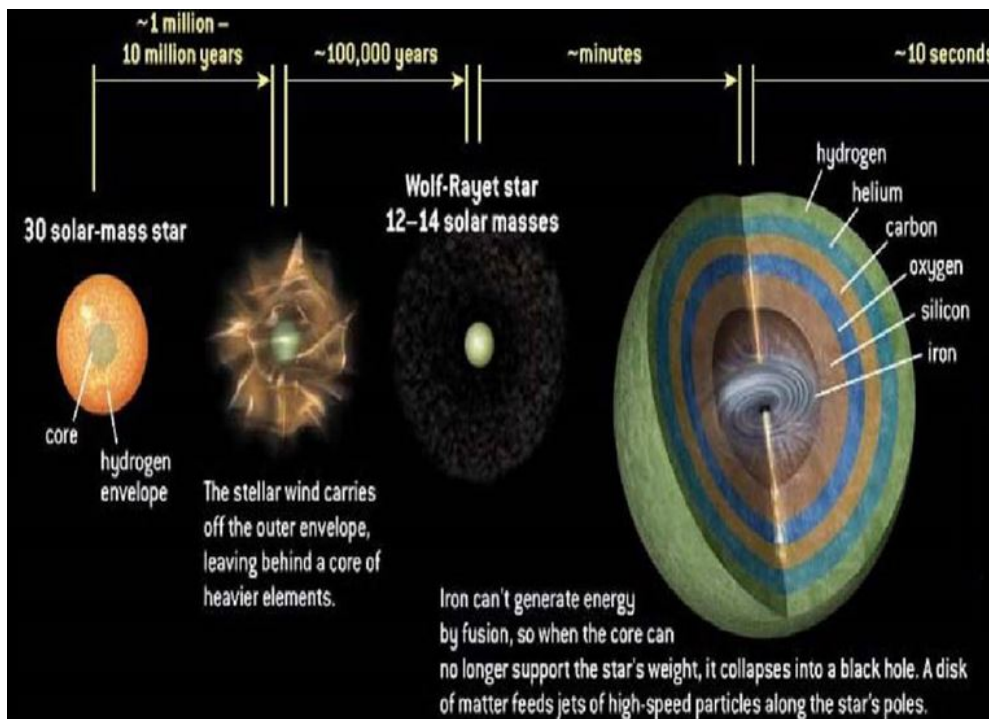


Figure 2.4.2: Sketch of the collapsar model summarizing the main phases from the progenitor star until the collapse. Courtesy of Dr. L. Vetere.

Woosley (1993) suggested that GRBs are produced through the collapse of a fast rotating Wolf-Rayet star. Paczyński (1998) concluded that GRBs are associated with the collapse of stars with $M > 30 M_{\odot}$. MacFadyen and Woosley (1999) investigated the propagation of a jet moving with relativistic velocities through the stellar envelope of the collapsing star and Mészáros and Rees (2001) investigated the collimation of the jet. Finally, Zhang et al. (2003) validated and enlarged the characteristics of the jet collimation. All these aspects give rise to the collapsar model.

Very massive stars fuse material in their core up to the iron layer, and when they cannot produce energy by fusion they collapse generating a BH. The central matter of the star produces an accretion disk with mass $0.1 M_{\odot}$. The fall down of this material into the BH causes a couple of jets (with $\theta_{\text{jet}} < 10^\circ$) generating a relativistic shock wave at the front

(Blandford and McKee, 1976). The core collapse, the accretion, and the jet emission last ~ 10 s (MacFadyen and Woosley, 1999), while the accretion onto the BH should last several dozens of seconds. The jet motion, as it breaks the envelope of the star, is influenced by its interaction with the surrounding medium. In this way the collapsar scenario attempts to model the time evolution of the prompt emission. In addition, this model accounts for a variable Γ for the production of the internal shocks (Woosley and Bloom, 2006a). This model is also able to predict that the activity of the central engine lasts long after the prompt phase is ended (Burrows et al., 2005). This is allowed within this model because jet and disk are inefficient at ejecting all the material in the equatorial plane of the star before the collapse. Indeed, a part of this material keeps falling back and accreting (MacFadyen et al., 2001). If the hydrogen layer of the star is not thick, the stellar surface will be crossed by the jet. In the case the density of the stellar matter decreases, the shock accelerates, and at the surface it has a value of Γ around 100 or larger with its energy emitted as gamma-rays. A sketch of the collapsar model is presented in Figure 2.4.2.

Evidence and problems for the collapsar view In the collapsar model three constraints are present for a star to produce a GRB:

- the mass of the star needs to be large (at least 30 solar masses on the main sequence) to produce a BH,
- to generate a torus able to emit jet, the rotation of the star has to be high,
- low metallicity of the star is requested to remove its hydrogen layer, so the surface can be reached from the jets.

In order to satisfy all these requirements, it happens that core collapse SNe are more frequent than GRBs. The accomplishment of this model is provided by the fact that LGRBs are observed in systems with high star formation, like irregular galaxies and spiral galaxies (Pontzen et al., 2010).

In addition, for systems at low redshift many cases of GRBs associated with SNe Ib/c are observed. In particular, this type of SNe misses hydrogen absorption lines. The most important GRBs associated with SNe are: GRB 980425/SN 1998bw (Galama et al., 1998), GRB 030329/SN 2003dh (Stanek et al., 1999; Hjorth et al., 2003), GRB 031203/SN 2003lw (Malesani et al., 2004), GRB 060218/SN 2006aj (Della Valle et al., 2006), GRB 111209A/SN 2011kl (Greiner et al., 2015), GRB 130215A/SN 2013ez, GRB 130831A/SN 2013fu (Cano et al., 2014), GRB 130702A/SN 2013DX (Toy et al., 2016), GRB 161219B/SN 2016jca (Cano et al., 2017) and a few GRBs with SN bumps in their afterglow light curves.

However, Fynbo et al. (2006) pointed out that GRB 060614 and GRB 060505 do not have any associated SN, but they are observed in a high star formation region. Therefore, they concluded that, if the BH absorbs the star before the SN burst reaches the surface, the SN

could not appear.

2.4.2 Short GRB models

Magnetar model

Regarding SGRBs, a possible scenario was developed by Usov (1992) in which a strongly magnetised NS (namely a magnetar) can be an engine for GRBs (see Fig. 2.4.3). In this model a magnetar with $B \sim 10^{14\div 15}$ G created in a freshly collapsed massive star releases a huge amount of energy allowing to power the jet of an SGRB (Metzger et al., 2011; Dall’Osso et al., 2011; Rowlinson et al., 2013, 2014). The magnetars involved in this process need to have a rotation period of ~ 1 ms, or even shorter, to fulfill the budget of total and emitted energies (Zhang and Mészáros, 2001).

There are also studies in which magnetars connected to SNe and magnetars connected to LGRBs were compared finding similarities between these two phenomena, as for example in Dall’Osso et al. (2011); Rowlinson et al. (2014) and Yu et al. (2017). Indeed, the host galaxies of both GRBs and SNe seem to have high star formation rate and low metallicity (Lunnan et al., 2014). One should note that in the magnetar model it is often hard to distinguish between wind-like and constant external media surrounding the GRB (Gompertz and Fruchter, 2017), while this detail can play a crucial role because different external medium densities can imply different energy emission processes.

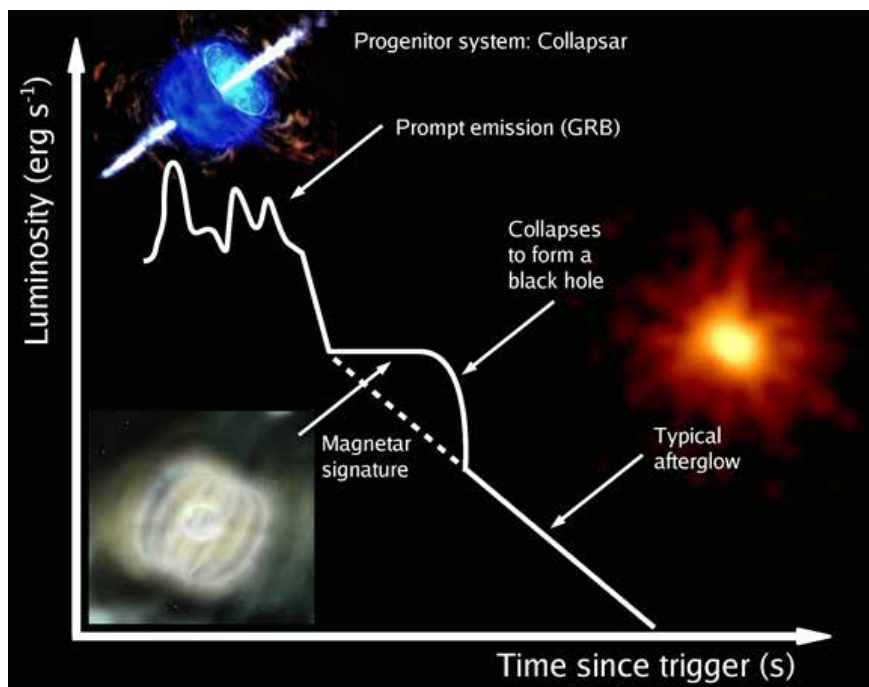


Figure 2.4.3: A sketch of the magnetar model. (Figure from Rowlinson et al. (2011). Copyright © 2011 AIP Publishing.)

Supranova model

An alternative model for SGRBs is provided by the supranova model (Vietri and Stella, 1998). A supranova is a very luminous SN remnant ($\sim 10 \times$ SN luminosity) obtained from the collapse of a massive star (few M_{\odot}). In their work, Vietri and Stella (1998) assumed that the main reason for the collapse is the missing angular momentum of the massive star or the instability generated by the cooling of the massive star. In this scenario, a really massive NS (few M_{\odot}) collapses onto a BH and the radiation gives rise to an SGRB (Piran, 2004). The model is composed of two phases: in the first, the NS is generated from a supranova (really luminous massive star), and then in the second one the NS gives rise to an SGRB through its collapse. Recently, this model allowed for the investigation of the really massive GRB progenitor that can give important information about the environment in which GRBs occur (Lazzati et al., 1999; Böttcher and Fryer, 2001). Indeed, such constraints are in agreement with the observations of the density of the medium, the initial energy, and the mass.

Even if this model appears similar to the collapsar model, they differ for the following reason: in the collapsar model an SN bump is present as a characteristic feature of the afterglow light curve, while in the supranova model it is absent. The difference among the supranova and the collapsar is evident, because the energy of the latter is higher than the first one (10^{52} versus 10^{51} erg), see Woosley and Bloom (2006b) and Piran et al. (2017).

A model of merging neutron stars

Finally, for SGRBs there is the widely accredited model involving the collision of two NSs (Duncan and Thompson, 1992; Narayan et al., 1992b). Within this scenario, a BH accreting the disk around the coalescent NS system can be generated (Fryer et al., 1999a). The energy released during this process will lead to the creation of the SGRB, given the energy budget and the timescale of this phenomenon. In more detail, Narayan et al. (1992b) investigated NS–NS and BH–NS systems, taking into account different interaction mechanisms such as magnetic flares and neutrino interactions. From their model they assumed the distance of the GRB and predicted the possible detection of GWs from these cosmological systems based on the LIGO technical specification.

On the other hand, considering other merging system, Fryer et al. (1999a) analysed the BH accretion phenomenon in different kinds of stellar binary systems to provide some limits for the progenitors and the formation rate of the merging binary systems. They also investigated the merging NS–helium star system and concluded that to have the highest formation rate of merging binary systems the helium core in the NS–helium star system is relevant. In fact, the presence of a NS merging with its helium companion star leads to a formation rate of merging binary systems one order of magnitude smaller. Nevertheless, the formation rate of the NS–helium star merging system is sufficient to allow the formation of an SGRB.

According to several authors, the merging NSs model seems to represent the main explanation for the origin of SGRBs (Berger, 2014a). Unfortunately, this model has to face two issues: the first is the occurrence of an extended emission in some SGRB light curves (Norris and Bonnell, 2006), and the second is the detection of optical flares at late times ($> 10^5$ s, Gehrels et al. 2009). Indeed, the timescales computed for this model are shorter than those required by these observational features. However, as already pointed out in the beginning of Chapter 1 the observation of GW170817 leaves no doubt that this scenario is definitely favoured among the plausible scenarios for the creation of SGRBs.

2.5 Additional Models

Several models for the GRB emission that do not focus on the central engine have been also presented in the literature. Below, for a more complete overview, several models are described. In those the GRB emission a) relies on microphysical parameters evolving with the Lorentz factor; b) is influenced by a jet observed off-axis; c) is modified by scattering in the ISM or d) is affected by the GRB photosphere.

Microphysical parameters model evolving with the Lorentz factor

To explain the differences between the GRB emission in optical and X-ray wavelengths in a context of a model which involves microphysical parameters (Panaiteescu et al., 2006), the physical quantities describing the GRB shock are assumed to be power-laws. Therefore, the required parameters should be the injected energy larger than a given Γ , $E(> \Gamma) \propto \Gamma^{-e}$, the energy density of the magnetic field $\epsilon_B \propto \Gamma^{-b}$, the energy density of the electric field $\epsilon_E \propto \Gamma^{-i}$, and the ambient medium density $n(r) \propto r^{-s}$. e , i , and b are the exponents for the Lorentz factor. In this model, the difference between the temporal decay indices in X-ray ($\alpha_{X,a}$) and optical ($\alpha_{O,a}$) wavelengths is given by Urata et al. (2007):

$$\alpha_{X,a} - \alpha_{O,a} = \frac{s}{8-2s} - \frac{1}{4} + \frac{3-s}{e+8-2s} \left[\left(\frac{s}{8-2s} - \frac{1}{4} \right) e - \frac{3}{4} b \right]. \quad (2.16)$$

Hence, for a constant ($s = 0$) medium density, the magnetic field and the amount of energy injected are the only quantities influencing the difference between the optical and the X-ray decay rates of the GRB light curve, as claimed by Panaiteescu et al. (2006) and Urata et al. (2007).

GRB model for a jet observed off-axis

For the GRB jet observed off-axis in the afterglow phase the viewing angle should be slightly larger than θ_{jet} . This would be the main physical explanation for the shallow plateau phase,

because the viewing angle affects the emission detected shortly after the prompt phase, and the observed emission is dimmer off-axis.

As shown by Yamazaki et al. (2003), the off-axis observation of the GRB emission can lead to a detection of phenomena looking much weaker than they actually are. As pointed out by Ioka and Nakamura (2001) (see Fig. 2.5.1), this effect could allow to interpret XRFs as LGRBs seen off-axis. Also Oates et al. (2012) and Oates et al. (2015) claimed that the observation of GRBs off-axis can be an explanation for the behaviour of the afterglow phase of the GRB light curve, when accompanied with a complex jet structure.

Ryan et al. (2015), investigating a sample of 226 Swift GRBs through hydrodynamic simulations, found that most of their afterglow phases were observed off-axis. In addition, they claimed that this aspect could affect the jet break behaviour in the GRB light curves.

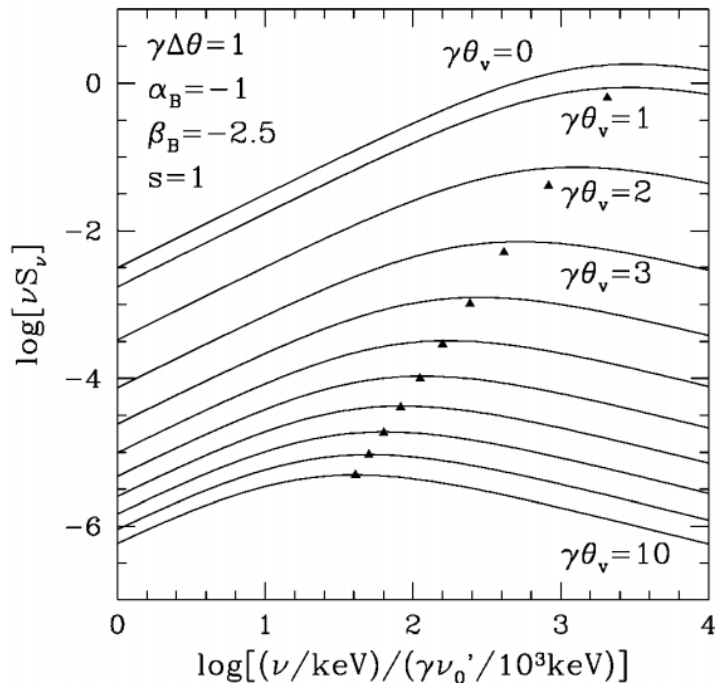


Figure 2.5.1: GRB model for a jet observed off-axis. Total fluence, S_ν , is plotted versus the observed frequency at different viewing angles. (Figure from Ioka and Nakamura (2001). @ AAS. Reproduced with permission.)

GRB emission modified by scattering in the interstellar dust

The dust scattering model was developed to describe the plateau phase at the beginning of the GRB afterglow emission. This model was introduced by Shao and Dai (2007) and Shao et al. (2008). They used the analysis carried out by Miralda-Escudé (1999). In this approach the scattering of the X-ray afterglow radiation along the GRB line of sight is due to the dust inside the parent galaxy. The authors claimed that the afterglow phase would result from

the scattering of the prompt emission radiation by the dust in the medium surrounding the GRB progenitor (Shao and Dai, 2007; Shao et al., 2008).

In addition, in the framework of this model $\beta_{X,a}$ should increase, and the spectrum of the steep decay of the afterglow phase should be softer than the one of the plateau phase. However, as noted by Shen et al. (2009), such spectral softening is not observed in the sample they analysed. On the contrary, a hardening behaviour of $\beta_{X,a}$ was found, but from the analysis they could not rule out the model.

GRB photospheric model

As it has already been discussed for the compactness problem, in the inner part of the outflow the optical depth is too high ($\tau_{\gamma\gamma} \sim 10^{15}$). Therefore, this region is defined as the most internal part of the outflow from which the radiation can be observed. To explain the prompt phase, a signature from this region should be present in the GRB spectra, but instead the observed spectrum is non-thermal. This situation is well summarized by Pe'er (2015), where the study of this inconsistency leads to the discovery of two aspects: the spectrum from the photosphere is difficult to reconstruct, and the photosphere can be affected by energy dissipation. The first aspect was presented by Pe'er (2008) and Beloborodov (2011). From their analysis it was concluded that during the emission the comoving energy is different for each photospheric photon causing the widening of the photospheric spectrum. In this way the spectrum becomes non-thermal. Alternatively, the second aspect, investigated by Giannios (2006, 2008) and Lazzati and Begelman (2010), states that a fraction of the kinetic energy during the prompt emission is dissipated in regions of moderate or low optical depth. The electrons are accelerated at ultra-relativistic velocity if they receive a broad fraction of this dissipated energy. Subsequently, these particles release energy through synchrotron radiation and scatter the thermal photons to higher energy, generating non-thermal spectra. In addition, the photons do not have enough time to thermalize before separating from the plasma, providing a non-thermal photospheric spectrum. For a recent review on the photospheric model see Beloborodov and Mészáros (2017).

To have a more complete picture, sometimes the photospheric model and the external shock model are employed together. The GRB photosphere and external shock model assumes the X-ray emission subject to the jet photospheric emission, while the synchrotron radiation from the external shocks in the jet controls the optical emission. Sometimes it is observed that if the central engine emission has a break, also the optical and X-ray GRB emissions will present an achromatic (independent of the frequency) break at the same time (Ghisellini et al., 2009).

As presented in Figure 2.5.2, in this model the external medium structure plays an important role. Panaitescu and Kumar (2000) analysed the differences between the wind-like medium and the constant density medium. The equation for the density medium is the following:

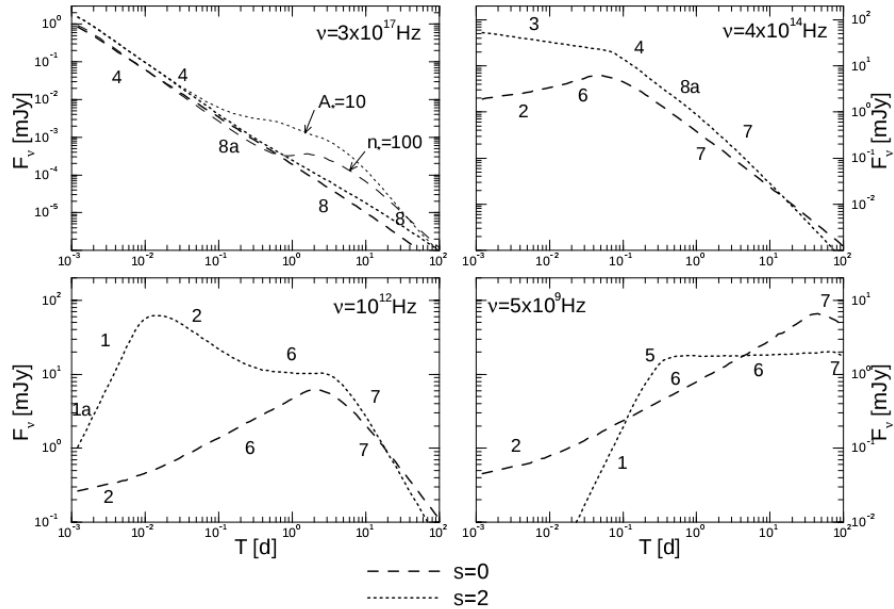


Figure 2.5.2: GRB afterglow light curve flux F_ν in the GRB photosphere and external shock model in four emission frequencies, see detailed description of presented cases in Panaiteescu and Kumar (2000). The case $s = 0$ represents the constant external medium density, while the case $s=2$ stands for the external medium formed by the stellar wind, see Equation 2.17. (Figure from Panaiteescu and Kumar (2000). @ AAS. Reproduced with permission.)

$$n(r) = A \times r^{-s}, \quad (2.17)$$

where $s = 0$ for a constant density medium and $s = 2$ for a wind-like medium. Panaitescu and Kumar (2000) examined the emission behaviour in the cases in which the electrons interacting with these two kinds of media cool adiabatically or radiatively. They found a number of differences, for example in the frequency ranges characterising the electron cooling spectra, in the plateau phases, and in the decaying parts of the afterglow phase of the light curve. However, these results are not adequately constraining the physical parameters describing GRBs.

2.6 The SNe Ib/c models

The position of the SNe in the galaxy can give information about their nature and the mass of the progenitor. Indeed, SNe II, Ib, and Ic are mostly found in the surrounding of spiral arms and HII regions (Filippenko, 1988), suggesting a mass of $8 - 10 M_\odot$ for the progenitor. Filippenko (2005) studied the progenitor of SNe II and he found that some of the SNe II can be originated from an ejecta interacting with high density circumstellar

medium, while some others from highly luminous and variable stars. From their analysis, James and Anderson (2006) claimed that SNe Ib, Ic and II fractions are proportional to the luminosity and the host galaxy star formation rate (SFR). SNe Ib and SNe Ic prefer bright host galaxies, while SNe II are most likely found in dim host galaxies. Instead, SNe Ia are found in each kind of galaxies, with some of them favouring the spiral ones. Della Valle and Livio (1994) concluded that, due to the growing rate from early to late Hubble type, the progenitor star for SNe Ia has most likely mass around $4 - 7 M_{\odot}$ and age 0.1-0.5 billion years. Li et al. (2011) investigated the luminosity functions of different SNe. They found there is no correlation between the SN luminosity function and the host galaxy dimension. Additionally, they claimed that SNe Ib and SNe Ic appear originated from luminous galaxies. Fink et al. (2007) analysed a model in which the white dwarf explodes before reaching the Chandrasekhar limit, but this model looks unlikely for SNe Ia.

Instead, Ouyed and Staff (2013) developed a model in which a quark-nova ejecta colliding with a white dwarf at the Chandrasekhar limit can generate a phenomenon similar to SNe Ia. The few investigated SNe Ib/c present a light curve with a rise time and fast-decline phase lasting 15 – 20 days and 30 days, respectively and a decaying phase with rate $0.01 - 0.03 \text{ mag day}^{-1}$. SNe Ib/c light curves are fuelled by the process $Ni^{56} \rightarrow Co^{56} \rightarrow Fe^{56}$, differently from those for SNe IIP. A good pattern of all the types of SNe is well represented by Figure 2.6.1. While the amount of produced nickel provides the peak of the emission, the photon diffusion indicates the width. This diffusion is constrained by the envelope mass and the expansion velocity.

The determination of the kinetic energy is derived from the Doppler effect widening the spectral lines. The decaying at late time shows that a part of the gamma-rays leaves SN ejecta not thermalized, and thus able to estimate the amount of Ni^{56} in the SN core. Jerkstrand et al. (2015) found that the burning silicon amount can give constraints on the progenitor and the explosion mechanism. Nomoto and collaborators, assuming a spherically symmetric emission, described SNe Ib as helium stars lacking of hydrogen layer, while SNe Ic as carbon/oxygen nuclei without helium layer.

For SNe Ib/c as for SNe II heavier envelope masses lead to more energetic explosions, but SNe Ib/c undergo to a larger mass loss. These phenomena are called hypernova due to their extreme energy. In spite of the higher than normal energies, none of these phenomena generates high nickel masses in comparison with lower energy SNe Ib/c (see Fig. 2.6.2). This result confirms that the core physics of SNe Ib/c and SNe II could be similar. Taking into account all SNe II and SNe Ib/c, it seems that there is a continuous distribution of energies below 8 foes ($1foe \sim 10^{51} \text{ erg}$). During the explosion, in this model, SNe II can emit energies in agreement with those of SN 1997ef and SN 2002ap. Even though the process responsible for the hypernova is not clear, if SN 1997ef and SN 2002ap are explained within this model (Nomoto et al., 2000; Deng et al., 2003), then at least one SN II (SN 1992am) can be regarded as a hypernova. To confirm that the energy distribution is continuous more data are needed.

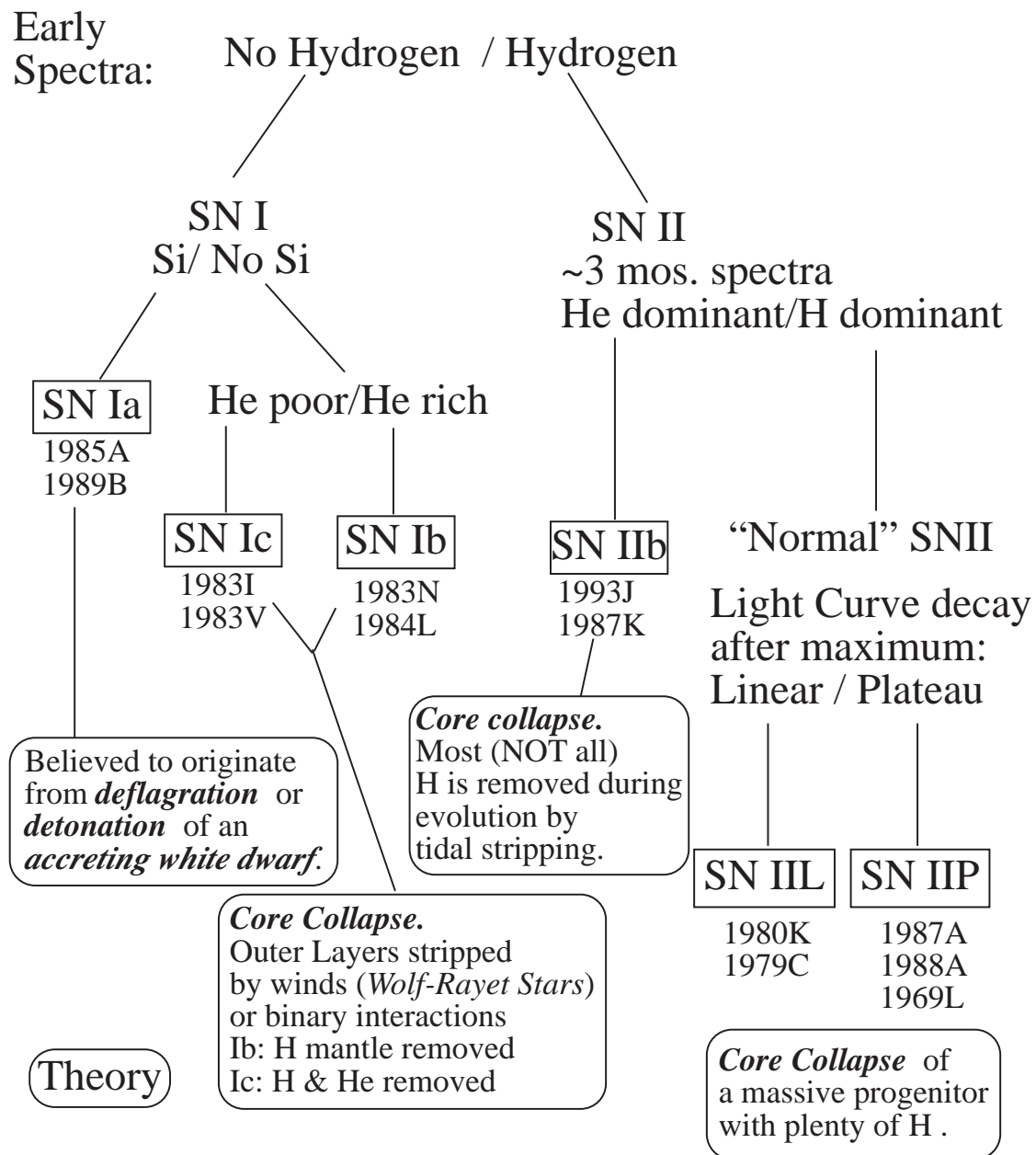
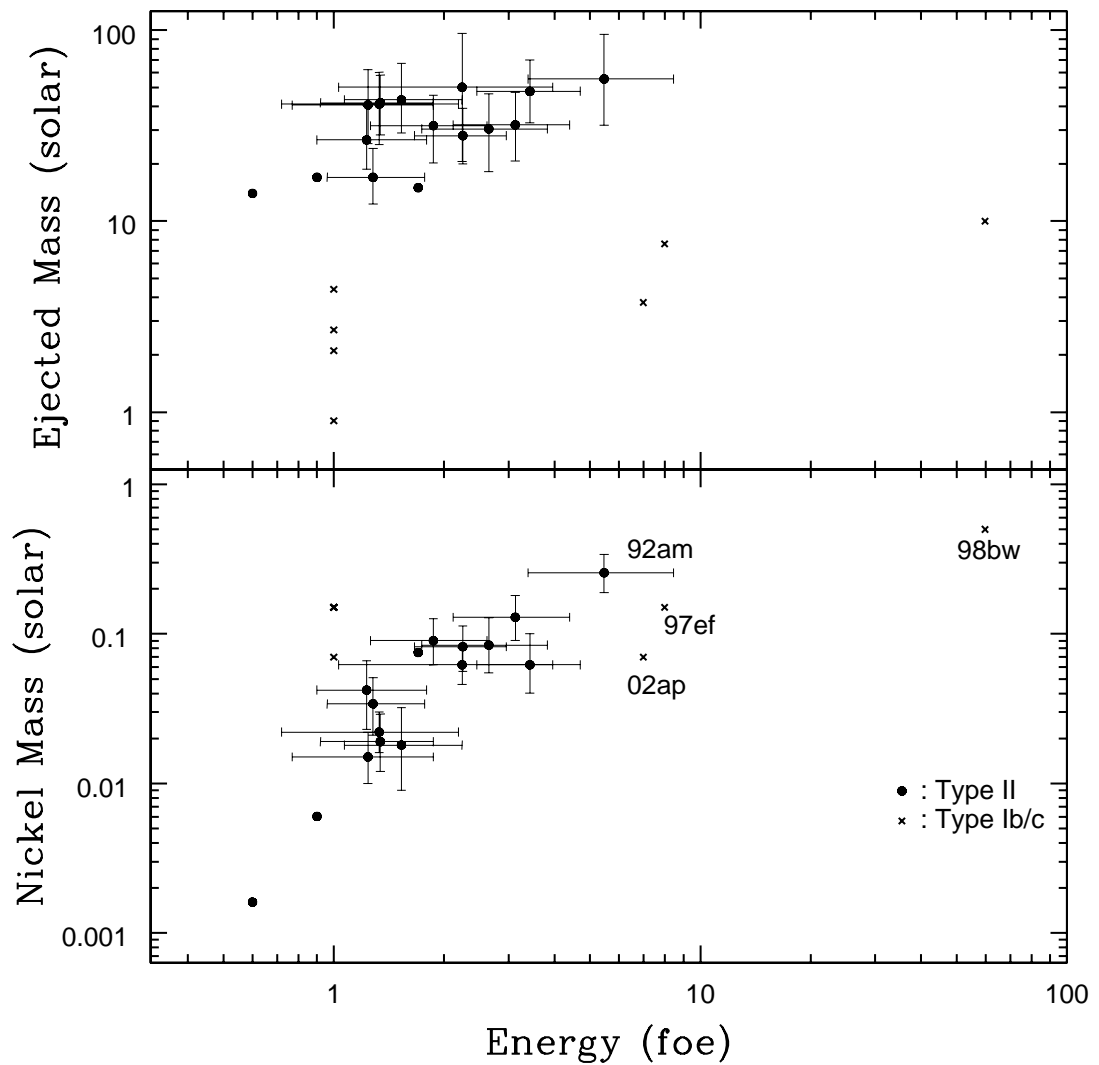


Figure 2.6.1: A sketch summarizing the SNe types. Courtesy of Dr. M.G. Dainotti.



Smartt et al. (2002) analysed the images of the galaxy M74 before SN 2002ap. Even if they did not find any possible progenitor, they could not discard the Wolf-Rayet star scenario. They claimed that another possible description is that SN 2002ap can be originated from a star in a binary system which has all the hydrogen and helium cores removed via mass transfer. Van Dyk et al. (2003) could not conclude if the Wolf-Rayet star or the massive interacting binary system are the most plausible scenarios for the SN Ib/c progenitors.

CHAPTER 3

The GRB correlations among prompt parameters

3.1 Why Standard candles and sirens are important for cosmology?

One of the main problems of astronomy is the computation of the distances and, as shown in Figure 3.1.1, there are a lot of methods to be applied at different distance ranges. Parallax measurements are used for computing distances of nearby stars, the periodicity of Cepheids is considered for deriving distances of nearby galaxies, while for more distant objects the method of SNe Ia, which are the most popular standard candles, is used. Standard candles are astronomical objects for which the luminosity is known or it can be computed through other well established correlations. Consequently, the luminosity distance can be derived through the luminosity of the objects or through these correlations. Standard sirens are astrophysical objects for which the luminosity distance is computed from the waveform created by a binary system. Thus, GW sources are standard distance indicators. For GW the main issue is to calculate the redshift of the object through an electromagnetic counterpart (EM) such as EM emission from the merger or through the hosting galaxy. Here a comparison between standard candles and standard sirens is described pinpointing advantages and drawbacks.

With EM waves:

- Measuring redshift is easy throughout the comparison of EM spectra.
- Measuring distance is hard, because objects with known luminosity such as SNe Ia are needed.

With GWs:

- Measuring distance is simple, because it can be derived directly from the waveform (standard sirens).
- Measuring redshift is hard, because the problem of the mass degeneracy in the waveform has to be faced. The main aim is to identify an EM counterpart such as optical, radio, X-rays, gamma-rays emissions, together with its precise distance from the GW to distinguish the object or the host galaxy.

GWs were not observed until 2016 Abbott et al. (2016b), because they are not interacting through electromagnetic forces and instruments with sufficient sensitivity were lacking. Nevertheless, Schutz (1986) suggested that with the instruments in preparation, the GW signal coming from the coalescence of a NS binary system has the potential for constraining the value of the present-day Hubble constant, H_0 . Schutz (2002) claimed that the observations of GWs from binary systems through the future GW detectors, especially the LISA mission, will be able to determine the beginning of the star formation epoch and, together with telescopes providing electromagnetic observations, to measure the expansion of the galaxies with high precision.

In addition, Holz and Hughes (2005) yielded that the GW signal coming from a coalescent supermassive binary BH system and detected by the future LISA mission will be able to compute the luminosity distances with 1%-10% accuracy. In particular, with an additional EM counterpart those observations will allow also the measurement of the redshift; thus the coalescent binary BH systems could be conceived as standard candles.

Recently, Abbott et al. (2016b) claimed the detection of the first GW signal from a binary BH system by the LIGO and VIRGO collaborations, without an EM counterpart, though. Nevertheless, this opened a new branch of study in astronomy. As a further step Abbott et al. (2017b) presented the detection of the first GW signal from a NS binary system by the LIGO and VIRGO collaborations with a following optical counterpart detected by other space missions. Furthermore, from the analysis of Abbott et al. (2017a) the value of H_0 was retrieved using only the GW signal associated with one GRB and it was found in agreement with the previous values present in the literature. Indeed, they found $H_0 = 70.0^{+12.0}_{-8.0}$ $\text{Km s}^{-1} \text{ Mpc}^{-1}$ in agreement with the estimate ($67.74 \pm 0.46 \text{ km s}^{-1} \text{ Mpc}^{-1}$) by Planck (Planck Collaboration et al., 2016) and the value ($73.24 \pm 1.74 \text{ km s}^{-1} \text{ Mpc}^{-1}$) from SHoES observations of SNe Ia (Riess et al., 2016). This result will allow for the measurement of the luminosity distance up to cosmological scales, using just the GW signal.

GRBs are good candidates for standard candles because they would allow for an extension of the Hubble Diagram (HD) an order of magnitude further than SNe Ia. In fact, GRBs are detected until redshift $z = 9.4$ (Cucchiara et al., 2011), while SNe Ia until $z = 2.26$ (Rodney et al., 2015). This is very helpful for analysing the dark energy (DE). SNe are so well known standard candles that their measurement of the universe expansion (Riess et al., 1998; Perlmutter et al., 1998) has been worth the Nobel Prize in 2011. The estimation through SNe Ia of H_0 is even more precise if associated with Cosmic Microwave Background Radiation (CMBR) and Baryon Acoustic Oscillation (BAO) estimations (Weinberg et al., 2013). For this reason, evaluations from GRBs also would validate or limit the parameter H_0 . Nevertheless, the isotropic energy of GRBs extends over 8 orders of magnitude (Lin et al., 2015), but these phenomena can trace the cosmic SFR (Totani, 1997; Porciani and Madau, 2001; Bromm and Loeb, 2006; Kistler et al., 2009; de Souza et al., 2011) and report on the intergalactic medium physics (Barkana and Loeb, 2004; Ioka and Mészáros, 2005; Inoue et al., 2007). Therefore, GRB correlations are potential extremely powerful tools to

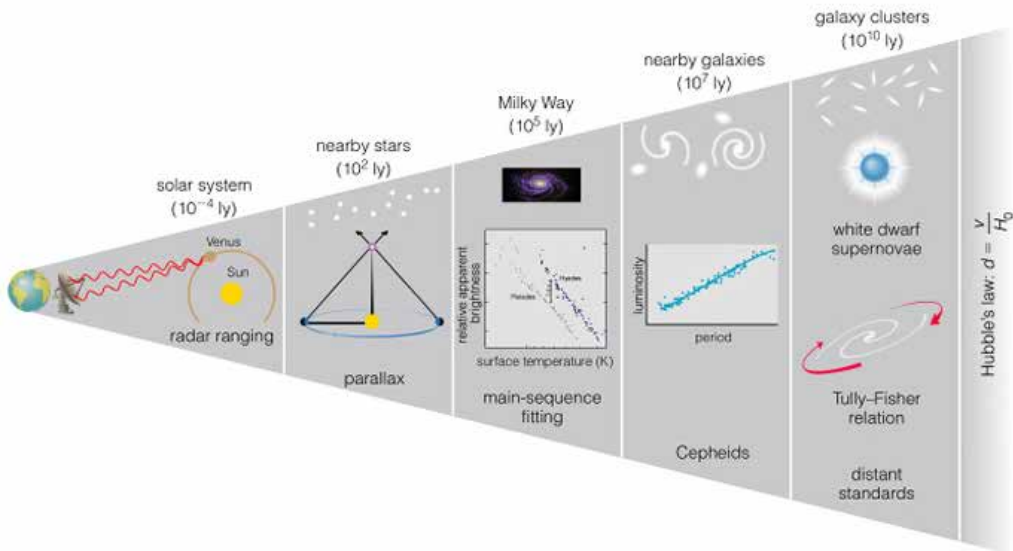


Figure 3.1.1: Distance indicators used in astronomy (from <http://astronomy.nmsu.edu/tharris/ast105/Ast105week14.html>).

explain the physics of GRBs, define a good distance indicator, and examine the universe at high redshift (Salvaterra, 2015).

3.2 Notations, nomenclature and abbreviations

The work presented in this Chapter is based on the article M. G. Dainotti, R. Del Vecchio, and M. Tarnopolski, Advances in Astronomy, Volume 2018, Article ID 4969503, 31 pages, (2018). In this work led by Dr. M.G. Dainotti, the contribution of the thesis author was to select some interesting papers about GRB correlations among prompt emission parameters and to help with figures and text during the manuscript preparation. She was also involved in the discussion about the reply to the referee's comments.

Here a summary of the nomenclature employed in this manuscript is presented. This is mostly taken from the nomenclature used in Dainotti, Del Vecchio, and Tarnopolski (2018) and Dainotti and Del Vecchio (2017). L , F , E , S and T represent the luminosity, the flux, the energy, the fluence and the timescale, respectively. The first subscript indicates the wavelength in which they are computed, while the second displayed the different times or part of the light curve. L indicates the luminosity, and in particular L_{peak} and L_{iso} represent the peak luminosity and the total isotropic luminosity in a given energy band. L_{peak} is computed in this way:

$$L_{\text{peak}} = 4\pi D_L(z, \Omega_M, \Omega_\Lambda)^2 F_{\text{peak}}, \quad (3.1)$$

with $D_L(z, \Omega_M, \Omega_\Lambda)$ the luminosity distance given by

$$D_L(z, \Omega_M, \Omega_\Lambda) = \frac{c(1+z)}{H_0} \int_0^z \frac{dz'}{\sqrt{\Omega_M(1+z')^3 + \Omega_\Lambda}}, \quad (3.2)$$

with Ω_M and Ω_Λ the matter and dark energy density parameters, and z the redshift. Similarly, L_{iso} is obtained:

$$L_{\text{iso}} = 4\pi D_L(z, \Omega_M, \Omega_\Lambda)^2 F_{\text{tot}}. \quad (3.3)$$

Furthermore, α , β and ν , indicate the temporal and spectral decay indices and the frequencies.

Here the nomenclature is shown in detail:

- T_{90} is the time in which 90% of the GRB's fluence, starting from the 5%, is radiated (Kouveliotou et al., 1993).
- T_{45} is the time in which the 45% of the total counts are detected above background (Reichart et al., 2001).
- T_{break} represents the break time in the afterglow light curve (Sari et al., 1999; Willingale et al., 2010).
- T_{peak} is the time at which a given pulse (Fishman et al., 1994; Norris et al., 1996a; Stern and Svensson, 1996; Ryde and Svensson, 2002) in the prompt light curve peaks.
- τ_{lag} and τ_{RT} are the time difference in the arrival to the observer of the high energy (100 – 300 keV) photons and low energy (25 – 50 keV) photons, and the shortest time over which the light curve rises by 50% of the peak flux of the pulse.
- $T_{X,a}$ and $T_{O,a}$ are the time in the X-ray at the end of the plateau and the equivalent in the optical wavelength, respectively. $F_{X,a}$ and $F_{O,a}$ represent their respective fluxes, while $L_{X,a}$ and $L_{O,a}$ denote their respective luminosities. The energy of the plateau can be approximated by $E_{X,\text{plateau}} = (L_{X,a} \times T_{X,a}^*)$.
- $T_{O,\text{peak}}$ and $T_{X,f}$ represent the peak time in the optical band and the time since ejection of the pulse (T_{ej}). $L_{O,\text{peak}}$ and $L_{X,f}$ indicate their respective luminosities. $F_{O,\text{peak}}$ is the flux at time $T_{O,\text{peak}}$.
- $T_{X,\text{peak}}$ defines the peak time in the X-ray range and $F_{X,\text{peak}}$ and $L_{X,\text{peak}}$ indicate its flux and luminosity, respectively.
- $T_{X,p}$ and $T_{X,t}$ display the time at the end of the prompt emission in the W07 model and the time at which the flat and the step decay trends of the light curves join, respectively.
- E_{peak} , E_{iso} , E_γ and E_{prompt} are the spectral peak energy (Mallozzi et al., 1995), the total isotropic energy emitted during the whole burst (e.g., Amati et al. 2002), the

total energy corrected for the beaming factor, and the isotropic energy emitted in the prompt phase, respectively.

- F_{peak} and F_{tot} are the peak and the total fluxes, respectively (Lee and Petrosian, 1996).
- $L_{X,p}$ is the luminosity at the time $T_{X,p}$ in the X-ray band.
- $L_{X,200s}, L_{X,10}, L_{X,11}, L_{X,12}, L_{X,1d}$ and $L_{O,200s}, L_{O,10}, L_{O,11}, L_{O,12}, L_{O,1d}$ represent the X-ray and optical luminosities at 200 s, at 10, 11, 12 hours and at 1 day, respectively; $L_{O,100s}, L_{O,1000s}, L_{O,10000s}, L_{O,7}$ denote the optical luminosity at 100 s, 1000 s, 10000 s and 7 hours; $L_L(\nu, T_{X,a})$ is the optical or X-ray luminosity of the late prompt emission at the time $T_{X,a}$.
- $F_{X,11}, F_{X,1d}$ and $F_{O,11}, F_{O,1d}$ indicate the X-ray and optical fluxes at 11 hours and at 1 day respectively;
- $F_{\gamma,\text{prompt}}, F_{X,\text{afterglow}}$ represent the gamma-ray flux in the prompt and the X-ray flux in the afterglow phase, respectively. $E_{\gamma,\text{prompt}}$ and $E_{X,\text{afterglow}}$ indicate their respective isotropic energies, while $L_{\gamma,\text{prompt}}$ and $L_{X,\text{afterglow}}$ indicate their respective luminosities.
- $E_{O,\text{afterglow}}$ and $E_{X,f}$ represent the optical isotropic energy in the afterglow phase and the break energy of the pulse.
- $E_{k,aft}$ represents the isotropic kinetic afterglow energy in the X-ray band.
- $\alpha_{X,a}, \alpha_{O,>200s}, \alpha_{X,>200s}, \alpha_{\nu,fl}$ and $\alpha_{\nu,st}$ indicate the X-ray temporal decay index in the afterglow phase, in the optical band after 200 s, in the X-ray band after 200 s and the optical or X-ray flat and steep temporal decay indices, respectively.
- $\beta_{X,a}, \beta_{OX,a}$ and $\beta_{O,>200s}$ represent the spectral index of the plateau emission in the X-ray band, the optical-to-X-ray spectral index for the end time of the plateau and the optical spectral index after 200 s.
- $\nu_X, \nu_O, \nu_c, \nu_m$ designate the X-ray and optical frequencies, and the cooling and the peak frequencies of the synchrotron radiation.
- $S_{\text{obs}}, S_{\text{tot}}$, and $S_{\gamma,\text{prompt}}$ represent the observed fluence in the range 50 – 300 keV, the total fluence in the 20 keV – 1.5 MeV energy band, and the prompt fluence in the gamma band correspondent to the rest-frame isotropic prompt energy.
- V indicates the variability of the GRB's light curve. It is calculated from the difference between the observed light curve and its smoothed version, squaring and adding these squared differences over time intervals, and normalizing the result of this sum (Reichart et al., 2001). Different smoothing filters may be applied (see also Li and Paczyński 2006). V_f indicates the variability for a specific fraction of the smoothing timescale for the light curve.

Majority of the parameters mentioned above are presented in the observer frame, except for E_{iso} , E_{prompt} , L_{peak} and L_{iso} . With the upper symbol “ $*$ ” the rest-frame quantities are indicated, like $T_{X,a}^* = T_{X,a}/(1+z)$ and $E_{\text{peak}}^* = E_{\text{peak}}(1+z)$.

The Pearson correlation coefficient (Bevington and Robinson, 2003) is indicated by r , the Spearman correlation coefficient¹ (Spearman, 1904) by ρ , the Kendall correlation coefficient² (Kendall, 1938) by τ , and the p -value (the probability that a correlation is due by chance) is represented by P . Given that almost all the correlations described here are represented by power-laws, the slope is the one of the equivalent log-log correlation.

The Table below (mostly taken from Dainotti, Del Vecchio, and Tarnopolski 2018 and Dainotti and Del Vecchio 2017) presents the abbreviations and acronyms adopted in all the manuscript:

¹This coefficient measures the level of correlation between two quantities using a monotonic function. Its value ranges between -1 and $+1$.

²The Kendall coefficient τ calculates non-parametrically the rank correlation between two variables.

Abbreviation	Meaning
a	Normalization of the correlation
b	Slope of the correlation
b_{int}	Intrinsic slope of the correlation
BH	Black Hole
CL	Confidence Level
DE	Dark Energy
EoS	Equation of State
E4	Sample with $\sigma_E = (\sigma_{\log L_{X,a}}^2 + \sigma_{\log T_{X,a}^*}^2)^{1/2} < 4$
E0095	Sample with $\sigma_E = (\sigma_{\log L_{X,a}}^2 + \sigma_{\log T_{X,a}^*}^2)^{1/2} < 0.095$
FS	Forward Shock
γ	Electron energy distribution power-law index
Γ	Lorentz Factor
GFR	GRB Formation rate, the number of the GRBs as a function of the redshift
H_0	Present-day Hubble constant
h	Hubble constant divided by 100
HD	Hubble Diagram
IC	Intermediate Class GRB
LGRB	Long GRBs
NS	Neutron star
Ω_M	Matter density in Λ CDM model
Ω_Λ	Dark Energy density in Λ CDM model
Ω_k	Curvature in Λ CDM model
RS	Reverse Shock
SNe	Supernovae
SGRB	Short GRB
SFR	Star Formation Rate
$\sigma_{\log L_{X,a}}$	Error in the luminosity
$\sigma_{\log T_{X,a}^*}$	Error in the time
σ_{int}	Intrinsic scatter of the correlation
ULGRB	Ultra Long GRB
V	Variability of the GRB light curve
W07	Willingale et al. (2007)
w_0, w_a	Coefficients of the DE EoS $w(z) = w_0 + w_a z(1+z)^{-1}$
XRFs	X-ray Flashes
z	Redshift

Table 3.1: Table with abbreviations from Dainotti and Del Vecchio (2017).

3.3 The GRB correlations among prompt parameters

Here physical phenomenological correlations between important observables in GRBs are described. Each section briefly summarizes the discovery of the correlations, their discussion in literature, and their physical interpretation.

3.3.1 The $L_{\text{peak}} - \tau_{\text{lag}}$ correlation

Liang and Kargatis (1996) discovered, employing 34 bright GRBs detected by BATSE, that E_{peak} depends linearly to the instantaneous luminosity. Quantitatively,

$$\frac{L_{\text{peak}}}{N} = -\frac{dE_{\text{peak}}}{dt}, \quad (3.4)$$

where N is a normalization constant denoting the pulse luminosity.

The $L_{\text{peak}} - \tau_{\text{lag}}$ anti-correlation was discovered by Norris et al. (2000) with a sample of 6 GRBs with firm redshift (see the left panel of Fig. 3.3.1)

$$\log L_{\text{peak}} = 55.11 - 1.14 \log \tau_{\text{lag}}^*, \quad (3.5)$$

with L_{peak} , in units of $10^{53} \text{ erg s}^{-1}$, calculated between 50 and 300 keV, and τ_{lag}^* in seconds. A correlation in agreement with the previous one was retrieved by Schaefer et al. (2001) with 112 BATSE GRBs:

$$\log L_{\text{peak}} = 52.46 - (1.14 \pm 0.20) \log \tau_{\text{lag}}. \quad (3.6)$$

This correlation well agrees with the outcome found by Norris et al. (2000). In this work, instead L_{peak} is in units of $10^{51} \text{ erg s}^{-1}$. This correlation has been object of discussion and investigation (e.g. Salmonson 2000; Daigne and Mochkovitch 2003; Zhang et al. 2006b).

Schaefer (2004) suggested that the $L_{\text{peak}} - \tau_{\text{lag}}$ correlation is derived by the Liang and Kargatis (1996) correlation from Equation 3.4. This correlation was useful (Schaefer et al., 2001) to infer pseudo-redshifts. Kocevski and Liang (2003) varied the predicted z until the $D_L(z, \Omega_M, \Omega_\Lambda)$ computed through the estimated redshift is in agreement with the measured $D_L(z, \Omega_M, \Omega_\Lambda)$ with a precision of the convergence of these two values of 10^{-3} . This has been performed always fixing a flat Λ CDM model. Additionally, Kocevski and Liang (2003) demonstrated that the GRB's spectral evolution is related to L_{peak} . Instead, Hakkila et al. (2008), finding a different slope (-0.62 ± 0.04), concluded that the $L_{\text{peak}} - \tau_{\text{lag}}$ correlation is a characteristic of the pulse, not a burst's feature.

Tsutsui et al. (2008), using pseudo-redshifts estimated with the use of the Yonetoku correlation (see Section 3.3.6), found that the $L_{\text{peak}} - \tau_{\text{lag}}$ correlation has a small correlation coefficient $\rho = 0.38$ (see the right panel of Fig. 3.3.1). Taking into account the dependence of the

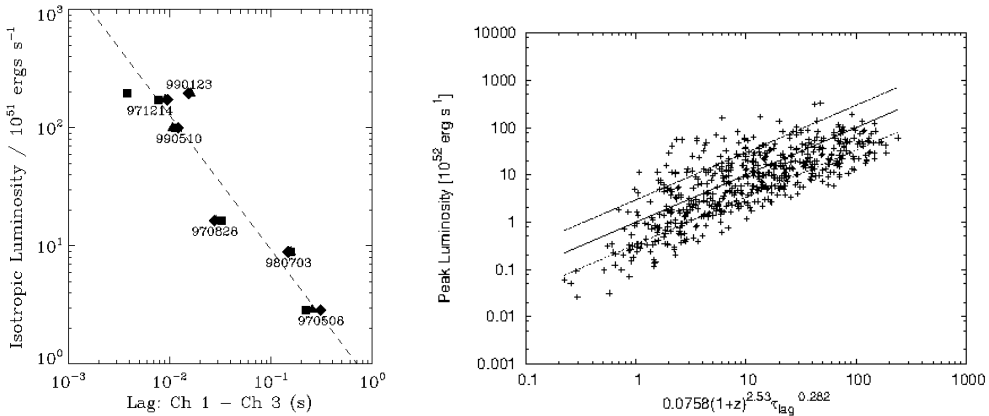


Figure 3.3.1: Left panel: the $L_{\text{peak}} - \tau_{\text{lag}}^*$ correlation adopting six GRBs with known redshift. The power-law fit employing channel 1 (25 – 50 keV) and channel 3 (100 – 300 keV) of the BATSE instrument is displayed by the dashed line. (Figure from Norris et al. (2000). © AAS. Reproduced with permission.) Right panel: the $\log L_{\text{peak}} \sim 2.53 \log(1 + z) - 0.282 \log \tau_{\text{lag}}$ distribution with correlation coefficient $\rho = 0.77$, $P = 7.9 \times 10^{-75}$. The best fit line is represented by the solid line. (Figure from Tsutsui et al. (2008). Copyright © 2008 AIP Publishing.)

luminosity on both redshift and τ_{lag} , they obtained

$$\log L_{\text{peak}} = 50.88 + 2.53 \log(1 + z) - 0.282 \log \tau_{\text{lag}}, \quad (3.7)$$

with L_{peak} in units of $10^{50} \text{ erg s}^{-1}$, τ_{lag} in seconds, $\rho = 0.77$ and $P = 7.9 \times 10^{-75}$. This outcome infers that an eventual $L_{\text{peak}} - \tau_{\text{lag}}$ correlation recovered using Swift data should show dependence on the redshift.

Following this track, Sultana et al. (2012) presented a correlation between the z - and k -corrected τ_{lag} (computed between 50 and 100 keV and between 100 and 200 keV) and L_{peak} for 12 Swift LGRBs. The correction for the time dilatation effect together with the k -correction in the energy bands (Gehrels et al., 2006) makes τ_{lag}^* to be equal to $(1 + z)^{-0.67} \tau_{\text{lag}}$. Sultana et al. (2012) showed that $L_{\text{peak}} - \tau_{\text{lag}}^*$ correlation can be the extrapolation of the LT correlation within the prompt emission. The slope of the $L_{\text{peak}} - \tau_{\text{lag}}^*$ correlation is compatible within 1σ with the slope of the LT correlation (Dainotti et al., 2008, 2010, 2011a, 2013b).

Sultana et al. (2012) retrieved³:

$$\log L_{\text{peak}} = (54.87 \pm 0.29) - (1.19 \pm 0.17) \log [(1 + z)^{-0.67} \tau_{\text{lag}}], \quad (3.8)$$

and

$$\log L_{X,a} = (51.57 \pm 0.10) - (1.10 \pm 0.03) \log T_{X,a}^*. \quad (3.9)$$

³In Sultana et al. (2012) the peak isotropic luminosity is represented by L_{iso} .

with τ_{lag} in ms, T_a^* in seconds, and L in erg s^{-1} . These two correlations have both significant correlation coefficients ($\rho = -0.65$ for the $L_{\text{peak}} - \tau_{\text{lag}}$ correlation and $\rho = -0.88$ for the LT correlation) and have analogous values of the slopes (-1.19 ± 0.17 for the $L_{\text{peak}} - \tau_{\text{lag}}$ and -1.10 ± 0.03 for the LT correlation). Although τ_{lag} and $T_{X,a}^*$ represent different GRB time variables, it is clear that the $L_{\text{peak}} - \tau_{\text{lag}}$ correlation extrapolates into the LT one for timescales $\tau_{\text{lag}} \simeq T_{X,a}^*$.

Ukwatta et al. (2010) confirmed the existence of a correlation between L_{peak}^* and both the time dilated and k -corrected τ_{lag} for 31 Swift GRBs. From their analysis they found $r = -0.68$, $P = 7 \times 10^{-2}$, and the slope equal to -1.4 ± 0.3 , although with a large scatter. In addition, Ukwatta et al. (2012) with a sample of 43 Swift GRBs with measured redshift yielded $r = -0.82$, $P = 5.5 \times 10^{-5}$, and a slope -1.2 ± 0.2 , compatible with earlier findings.

Finally, Margutti et al. (2010) concluded that the X-ray flares follow the same $L_{\text{peak}} - \tau_{\text{lag}}^*$ correlation (between 0.3 and 10 keV in the rest-frame) of the GRBs, and claimed that the emission process of both X-ray flares and GRBs is analogous.

Physical interpretation of the $L_{\text{peak}} - \tau_{\text{lag}}$ correlation

The main hypothesis of Norris et al. (2000) is that the energy formation process is much more important than dissipation in the pulse dynamics. Investigating several pulses in the very luminous LGRB detected by BATSE, it was found that the rise-to-decay ratio is ≤ 1 for pulses with well-defined shape. Moreover, when the ratio becomes lower the pulse appears broader and dimmer. Another interpretation of the $L_{\text{peak}} - \tau_{\text{lag}}$ correlation is the one given by Salmonson (2000) for which this correlation is due to a kinematic effect. In this framework, an emitting region with constant luminosity is the origin of the GRB's emission. Additionally, in this scenario the observed luminosity should be proportional to Γ , while the apparent τ_{lag} to $1/\Gamma$. Nevertheless, Schaefer (2004) noted that several drawbacks are associated with this scenario:

- the variation in the velocity along the line of sight is due to the velocity of the jet expansion together with the cosmological expansion;
- the discrepancies in luminosity and τ_{lag} among GRBs are caused by the different velocities of the emitting regions. This gives consistent results with the $L_{\text{peak}} - \tau_{\text{lag}}$ correlation. Although, such an explanation demands a constant comoving luminosity for all GRBs, which represents a severe requirement;
- Γ and luminosity should vary consistently. This is not the case, because the observed L_{peak} spans more than three orders of magnitude (e.g., Schaefer et al. 2001), while Γ varies less than one order of magnitude (Panaiteescu and Kumar, 2002);
- the observed luminosity should depend linearly on the parameter Γ of the jet. However,

this requirement is not fulfilled. In fact, a number of corrections that produce a nonlinear dependence should be accounted for. For example, the forward jet motion adds a quadratic dependence (Fenimore et al., 1996).

Another interpretation of the $L_{\text{peak}} - \tau_{\text{lag}}$ correlation was suggested by Ioka and Nakamura (2001). They required that the L_{peak} depends on the viewing angle pointing out that a jet with a tiny viewing angle leads to high-luminosity peak in GRBs with a short τ_{lag} . The viewing angle affects also other correlations (see the $L_{\text{peak}} - V$ correlation presented in Section 3.3.2). Additionally, XRFs may be considered as GRBs observed from large viewing angles with large τ_{lag} and negligible variability. However, under the assumption of a particular jet angle distributions, that the rate of GRBs is the same as the SFR, and accounting for selection effects, Lü et al. (2012b) found an anti-correlation between θ_{jet} and the redshift for 77 GRBs. This correlation reads as follows:

$$\log \theta_{\text{jet}} = (-0.90 \pm 0.09) - (0.94 \pm 0.19) \log(1 + z), \quad (3.10)$$

with $\rho = 0.55$ and $P < 10^{-4}$.

Through simulations, they pointed out that the instrumental selection effects play a major role in the observed $\theta_{\text{jet}} - z$ as well as in the $\tau_{\text{lag}} - z$ correlations (Yi et al., 2008). These biases are also relevant in the dependence on the redshift of the shallow decays in the X-ray afterglow phases (Stratta et al., 2009). Recently, Ryan et al. (2015) explored 226 jet opening angles of Swift/XRT GRB light curves with known redshift. As a result, majority of the GRBs was observed off-axis, giving an important role to the viewing angle for the behaviour of the afterglow light curves. Regarding its physical interpretation, Zhang et al. (2009) claimed a connection between the $L_{\text{peak}} - \tau_{\text{lag}}$ correlation and the $L_{\text{peak}} - V$ one (see Section 3.3.2), giving an explanation for the latter correlation through the internal shock scenario (see Section 3.3.2). Later, Uhm and Zhang (2016) employed the synchrotron radiation mechanism to describe the values of τ_{lag} and this explanation is in agreement with observations. An additional possibility to interpret the origin of the $L_{\text{peak}} - \tau_{\text{lag}}$ correlation is provided by Sultana et al. (2012). They interpreted the $L_{\text{peak}} - \tau_{\text{lag}}$ correlation using the following parameter:

$$D = \frac{1}{\Gamma(1 - \beta_0 \cos \theta)(1 + z)}, \quad (3.11)$$

where D is the Doppler factor of a jet at a viewing angle θ and with velocity $\beta_0 \equiv v/c$ at redshift z . D is also related to the rest-frame timescale τ and the observed time t as follows:

$$t = \frac{\tau}{D}. \quad (3.12)$$

Thus, assuming a timescale $\Delta\tau$ in the GRB rest-frame, Equation 3.12 will become $\Delta t = \Delta\tau/D$

in the observer frame. Then, L_{peak} , assuming a power-law spectrum, is given by

$$L_{\text{peak}} \propto D^\alpha, \quad (3.13)$$

with $\alpha \approx 1$. This result reproduced, together with Equation 3.12, the $L_{\text{peak}} - \tau_{\text{lag}}$ correlation. In conclusion, a similar description for the $L_{\text{peak}} - \tau_{\text{lag}}$ and LT correlations is suggested by Sultana et al. (2012) given the similar correlation coefficients and best fit slopes of the two correlations, as already discussed in Section 3.3.1.

3.3.2 The $L_{\text{peak}} - V$ correlation

Fenimore and Ramirez-Ruiz (2000) found the following correlation between L_{peak} and V :

$$\log L_{\text{peak}} = 56.49 + 3.35 \log V, \quad (3.14)$$

L_{peak} , in erg s^{-1} , is computed in the rest-frame between 50 and 300 keV. After calibrating the correlation, a sample of 220 GRBs detected by BATSE were used to compute luminosities, distances, and the GRB formation rate (GFR). Nevertheless, the authors state that further analysis for the validation of this $L_{\text{peak}} - V$ correlation was needed.

Employing a sample of 20 GRBs detected by CGRO/BATSE, KONUS/Wind and Ulysses/GRB, Reichart et al. (2001) discovered the following correlation:

$$\log L_{\text{peak}} \sim (3.3_{-0.9}^{+1.1}) \log V. \quad (3.15)$$

with $\rho = 0.8$ and $P = 1.4 \times 10^{-4}$ (see the left panel of Fig. 3.3.2); L_{peak} was calculated between 50 and 300 keV in the observer frame. The $\log L_{\text{peak}} - \log V_f$ correlation can be represented in this way:

$$\log V_f(L) = \log \bar{V}_f + b + m(\log L_{\text{peak}} - \log \bar{L}_{\text{peak}}), \quad (3.16)$$

where $b = 0.013_{-0.092}^{+0.075}$, $m = 0.302_{-0.075}^{+0.112}$, and \bar{V}_f and \bar{L}_{peak} are the median values of V_f and L_{peak}

An update of the $\log L_{\text{peak}} - \log V$ correlation was described in Guidorzi et al. (2005). Employing 32 GRBs detected by BeppoSAX, CGRO/BATSE, HETE-2 and KONUS, they found the following correlation (see the right panel of Fig. 3.3.2):

$$\log L_{\text{peak}} = 3.36_{-0.43}^{+0.89} + 1.30_{-0.44}^{+0.84} \log V, \quad (3.17)$$

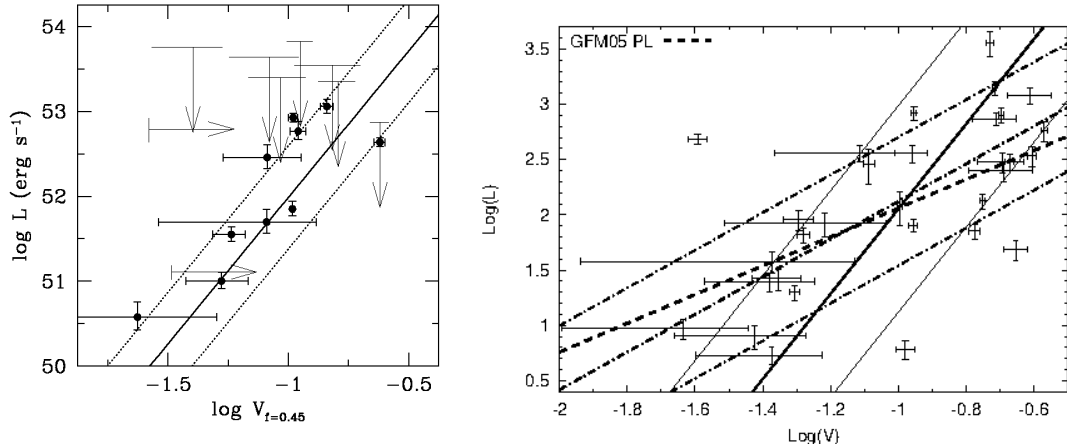


Figure 3.3.2: Left panel: the $L_{\text{peak}} - V_{f=0.45}$ correlation with the solid and dotted lines the best fit line and 1σ deviation, respectively. (Figure from Reichart et al. (2001). © AAS. Reproduced with permission.) Right panel: the $\log L_{\text{peak}} - \log V$ correlation for a data set of 32 GRBs. The solid lines are obtained through the Reichart et al. (2001) method, dashed-dotted lines through the D'Agostini (2005) method and the dashed lines are retrieved by Guidorzi et al. (2005). (Figure from Guidorzi et al. (2006).)

with $\rho = 0.625$ and $P = 10^{-4}$, and L_{peak} in units of $10^{50} \text{ erg s}^{-1}$.

The last result was criticized by Reichart and Nysewander (2005), who pointed out that in Guidorzi et al. (2005) the variance of the sample in their fit was not taken into account. Reichart and Nysewander (2005) with an updated data set confirmed the results obtained in Reichart et al. (2001), finding a correlation with slope $3.4^{+0.9}_{-0.6}$ and variance $\sigma_V = 0.2 \pm 0.04$.

Later, Guidorzi et al. (2006) analysed the $L_{\text{peak}} - V$ correlation by applying the statistical fitting methods described in Reichart et al. (2001) and D'Agostini (2005). The former method recovered a $L_{\text{peak}} - V$ correlation compatible with earlier works:

$$\log L_{\text{peak}} \sim 3.5^{+0.6}_{-0.4} \log V. \quad (3.18)$$

Instead, the latter method retrieved a correlation slope lower than the one by Reichart et al. (2001):

$$\log L_{\text{peak}} \sim 0.88^{+0.12}_{-0.13} \log V. \quad (3.19)$$

The latter slope is in agreement with the outcomes by Guidorzi et al. (2005), but incompatible with those by Reichart and Nysewander (2005).

Rizzuto et al. (2007), using 36 Swift LGRBs with known redshifts and $L_{\text{peak}} > 5 \times 10^{50} \text{ erg s}^{-1}$ between 100 and 1000 keV, investigated the $L_{\text{peak}} - V$ correlation. Rizzuto et al. (2007) assumed two definitions for the variability V : the first by Reichart et al. (2001), V_R , and the latter by Li and Paczyński (2006), V_{LP} , which selects only high-frequency variability. In this way, Rizzuto et al. (2007) obtained:

$$\log L_{\text{peak}} \sim (2.3 \pm 0.17) \log V_{\text{LP}}, \quad (3.20)$$

with $\rho = 0.758$ and $P = 0.011$, and

$$\log L_{\text{peak}} \sim (1.7 \pm 0.4) \log V_{\text{R}}, \quad (3.21)$$

with $\sigma_{\log L} = 0.58^{+0.15}_{-0.12}$, $\rho = 0.115$, and $P = 0.506$. From their work six dim GRBs (GRB 050223, GRB 050416A, GRB 050803, GRB 051016B, GRB 060614 and GRB 060729) were classified as outliers of the correlation due to their high values of V_{R} . For this reason, the correlation appears to be valid for luminous GRBs only. In conclusion, the variance in this correlation is more significant than in other ones. Thus, this outcome show that this correlation is less robust. Nevertheless, it is worth examining the physical interpretation of this correlation for additional studies.

Physical interpretation of the $L_{\text{peak}} - V$ correlation

In the framework of the internal and external shock model (Piran, 2004; Mészáros, 2006), Fenimore and Ramirez-Ruiz (2000) pointed out that the interpretation of the $L_{\text{peak}} - V$ correlation is not clear. Indeed, larger initial Γ values should generate more efficient collisions. After modifying several variables, i.e. Γ , the initial shells' mass, and the external medium density, it is not possible to reproduce the observed variability V . Therefore, the central engine seems to be crucial in the description of this correlation. Salmonson and Galama (2002) investigated the correlation assuming that the GRB variability is due to a variation in the value of the opening angles of the jets. Small values of θ_{jet} produce faster outflows. They found out that under these assumptions it is possible to explain high luminosities, high variability values, short pulse lags, and a jet break at early time for GRBs observed on-axis. Instead, low luminosities, flatter light curves, broader pulse lags, and jet breaks at later times suggest larger viewing angles.

Guidorzi et al. (2006) suggested that a stronger dependence of Γ on θ_{jet} is needed to interpret this correlation within the jet-emission model. However, given that V and L_{peak} are proportional to Γ and fast rise times and short pulse durations lead to high variability, Schaefer (2007) attributed the origin of the $L_{\text{peak}} - V$ correlation to be based on relativistically shocked jets.

3.3.3 The $L_{\text{iso}} - \tau_{\text{RT}}$ correlation and its physical interpretation

Schaefer (2002) proposed the correlation between τ_{RT} and L_{iso} :

$$L_{\text{iso}} \propto \tau_{\text{RT}}^{-N/2}, \quad (3.22)$$

with the exponent $N \simeq 3$ (see also Schaefer 2002, 2007). From this correlation it follows that high luminosities are produced by fast rises and low luminosities from slow rises. Regarding the physics of the shocked jet, τ_{RT} represents the largest delay between the time of the arrival of photons from the center of the visible region and their arrival time from the edge of the same region.

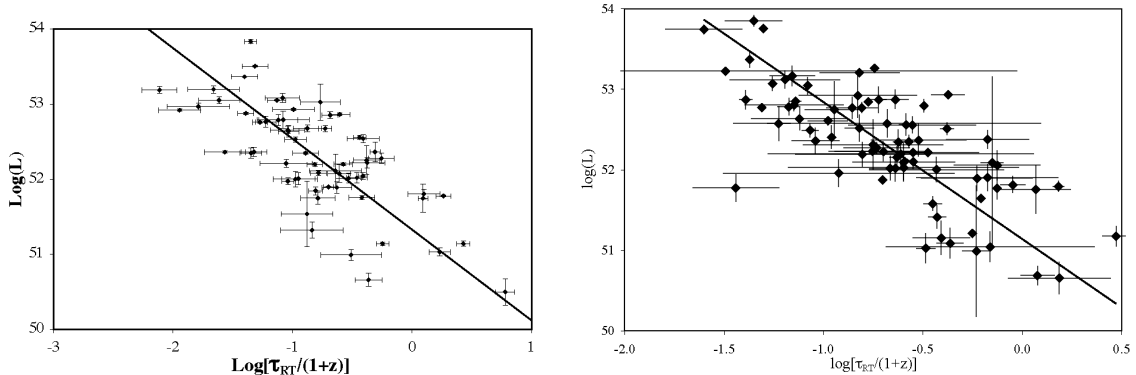


Figure 3.3.3: Left panel: the $\log L_{\text{iso}} - \log \tau_{\text{RT}}^*$ correlation with best fit line and errors displayed. (Figure from Schaefer (2007). @ AAS. Reproduced with permission.) Right panel: the $\log L_{\text{iso}} - \log \tau_{\text{RT}}^*$ correlation and its best fit line. (Figure from Xiao and Schaefer (2009). @ AAS. Reproduced with permission.)

This delay generating the $\tau_{\text{RT}} \propto \Gamma^{-2}$ correlation is due to the angular opening of the emitted jet. Panaiteescu and Kumar (2002) claimed the existence of a minimum radius similar for all the GRBs under which the emission from the material is not efficient anymore.

Using the common dependence on Γ of τ_{RT} and L_{iso} , Schaefer (2007) confirmed that $\log L_{\text{iso}}$ is $\sim -N/2 \log \tau_{\text{RT}}$. With a sample of 69 BATSE and Swift GRBs, the correlation reads as follows:

$$\log L_{\text{iso}} = 53.54 - 1.21 \log \tau_{\text{RT}}^*, \quad (3.23)$$

with L_{iso} in erg s^{-1} and τ_{RT}^* in seconds. The 1σ errors are represented in the left panel of Figure 3.3.3. The error in $\log L_{\text{iso}}$ is

$$\sigma_{\log L_{\text{iso}}}^2 = \sigma_a^2 + \left[\sigma_b \log \frac{\tau_{\text{RT}}^*}{0.1 \text{ s}} \right]^2 + \left(\frac{0.43 b \sigma_{\text{RT}}}{\tau_{\text{RT}}} \right)^2 + \sigma_{\text{RT,sys}}^2, \quad (3.24)$$

where Schaefer (2007) took into account an additional scatter, $\sigma_{\text{RT,sys}}$. When $\sigma_{\text{RT,sys}} = 0.47$, the χ^2 of the best fit is equal to 1. With a sample of 107 GRBs detected by BATSE, HETE-2, KONUS and Swift, with measured spectroscopic redshift (see the right panel of Fig. 3.3.3), Xiao and Schaefer (2009) pointed out, accounting also for the Poisson noise, the following correlation:

$$\log L_{\text{iso}} = 53.84 - 1.70 \log \tau_{\text{RT}}^*, \quad (3.25)$$

with the same units as in Equation 3.23.

From this analysis they yielded that the smoothing of the light curve to calculate the τ_{RT} is relevant because can lead to underestimation/overestimation of this parameter. This problem can be very significant for the low luminosity bursts. In conclusion, Schaefer (2007) provided the physical interpretation of this correlation. Indeed, in his analysis the quickest increase in a light curve is linked to Γ . The luminosity of the burst is proportional to Γ^N with $3 < N < 5$. For this reason, the $\tau_{\text{RT}} - \Gamma$ and the $L_{\text{iso}} - \Gamma$ correlations are able to retrieve the $L_{\text{iso}} - \tau_{\text{RT}}$ one.

3.3.4 The $\Gamma_0 - E_{\text{prompt}}$ and $\Gamma_0 - L_{\text{iso}}$ correlations and their physical interpretation

Freedman and Waxman (2001), within the fireball scenario, pointed out that the emission reaching the observer is beamed in an angle $\simeq 1/\Gamma(t)$, the total energy E should be interpreted as released spherically symmetric, $\epsilon_e = \xi_e E/4\pi$, the energy of the fireball divided by the solid angle, where ξ_e is the electron energy fraction. Within this scenario it was found that

$$\Gamma(t) = 10.6 \left(\frac{1+z}{2} \right)^{3/8} \left(\frac{E_{\text{prompt}}}{n_0} \right)^{1/8} t^{-3/8}, \quad (3.26)$$

where E_{prompt} is in units of 10^{53} erg, n_0 is the fireball uniform ambient medium in units of cm^{-3} , and t is the duration of the expansion of the fireball measured in days. As previously found by Waxman (1997); Wijers and Galama (1999) and Granot et al. (1999) for GRB 970508, ξ_e from the afterglow observations should have value close to equipartition, namely $\xi_e \simeq \frac{1}{3}$. A particular case is given by Wijers and Galama (1999) for GRB 971214, where $\xi_e \simeq 1$.

Later, Liang et al. (2010) found a $\log \Gamma_0 - \log E_{\text{prompt}}$ correlation with the Lorentz factor at the beginning of the fireball emission Γ_0 (see the left panel of Fig. 3.3.4) using a data set of 20 optical and 12 X-ray Swift GRBs:

$$\log \Gamma_0 = (2.26 \pm 0.03) + (0.25 \pm 0.03) \log E_{\text{prompt}}, \quad (3.27)$$

giving $\rho = 0.89$, $P < 10^{-4}$, and $\sigma = 0.11$.

The majority of GRBs with a lower limit of Γ_0 are inside the 2σ region (see the dashed lines in the left panel of Fig. 3.3.4), while GRBs with a tentative Γ_0 computed from the afterglow or the RS peaks are usually found above the best fit line. Smaller values of Γ_0 were in agreement with this correlation. This evidence happens when Γ_0 are computed through a sample of optical afterglow light curves displaying a decay since the beginning of the observation.

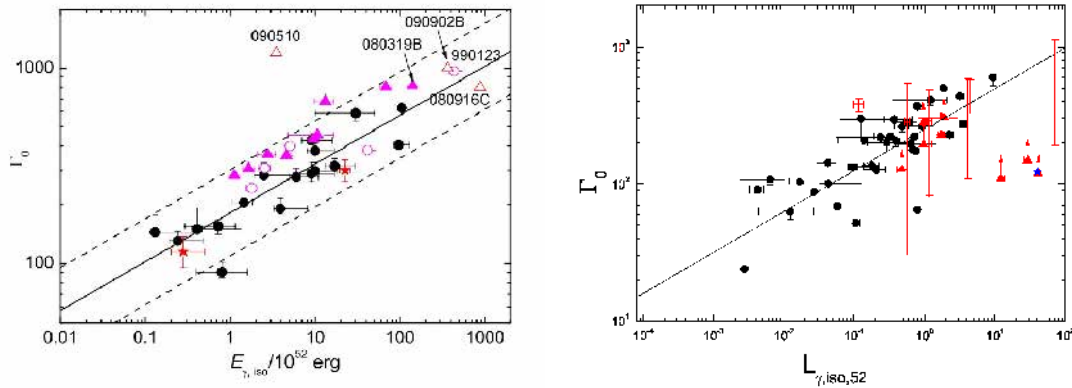


Figure 3.3.4: Left panel: the $\log \Gamma_0 - \log E_{\text{prompt}}$ distribution. The red stars represent GRBs 070208 and 080319C, which have visible afterglow phase in X-ray, pink open circles indicate the GRBs with Γ_0 obtained by RS peaks or possible afterglow peaks, pink solid triangles show the GRBs with lower values of Γ_0 calculated from single power-law decay light curves, and red open triangles display GRBs with strong lower values of Γ_0 for GRBs 080916C, 090902B, and 090510 retrieved from the limits on the opacity through the detections by Fermi/LAT. The best fit line is represented by the solid line. The 2σ deviation is indicated by the two dashed lines. (Figure from Liang et al. (2010). @ AAS. Reproduced with permission.) Right panel: the $\log \Gamma_0 - \log L_{\text{iso}}$ correlation. The triangles indicates the GRBs with only lower limits and the star represents the SGRB 090510. (Figure from Lü et al. (2012a). @ AAS. Reproduced with permission.)

More recently, Ghirlanda et al. (2011) and Lü et al. (2012a) validated the $\log \Gamma_0 - \log E_{\text{prompt}}$ correlation. The first analysed the spectra between 8 keV and 35 MeV of 13 Fermi/GBM SGRBs. Their findings verified the previous results.

To compute Γ_0 , Lü et al. (2012a) applied three approaches to a data set of 51 GRBs with spectroscopic redshifts. The first method requires T_{peak} of the afterglow phase as the time at which the external FS slows down (Sari and Piran, 1999); the second one assumes that the gamma-rays in the GeV band are transparent to the creation of electron-positron pair, providing a lower constraint on Γ_0 of the emitting region (Lithwick and Sari, 2001a); the last one considers that an upper limit on Γ_0 can be computed from the inactivity interval among the prompt pulses (Zou and Piran, 2010), in which the external shock must vanish. Employing 38 GRBs with Γ_0 obtained through the first method, they found out:

$$\log \Gamma_0 = (1.96 \pm 0.002) + (0.29 \pm 0.002) \log E_{\text{prompt}}, \quad (3.28)$$

with $r = 0.67$ and E_{prompt} in units of 10^{52} erg. Furthermore, correcting the energy for the beaming effect, they found also a correlation between Γ_0 and L_{iso} (see the right panel of Fig. 3.3.4) given by:

$$\log \Gamma_0 = (2.40 \pm 0.002) + (0.30 \pm 0.002) \log L_{\text{iso}}, \quad (3.29)$$

with $r = 0.79$.

In regard to the physical interpretation, Liang et al. (2010) interpreted this correlation due to the connection of E_{prompt} with Γ_0 , stressing the validity of the fireball deceleration model. Lü et al. (2012a) claimed that a jet fuelled by neutrino-annihilation well describes the correlation. This suggests the presence of a BH spin not very swift and a high rate of accretion. Zhang and Pe'er (2009), Fan (2010), and Zhang and Yan (2011) proposed a model consisting of a magnetic dominated jet, because it has already been shown that magnetic fields are an important characteristic for the BH central engine models (Lei et al., 2009).

3.3.5 Correlations between the energetics and the peak energy

The $\langle E_{\text{peak}} \rangle - F_{\text{peak}}$ and the $E_{\text{peak}} - S_{\text{tot}}$ correlations

Selecting 399 GRBs with $F_{\text{peak}} \geq 1 \text{ ph cm}^{-2} \text{ s}^{-1}$ between 50 and 300 keV Mallozzi et al. (1995) found out a correlation between $\langle E_{\text{peak}} \rangle$ and F_{peak} with $\rho = 0.90$ and $P = 0.04$. E_{peak} is given by the Comptonized photon model:

$$\frac{dN}{dE} = A e^{-E(2+\beta_S)/E_{\text{peak}}} \left(\frac{E}{E_{\text{piv}}} \right)^{\beta_S}, \quad (3.30)$$

where A indicates the normalization, β_S represents the spectral index, and the pivotal energy, $E_{\text{piv}} = 100 \text{ keV}$. Indeed, dividing the data set in 5 bins of F_{peak} (see Fig. 3.3.5) it appeared that dim GRBs had a smaller $\langle E_{\text{peak}} \rangle$.

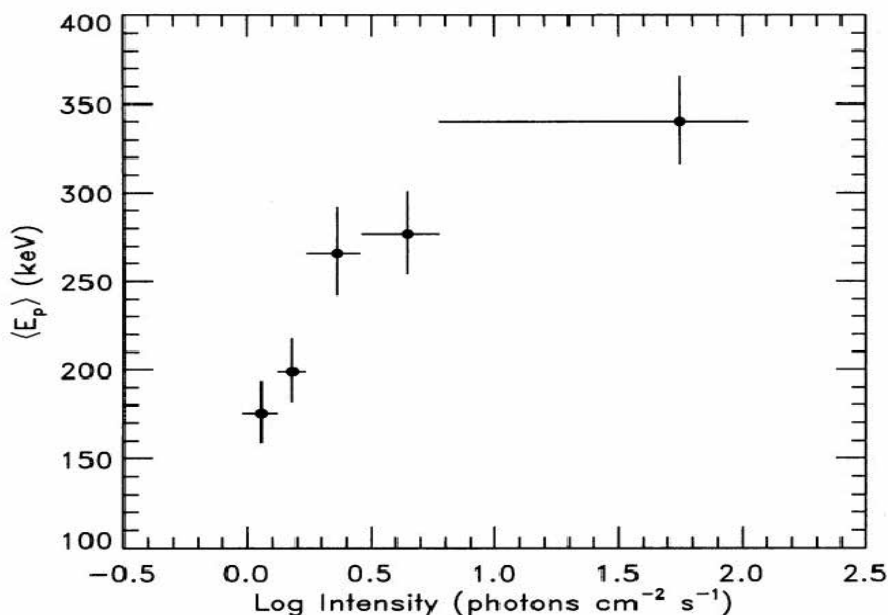


Figure 3.3.5: Peak energies versus intensity with displayed error bars for five GRB sets. The log intensity bin widths are indicated by the horizontal bars. (Figure from Mallozzi et al. (1995). © AAS. Reproduced with permission.)

Then, adopting 1000 simulated GRBs at similar energies to those by Mallozzi et al. (1995), Lloyd et al. (2000a) found a significant $E_{\text{peak}} - S_{\text{tot}}$ correlation (see the left panel of Fig. 3.3.6) given by:

$$\log E_{\text{peak}} \sim 0.29 \log S_{\text{tot}}, \quad (3.31)$$

with $\tau = 0.80$ and $P = 10^{-13}$.

Moreover, they compared the $E_{\text{peak}} - S_{\text{tot}}$ correlation to the $E_{\text{peak}} - F_{\text{peak}}$ one (see the right panel of Fig. 3.3.6). They selected a subsample composed of only the brightest GRBs, namely with the following selection criteria: $F_{\text{peak}} \geq 3 \text{ ph cm}^{-2} \text{ s}^{-1}$, $S_{\text{obs}} \geq 10^{-6} \text{ erg cm}^{-2}$, and $S_{\text{tot}} \geq 5 \times 10^{-6} \text{ erg cm}^{-2}$. This choice guarantees that only the spectral parameters that are robust and not close to the detector threshold are taken into account in this analysis. Indeed, the sensitivity over a specific interval of energies of the instruments, in particular BATSE, and the limits on the trigger do not allow to avoid the observational biases. However, the brightest GRBs show a weak $E_{\text{peak}} - F_{\text{peak}}$ correlation. On the other hand, a tight $E_{\text{peak}} - S_{\text{tot}}$ correlation was found for both the whole sample and the sample composed of the brightest GRBs, for which it is simpler to treat the truncation biases and the interpretation of the cosmology is easier.

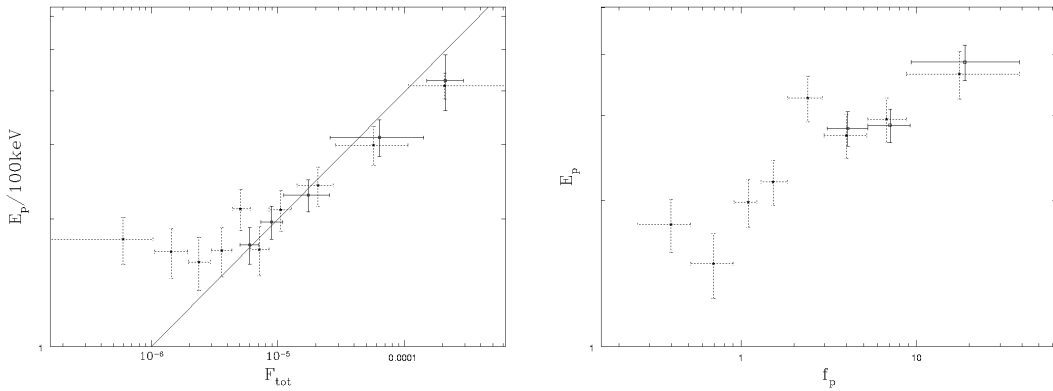


Figure 3.3.6: E_{peak} versus (left panel) S_{tot} and (right panel) F_{peak} distributions for the complete and sub spectral samples indicated with dashed and solid points. The best fit is represented by the solid line. (Figures from Lloyd et al. (2000a). @ AAS. Reproduced with permission.)

The study of the Amati (see Section 3.3.5) and the Ghirlanda (see Section 3.3.5) correlations is grounded on this correlation. The outcomes by Lloyd et al. (2000a) are independent of the number of GRBs or other parameters' distribution. Nevertheless, the results from GRBs with known redshift are in disagreement with the narrow distributions for the radiated energy or luminosity. So farther investigation was needed.

Later, Goldstein et al. (2010) yielded that the $E_{\text{peak}}/S_{\text{tot}}$ can be a useful estimator of the ratio between the energy at which majority of gamma-rays are emitted and the total energy. They found out that the $E_{\text{peak}} - S_{\text{tot}}$ correlation is important for distinguishing LGRBs

from SGRBs. The most important point of this correlation is that since the energy ratio is proportional only to the square of the luminosity distance (hereafter $D_L(z, \Omega_M, \Omega_\Lambda)$), it is easy to remove the cosmological dependence from the discussed parameters. This allows for the use of the energy ratio to classify GRBs.

Finally, using 51 LGRBs and 11 bright SGRBs detected by Fermi/GBM, Lu et al. (2012) investigated the $E_{\text{peak}} - S_{\text{tot}}$ correlation. They calculated the distance of the data from the best fit line of the correlation obtaining a value for the scatter of 0.17 ± 0.08 . This outcome was already presented by Golenetskii et al. (1983); Borgonovo and Ryde (2001); Ghirlanda et al. (2010); Guiriec et al. (2010), and Ghirlanda et al. (2011).

The $E_{\text{peak}} - E_{\text{iso}}$ correlation

Due to the limited number of GRBs observed with precise redshift, the correlation between E_{peak} and S_{tot} was discovered in the observer frame, as shown in Section 3.3.5. Amati et al. (2002) found a tighter $E_{\text{peak}} - E_{\text{iso}}$ correlation, also known as the Amati correlation, using 12 GRBs with known redshifts detected by BeppoSAX. The correlation is given by:

$$\log E_{\text{peak}} \sim (0.52 \pm 0.06) \log E_{\text{iso}}, \quad (3.32)$$

with $r = 0.949$, $P = 0.005$, and E_{iso} :

$$E_{\text{iso}} = 4\pi D_L(z, \Omega_M, \Omega_\Lambda)^2 S_{\text{tot}} (1+z)^{-2}. \quad (3.33)$$

Differently from Bloom et al. (2001), Amati et al. (2002) computed the GRB spectra in the rest-frames and obtained the radiated energy using the Band et al. (1993) functional form between 1 and 10^4 keV. In this work a Friedman-Lemaître-Robertson-Walker cosmological model was assumed with $H_0 = 65 \text{ km s}^{-1} \text{ Mpc}^{-1}$, $\Omega_M = 0.3$, $\Omega_\Lambda = 0.7$. The cosmological time dilation and spectral redshift have also been taken into consideration.

Adding 10 BeppoSAX GRBs with measured redshift to the sample used in Amati et al. (2002), Amati (2003) pointed out the following correlation:

$$\log E_{\text{peak}} = (2.07 \pm 0.03) + (0.35 \pm 0.06) \log E_{\text{iso}}, \quad (3.34)$$

with $r = 0.92$, $P = 1.1 \times 10^{-8}$, E_{peak} in keV, and E_{iso} in units of 10^{52} erg. The correlation is highly significant given that it has been established through a bigger sample than the one used in Amati et al. (2002), but with a compatible correlation coefficient.

Using HETE-2 GRBs and enlarging the sample to XRRs and XRFs also, Lamb et al. (2004) and Sakamoto et al. (2004) obtained similar outcomes to the earlier ones with a correlation spanning over three orders of magnitude in E_{peak} and five orders of magnitude in E_{iso} . These

results were improved by Ghirlanda et al. (2004b), who, with new 29 events with known redshifts, retrieved a correlation with $r = 0.803$ and $P = 7.6 \times 10^{-7}$ (see the left panel in Fig. 3.3.8). The rise in the number of GRBs was possible due to the additional measurements of the redshift.

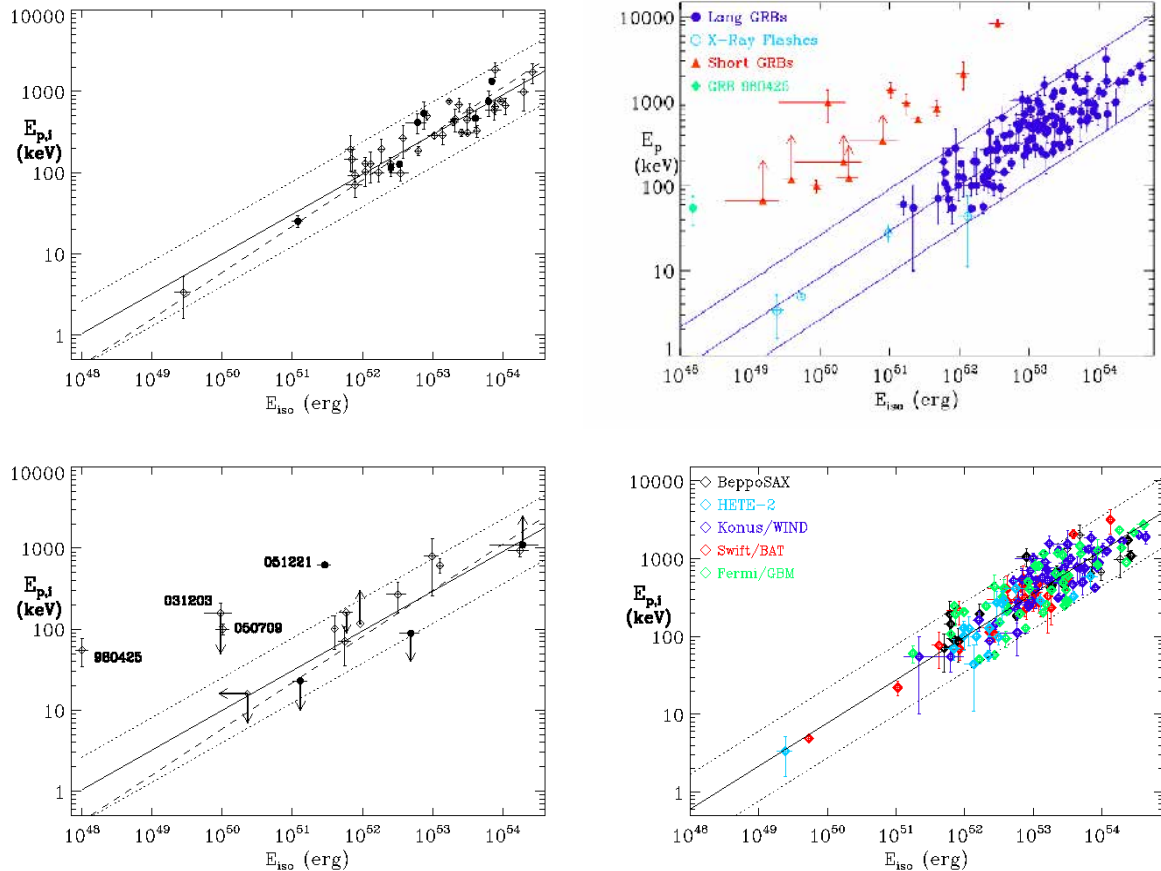


Figure 3.3.7: Upper left panel: the $E_{\text{peak}} - E_{\text{iso}}$ distribution for 41 GRBs/XRFs. Swift GRBs are represented by the filled circles. The best fit line is indicated by the solid line, while the best fit line without the sample variance is displayed by the dashed line. (Figure from Amati (2006).) Upper right panel: the $E_{\text{peak}} - E_{\text{iso}}$ correlation with the best fit line and the $\pm 2\sigma$ confidence area for LGRBs and XRFs displayed. (Figure from Amati (2012). Copyright @ 2012 World Scientific Publishing Company.) Bottom left panel: the $E_{\text{peak}} - E_{\text{iso}}$ correlation for 12 GRBs, the sub-energetic event GRB 980425 and for the SGRBs 050709 and 051221. Swift GRBs are indicated by filled circles. The best fit line is represented by the solid line, while the best fit line calculated without the sample variance is displayed from the dashed line. (Figure from Amati (2006).) Bottom right panel: the $E_{\text{peak}} - E_{\text{iso}}$ correlation with the best fit line indicated by the black line. (Figure from Amati and Della Valle (2013). Copyright @ 2013 World Scientific Publishing Company.)

Ghirlanda et al. (2005a) confirmed the $E_{\text{peak}} - E_{\text{iso}}$ correlation obtained from 442 BATSE LGRBs for which the estimate of E_{peak} was possible and with pseudo-redshifts obtained through the $L_{\text{peak}} - \tau_{\text{lag}}$ correlation. They compared the correlation derived from this sample with the one retrieved from a sample of 27 GRBs with measured spectroscopic redshifts. Due to the negligible influence of the outliers, the scatter of the data in both the correlations has compatible values, but the slope of the correlation for the 442 BATSE LGRBs is slightly

smaller (0.47) than the one for the 27 GRBs with measured spectroscopic redshifts (0.56).

Amati (2006) investigated further the $E_{\text{peak}} - E_{\text{iso}}$ correlation (see the upper left and bottom left panels of Fig. 3.3.7) by employing the following requirements: a) 41 LGRBs/XRFs with measured z and E_{peak} , b) 12 GRBs with uncertain z and/or E_{peak} , c) 2 SGRBs with confirmed z and E_{peak} , and d) the low-energetic GRB 980425/SN 1998bw and GRB 031203/SN 2003lw. The upper right panel of Figure 3.3.7 presents the samples. They obtained:

$$\log E_{\text{peak}} = 1.98_{-0.04}^{+0.05} + (0.49_{-0.05}^{+0.06}) \log E_{\text{iso}}, \quad (3.35)$$

with $\rho = 0.89$, $P = 7 \times 10^{-15}$, and the same units as in Equation 3.34. From this analysis it was found that this correlation can be a significant discriminant among distinct GRB types, because some of the low-energetic GRBs (980425 and possibly 031203) and SGRBs appear to not follow the $E_{\text{peak}} - E_{\text{iso}}$ correlation, while the case of GRB 060218 is consistent with the correlation. Thus, more data can shed light on this topic. The normalization of the correlation obtained by Amati (2006) is comparable to those retrieved by different space missions.

Ghirlanda et al. (2008) found out that XRFs obey the $E_{\text{peak}} - E_{\text{iso}}$ correlation. Using 76 GRBs detected by HETE-2, KONUS/Wind, Swift and Fermi/GBM, they found the following correlation:

$$\log E_{\text{peak}} \sim (0.54 \pm 0.01) \log E_{\text{iso}}. \quad (3.36)$$

This result suggested a strong correlation without additional outliers (except for the well known outliers GRB 980425 and GRB 031203).

Later, using 95 Fermi GRBs with known z , Amati et al. (2009) found out the following $E_{\text{peak}} - E_{\text{iso}}$ correlation:

$$\log E_{\text{peak}} \sim 0.57 \log E_{\text{iso}}, \quad (3.37)$$

with $\rho = 0.88$ and $P < 10^{-3}$. Analysing the highly energetic LGRBs 080916C and 090323 and the SGRB 090510, Amati et al. (2009) found that LGRBs whether they are very energetic or low luminous, anyway follow the $E_{\text{peak}} - E_{\text{iso}}$ correlation. While, SGRBs do not follow the correlation, as in the case of GRB 090510, again independently of their luminosities. They concluded that in the brightest and most energetic LGRBs the emission mechanism should be the same as for other long events with an average luminosity and XRFs, because they all satisfy the Amati correlation.

Using a broadened sample of 120 GRBs, Amati (2012) updated the work by Amati et al. (2008) (see the upper right panel of Fig. 3.3.7) pointing out the correlation:

$$\log E_{\text{peak}} = 2 + 0.5 \log E_{\text{iso}}, \quad (3.38)$$

with the same units as in Equations 3.34 and 3.35. Employing a set of 153 GRBs with known z , E_{peak} , E_{iso} and T_{90} detected by several instruments, Qin and Chen (2013) studied the discrepancy between measured E_{peak} and those derived by the best fit line of the Amati correlation. They discovered an explicit bimodality: the Amati GRBs, obeying the Amati correlation, and the non-Amati GRBs, not obeying it. In the case of Amati type GRBs it was obtained:

$$\log E_{\text{peak}} = (2.06 \pm 0.16) + (0.51 \pm 0.12) \log E_{\text{iso}} \quad (3.39)$$

with $r = 0.83$ and $P < 10^{-36}$, instead adopting the set of non-Amati GRBs:

$$\log E_{\text{peak}} = (3.16 \pm 0.65) + (0.39 \pm 0.33) \log E_{\text{iso}} \quad (3.40)$$

with $r = 0.91$, $P < 10^{-7}$, E_{peak} in keV, and E_{iso} in units of 10^{52} erg. Furthermore, they claimed that Amati GRBs are connected with energetic LGRBs, while non-Amati GRBs are for the majority of the cases associated with SGRBs. The two groups of GRBs are noticeably divided, thus these two types of GRBs can be catalogued without difficulties.

Selecting 43 Fermi GRBs (with measured redshifts) based on specific criteria regarding the duration and spectral indices, Heussaff et al. (2013) retrieved the correlation:

$$\log E_{\text{peak}} = 2.07 + 0.49 \log E_{\text{iso}}, \quad (3.41)$$

with $\rho = 0.70$, $P = 1.7 \times 10^{-7}$. The correlation has been computed with analogous units to the earlier Amati correlations.

Employing 156 LGRBs with measured z and E_{peak} , Amati and Della Valle (2013) validated the Amati correlation showing a slope $\simeq 0.5$ (see the bottom right panel of Fig. 3.3.7). Then, Basak and Rao (2012) claimed that a time-resolved Amati correlation is verified also in each GRB with normalization and slope compatible with those obtained with time-averaged spectra. Actually, this correlation appears even stronger than the time-integrated correlation (Basak and Rao, 2013). Time-resolved E_{peak} and E_{iso} were computed at distinct moments of the prompt phase (see also Ghirlanda et al. 2010; Lu et al. 2012; Frontera et al. 2012 and Section 3.3.6).

The $E_{\text{peak}} - E_{\gamma}$ correlation

Ghirlanda et al. (2004b) determined for the first time the $E_{\text{peak}} - E_{\gamma}$ correlation where E_{γ} is the energy corrected for the beaming factor:

$$E_{\gamma} = (1 - \cos \theta_{\text{jet}}) \times 4\pi \times D_L^2(z, \Omega_M, h) \times S_{\gamma, \text{prompt}} / (1 + z)^2. \quad (3.42)$$

This correlation is also called the Ghirlanda correlation. It was obtained by employing a

set of 40 GRBs with measured z and E_{peak} . To compute E_{γ} using E_{iso} , θ_{jet} , which however is observed only for less than half of the bursts, is needed. For computing this parameter, a theoretical assumptions need to be made regarding the density medium, the radiative efficiency and the energy (see Equation 2.7 in Section 2.2). They retrieved a correlation with slope 0.7, $\rho = 0.88$, and $P = 2.7 \times 10^{-8}$.

Opposed to Ghirlanda et al. (2004b), Liang and Zhang (2005) took into account a sample composed of 15 GRBs with known z , E_{peak} and a purely phenomenological time T_{break} of the afterglow phase in the optical band. Thus, circumventing any hypotheses on the theoretical model regarding T_{break} , they found the following correlation:

$$\log E_{\gamma} = (0.85 \pm 0.21) + (1.94 \pm 0.17) \log E_{\text{peak}}^* - (1.24 \pm 0.23) \log T_{\text{break}}^*, \quad (3.43)$$

where E_{γ} is in units of 10^{52} erg, E_{peak}^* in units of 100 keV, T_{break}^* is measured in days, with $\rho = 0.96$ and $P < 10^{-4}$.

From their analysis, Nava et al. (2006) claimed that the Ghirlanda correlation for a wind-like circumburst medium is as tight as the one for a homogeneous medium. Drawing a comparison between the observed and the comoving frame correlations, the wind-like Ghirlanda correlation remains linear also in the comoving frame regardless the Γ values. While, for the homogeneous density medium case a significant correlation between Γ and the total energy should exist, thus further constraining the emission models of the prompt radiation. A data set of 18 GRBs with firm z , E_{peak} and T_{break} was used by Nava et al. (2006) for the homogeneous density case, obtaining:

$$\log \frac{E_{\text{peak}}^*}{100 \text{ keV}} = 0.45^{+0.02}_{-0.03} + (0.69 \pm 0.04) \log \frac{E_{\gamma}}{2.72 \times 10^{52} \text{ erg}}, \quad (3.44)$$

with $\rho = 0.93$ and $P = 2.3 \times 10^{-8}$. For the wind case, they found:

$$\log \frac{E_{\text{peak}}^*}{100 \text{ keV}} = 0.48^{+0.02}_{-0.03} + (1.03 \pm 0.06) \log \frac{E_{\gamma}}{2.2 \times 10^{50} \text{ erg}}, \quad (3.45)$$

with $\rho = 0.92$ and $P = 6.9 \times 10^{-8}$.

Ghirlanda et al. (2007) employing a sample of 33 GRBs (16 Swift GRBs with measured z and E_{peak} , and 17 GRBs detected by pre-Swift missions) investigated the $E_{\text{peak}} - E_{\gamma}$ correlation. To calculate the T_{break} they suggested that:

1. the jet break has to be observed in the optical wavelengths,
2. the optical light curve should last long after T_{break} ,
3. the flux from a plausible SN and the host galaxy emission should not be taken into

account,

4. the optical break should not be influenced by the frequency, and an X-ray break at the same time is not needed,
5. T_{break} should not coincide with $T_{X,a}$ from W07, otherwise the characteristic influencing the X-ray flux is also affecting the optical one.

From all these assumptions, the final set dropped down to 16 GRBs which obey the following correlation:

$$\log \frac{E_{\text{peak}}}{100 \text{ keV}} = (0.48 \pm 0.02) + (0.70 \pm 0.04) \log \frac{E_{\gamma}}{4.4 \times 10^{50} \text{ erg}}. \quad (3.46)$$

In this data set there were no outliers, thus the decreased value of the scatter in this correlation strengthened the possibility to conceive GRBs as standardizable candles.

Physical interpretation of the energetics vs. peak energy correlations

Under the assumption of the synchrotron radiation process from internal and external shocks Lloyd et al. (2000a) enquired into the physical explanation of the $E_{\text{peak}} - S_{\text{tot}}$ correlation. The synchrotron emission from electrons with a power-law distribution and Γ larger than some minimum threshold value, Γ_m , is able to explain the correlation. Moreover, the internal shock model explains the $E_{\text{peak}} - S_{\text{tot}}$ correlation and the radiated energy better than the external shock model.

Lloyd-Ronning and Petrosian (2002) stated that the GRB particle acceleration problem needs further investigation. The common hypothesis is that the repeated scatterings through the (internal) shocks accelerate the emitted particles. The recurrent shocks are generated by particles with a power-law distribution and a large photon index. The link between E_{peak} and the photon flux can be clarified by the fluctuation in the magnetic field or electron energy. In conclusion, it was yielded that in almost all GRBs the particle acceleration is not an isotropic process, but it happens along the magnetic field lines.

In their analysis Amati et al. (2002) validated the result that the $\log E_{\text{peak}} \sim 0.5 \log E_{\text{iso}}$ correlation is obtained considering an optically thin synchrotron shock model, as already shown by Lloyd et al. (2000b). In the framework of this model electrons follow the $N(\Gamma) = N_0 \Gamma^{-p}$ distribution for $\Gamma > \Gamma_m$ with Γ_m , GRB duration, and N_0 , the normalization, which are constant factors for each GRBs. A caveat must be posed regarding these assumptions, because each GRB has different duration and E_{iso} might be smaller when the emission is beamed.

The effect of this correlation on the theoretical interpretation of the prompt emission and on the probable union of the two classes of GRBs and XRFs were presented by Amati (2006).

As shown by Zhang and Mészáros 2002 and Ghirlanda et al. (2013), this correlation can be employed also for verifying the GRB synthesis models.

E_{peak} and E_{iso} are dependent on Γ and the $E_{\text{peak}} - E_{\text{iso}}$ correlation is a useful tool to link the parameters of the synchrotron shock model. Indeed, Zhang and Mészáros (2002) and Rees and Mészáros (2005) concluded that, for a power-law electron distribution generated from an internal shock in a fireball with velocity Γ , the peak energy is

$$\log E_{\text{peak}}^* \sim -2 \log \Gamma + 0.5 \log L - \log t_\nu, \quad (3.47)$$

where L is the total fireball luminosity and t_ν the variability timescale. To retrieve the $E_{\text{peak}} - E_{\text{iso}}$ correlation a complex assumption has to be made: Γ and t_ν should be similar for each GRB. This assumption causes problems when $L \propto \Gamma^N$, with N between 2 and 3 (Zhang and Mészáros, 2002; Schaefer, 2003b; Ramirez-Ruiz, 2005). A possible interpretation could be given by the fact that the GRB prompt emission is affected by direct or Comptonized thermal radiation produced by the photospheric region of the fireball (Zhang and Mészáros, 2002; Ramirez-Ruiz, 2005; Ryde, 2005; Rees and Mészáros, 2005; Beloborodov, 2010; Guiriec et al., 2011; Hascoët et al., 2013; Guiriec et al., 2013; Vurm and Beloborodov, 2016; Guiriec et al., 2015a,b). This explanation is particularly suitable for really energetic (Frontera et al., 2000; Preece et al., 2000; Ghirlanda et al., 2003) and flat average spectra. In these circumstances, E_{peak} is a function of the peak temperature, $T_{bb,\text{peak}}$, of the photons distributed as in a blackbody, and for this reason it is related to the luminosity or emitted energy. In the case of Comptonized radiation from the photosphere $\log E_{\text{peak}}$ can be written as:

$$\log E_{\text{peak}} \sim \log \Gamma + \log T_{bb,\text{peak}} \sim 2 \log \Gamma - 0.25 \log L \quad (3.48)$$

or

$$\log E_{\text{peak}} \sim \log \Gamma + \log T_{bb,\text{peak}} \sim -0.5 \log r_0 + 0.25 \log L, \quad (3.49)$$

where r_0 is the distance between the region of the energy emission and the central engine, such that $\Gamma \simeq r/r_0$ grows up to some saturation radius r_s (Rees and Mészáros, 2005). Rees and Mészáros (2005) claimed that in this case the $E_{\text{peak}} - E_{\text{iso}}$ correlation can be retrieved just below the photosphere, though it would be a function of an uncertain amount of unknown parameters.

The non-thermal synchrotron emission model can have an important role in explaining the $E_{\text{peak}} - E_{\text{iso}}$ correlation for highly energetic GRBs (i.e., $E_{\text{iso}} \approx 10^{55}$ erg). As shown by Lloyd et al. (2000b) and Zhang and Mészáros (2002) this can be achieved in two ways: a) supposing the minimum Γ and the normalization of the electron distribution, approximated as a power-law, constant in each GRB; b) by bounding the slope of the correlation between

Γ and the luminosity.

Panaitescu (2009) from the study of 76 GRBs with measured redshifts concluded that the $\log E_{\text{peak}} \sim 0.5 \log E_{\text{iso}}$ correlation for LGRBs is generated from the external shock interacting with an external medium which is radially stratified, for example with a particle density distribution which does not follow the usual R^{-2} trend, with R the distance from the produced GRB radiation.

To investigate the connection between the $E_{\text{peak}} - E_{\text{iso}}$ correlation and the internal shock scenario, Mochkovitch and Nava (2015) simulated GRB sets with different model parameter distributions (e.g., the radiated power in the relativistic emission and Γ). Then, they compared the $E_{\text{peak}} - E_{\text{iso}}$ correlations obtained through the simulated data set with the observed correlation recovered using 58 Swift GRBs with $F_{\text{peak}} > 2.6 \text{ ph cm}^{-2} \text{ s}^{-1}$ between 15 and 150 keV. As a result, an agreement between observations and simulations was obtained only with the following assumptions:

1. the diffused energy should be emitted in a small amount of electrons;
2. the difference between the highest and the lowest Γ should be irrelevant;
3. if $\bar{\Gamma} \propto \dot{E}^{1/2}$ (with \dot{E} the rate of injected energy in the relativistic jet), the $E_{\text{peak}} - E_{\text{iso}}$ correlation is not recovered and E_{peak} decreases with greater values of E_{iso} . Nevertheless, the $E_{\text{peak}} - E_{\text{iso}}$ correlation can be retrieved if $\bar{\Gamma} \propto \dot{E}^{1/2}$ is a lower limit for a specific \dot{E} ;
4. the $E_{\text{peak}} - E_{\text{iso}}$ correlation is retrieved in the case the amplitude of the Γ variability is related to $\bar{\Gamma}$.

The Ghirlanda correlation (Ghirlanda et al., 2004b) has been considered invariant under the transition from the rest-frame to the comoving frame, assuming that θ_{jet} is along the line of sight. The number of emitted photons for each GRB is similar and around 10^{57} . This aspect could be significant to understand the GRB dynamics and the radiation processes (see also right panel of Fig. 3.3.8).

Collazzi et al. (2011) investigated the mean E_{peak}^* , yielding that it is close to the electron rest-mass energy value, 511 keV. This result suggests that the shape of the E_{peak} distribution is not caused by selection biases only. Nevertheless, this effect is not explained by any known mechanism, but the almost steady temperature indicates the necessity of some mechanism holding the temperature at a constant value, like an electron-positron annihilation.

From their analysis of a simulated data set, Ghirlanda et al. (2013) yielded that the correlation between Γ and θ_{jet} with the highest agreement between simulations and observations is given by $\theta_{\text{jet},\text{max}}^{2.5} \Gamma_{\text{max}} = \text{const.}$ Using a set of ≈ 30 GRBs with computed θ_{jet} or Γ a correlation between E_{γ} and E_{peak} was found:

$$\log E_{\text{peak}} \sim \log \frac{E_{\gamma}}{5 - 2\beta_0}. \quad (3.50)$$

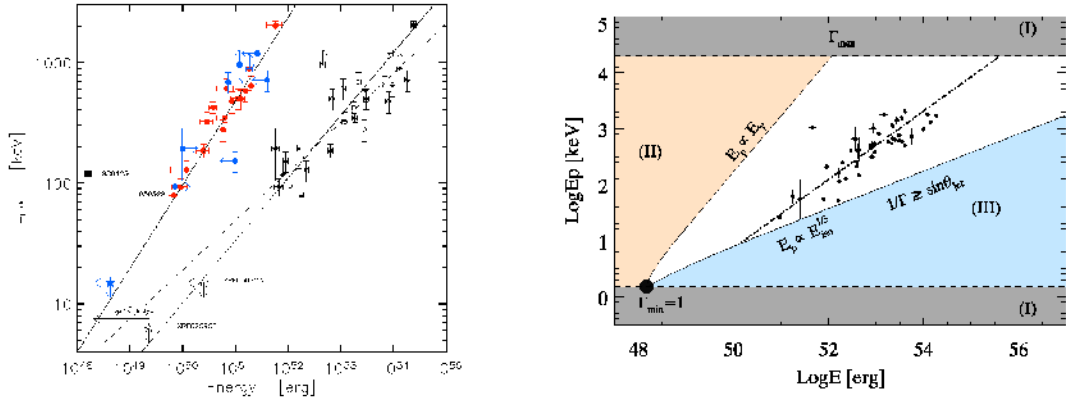


Figure 3.3.8: Left panel: the $E_{\text{peak}}^* - E_{\gamma}$ correlation for GRBs with measured redshift. E_{γ} for GRBs where a jet break was detected is indicated by filled circles. Lower/upper limits are represented by grey symbols. The best fit is displayed by the solid line, while open circles indicate E_{iso} for the GRBs. The best fit to these points is given by the dashed line and the correlation shown by Amati et al. (2002) is represented by the dash-dotted line. (Figure from Ghirlanda et al. (2004b). @ AAS. Reproduced with permission.) Right panel: rest-frame distribution of the Ghirlanda correlation. The large black dot represents the simulated GRBs with $E_{\text{peak}}^* = 1.5 \text{ keV}$ and $E_{\gamma}^* = 1.5 \times 10^{48} \text{ erg}$. Region I, II, III are not allowed. Region I is forbidden because $\Gamma > 1$ but less than 8000, region II, because $\theta_{\text{jet}} \leq 90^\circ$, region III because in the case Γ is tiny, the area of the beaming cone appears wider than the one individuated by the jet. The black dots represent the Swift GRBs of the sample. The dot-dashed line displays the fit to the Swift sample. (Figure from Ghirlanda et al. (2013).)

Even if Γ and θ_{jet} estimations are based on incomplete sets and can be affected by selection effects, Ghirlanda et al. (2013) concluded that the higher the value of Γ , the smaller its θ_{jet} , namely the faster a GRB, the narrower its jet.

Ghirlanda et al. (2013) claimed that just $\approx 6\%$ of the on-axis GRBs should have $\sin \theta_{\text{jet}} < 1/\Gamma$, not displaying any jet break feature in the afterglow light curve. Most importantly they concluded that the local rate of GRBs is $\approx 0.3\%$ of the local SNe Ib/c, and $\approx 4.3\%$ of the local hypernovae.

3.3.6 Correlations between the luminosity and the peak energy

The $E_{\text{peak}} - L_{\text{iso}}$ correlation

Schaefer (2003a) was the first to discover the $E_{\text{peak}} - L_{\text{iso}}$ correlation. For 20 GRBs with luminosities based on optically known redshift (Amati et al., 2002; Schaefer, 2003a) it was obtained (see Fig. 3.3.9):

$$\log E_{\text{peak}} \sim (0.38 \pm 0.11) \log L_{\text{iso}}, \quad (3.51)$$

with $r = 0.90$ and $P = 3 \times 10^{-8}$, while for 84 GRBs with computed E_{peak} from the BATSE catalogue (Schaefer et al., 2001) the correlation was given by

$$\log E_{\text{peak}} \sim (0.36 \pm 0.03) \log L_{\text{iso}}. \quad (3.52)$$

Given that both E_{peak} and L_{iso} are functions of Γ , their common dependence on Γ simply relates these two physical quantities. Assuming that the luminosity is proportional to Γ^N and E_{peak} is proportional to Γ^M , $\log E_{\text{peak}}$ will be a function of $(M + 1)/N \times \log L_{\text{iso}}$.

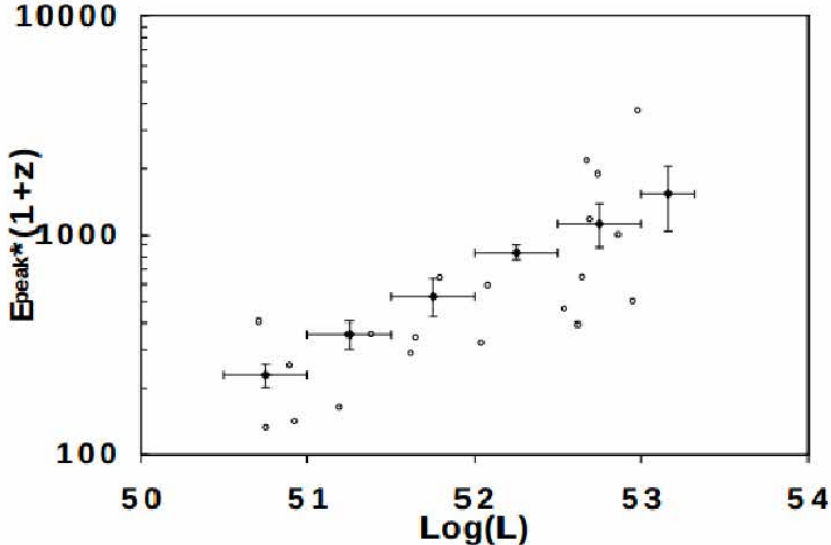


Figure 3.3.9: Fit of the $\log E_{\text{peak}} - \log L_{\text{iso}}$ correlation. The open circles represent 20 GRBs of the sample with known redshift; instead the filled diamonds indicate the binned values of the 84 GRBs with luminosity (and then redshift) computed by using the spectral lag and variability. (Figure from Schaefer (2003b). © AAS. Reproduced with permission.)

Investigating the time-resolved prompt emission spectra between 2 and 2000 keV of 9 GRBs observed simultaneously with the Wide Field Camera and the BATSE instrument, Frontera et al. (2012) obtained the correlation (see Fig. 3.3.10):

$$\log E_{\text{peak}}^* \sim (0.66 \pm 0.03) \log L_{\text{iso}}, \quad (3.53)$$

with $\rho = 0.94$ and $P = 1.57 \times 10^{-13}$.

Additionally, employing 46 Swift GRBs with known z and E_{peak} , Nava et al. (2012) retrieved a significant $E_{\text{peak}} - L_{\text{iso}}$ correlation represented by

$$\log E_{\text{peak}}^* = -(25.33 \pm 3.26) + (0.53 \pm 0.06) \log L_{\text{iso}}, \quad (3.54)$$

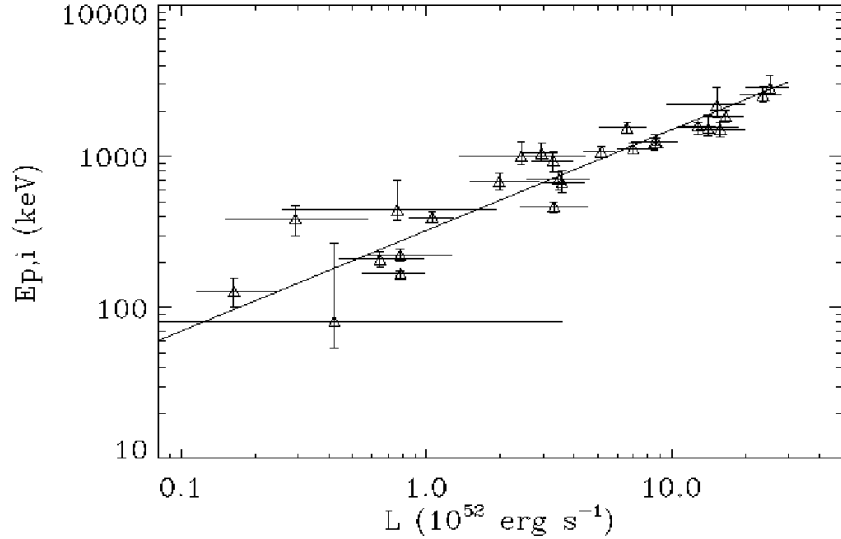


Figure 3.3.10: The $E_{\text{peak}}^* - L_{\text{iso}}$ correlation obtained from data for GRBs 990123 and 990510 computed at different time intervals. The solid line displays the best fit power-law. (Figure from Frontera et al. (2012). @ AAS. Reproduced with permission.)

with $\rho = 0.65$, $P = 10^{-6}$, E_{peak} in keV, and L_{iso} is in units of $10^{51} \text{ erg s}^{-1}$. Nevertheless, they showed that, even using GRBs with no estimation or just an upper or lower limit on z and E_{peak} , this $E_{\text{peak}} - L_{\text{iso}}$ correlation is still valid.

The $L_{\text{peak}} - E_{\text{peak}}$ correlation

Even replacing E_{iso} with L_{iso} or L_{peak} , a correlation is still present. The Yonetoku correlation (Yonetoku et al. 2004, see the left panel of Fig. 3.3.11), between E_{peak} and L_{peak} , was recovered with a sample of 11 BATSE GRBs with measured redshifts and BeppoSAX GRBs from (Amati et al., 2002). Considering L_{peak} of the burst instead of L_{iso} , this correlation appears more significant than other correlations among prompt phase parameters:

$$\log L_{\text{peak}} \sim (2.0 \pm 0.2) \log E_{\text{peak}}^*, \quad (3.55)$$

with $r = 0.958$, $P = 5.31 \times 10^{-9}$, and the uncertainties are 1σ errors. Indeed, this correlation, compatible with the standard synchrotron model (Zhang and Mészáros, 2002; Lloyd et al., 2000b), has been employed to compute the pseudo-redshifts of 689 BATSE LGRBs with not measured distances and to calculate the formation rate versus z .

From a sample of 36 bright BATSE SGRBs, Ghirlanda et al. (2004a) chose the GRBs with F_{peak} , measured at the 64 ms timescale and in the energy band between 50 and 300 keV,

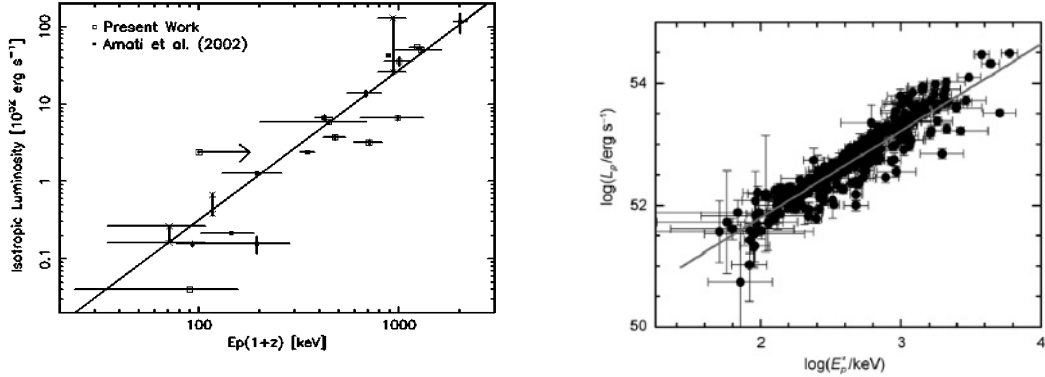


Figure 3.3.11: Left panel: the $\log L_{\text{peak}} - \log E_{\text{peak}}$ correlation with BATSE data represented by the open squares and the BeppoSAX GRBs indicated by the filled squares and the cross points. The best fit line is displayed by the solid line. (Figure from Yonetoku et al. (2004). © AAS. Reproduced with permission.) Right panel: the $\log L_{\text{peak}} - \log E_{\text{peak}}$ correlation using a sample of 276 GRB time-resolved spectra within the decay pulses. The best fit to the set is indicated by the solid line. (Figure from Lu and Liang (2010). Copyright © 2010 Springer.)

larger than $10 \text{ ph cm}^{-2} \text{ s}^{-1}$ and with a significant signal to noise ratio (S/N), obtaining in the end a data set of 28 SGRBs. From the analysis of this sample, it was yielded that SGRBs follow the $L_{\text{peak}} - E_{\text{peak}}^*$ correlation, but not the Amati correlation. So, the pseudo-redshifts for SGRBs were calculated using the Yonetoku correlation and, as a result, their distribution resembles the one for LGRBs, but centered at a smaller redshift.

Later, Yonetoku et al. (2010) with a sample of 101 GRBs with known redshifts, reported F_{peak} , and observed by KONUS, Swift, HXD-WAM and RHESSI changed the parameter values of the correlation as follows:

$$\log L_{\text{peak}} = (52.43 \pm 0.037) + (1.60 \pm 0.082) \log E_{\text{peak}}^*, \quad (3.56)$$

with $r = 0.889$, $P = 2.18 \times 10^{-35}$, L_{peak} expressed in erg s^{-1} , and E_{peak}^* in units of 355 keV. In conclusion, it was yielded that this correlation is intrinsic to GRBs, but the selection effects due to the detector threshold severely influence it.

With time-resolved spectral data for 30 pulses in 27 bright BATSE GRBs, Lu and Liang (2010) studied the decaying parts of the pulses (see the right panel of Fig. 3.3.11) obtaining:

$$\log L_{\text{peak}} \sim (1.42 \pm 0.03) \log E_{\text{peak}}^*, \quad (3.57)$$

with $r = 0.91$ and $P < 10^{-4}$. The statistical or observational effects are not alone sufficient to justify the wide scatter of the power-law index. Thus, this may be an intrinsic characteristic, suggesting that there is no common $L_{\text{peak}} - E_{\text{peak}}$ correlation expected for all GRB pulses.

Considering the Fermi observations deviating from the Band function (Abdo et al. 2009a; Guiriec et al. 2010; Ackermann et al. 2010, 2011, 2013; see also Lin et al. 2016b), Guiriec et al. (2013, 2015a,b, 2016) suggested that the GRB spectra should be described not only by the Band function, but also by a blackbody (thermal) and a power-law (non-thermal) components. Synchrotron radiation from the jet particles well interpreted the non-thermal component, instead the radiation generated from the jet photosphere described the thermal component. Most likely, the inverse Compton process produced the power-law component, but the outcomes suggest a general $L_{\text{peak}} - E_{\text{peak}}^*$ correlation due to the non-thermal components.

In a sample of 13 SGRB candidates, Tsutsui et al. (2013) chose 8 well-defined SGRBs (defined by a scatter larger than $3\sigma_{\text{int}}$ around the Amati correlation for LGRBs) in order to study the $L_{\text{peak}} - E_{\text{peak}}$ correlation. It was found:

$$\log L_{\text{peak}} = (52.29 \pm 0.066) + (1.59 \pm 0.11) \log E_{\text{peak}}^*, \quad (3.58)$$

with $r = 0.98$, $P = 1.5 \times 10^{-5}$, E_{peak}^* in units of 774.5 keV from the time-integrated spectrum, and L_{peak} in erg s^{-1} integrated for 64 ms. Employing this correlation on 71 luminous BATSE SGRBs allowed to compute their pseudo-redshifts, which were spread in the range $z \in [0.097, 2.258]$, with mean value $\langle z \rangle = 1.05$, smaller than $\langle z \rangle = 2.2$ for LGRBs. In conclusion, Yonetoku et al. (2014), considering a sample of 72 SGRBs with well known spectral characteristics detected by BATSE, used the $L_{\text{peak}} - E_{\text{peak}}$ correlation for SGRBs obtained by Tsutsui et al. (2013) to calculate their pseudo-redshifts and luminosities. The measured redshift distribution for $z \leq 1$ was comparable to the one for 22 Swift SGRBs, confirming the accuracy of the redshift estimation through the $L_{\text{peak}} - E_{\text{peak}}^*$ correlation.

Physical interpretation of the luminosity vs. peak energy correlations

Schaefer et al. (2001) and Schaefer (2003b) showed that E_{peak} and L_{iso} are linked due to their common proportionality to the factor Γ . As claimed by Lloyd-Ronning and Ramirez-Ruiz (2002), the $E_{\text{peak}} - L_{\text{iso}}$ correlation could help to explain the structure of the ultra-relativistic jet, the shock acceleration and the production of the magnetic field. Nevertheless, the small amount of SGRBs present in the data sets allows the correlation to be used for LGRBs only.

Even if Schaefer et al. (2001) and Schaefer (2003b) concluded that E_{peak} is the same for all GRBs at redshifts $z \geq 5$, the use of GRBs as standard candles is still an open issue. The most important result would be to find out common features in some GRB quantities, regardless the complexity and the difference of each GRB light curve, to use GRBs as cosmological tools (Wang et al., 2015).

Introducing the quantity $\omega = (L_{\text{iso}}/10^{52} \text{ erg s}^{-1})^{0.5}/(E_{\text{peak}}/200 \text{ keV})$, Liang et al. (2004) constrained ω to the values $\simeq 0.1 - 1$ and investigated the consequences of the $E_{\text{peak}} - L_{\text{iso}}$

correlation within the fireball model. Other parameters were discussed, such as the combined internal shock parameter, ζ_i , for both the internal and external shocks scenarios. With the hypothesis of uncorrelated parameters, they concluded that the production of prompt gamma-rays within internal shocks dominated by kinetic energy fulfills the requirements of the standard internal shock model. The same is valid for the gamma-rays generated from external shocks subjected to magnetic dissipation, namely both models give a valid explanation of the $L_{\text{iso}} \propto E_{\text{peak}}^2$ correlation and ω .

Another interpretation of this correlation was given by Mendoza et al. (2009). They considered a source-ejecting matter in a particular x direction with a speed $v(t)$ and a rate of mass ejection $\dot{m}(t)$, both dependent on time t as computed from the source of the outflow. Then, they investigated the uniform release of mass and, assuming simple periodic oscillations of the particle velocity (an ordinary hypothesis in the internal shock model scenario), they computed the luminosity.

In the photospheric context, Ito et al. (2013) proposed that if a velocity shear with a significant change in Γ is observed at the edge of the spine and the sheath region, the high energy component of the GRB photon spectrum is described by a Fermi-like acceleration mechanism. This acceleration phenomenon explains also the power-law slope above the thermal-like peak bump visible in a few GRBs (090510, 090902B, 090926A). Additionally, they claimed that time-integrated spectra can recover the low energy part of the GRB spectrum in the case the time evolution of the jet is taken into account.

For the Yonetoku correlation, Yonetoku et al. (2004) claimed that the luminosity evolution of GRBs may be linked to the evolution of GRB progenitor mass or to the jet evolution. To investigate the evolution of the jet opening angle two cases were taken into account: the maximum jet opening angle drops or the total jet energy rises. Although, in the first scenario, the GFR is underestimated due to the fact that the probability to detect GRBs at high redshift would be reduced. In this case the evolution of the ratio of the GFR to the SFR would be faster. Instead in the second scenario, the evaluation of the GFR appears reliable.

Finally, to explain the $L_{\text{iso}} - E_{\text{peak}}$ correlation Frontera et al. (2016) started from the model developed by Titarchuk et al. (2012). This model is characterized by an expanding plasma shell deriving from a star explosion and soft photons. Through this model, Frontera et al. (2016) concluded that, if $\tau_{\gamma\gamma} \gg 1$ (see Section 2.1), the $\log L_{\text{iso}} - \log E_{\text{peak}}$ correlation has a slope of 0.5, thus implying the physical ground for the Amati correlation (see Section 3.3.5).

3.3.7 Comparisons between $E_{\text{peak}} - E_{\text{iso}}$ and $L_{\text{peak}} - E_{\text{peak}}$ correlation

Here, the $E_{\text{peak}} - E_{\text{iso}}$ correlation and the $L_{\text{peak}} - E_{\text{peak}}$ correlation are examined. With this aim, Ghirlanda et al. (2005b) determined the $L_{\text{peak}} - E_{\text{peak}}$ correlation, using 22 GRBs

with measured z , with a slope of 0.51. This is comparable to the one found by Yonetoku et al. (2004) using 12 GRBs, but it presents a larger scatter than the one by Yonetoku et al. (2004).

Employing 33 low redshift GRBs with $z \leq 1.6$, Tsutsui et al. (2009a) studied these two correlations finding in both of them a significant correlation coefficient together with a relevant scatter though. Additionally, a partial linear correlation degree, which represents the measure of the correlation between two quantities, was $\rho_{L_{\text{peak}}, E_{\text{iso}}, E_{\text{peak}}} = 0.38$. To attenuate the scatter of the Yonetoku correlation, a parameter $T_L = E_{\text{iso}}/L_{\text{peak}}$ was inserted by Tsutsui et al. (2009a) as a third parameter, giving a new correlation:

$$\log L_{\text{peak}} = (-3.87 \pm 0.19) + (1.82 \pm 0.08) \log E_{\text{peak}} - (0.34 \pm 0.09) \log T_L, \quad (3.59)$$

with $r = 0.94$, $P = 10^{-10}$, L_{peak} in units of $10^{52} \text{ erg s}^{-1}$, E_{peak} in keV, and T_L in seconds. Through this correlation the systematic errors were diminished by 40%, and the plane displayed by this correlation might be a “fundamental plane” for GRBs observed during their prompt emission phase.

Using the database developed by Yonetoku et al. (2010) (composed of 109 GRBs with known redshifts, E_{peak} , L_{peak} and E_{iso}), Tsutsui et al. (2010) analysed the correlations among E_{peak} , L_{peak} and E_{iso} . In this sample GRBs were separated into two groups: the gold and the bronze data sets. The first is composed of GRBs with E_{peak} given by the Band function with four free parameters. The latter is composed of GRBs with such a poor energy spectra that E_{peak} must be given either by the Band function with only three free parameters (instead of 4, for example with one fixed spectral index) or by the three free parameters of the cut-off power-law (CPL) model. E_{peak} for the GRBs in the bronze data set had larger value than that estimated for the GRBs in the gold data set, suggesting that the quality of the data set affected the scatter of the correlations among E_{peak} , L_{peak} , and E_{iso} .

The presence of GRB 060218 in the LGRB sample induces a difference between the $L_{\text{peak}} - E_{\text{peak}}$ correlation found by Ghirlanda et al. (2010) from the one analysed by Yonetoku et al. (2010). For Ghirlanda et al. (2010) GRB 060218 was an ordinary LGRB, while for Yonetoku et al. (2010) this GRB was removed from the sample, since it was an outlier situated at more than 8σ from the $L_{\text{peak}} - E_{\text{peak}}$ correlation. This GRB removal gave as a result a much steeper best fit line.

Employing 13 highly energetic Fermi GRBs until July 2009, and with measured redshift, Ghirlanda et al. (2010) retrieved a significant correlation:

$$\log E_{\text{peak}}^* \sim 0.4 \log L_{\text{iso}}, \quad (3.60)$$

with a scatter of $\sigma = 0.26$. Likewise, for E_{peak}^* and E_{iso} :

$$\log E_{\text{peak}}^* \sim 0.5 \log E_{\text{iso}}. \quad (3.61)$$

The time-integrated spectra of 8 Fermi GRBs with known redshift were compatible with both the $E_{\text{peak}} - E_{\text{iso}}$ and the $E_{\text{peak}} - L_{\text{iso}}$ correlations obtained from a sample of 100 GRBs observed by missions previous to Fermi.

In the framework of these two correlations, 8 SGRBs were employed by Tsutsui et al. (2013) to verify whether the $E_{\text{peak}} - E_{\text{iso}}$ and $L_{\text{peak}} - E_{\text{peak}}$ correlations are valid for SGRBs also. For the first time they concluded that the $E_{\text{peak}} - E_{\text{iso}}$ correlation for SGRBs was given by

$$\log E_{\text{iso}} = (51.42 \pm 0.15) + (1.58 \pm 0.28) \log E_{\text{peak}}^*, \quad (3.62)$$

with $r = 0.91$, $P = 1.5 \times 10^{-3}$, E_{iso} in erg s^{-1} , and E_{peak}^* in units of 774.5 keV. Furthermore, the $L_{\text{peak}} - E_{\text{peak}}$ correlation for SGRBs in Equation 3.58 is more significant than the $E_{\text{peak}} - E_{\text{iso}}$ one. For equal value of E_{peak} SGRBs are dimmer than LGRBs by $\simeq 100$ for the $E_{\text{peak}} - E_{\text{iso}}$ correlation, and $\simeq 5$ for the $L_{\text{peak}} - E_{\text{peak}}$ correlation.

3.3.8 The $L_{X,p} - T_{X,p}^*$ correlation and its physical interpretation

W07 developed a phenomenological model to compute both prompt and afterglow variables contemporaneously. Both parts are nicely described by the same function:

$$f_i(t) = \begin{cases} F_i e^{\alpha_i(1-\frac{t}{T_i})} e^{-\frac{t_i}{t}}, & t < T_i, \\ F_i (\frac{t}{T_i})^{-\alpha_i} e^{-\frac{t_i}{t}}, & t \geq T_i. \end{cases} \quad (3.63)$$

The index i denotes p or a representing the prompt and afterglow phases, respectively. The whole light curve, $f_{\text{tot}}(t) = f_p(t) + f_a(t)$, is characterized by two groups of four quantities each: $\{T_i, F_i, \alpha_i, t_i\}$, where α_i is the temporal power-law decay index, the time t_i is the initial rise timescale, F_i is the flux and T_i is the break time. Figure 1.2.1 depicts this function.

Following Dainotti et al. (2008), employing 107 GRB light curves detected by the XRT, Qi and Lu (2010) studied the prompt phase, discovering a correlation between $L_{X,p}$ and $T_{X,p}^*$. Due to the lack of redshift measurements and solid prompt spectral parameters only 47 GRBs were employed in the final sample. Among those there were 37 GRBs with $T_{X,p}^* > 2$ s and 3 GRBs with $T_{X,p}^* > 100$ s.

They obtained that the correlation can have the form:

$$\log L_{X,p} = a + b \log T_{X,p}^*, \quad (3.64)$$

where $L_{X,p}$ is in erg s^{-1} , and $T_{X,p}^*$ is in seconds. The D'Agostini (2005) fitting method was employed to the samples:

1. the whole data set of 47 GRBs (see the left panel of Fig. 3.3.12),
2. 37 GRBs with $T_{X,p}^* > 2\text{ s}$ (see the middle panel of Fig. 3.3.12),
3. 34 GRBs with $2\text{ s} < T_{X,p}^* < 100\text{ s}$ (see the right panel of Fig. 3.3.12).

From these fits different trends compared to Equation 3.64 were retrieved. For the first sample, the results of the fit yield a normalization $a = 50.91 \pm 0.23$ and a slope $b = -0.89 \pm 0.19$. For the other two samples, other values were recovered, $b = -1.73$ and $b = -0.74$, respectively. It was observed that the third sample gave the smallest scatter value σ_{int} , and most importantly a slope ($-0.74^{+0.20}_{-0.19}$) comparable within 1σ to the one of the LT correlation (Dainotti et al., 2008).

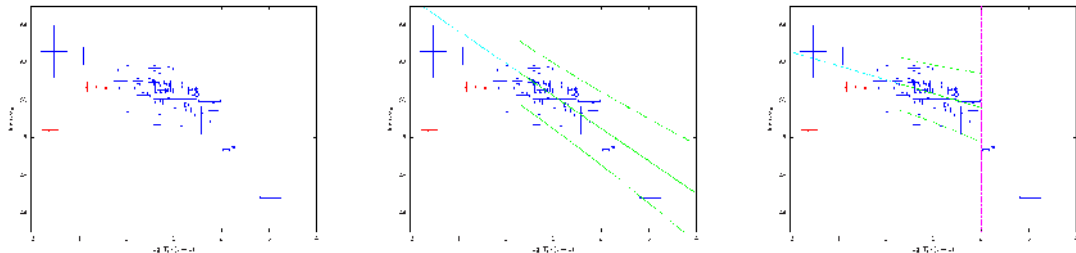


Figure 3.3.12: Left panel: the $\log L_{X,p} - \log T_{X,p}^*$ correlation for the set of 47 GRBs. (i.e., $T_{90} < 2\text{ s}$). (Figure from Qi and Lu (2010). @ AAS. Reproduced with permission.) Middle panel: best fit of the $\log L_{X,p} - \log T_{X,p}^*$ correlation for only GRBs with $T_{X,p}^* > 2\text{ s}$. (Figure from Qi and Lu (2010). @ AAS. Reproduced with permission.) Right panel: Best fit of the $\log L_{X,p} - \log T_{X,p}^*$ correlation for the 34 GRBs with $2\text{ s} < T_{X,p}^* < 100\text{ s}$. (Figure from Qi and Lu (2010). @ AAS. Reproduced with permission.)

As claimed by Qi and Lu (2010), an indication of curvature appears in the $L_{X,p} - T_{X,p}^*$ correlation (see the middle panel of Fig. 3.3.12). Particularly, all GRBs which present $T_{X,p}^* < 2\text{ s}$ are placed below the best fit line, but the small number of GRBs used in their study does not allow for any definitive statements on the reliability of this effect. Indeed, it can be due to selection effects from outliers. In the case the effect is real, $T_{X,p}^*$ could be used to pursue a new classification of GRBs into LGRBs and SGRBs, as already suggested by O'Brien and Willingale (2007). Both T_{90} and $T_{X,p}$ evaluate the GRB duration: T_{90} is based on the energetics of the GRB, while $T_{X,p}$ on the GRB time evolution of the light curves. Nevertheless, substituting $T_{X,p}$ with T_{90} does not allow for the recovery of the correlation. For an investigation of an updated data set and comparison of $T_{X,p}$ with T_{45} see Dainotti et al. (2011b).

To physically interpret this correlation, it is needed to remind that both the existence of few GRBs with a high value of $T_{X,p}^*$ and several physical emission processes can be the reason for the existence of this curvature in the $L_{X,p} - T_{X,p}^*$ correlation in Qi and Lu (2010). However, this issue cannot be solved due to the small number of GRBs in the given data set and the

existence of possible outliers in the sample. To additionally confirm this correlation and its interpretation further study is essential.

3.3.9 The $L_{X,f} - T_{X,f}$ correlation and its physical interpretation

As claimed by Nousek et al. (2006), a rapid decay phase (RDP) following the prompt emission is detected in several GRBs. Due to the fact that this RDP is smoothly prolonged after the prompt phase, as concluded by O'Brien et al. (2006), it can be considered as the prompt phase's tail. Among the several models (see Zhang et al. 2007b) trying to investigate the RDP, it is included the high latitude emission (HLE) one. The HLE scenario asserts that given the additional path length due to the curvature of the emitting region, the photons reach the observer from angles which appear to be wider respect to the line of sight. This happens when the prompt phase radiation from a spherical shell switches off at a given radius. In such a situation the Doppler factor of these photons is small.

Willingale et al. (2010) improved the procedure developed by W07 to investigate the pulses in the prompt phase and the late X-ray flares detected by Swift/BAT+XRT. The pulse profile is fitted by this function:

$$P = \left\{ \left[\min \left(\frac{T - T_{\text{ej}}}{T_{X,f}}, 1 \right)^{\alpha+2} - \left(\frac{T_{X,f} - T_{\text{rise}}}{T_{X,f}} \right)^{\alpha+2} \right] \left[1 - \left(\frac{T_{X,f} - T_{\text{rise}}}{T_{X,f}} \right)^{\alpha+2} \right]^{-1} \right\} \left(\frac{T - T_{\text{ej}}}{T_{X,f}} \right)^{-1}, \quad (3.65)$$

where $T_0 = T_{X,f} - T_{\text{rise}}$ is the time of the arrival of the first photon radiated from the shell, and T_{rise} the rise time of the pulse. The emission is supposed to originate from an ultra-relativistic thin shell expanding on limited values of radii along the line of sight, computed in the observer frame since the ejection time, T_{ej} . In this way, the rise of the pulse can be shaped using α , T_{rise} and $T_{X,f}$.

The rise and decay of the pulse is due to the union of the pulse profile $P(t, T_{X,f}, T_{\text{rise}})$ and $B(x)$, roughly represented by the Band function:

$$B(x) = B_{\text{norm}} \times \begin{cases} x^{(\alpha-1)} e^{-x}, & x \leq \alpha - \beta \\ x^{(\beta-1)} (\alpha - \beta)^{(\alpha-\beta)} e^{-(\alpha-\beta)}, & x > \alpha - \beta \end{cases} \quad (3.66)$$

where $x = (E/E_{X,f}) [(T - T_{\text{ej}})/T_{X,f}]^{-1}$, $E_{X,f}$ the spectral break energy, and B_{norm} the normalization.

Adopting a sample of 12 Swift GRBs detected in the BAT and XRT energy ranges, Willingale et al. (2010) discovered that $L_{X,f}$ is anti-correlated with $T_{X,f}^*$ through the equation:

$$\log L_{X,f} \sim -(2.0 \pm 0.2) \log T_{X,f}^*. \quad (3.67)$$

This correlation shows that bright pulses take place just after ejection, while dim pulses take place at later time (see the left panel of Fig. 3.3.13). In Willingale et al. (2010) a correlation between $L_{X,f}$ and E_{peak} was also claimed, as shown in the right panel of Figure 3.3.13, in accordance with the already known Yonetoku correlation between L_{peak} and E_{peak} of the spectrum during the time T_{90} (Yonetoku et al., 2004; Tsutsui et al., 2013), see also Section 3.3.6.

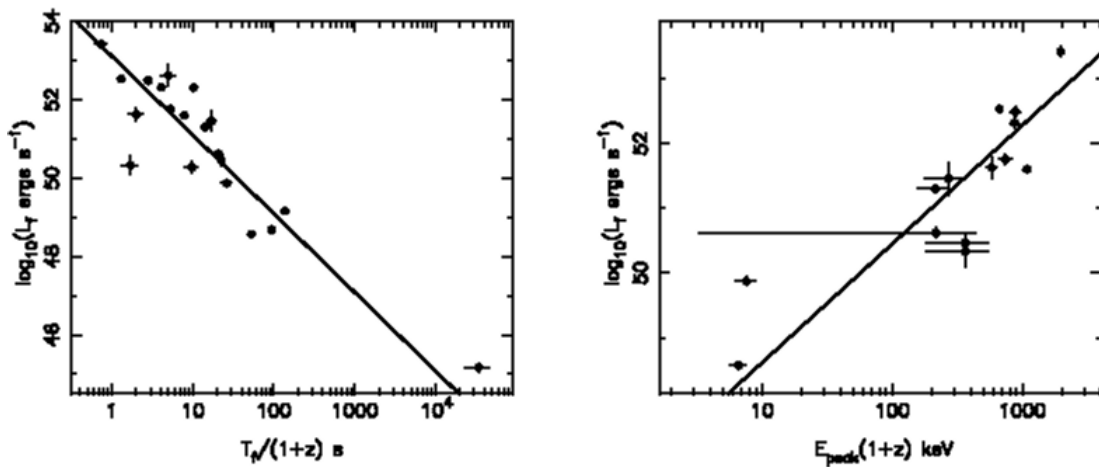


Figure 3.3.13: Left panel: the $L_{X,f} - T_{X,f}^*$ distribution. Right panel: $L_{X,f} - E_{\text{peak}}$ distribution. (Figures from Willingale et al. (2010).)

From the sample analysed by Willingale et al. (2010), 49 pulses were adequately fitted with the RDP function indicating the HLE model as the correct one to describe the GRB prompt phase, except for some hard peak pulses. Although, an anomaly is represented by the hard pulse in GRB 061121 which demands a spectral index $\beta_S = 2.4$, which is different from the value assumed for synchrotron emission, i.e. $\beta_S = 1$.

An example of similar correlations were given by Lee et al. (2000) and Quilligan et al. (2002), which analysed the width of a pulse instead of $T_{X,f}$. Later, other authors (Littlejohns et al., 2013; Bošnjak and Daigne, 2014; Evans et al., 2014; Hakkila and Preece, 2014; Laskar et al., 2014; Littlejohns and Butler, 2014; Roychoudhury et al., 2014; Ceccobello and Kumar, 2015; Kazanas et al., 2015; Laskar et al., 2015; Peng et al., 2015) employed the pulse profile by Willingale et al. (2010) to investigate the prompt radiation features of the pulses.

Regarding the physical interpretation of this correlation, in Willingale et al. (2010) the emission is assumed generated from a thin shell, as previously seen in this section. Furthermore, Genet and Granot (2009) showed that the HLE is the right model to explain the decaying

phase after the peak along the shell, which is slowed down and changed by the different Doppler factor responsible of the curvature of the surface (Ryde and Petrosian, 2002; Dermer, 2007).

For the sake of completeness, in the next three sections of this chapter, a part based on the article Dainotti & Amati, Publications to the Astronomical Society of the Pacific, Volume 130, number 987, (2018) is presented. Indeed, in this work led by Dr. M.G. Dainotti, the thesis author started to be involved in the survey of the redshift estimators for the GRB correlations among prompt parameters and the applications to cosmology of the GRB correlations among prompt parameters. She provided and discussed with the other authors interesting papers about these topics. Nevertheless, She could not help with the entire version of the work and its subsequent submission to the journal, but her initial contribution is confirmed in the acknowledgements section of the paper.

3.3.10 Redshift estimator for correlations among prompt parameters

Here, some emblematic cases regarding the correlations used to build a redshift indicator among prompt parameters (Atteia, 2003; Yonetoku et al., 2004; Tsutsui et al., 2013) are described. To retrieve pseudo-redshifts of 17 BeppoSAX GRBs, Atteia (2003) investigated the $E_{\text{peak}} - E_{\text{iso}}$ correlation, given that these parameters are dependent on the luminosity distance. Defining the quantity $X = \frac{n_\gamma \sqrt{T_{90}}}{E_{\text{peak}}}$, with n_γ the observed photons' amount, the theoretical evolution of this quantity was given by:

$$X = A \times f(z), \quad (3.68)$$

with A a constant and $f(z)$ is the redshift evolution in the case of a “standard” GRB in a Λ CDM model ($H_0 = 65 \text{ km s}^{-1} \text{ Mpc}^{-1}$, $\Omega_M = 0.3$, $\Omega_\Lambda = 0.7$). Namely, the “standard” GRBs are defined as GRBs having parameters of the Band function $\alpha = -1.0$, $\beta = -2.3$, and $E_0 = 250 \text{ keV}$. Inverting the relation of the theoretical evolution, a redshift indicator was obtained through the observables. This redshift estimator is represented by the formula $z = \frac{1}{A} f^{-1}(X)$. This indicator can be able to make a quick classification of GRBs at $z > 3$, a comparison at a statistical level of the distance distributions of several GRB groups, and the evaluation of the high z SFR.

With 689 highly luminous BATSE LGRBs, Yonetoku et al. (2004) studied their spectra through the Band function. To retrieve significant S/N, the lowest value for the flux was established $F_{\text{lim}} = 2 \times 10^{-7} \text{ erg cm}^{-2} \text{ s}^{-1}$. Furthermore, they computed F_{peak} and E_{peak}^* . Then, considering the dependence of these quantities on $D_L(z, \Omega_M, h)$, they inverted the equation:

$$\log L_{\text{peak}} = (47.37 \pm 0.37) + (2.0 \pm 0.2) \log E_{\text{peak}}^*. \quad (3.69)$$

and the GRBs' pseudo-redshifts were recovered.

In addition, Tsutsui et al. (2013) studied the $E_{\text{peak}} - E_{\text{iso}}$ and the $L_{\text{peak}} - E_{\text{peak}}$ correlations for 71 BATSE SGRBs. From their analysis, the $L_{\text{peak}} - E_{\text{peak}}$ correlation appears stronger than the $E_{\text{peak}} - E_{\text{iso}}$ one, thus the first correlation seems to be a better redshift indicator. Considering a different form of the $L_{\text{peak}} - E_{\text{peak}}$ correlation:

$$\frac{D_L^2(z, \Omega_M, \Omega_\Lambda)}{(1+z)^{1.59}} = \frac{10^{52.29}}{4\pi F_{\text{peak}}} \left(\frac{E_{\text{peak}}}{774.5} \right)^{1.59}, \quad (3.70)$$

and $(\Omega_M, \Omega_\Lambda) = (0.3, 0.7)$, they computed the pseudo-redshifts from $D_L(z, \Omega_M, \Omega_\Lambda)$ (see Fig. 3.3.14). The application of the LT correlation as a redshift estimator was studied by Dainotti et al. (2011a). They concluded that reliable outcomes can be retrieved only in the case the scatter of the correlation is less than 20% and the errors in the parameters of the analysed GRBs are small. Given its smaller scatter, better outcomes for this redshift estimator are anticipated from the recent 3D (Dainotti et al., 2016) correlation.

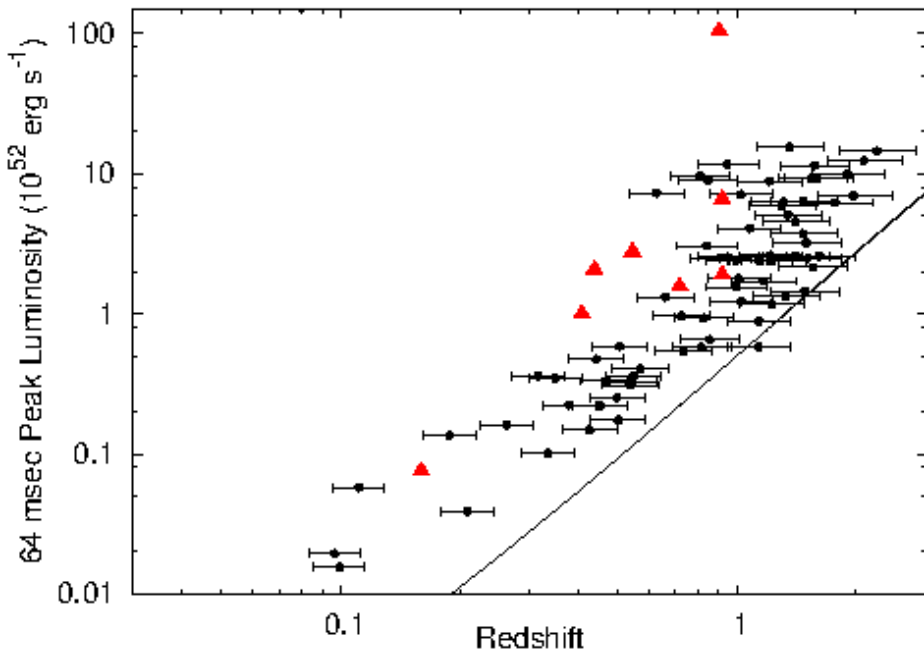


Figure 3.3.14: The distribution of z through the $\log L_{\text{peak}} - \log E_{\text{peak}}$ correlation for 71 bright BATSE SGRBs from (Ghirlanda et al., 2009). The pseudo-redshifts and L_{peak} are indicated by black dots, and secure SGRBs are displayed by red filled triangles; $z \in (0.097, 2.581)$ with $\langle z \rangle = 1.05$, while for Swift LGRBs $\langle z \rangle \approx 2.16$. The flux limit of $F_{\text{peak}} = 10^{-6} \text{ erg cm}^{-2} \text{ s}^{-1}$ is shown by the solid line. (Figure from Tsutsui et al. (2013).)

To investigate its use as redshift estimator, the hardness-intensity correlation, namely

the Golenetskii correlation, between the GRB spectral peak energy and its instantaneous luminosity, was analysed by Burgess (2015). For this reason, they applied a hierarchical Bayesian analysis. Employing a power-law form for the correlation, the indices were found around specific value, with scatter larger than those previously obtained, though. In addition, the rest-frame normalization of the correlation span between 10^{51} and $10^{53} \text{ erg s}^{-1}$, suggesting the presence of several quantity related to the radiation like the strength of the magnetic field, the number of emitting electrons, the photospheric radius, the viewing angle, and so forth. Therefore, it was concluded that the hardness-intensity correlation cannot be a reliable redshift estimator. Nevertheless, an improved estimation of the correlation properties in the rest-frame is retrieved through the Bayesian analysis applied here, providing tighter constraints for the physics of the radiation models.

Guiriec et al. (2013, 2016); Guiriec (2016) investigated the use of a correlation similar to the Yonetoku one (Yonetoku et al., 2004) as a redshift indicator. This correlation, between the non-thermal component luminosity, L_i^{nTh} , and its rest-frame spectral peak energy, $E_{\text{peak},i}^{nTh,\text{rest}}$, allowed for the evaluation of three redshifts.

An additional issue of this correlation is the measurement of the intrinsic scatter. Andreon (2013) investigated this problem as well as the controversial features of the data in astronomy, such as upper/lower limits, selection biases, intrinsic scatter, effect of the Malmquist bias on the samples, non-Gaussianity aspect of the observational data sample, so forth. It was claimed that the Bayesian analysis is a good choice for the description of the data characteristics. Indeed, after the data analysis, the posterior probability distribution provides all the available pieces of information about the analysed variables, and then the Monte Carlo simulations are employed for the numerical evaluation. As a main result, Andreon (2013) provided a way to bound the cosmological parameters computed through a sample of SNe and to confirm the functional form of the fit.

3.3.11 Applications to cosmology of GRB correlations among prompt parameters

To constrain the parameters of the cosmological model through a given sample of GRBs, Dai et al. (2004) and Xu et al. (2005) investigated a procedure based on the $E_{\text{peak}} - E_{\gamma}$ correlation using 12 and 17 GRBs, respectively. Dai et al. (2004) recovered $\Omega_M = 0.35^{+0.15}_{-0.15}$, while Xu et al. (2005) $\Omega_M = 0.15^{+0.45}_{-0.13}$, within 1σ confidence level (CL). These outcomes are in agreement with the one from SNe Ia.

Ghirlanda et al. (2006) studying a sample of 19 GRBs concluded that $E_{\text{peak}} - E_{\gamma}$ and $E_{\text{peak}} - E_{\text{iso}} - T_{\text{break}}$ correlations can be employed for cosmological purposes for the homogeneous (HM, see left panel in Fig. 3.3.15) and wind circumburst medium (WM, see middle panel in Fig. 3.3.15) events. Later, Ghirlanda (2009) using an updated sample of 29 GRBs confirmed earlier outcomes (see right panel in Fig. 3.3.15).

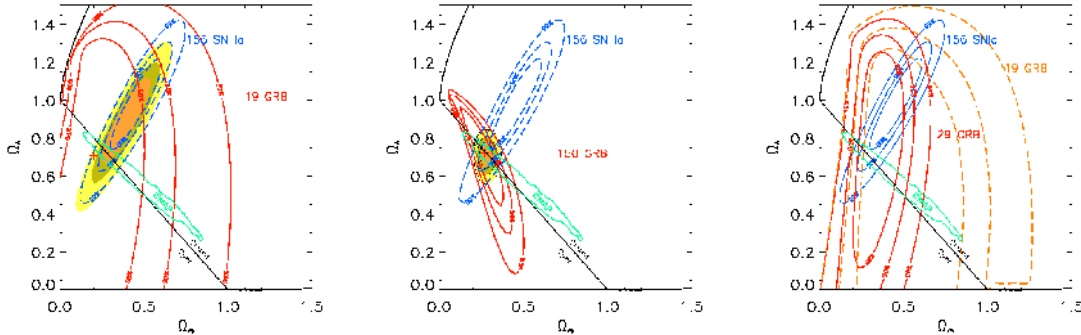


Figure 3.3.15: Left panel: The 68.3%, 90% and 99% contours of Ω_M and Ω_Λ from the $E_{\text{peak}} - E_\gamma$ correlation for a data set of 19 GRBs and HM (Ghirlanda et al., 2006) are indicated by the solid red line. The red cross represents the middle of these areas. The smallest χ^2 is provided by this point, together with values $\Omega_M = 0.23$, $\Omega_\Lambda = 0.81$. (Figure from Ghirlanda et al. (2006).) Middle panel: like in the left panel but retrieved through 150 simulated GRBs and the $E_{\text{peak}} - E_\gamma$ correlation for the WM. (Figure from Ghirlanda et al. (2006).) In both panels, the dashed blue lines indicate the contours for 156 SNe Ia from the “Gold” data set by Riess et al. (2004). The shaded contours display the boundaries retrieved from GRBs and SNe together. In this picture, 90% contours recovered through a WMAP sample are also plotted. Right panel: like in the previous panels, but with data extended to January 2009. The solid line indicates the updated sample of 29 GRBs, while the dashed line represents the earlier data set of 19 GRBs. The blue thin line displays the boundaries for a sample of 156 SNe Ia by Riess et al. (2004), while the green line depicts the constraints for a WMAP data set. (Figure from Ghirlanda (2009). Copyright @ 2009 AIP Publishing.)

Ghirlanda et al. (2006) employed three distinct procedures for the fitting of the cosmological parameters, using a sample of GRBs, to avoid the circularity problem:

1. The scatter procedure in which the cosmological parameters, such as Ω_M and Ω_Λ , required to be constrained. These parameters are selected to fit the correlation. In this procedure a χ^2 surface dependent on these quantities is retrieved. The minimum value of this surface gives the best cosmological model.
2. The luminosity distance procedure is divided in few stages: (1) select the cosmological parameters to fit the $E_{\text{peak}} - E_\gamma$ correlation; (2) retrieve the best value of $\log E_\gamma$; (3) compute $\log E_{\text{iso}}$ from $\log E_\gamma$ and consequently $D_L(z, \Omega_M, \Omega_\Lambda)$; (4) compare $D_L(z, \Omega_M, \Omega_\Lambda)$ with that from the cosmological model to compute χ^2 . After several selections of the values of the cosmological parameters, a χ^2 surface is recovered. Like in the previous procedure, the best cosmological model is provided by the minimum χ^2 .
3. The Bayesian procedure: the first two procedures rely on the statement that the origin of some correlations, e.g. the $E_{\text{peak}} - E_\gamma$ one, relies on the physical quantities characterizing them. Nevertheless, these procedures do not explain the point that also the GRB physics influences the correlations and, for this reason, they may be unique. A more composite procedure ground on the Bayesian analysis was developed by Firmani et al. (2005, 2007) using a sample of both GRBs and SNe Ia.

Also the $E_{\text{peak}} - E_{\text{iso}}$ correlation can be used for computing Ω_M , as shown in Amati et al. (2008). The scatter of this correlation can be properly estimated through the maximum likelihood method, providing in the case of a flat universe $\Omega_M = 0.04 - 0.40$ (68% CL) with best value $\Omega_M = 0.15$. The value $\Omega_M = 1$ is ruled out at $> 99.9\%$ CL. In this case the circularity problem (see Section 4.5.1) does not influence the results because no particular statements on the $E_{\text{peak}} - E_{\text{iso}}$ correlation are asserted. For computing the normalization further calibrators are not employed. In addition, their findings are independent of those from a sample of SNe Ia. Due to the expectations of the present and forthcoming space missions the errors in Ω_M and Ω_Λ can be considerably diminished.

To analyse the constraints on Ω_M and Ω_Λ , Tsutsui et al. (2009a) applied three correlations to 31 low z GRBs and 29 high z GRBs. The first correlation was the $E_{\text{peak}} - T_L - L_{\text{peak}}$ correlation, the second one was the $L_{\text{peak}} - E_{\text{peak}}$ one, and the third $E_{\text{peak}} - E_{\text{iso}}$ one. The last two correlations were calibrated through GRBs at $z \leq 1.8$ (see upper left and upper middle panels in Fig. 3.3.16, respectively). In the case of ΛCDM model with $\Omega_k = \Omega_M + \Omega_\Lambda - 1$, and Ω_k the density of the spatial curvature, the constraints for the $L_{\text{peak}} - E_{\text{peak}}$ and $E_{\text{peak}} - E_{\text{iso}}$ correlations are incompatible within 1σ , but comparable in 2σ . For this reason, they defined the quantity $T_L = E_{\text{iso}}/L_{\text{peak}}$, and the following correlation was retrieved:

$$\log L_{\text{peak}} = (49.87 \pm 0.19) + (1.82 \pm 0.08) \log E_{\text{peak}} - (0.34 \pm 0.09) \log T_L. \quad (3.71)$$

With the introduction of this quantity, the uncertainty of this correlation presented a decrease of 40%. For GRBs at $1.8 < z < 5.6$ the correlation recovered $(\Omega_M, \Omega_\Lambda) = (0.17^{+0.15}_{-0.08}, 1.21^{+0.07}_{-0.61})$, in agreement with the ΛCDM model (see upper right panel in Fig. 3.3.16). In the lower right and lower left panel of Fig. 3.3.16 are plotted the $\Omega_M - \Omega_\Lambda$ space and the HD employing the Amati correlation.

To stretch out the HD to $z = 5.6$, Tsutsui et al. (2009b) analysed the $L_{\text{peak}} - E_{\text{peak}}$ correlation using 63 GRBs and 192 SNe Ia (see Fig. 3.3.17). They applied three cosmological model: the ΛCDM model, a non-dynamical DE model (with the parameter of the DE EoS, $w_a = 0$), and a dynamical DE model (with the DE EoS $w(z) = w_0 + w_a z/(1+z)$). Their results obtained with the GRB sample were compatible with the ΛCDM model ($\Omega_M = 0.28$, $\Omega_\Lambda = 0.72$, $w_0 = -1$, $w_a = 0$) at 2σ CL. Then, they employed Monte Carlo simulations to compute the boundaries of the DE EoS parameters predicted by Fermi and Swift detections. It was found out that with further 150 GRBs these boundaries should become considerably tighter.

Later, Tsutsui et al. (2010) claimed that $D_L(z, \Omega_M, \Omega_\Lambda)$ can be computed with an uncertainty of $\sim 16\%$ through the $E_{\text{peak}} - T_L - L_{\text{peak}}$ correlation. This level of precision can be advantageous for investigating the DE at $z > 3$. Furthermore, Wang et al. (2011) claimed that correlations like the LT (Dainotti et al., 2008) and the $L_{X,p} - T_{X,p}^*$ (Qi and Lu, 2010)

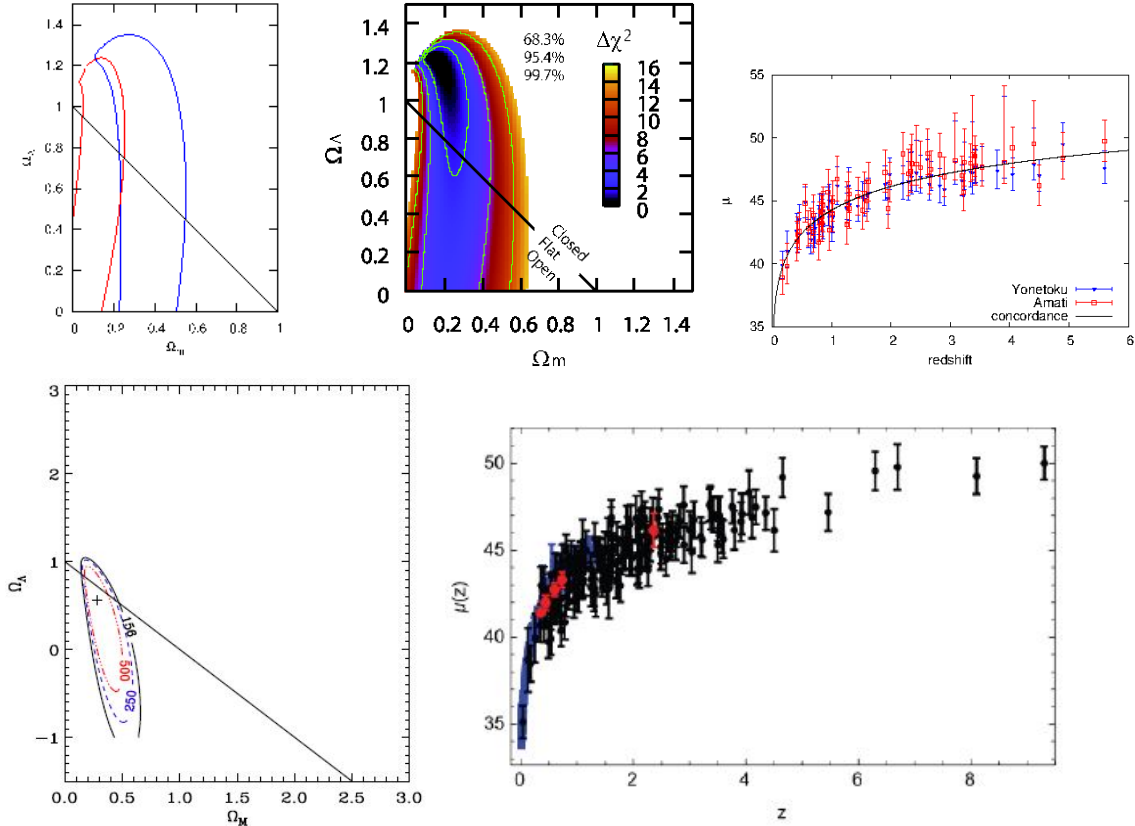


Figure 3.3.16: Upper left panel: 68.3% CL contours for Ω_M and Ω_Λ recovered through the Amati (presented in red) and the Yonetoku (indicated in blue) correlations. The flat universe is displayed by a black solid line. The constraints are in agreement within 2σ . (Figure from Tsutsui et al. (2009a). © SISSA Medialab Srl. Reproduced by permission of IOP Publishing. All rights reserved.) Upper middle panel: contours for Ω_M and Ω_Λ recovered through the $E_{\text{peak}} - T_L - L_{\text{peak}}$ correlation. (Figure from Tsutsui et al. (2009a). © SISSA Medialab Srl. Reproduced by permission of IOP Publishing. All rights reserved.) Upper right panel: HD obtained considering the Amati (presented in red) and the Yonetoku (indicated in blue) correlations. At high z a systematic discrepancy of HD, not observed at low z , shows up. (Figure from Tsutsui et al. (2009a). © SISSA Medialab Srl. Reproduced by permission of IOP Publishing. All rights reserved.) Lower left panel: Contours at 68% CL in the $\Omega_M - \Omega_\Lambda$ space considering 156 GRBs until the end of 2012, indicated by black dots, and GRB data predicted through the Amati correlation in the case of higher number of GRBs in the future, indicated by red and blue dots. (Figure from Amati and Della Valle (2013). Copyright © 2013 World Scientific Publishing Company.) Lower right panel: black dots indicate the HD for a GRB sample, while the blue and red dots represent the HD for a sample of SNe Ia and a sample of BAO data, respectively. (Figure from Demianski et al. (2017). Reproduced with permission © ESO.)

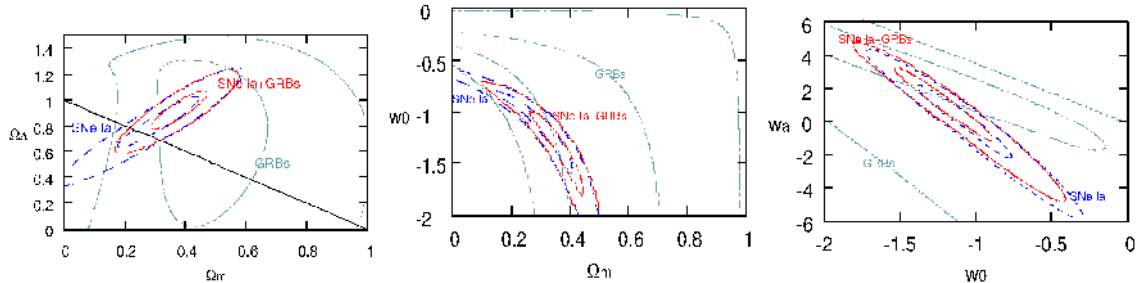


Figure 3.3.17: Maximum likelihood $\Delta\chi^2$ contours, at 68.3% and 99.7% CL, for the $(\Omega_M, \Omega_\Lambda)$ (left panel), the (Ω_M, w_0) (middle panel), and the (w_0, w_a) (right panel) distributions. Light blue dash-dotted lines indicate the constraints for GRBs, the blue dotted lines the ones for the SNe Ia, and the red solid lines the ones for SNe Ia and GRBs together. The flat universe is indicated by a black solid line. (Figures from (Tsutsui et al., 2009b).)

ones can be regarded as standard candles after suitable calibration. Wang et al. (2011) showed that this result can be achieved through the minimization of χ^2 , obtained by the maximum likelihood procedure, over both the correlation coefficients and the cosmological parameters. Indeed, through these correlations, the cosmic acceleration at high redshift could be better established and contemporaneously the constraints on the cosmic acceleration at low redshift may be enhanced. To differentiate between DE and modified gravity models, GRBs are in principle good tools to determine the cosmological parameters (Wang et al., 2009; Wang and Dai, 2009; Vitagliano et al., 2010; Capozziello and Izzo, 2008).

With a data set of 120 GRBs, Amati (2012) and Amati and Della Valle (2013) continued the work by Amati et al. (2008). To examine the DE, they simulated a data set of 250 GRBs (pink region in Fig. 3.3.18) to recover the 68% CL contours in the $\Omega_M - \Omega_\Lambda$ space. Then, these contours were brought into comparison together with those from SNe Ia, CMB and galaxy clusters (blue, green and yellow regions, respectively, in Fig. 3.3.18).

Amati and Della Valle (2013) applied a Monte Carlo method to simulate the sample. They considered the observed z distribution of the sample, the coefficients and the scatter of the $E_{\text{peak}} - E_{\text{iso}}$ correlation, and the errors in E_{peak} and E_{iso} quantities. From the simulation it was found that ≈ 250 GRBs are enough to recover Ω_M with a precision in agreement with that from SNe Ia. They also predicted values of Ω_M and w_0 from present and forthcoming detections. It was claimed that the $E_{\text{peak}} - E_{\text{iso}}$ correlation is calibrated with a precision of 10%. Indeed, they employed $D_L(z, \Omega_M, \Omega_\Lambda)$ obtained from a sample of SNe Ia and a GRB sample wide enough in a narrow interval ($\Delta z \sim 0.1 - 0.2$) to self-calibrate the GRB correlation. Finally, they yielded that the precision and reliability of the self-calibration of the $E_{\text{peak}} - E_{\text{iso}}$ correlation may improve for a larger sample of GRBs in each redshift bin.

Lin et al. (2016a) separated the data set of 116 GRBs, with z between 0.17 and 8.2 and used by Wang et al. (2011) into two subsamples: GRBs with $z < 1.4$ and GRBs with

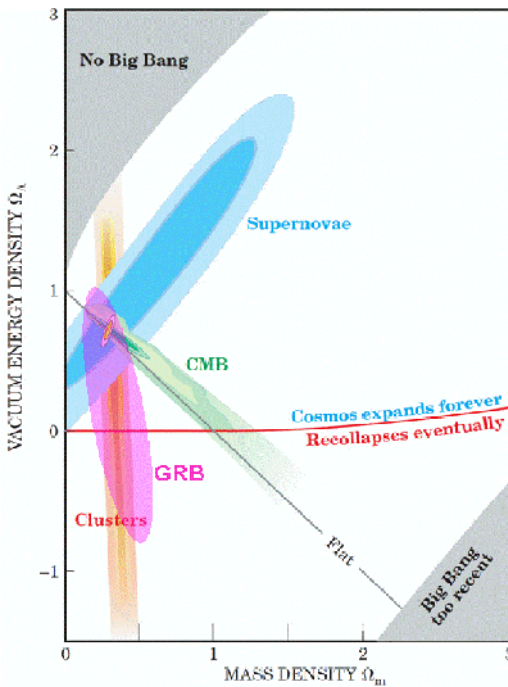


Figure 3.3.18: Contours at 68% CL in the $\Omega_M - \Omega_\Lambda$ space retrieved through 250 simulated GRBs from forthcoming missions (pink region) together with the ones from SNe Ia, CMB and galaxy clusters. (Figure from Amati and Della Valle (2013). Adapted and reproduced from Perlmutter (2003), with the permission of the American Institute of Physics.)

$z > 1.4$. The main aim was to analyse the redshift dependence of the $L_{\text{peak}} - \tau_{\text{lag}}$, $L_{\text{peak}} - V$, $L_{\text{peak}} - E_{\text{peak}}$, $E_{\text{peak}} - E_\gamma$, $L_{\text{iso}} - \tau_{\text{RT}}$, and $E_{\text{peak}} - E_{\text{iso}}$ correlations. From their analysis, GRBs at $z < 1.4$ retrieved a $E_{\text{peak}} - E_\gamma$ correlation compatible in 1σ CL with the one for GRBs at $z > 1.4$. The substantial value of the scatter for the $L_{\text{peak}} - V$ did not allow for any definitive statement. In the case of the other correlations, GRBs at $z < 1.4$ and those at $z > 1.4$ are incompatible at more than 3σ CL. For this reason, GRBs were calibrated, regardless of the model assumed, through the $E_{\text{peak}} - E_\gamma$ correlation. $\Omega_M = 0.302 \pm 0.142$ was recovered for GRBs at $z > 1.4$ at 1σ CL in the Λ CDM model. This result was completely compatible with the Planck 2015 ones (Planck Collaboration et al., 2016). To summarize, an independent estimation of Ω_M have been already supplied by GRBs, and it was supported by simulations that a precision similar to the one of SNe Ia can be accomplished by GRBs in the future.

3.3.12 Statistical approaches related to SNe Ia Cosmology

In this section, works about the cosmology of SNe Ia and their current status are investigated to improve the knowledge of the cosmological usage of GRBs. Indeed, some difficulties with the statistical procedures for the analysis of SNe Ia are presented in the literature, even if they

are well established standard candles. For this reason, in the case of GRBs, which are physical phenomena considerably less known, the errors of the GRB correlations are significant, with the selection biases influencing the outcomes, and the data set of the luminosity indicators is much more exiguous. Statistical methods and procedure of standardization for SNe Ia and GRBs are described. In particular, the methods for SNe Ia that could be more useful and efficient for cosmological studies of GRBs are discussed.

Considering random selection biases, Mandel et al. (2009) developed a description of the Near Infrared (NIR) light curves of SNe Ia. This seemed a very encouraging procedure, because NIR radiation is not affected by dust extinction and additionally NIR luminosities provide reliable standard candles. To rule out the random influences of diverse SNe, a large number of light curves were employed. This choice favoured those light curves in which dust absorption is not very relevant. In fact, the dust extinction is the main uncertainty that reduces the precision of the optical light curves. A hierarchical Bayesian analysis was applied to retrieve NIR light curves of SNe Ia, distribution of the intrinsic fluctuation of the light curves, and dust distribution. This Bayesian method was employed to evaluate the yet not explored SN parameters. Through a non-parametric method, they shaped locally the light curves assuming local parameters. The lack of data can be also managed using this method, deducing them in the case of incomplete time coverage or variability in the light curves. A hierarchical Bayesian method was employed by Mandel (2011) to properly describe randomized effects on the redshift like dust extinction, intrinsic fluctuations of the light curves and distances. Inferential models were also developed for optical and NIR ranges. Applying a Markov Chain Monte Carlo algorithm re-sampling the global posterior probability density, this work was an update of the one by Mandel et al. (2009). The advantage of employing both NIR and optical samples is dual: the dust extinction is attenuated and the estimation of the SNe Ia distances is more accurate by 60%. Indeed, through cross-validation, for SNe with optical and NIR data the error in the distance modulus ($\mu(z)$) was of 0.11 mag in comparison to 0.15 mag for optical SNe only. For this reason, to use these objects as distance indicators, it was strongly recommendable further investigation of SNe Ia in the NIR range.

Unlike this method, for cosmological studies of GRBs, a Bayesian analysis was applied (Reichart, 1999; D'Agostini, 2005). It was stressed that this method is not hierarchical. In this way the intrinsic scatter (σ_{int}) was characterized by global, not local, parameters. On the other hand, randomness, errors, intrinsic SN fluctuation, dust extinction, reddening, velocities and distances for each SN were included in this parametric approach. The main quantities of the SN Ia light curves were: intrinsic fluctuation, colour and luminosity in several wavelengths. The distribution of host galaxy dust was dominated by the dust parameters. The approach associated randomly the dust parameters to every SN light curve from the distribution of the real parameters. To produce a light curve with noise similar to the observed multi-wavelength light curve, the dust parameters were combined with $\mu(z)$ and

the light curves. For the near universe $\mu(z)$ is a function not only of the redshift through the Hubble law, but also of a noise component indicating random velocities of the host galaxies. This random procedure was applied to each SN of the sample.

To tighten the constraints of the cosmological parameters for SNe Ia data from the SALT-II light curve fitter, March et al. (2011) employed a Bayesian hierarchical method. Diminishing biases by 2 – 3 times through a simulated sample, their analysis reduced the confidence range of the cosmological parameters. Furthermore, they recovered a posterior probability distribution for the scatter of the intrinsic magnitude of SNe. Through this procedure, for the up-to-date SNe Ia and BAO and CMB samples, $\Omega_M = 0.28 \pm 0.02$ and $\Omega_\Lambda = 0.73 \pm 0.01$ were found for $w = -1$, and $\Omega_M = 0.28 \pm 0.01$ and $w = -0.90 \pm 0.05$ were found for the flat model. Finally, σ_{int} of the B magnitude of SNe Ia data was constrained providing $\sigma_\mu = 0.13 \pm 0.01$ mag.

Employing a BAyesian HierArchical Modeling for the Analysis of Supernova cosmology (the BAHAMAS software), 740 SNe Ia from the sample of the “Joint Light-curve Analysis” (JLA) were investigated by Shariff (2016). Joining JLA and Planck CMB samples, the cosmological parameters were evaluated in comparison with the standard analysis. They pointed out significant differences in these quantities: $\Omega_M = 0.399 \pm 0.027$ and $w = -0.910 \pm 0.045$, 2.8 σ and 1.6 σ larger than earlier results, respectively. A question arose naturally: Is this difference due to two subsamples with distinct host galaxy masses or to a 4 σ discrepancy between the colour corrections at $z = 0.662$? It was concluded that neither of the two was the reason of the difference in the results. Therefore, this is still an unsolved question.

Furthermore, the issues of the SNe cosmological methods regarding the outliers’ treatment, selection biases, diverse observations, σ_{int} , shape and colour standardization of the correlations were investigated by Rubin et al. (2015). Employing a brand new Bayesian model, UNITY (Unified Nonlinear Inference for Type-Ia cosmologY), to a number of observed SNe light curves, they improved the outcomes retrieving smaller statistical and systematic errors. They confirmed that SNe Ia demand nonlinear shape and colour standardizations, but these nonlinear correlations were taken into account in a proper statistical way in this procedure. In this analysis, the validation of the procedure was first made on a simulated sample, and then reiterated with a real sample. They did not find any change in the results.

Considering the larger up-to-date sample of SNe Ia, Nielsen et al. (2016) examined the standard cosmological model to check if a larger sample can reproduce the same results obtained with the SNe sample employed for the discovery of the cosmic acceleration. Employing the corrections to the absolute magnitudes to describe the fluctuation of the light curve and the dust extinction, the rate of expansion was found almost constant. This surprising result provided only a negligible proof for the cosmic acceleration.

From all these analyses, GRBs, observed at higher redshift than SNe Ia, may explain the differences in the cosmological parameters claimed by March et al. (2011). In addition, the

study of GRBs have the potential to cast light on the cosmic acceleration as investigated in Nielsen et al. (2016). To have a precision cosmology in agreement with that for SNe Ia, the strategy for the study of GRBs for cosmological purposes should be enhanced. This is the main goal of forthcoming space missions like SVOM (Cordier et al., 2015) and Theseus (Amati et al., 2017).

Finally, analogies and differences in the methodology adopted to use GRBs and SNe Ia as cosmological tools are described. The circularity problem affecting GRBs (see Section 4.5.1) can be eluded through parameters independent of the cosmological model. Instead, the Cepheids can properly calibrate SNe Ia in the same galaxy, especially those at low z . Therefore, the calibration is not a relevant problem for SNe Ia. Furthermore, unlike the non-parametric method by Mandel (2011), the procedure for GRBs is parametric and employed through established correlations, not through individual light curves. Indeed, in the non-parametric procedure, first of all the light curve has to be reproduced locally to represent its behaviour in every phase and energy range. Only after that it is possible to obtain the description of the whole light curve in all the energy ranges. A method to treat lack of data is given also by the probabilistic hierarchical approach. But, for GRBs there is still no such elaborated procedure for analysing correlations among prompt parameters. For this reason, selection effects can be present. Nevertheless, tighter cosmological parameters could be provided by the local description through the application of this procedure to GRBs. The light curves in the Swift repository are already unabsorbed, for details see Evans et al. (2009). Thus, the dust extinction is not a variable of the hierarchical method. Moreover, the GRB intrinsic scatter, σ_{int} , is evaluated parametrically. Furthermore, from the GRB investigation a training sample in the light curves has not been determined yet. To choose this training set and extend the approaches for SNe Ia to GRBs, the gold set of GRBs with flat plateau phases (Dainotti et al., 2016) alone can supply a fundamental aid, without any additional GRB observational sample (Dainotti et al., 2017b).

CHAPTER 4

Correlations among afterglow and prompt-afterglow parameters

This Chapter is based on the article Dainotti, M.G & Del Vecchio, R., New Astronomy Reviews, Volume 77, p. 23-61, (2017). In this work lead by Dr. M.G. Dainotti, the contribution of the thesis author was to select some interesting papers about GRB correlations among afterglow phase parameters and prompt-afterglow parameters. She also helped with tables, figures and text during the manuscript preparation, and took part in the discussion about the reply to the referee's comments.

4.1 The correlations among afterglow parameters

The main correlations among physical parameters of the afterglow phase presented in the literature are: the LT correlation (Dainotti et al., 2008), the unified $L_{X,a}$ - $T_{X,a}^*$ and $L_{O,a}$ - $T_{O,a}^*$ correlations (Ghisellini et al., 2009) and the $L_{O,200s}$ - $\alpha_{O,>200s}$ correlation (Oates et al., 2012).

4.1.1 The LT correlation ($L_{X,a}$ - $T_{X,a}^*$)

The LT correlation is the first to investigate the plateau phase features. This is an anti-correlation between $L_{X,a}$ and $T_{X,a}^*$, for definitions see Section 3.2.

It was discovered by Dainotti et al. (2008) employing 33 LGRBs detected by XRT. This sample is derived from the one analysed by W07 by selecting GRBs with known z and reliable spectral parameters. The LT correlation reads as follows:

$$\log L_{X,a} = a + b \times \log T_{X,a}^*, \quad (4.1)$$

with $\log L_{X,a}$ in erg s^{-1} and $T_{X,a}^*$ in seconds, a normalization $a = 48.54$, a slope $b = -0.74^{+0.20}_{-0.19}$, $\sigma_{int} = 0.43$, and a Spearman correlation coefficient $\rho = -0.74$. $L_{X,a}$ has been calculated in the Swift XRT energy band using the formula:

$$L_{X,a}(z) = 4\pi D_L^2(z, \Omega_M, h) F_{X,a} \times K \quad (4.2)$$

where $D_L(z, \Omega_M, h)$ is the GRB luminosity distance for a given z , $F_{X,a}$ the flux in the X-ray energy band at the end of the plateau phase, and $K = \frac{1}{(1+z)^{(1-\beta_{X,a})}}$ the K-correction for cosmic expansion (Bloom et al., 2001). From this anti-correlation it is suggested that the shorter the plateau phase duration, the brighter the plateau phase. Since the errors in both the variables $\log T_{X,a}$ and $\log L_{X,a}$ are comparable, it is more appropriate to employ a method that takes into account both the error bars rather than the simple method of the Levenberg-Marquardt algorithm. The latter method considers that the errors in one variable are negligible compared to the errors in the other variable. Thus, the fitting method by D'Agostini (2005), which relies on Bayesian assumptions and account also for σ_{int} of an unknown nature, have to be employed. However, Dainotti et al. (2008) checked that the results of both the D'Agostini method and the Levenberg-Marquardt algorithm are in agreement within 1σ . Clearly, if the final goal is to employ this correlation as a model discriminator and as a cosmological tool, it is mandatory to reduce as much as possible the scatter of this correlation. To this end, a subset of GRBs taken from the initial sample of 33 GRBs has been chosen with definite selection criteria: $\log L_{X,a} > 45$ and $1 \leq \log T_{X,a}^* \leq 5$. With this choice the sample dropped to 28 GRBs obtaining a correlation with a much smaller scatter (23%) and with $(a, b, \sigma_{int}) = (48.09, -0.58 \pm 0.18, 0.33)$.

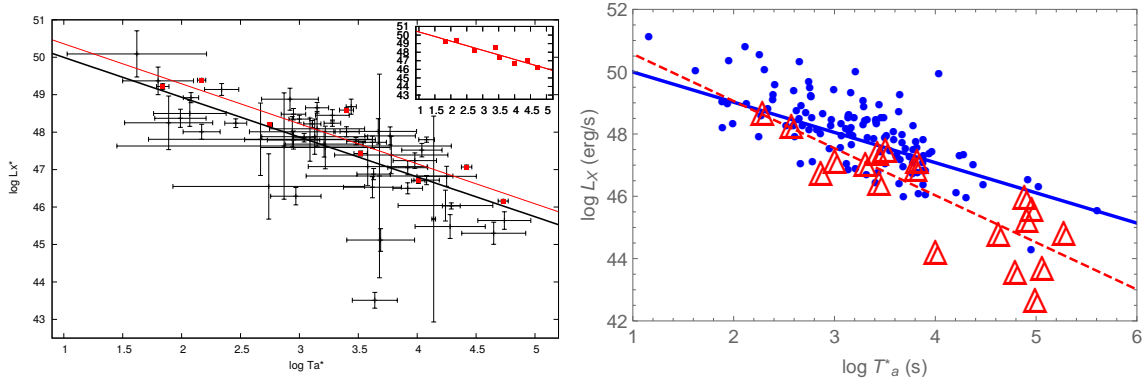


Figure 4.1.1: Left panel: the $\log L_{X,a}$ ($\log L_X^*$ in the plot)- $\log T_{X,a}^*$ distribution for 62 LGRBs with $\sigma_E < 4$ and the best fit indicated by the black line. The 8 red points with the lowest errors in the sample are fitted with a red line and displayed also in the subpanel at the upper right corner. (Figure from Dainotti et al. (2010). @ AAS. Reproduced with permission.) Right panel: the blue points (fitted with a solid line of the same colour) indicate 128 GRBs of the LONG-NO-SNe set, while the red empty triangles (fitted with a dashed line of the same colour) represent 19 GRBs of the LONG-SNe set (Figure from Dainotti et al. (2017b). Reproduced with permission @ ESO.)

From the investigation of 33 LGRBs during the late prompt phase in optical and X-ray bands, Ghisellini et al. (2009) confirmed the value of the slope for the LT correlation, $b = -0.58^{+0.18}_{-0.18}$, when this particular selection choice is applied: $1 \leq \log T_{X,a}^* \leq 5$.

Afterwards, a slope $b = -1.06^{+0.27}_{-0.28}$ was recovered by Dainotti et al. (2010), considering 62 LGRBs. While taking into account only the 8 IC GRBs in the sample $b = -1.72^{+0.22}_{-0.21}$ was

obtained. Additionally, introducing the quantity $\sigma_E = (\sigma_{\log L_{X,a}}^2 + \sigma_{\log T_{X,a}^*}^2)^{1/2}$, with $\sigma_{\log L_{X,a}}$ and $\sigma_{\log T_{X,a}^*}$ the errors in luminosity and time respectively, Dainotti et al. (2010) claimed that for the 8 GRBs with the smallest errors ($\sigma_E < 0.095$) the LT correlation has a slope $b = -1.05^{+0.19}_{-0.20}$ (see the left panel of Fig. 4.1.1, the right panel of Fig. 4.1.2, and Table 4.1). Likewise, Bernardini et al. (2012b) and Sultana et al. (2012), from the analysis of 64 and 14 LGRBs respectively, retrieved a slope $b \approx -1$ (for details see Table 4.1).

Later, Dainotti et al. (2011a) retrieved a correlation with $b = -1.20^{+0.27}_{-0.30}$, using an enlarged data set of 77 LGRBs. Instead, Mangano et al. (2012) obtained a steeper slope ($b = -1.38^{+0.16}_{-0.16}$), but mostly due to the fact that they used in their set of 50 LGRBs some GRBs with no evident plateau phase. They fitted this sample with a broken power-law as a fitting function instead of the W07 model. From the outcomes of all these works, it was concluded that when the number of GRBs is enlarged a steepening of the slope is pointed out.

For this reason, Dainotti et al. (2013b) studied the selection biases affecting the correlation. They found that, even if the steepening of the correlation slope is caused by selection biases, the intrinsic (namely, after it has been fully corrected for selection biases) slope (b_{int}) of the correlation can be computed through a robust statistical analysis. Eventually it has value $b_{int} = -1.07^{+0.09}_{-0.14}$, (see Section 4.3). In conclusion, Dainotti et al. (2013b) and Rowlinson et al. (2014) corroborated the outcomes from Dainotti et al. (2010) by using enlarged samples of 101 and 159 GRBs, respectively.

The previous results by Dainotti et al. (2013b) were validated from Dainotti et al. (2015a) using a wider data set of 123 LGRBs detected by Swift/XRT.

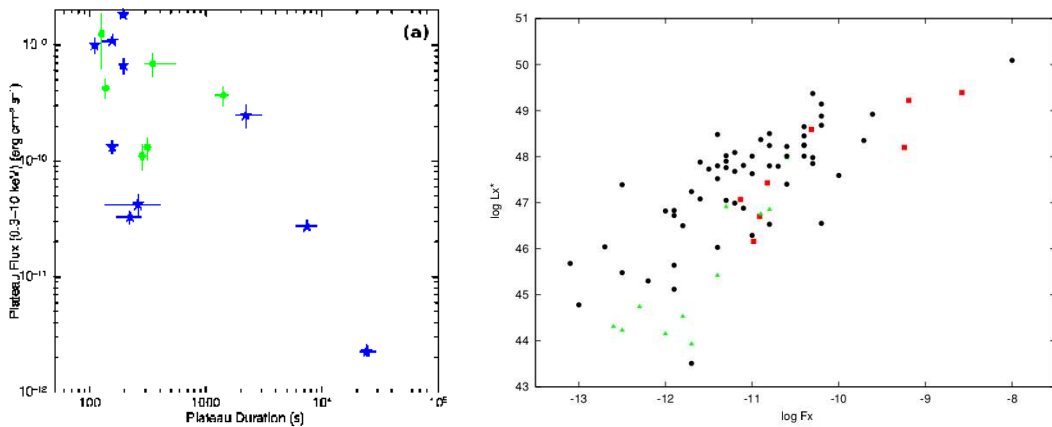


Figure 4.1.2: Left panel: flux versus time for the plateau phase of 22 SGRBs. GRB light curves with two or more breaks are shown as blue stars, while GRB light curves with only one break are represented by green circles (Figure from Rowlinson et al. (2013).) Right panel: the $\log L_{X,a} - \log F_{X,a}$ distribution for the whole GRB set. Red squares represent the 8 GRBs with the lowest errors in the sample, while the green triangles the IC GRBs. (Figure from Dainotti et al. (2010). © AAS. Reproduced with permission.)

To diminish the scatter of the LT correlation, using 176 Swift GRBs Del Vecchio et al. (2016) studied the temporal decay indices after the plateau phase, $\alpha_{X,a}$, obtained through two different fitting functions: a simple power-law, taking into account the declining part after

Author	N	Type	Slope	Norm	Corr.coeff.	P
Dainotti et al. (2008)	28	$1 < T_{X,a}^* < 5$	$-0.58^{+0.18}_{-0.18}$	48.09	-0.80	1.6×10^{-7}
Dainotti et al. (2008)	33	All GRBs	$-0.74^{+0.20}_{-0.19}$	48.54	-0.74	10^{-9}
Cardone et al. (2009)	28	L	$-0.58^{+0.18}_{-0.18}$	48.09	-0.74	10^{-9}
Ghisellini et al. (2009)	33	L	$-0.58^{+0.18}_{-0.18}$	48.09	-0.74	10^{-9}
Cardone et al. (2010)	66	L	$-1.04^{+0.23}_{-0.22}$	$50.22^{+0.77}_{-0.76}$	-0.68	7.6×10^{-9}
Dainotti et al. (2010)	62	L	$-1.06^{+0.27}_{-0.28}$	$51.06^{+1.02}_{-1.02}$	-0.76	1.85×10^{-11}
Dainotti et al. (2010)	8	high luminosity	$-1.05^{+0.19}_{-0.20}$	$51.39^{+0.90}_{-0.90}$	-0.93	1.7×10^{-2}
Dainotti et al. (2010)	8	IC	$-1.72^{+0.22}_{-0.21}$	$52.57^{+1.04}_{-1.04}$	-0.66	7.4×10^{-2}
Dainotti et al. (2011a)	77	L	$-1.20^{+0.27}_{-0.30}$	$51.04^{+0.27}_{-0.30}$	-0.69	7.7×10^{-8}
Sultana et al. (2012)	14	L	$-1.10^{+0.03}_{-0.03}$	$51.57^{+0.10}_{-0.10}$	-0.88	10^{-5}
Bernardini et al. (2012)	64	L	$-1.06^{+0.06}_{-0.06}$	51.06	-0.68	7.6×10^{-9}
Mangano et al. (2012)	50	L	$-1.38^{+0.16}_{-0.16}$	$52.2^{+0.06}_{-0.06}$	-0.81	2.4×10^{-10}
Dainotti et al. (2013a)	101	simulated	$-1.52^{+0.04}_{-0.24}$	$53.27^{+0.54}_{-0.48}$	-0.74	10^{-18}
Dainotti et al. (2013b)	101	ALL intrinsic	$-1.07^{+0.09}_{-0.14}$	52.94	-0.74	10^{-18}
Dainotti et al. (2013b)	101	All GRBs	$-1.32^{+0.18}_{-0.17}$	$52.8^{+0.9}_{-0.3}$	-0.74	10^{-18}
Dainotti et al. (2013b)	101	without short	$-1.27^{+0.18}_{-0.26}$	52.94	-0.74	10^{-18}
Postnikov et al. (2014)	101	L ($z < 1.4$)	$-1.51^{+0.26}_{-0.27}$	$53.27^{+0.54}_{-0.48}$	-0.74	10^{-18}
Rowlinson et al. (2014)	159	intrinsic	$-1.07^{+0.09}_{-0.14}$	52.94	-0.74	10^{-18}
Rowlinson et al. (2014)	159	observed	$-1.40^{+0.19}_{-0.19}$	$52.73^{+0.52}_{-0.52}$	-0.74	10^{-18}
Rowlinson et al. (2014)	159	simulated	$-1.30^{+0.03}_{-0.03}$	$52.73^{+0.52}_{-0.52}$	-0.74	10^{-18}
Dainotti et al (2015)	123	L	$-0.90^{+0.19}_{-0.17}$	$51.14^{+0.58}_{-0.58}$	-0.74	10^{-15}
Dainotti et al. (2017)	19	L-SNe	$-1.5^{+0.3}_{-0.3}$	$51.85^{+0.94}_{-0.94}$	-0.83	5×10^{-6}

Table 4.1: Summary of the LT correlation. All GRBs are observed by Swift. The authors are indicated in the first column, the size of the data set is displayed in the second one, the type of GRB (S=Short, L=Long, IC=Intermediate) is listed in the third one. The slope and normalization of the correlation are shown in the fourth and the fifth columns, respectively. The correlation coefficient and the chance probability, P, are presented in the last two columns, respectively. (Table from Dainotti and Del Vecchio (2017).)

the plateau phase, and the W07 one (see Section 1.2). Given that the findings do not depend on the chosen function, Del Vecchio et al. (2016) looked for some common characteristics in GRBs to use them as standard candles and to constrain the physical models presented by Hascoët et al. (2014) for the plateau phase emission. As a result, it was pointed out that the $\alpha_{X,a}$ parameter can give rise to different LT correlations for the low and high luminosity GRBs, indicating a difference in the density of the external medium.

Recently, using a data set of 176 Swift GRBs with measured redshifts Dainotti et al. (2017b) found out that the group of LGRBs connected with SNe (LONG-SNe) displays a LT correlation with a significant Spearman correlation coefficient, ρ (see the right panel of Fig. 4.1.1). Comparing the group of LONG GRBs associated with SNe to that of LGRBs with no associated SNe (hereafter LONG-NO-SNe, 128 GRBs), they employed the Efron and Petrosian (1992) method to investigate whether there is an intrinsic difference among the slopes of these two subsamples. To this end, the first step was to verify if there is a different redshift evolution pertained to the 128 LONG-NO-SNe sample compared to the evolution associated with the previous analysed sample of 101 GRBs. In the latter sample all the GRB categories were considered together (Dainotti et al., 2013b). This step is mandatory because the two subsamples are observed at different redshifts, namely the LONG-NO-SNe sample is observed at higher z than the LONG-SNe sample. The second step is to test if the intrinsic slope, b_{int} , of the 128 LONG-NO-SNe sample is different from the observed one of the same sample. The third step is to compare b_{int} of the two samples assuming the sample of the GRB-SNe is not affected by redshift evolution since it is observed at small redshifts. Through this analysis, they concluded that b_{int} for the LONG-NO-SNe group is the same as the observed one, thus no steepening of the slope for this sample is found. Therefore, they compared the slopes of the two samples retrieving a statistical difference ($P = 0.005$) between the LONG-SNe sample with firm spectroscopic evidence and the LONG-NO-SNe sample. Since the observed slope of the LONG-SNe sample with firm spectroscopic evidence is -1.9 , this value highly likely implies that this sample does not demand a typical energy reservoir for the plateau phase. As a result, this study might envision a new path for future theoretical modelling. In this work it was also investigated how θ_{jet} can affect these results. If the same beaming angle of 10° is chosen for the all LONG-NO-SNe sample the slope of the sample does not change, but it experiences only a shift in the normalization. However, the beaming angle is larger for low luminous GRBs. Thus, assuming the beaming correction, the discrepancies between the two groups are only statistically significant at the 10%. Therefore, this evidence opens two possible scenarios: the differences in the slopes may be due to the poor accuracy in the determination of θ_{jet} or to the presence of dim GRBs in the LONG-SNe sample which have not been previously corrected for the beaming angles. For these reasons, the discussion is not concluded, thus it will be very helpful to collect new data for further analysis. In Table 4.1, the parameters a and b with ρ and P for the LT correlation are displayed.

Physical interpretation of the ($L_{X,a}$ - $T_{X,a}^*$) correlation

In this section the theoretical interpretation of the LT correlation is presented. The accretion (Cannizzo and Gehrels, 2009; Cannizzo et al., 2011) and the magnetar models (Zhang and Mészáros, 2001; Dall’Osso et al., 2011; Rowlinson and O’Brien, 2012; Rowlinson et al., 2013, 2014) are the main theoretical descriptions for the LT correlation. In the first model the material moving around the GRB progenitor star and collapsing towards the core of the progenitor generates an accretion disk. After the material around the disk is squeezed by the gravitational forces, the GRB is emitted. Kumar et al. (2008) suggested that in LGRBs the early steep decay phase slope can give constraints on the distribution of the radial density in the progenitor.

A steeper correlation slope (-3/2) than the observed one (~ -1) was obtained by Cannizzo and Gehrels (2009), nevertheless it was comparable with the one retrieved from the model by Yamazaki (2009). With a set of 62 LGRBs and few SGRBs Cannizzo et al. (2011) analysed the simulated fall-back disks around the BH. They pointed out that a circularization radius with value $10^{10} - 10^{11}$ cm provides a value for the plateau phase duration of 10^4 s for LGRBs, with the starting fall-back mass $10^{-4} M_\odot$ (see the left panel of Fig. 4.1.3). In the case of SGRBs the radius is evaluated to be around 10^8 cm. A lower limit for the accreting mass is provided by the LT correlation and it has a value between 10^{-4} and $10^{-3} M_\odot$ ¹. Therefore, it was concluded that if a standard energy reservoir for the fall-back mass is taken into account, the LT correlation can be recovered (see the right panel of Fig. 4.1.3). Although, in this work the very steep decay following the prompt phase is not examined, differently from Lindner et al. (2010).

Instead, in regard to the magnetar model, Zhang and Mészáros (2001) investigated the effects of a strongly magnetized millisecond pulsar on the GRB afterglow phase. They concluded that, for particular initial pulsar rotation period and magnetic field, the afterglow phase should display an achromatic bump lasting from minutes to months. This feature can determine some limits on the progenitor models. Later, Dall’Osso et al. (2011) recovered the GRB shallow decay phase characteristics by fitting few Swift XRT light curves and computing the parameters for the magnetar model (i.e. spin period of 1 – 3 ms and magnetic field $\sim 10^{14} - 10^{15}$ G). They also reproduced within this scenario the LT correlation (see the left panel of Fig. 4.1.4).

Similarly to Dall’Osso et al. (2011), Bernardini et al. (2012b), analysing a data set of 64 LGRBs, verified that the GRB light curve phase, displaying a shallow decay which obey the LT correlation, can be well described in the framework of the magnetar model. Rowlinson and O’Brien (2012) and Rowlinson et al. (2013) claimed that the energy injection, produced by a magnetar, is able to nicely represent most SGRBs.

¹The following estimate can be calculated assuming the total accretion mass $\Delta M/M = \Delta E_X/f^{-1} * \epsilon_{acc} * c^2$, with c the light speed, f the beaming factor, ϵ_{acc} the efficiency of accretion onto the BH, and E_X the plateau energy plus later decaying stages.

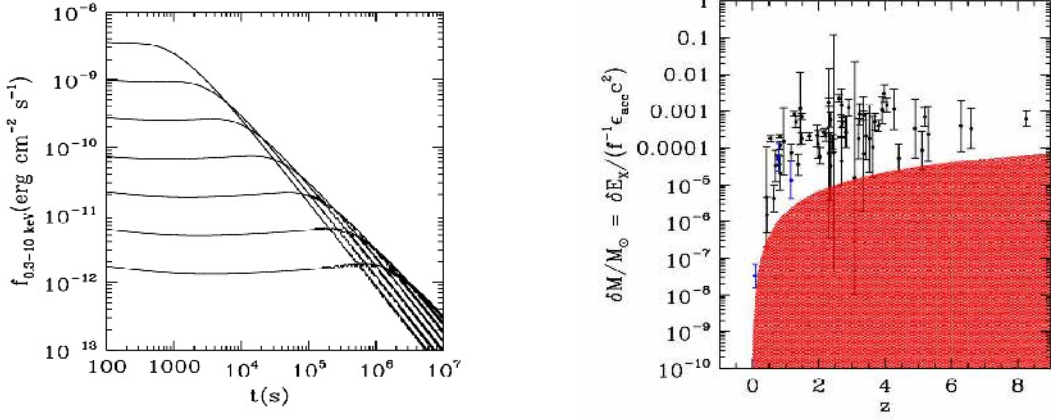


Figure 4.1.3: Left panel: light curves for LGRBs obtained through the constant ($10^{-4} M_\odot$) fall-back disk mass but modifying the normalization and initial radius. (Figure from Cannizzo et al. (2011). @ AAS. Reproduced with permission.) Right panel: the total accretion mass for the plateau phase added to the later decay phases of GRBs for 62 LGRBs from Dainotti et al. (2010). A limiting XRT detection flux level of $10^{-12} \text{ erg cm}^{-2} \text{s}^{-1}$ with a plateau phase lasting 10^4 s is displayed by the red area. A value of the beaming factor $f = 1/300$ and a value of the net efficiency fuelling the X-ray flux $\epsilon_{\text{net}} = \epsilon_{\text{acc}} \epsilon_X = 0.03$ are considered. (Figure from Cannizzo et al. (2011). @ AAS. Reproduced with permission.)

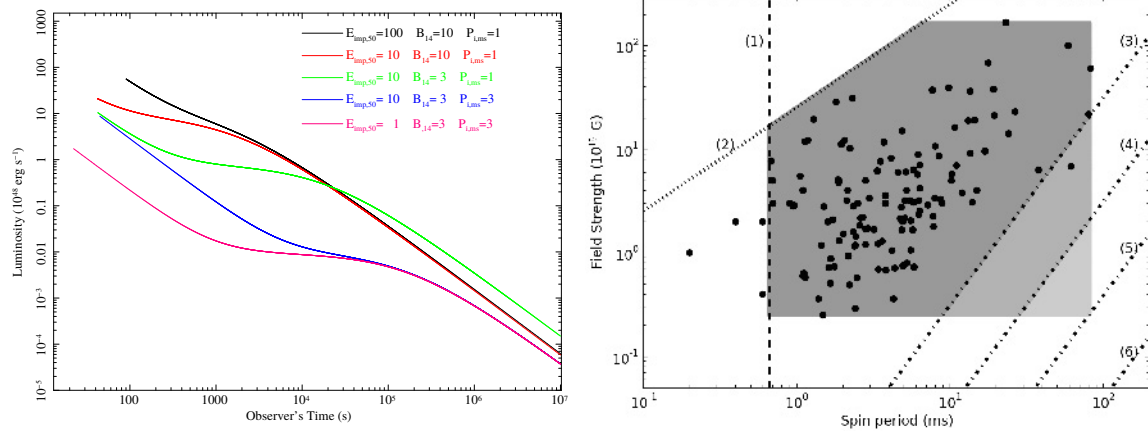


Figure 4.1.4: Left panel: five light curves computed through the variation of the afterglow energy and the NS spin period, P , at the beginning and the dipole magnetic field, B . (Figure from Dall'Osso et al. (2011). Reproduced with permission @ ESO.) Right panel: the regular distributions of B and P assumed in the simulation of the observed magnetar plateau phases are indicated with grey shaded area. The magnetar model (Lyons et al., 2010; Dall'Osso et al., 2011; Bernardini et al., 2012b; Gompertz et al., 2013; Rowlinson et al., 2013; Yi et al., 2014; Lü and Zhang, 2014) was used for the fit of the light curves to recover upper and lower boundaries on B and P . For an explanation of the different areas of the plot see Rowlinson et al. (2014). From these distributions it was concluded that the efficiencies and the beaming angles of the GRBs in their sample are small. (Figure from Rowlinson et al. (2014).)

Additionally, by employing 159 Swift GRBs Rowlinson et al. (2014) proved that the central engine model recovers the LT correlation. This result was obtained assuming that the compact object is emitting energy into the FS. The luminosity and plateau phase duration are given by:

$$\log L_{X,a} \sim \log(B_p^2 P_0^{-4} R^6) \quad (4.3)$$

and

$$\log T_{X,a}^* = \log(2.05 \times I B_p^{-2} P_0^2 R^{-6}), \quad (4.4)$$

where $T_{X,a}^*$ is in units of 10^3 s, $L_{X,a}$ is in units of 10^{49} erg s $^{-1}$, the moment of inertia in units of 10^{45} g cm 2 is expressed by I , the strength of the magnetic field at the poles in units of 10^{15} G is indicated by B_p , the NS radius in units of 10^6 cm is given by R , and the initial period of the compact object in milliseconds is described by P_0 . After, replacing the radius from Equation 4.4 into Equation 4.3, it was obtained that:

$$\log(L_{X,a}) \sim \log(10^{52} I^{-1} P_0^{-2}) - \log(T_{X,a}^*). \quad (4.5)$$

This indicates the existence of an intrinsic $\log L_{X,a} \sim -\log T_{X,a}^*$ correlation. Even if some magnetar plateau phases seem in disagreement with energy injection into the FS, Rowlinson et al. (2014) pointed out that the rotational energy transfer from the compact object to the luminosity of the plateau phase has $\leq 20\%$ efficiency and this emission is narrowly beamed. Moreover, the intrinsic LT correlation slope is recovered within the framework of the spin-down of a recently produced magnetar at 1σ level (see the right panel of Fig. 4.1.4). The scatter in this correlation is caused by the different initial spin periods.

Contributing to the discussion of all these papers on the connection of the LT correlation with the magnetar model, Rea et al. (2015) employed a sample of Swift GRBs with measured z observed from its launch until August 2014. They pointed out that the initial magnetic field distribution of GRB-magnetars is not in agreement with the one of the Galactic magnetars. For this reason, the GRB-magnetar model is correct only if two types of magnetar progenitors are allowed. In particular, GRB-magnetars should be regarded as supermagnetars (magnetars with a huge initial magnetic field) and separately from Galactic magnetars. Furthermore, from their analysis they put a constraint on the number of stable magnetars generated by a GRB in the Milky Way in the past Myr (about ≤ 16). Nevertheless, the core collapse SNe rate is lower by 10% than the Galactic magnetar rate, while the rate of GRBs is much smaller. Thus, Galactic magnetars cannot explain the production of GRBs. Besides that, the GRB magnetars spin-down rates have to be very fast in comparison to the default spin-down rates measured for magnetars, and the low GRB rate would not easily allow the observation of these supermagnetars. In conclusion, it was claimed that the results from this paper are in agreement with those from previous ones.

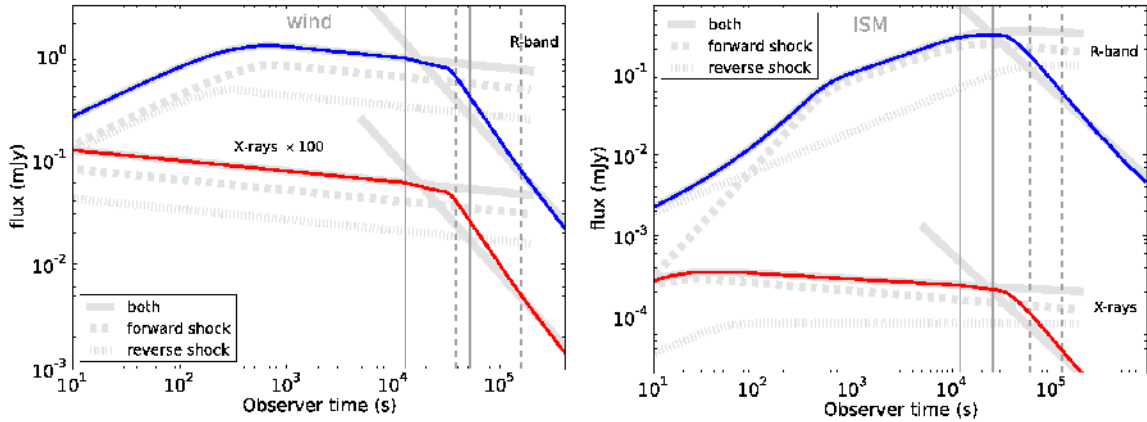


Figure 4.1.5: Light curves in the optical and X-ray ranges in the case of wind (left panel) and ISM (right panel) external media. The analytical curves for prolonged and impulsive energy injection are displayed by thick light grey curves. The area of FS radiation alone and the one of RS radiation alone are represented by thick dashed light grey and the thick dotted light grey function, respectively. For additional details of the plots see van Eerten (2014a). (Figures from van Eerten (2014a).)

Still in the framework of the energy injection models, van Eerten (2014a) retrieved a correlation between $F_{O,a} \sim T_{O,a}^{-0.78 \pm 0.08}$ (Panaitescu and Vestrand, 2011; Li et al., 2012), for definitions see Section 3.2. The range of E_{iso} , the fraction of the magnetic energy, ϵ_B , and the initial density, n_0 , generate the scatter in the correlation without varying the slope. They concluded that both the medium characterized by the wind profile ($\propto A/r^2$, where A is a constant) and the ISM recovered the observed correlation within both the RS and FS models (see Fig. 4.1.5).

Alternatively, Sultana et al. (2013) investigated the evolution of Γ during the whole light curve in the framework of the Supercritical Pile Model. As a result, they retrieved the LT correlation. The Supercritical Pile model supplies with the description for the steep-decline and the plateau phase or the steep-decline and the power-law decay of the afterglow phase. Their main outcome was that the plateau phase in the evolution of Γ lasts less as long as the value of $M_0 c^2$ diminishes, with M_0 indicating the initial rest mass of the flow. For this reason, the brighter the plateau phase, the shorter its duration. This implies a tinier value of $M_0 c^2$, namely the energy.

In the framework of the thick shell model, from the analysis of the synchrotron emission Leventis et al. (2014) claimed that this radiation is in agreement with the existence of the plateau phase (see the left panel of Fig. 4.1.6). From the study of the $\log F_{X,a} - \log T_{X,a}$ correlation they concluded that the energy emission through the RS is preferred to the one through the FS (see the right panel of Fig. 4.1.6).

From the simulation of a GRB data set by van Eerten (2014b), it was obtained that the observed LT correlation rejects thin shell models, but not basic thick ones. For thin shell models, the pre-deceleration radiation coming from a slow-moving component in a

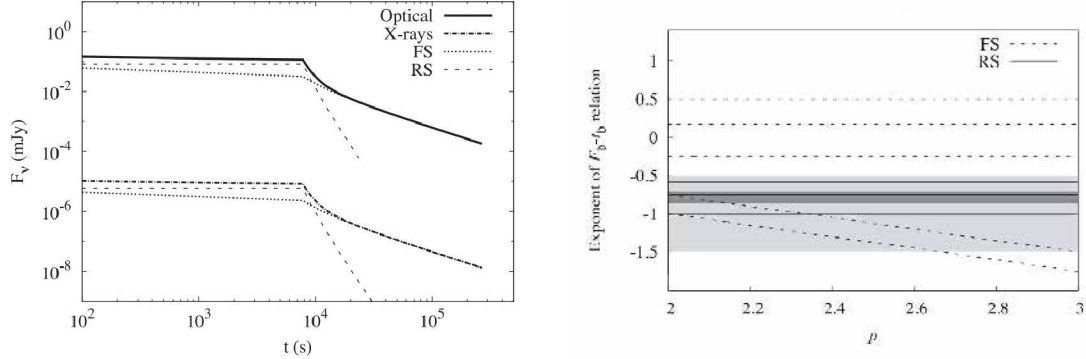


Figure 4.1.6: Left panel: light curves in optical and X-ray wavelengths before and after the injection break. The FS emission is indicated by a dotted line, while the RS one is displayed by the dashed line. The values of the variables assumed for the physical model are $E = 10^{51}$ erg, $n_1 = 50$ cm $^{-3}$, $\Delta t = 5 \times 10^3$ s, $\eta = 600$, $q=0$, $\epsilon_e = \epsilon_B = 0.1$, $p = 2.3$, $\theta_j = 90^\circ$, $d = 10^{28}$ cm and $z = 0.56$. (Figure from Leventis et al. (2014).) Right panel: the $F_{X,a} - T_{X,a}$ correlation slope versus the electron distribution index for the FS and the RS. Results obtained by Panaiteescu and Vestrand (2011) are presented by a lightly shaded area, while results by Li et al. (2012) are displayed by a darker region. The five plausible indices for the FS are represented by the five dashed lines, while for the RS case the three plausible indices (not depending on the electron distribution index) are indicated by the three solid lines. (Figure from Leventis et al. (2014).)

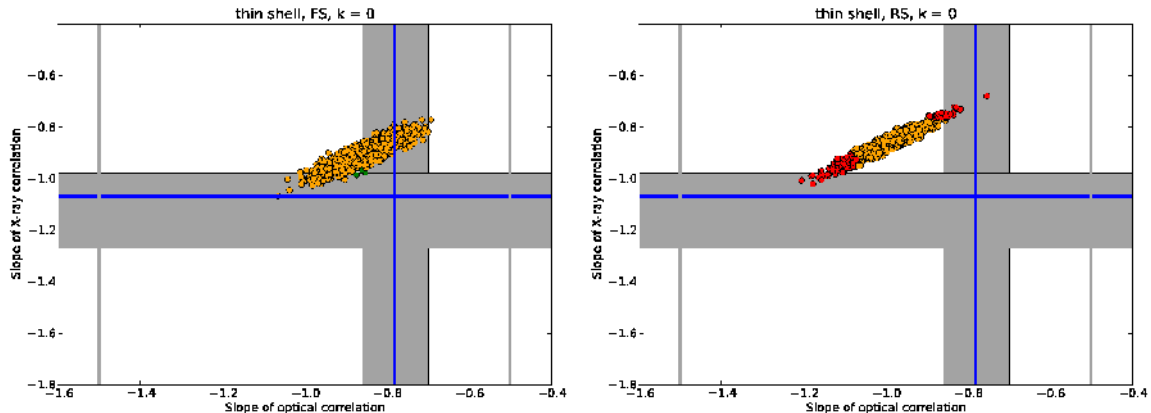


Figure 4.1.7: Simulated slopes of the X-ray (vertical axis) and optical (horizontal axis) LT correlations for 1000 thin shell samples considering the FS (left panel) or the RS (right panel) scenario. 1σ errors in both the optical and X-ray correlations are represented by a grey region. Green dots and orange dots are compatible for both correlations within 1σ and 3σ , respectively. Red dots are not consistent either in 1 or 3σ in neither of the two correlations. The errors in the optical LT correlation from Panaiteescu and Vestrand (2011) are displayed by the vertical grey lines. (Figures from van Eerten (2014b).)

two-components or jet-type model leads to the plateau phase, but this description does not explain the observed LT correlation (see Fig. 4.1.7). On the other hand, this does not necessarily suggest that reliable fits are not feasible using a thin shell model. Therefore, additional investigation is mandatory to definitely rule out thin shell models. Instead, for the thick models, the late activity of the central engine, or further kinetic energy transfer from slower ejecta which interacts with the blast wave, generate the plateau phase. Nevertheless, in this case it is hard to differentiate between FS and RS radiations, or homogeneous and stellar wind-type external media. Finally, another possibility would be the photospheric model from stratified jets (Ito et al., 2014), which has not been examined yet on the LT correlation.

4.1.2 The unified $L_{X,a}$ - $T_{X,a}^*$ and $L_{O,a}$ - $T_{O,a}^*$ correlations

To analyse the X-ray and optical afterglow phases as a unique picture, it is mandatory to consider important characteristics of the optical luminosities. For this purpose, Boér and Gendre (2000) with a sample of 8 GRBs claimed that in the X-ray range the afterglow decay index ($\alpha_{X,a}$) distribution presents a bimodality, with the most luminous GRBs clustering around the value 1.6 and the faintest ones around the value 1.11. In the optical range, possibly due to the host galaxy absorption, this behaviour is not visible.

Following, Nardini et al. (2006) pointed out the existence of a group of dark GRBs, namely GRBs with optical-to-X-ray spectral index, $\beta_{OX,a}$, smaller than 0.5, $\beta_{OX,a} \leq 0.5$. Indeed, the monochromatic $L_{O,12}$ (for definitions see Section 3.2) of 24 LGRBs clustered at $\log L_{O,12} = 30.65 \text{ erg s}^{-1} \text{ Hz}^{-1}$ with $\sigma_{int} = 0.28$. The dispersion of this distribution was smaller than the one of $L_{X,12}$ and the one of the ratio $L_{O,12}/E_{\gamma,prompt}$, for definitions see Section 3.2. From their analysis, three outliers were found with luminosity lower by a factor of ~ 15 .

Liang and Zhang (2006a) with a sample of 44 GRBs recovered a bimodal distribution of $L_{O,1d}$, for definitions see Section 3.2, validating the previous results. Nardini et al. (2008a) enlarged the data set to 55 Swift LGRBs with measured z and rest-frame optical extinction and investigated the selection biases in their observations. Their results were in agreement with previous works. Instead, no evidence of bimodality was retrieved in the distributions of $L_{O,12}$, $L_{O,1d}$ and $L_{O,11}$ by Melandri et al. (2008), Oates et al. (2009), Zaninoni et al. (2013) and Melandri et al. (2014), who used 44, 24, 40 and 47 GRBs, respectively.

With the scope of looking for a common description of the GRB afterglow phase, Ghisellini et al. (2009) analysed 33 Swift LGRBs in the X-ray range between 0.3 and 10 keV and in the optical R range (see the left and middle panels of Fig. 4.1.8). They employed the following function:

$$L_L(\nu, t) = L_L(\nu, T_{X,a}) \frac{(t/T_{X,t})^{-\alpha_{\nu,fl}}}{1 + (t/T_{X,t})^{\alpha_{\nu,st} - \alpha_{\nu,fl}}} \quad (4.6)$$

As a result, with this approximation they found a good agreement with the GRB light curves, and they were able to reproduce the X-ray LT correlation.

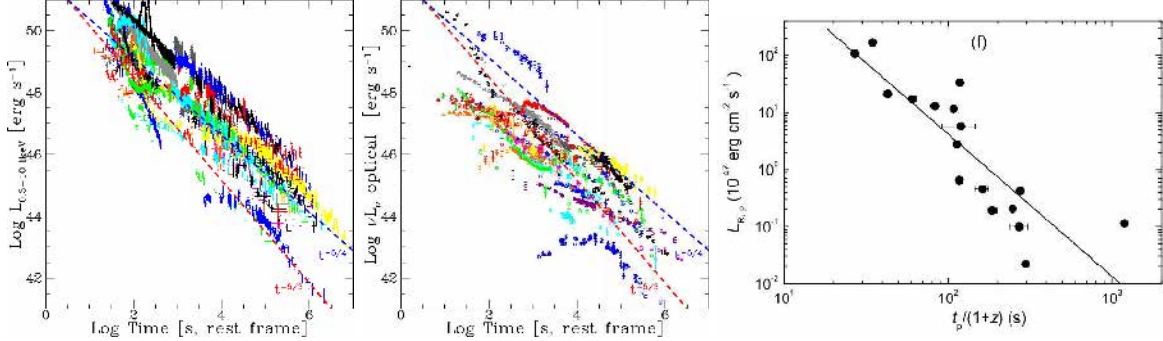


Figure 4.1.8: The X-rays (left panel) and optical (middle panel) light curves for the GRB data set. $\log L_{X,12}$ and $\log L_{O,12}$ at a given rest-frame time are indicated by vertical lines, while the $\log t^{-5/4}$ (blue) and the $\log t^{-5/3}$ (red) trends are represented by the dashed lines. (Figures from Ghisellini et al. (2009).) Right panel: the $L_{O,\text{peak}} - T_{O,\text{peak}}^*$ correlation with the best fit line. In the picture, $L_{O,\text{peak}}$ is equivalent to $L_{R,p}$. (Figure from Liang et al. (2010). © AAS. Reproduced with permission.)

Employing 32 Swift GRBs, Liang et al. (2010) concluded that $L_{O,\text{peak}}$ in the R filter and $T_{O,\text{peak}}^*$ are anti-correlated (for definitions see Section 3.2) with a slope $b = -2.49 \pm 0.39$ and $\rho = -0.90$ (see the right panel of Fig. 4.1.8). In conclusion, they claimed that a dimmer bump shows its maximum later than more luminous ones as well as a longer duration. Similarly, Panaitescu and Vestrand (2011) recovered a $\log F_{O,a} \sim \log T_{O,a}^{-1}$ anti-correlation with a sample of 37 Swift GRBs. They claimed the existence of a common process for the afterglow phase in the optical range, despite the large scatter in the optical band.

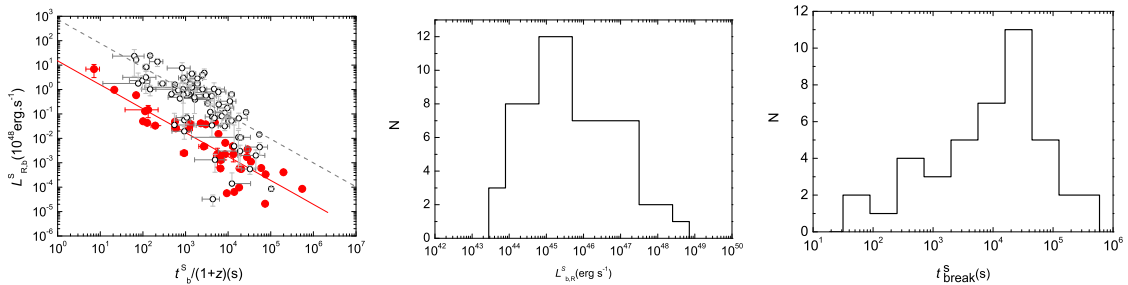


Figure 4.1.9: Left panel: the $L_{O,a}^S$ ($L_{R,p}$ in the picture)– $T_{O,a}^{S,*}$ (t_b in the picture) correlation represented by red circles, while the X-ray data from Dainotti et al. (2010) are indicated by grey circles and the lines show the best fit lines. (Figure from Li et al. (2012). © AAS. Reproduced with permission.) Middle and Right panels: the distributions of $L_{O,a}^S$ and $T_{O,a}^S$ for the whole GRB sample (Figures from Li et al. (2012). © AAS. Reproduced with permission.)

Later, Li et al. (2012) found a correlation (see the left panel of Fig. 4.1.9) analogous to the LT one, but in the R energy range. They employed 39 GRBs with data in the optical range retrieved from the literature. This correlation was between $L_{O,a}$, in units of $10^{48} \text{ erg s}^{-1}$, and $\log T_{O,a}^*$, for definitions see Section 3.2. The quantities were defined for the shallow decay phase of the GRB light curves and denoted with the superscript S. They retrieved a slope $b = -0.78 \pm 0.08$, $\rho = 0.86$ and $P < 10^{-4}$.

Correlations	Author	N	Slope	Corr.coeff.	P
$L_{O,peak} - T_{O,peak}$	Liang et al. (2010)	32	-2.49 ± 0.39	-0.90	
$L_{O,a} - T_{O,a}$	Panaiteescu & Vestrand (2011)	37	-1		
$L_{O,a}^S - T_{O,a}^S$	Li et al. (2012)	39	-0.78 ± 0.08	0.86	$< 10^{-4}$

Table 4.2: Summary of the correlations presented in this section. The correlation in log scale is listed in the first column, the authors are presented in the second one, and the size of the data set is displayed in the third one. The correlation slope is indicated in the fourth column, while the correlation coefficient and the chance probability, P, are shown in the last two columns. (Table from Dainotti and Del Vecchio (2017).)

$L_{O,a}^S$ fluctuated between 10^{43} and 10^{47} erg s $^{-1}$, and in several GRBs with an early break arrived at $\sim 10^{49}$ erg s $^{-1}$ (see the middle panel of Fig. 4.1.9). $T_{O,a}^S$ varied between tens of seconds and days after the trigger of the GRB, with a peak at $T_{O,a}^S \sim 10^4$ seconds (see the right panel of Fig. 4.1.9). They concluded that optical light curves have a similar behaviour compared to the X-ray light curves. Indeed, the correlation displayed in the left panel of Figure 4.1.9, with a slope $b = -0.78 \pm 0.08$, reproduces the LT correlation for the X-ray flares (see Section 4.2.6). Table 4.2 summarizes b and P of the correlations mentioned in this section.

Physical interpretation of the unified $L_{X,a}$ - $T_{X,a}^*$ and $L_{O,a}$ - $T_{O,a}^*$ correlations

In the unified $L_{X,a}$ - $T_{X,a}^*$ and $L_{O,a}$ - $T_{O,a}^*$ correlations Ghisellini et al. (2009) assumed the flux to be the sum of two component: one is the synchrotron radiation caused by the standard FS, see Section 2.3.1 for additional details, and the latter might be generated by a long-lived central engine responsible for the “late prompt” emission. Though this treatment relies on an observational model, the achromatic and chromatic jet breaks in the data can be reliably described. Furthermore, they claimed that the decay slope of the late prompt phase ($-5/4$) has a value analogous within the error bars to the estimate of the rate of the accretion of the fall-back material ($\sim -5/3$). This situation is well represented by the blue and red dashed lines for X-ray and optical emissions in the left and middle panels of Figure 4.1.8, respectively. This result accounts for a very long central engine activity. For an analogous analysis in the framework of the BH accretion concerning the explanation of the LT correlation see Section 4.1.1. Given that later deceleration time suggests slower ejecta and a dimmer emission, Liang et al. (2010) concluded that the external shock model well recovers the $L_{O,peak} - T_{O,peak}$ anti-correlation.

Panaiteescu and Vestrand (2008) claimed that the peaky afterglow phases (with $L_{O,a} \propto T_{O,a}^{-1}$) are phenomena observed slightly outside the cone of view, while the plateau afterglow phases are off-axis phenomena caused by the angular structure of the jet. Later, Panaiteescu and Vestrand (2011) proposed a theoretical framework such that the peaky and plateau afterglow phases rely on how long the energy injection from the central engine lasts. In

particular, the peaky afterglow phases are originated from the impulsive ejecta with a small range of Γ , while the plateau afterglow phases stem from a distribution of initial Γ which feeds the energy injection up to 10^5 s.

Finally, Li et al. (2012) claimed that optical flares and the optical shallow decay segments are both described by late GRB central engine activities, which can be irregular (in the case of flares) or constant (in the case of internal plateaus). Usually, after the external plateau phases a normal decay with $\alpha_{X,a}$ around -1 is encountered. These plateau phases are maybe created from an external shock with the shallow decay part produced by continuous energy injection pumping into the blast wave (Rees and Mészáros, 1998; Dai and Lu, 1998; Sari and Mészáros, 2000; Zhang and Mészáros, 2001). On the other hand, the internal plateau phases, discovered for the first time by Troja et al. (2007) in GRB 070110 and later investigated statistically by Liang et al. (2007), are characterized by a much steeper decay ($\alpha_{X,a}$ steeper than -3) after the plateau phase. These internal plateau phases are highly likely fuelled by internal dissipation of a late emission. In conclusion, the afterglow phase is well modelled by a mixture of internal and external components.

4.1.3 The $L_{O,200s}$ - $\alpha_{O,>200s}$ correlation and its physical interpretation

A correlation between $\log L_{O,200s}$ and $\alpha_{O,>200s}$ (for definitions see Section 3.2) was pointed out for the first time by Oates et al. (2012) (see the right panel of Fig. 4.1.10), with a data set of 48 UVOT LGRB light curves at 1600 Å (see the left panel of Fig. 4.1.10). This correlation is represented in the following way:

$$\log L_{O,200s} = (28.08 \pm 0.13) - (3.636 \pm 0.004) \times \alpha_{O,>200s}, \quad (4.7)$$

with $\log L_{O,200s}$ in $\text{erg s}^{-1} \text{Hz}^{-1}$, $\rho = -0.58$ and a significance of 99.998% (4.2σ). Therefore, the more luminous the GRB, the faster the afterglow decay. To recover the light curves used for the analysis, they employed the following selection criteria to ensure a high S/N of the UVOT light curve: the optical/UV light curve is detected in the V filter with a magnitude ≤ 17.8 , UVOT observation begins during the first 400 s since the BAT trigger, and the afterglow phase should last at least 10^5 s after the trigger (Oates et al., 2009). Their outcomes showed that this correlation significantly depends on the discrepancies in the observing angle and in the rate of the energy emission from the central engine.

Additionally, Oates et al. (2015) compared the same correlation in optical and in X-ray bands, using the same data set as Oates et al. (2012). Their main results was the achievement of a similar value for the slope b of both correlations. As a further step, studying the connection between $\alpha_{X,>200s}$ and $\alpha_{O,>200s}$ (for definitions see Section 3.2), Oates et al. (2015) claimed that the best fit correlation is $\alpha_{X,>200s} = \alpha_{O,>200s} - 0.25$ (see the left panel of Fig. 4.1.11). Even if some correspondences between optical and X-ray components of GRBs were pointed out from this work, the outcomes were not in agreement with the ones

by Urata et al. (2007). Indeed, Urata et al. (2007) found many outliers in the study of the correlation between $\alpha_{X,>200s}$ and $\alpha_{O,>200s}$ in the context of the external shock model.

Employing 237 Swift LGRBs, Racusin et al. (2016) focused on a comparable correlation in X-ray. They retrieved a $b = -0.27 \pm 0.04$ and a convincing link between optical and X-ray components of GRBs. The Monte Carlo simulations and the statistical tests recovered the $\log L_{O,200s} - \alpha_{O,>200s}$ correlation by Oates et al. (2012). Finally, a possible association with the LT correlation was displayed, suggesting a common emission process describing both of them. In Table 4.3 a summary of the correlations presented in this section is given.

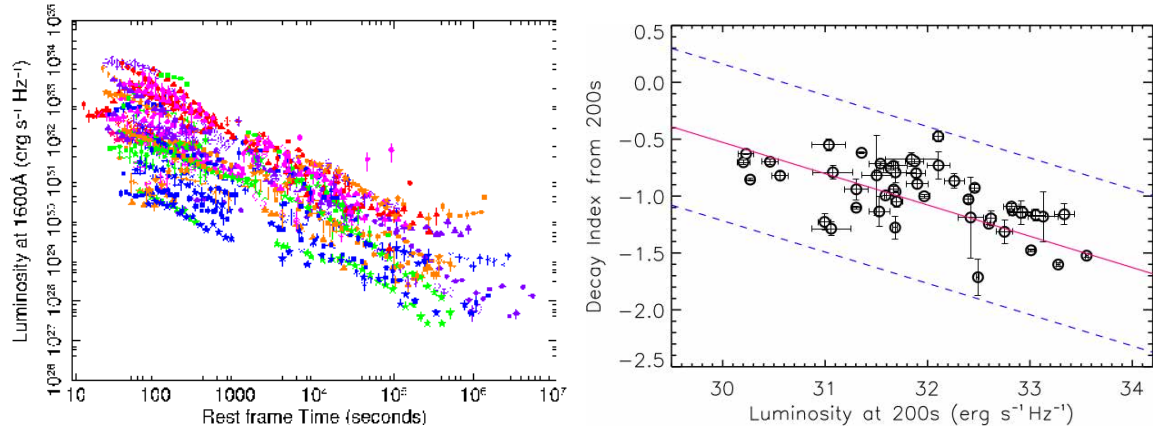


Figure 4.1.10: Left panel: the light curves in the optical range of the GRB data set. (Figure from Oates et al. (2012).) Right panel: the $\log L_{O,200s} - \alpha_{O,>200s}$ correlation with the best fit line displayed by a red solid line and the 3σ region indicated by a blue dashed line. (Figure from Oates et al. (2012).)

To explain the $\log L_{O,200s} - \alpha_{O,>200s}$ correlation, Oates et al. (2012) investigated different possibilities. In the first one, considering the collision of the jet with the external medium, $\alpha_{O,>200s}$ is not a fixed quantity and all the optical afterglow phases are generated from a single closure relation with $\alpha_{O,>200s}$ and $\beta_{O,>200s}$ (for definitions see Section 3.2) linearly correlated. As a consequence, a correlation between $\log L_{O,200s}$ and $\beta_{O,>200s}$ should be pointed out. However, from the observations $\alpha_{O,>200s}$ and $\beta_{O,>200s}$ result weakly related (see the right panel of Fig. 4.1.11) and no correlation between $\beta_{O,>200s}$ and $\log L_{O,200s}$ is recovered. For these reasons, this theoretical interpretation is ruled out as possible explanation of the $\log L_{O,200s} - \alpha_{O,>200s}$ correlation.

For an alternative description, they considered that the $\log L_{O,200s} - \alpha_{O,>200s}$ correlation is originated from a few closure relations (see the lines in the right panel of Fig. 4.1.11). But, in this case the $\alpha_{O,>200s}$ and $\beta_{O,>200s}$ values with similar luminosities did not cluster around a specific closure relation. Therefore, also the standard model does not well describe the $\log L_{O,200s} - \alpha_{O,>200s}$ correlation. They concluded that the afterglow model should be more complicated than the one supposed in previous works. It is plausible that still unknown physical features rule the radiation process and the decay rate.

For this reason, Oates et al. (2012) indicated two further options: the first claimed that

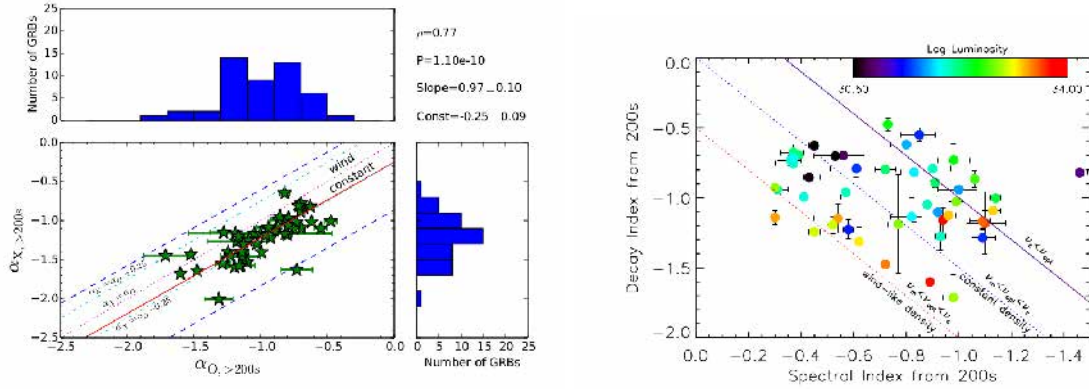


Figure 4.1.11: Left panel: the $\alpha_{O,>200s} - \alpha_{X,>200s}$ correlation with the best fit line represented by a red solid line and the 3σ region indicated by blue dashed lines. The closure relations are also displayed. The $\alpha_{O,>200s} = \alpha_{X,>200s}$ correlation is given by the pink dotted line, while the $\alpha_{X,>200s} = \alpha_{O,>200s} \pm 0.25$ correlation is displayed by the light blue dotted-dashed lines. ρ , P , and the best fit coefficients are shown in the top right corner (Figure from Oates et al. (2015).) Right panel: the $\alpha_{O,>200s} - \beta_{O,>200s}$ correlation for 48 GRBs with different $\log L_{O,200s}$ displayed by a colour scale and 3 closure relations indicated by lines. (Figure from Oates et al. (2012).)

the $\log L_{O,200s} - \alpha_{O,>200s}$ correlation is associated with some characteristics of the central engine which control the rate of energy emission. Thus, for weaker afterglow phases, the energy is radiated more slowly. The second option stated that the $\log L_{O,200s} - \alpha_{O,>200s}$ correlation may be caused by different observing angles. In this scenario faster and more luminous decaying light curves are seen by the observers at smaller viewing angles.

Correlations	Author	N	Slope	Norm	Corr.coeff.	P
$L_{O,200s} - \alpha_{O,>200s}$	Oates et al. (2012)	48	-3.636 ± 0.004	28.08 ± 0.13	-0.58	2×10^{-4}
	Oates et al. (2015)	48	-3.636 ± 0.004	28.08 ± 0.13	-0.58	2×10^{-4}
$L_{X,200s} - \alpha_{X,>200s}$	Racusin et al. (2016)	237	-0.27 ± 0.04	-6.99 ± 1.11	0.59	10^{-6}

Table 4.3: Summary of the correlations presented in this section. The correlation in log scale is listed in the first column, the authors are presented in the second one, and the size of the data set is displayed in the third one. The correlation slope and normalization are indicated in the fourth and fifth columns, while the correlation coefficient and the chance probability, P , are shown in the last two columns. (Table from Dainotti and Del Vecchio (2017).)

In conclusion, Dainotti et al. (2013b) claimed that the $\log L_{O,200s} - \alpha_{O,>200s}$ and the LT correlations are connected and that it would be important to point out how they are associated as well as the physical mechanisms leading both of them. With this aim, Oates et al. (2015) investigated the observed correlations and the simulated ones, yielding that the $\log L_{O,200s} - \alpha_{O,>200s}$ correlation and the equivalent in the X-ray band are compatible. This result indicated a similar physical process for both correlations.

4.2 Correlations among prompt-afterglow parameters

As described in previous sections, the plateau phase is still a mystery and the correlations connected to it still need to be studied and fully understood. Thus, many models have been developed. To better understand this plateau phase the investigation of the relationship between plateau and prompt phases is needed. Here, the correlations among prompt-afterglow physical parameters are presented, providing a more exhaustive description of the plateau phase.

4.2.1 The $E_{X,\text{afterglow}} - E_{\gamma,\text{prompt}}$ correlation and its physical interpretation

Employing 107 Swift GRBs, W07 investigated the correlation between $F_{\gamma,\text{prompt}}$ and $F_{X,\text{afterglow}}$ (see the upper left panel of Fig. 4.2.1), measured in the BAT and XRT bands and in the XRT band, respectively. For definitions of these quantities see Section 3.2. In the case of measured redshift, the isotropic energies ($E_{\gamma,\text{prompt}}$ and $E_{X,\text{afterglow}}$) were studied supposing a cosmological model given by $H_0 = 71 \text{ km s}^{-1} \text{ Mpc}^{-1}$, $\Omega_\Lambda = 0.73$ and $\Omega_M = 0.27$ (see the upper right panel of Fig. 4.2.1).

Contemporaneously, Liang et al. (2007), with 53 LGRBs, analysed the $E_{\gamma,\text{prompt}} - E_{X,\text{afterglow}}$ correlation obtaining $b = 1 \pm 0.16$ (see the bottom left panel of Fig. 4.2.1). Later, choosing distinct energy ranges from those employed in Liang et al. (2007), Liang et al. (2010) and Panaiteescu and Vestrand (2011) examined the same correlation with data sets composed of 32 and 37 GRBs, respectively. From their analysis they found out slopes $b = 0.76 \pm 0.14$ and $b = 1.18$, respectively. These correlations are represented in the left and middle panels of Figure 4.2.2.

From the analysis of 43 SGRBs and 232 Swift GRBs with measured spectroscopic redshifts respectively, Rowlinson et al. (2013) and Grupe et al. (2013) claimed an $E_{X,\text{afterglow}} - E_{\gamma,\text{prompt}}$ correlation with $b \sim 1$ in agreement with earlier outcomes (see the left and middle panels of Fig. 4.2.3). To put some limits on the ratio of $E_{X,\text{afterglow}}$ to $E_{\gamma,\text{prompt}}$, also Dainotti et al. (2015a) studied this correlation with a data set of 123 LGRBs (see the right panel of Fig. 4.2.3). On the other hand, using the X-ray plateau energy, $E_{X,\text{plateau}}$, as an evaluation of $E_{X,\text{afterglow}}$, Ghisellini et al. (2009) examined an analogous correlation for a set of 33 LGRBs. They obtained $b = 0.86$ (see the bottom right panel of Fig. 4.2.1).

Furthermore, Ghisellini et al. (2009) with the same data set analysed the correlation between $E_{\gamma,\text{prompt}}$ and $E_{k,aft}$, for definitions see Section 3.2. They retrieved $b = 0.42$. Analogously, this correlation was also examined by Racusin et al. (2011), with a sample of 69 GRBs. In their analysis they selected different values for the efficiency to constrain $E_{k,aft}$ and $E_{\gamma,\text{prompt}}$ (see the right panel of Fig. 4.2.2). The main purpose of the use of this correlation was to test the difference in detection limits of many instruments and to study the transfer of kinetic energy in the prompt radiation. Among the works mentioned above

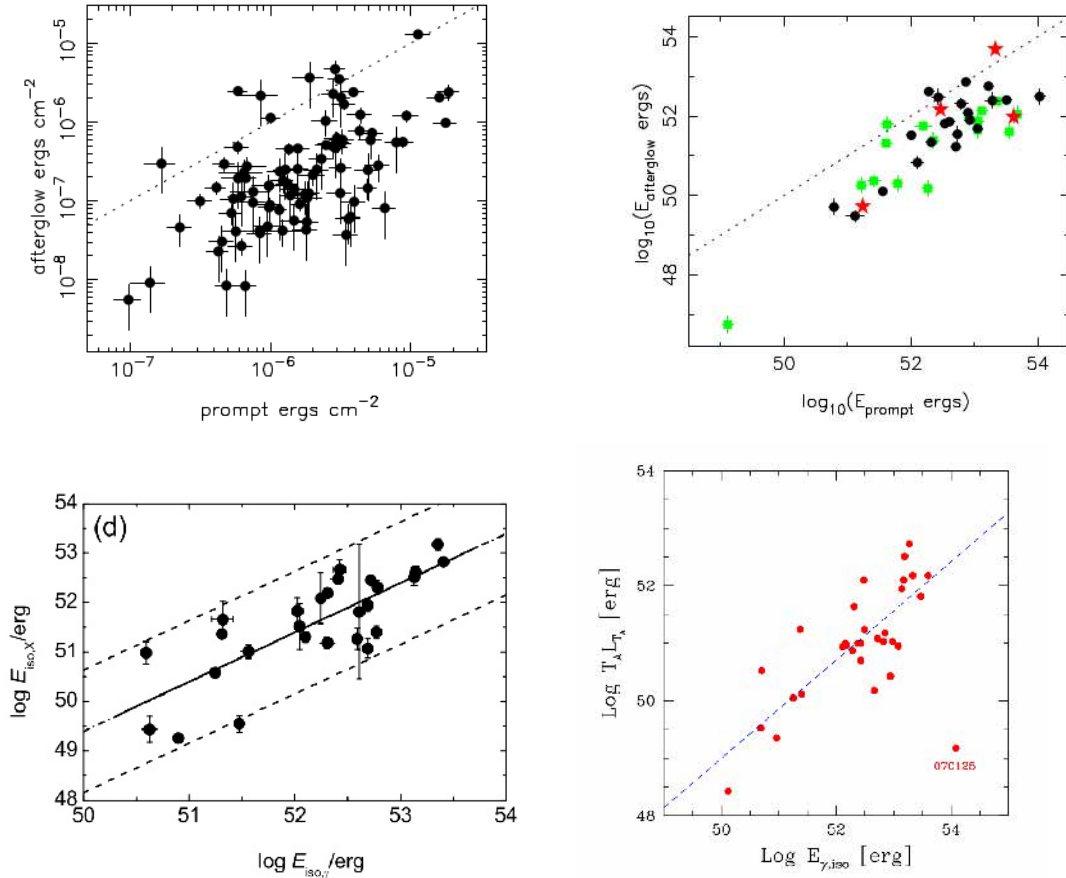


Figure 4.2.1: Upper left panel: the correlation between prompt and afterglow fluences obtained from the BAT flux and the XRT flux, respectively. The points were the fluences have the same values are shown by a dotted line. (Figure from Willingale et al. (2007). @ AAS. Reproduced with permission.) Upper right panel: the $\log E_{X,\text{afterglow}} - \log E_{\gamma,\text{prompt}}$ correlation. GRBs in the pre-jet break area of the $\beta_{X,a}$ - $\alpha_{X,a}$ plane are represented by dots, GRBs in the post-jet break area of the $\beta_{X,a}$ - $\alpha_{X,a}$ plane are indicated by stars, while GRBs below the pre-jet break area of the $\beta_{X,a}$ - $\alpha_{X,a}$ plane are displayed by squares. $\log E_{\gamma,\text{prompt}} = \log E_{X,\text{afterglow}}$ is shown by a dotted line. (Figure from Willingale et al. (2007). @ AAS. Reproduced with permission.) Bottom left panel: the $\log E_{X,\text{afterglow}} - \log E_{\gamma,\text{prompt}}$ ($E_{X,\text{iso}}$ and $E_{\gamma,\text{iso}}$ respectively in the plot) correlation with the best fit line represented by a solid line and the 2σ region displayed by a dashed line. (Figure from Liang et al. (2007). @ AAS. Reproduced with permission.) Bottom right panel: the $\log E_{X,\text{plateau}} - \log E_{\gamma,\text{prompt}}$ ($L_{T_a} T_a$ and $E_{\gamma,\text{iso}}$ respectively in the picture) with the best fit indicated by a dashed line. (Figure from Ghisellini et al. (2009).)

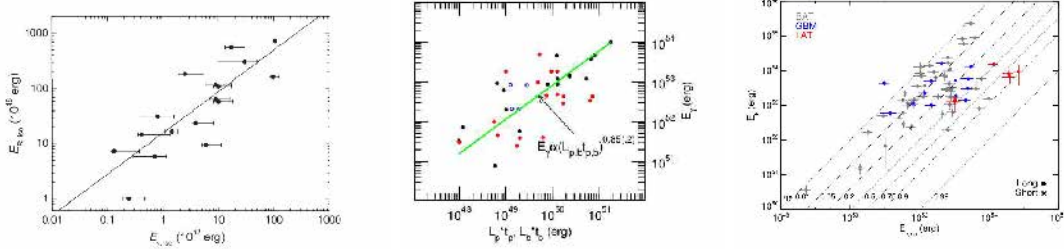


Figure 4.2.2: Left panel: the $E_{O,\text{afterglow}} - E_{\gamma,\text{prompt}}$ correlation ($E_{R,\text{iso}}$ and $E_{\gamma,\text{iso}}$ respectively in the plot) for the optically selected data set with the best fit indicated by a line. (Figure from Liang et al. (2010). @ AAS. Reproduced with permission.) Middle panel: the $E_{\gamma,\text{prompt}} - E_{O,\text{afterglow}}$ correlation ($E_{\gamma,\text{iso}}$ and $L_p \times t_p$ respectively in the plot). Afterglow phases with peaks in the optical band are indicated by black symbols, optical plateau phases are represented by red symbols, and afterglow of uncertain type are displayed by open circles. For all the sample of 37 afterglow phases it is obtained $r(\log E_{O,\text{afterglow}}, \log E_{\gamma,\text{prompt}}) = 0.66$ and $P = 10^{-5.3}$ (Figure from Panaiteescu and Vestrand (2011).) Right panel: the $E_{k,\text{aft}} - E_{\gamma,\text{prompt}}$ ($E_{\gamma,\text{iso}}$ in the plot) correlation with distinct values of the efficiency shown by dashed lines. $E_{\gamma,\text{prompt}}$ for LAT GRBs appears higher than the one for BAT and GBM GRBs, while $E_{k,\text{aft}}$ has an ordinary value. Thus, the efficiency for LAT GRBs will be greater than that for BAT and GBM GRBs. (Figure from Racusin et al. (2011). @ AAS. Reproduced with permission.)

the correlation presented by Racusin et al. (2011) is considered the most robust.

In conclusion, the $E_{X,\text{afterglow}} - E_{\gamma,\text{prompt}}$ correlation, investigated by Liang et al. (2007) and confirmed by Rowlinson et al. (2013), Grupe et al. (2013) and Dainotti et al. (2015a), is useful for relating the energies in the prompt and the afterglow phases. The $E_{k,\text{aft}} - E_{\gamma,\text{prompt}}$ correlation analysed by Ghisellini et al. (2009) and confirmed by Racusin et al. (2011) can help to examine the efficiency of the emission processes in the transition from the prompt to the afterglow phases. Additionally, this correlation is able to well describe the relationship between these two phases. Ghisellini et al. (2009) and Racusin et al. (2011) concluded that the transferred kinetic energy from the prompt to the afterglow phases is approximately 10% for a data set of BAT GRBs. This outcome is compatible with those by Zhang et al. (2007a). Particularly, the internal shock model well explains the 10% for the energy efficiency when a late energy transfer occurs from the fireball to the external medium (Zhang and Kobayashi, 2005).

In Table 4.4, the parameters of the correlations mentioned in this section are described. To physically describe the $E_{X,\text{afterglow}} - E_{\gamma,\text{prompt}}$ correlation it is important to consider that the outcomes by Racusin et al. (2011) about the efficiency of a BAT data set are in agreement with the results by Zhang et al. (2007a), for which $\sim 57\%$ of BAT bursts have energy efficiency $< 10\%$. From the sets of GRBs detected by the GBM and LAT instruments, it was yielded that only 25% of the GBM GRBs and none of the LAT GRBs have efficiency $< 10\%$. Therefore, it was proposed that the efficiency of the kinetic energy transfer to prompt emission of Fermi GRBs is higher than that of Swift GRBs.

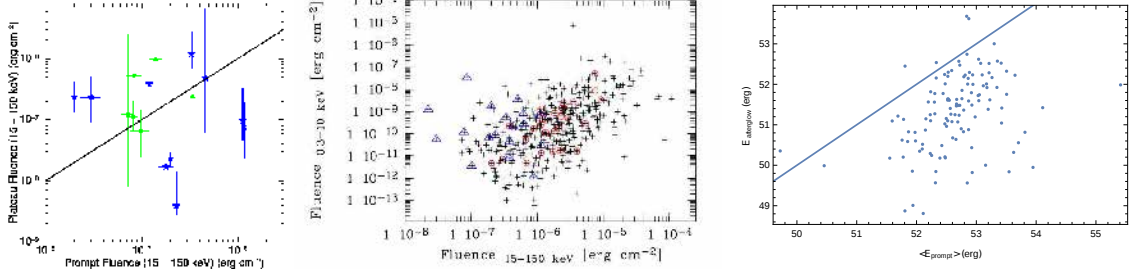


Figure 4.2.3: Left panel: the X-ray fluence versus the prompt fluence correlation where GRBs possessing 2 or more breaks in their light curves are indicated by blue stars, and GRBs with 1 break are represented by green circles. The equality line between the values of the shallow decay phase fluence and the prompt fluence is displayed by a black line. (Figure from Rowlinson et al. (2013).) Middle panel: XRT fluence–BAT fluence correlations with triangles indicating SGRBs and circles representing high redshift ($z > 3.5$) GRBs (Figure from Grupe et al. (2013). @ AAS. Reproduced with permission.) Right panel: the $\log E_{X,\text{afterglow}} - \log E_{\gamma,\text{prompt}} < 0$ correlation for a sample of 123 LGRBs with $\log E_{\gamma,\text{prompt}} = \log E_{X,\text{afterglow}}$ indicated by a solid line. (Figure from Dainotti et al. (2015a).)

Correlations	Author	N	Slope	Norm	Corr.coeff.	P
$E_{X,\text{afterglow}} - E_{\gamma,\text{prompt}}$	Liang et al. (2007)	53	$1.00^{+0.16}_{-0.16}$	$-0.50^{+8.10}_{-8.10}$	0.79	$< 10^{-4}$
$E_{O,\text{afterglow}} - E_{\gamma,\text{prompt}}$	Liang et al. (2010)	32	$0.76^{+0.14}_{-0.14}$	$1.30^{+0.14}_{-0.14}$	0.82	$< 10^{-4}$
	Panaiteescu & Vestrand (2011)	37	1.18		0.66	$10^{-5.3}$
$E_{X,\text{plateau}} - E_{\gamma,\text{prompt}}$	Ghisellini et al. (2009)	33	0.86			2×10^{-7}
$E_{k,aft} - E_{\gamma,\text{prompt}}$	Ghisellini et al. (2009)	33	0.42			10^{-3}

Table 4.4: Summary of the correlations presented in this section. The correlation in log scale is listed in the first column, the authors are presented in the second one, and the size of the data set is displayed in the third one. The correlation slope and normalization are indicated in the fourth and fifth columns, while the correlation coefficient and the chance probability, P, are shown in the last two columns. (Table from Dainotti and Del Vecchio (2017).)

4.2.2 The $L_{X,\text{afterglow}} - E_{\gamma,\text{prompt}}$ correlation and its physical interpretation

Examining the observed energies of 16 SGRBs in the prompt and afterglow phases, Berger (2007) pointed out that the 80% fulfills a linear correlation between $S_{\gamma,\text{prompt}}$ and $F_{X,1d}$ in the BAT and XRT range, respectively. For definitions see Section 3.2. The correlation among these quantities is the following:

$$\log F_{X,1d} \sim (1.01 \pm 0.09) \times \log S_{\gamma,\text{prompt}}, \quad (4.8)$$

with $\rho = 0.86$ and $P = 5.3 \times 10^{-5}$. Using $F_{X,11}$ instead of $F_{X,1d}$, for definitions see Section 3.2, Gehrels et al. (2008) verified this correlation found by Berger (2007) (see Fig. 4.2.4).

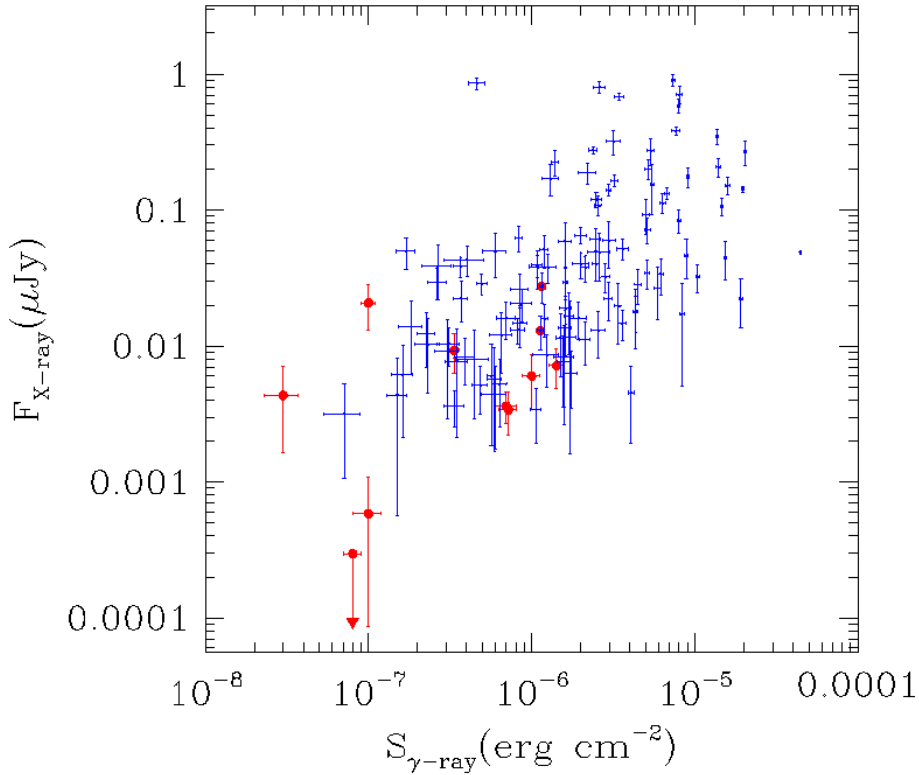


Figure 4.2.4: The $F_{X,11}$ - $S_{\gamma,\text{prompt}}$ distribution ($F_{X,\text{ray}}$ and $S_{\gamma,\text{ray}}$ respectively in the picture) for SGRBs (indicated by red points) and LGRBs (indicated by blue points) detected by Swift. The XRT $F_{X,11}$ are computed at 3 keV and the BAT $S_{\gamma,\text{prompt}}$ are detected in the whole BAT energy range. (Figure from Gehrels et al. (2008). @ AAS. Reproduced with permission.)

Following, Nysewander et al. (2009) with 37 SGRBs and 421 LGRBs observed by Swift obtained a roughly linear correlation between $F_{X,11}$ or $F_{O,11}$ and $E_{\gamma,\text{prompt}}$ (see Fig. 4.2.5). For definitions see Section 3.2. An analogous correlation between $E_{\gamma,\text{prompt}}$ and $F_{O,a}$ with a steeper slope $b = 1.67$ was retrieved by Panaitescu and Vestrand (2011) employing 37 GRBs

(see the left panel of Fig. 4.2.6).

Additionally, using four long events associated with SNe and 27 “regular” energetic LGRBs ($E_{\gamma,prompt} \sim 10^{52} - 10^{54}$ erg), Kaneko et al. (2007) pointed out a linear correlation $L_{X,10} \propto E_{\gamma,prompt}$. For definitions see Section 3.2. $L_{X,10}$ is in the energy band between 2 and 10 keV, while $E_{\gamma,prompt}$ is computed between 20 and 2000 keV (see the left panel of Fig. 4.2.7). From their analysis, it was claimed the possibility of a similar efficiency value in the kinetic energy transformation for the four events associated with SNe and for the “regular” energetic LGRBs.

This correlation was investigated for the low luminosity versus normal luminosity GRBs. Amati et al. (2007) investigated the correlation between $L_{X,10}$, in the range between 2 and 10 keV, and $E_{\gamma,prompt}$, in the range between 1 and 10000 keV. From their analysis, it was concluded that this correlation is tighter ($P \sim 10^{-11}$) when sub-energetic GRBs as GRB 060218, GRB 980425 and GRB 031203 are taken into account (see the middle panel of Fig. 4.2.7). Sub-energetic GRBs are intrinsically dim and they can be regarded as normal cosmological GRBs. As a further step, the correlation between $L_{X,1d}$ and $E_{\gamma,prompt}$, for definitions see Section 3.2, was examined by Berger (2007) with a sample of 13 SGRBs with known z . They recovered a slope $b = 1.13 \pm 0.16$ (see the right panel of Fig. 4.2.6).

In agreement with previous outcomes, Liang et al. (2010) obtained with 32 Swift GRBs an $L_{O,peak} - E_{\gamma,prompt}$ correlation in the optical band with $b = 1.40 \pm 0.08$ (see the right panel of Fig. 4.2.7). Moreover, Kann et al. (2010) retrieved, using 76 LGRBs, an $L_{O,1d} - E_{\gamma,prompt}$ correlation with $b = 0.36$ (see the left panel of Fig. 4.2.8) confirming the results by Berger (2007).

Analogously, a correlation between $\log L_{X,a}$ and $\log E_{\gamma,prompt}$ was studied by Dainotti et al. (2011b) for a data set of 66 Swift BAT+XRT LGRBs, http://www.swift.ac.uk/burst_analyser/. Employing σ_E as a quantity indicating the goodness of the fit, the data set was separated into the E4 subsample, composed of 62 LGRBs, and the E0095 subsample, formed of 8 LGRBs. In the case of the E4 subsample it was recovered:

$$\log L_{X,a} = 28.03_{-2.97}^{+2.98} + 0.52_{-0.06}^{+0.07} \times \log E_{\gamma,prompt}, \quad (4.9)$$

with $\rho = 0.43$ and $P = 1.4 \times 10^{-5}$, while for the E0095 subsample it was obtained

$$\log L_{X,a} = 29.82_{-7.82}^{+7.11} + 0.49_{-0.16}^{+0.21} \times \log E_{\gamma,prompt}, \quad (4.10)$$

with $\rho = 0.83$ and $P = 3.2 \times 10^{-2}$. From this analysis, it was yielded that the subset with the smallest σ_E shows a tighter correlation. In principle this result could allow for the use of this subsample of GRBs as standardizable candle. Furthermore, since the LT slope, b , is roughly -1 , thus the energy reservoir of the plateau phase, $\log E_{X,plateau}$, is roughly constant. Since $\log E_{peak}$ and $\log E_{\gamma,prompt}$ are both correlated with $\log E_{X,plateau}$,

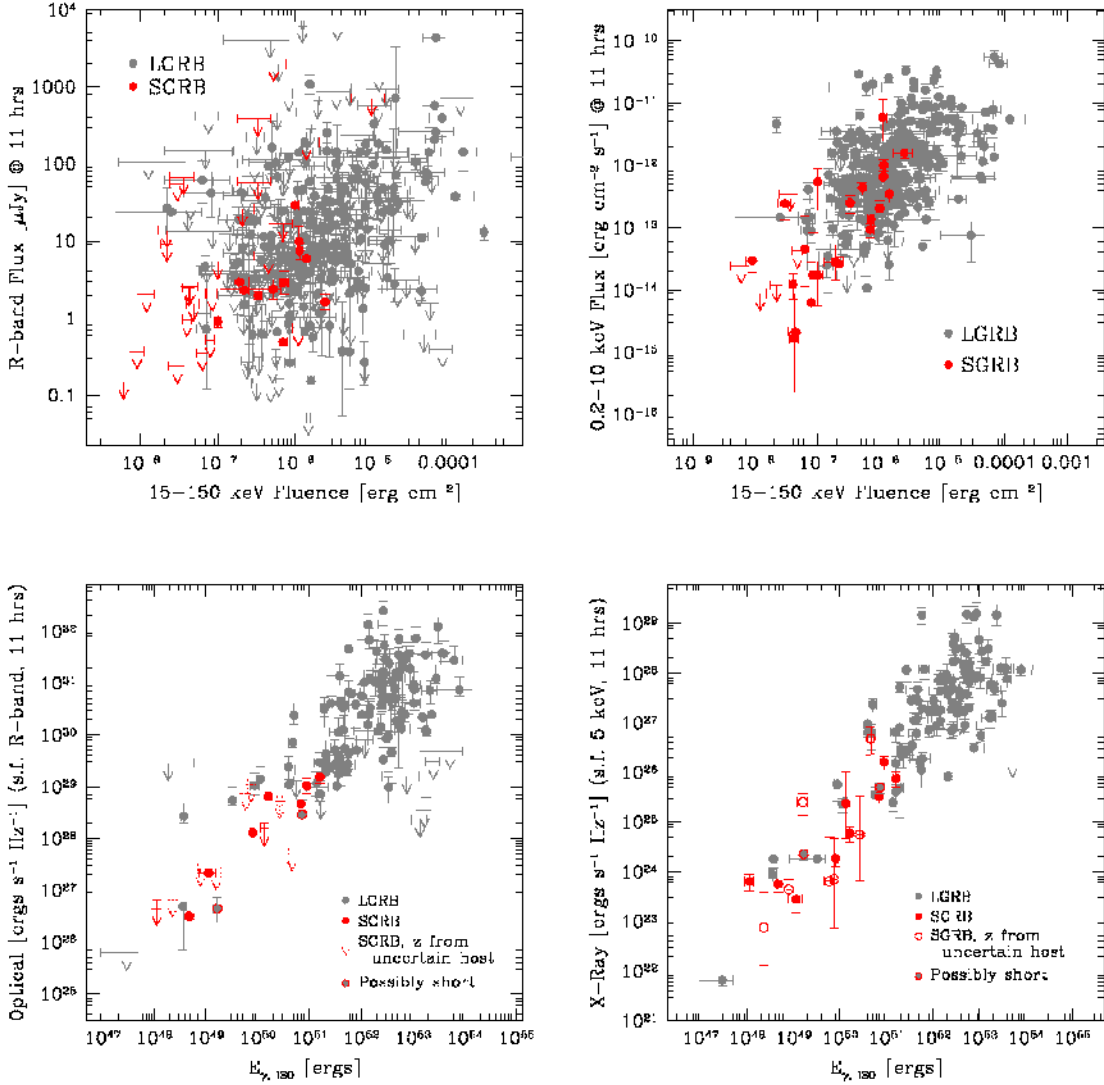


Figure 4.2.5: Upper left panel: the $F_{O,11} - S_{\gamma,prompt}$ correlation using LGRBs (presented in grey) and SGRBs (presented in red). $F_{O,11}$ is corrected for galactic extinction, and $S_{\gamma,prompt}$ is computed in the BAT band. Optical afterglow phases for SGRBs are not found for value of the fluence lower than 10^{-7} erg cm⁻², while for fluence values higher than 10^{-7} erg cm⁻², optical afterglow phases are observed for all GRBs in the sample, except for GRB 061210. Upper right panel: the $F_{X,11} - S_{\gamma,prompt}$ correlation using LGRBs (presented in grey) and SGRBs (presented in red). Bottom left panel: the $L_{O,11} - E_{\gamma,prompt}$ ($E_{\gamma,iso}$ in the plot) correlation with GRB 060614 and GRB 060505 indicated as “possibly short”. $L_{O,11}$ is corrected for Galactic extinction. SGRBs with a host galaxy computed by XRT error circle are indicated by dashed upper limits. Bottom right panel: the $L_{X,11} - E_{\gamma,prompt}$ ($E_{\gamma,iso}$ in the plot) correlation with GRB 060614 and GRB 060505 indicated as “possibly short”. SGRBs with a host galaxy computed by XRT error circle are indicated by open circles. (Figures from Nysewander et al. (2009). © AAS. Reproduced with permission.)

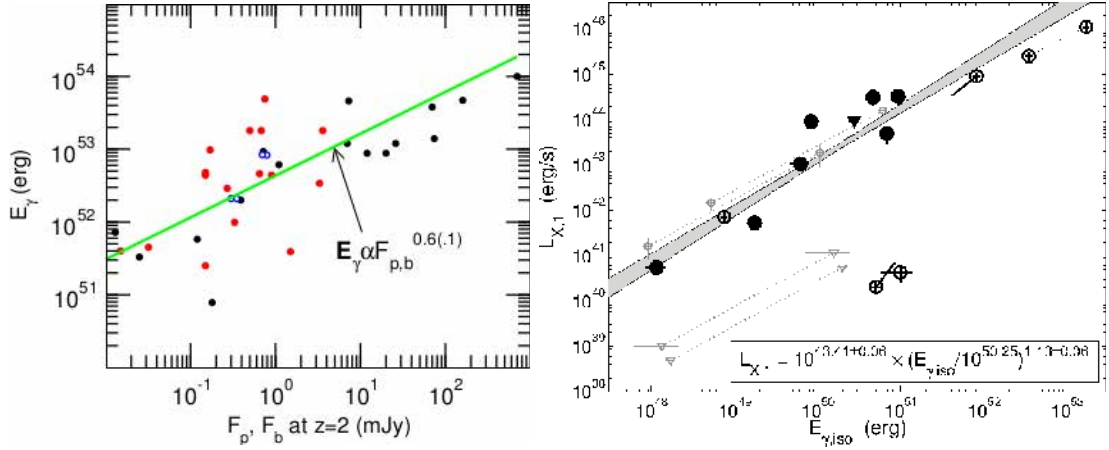


Figure 4.2.6: Left panel: the $E_{\gamma, \text{prompt}} - F_{O,a}$ correlation ($E_{\gamma, \text{iso}}$ and F_p respectively in the plot). Afterglow phases with optical peaks are indicated by black symbols, optical plateau phases are represented by red symbols, and afterglow phases of unknown type are displayed by open circles. (Figure from Panaiteescu and Vestrand (2011).) Right panel: the $L_{X,1d} - E_{\gamma, \text{prompt}}$ correlation ($E_{\gamma, \text{iso}}$ in the plot). SGRBs with measured z are indicated by solid black circles, SGRBs with redshift constraints are presented by open black circles, while SGRBs without measured redshift are displayed by grey symbols connected by dotted lines. (Figure from Berger (2007). @ AAS. Reproduced with permission.)

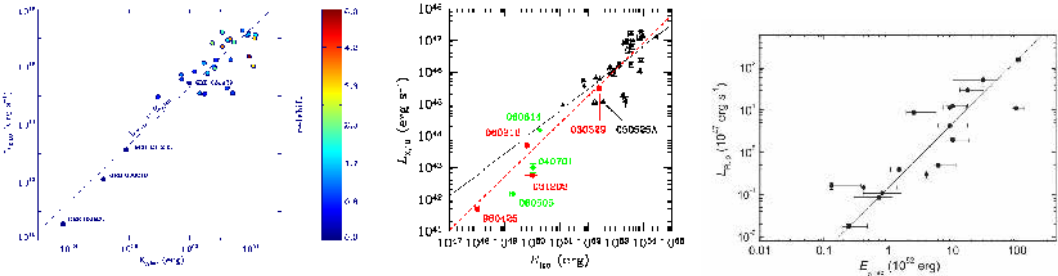


Figure 4.2.7: Left panel: the $L_{X,10} - E_{\gamma, \text{prompt}}$ ($E_{\gamma, \text{iso}}$ in the picture) correlation for GRBs connected with SNe. $E_{\gamma, \text{prompt}}$ is computed between 20 and 2000 keV, while $L_{X,10}$ between 2 and 10 keV. A coloured bar displayed the redshift scale. (Figure from Kaneko et al. (2007). @ AAS. Reproduced with permission.) Middle panel: the $L_{X,10} - E_{\gamma, \text{prompt}}$ ($E_{\gamma, \text{iso}}$ in the picture) correlation. GRBs by Nousek et al. (2006) are indicated by triangles, the 3 sub-energetic GRB 980425, GRB 031203, GRB 060218, and the GRB connected with SN, GRB 030329, are represented by circles, while the 3 GRBs with measured z and deep constraints on the peak magnitude of the associated SN, XRF 040701, GRB 060505 and GRB 060614 are displayed by diamonds. Empty triangles show GRBs with $E_{\gamma, \text{prompt}}$ in the range of 1 – 10000 keV calculated from $E_{\gamma, \text{prompt}}$ in the 100-500 energy keV tabulated by Nousek et al. (2006) considering an average spectral index. The best fit calculated without sub-energetic GRBs and GRB 030329 is indicated by the dotted line, while that with sub-energetic GRBs and GRB 030329 is indicated by the dashed line. (Figure from Amati et al. (2007). Reproduced with permission @ ESO.) Right panel: the $L_{O, \text{peak}} - E_{\gamma, \text{prompt}}$ correlation ($L_{O, \text{peak}}$ and $E_{\gamma, \text{iso}}$ respectively in the plot) using the optically selected sample with the best fit indicated by the line. (Figure from Liang et al. (2010). @ AAS. Reproduced with permission.)

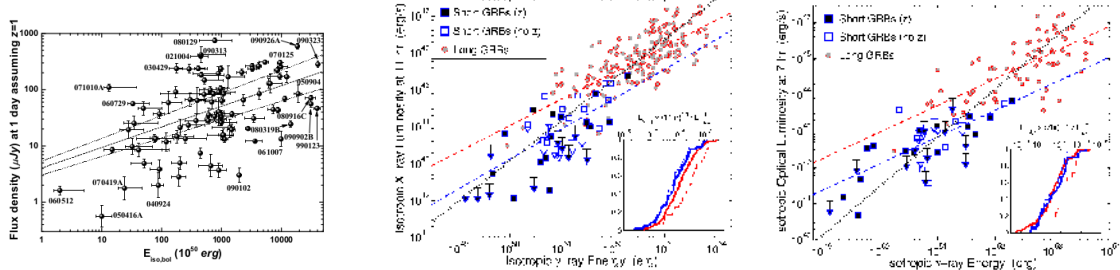


Figure 4.2.8: Left panel: the $F_{O,1d} - E_{\gamma,\text{prompt}}$ ($E_{\text{iso,bol}}$ in the picture) correlation for the optically selected sample with the best fit line represented by a dashed line and the 3σ error indicated by a dotted line. GRB 991208, 060210, 060607A, 060906 and 080319C are not included. The first because observed after few days, and the others because the detection stopped before one day. Particular GRBs are displayed with their own names. (Figure from Kann et al. (2010). @ AAS. Reproduced with permission.) Middle panel: the $L_{X,11} - E_{\gamma,\text{prompt}}$ correlation using SGRBs (indicated in blue) and LGRBs (indicated in grey). SGRBs without measured redshift, but with a selected fiducial value $z = 0.75$, are represented by open markers. The best fit for SGRBs and LGRBs are indicated by dashed blue and red lines, respectively. The correlation predicted by the afterglow synchrotron model with $\nu_X > \nu_c$ and $\gamma = 2.4$ ($\log L_{X,11} \propto 1.1 \times \log E_{\gamma,\text{prompt}}$) is displayed by a dotted black line. In the inset panel thick lines indicate the distribution of the quantity $\log(L_{X,11} \times (11 \text{ hr})^{1.3} / E_{\gamma,\text{prompt}}^{1.1})$ for the complete data set, while thin lines display the same distribution but for the area where values of $E_{\gamma,\text{prompt}}$ for SGRBs and LGRBs are identical. For SGRBs, $L_{X,11}$ at the same value of $E_{\gamma,\text{prompt}}$ appears clearly smaller than the one for LGRBs. (Figure from Berger (2014a).) Right panel: the $L_O,7 - E_{\gamma,\text{prompt}}$ correlation using SGRBs (indicated in blue) and LGRBs (indicated in grey). The correlation predicted by the afterglow synchrotron model for $\nu_m < \nu_O < \nu_c$ and $\gamma = 2.4$ ($\log L_{O,7} \propto 1.35 \times \log E_{\gamma,\text{prompt}}$) is represented by a dotted black line. In the inset panel the thick lines display the distribution of the quantity $\log(L_{O,7} \times (7 \text{ hr})^{1.05} / E_{\gamma,\text{prompt}}^{1.35})$ for the complete data set, while thin lines display the same distribution for the region where values of $E_{\gamma,\text{prompt}}$ for SGRBs and LGRBs are identical. For SGRBs, $L_{O,7}$ at the same value of $E_{\gamma,\text{prompt}}$ appears clearly smaller than the one for LGRBs. (Figure from Berger (2014a).)

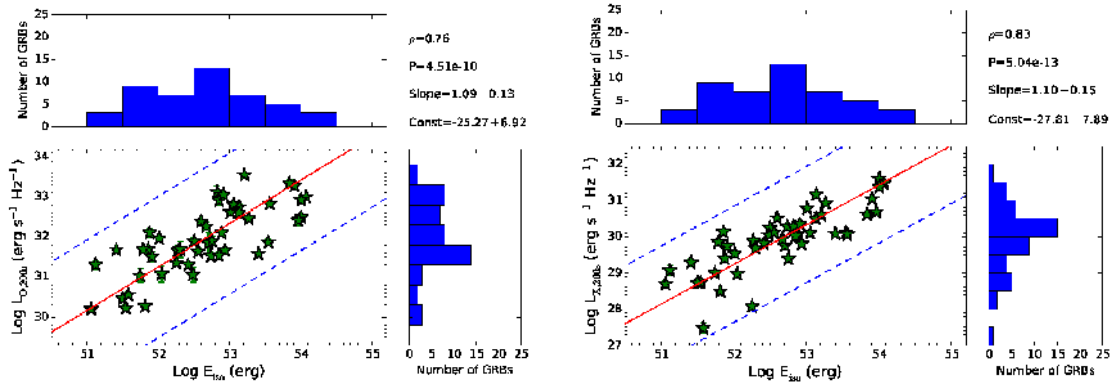


Figure 4.2.9: Left panel: the $\log L_{O,200s} - \log E_{\gamma,\text{prompt}}$ correlation. (Figure from Oates et al. (2015).) Right panel: the $\log L_{X,200s} - \log E_{\gamma,\text{prompt}}$ correlation. (Figure from Oates et al. (2015).) In both panels $E_{\gamma,\text{prompt}}$ is labelled E_{iso} .

the $\log E_{\text{peak}} - \log E_{\gamma,\text{prompt}} - \log E_{X,\text{plateau}}$ correlation is easily retrieved. Bernardini et al. (2012a) investigated a variation of the $\log E_{\text{peak}} - \log E_{\gamma,\text{prompt}} - \log E_{X,\text{plateau}}$ correlation employing $\log E_{\text{iso}}$ of the complete light curve in the X-ray energy band. In conclusion, with data sets of 58 and 297 LGRBs from Swift respectively, D’Avanzo et al. (2012) and Margutti et al. (2013) verified the $L_{X,a} - E_{\gamma,\text{prompt}}$ correlation, pointing out $b \sim 1$ and $\rho \approx 0.70$.

Correlations	Author	N	Slope	Norm	Corr.coeff.	P
$F_{X,1d} - S_{\gamma,\text{prompt}}$	Berger (2007)	16	$1.01^{+0.09}_{-0.09}$		0.86	5.3×10^{-5}
$F_{X,11} - S_{\gamma,\text{prompt}}$	Gehrels et al. (2008)	111	$0.63^{+0.04}_{-0.04}$	$2.11^{+0.21}_{-0.21}$	0.53	4×10^{-9}
	Gehrels et al. (2008)	10	$0.36^{+0.17}_{-0.17}$	$0.06^{+1.07}_{-1.07}$	0.35	0.31
$F_{O,11} - E_{\gamma,\text{prompt}}$	Nysewander et al. (2009)	421	~ 1			
$F_{O,11} - E_{\gamma,\text{prompt}}$	Nysewander et al. (2009)	37	~ 1			
$F_{X,11} - E_{\gamma,\text{prompt}}$	Nysewander et al. (2009)	421	~ 1			
	Nysewander et al. (2009)	37	~ 1			
$F_{O,a} - E_{\gamma,\text{prompt}}$	Panaiteescu&Vestrand (2011)	37	1.67		0.75	$10^{-7.3}$
$L_{X,1d} - E_{\gamma,\text{prompt}}$	Berger (2007)	13	$1.13^{+0.16}_{-0.16}$	$43.43^{+0.20}_{-0.20}$	0.94	3.2×10^{-6}
$L_{O,\text{peak}} - E_{\gamma,\text{prompt}}$	Liang et al. (2010)	32	$1.40^{+0.08}_{-0.08}$	$0.83^{+0.15}_{-0.15}$	0.87	10^{-4}
$L_{O,1d} - E_{\gamma,\text{prompt}}$	Kann et al. (2010)	76	0.36			
$L_{X,a} - E_{\gamma,\text{prompt}}$	Dainotti et al. (2011b)	62	$0.52^{+0.07}_{-0.06}$	$28.03^{+2.98}_{-2.97}$	0.43	1.4×10^{-5}
	Dainotti et al. (2011b)	8	$0.49^{+0.21}_{-0.16}$	$29.82^{+7.11}_{-7.82}$	0.83	3.2×10^{-2}
	D’Avanzo et al. (2012)	58	~ 1		≈ 0.70	
	Margutti et al. (2013)	297	~ 1		≈ 0.70	
$L_{X,11} - E_{\gamma,\text{prompt}}$	Berger (2014)	73	0.72	44.75		
	Berger (2014)	70	0.83	43.93		
$L_{O,7} - E_{\gamma,\text{prompt}}$	Berger (2014)	73	0.73	43.70		
	Berger (2014)	70	0.74	42.84		
$L_{X,200s} - E_{\gamma,\text{prompt}}$	Oates et al. (2015)	48	$1.10^{+0.15}_{-0.15}$	$-27.81^{+7.89}_{-7.89}$	0.83	5.04×10^{-13}
$L_{O,200s} - E_{\gamma,\text{prompt}}$	Oates et al. (2015)	48	$1.09^{+0.13}_{-0.13}$	$-25.27^{+6.92}_{-6.92}$	0.76	4.51×10^{-10}

Table 4.5: Summary of the correlations presented in this section. The correlation in log scale is listed in the first column, the authors are presented in the second one, and the size of the data set is displayed in the third one. The correlation slope and normalization are indicated in the fourth and fifth columns, while the correlation coefficient and the chance probability, P, are shown in the last two columns. (Table from Dainotti and Del Vecchio (2017).)

The correlations between $L_{X,11}$ and $E_{\gamma,\text{prompt}}$ and $L_{O,7}$ and $E_{\gamma,\text{prompt}}$, for definitions see Section 3.2, were investigated by Berger (2014a) employing 70 SGRBs and 73 LGRBs. The recovered correlations were flatter than those obtained by Kann et al. (2010) through the simulations (see the middle and right panels of Fig. 4.2.8).

Besides, a tight correlation between $L_{O,200s}$ or $L_{X,200s}$ and $\log E_{\gamma,\text{prompt}}$ was found by Oates et al. (2015) employing a data set of 48 LGRBs (see Fig. 4.2.9 and Table 4.5). From their analysis, it was concluded that this correlation allows for a deeper investigation of the

spectral features of GRBs, the emission mechanism in the optical and X-ray energy ranges, and the standard afterglow model. In Table 4.5, the correlations presented in this section are displayed.

For the physical interpretation of the $L_{X,\text{afterglow}} - E_{\gamma,\text{prompt}}$ correlation, Gehrels et al. (2008) stressed that $\beta_{OX,a} \approx 0.75$ identifies the optical and X-ray emissions. Nevertheless, this value of $\beta_{OX,a}$ is similar to the one for the slow cooling case, when $\gamma = 2.5$ for $\nu_m < \nu_O < \nu_X < \nu_c$. γ is the electron energy distribution power-law index, ν_X indicates the X-ray frequency, ν_O represents the optical frequencies, ν_c is the cooling frequency, and ν_m designates the peak frequencies of the synchrotron radiation. Oates et al. (2015) yielded that the standard afterglow model anticipates the $(\log L_{O,200s}, \log L_{X,200s}) - \log E_{\gamma,\text{prompt}}$ correlations. However, the slopes of the simulated and observed correlations are not compatible at $> 3\sigma$ as a consequence of the values of the efficiency, η . The scatter of the correlation will be more significant if the efficiency range is not sufficiently small. For example, the simulations carried out assuming efficiency $\eta = 0.1$ and $\eta = 0.9$ pointed out inconsistent outcomes between the simulated and observed slopes by more than 3σ .

4.2.3 The $L_{X,a} - L_{O,a}$ correlation and its physical interpretation

Jakobsson et al. (2004) investigated the $\log F_{O,11} - \log F_{X,11}$ distribution in the optical R band and in the 2 – 10 keV energy range, respectively. Using all GRBs with an observed X-ray afterglow phase (see the left panel of Fig. 4.2.10), they recovered 5 dark bursts among 52 BeppoSAX bursts. Unlike earlier definition, they denoted dark bursts as those GRBs with $\beta_{OX,a}$ smaller than 0.5, namely $\beta_{OX,a} \leq 0.5$. This definition was later employed by Nardini et al. (2006). Their purpose was to extend the investigation of dark burst to Swift data. Later, Gehrels (2007) and Gehrels et al. (2008), with 19 SGRBs and 37 LGRBs+6 SGRBs respectively, validated previous outcomes (see the middle and right panels of Fig. 4.2.10), recovering $b = 0.38 \pm 0.03$ for LGRBs and $b = 0.14 \pm 0.45$ for SGRBs (Gehrels et al., 2008).

Regarding the rest-frame, Berger (2014a) pointed out some resemblances between SGRBs and LGRBs, and a common average value of the ratio $\langle L_{O,7}/L_{X,11} \rangle \approx 0.08$, by investigating the correlation between $L_{O,7}$ and $L_{X,11}$ for 70 SGRBs and 73 LGRBs (see the left panel of Fig. 4.2.11). Oates et al. (2015) enriched this analysis by examining $L_{O,200s}$ and $L_{X,200s}$ for 48 LGRBs (see the right panel of Fig. 4.2.11) and by computing $b = 0.91 \pm 0.22$. The main aim of this correlation is to investigate the GRB synchrotron spectrum and to recover some limits on the external medium for both LGRBs and SGRBs. In Table 4.6 the parameters of the correlations presented in this section are shown.

For the physical interpretation of the $L_{X,a} - L_{O,a}$ correlation, Berger (2014a) claimed that in the framework of the synchrotron model the correlation between $L_{O,7}$ and $L_{X,11}$ implies that often ν_c is around or greater than the X-ray frequency range. This leads to the conclusion that the external medium densities for LGRBs are usually ~ 50 times higher than those for

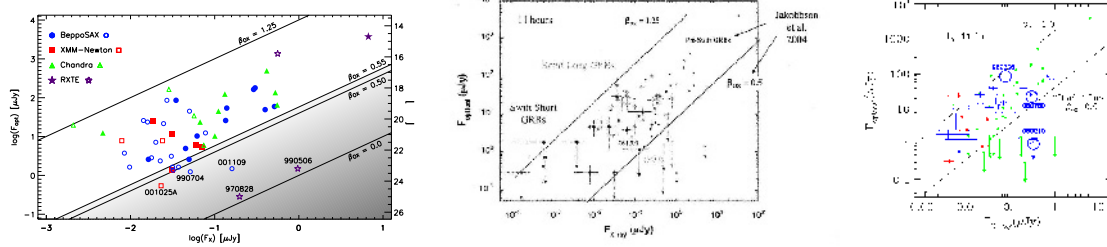


Figure 4.2.10: Left panel: the $\log F_{O,11} - \log F_X,11$ correlation (F_{opt} and F_X respectively in the plot) with optical observations displayed by filled symbols and upper limits indicated by open symbols. Constant $\beta_{OX,a}$ lines are displayed with their respective values. GRBs with $\beta_{OX,a} < 0.5$ are called dark bursts. (Figure from Jakobsson et al. (2004). © AAS. Reproduced with permission.) Middle panel: the $F_{O,11} - F_{X,11}$ correlation for Swift SGRBs and LGRBs. The pre-Swift GRBs and $\beta_{OX,a}$ values from Jakobsson et al. (2004) are inserted for analogy. The grey points display LGRBs, the black points indicate SGRBs and the small black points without error bars show the pre-Swift GRBs. (Figure from Gehrels (2007).) Right panel: the $F_{O,11} - F_{X,11}$ correlation using a sample of Swift SGRBs (indicated by red dots) and LGRBs (indicated by blue dots). The three GRBs with $z > 3.9$ are presented inside a circle, while in green are displayed the pre-Swift GRBs from Jakobsson et al. (2004). The line $\beta_{OX,a} = 0.5$ for dark bursts (Jakobsson et al., 2004) and a line for $\beta_{OX,a} = 1.0$ are described. (Figure from Gehrels et al. (2008). © AAS. Reproduced with permission.)

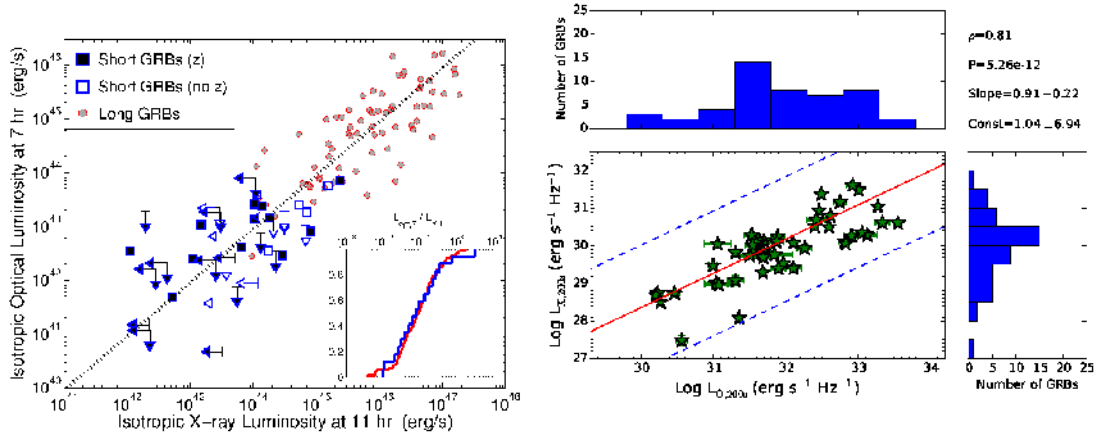


Figure 4.2.11: Left panel: the $L_{O,7} - L_{X,11}$ correlation. The correlation predicted by $\nu_X \sim \nu_c$ is represented with a dotted black line. In the inset panel the distribution of the quantity $L_{O,7}/L_{X,11}$ is displayed. These distributions are analogous for both SGRBs and LGRBs, with $L_{O,7}/L_{X,11} \leq 1$. This finding suggests that $\nu_X \sim \nu_c$ for SGRBs. (Figure from Berger (2014a).) Right panel: the $\log L_{X,200s} - \log L_{O,200s}$ correlation with the best fit line presented by a red solid line and the 3σ error region shown by a blue dashed line. ρ , P and the best fit coefficients are displayed in the top right edge. (Figure from Oates et al. (2015).)

SGRBs, thus $\nu_c \sim \nu_X$.

Correlations	Author	N	Slope	Norm	Corr.coeff.	P
$F_{O,11} - F_{X,11}$	Gehrels et al. (2008)	6	0.14 ± 0.45	0.72 ± 0.94	0.06	0.68
		37	0.38 ± 0.03	1.62 ± 0.04	0.44	0.006
$L_{O,7} - L_{X,11}$	Berger (2014)	70	0.08			
		73	0.08			
$L_{X,200s} - L_{O,200s}$	Oates et al. (2015)	48	0.91 ± 0.22	1.04 ± 6.94	0.81	5.26×10^{-12}

Table 4.6: Summary of the correlations presented in this section. The correlation in log scale is listed in the first column, the authors are presented in the second one, and the size of the data set is displayed in the third one. The correlation slope and normalization are indicated in the fourth and fifth columns, while the correlation coefficient and the chance probability, P, are shown in the last two columns. (Table from Dainotti and Del Vecchio (2017).)

4.2.4 The $L_{X,a} - L_{\text{iso}}$ correlation

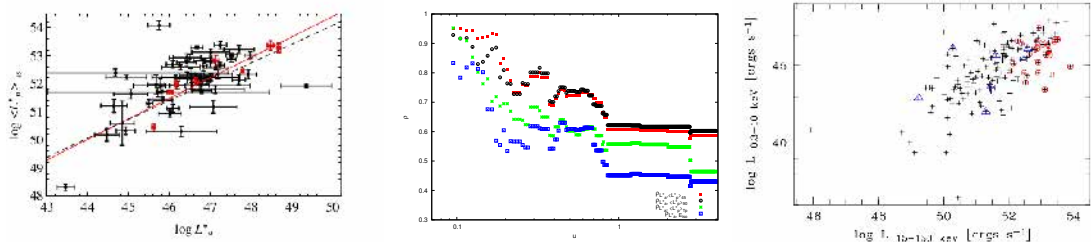


Figure 4.2.12: Left panel: the $\log < L_{\text{iso}} >_{45} - \log L_{X,a}$ correlation ($\log L_p^*$ and $\log L_a^*$ respectively in the plot) for the E4 sample (black points). The black dashed line presents the best fit, while the E0095 sample (red points) best fit is indicated by the red line. (Figure from Dainotti et al. (2011b).) Middle panel: the correlation coefficients for a few correlations versus $u = \sigma_E$ for LGRBs subsets. The $\log L_{X,a} - \log < L_{\text{iso}} >_{45}$ correlation is indicated by red squares, the $\log L_{X,a} - \log < L_{\text{iso}} >_{90}$ one is marked by black circles, the $\log L_{X,a} - \log < T_{X,p} >$ one is presented by green asterisks, and the $\log L_{X,a} - \log E_{\gamma,\text{prompt}}$ one is displayed by blue squares. (Figure from Dainotti et al. (2011b).) Right panel: the $L_{X,a} - L_{\text{iso}}$ correlation with triangles indicating SGRBs and circles marking high redshift ($z > 3.5$) GRBs. $L_{X,a}$ is computed in the XRT range, while L_{iso} in the BAT range. (Figure from Grupe et al. (2013). @ AAS. Reproduced with permission.)

Employing 77 Swift LGRBs, Dainotti et al. (2011b) investigated the relationships between the prompt emission and $\log L_{X,a}$. They obtained a correlation between $\log L_{X,a}$, in the XRT range, and $\log < L_{\text{iso}} >_{45} \equiv \log(E_{\gamma,\text{prompt}}/T_{45})$ in the BAT range, for definitions see Section 3.2. From the sample of 77 GRBs they selected a subsample of LGRBs for which $\sigma_E < 4$ is fulfilled, similarly to what has been done for the LT correlation, see Section 4.1.1. This new sample is composed of 62 LGRBs and the correlation (see the left panel of Fig. 4.2.12) associated with it is:

$$\log L_{X,a} = 20.58^{+6.66}_{-6.73} + 0.67^{+0.14}_{-0.15} \times \log < L_{\text{iso}} >_{45}, \quad (4.11)$$

with $\rho = 0.59$ and $P = 7.7 \times 10^{-8}$. Additionally, $\log L_{X,a}$ was correlated to other prompt luminosities determined by employing different timescales, such as T_{90} , T_{45} , and $T_{X,p}$, for definitions see Section 3.2. The E4 subsample made of 62 LGRBs with measured z and the E0095 subsample composed of 8 GRBs with regular light curves were employed in the analysis (see black and red points in the left panel of Fig. 4.2.12). They concluded that the GRB group providing the highest correlation coefficient, ρ , for the LT correlation also suggests the most significant correlations among prompt-afterglow parameters. Namely, the higher ρ , the smaller the σ_E parameter, as one can see in the middle panel of Figure 4.2.12. In this Figure ρ are displayed for the correlations: $\log L_{X,a} - (\log < L_{\text{iso}} >_{45}, \log < L_{\text{iso}} >_{90}, \log < L_{\text{iso}} >_{T_{X,p}}, \log E_{\gamma, \text{prompt}})$, indicated by red, black, green and blue colours, respectively. Thus, the increase in the value of ρ can help to choose the appropriate data set which can be used for achieving a more accurate determination of the plateau phase nature. Additionally, this set can be used for cosmological purposes. For the IC bursts no tight correlations were pointed out, due to the small amount of data, and it was claimed that their presence does not improve the significance of the correlations.

	E4		E0095	
Correlations	ρ	(b, a)	ρ	(b, a)
	P		P	
$L_{X,a} - < L_{\text{iso}} >_{45}$	0.59	$(0.67^{+0.14}_{-0.15}, 20.58^{+6.66}_{-6.73})$	0.95	$(0.73^{+0.16}_{-0.11}, 17.90^{+5.29}_{-6.0})$
	0.62	7.7×10^{-8}	0.90	2.3×10^{-3}
$L_{X,a} - < L_{\text{iso}} >_{90}$	0.60	$(0.63^{+0.15}_{-0.16}, 22.05^{+7.14}_{-7.31})$	0.93	$(0.84^{+0.11}_{-0.12}, 11.86^{+3.43}_{-3.44})$
	0.62	7.7×10^{-8}	0.94	2.7×10^{-3}
$L_{X,a} - < L_{\text{iso}} >_{T_{X,p}}$	0.46	$(0.73^{+0.09}_{-0.14}, 16.61^{+4.35}_{-4.35})$	0.95	$(0.93^{+0.20}_{-0.23}, 7.70^{+3.47}_{-3.46})$
	0.56	2.21×10^{-6}	0.90	2.3×10^{-3}
$L_{X,a} - E_{\gamma, \text{prompt}}$	0.43	$(0.52^{+0.07}_{-0.06}, 28.03^{+2.98}_{-2.97})$	0.83	$(0.49^{+0.21}_{-0.16}, 29.82^{+7.11}_{-7.82})$
	0.52	1.4×10^{-5}	0.75	3.2×10^{-2}
$T_{X,a}^* - E_{\gamma, \text{prompt}}$	-0.19	$(-0.49^{+0.09}_{-0.08}, 54.51^{+0.37}_{-0.30})$	-0.81	$(-0.96^{+0.21}_{-0.22}, 54.67^{+0.69}_{-0.69})$
	-0.21	1.0×10^{-1}	-0.69	5.8×10^{-2}
$L_{X,a} - E_{\text{peak}}$	0.54	$(1.06^{+0.53}_{-0.23}, 43.88^{+0.61}_{-1.00})$	0.74	$(1.5^{+0.65}_{-0.94}, 43.10^{+2.53}_{-2.26})$
	0.51	2.2×10^{-5}	0.80	1.7×10^{-2}
$T_{X,a}^* - E_{\text{peak}}$	-0.36	$(-0.66^{+0.20}_{-0.29}, 4.96^{+0.81}_{-0.80})$	-0.74	$(-1.40^{+0.66}_{-0.65}, 7.04^{+1.79}_{-1.77})$
	-0.35	5.2×10^{-3}	-0.77	2.5×10^{-2}
$< L_{\text{iso}} >_{45} - E_{\text{peak}}$	0.81	$(1.14^{+0.22}_{-0.25}, 49.27^{+0.61}_{-0.60})$	0.76	$(1.45^{+0.26}_{-0.54}, 48.48^{+1.05}_{-1.04})$
	0.67	2.6×10^{-9}	0.92	1.2×10^{-3}

Table 4.7: In this table are listed: the correlation coefficients ρ , the respective best fit quantities (a, b), the correlation coefficient r and the occurrence probability P , for the correlations among prompt and prompt-afterglow parameters mentioned in this section. (Table from Dainotti et al. (2011b).)

In conclusion, Dainotti et al. (2011b) stressed the concept that the plateau phase is related to the central engine. In this work, other correlations between $\log L_{X,a}$ and parameters of the

prompt phase such as $\log E_{\text{peak}}$ and the variability, $\log V$, were also investigated, recovering (except for V) significant correlations (see Table 4.7).

As displayed in Table 4.7, the $\log T_{X,a}^* - \log E_{\gamma,\text{prompt}}$ correlation has a low $\rho = -0.19$. The occurrence of the $\log L_{X,a} - \log < L_{\text{iso}} >_{90}$ (see the right panel of Fig. 4.2.12) and the $\log < L_{\text{iso}} >_{90} - \log T_{X,a}^*$ correlations was recovered also by Grupe et al. (2013), who analysed a data set of 232 GRBs. Given that $\log < L_{\text{iso}} >_{90} = \log(E_{\gamma,\text{prompt}}/T_{90})$, the $\log < L_{\text{iso}} >_{90} - \log T_{X,a}^*$ correlation logically follows from the $\log T_{X,a}^* - \log E_{\gamma,\text{prompt}}$ one.

4.2.5 The $L_{X,a} - L_{X,\text{peak}}$ correlation

Dainotti et al. (2015a) upgraded the analysis of the correlations among prompt and afterglow parameters employing 123 LGRBs detected by Swift BAT+XRT with measured z and clear plateau phase. From their work, a correlation between $\log L_{X,\text{peak}}$ and $\log L_{X,a}$ was obtained (for definition see Section 3.2):

$$\log L_{X,a} = A + B \times \log L_{X,\text{peak}}, \quad (4.12)$$

with $A = -14.67 \pm 3.46$, $B = 1.21^{+0.14}_{-0.13}$, $\rho = 0.79$ and $P < 0.05$ (see the left panel of Fig. 4.2.13). $L_{X,\text{peak}}$ is given by:

$$L_{X,\text{peak}} = 4\pi \times D_L(z, \Omega_M, h)^2 \times F_{X,\text{peak}} \times K. \quad (4.13)$$

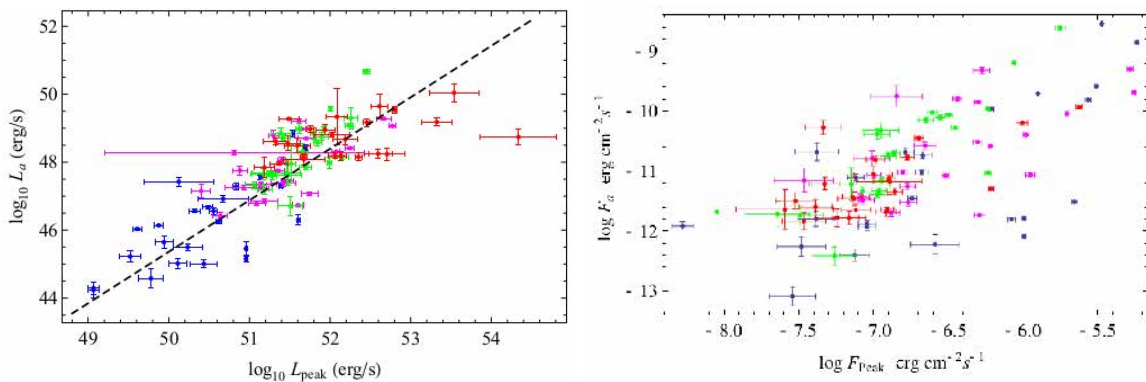


Figure 4.2.13: Left panel: the $\log L_{X,a} - \log L_{X,\text{peak}}$ correlation with the data set divided in 4 different equally populated redshift bins: $z \leq 0.84$, presented by blue dots, $0.84 \leq z < 1.8$ indicated by magenta dots, $1.8 \leq z < 2.9$ represented by green dots, and $z \geq 2.9$ displayed by red dots. The best fit line is marked by a dashed line. (Figure from Dainotti et al. (2015a).) Right panel: the $\log F_{X,a} - \log F_{X,\text{peak}}$ correlation with the sample divided as in the left panel. $\log F_{X,\text{peak}}$ is retrieved as described in the Second BAT Catalogue in both panels. (Figure from Dainotti et al. (2015a).)

ρ of the $\log L_{X,a} - \log L_{\text{iso}}$ correlation (Dainotti et al., 2011b) for 62 LGRBs, namely $\rho = 0.60$, was found to be lower than the one of the $\log L_{X,a} - \log L_{X,\text{peak}}$ correlation (see Section 4.2.4). This outcome indicates that a more suitable definition of the luminosity or

energy increases ρ by 24%. In the left panel of Figure 4.2.13 $\log L_{X,peak}$ is computed from the peak flux in X-ray, $F_{X,peak}$, through a broken or a simple power-law lines as the best fit of the spectrum. This computation has been performed without taking into account the error propagation due to time and energy, and thus, it differs from the previously defined luminosities. Given that $\log E_{\gamma,prompt}$ and $\log E_{peak}$ can be affected by the truncation effect caused by the detector threshold at high and low energies, Dainotti et al. (2015a) preferred the $\log L_{X,a} - \log L_{X,peak}$ correlation to those described in Dainotti et al. (2011b). Indeed, this truncation issue does not exist for $\log L_{X,peak}$ (Lloyd and Petrosian, 1999). Moreover, the redshift dependence caused by $D_L(z, \Omega_M, h)$ in the $\log L_{X,a} - \log L_{X,peak}$ correlation was taken out employing fluxes rather than luminosities. The main aim was to test its robustness. This analysis recovered a correlation between $\log F_{X,a}$ and $\log F_{X,peak}$ with $\rho = 0.63$ (see the right panel of Fig. 4.2.13). For a quantitative investigation of the selection effects see Section 4.3.

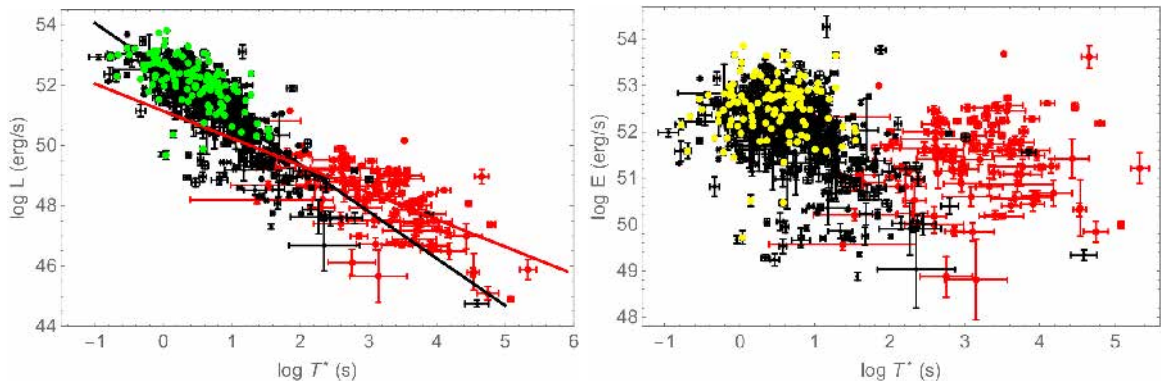


Figure 4.2.14: Left panel: the $\log L - \log T^*$ correlation for all the prompt and afterglow pulses represented by black and red symbols, respectively. The maximum luminosity of the pulses in the prompt phase ($\log T_{Lmax}$, $\log L_{max}$) are marked by green dots. (Figure from Dainotti et al. (2015a).) Right panel: the $\log E - \log T^*$ correlation for all the prompt and afterglow pulses represented by black and red symbols, respectively. The maximum energy of the pulses in the prompt phase ($\log T_{Emax}$, $\log E_{max}$) are displayed by yellow dots. (Figure from Dainotti et al. (2015a).) For both figures in the prompt pulses $\log L$ is $\log L_{X,f}$ and $\log T^*$ is $\log T_{X,f}^*$, while in the afterglow pulses $\log L$ is $\log L_{X,a}$ and $\log T^*$ is $\log T_{X,a}^*$.

Dainotti et al. (2015a) concluded that the LT correlation and its equivalent in the prompt phase, $\log L_{X,f} - \log T_{X,f}^*$ (Willingale et al. 2010, see the left panel of Fig. 4.2.14) have slopes incompatible at more than 2σ . This result indicated also a difference in the energy and time distributions (see the right panel of Fig. 4.2.14). This outcome gave rise to a new interpretation of these observations, see the next section for details.

Later, using 122 LGRBs without XRFs and GRBs associated with SNe, Dainotti et al. (2016) added a third parameter, $T_{X,a}$, to the $\log L_{X,a} - \log L_{X,peak}$ correlation retrieving:

$$\log L_{X,a} = (15.69 \pm 3.8) + (0.67 \pm 0.07) \times \log L_{X,peak} - (0.80 \pm 0.07) \log T_{X,a}, \quad (4.14)$$

with $r = 0.93$, $P \leq 2.2 \times 10^{-16}$, and $\sigma_{int} = 0.44 \pm 0.03$. Then, to diminish the scatter of the correlation, they employed only the group of 40 LGRBs with a good number of data and flat plateau phase. These assumptions gave:

$$\log L_{X,a} = (15.75 \pm 5.3) + (0.67 \pm 0.1) \times \log L_{X,peak} - (0.77 \pm 0.1) \times \log T_{X,a}, \quad (4.15)$$

with $r = 0.90$, $P = 4.41 \times 10^{-15}$, and $\sigma_{int} = 0.27 \pm 0.04$. From these outcomes it was concluded that the plane defined by this correlation can be regarded as a “fundamental” plane for GRBs. This can be employed for a better understanding of the theoretical framework of the relation between the prompt and the plateau emissions and as an effective cosmological probe.

As a follow up of Dainotti et al. (2016), Dainotti et al. (2017a) analysed the fundamental plane created by the 3D correlation $L_{X,a} - L_{X,peak} - T_{X,a}$. They divided their sample of 183 Swift GRBs in several groups: XRFs (27), SNe (22), SEE-GRBs (15), LGRBs (132) and gold (45). Like in Dainotti et al. (2016) they defined the gold sample as the set of GRBs with a flat plateau phase and at least 5 points in the light curve. For this category they obtained the correlation:

$$\log L_{X,a} = (17.65 \pm 5.7) - (0.83 \pm 0.10) \times \log T_{X,a} + (0.64 \pm 0.11) \times \log L_{X,peak}, \quad (4.16)$$

with $\sigma_{int} = 0.316 \pm 0.039$, $r = 0.90$, and $P = 1.75 \times 10^{-17}$. The scatter of the correlation computed for this group is the smallest among those of all the categories analysed in this work. This result was in agreement with the one from Dainotti et al. (2016) within 1σ . They investigated the fundamental planes created by this 3D correlation for each group of GRBs. As a result, they obtained that all the planes, except the one for SEE-GRBs, are statistically similar to the one computed for the gold sample. Therefore, the distance of GRBs from this fundamental plane is an important tool to classify LGRBs and SGRBs. Furthermore, they investigated the correlation assuming $T_{X,a}$ as the dependent variable:

$$\log T_{X,a} = C_0 - C_1 \times \log L_{X,a} + C_2 \times \log L_{X,peak}. \quad (4.17)$$

with C_0 , C_1 and C_2 the correlation coefficients. From this attempt they achieved smaller values of the scatter (for LGRBs sample the reduction of the scatter is 24%). Finally, they compared their samples to those obtained by using $L_{X,peak}$ through Fermi/GBM data to verify if the fundamental plane does not depend on the particular energy range assumed. They not only confirmed the existence of the fundamental plane, but they even showed that the scatter is reduced by 27% for the gold sample. This suggested that the correlation

does not depend on the energy range and indeed its existence is very robust. To verify if the correlation is independent of other parameters, they built several four parameter correlations by employing some of the prompt and afterglow parameters ($\alpha_{X,a}$, T_{90}^* , E_{peak}^* , and θ_{jet}). None of these four parameters correlations are statistically significant. Thus, the fundamental plane is robust in its 3D configuration.

Physical interpretation of the $L_{X,a} - L_{\text{iso}}$ and the $L_{X,a} - L_{X,\text{peak}}$ correlations

Dainotti et al. (2015a) showed two different values of the slope for the $L - T^*$ and the $E - T^*$ correlations of prompt and afterglow pulses. These values may imply that the prompt pulses can be produced by the internal shocks, while the afterglow pulses by the external shocks. In the case where the plateau phase is due to synchrotron emission from the external shocks, then all the pulses should present similar initial physical conditions. The association between prompt and afterglow phases was examined to understand the GRB physical models explaining the $\log L_{X,a} - \log L_{\text{iso}}$, the $\log L_{X,a} - \log L_{X,\text{peak}}$, and the LT correlations. The best framework describing this association is the one by Hascoët et al. (2014), which analysed two scenarios. The first one in the FS model assumes modified microphysics quantities to reduce the initial efficiency of the GRB phenomenon. In the second one, the early afterglow phase is produced from a long-lived RS in the FS scenario. In the first case, a wind external medium is presumed together with the internal energy transferred into electrons (or positrons), $\epsilon_e \propto n^{-\nu}$, with n the density medium. When $\nu \approx 1$ a flat plateau phase is retrieved. This showed that it is possible to obtain a plateau phase satisfying the $\log L_{X,a} - \log L_{\text{iso}}$ and the $\log L_{X,a} - \log L_{X,\text{peak}}$ correlations even modifying one parameter only. In the second case, the correlations among prompt-afterglow quantities are recovered when Γ of the jet increases with the energy of the burst.

On the other hand, Ruffini et al. (2014) yielded that the $\log L_{X,a} - \log L_{\text{iso}}$ and the $\log L_{X,a} - \log L_{X,\text{peak}}$ correlations can be explained by the induced gravitational collapse paradigm taking into account the energetic ($10^{52} - 10^{54}$ erg) LGRBs with the observed associated SNe. In this case, the external medium well fits the plateau and the prompt emissions of the light curves. Indeed, for the external medium either a radial structure of the wind (Guida et al., 2008; Bernardini et al., 2006, 2007; Caito et al., 2009) or a division of the shell (Dainotti et al., 2007) was supposed.

Also the Supercritical Pile GRB Model seems to explain the $\log L_{X,a} - \log L_{\text{iso}}$ and the $\log L_{X,a} - \log L_{X,\text{peak}}$ correlations. Indeed, Kazanas et al. (2015), using this model, concluded that: 1) the ratio, R , between the luminosities is in agreement with the one between the mean prompt flux in the BAT range and the plateau flux in the XRT band; 2) the ratio, R , has value analogous to that of the proton to electron mass ratio (see Fig. 4.2.15). Thus, they pointed out that the $\log L_{X,a} - \log L_{\text{iso}}$ and the $\log L_{X,a} - \log L_{X,\text{peak}}$ correlations can be retrieved. In conclusion, this appears to be a demanding task for the ones who aim to better describe the phenomenology of the correlations taking into account all the aspects

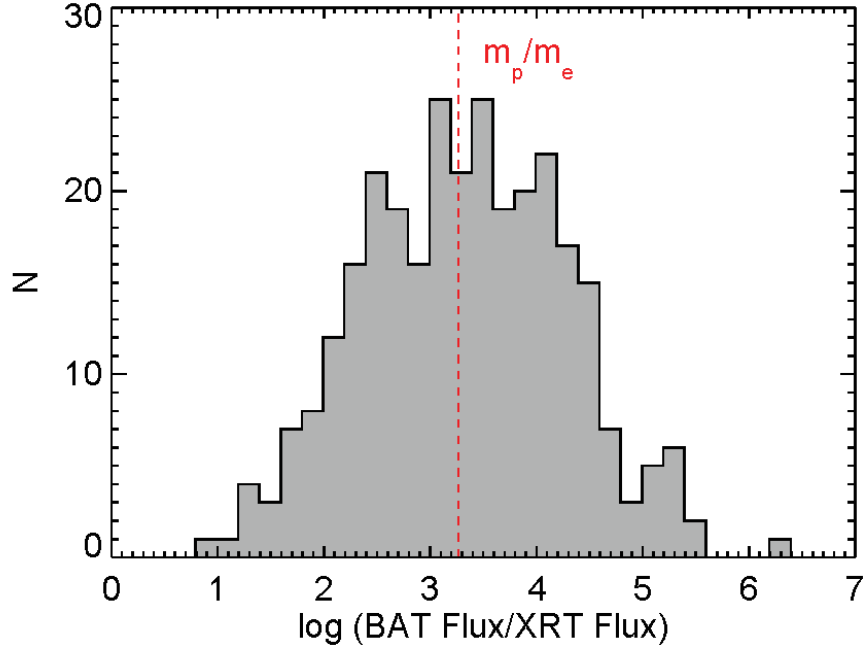


Figure 4.2.15: Distribution of the ratio of the BAT to XRT fluxes considering a set of Swift GRBs. The mean value of this distribution is $\sim 10^3 - 10^4$. The ratio of the proton to electron masses m_p/m_e is indicated by the vertical line. (Figure from Kazanas et al. (2015).)

mentioned above.

4.2.6 The $L_{O,peak}^F - T_{O,peak}^{*F}$ correlation and its physical interpretation

The correlation between the width, w , and $T_{O,peak}$ of the light curve flares, expressed by the superscript F, was investigated by Liang et al. (2010) (for definitions see Section 3.2). They employed 32 GRBs detected by Swift (see the left panel of Fig. 4.2.16). The correlation obtained is the following:

$$\log w^F = (0.05 \pm 0.27) + (1.16 \pm 0.10) \times \log T_{O,peak}^F, \quad (4.18)$$

with $\rho = 0.94$.

Then, employing 24 flares from 19 single-pulse CGRO/BATSE GRBs, Li et al. (2012) examined a similar correlation, but with smaller values of normalization and slope (see the right panel of Fig. 4.2.16). Adopting only the 14 GRBs with a clear flare activity, they obtained:

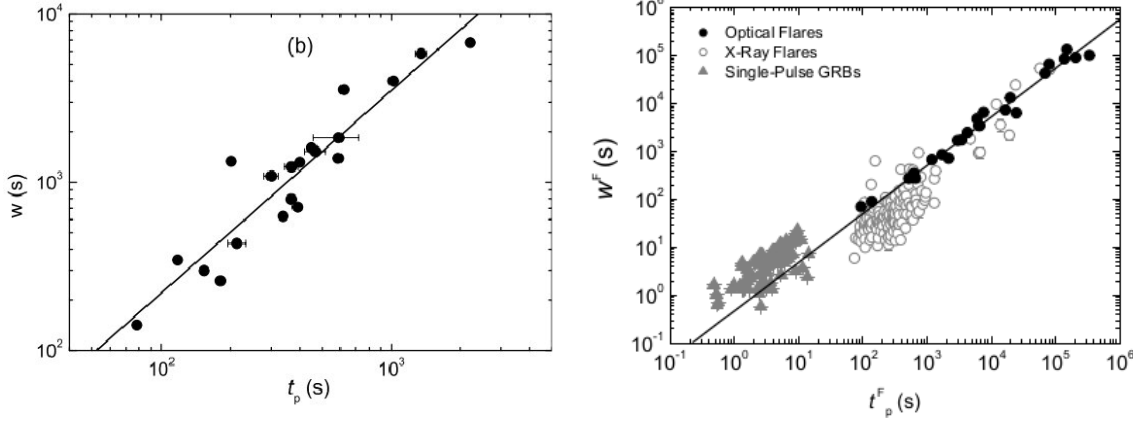


Figure 4.2.16: Left panel: the $\log w^F$ - $\log T_{O,peak}^F$ correlation. (Figure from Liang et al. (2010). @ AAS. Reproduced with permission.) Right panel: the $\log w^F$ - $\log T_{O,peak}^F$ correlation. (Figure from Li et al. (2012). @ AAS. Reproduced with permission.) In both panels the best fit is indicated by a line.

$$\log w^F = -0.32 + 1.01 \times \log T_{O,peak}^F. \quad (4.19)$$

From this correlation it was yielded that flares at earlier times are more luminous and narrower than those at later times. In addition, they claimed that X-ray flares observed by Swift/XRT and optical flares observed in the R filter showed an analogous behaviour in regard to the $w^F - T_{O,peak}^F$ correlation (Chincarini et al. 2007; Margutti et al. 2010, see the right panel of Fig. 4.2.16). In their analysis, a new correlation in the rest-frame was also recovered between $L_{O,peak}$ in the R filter, in units of 10^{48} erg s $^{-1}$, and $T_{O,peak}^*$ of the flares for a sample of 19 GRBs (see Fig. 4.2.17). The best fit of this correlation is established by:

$$\log L_{O,peak}^F = (1.89 \pm 0.52) - (1.15 \pm 0.15) \times \log T_{O,peak}^*, \quad (4.20)$$

with $\rho = 0.85$ and $P < 10^{-4}$. $T_{O,peak}^F$ was found in the range between \sim tens of seconds and $\sim 10^6$ seconds, while $L_{O,peak}^F$ was in the interval between 10^{43} and 10^{49} erg s $^{-1}$, with mean 10^{46} erg s $^{-1}$. Furthermore, employing only the brightest GRBs of the data set, they concluded that $T_{O,peak}^*$ was significantly anti-correlated with $E_{\gamma,prompt}$ in the range between 1 and 10^4 keV:

$$\log T_{O,peak}^* = (5.38 \pm 0.30) - (0.78 \pm 0.09) \times \log E_{\gamma,prompt}/10^{50}, \quad (4.21)$$

with $\rho = 0.92$. The correlations mentioned in this section suggest that in the optical band the GRB flares which are more energetic (high values of $E_{\gamma,prompt}$) display a peak at earlier times and are much brighter. In Table 4.8 the correlations presented in this section are shown.

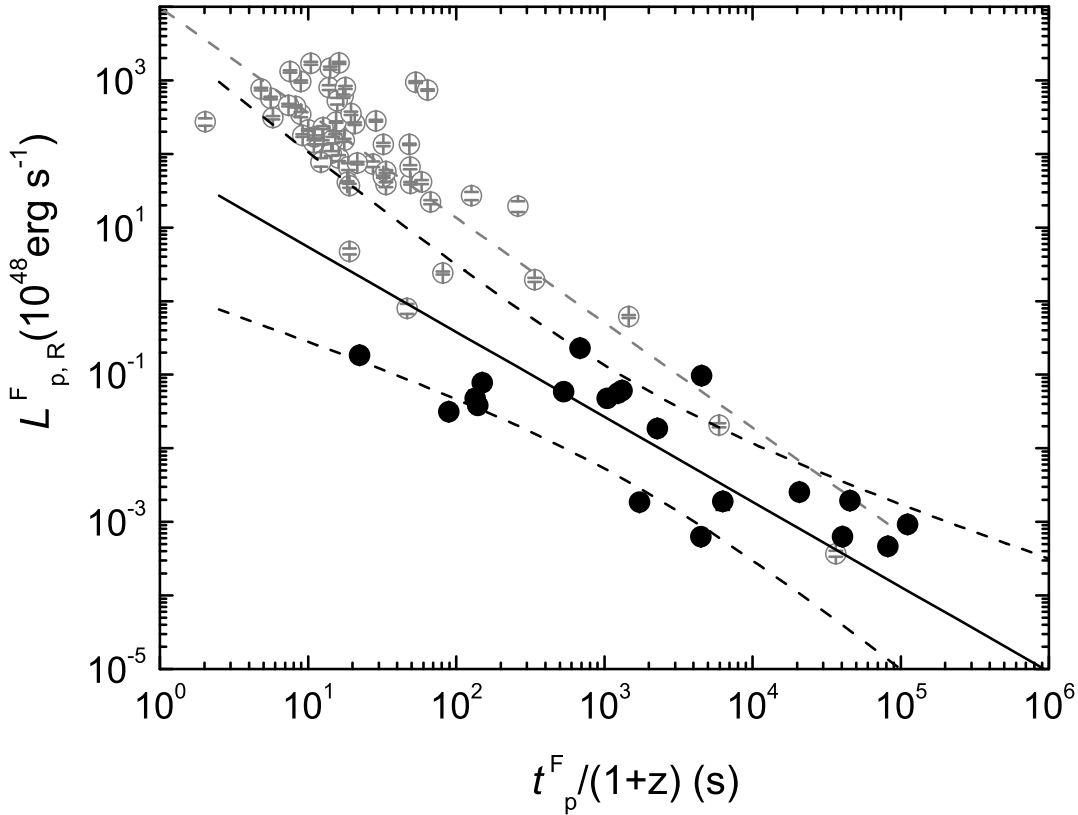


Figure 4.2.17: The $\log L_{O,peak}^F$ - $\log T_{O,peak}^{*F}$ correlation with optical flares represented by black dots, and X-ray flares related to the optical flares displayed by grey circles. Best fits are indicated by lines. (Figure from Li et al. (2012). @ AAS. Reproduced with permission.)

Correlations	Author	N	Slope	Norm	Corr.coeff.	P
$w^F - T_{O,peak}^F$	Liang et al. (2010)	32	$1.16^{+0.10}_{-0.10}$	$0.05^{+0.27}_{-0.27}$	0.94	$< 10^{-4}$
	Li et al. (2012)	19	1.01	-0.32		
$L_{O,peak}^F - T_{O,peak}^{*F}$	Li et al. (2012)	19	$-1.15^{+0.15}_{-0.15}$	$1.89^{+0.52}_{-0.52}$	0.85	$< 10^{-4}$
$T_{O,peak}^{*F} - E_{\gamma,prompt}$	Li et al. (2012)	19	$-0.78^{+0.09}_{-0.09}$	$5.38^{+0.30}_{-0.30}$	0.92	$< 10^{-4}$

Table 4.8: Summary of the correlations presented in this section. The correlation in log scale is listed in the first column, the authors are presented in the second one, and the size of the data set is displayed in the third one. The correlation slope and normalization are indicated in the fourth and fifth columns, while the correlation coefficient and the chance probability, P, are shown in the last two columns. (Table from Dainotti and Del Vecchio (2017).)

For the physical interpretation of the $L_{O,peak}^F - T_{O,peak}^{*F}$ correlation, Li et al. (2012) claimed that the flares are distinct from the afterglow phase. In addition, they concluded that the association between $L_{O,peak}^F$ and $T_{O,peak}^{*F}$ implies a common mechanism for the prompt gamma-ray and late optical flare radiations, i.e. a central engine repeatedly emitting shells during radiation. Magnetic turbulent reconnection or internal shocks, which possibly stem from the variability (Kobayashi et al., 1997; Zhang and Yan, 2011), could be produced from the collisions among the shells. Nevertheless, Fenimore et al. (1995) pointed out that no relevant pattern for the intensity and width of the flare is found by employing GRBs only in the BATSE gamma-ray range. Later, Maxham and Zhang (2009) concluded that it is needed a central engine emitting thicker and dimmer shells at late times to understand the $w^F - T_{O,peak}^F$ correlation. As shown by Perna et al. (2006) and Proga and Zhang (2006), this could be described with flares produced by blobs, such that the diffusion during the accretion would prolong the accretion time onto the BH.

4.3 Selection Effects

GRB correlations are often influenced by selection effects. Selection biases are distortions or biases that appear when the considered sample is not fully characterizing the “true” distribution. It was stressed by Efron and Petrosian (1992), Lloyd and Petrosian (1999), Dainotti et al. (2013b, 2015a) and Petrosian et al. (2013) that in the analysis of a multivariate sample a significant point is to recover the correlations without selection biases (intrinsic correlations) and to compute the correct distribution for each parameter.

The correlations mentioned in previous sections are mostly affected by two types of biases: the first caused by the redshift dependence of the parameters and the latter originated from the threshold of the detector employed. Several methods to deal with selection biases are here presented. In Section 4.3.1, the redshift induced correlations are presented through a qualitative procedure, in Section 4.3.2 a more quantitative procedure through the EP method is discussed. In Section 4.3.3, how to obtain the intrinsic correlations corrected for selection biases is described. In Section 4.3.4 the selection biases for the optical and X-ray luminosities are summarized. Finally, in Section 4.3.5 the estimation of the intrinsic correlation through Monte Carlo simulations is displayed.

4.3.1 Redshift induced correlations

Given that a modification of the correlation slope, b , of the LT correlation has been pointed out by different analyses (Dainotti et al., 2008, 2010), Dainotti et al. (2011a) investigated the redshift dependence of the LT correlation to understand the motivation of this variation. Indeed, even if the values are compatible within 1σ , Dainotti et al. (2008) obtained as the central value $b = -0.74^{+0.20}_{-0.19}$, while Dainotti et al. (2010) computed $b = -1.06^{+0.27}_{-0.28}$.

Although the 62 LGRBs of the data set were found not equally distributed in the interval $(z_{min}, z_{max}) = (0.08, 8.26)$, the main point was to examine if the coefficients (a, b, σ_{int}) were compatible within the errors in the whole redshift range (see the left panel of Fig. 4.3.1).

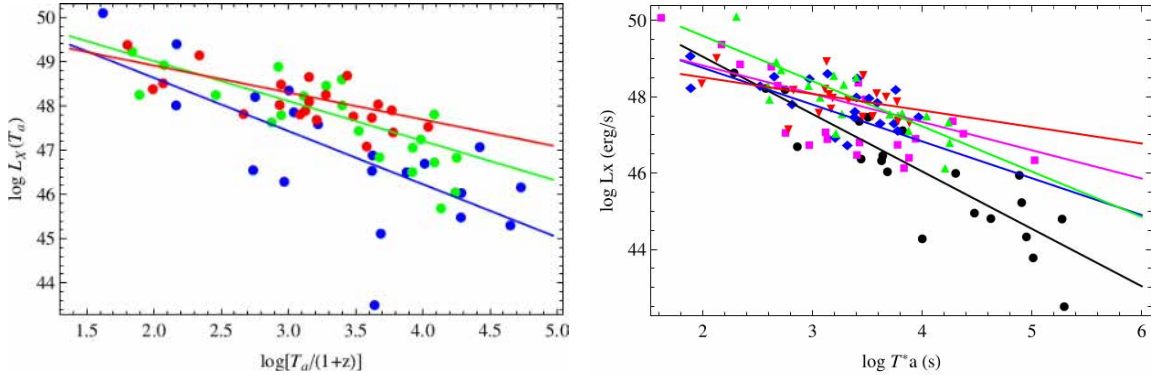


Figure 4.3.1: Left panel: the LT correlation with the data set split in the three redshift ranges: $Z1 = (0.08, 1.56)$, presented by blue dots, $Z2 = (1.71, 3.08)$, displayed by green dots, and $Z3 = (3.21, 8.26)$, indicated by red dots. With the same colours the best fit line are drawn. (Figure from Dainotti et al. (2011a). @ AAS. Reproduced with permission.) Right panel: the LT correlation using 101 GRBs split into five redshift intervals: $z < 0.89$ presented by black dots, $0.89 \leq z \leq 1.68$ indicated by magenta dots, $1.68 < z \leq 2.45$ displayed by blue dots, $2.45 < z \leq 3.45$ represented by green dots, and $z \geq 3.45$ marked by red dots. The best fits are indicated by solid lines. (Figure from Dainotti et al. (2013b). @ AAS. Reproduced with permission.)

Consequently, the sample was divided in three redshift groups with equal number of GRBs, $Z1 = (0.08, 1.56)$, $Z2 = (1.71, 3.08)$ and $Z3 = (3.21, 8.26)$, displayed as blue, green and red points, respectively, in the left panel of Figure 4.3.1. Table 4.9 shows the outcomes.

Id	ρ	$(b, a, \sigma_{int})_{bf}$	b_{median}	$(\sigma_{int})_{median}$
Z1	-0.69	(-1.20, 51.04, 0.98)	$-1.08^{+0.27}_{-0.30}$	$1.01^{+0.20}_{-0.16}$
Z2	-0.83	(-0.90, 50.82, 0.43)	$-0.86^{+0.18}_{-0.16}$	$0.45^{+0.09}_{-0.08}$
Z3	-0.63	(-0.61, 50.14, 0.26)	$-0.58^{+0.14}_{-0.15}$	$0.26^{+0.07}_{-0.06}$

Table 4.9: Calibration results for GRBs split in three equally populated redshift bins. The $Z1$, $Z2$, $Z3$ bins are in the following ranges respectively: $(z_{min}, z_{max}) = (0.08, 1.56)$, $(1.71, 3.08)$, $(3.21, 8.26)$. The best fit values are indicated by the subscript bf , while the median values are represented by the $median$ subscript. (Table from Dainotti et al. (2011a).)

The computed ρ was significant in each redshift bin, corroborating the redshift independence of the LT correlation. Indeed, if ρ was not significant in one or more redshift bins, this would have implied that the correlation as a whole would have been reproduced merely as an effect of the redshift dependence. As visible from Table 4.9, b for groups $Z1$ and $Z2$ are compatible at the 68% CL, while b for groups $Z1$ and $Z3$ only at the 95% CL. On the other hand, the normalization a is similar in all the groups. Given the paucity of GRBs in the sample and the existence of high σ_E GRBs, it could not be verified if the LT correlation is shallower for higher z GRBs. Therefore, it was concluded that broader data sets with low σ_E and a more regular binning of z are needed to solve this issue.

Using 101 GRBs, Dainotti et al. (2013b) analysed the updated sample dividing it in 5

redshift ranges with equal number of GRBs, thus having 20 GRBs in each redshift range. The bins are displayed in the right panel of Figure 4.3.1 by distinct colours: black for $z < 0.89$, magenta for $0.89 \leq z \leq 1.68$, blue for $1.68 < z \leq 2.45$, green for $2.45 < z \leq 3.45$ and red for $z \geq 3.45$. The best fit line for each redshift bin is presented with the same colours. In each bin b is distinct for the different samples. In addition, GRBs in each redshift range in the different bins are well separated in the LT plane. In the left panel of Figure 4.3.2 the evolution of the slope of the LT correlation is shown for each redshift range as a function of the average redshift of each bin.

Later, Dainotti et al. (2015b) split the data set of 176 GRBs into 5 redshift bins, as displayed in the right panel of Figure 4.3.2. It was found a weak dependence on z given by: $b(z) = 0.10z - 1.38$.

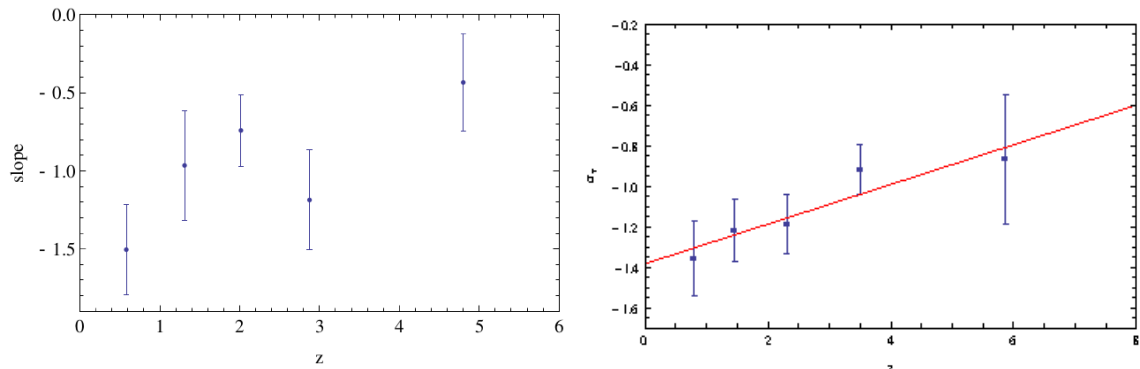


Figure 4.3.2: Left panel: the slope b as a function of the average value of the redshift intervals. (Figure from Dainotti et al. (2013b). © AAS. Reproduced with permission.) Right panel: α_τ , corresponding to the slope b , as a function of z . The best fit function is given by $\alpha_\tau = 0.10z - 1.38$. (Figure from Dainotti et al. (2015b). © AAS. Reproduced with permission.)

Furthermore, dividing the data set in 4 redshift bins (see the left panel of Fig. 4.2.13), Dainotti et al. (2015a) concluded that the $\log L_{X,a} - \log L_{X,peak}$ correlation is not dependent on the redshift. Indeed, the distribution of the GRBs is not clustered around a particular area, suggesting no significant redshift evolution. Regarding the luminosity, a weak redshift evolution for $\log L_{X,a}$ was claimed by Dainotti et al. (2013b), instead an important redshift evolution for $\log L_{X,peak}$ was computed by Yonetoku et al. (2004), Petrosian et al. (2013), and Dainotti et al. (2015a). For more details, see Sections 4.3.2 and 4.3.2.

4.3.2 Redshift induced correlations through Efron and Petrosian method

To examine quantitatively the dependence on the redshift of the physical quantities and to remove the selection effects, the EP method was employed for the analysis of incomplete GRB samples (Petrosian et al., 2009; Lloyd and Petrosian, 1999; Lloyd et al., 2000b). This method calculates the redshift evolution and the instrumental selection biases with the aim of overcoming them. The final goal of using this method is to allow the computation of the intrinsic correlation slope b_{int} by defining new bias-free quantities, the so-called local

variables, indicated with the symbol $'$. Namely, these are the variables as they are computed at $z = 0$ in the local universe. Then, the EP method employs a variation to the Kendall tau test, τ , to calculate the most reliable estimates of the parameters in the functions describing the luminosity and time evolution. For details on the meaning and determination of τ see Efron and Petrosian (1992).

Luminosity evolution

To investigate the relation between luminosity and redshift (the so-called luminosity evolution) for both prompt and plateau phases, the limiting plateau flux, F_{lim} , should be parameterised before employing the EP method. F_{lim} is the smallest observed flux at a certain z . The limit given by XRT, $F_{\text{lim},XRT} = 10^{-14}$ erg cm $^{-2}$ s $^{-1}$, does not well describe the sample incompleteness. The best evaluation for the flux threshold is given by Cannizzo et al. (2011), (10^{-12} erg cm $^{-2}$ s $^{-1}$). Among several threshold fluxes, Dainotti et al. (2013b) chose the value $F_{\text{lim},XRT} = 1.5 \times 10^{-12}$ erg cm $^{-2}$ s $^{-1}$, which allowed for the inclusion of 90 GRBs (the initial sample was composed of 101 GRBs, see the left panel of Fig. 4.3.3). Instead, for the prompt phase, Dainotti et al. (2015a) computed a prompt limiting flux $F_{\text{lim},BAT} = 4 \times 10^{-8}$ erg cm $^{-2}$ s $^{-1}$, which also included 90% of the data sample (see the right panel of Fig. 4.3.3).

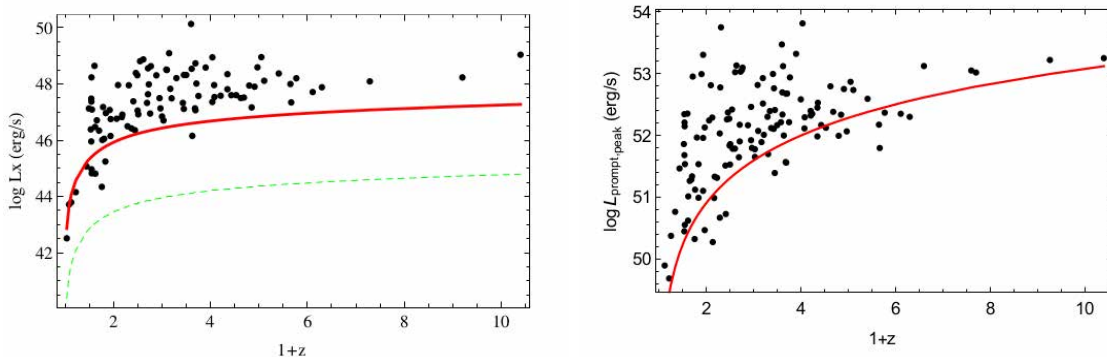


Figure 4.3.3: Left panel: the $\log L_{X,a} - z$ distribution with the XRT flux limit, 1.0×10^{-14} erg cm $^{-2}$ s $^{-1}$, represented by a dashed green line. This value does not well describe the limit of the flux. The best flux limit for the considered data set, 1.5×10^{-12} erg cm $^{-2}$ s $^{-1}$, is indicated by a solid red line. (Figure from Dainotti et al. (2013b). @ AAS. Reproduced with permission.) Right panel: the $\log L_{X,peak} - z$ distribution, with the BAT flux limit (4.0×10^{-8} erg cm $^{-2}$ s $^{-1}$) and K correction $K = 1$, well describes the flux limit for the considered data set, displayed by a solid red line. (Figure from Dainotti et al. (2015a).)

From the analysis by Dainotti et al. (2013b), it was chosen a correlation function, $g(z)$, in a way that $L'_{X,a} \equiv L_{X,a}/g(z)$ does not depend on z . This function is simply given by:

$$g(z) = (1 + z)^{k_{L_{X,a}}}. \quad (4.22)$$

More complicated functional forms were also considered by Dainotti et al. (2013b, 2015a), although they provided similar outcomes.

From this analysis, Dainotti et al. (2013b) computed the value of $k_{L_{X,a}}$ for which $\tau_{L_{X,a}} = 0$. This is the best definition of the luminosity evolution at 1σ level. They calculated $k_{L_{X,a}} = -0.05^{+0.35}_{-0.55}$, pointing a weak evolution (see the left panel of Fig. 4.3.4). In the same picture, using the data set of 47 GRBs (green dotted line) in common with the sample of 77 LGRBs employed in Dainotti et al. (2011a), the analogous distribution for this smaller sample is displayed. It was claimed that the outcomes of the afterglow luminosity evolution for these two sets are in agreement within 2σ .

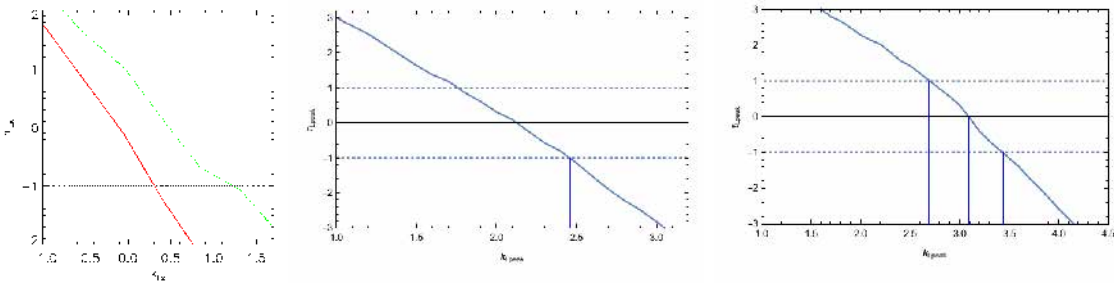


Figure 4.3.4: Left panel: the $\tau - k_{L_{X,a}}$ distribution for the complete data set shown by a red line. The green dotted line represents the distribution for 47 GRBs in common with the 77 GRB sample used by Dainotti et al. (2011a). (Figure from Dainotti et al. (2013b). @ AAS. Reproduced with permission.) Middle panel: the $\tau - k_{L_{X,peak}}$ distribution obtained through the Equation 4.22. (Figure from Dainotti et al. (2015a).) Right panel: the $\tau - k_{L_{X,peak}}$ distribution computed through the Equation 4.23. (Figure from Dainotti et al. (2015a).)

In the prompt phase, for the evolution of $L_{X,peak}$, Dainotti et al. (2015a) employed both a simple relation function (see Equation 4.22) and a more complex one:

$$g(z) = \frac{Z^{k_L}(1 + Z_{cr}^{k_L})}{Z^{k_L} + Z_{cr}^{k_L}}, \quad (4.23)$$

where $Z = 1+z$ and $Z_{cr} = 3.5$. For the prompt phase it was recovered a significant luminosity evolution, $k_{L_{X,peak}} = 2.13^{+0.33}_{-0.37}$, through the simple relation, and $k_{L_{X,peak}} = 3.09^{+0.40}_{-0.35}$ in the case of the more complex function (see the middle and right panels of Fig. 4.3.4). In conclusion, the outcomes of the prompt luminosity evolution for these two functions are in agreement within 2σ .

Time Evolution

As already done for the luminosity, also the limit of the plateau end time should be computed. Dainotti et al. (2013b) retrieved $T_{X,a,lim}^* = 242/(1+z)$ s, while (Dainotti et al., 2015a) claimed that for the prompt phase $T_{X,prompt,lim}^* = 1.74/(1+z)$ s (see Fig. 4.3.5 and Fig. 4.3.6). To analyse the time evolution, Dainotti et al. (2013b) defined the function $f(z)$, again such that $T'_{X,a} \equiv T_{X,a}^*/f(z)$ is independent of z . This is equivalent to the Equation 4.22 in which $k_{L_{X,a}}$ is substituted by the coefficient of the time evolution, $k_{T_{X,a}^*}$.

Similarly to the luminosity evolution, also for the time evolution the best value of $k_{T_{X,a}^*}$ is the one for which $\tau_{T_{X,a}^*} = 0$. As a result, $\tau_{T_{X,a}^*}$ versus $k_{T_{X,a}^*}$ distribution indicates a significant evolution for $T_{X,a}^*$ ($k_{T_{X,a}^*} = -0.85^{+0.30}_{-0.30}$, see the left panel of Fig. 4.3.7). The analogous distribution for a smaller set of 47 GRBs, in common with 77 GRBs employed in Dainotti et al. (2011a), is displayed in the same picture with a green dotted line. The findings of the afterglow time evolution for these two sets are in agreement within 1.5σ .

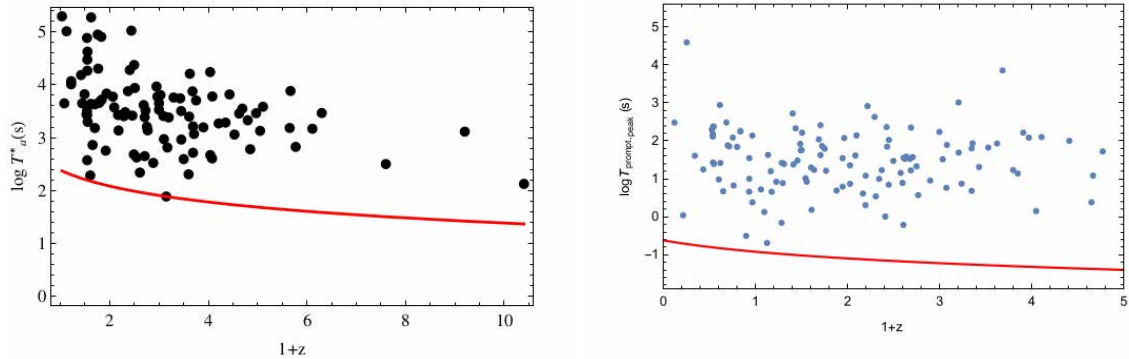


Figure 4.3.5: Left panel: the $\log T_{X,a}^* - z$ distribution with the limiting time in the rest-frame indicated by a red line. For this data set the limiting end-time of the plateau phase in the observed frame is set at $T_{X,a,lim} = 242$ s. (Figure from Dainotti et al. (2013b). @ AAS. Reproduced with permission.) Right panel: the $\log T_{X,prompt}^* - z$ distribution with the limiting rest-frame time, $\log(T_{X,prompt,lim}/(1+z))$, displayed by a red line. $\log T_{X,prompt}^*$ is the total width of the peak pulses in each GRB pulse. For this data set the limiting pulse width in the observed frame is set at $\log T_{X,prompt,lim} = 0.24$ s. (Figure from Dainotti et al. (2015a).)

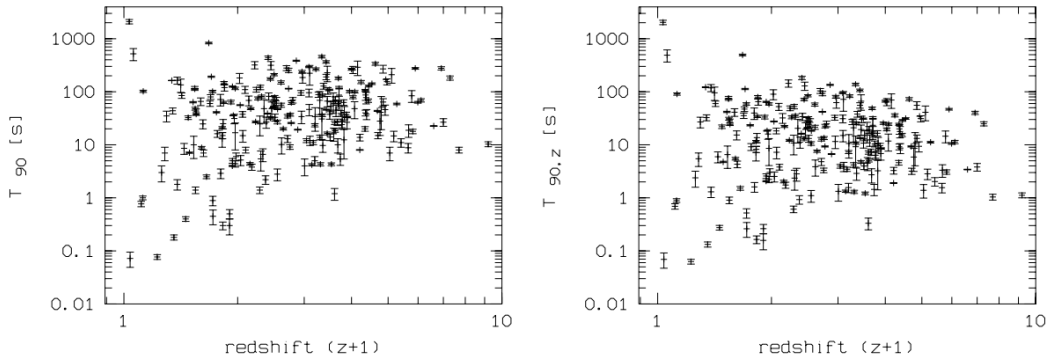


Figure 4.3.6: T_{90} in the BAT energy band in the observed (displayed in the left panel) and in the rest-frame (displayed in the right panel) versus the redshift. (Figure from Grupe et al. (2013). @ AAS. Reproduced with permission.)

In the analysis of the prompt time evolution, besides the simple relation function, Dainotti et al. (2015a) employed a more complex function. This is the same as the Equation 4.23, but with $k_{L_X,peak}$ substituted by the coefficient of the time evolution, $k_{T_{X,prompt}^*}$.

Finally, for both the simple function and the more complex one, a not significant time evolution in the prompt was retrieved ($k_{T_{X,prompt}^*} = -0.62^{+0.38}_{-0.38}$ and $k_{T_{X,prompt}^*} = -0.17^{+0.24}_{-0.27}$ respectively, see the middle and right panels of Fig. 4.3.7). It was concluded that the outcomes of the prompt time evolution for these two functions agree within 1σ .

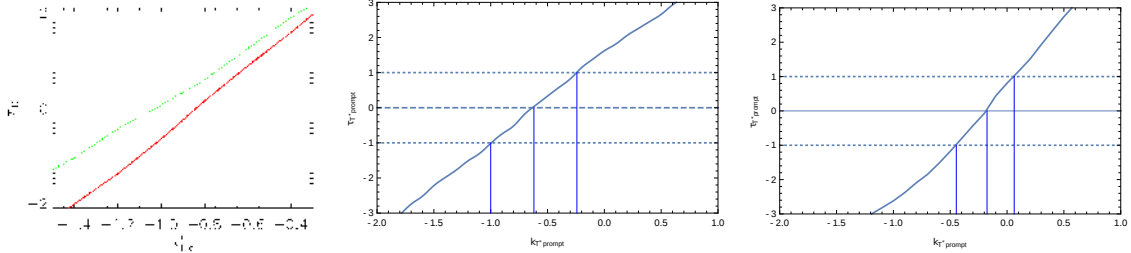


Figure 4.3.7: Left panel: the $\tau - k_{T_{X,a}}$ distribution with the complete data set indicated by a red line. The green dotted line represents 47 GRBs in common with the 77 GRB sample shown in Dainotti et al. (2011a). (Figure from Dainotti et al. (2013b). @ AAS. Reproduced with permission.) Middle panel: the $\tau - k_{T_{X,prompt}^*}$ distribution obtained through the equivalent Equation 4.22 for the time. (Figure from Dainotti et al. (2015a).) Right panel: the $\tau - k_{T_{X,prompt}^*}$ distribution computed through the equivalent Equation 4.23 for the time. (Figure from Dainotti et al. (2015a).)

4.3.3 Evaluation of the intrinsic slope

Computing the “true” slope of the correlation is the next stage to study an intrinsic correlation. Dainotti et al. (2013b) considered the EP method in the local time ($T'_{X,a}$) and luminosity ($L'_{X,a}$) space to compute b_{int} for the LT correlation, $b_{int} = -1.07^{+0.09}_{-0.14}$, at 12σ CL. This result is clearly visible from the left panel of Figure 4.3.8 (Dainotti et al., 2013b). Otherwise, in the case of no correlation it would have been resulted that $\tau = 0$ for $b_{int} = 0$ at 1σ . On the other hand, for computing b_{int} of the $\log L_{X,a} - \log L_{X,peak}$ correlation, Dainotti et al. (2015a) applied the partial correlation coefficient. The partial correlation coefficient represents the level of correlation between two quantities as a function of b_{int} given by:

$$r_{L'_{X,peak} L'_{X,a}, D_L} = \frac{r_{L'_{X,peak}, L'_{X,a}} - r_{L'_{X,peak}, D_L} * r_{L'_{X,a}, D_L}}{(1 - r_{L'_{X,peak}, D_L}^2) * (1 - r_{L'_{X,a}, D_L}^2)}, \quad (4.24)$$

where $\log L'_{X,a} = L'_{X,a}$ and $\log L'_{X,peak} = L'_{X,peak}$.

The right panel of Figure 4.3.8 pointed out that the correlation is particularly relevant when $b_{int} = 1.14^{+0.83}_{-0.32}$, which is within 1σ from the observed slope, b . Besides, in the same way as Butler et al. (2010), Dainotti et al. (2015b) mimicked a set with biases on both time and luminosity. These selection effects were similar for every monotonic efficiency function related to the detection of luminosity and time. The final aim was to display how an unknown efficiency function influences b and the density rate of GRBs. In addition, biases in slope or normalization due to truncation were examined resulting in different estimates. In this way, also the scatter of the correlation and its selection effects were investigated.

In conclusion, this work and the one by Dainotti et al. (2013b) have displayed, that the LT correlation can be corrected for selection effects and employed as redshift estimator (see Section 4.4) and cosmological tool (see Section 4.5). The partial correlation coefficient

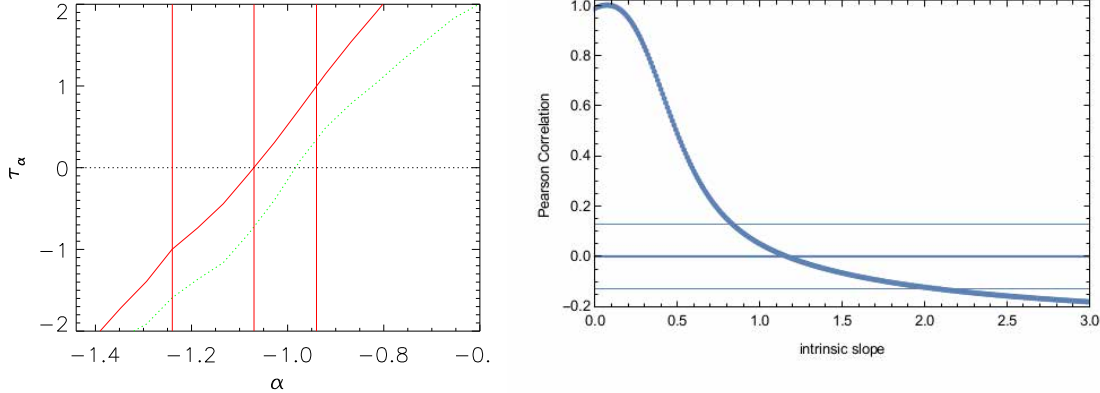


Figure 4.3.8: Left panel: the τ - b_{int} distribution. In the plot b_{int} is represented by α . (Figure from Dainotti et al. (2013b). @ AAS. Reproduced with permission.) Right panel: the Pearson correlation coefficient, r , versus b_{int} for the $\log L_{X,a} - \log L_{X,peak}$ correlation with the best fit indicated by a thick line. The 0.05% probability that the distribution of data is due by chance is represented by two thinner lines. (Figure from Dainotti et al. (2015a).)

method was also applied by D'Avanzo et al. (2012) to the $L_{X,a} - E_{\gamma,prompt}$ correlation, by Oates et al. (2015) to the $L_{O,200s} - \alpha_{O,>200s}$ correlation, and by Racusin et al. (2016) to the $L_{X,200s} - \alpha_{X,>200s}$ correlation. Their aim was to prove that these correlations are not affected by the redshift dependence.

4.3.4 Selection effects for the optical and X-ray luminosities

Here, the selection biases affecting the optical and X-ray luminosities are presented for the correlations discussed so far. Studying the optically dark afterglow phase, Nardini et al. (2008b) analysed if the observed luminosity distribution is the result of selection effects. They simulated the $\log L_{O,12}$, z , the host galaxy dust absorption, A_V^{host} , and the telescope limiting magnitude for the whole sample of 30000 GRBs to compare the observed optical luminosity distribution to the simulated one. They claimed that only GRBs with a flux greater than the detector threshold flux need to be considered. This is equivalent to a lower luminosity truncation around $\log L_{O,12} \approx 31.2$ ($\text{erg s}^{-1} \text{Hz}^{-1}$). GRBs with such a luminosity are not detected, thus constraining the luminosity function. In addition, a group of low luminosity GRBs which are at 3.6σ away from the mean of the distribution were also investigated from a statistical point of view. They yielded that if the absorption depends on the frequency, the observed luminosity distribution does not fit with any unimodal one. Nevertheless, a unimodal luminosity distribution can be recovered if the majority of GRBs are absorbed by “grey” achromatic dust. Thus, an optically subluminous sample, or a group of GRBs for which a significant achromatic absorption is detected, could explain dark bursts.

For the investigation of the biases of $L_{O,peak}$, considerations on the selection effects of

$F_{O,peak}$ observations are required. Indeed, for a typical optical afterglow ($F_{O,a} \propto T_{O,a}^{-1}$), Panaitescu and Vestrand (2008) claimed that a shallower $\log F_{O,peak} - \log T_{O,peak}$ anti-correlation than the measured one can be produced by changes in the observer offset angle. Indeed, the slope of the $\log F_{O,peak} - \log T_{O,peak}$ anti-correlation becomes steeper due to an observational selection bias. Gehrels et al. (2008) found out that Swift SGRBs are fluence-limited, while Swift LGRBs are flux-limited due to the instrument trigger.

As yielded by Nysewander et al. (2009), the absorption of photons in the host galaxy can modify the ratio $F_{O,11}/F_{X,11}$. In addition, they claimed that $F_{X,11}$ should be correct, because the LGRBs detected in the XRT energy range do not show X-ray column absorptions, unlike most of LGRBs. The presence of optical absorption (A_V) in LGRB afterglow phases suggests column densities (N_H) with lower values than those in the X-ray, while A_V are roughly one-tenth to one magnitude (Schady et al., 2007; Cenko et al., 2009). Instead, in SGRBs the optical emission relative to the X-ray one is brighter than the one expected from the standard model. Kann et al. (2010) concluded that the clustering of $L_{O,1d}$ is not significant for Swift GRBs, as claimed by Liang and Zhang (2006b) and Nardini et al. (2006). Thus, the clustering observed in pre-Swift data can be caused by the selection effects alone. Finally, Berger (2014a) pointed out that the detection of the optical afterglow phase can modify the luminosity distribution favouring regions with particularly high density medium.

4.3.5 Selection effects in the $L_{O,200s} - \alpha_{O,>200s}$ correlation

Employing the criteria from Oates et al. (2009), Oates et al. (2012) assured the possibility of retrieving high S/N light curves at early and late times from the UVOT observations. If the dimmest optical/UV afterglow phases decay more slowly than the most luminous ones, the luminosity distribution at late time is narrower and ρ of the $\log L_{O,200s} - \alpha_{O,>200s}$ correlation have to eventually be almost marginal. Given that both of these effects were found in their sample, there was the possibility that the $\log L_{O,200s} - \alpha_{O,>200s}$ correlation could be caused by chance due to the choice of the data set. Therefore, they carried out Monte Carlo simulations to check this possibility. They concluded that, up to 10^6 trials, 34 have a correlation coefficient ρ with higher value than the original one. Their result implied that at 4.2σ CL the selection criteria do not affect the $\log L_{O,200s} - \alpha_{O,>200s}$ correlation, and that this correlation is not due by chance.

4.4 Redshift Estimator

Given that the value of the redshift z for the majority of GRBs is not measured, recovering a correlation able to deduce the GRB distance from parameters independent of z would improve the knowledge of GRB features. In addition, it would provide some clues on the GRB position. For the correlations among prompt parameters some redshift estimators were

developed by Atteia (2003), Yonetoku et al. (2004), and Tsutsui et al. (2013). Their works consisted in inverting numerically the GRB luminosity correlations to recover the distance as a function of z . This procedure can be implemented also for the correlations among afterglow or prompt-afterglow parameters.

For example, Dainotti et al. (2011a) developed a redshift estimator using the LT correlation. Firstly, the best fit slope and normalization for this correlation are determined and $\log F_{X,a}$, $\log T_{X,a}$, and $\beta_{X,a}$ are instead computed. Then, a value for z can be provided from inverting the LT correlation as done for the correlations among prompt parameters by Yonetoku et al. (2004). The Equation 4.2 can be rewritten as:

$$\begin{aligned}\log L_{X,a} &= \log (4\pi F_{X,a}) + 2 \log D_L(z, \Omega_M, h) - (1 - \beta_{X,a}) \log (1 + z) \\ &= \log (4\pi F_{X,a}) + (1 + \beta_{X,a}) \log (1 + z) + 2 \log r(z) + 2 \log (c/H_0) \\ &= a \log \left(\frac{T_{X,a}}{1 + z} \right) + b\end{aligned}\quad (4.25)$$

where $r(z) = D_L(z, \Omega_M, h) \times (H_0/c)$. Putting on one side the quantities depending on z , it was retrieved:

$$(1 + \beta_{X,a} + a) \log (1 + z) + 2 \log r(z) = a \log T_{X,a} + b - \log (4\pi F_{X,a}) - 2 \log (c/H_0). \quad (4.26)$$

For solving this equation numerically, some issues need to be considered: 1) the errors in $(\log T_{X,a}, \log F_{X,a}, \beta_{X,a})$ and the coefficient (a, b) of the LT correlation affect the physical quantities themselves; 2) the errors in (a, b) are not symmetric; and 3) σ_{int} is nonlinearly added to the entire error. For further details see Dainotti et al. (2011a). The solution was applied to the E4 and the E0095 samples indicating that the LT correlation cannot be regarded as a reliable redshift estimator. Considering $\Delta z = z_{obs} - z_{est}$, with z_{obs} and z_{est} the observed and the estimated redshifts respectively, it was concluded that $\sim 20\%$ of GRBs in the E4 sample (black, $0.3 \leq \sigma_E \leq 4$, and blue, $0.095 \leq \sigma_E \leq 0.3$, GRBs in Fig. 4.4.1) recover $|\Delta z/\sigma(z_{est})| \leq 1$. Instead for the E0095 set 28% of GRBs give $|\Delta z/\sigma(z_{est})| \leq 1$ (red GRBs in Fig. 4.4.1). The number of advantageous solutions improves in the case of $|\Delta z/\sigma(z_{est})| \leq 3$. Namely, it increases at $\sim 53\%$ ($\sim 57\%$) for the E4 (E0095) set, showing that σ_E has no significant effect on the evaluation of the redshift.

σ_{int} of the LT correlation is the main cause for the redshift indicator to be not reliable. Due to the large scatter of the LT correlation, it is worth testing if larger data sets will provide improved results. With this aim, they simulated an E0095 set from a distribution analogous to the E4 one. They provided $(\log T_{X,a}, \beta_{X,a}, z)$ and chose $\log L_{X,a}$ from a Gaussian distribution with mean value given by the LT correlation and variance σ_{int} . In this way,

they retrieved $\log F_{X,a}$ and the error bars for all the quantities such that the relative errors mimicked the observations. Through Markov chains, it is demonstrated that increasing the data set is not a proper way to improve the use of the LT correlation as a redshift estimator. Indeed, in the case $\mathcal{N} \simeq 50$, the percentage of GRBs for which $|\Delta z/\sigma(z_{est})| \leq 1$ first grows to $\sim 34\%$ and then is reduced to $\sim 20\%$ for $\mathcal{N} \simeq 200$. This does not come as a surprise. In fact, a large data set provides stronger constraints on the (a, b, σ_{int}) coefficients, but not on σ_{int} . In fact, σ_{int} is the main reason for the discrepancies between z_{obs} and z_{est} .

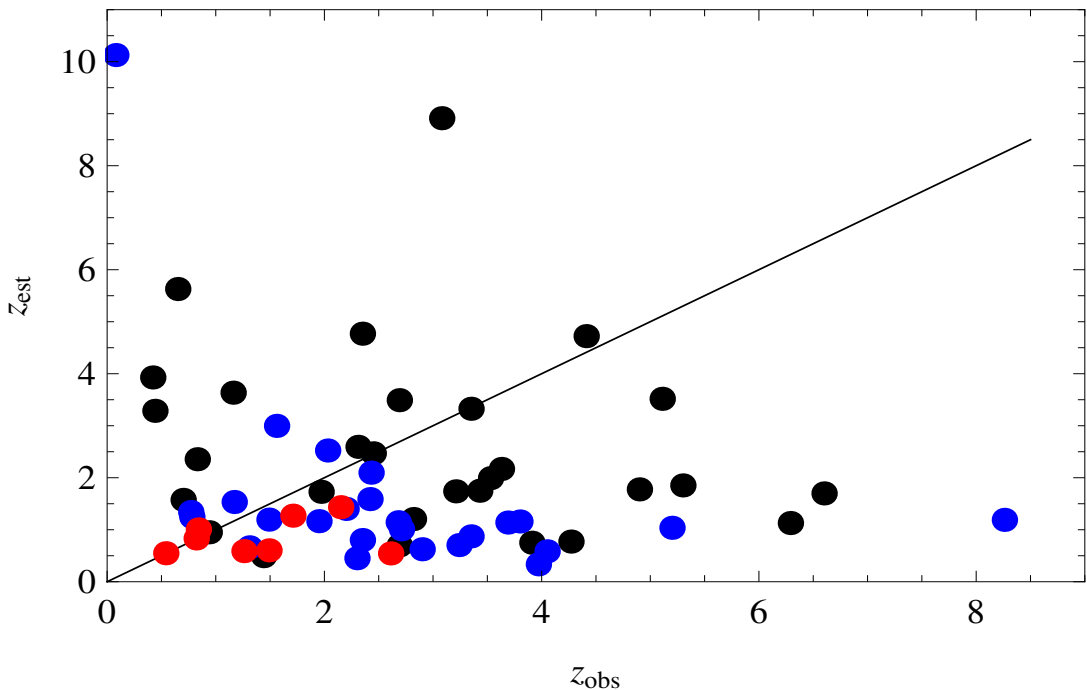


Figure 4.4.1: The z_{obs} - z_{est} correlation for the sample split in three σ_E intervals: $\sigma_E \leq 0.095$ indicated by red dots, $0.095 \leq \sigma_E \leq 0.3$ displayed by blue dots, and $0.3 \leq \sigma_E \leq 4$ shown by black dots. (Figure from Dainotti et al. (2011a). © AAS. Reproduced with permission.)

Alternatively it was observed that, assuming the best fit (a, b) quantities of the E0095 sample and fixing $\sigma_{int} = 0.10$ provides $f(|\Delta z/z_{obs}| \leq 1) \simeq 66\%$. This fact implied that the LT correlation can be applied as a redshift estimator only if the GRB set has $\sigma_{int} = 0.10 - 0.20$. Due to small number of elements in the E0095 set, it has not been yet determined when such a GRB set can be realistically gathered. Indeed, Dainotti et al. (2011a) yielded that to calibrate the LT correlation with $\sigma_{int} \sim 0.20$ and ~ 50 GRBs, ~ 600 GRBs with estimated $(\log T_{X,a}, \log F_{X,a}, \beta_{X,a}, z)$ are demanded. Nevertheless, it may be possible to discover some features of the afterglow phase which decrease σ_{int} of the LT correlation using a not so large data set. An example of this situation is represented by the extension of the LT correlation in 3D, with the so-called fundamental plane already discussed in Section 4.2.5. In conclusion, an interesting characteristic would be to correct for the biases all the parameters of the correlations introduced in previous sections to realise a more accurate redshift estimator.

4.5 Cosmology

The distribution of the distance modulus $\mu(z)$, which is the difference between the apparent (m) and the absolute (M) magnitudes, versus z of SNe Ia is named the Hubble Diagram (HD). This can be really helpful for the study of DE. It was already established in the literature that $\mu(z)$ is related to the $D_L(z, \Omega_M, h)$:

$$\mu(z) = 25 + 5 \times \log D_L(z, \Omega_M, h), \quad (4.27)$$

with $D_L(z, \Omega_M, h)$ associated with distinct DE EoS.

4.5.1 The problem of the calibration

The circularity problem is one of the main difficulties regarding the investigation of GRB correlations for cosmological purposes. The circularity problem implies that to calculate $D_L(z, \Omega_M, h)$ a cosmological model has to be assumed a priori. The main reason for this issue is that GRBs are not observed at $z < 0.01$, where there would not be any dependence on the cosmological model. Indeed, the only exception to this is GRB 980425 observed at $z = 0.0085$. To solve this problem, some solutions were proposed: a) to consider a significant sample of low z GRBs to calibrate these correlations (indeed at $z \leq 0.1$ Ω_M and Ω_Λ , for a certain H_0 between 65 and 72, do not affect $D_L(z, \Omega_M, h)$); b) to describe the observed 2D correlations taking into account a well-established theoretical model to determine their slopes and normalizations without any dependence on the cosmological model. Unfortunately, this plan seems not feasible; c) to calibrate the standard candles employing GRBs in a small redshift interval (Δz) around a particular value of the redshift, z_c . Now few ways of avoiding this circularity problem considering some correlations among prompt parameters are presented. Nevertheless, even in the case of the correlations among afterglow parameters or prompt-afterglow parameters, the circularity problem can be managed in the same way.

Liang and Zhang (2006b) outlined a new GRB luminosity indicator, dissimilar from earlier ones, given by $E_{\text{iso}} = aE_{\text{peak}}^{b_1} T_{O,a}^{b_2}$. From the analysis of this luminosity indicator it was yielded that a is dependent on the cosmological model assumed. This is not true for b_1 and b_2 until Δz is adequately small (see Fig. 4.5.1). Based on how large are the GRB sample and the errors in the observables, Δz can be selected appropriately. As claimed by Wang et al. (2011) and Wang et al. (2015), the most convenient method is to group GRBs within narrow redshift intervals centered at a particular z_c ($z_c \sim 1$ or $z_c \sim 2$, the range where the GRB z distribution has its maximum).

Employing the $\log E_{\text{peak}} - \log E_\gamma$ correlation (Ghirlanda et al., 2004b), also Ghirlanda et al. (2006) built a luminosity indicator given by $E_{\text{peak}} = a \times E_\gamma^b$. Using a data set of 19 GRBs observed by BeppoSAX and Swift they estimated the smallest amount of GRBs (N)

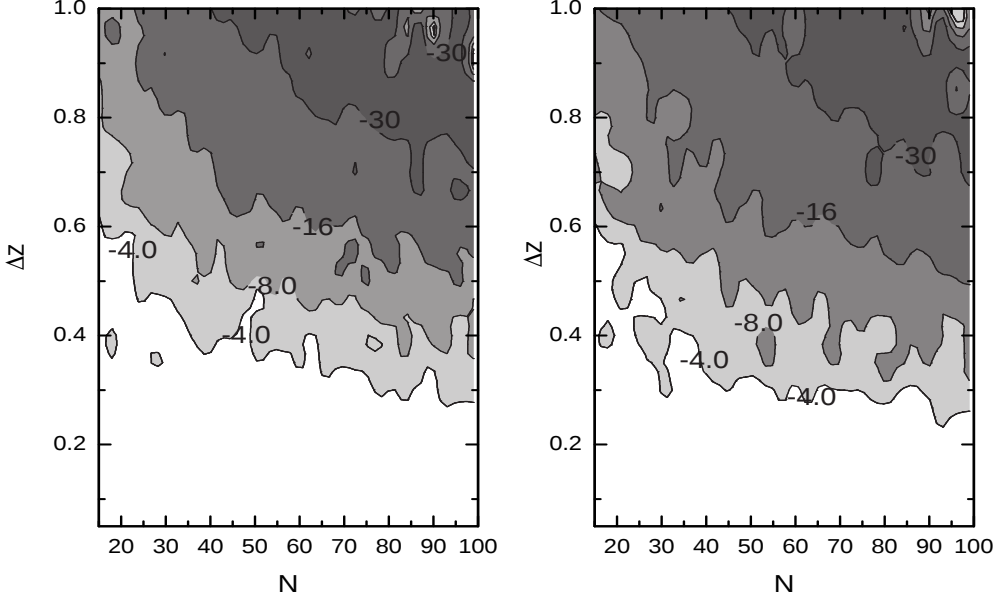


Figure 4.5.1: The $(N, \Delta z)$ space with the $\log P$ distribution. The regions where b_1 and b_2 are statistically dependent on Ω_M ($P < 10^{-4}$) are indicated by grey contours. The appropriate area for the calibration procedure is represented by the white zone. (Figure from Liang and Zhang (2006b).)

needed to calibrate the correlation. Considering N GRBs in the range Δz (distributed around z_c) they fitted the correlation for several values of Ω_M and Ω_Λ . If the slope, b , changed by less than 1% the correlation is calibrated. With N , Δz and z_c free parameters, distinct z_c and z intervals, $\Delta z \in (0.05, 0.5)$, were tested through Monte Carlo simulations. It was found that at each z the tinier the N the greater the slope variation, Δb , for equal values of Δz . The main reason for this finding is that in this case the scatter of the correlation is large. On the other hand, for higher z_c a narrower Δz is necessary to obtain tiny Δb . They pointed out that 12 GRBs with z in the range $(0.9, 1.1)$ are enough for the calibration of the $\log E_{\text{peak}} - \log E_\gamma$ correlation. At $z_c = 2$ a smaller redshift bin is required, such as z in the range $(1.95, 2.05)$. However, given that the GRB sample is not wide enough, this procedure may be not favourable.

Alternatively, it is possible to assume that $\mu(z)$ of a GRB at redshift z has the same value as that of an SN Ia at the same redshift. Thus, SNe Ia can be used as distance estimators for a calibration independent of the cosmological model assumed. In this procedure GRBs are filling the gap beyond SNe Ia, reaching very high redshift and providing an extended distance indicator. Thus, taking the value of $\mu(z)$ from the SNe Ia HD, it can be inferred also the value for GRBs at $z \leq 1.4$. Then, this value can be used to calibrate the correlations at higher z (Kodama et al., 2008; Liang et al., 2008; Wei and Zhang, 2009). $\mu(z)$ for SNe Ia is expressed by the equation:

$$\begin{aligned}\mu(z) &= 25 + (5/2)(\log y - k) \\ &= 25 + (5/2)(a + b \log x - k),\end{aligned}\quad (4.28)$$

with $y = kD_L^2(z, \Omega_M, h)$ where k is a constant independent of the redshift, and a and b are the correlation parameters. Considering this calibration independent of the redshift, the HD at higher z can be computed through the calibrated correlations.

The light curves of 8 LGRBs with associated SNe were studied by Li and Hjorth (2014), pointing out a correlation between the peak magnitude and the decay rate at 5, 10 and 15 days as observed in SNe Ia. Nevertheless, comparing it with the well known (Phillips, 1993) correlation for SNe Ia, it was concluded that the SNe associated with GRBs and SNe Ia have two distinct progenitors. In addition, this outcome gave the possibility to employ GRBs associated with SNe as plausible standard candles. Furthermore, the optical light curves of 8 LGRBs associated with SNe (7 light curves are in common with the ones used by Li and Hjorth (2014)) were analysed by Cano (2014). They pointed out a correlation between their luminosity and the width of the GRB light curves in relation to the SN 1998bw template. This finding also indicated that GRBs associated with SNe could be employed as standard candles.

4.5.2 Applications of GRB afterglow correlations

Here, the use of the LT correlation is presented for deriving cosmological parameters. Up-to-date this is the only correlation among afterglow parameters that has been employed for cosmological studies. Although, the procedure is really general and it can be applied to all the other correlations among afterglow parameters. Cardone et al. (2009, 2010) suggested the use of the afterglow phase as cosmological tool in 2009, when a new HD was obtained employing the LT correlation.

In particular, Cardone et al. (2009) added the LT correlation to the correlations analysed in Schaefer (2007). They employed a Bayesian fitting method, analogous to the one in Firmani et al. (2006) for the $\log E_{\text{peak}} - \log E_\gamma$ correlation. Then, they calibrated all the GRB correlations with a fiducial Λ CDM model in agreement with the data taken from the Wilkinson Microwave Anisotropy Probe, WMAP5. Analysing six correlations ($\log E_{\text{peak}} - \log E_\gamma$, $\log L_{\text{peak}} - \log V$, $\log L_{X,a} - \log T_{X,a}^*$, $\log L_{\text{peak}} - \log \tau_{\text{lag}}$, $\log L_{\text{iso}} - \log \tau_{RT}$, and $\log E_{\text{peak}} - \log L_{\text{iso}}$) they built a new HD including 83 GRBs (69 from Schaefer (2007) and 14 new GRBs from the LT correlation). To compute $\mu(z)$ from a data set of 307 SNe Ia with $0.015 \leq z \leq 1.55$ a local regression was applied with the purpose of avoiding the circularity problem (see Section 4.5.1). They calibrated the GRB correlations with a GRB set in the redshift range $z \leq 1.4$, the same interval of the SNe Ia sample. This procedure allows for the use of the SNe Ia set as input for the local regression of $\mu(z)$. To compute the best parameters

from the regression method shown in Cardone et al. (2009), firstly they simulated several data set. The model parameters (Ω_M, w_0, w_a, h) , with w_0 and w_a the coefficients of the DE EoS $w(z) = w_0 + w_a z(1+z)^{-1}$ (Schaefer, 2007), were chosen in the ranges $0.15 \leq \Omega_M \leq 0.45$, $-1.5 \leq w_0 \leq -0.5$, $-2.0 \leq w_a \leq 2.0$ and $0.60 \leq h \leq 0.80$. Then, they created a mock sample taking $\mu(z)$ from a normal distribution centered at the expected value with $\sigma_{int} = 0.15$, comparable with that of the SNe Ia absolute magnitude. This mock sample, with equal values of z and error distribution of the SNe Ia set, is compared with the input one. This regression procedure found reliable values of $\mu(z)$ for every cosmological model used at a given z . Afterwards, they examined the obtained HD and the one from Schaefer (2007). The Schaefer HD was investigated as follows: 1) updating the parameters of the Λ CDM model, 2) applying a Bayesian fitting method, and 3) summing to the other correlations the LT one also. To check the results of this analysis, the set of 69 GRBs used by Schaefer (2007) was also employed, and without taking into account the LT correlation the distance moduli were calculated through the new calibration. As a result, the ratio of the new to old $\mu(z)$ is around 1 within 5%. They concluded that the new procedure did not changed the outcomes in a significant way. Finally, they retrieved that the values of $\mu(z)$ for each of the GRBs in both Schaefer (2007) and Dainotti et al. (2008) data sets are in agreement with those calculated in Schaefer (2007). For this reason, adding the LT correlation does not imply further systematic effects. Additionally, they found that employing the LT correlation also broadens the sample from 69 to 83 GRBs and reduces the errors in $\mu(z)$ by $\sim 14\%$.

Later, Cardone et al. (2010) employed the LT correlation alone or together with additional cosmological tools to put some limits on the cosmological parameters at large z . They separated the sample of 66 LGRBs in E0095 and E4 data sets. The outcomes pointed out that the LT correlation constrains the cosmological parameters in agreement with earlier results. Indeed, the redshift domain of this current HD was broader: $(0.033, 8.2)$. As a further step, applying the Λ CDM, the CPL (Chevallier and Polarski, 2001) and the quintessence (QCDM) models, they concluded that the Λ CDM model is favoured. Then, the fit was reiterated with only SNe Ia and BAO, without GRBs, to investigate the influence of GRBs in the analysis. It was recovered that GRBs do not improve the estimation of the parameters, but they set the boundaries on w_a to 0. Therefore, a large set of E0095 GRBs could produce a constant DE EoS model. Unlike previous works, the HD for the E4 set is the only one obtained through a correlation between afterglow parameters with a statistically relevant subsample. Given the results obtained with the LT correlation alone, Cardone et al. (2010) suggested that it is not necessary to sum to the LT correlation other correlations to increase the GRB sample size with computed $\mu(z)$. This is important because biases and σ_{int} are present in each correlation, and employing all the correlations together in the HD can influence the estimation of the cosmological parameters. In conclusion, Cardone et al. (2010) pointed out that employing E0095 GRBs only, σ_{int} of the LT correlation will be severely reduced. While, using the whole set of 66 LGRBs, values of Ω_M and H_0 in agreement with those available in the literature are found. Therefore, using the LT correlation for the

GRB HD does not add any bias in the investigation of the cosmological quantities. Similar outcomes were obtained using E0095 GRBs only, even if they are only the 12% of the data set. Additional analysis of the E0095 sample can lead to regard them as a standard set for investigating DE.

Following, Dainotti et al. (2013a) investigated how much the cosmological studies are affected by a variation of 5σ (upwards and downwards) of the LT correlation slope, b , from its intrinsic value $b_{int} = -1.07^{+0.09}_{-0.14}$. They simulated through a Monte Carlo procedure a set of 101 GRBs with $b = -1.52$, $\sigma_{int} = 0.93$ (a wider value than the $\sigma_{int} = 0.66$ from the initial sample), and a Λ CDM model with $\Omega_M = 0.291$ and $H_0 = 71 \text{ Km s}^{-1} \text{ Mpc}^{-1}$. Then, they examined the behaviour of the scatter in the cosmological parameters for the total sample (hereafter Full) and a subgroup of bright GRBs with $\log L_{X,a} \geq 48.7$ (hereafter High Luminosity). This cut at a precise value of the luminosity was provided by Dainotti et al. (2013b), who claimed that the observed luminosity for $\log L_{X,a} \geq 48$ is in agreement with the local luminosity function. Resembling the same approach employed by Amati et al. (2008) for the $\log E_{\text{peak}} - \log E_{\text{iso}}$ correlation, they fit the correlation changing both the calibration parameters, $p_{GRB} = (a, b, \sigma_{int})$, and the cosmological parameters, $p_c = (\Omega_M, \Omega_\Lambda, w_0, w_a, h)$, for each model. In addition to GRBs, two samples of other cosmological probes were inserted in the data set to obtain tighter boundaries on the cosmological parameters. The first was the $H(z)$ sample ($H(z) = H_0 \times \sqrt{\Omega_M(1+z)^3 + \Omega_k(1+z)^2 + \Omega_\Lambda}$) in the interval $0.10 \leq z \leq 1.75$ (Stern et al., 2010) and the second was Union 2.1 SNe Ia set composed of 580 objects in the interval $0.015 \leq z \leq 1.414$ (Suzuki et al., 2012). Then, applying a Markov Chain Monte Carlo (MCMC) and the Gelman-Rubin test², they tested the convergence for a cosmological model defined by particular parameters p_c to be constrained. For the Full GRB sample b , a and σ_{int} of the LT correlation were independent of the cosmological model and the addition to the GRB set of the SNe Ia and $H(z)$ data. Although a 5σ scatter in b_{int} is considered, these outcomes for the Full sample were compatible with previous results (Dainotti et al., 2008, 2011a), where flat models only were analysed. However, the simulated data were affected by wide errors, thus hiding the cosmological variables in the calibration. The cosmological quantities would show up only using a wider sample with low uncertainties in $(\log T_{X,a}^*, \log L_{X,a})$. In addition, to complete the study of the Full sample, a model described by the present day values of Ω_M , Ω_Λ , and H_0 was used. It was employed to investigate the consequences of the deviation of b from b_{int} on the estimation of the cosmological quantities.

Even if H_0 was compatible with the results from both the local distance estimators (Riess et al., 2009) and CMBR data (Komatsu et al., 2011), the median Ω_M and Ω_Λ were wider than those obtained by Davis et al. (2007) ($\Omega_M \sim 0.27$). Therefore, analysing the Full sample, a different b_{int} implied a discrepancy of 13% from the best Ω_M (see the upper panels of Fig.

²This test is based on parallel chains of simulations to validate their convergence to an equal posterior distribution.

[4.5.2](#)). Although the fit of the set with SNe Ia and $H(z)$ data did not indicate flat models, a flat universe was comparable with the WMAP7 cosmological parameters within 95%, retrieving $\Omega_k = -0.080_{-0.093}^{+0.071}$. Nevertheless, in this case flat and not flat models were not distinguishable, even if SNe data were also taken into account. For this reason, a flat model, but with the DE EoS modelled by $w(z)$, led to distinct (w_0, w_a) , regardless of the presence of SNe Ia and $H(z)$ samples in the analysed data set. Instead, for the High Luminosity sample, the evaluation of the calibration parameters was not influenced by the cosmological model or whether SNe Ia and $H(z)$ data are added to the set. Indeed, for the High Luminosity sample the addition of SNe Ia and $H(z)$ data did not lead to an improvement in the estimation of the calibration parameters. In conclusion, the results for the Full sample were compatible with those of the flat cosmology for SNe Ia. Instead, for the High Luminosity sample the estimation of H_0 differed by 5% from the one computed by Petersen et al. (2010), and the scatter in Ω_M was underestimated by 13% (see the bottom panels of Fig. [4.5.2](#)). They concluded that the best method for this analysis would be to employ a High luminosity sample with cut at $\log L_{X,a} = 48$ to avoid the addition of the luminosity and time evolutions to the cosmological parameters estimation.

In addition, Postnikov et al. (2014) examined the DE EoS as a function of z without postulating any a priori $w(z)$ EoS. In this analysis, 580 SNe Ia taken from the Union 2.1 compendium (Suzuki et al., 2012) were employed together with 54 LGRBs in the overlapping redshift area ($z \leq 1.4$, see the left panel of Fig. [4.5.3](#)) to obtain a GRB HD. A standard $w = -1$ cosmological model was also considered.

In this work the correlation coefficients of the LT correlation are derived in the range of redshift overlapping with the one of SNe Ia. In this range the LT correlation reads as follows:

$$\log L_{X,a} = 53.27_{-0.48}^{+0.54} - 1.51_{-0.27}^{+0.26} \times \log T_{X,a}^*, \quad (4.29)$$

with $\rho = -0.74$ and $P = 10^{-18}$. Due to the use of the LT correlation, the redshift range was extended one order of magnitude up to $z = 8.2$. Postnikov et al. (2014) applied a Bayesian statistical analysis, like in Firmani et al. (2006) and Cardone et al. (2010). In this analysis the hypothesis is connected with a $w(z)$ function depending on H_0 and the present DE density parameter, $\Omega_{\Lambda 0}$. They assumed isotropy for the cosmological model, secure limits on the EoS, and a firm value for $w(z)$ in the $z \leq 0.01$ range. Furthermore, they employed many random $w(z)$ models. To check their analysis, they simulated samples retrieved through distinct input cosmological models with errors and z values equivalent to the real data sets. Employing the LT correlation, a set of Swift GRBs with z from 0.033 to 9.4 (see inset in the right panel of Fig. [4.5.3](#)) was employed to examine the history of the universe up to $z \approx 10$. Further analysis would be helpful if the GRB at photometric redshift $z = 9.4$ would be removed from the data set. In fact, in the sample of canonical GRBs considered by Cardone et al. (2010) this GRB is not present. They simulated 2000 constant EoSs between

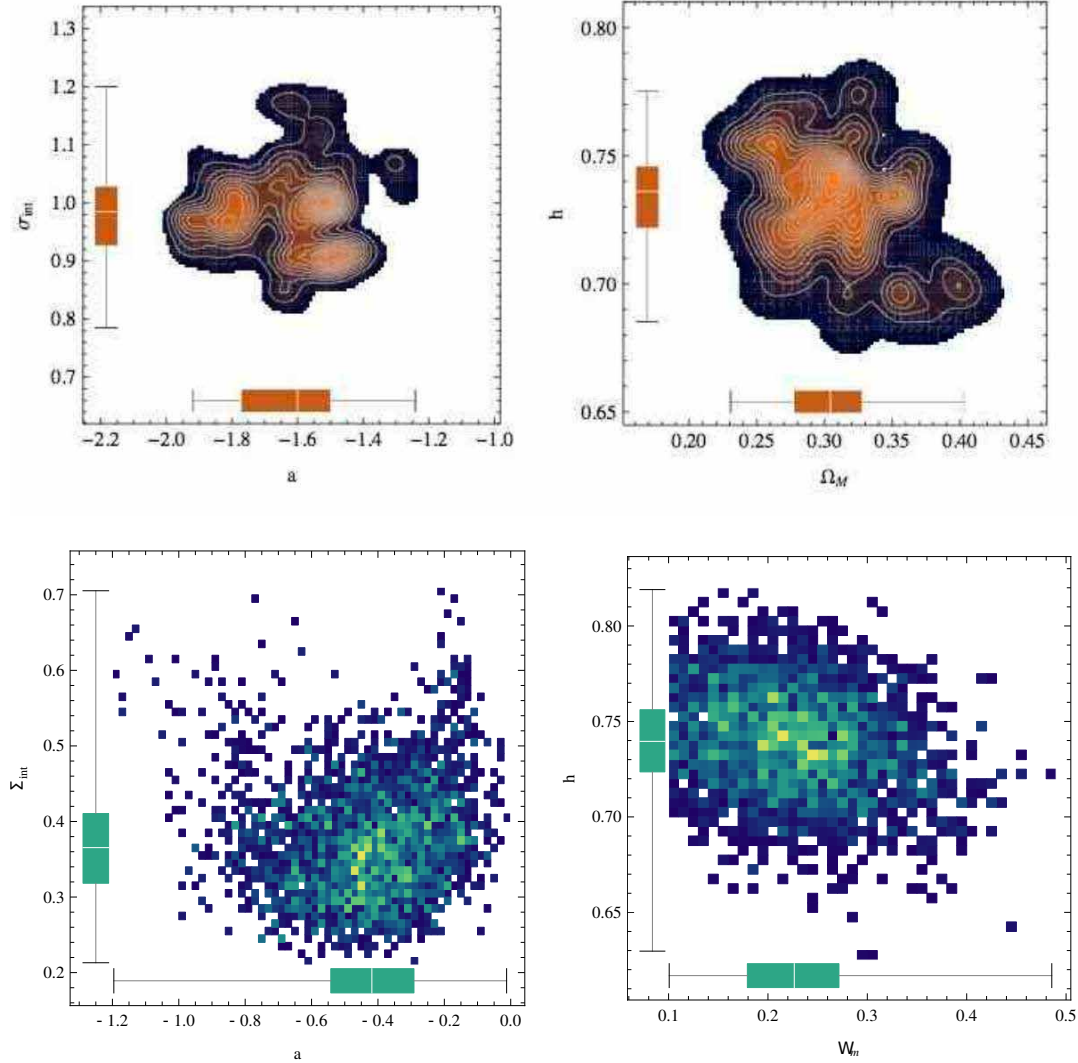


Figure 4.5.2: In all these panels b is labelled a . Upper left panel: confidence contours of the likelihood function $\mathcal{L}(b, \sigma_{int})$ for the Full data set. The 1σ (full zone) and 2σ (bright grey) regions of confidence are represented in bright brown regions. The box-and-whisker diagrams relatively to the b and σ_{int} parameters are presented on the axes. The 25th, 75th and 50th percentile are the bottom and top of the diagrams, and the band near the middle of the box, respectively. (Figure from Dainotti et al. (2013a).) Upper right panel: confidence contours of the likelihood function $\mathcal{L}(\Omega_M, h)$ for the Full data set. The explanation of this panel is the same as that of the left one. (Figure from Dainotti et al. (2013a).) Bottom left panel: confidence contours of the likelihood function $\mathcal{L}(b, \sigma_{int})$ for the High Luminosity data set. The 1σ (full zone) and 2σ (bright green) regions of confidence are represented in bright blue regions. The box-and-whisker diagrams relatively to the b and σ_{int} parameters are presented on the axes. The 25th, 75th and 50th percentile are the bottom and top of the diagrams, and the band near the middle of the box, respectively. (Figure from Dainotti et al. (2013a).) Bottom right panel: confidence contours of the likelihood function $\mathcal{L}(\Omega_M, h)$ for the High Luminosity data set. The explanation of this panel is the same as that of the left one. (Figure from Dainotti et al. (2013a).)

$-4 \leq w_\Lambda \leq 2$. For the SNe Ia sample, an exact solution was retrieved. It was comparable with the cosmological constant, $w = -0.99 \pm 0.2$ (see the right panel of Fig. 4.5.3). Although the BAO boundaries provided a solution similar to the one of the EoS for the SNe Ia sample, however it was found that the confidence interval is reduced dramatically ($w = -0.99 \pm 0.06$). Indeed, the confidence region of the solutions is relevantly constrained by BAO data. This is particularly true for $\Omega_{\Lambda 0}$, which is estimated to be $\Omega_{\Lambda 0} = 0.723 \pm 0.025$. Then, $w(z)$, which provides the best evaluation of $D_L(z, \Omega_M, h)$, z of the SNe Ia set, and BAO constraints, has to be chosen.

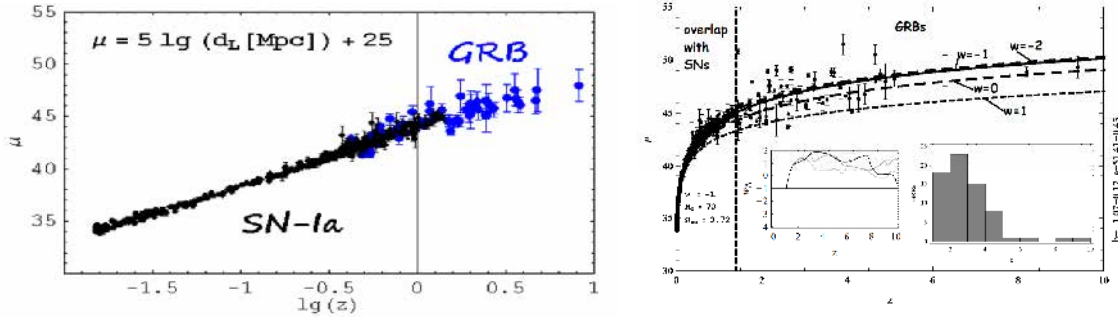


Figure 4.5.3: Left panel: HD for SNe Ia taken from the Union 2.1 compendium (Suzuki et al., 2012). GRBs are retrieved through the LT correlation and considering a flat $w = -1$ cosmology. Due to the significant errors in GRBs data, the HD appears with no gap and compatible with the $w = -1$ model. (Figure from Postnikov et al. (2014). © AAS. Reproduced with permission.) Right panel: HD for SNe Ia and GRBs together. GRBs in the SNe Ia overlapping region are employed to compute the intrinsic correlation coefficient. Furthermore, this correlation is applied to compute $D_L(z, \Omega_M, h)$ for high z GRBs. For comparison constant w solutions are presented. The farthest SN Ia is indicated by a vertical dashed line. The inset panel on the left side presents the most plausible EoS with a few tested models. Due to the extended confidence intervals, from this analysis only substantial modifications of $w = -1$ can be ruled out. The inset panel on the right side displays the GRB z distribution. (Figure from Postnikov et al. (2014). © AAS. Reproduced with permission.)

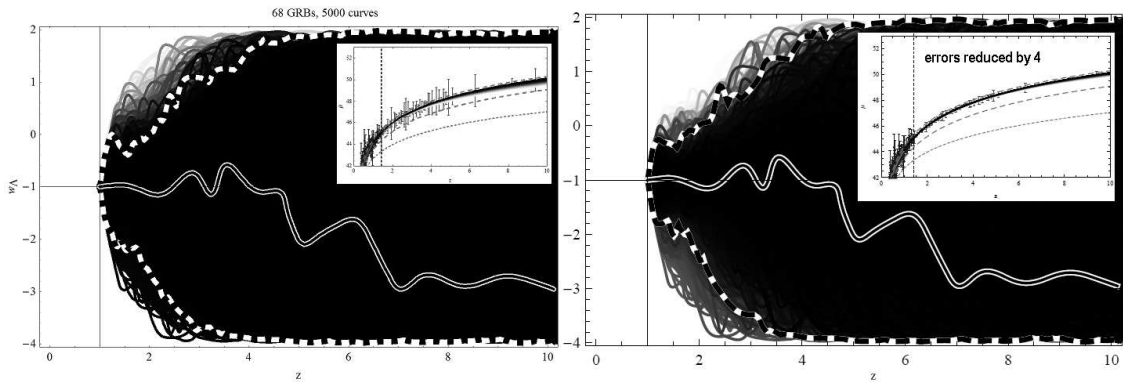


Figure 4.5.4: Left panel: a bunch of $w(z > 1)$ solutions computed through synthetic GRB data sets obtained for $w(z) = -1$. These solutions indicated how much the errors in GRBs bound $z > 1$ EoS. The considered GRB errors are from real data. Right panel: the same explanation as that of the left panel, but the assumed GRB errors are reduced by a factor 4. (Figure from Postnikov et al. (2014). © AAS. Reproduced with permission.)

Besides the extension of one order of magnitude in the redshift domain, GRB data should also reduce the degeneracy of the values of the cosmological parameters. Bounding the

high z $w(z)$ EoS was not straightforward, due to the small amount of data and the errors in these variables. In the left panel of Figure 4.5.4 a simulated GRB data set is displayed with z distribution and errors analogous to those for real data, but with an assumption of $w = -1$. It has been shown that strong $w(z)$ fluctuations alone are not possible. Then, more interesting high z DE limits were recovered reducing the uncertainties by 4 (see the right panel of Fig. 4.5.4). From the few GRB data, 54, in the SNe Ia overlapping region it was suggested that wide errors in the GRB correlation coefficients are present. Although, a shallow probability distribution (indicated by the dark area in the left panel of Fig. 4.5.4) was retrieved from the wide errors in high z GRBs for many EoSs analysed. For this reason, the $1 < z < 4$ region of the GRB HD would be really intriguing as soon as the GRB data set will be broad enough and the quality of data improved.

CHAPTER 5

Selection Effects in Gamma Ray Burst Correlations: Consequences on the Ratio between Gamma Ray Burst and Star Formation Rates

5.1 Preface

As shown in Section 4.3, selection effects are important issues for the study of GRB correlations, therefore they have to be analysed carefully to obtain reliable results. In the work presented in this Chapter the selection biases affecting the luminosity and time measurements are investigated. In particular, the detector efficiency functions are analysed to simulate data samples, to check how the correlation between luminosity and time varies. The results from this analysis confirmed within 1σ those from the literature. In addition, due to the fact that GRBs and further galaxies are tracers of remote epochs, their formation rates are compared using different SFR models. The evolution of the redshift-dependent ratio of SFR to GFR is found in agreement with Swift observations.

The following Chapter of the thesis is based on the article Dainotti, Del Vecchio, Nagataki & Capozziello, ApJ, Volume 800, 30, (2015). In this work led by Dr. M.G. Dainotti, the thesis author was involved in evaluation of the probability density distributions, and in deriving the efficiency functions and probabilities related to those efficiency functions. She also elaborated the relative plots and tables.

5.2 Main Analysis

The aim of this work was to study the selection effects due to the Swift detector's characteristics without knowing its efficiency. Although, this analysis can be extended to other detectors.

Because GRBs at high redshift and galaxies with star forming regions keep track of the important reionization era, the GFR and the SFR are compared. The LT correlation can be written in the following way:

$$\lambda = \alpha_0 + \alpha_\tau \tau + \alpha_\zeta \zeta, \quad (5.1)$$

where α_0 and α_τ are the normalization and the slope of the LT correlation respectively, $\lambda = \log L_{X,a}$, $\tau = \log T_{X,a}/(1+z)$, and $\zeta = \log(1+z)$. Furthermore, the GFR can be modelled by:

$$\frac{d\mathcal{N}}{d\lambda dz} \propto \Psi(z) \frac{\dot{\rho}_*(z)}{1+z} \frac{dV}{dz} \frac{\mathcal{F}_{\tau_U} - \mathcal{F}_{\tau_L}}{\sqrt{8\pi\sigma_\tau^2}} \exp\left(-\frac{1}{2} \left[\frac{\lambda - (\alpha_0 + \alpha_\tau \tau + \alpha_\zeta \zeta)}{\sqrt{\sigma_{int}^2}} \right]^2\right), \quad (5.2)$$

where $\Psi(z)$ is the factor denoting the redshift evolution, $\dot{\rho}_*(z)$ is the SFR, V is the volume, σ_{int} is the intrinsic scatter, and \mathcal{F}_{τ_U} and \mathcal{F}_{τ_L} represent the error functions of the lower and upper limits of the time distribution. It is shown that the SFR obtained by Li (2008) (see Fig. 5.2.1) describes the sample better than the models by Robertson and Ellis (2012) and Kistler et al. (2013), and it is given by

$$\dot{\rho}_*(z) = a + b \times \log(1+z), \quad (5.3)$$

where the parameters a and b are given as:

$$(a, b) = \begin{cases} (-1.70, 3.30) & z \leq 0.993, \\ (-0.727, 0.0549) & 0.993 \leq z \leq 3.80, \\ (2.35, -4.46) & z \geq 3.80. \end{cases} \quad (5.4)$$

In this case, to consider the efficiency of the detector, Equation 5.2 can be more precisely written as:

$$\frac{d\mathcal{N}_{obs}}{d\lambda dz} \propto \frac{d\mathcal{N}}{d\lambda dz} \times \mathcal{E}_\lambda(\lambda) \times \mathcal{E}_\tau(\tau), \quad (5.5)$$

where $\mathcal{E}_\lambda(\lambda)$ and $\mathcal{E}_\tau(\tau)$ are the efficiency functions for the luminosity and time measurements, respectively (see Fig. 5.2.2). Different efficiency functions for the luminosity measurements are considered with either a linear functional form:

$$\mathcal{E}_\lambda(\lambda) = \begin{cases} 0 & \lambda < \lambda_L, \\ \left(\frac{\lambda - \lambda_L}{\lambda_U - \lambda_L}\right)^{\mathcal{E}_\lambda} & \lambda_L \leq \lambda \leq \lambda_U, \\ 1 & \lambda > \lambda_U \end{cases} \quad (5.6)$$

or a polynomial one:

$$\mathcal{E}_\lambda(\lambda) = \begin{cases} 0 & \lambda < \lambda_L , \\ \frac{\mathcal{E}_1\tilde{\lambda} + \mathcal{E}_2\tilde{\lambda}^2 + \mathcal{E}_3\tilde{\lambda}^3 + \mathcal{E}_4\tilde{\lambda}^4}{\mathcal{E}_1 + \mathcal{E}_2 + \mathcal{E}_3 + \mathcal{E}_4} & \lambda_L \leq \lambda \leq \lambda_U , \\ 1 & \lambda > \lambda_U \end{cases} \quad (5.7)$$

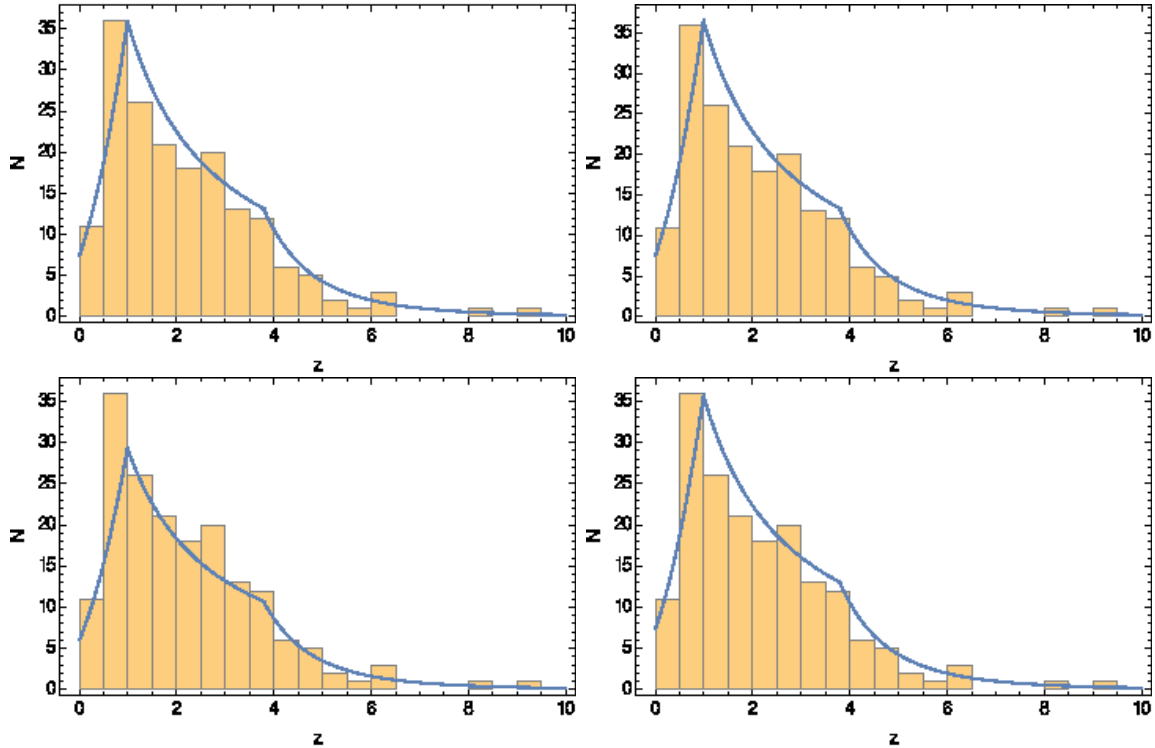


Figure 5.2.1: GRBs rate density using the method by Li (2008) and the observed GRBs rate density obtained by the linear efficiency functions (upper panel), and the polynomial efficiency function (lower panel) with the redshifts distribution of the data sample. The two linear efficiency functions used for the observed GRBs rate density in the upper panel have probability to fit the data $\leq 10^{-4}$ and 0.001, while the polynomial efficiency functions used for the observed GRBs rate density in the bottom panel have probability: $\leq 10^{-4}$ and 0.001. (Figure from Dainotti, Del Vecchio, Nagataki, and Capozziello (2015b).)

where λ_U and λ_L are the upper and lower limits of the luminosity distribution. The same formulae are valid for the time measurements. Dividing the original sample of 176 GRBs detected by Swift in 5 and 12 bins and assuming a redshift evolution, it is found that $\alpha_0 = -0.22z + 52.31$ for the linear case, while for the polynomial case $\alpha_0 = 55.87 - 8.13z + 5.53z^2 - 1.48z^3 + 0.13z^4$. Regarding α_τ , it is found that $\alpha_\tau = 0.10z - 1.38$ for the linear case, and $\alpha_\tau = 2.35 + 2.13z - 1.39z^2 + 0.37z^3 - 0.03z^4$ for the polynomial case. These results showed that both linear and fourth-polynomial models are good choices for fitting the redshift evolution of the parameters.

Assuming as a first simple case no cuts on the time measurements ($\mathcal{E}_\tau(\tau) = 1$), for each $(\alpha_0, \alpha_\tau, \sigma_{\text{int}})$ input parameters, new truncated (λ, τ) data samples are simulated using the different efficiency functions for the luminosity measurements. Then, these samples are used to calculate the best fit slope (α_τ) and normalization (α_0) of the LT correlation for each

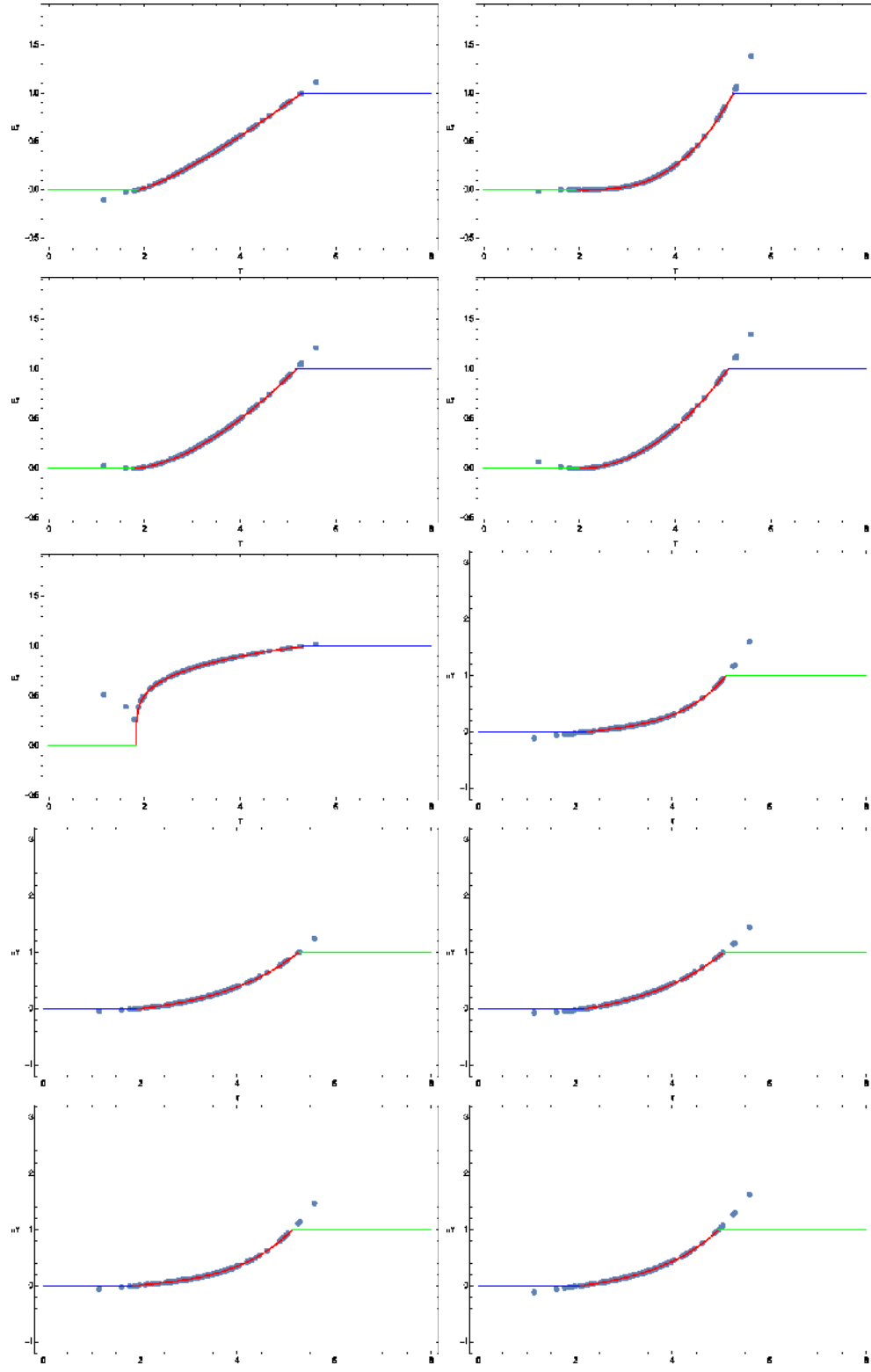


Figure 5.2.2: The first 5 panels (starting from the upper left one and going from the left to the right columns) represent examples of the efficiency function for the linear case versus the times, τ , of the GRBs in the data sample, while the last 5 panels the efficiency functions for the fourth order polynomial. The linear functions as well as the polynomial ones are computed according to Equation 5.6 and Equation 5.7. (Figure from Dainotti, Del Vecchio, Nagataki, and Capozziello (2015b).)

(λ, τ) simulated sample. From these correlation parameters, the discrepancies between the input and the best fit parameters are estimated. To calculate these differences between the observed and the best fit quantities the following formula is used:

$$\frac{\Delta x}{x} = \frac{x_{bf} - x_{inp}}{x_{inp}} = 1 - a - \frac{b}{x_{inp}}, \quad (5.8)$$

where x_{inp} is the input value of the parameter for the simulated (λ, τ) sample, while x_{bf} is the best fit value of the parameter obtained from the fit of the simulated (λ, τ) sample (see Tables 5.1 and 5.2). Finally, the case of cuts on the time measurements is also considered, and similar results are found.

5.3 Results

In most of the cases where only cuts on the luminosity measurements are considered the discrepancies between the input values and the best fit ones, given by Equation 5.8, are smaller than 0.006, and only few cases for the polynomial efficiency function give discrepancies larger than 0.006. Therefore, no significant differences are pointed out between the results from the two forms of the efficiency functions (see Tables 5.1 and 5.2). Instead, considering cuts on both luminosity and time measurements, the number of cases in which the discrepancy is greater than 0.006 is four times larger, meaning that the biases can be more relevant. Nevertheless, from this analysis the correlation coefficients of the intrinsic LT correlation by Dainotti et al. (2013b) are confirmed.

Using the simulated sample, the SFR from Li (2008), and the redshift-dependent ratio of the SFR to the GFR by Robertson and Ellis (2012) ($\Psi(z) = (1+z)^\alpha$), a weak evolution (-0.2 < α < 0.5) is found in agreement with the observations of a Swift plateau phase for $0.99 < z < 9.4$. This finding confirmed those by Robertson and Ellis (2012).

Id	$(a, b)_{bf}^\tau$	$(a, b)_{fit}^\tau$	$(a, b)_{bf}^{\alpha_0}$	$(a, b)_{fit}^{\alpha_0}$	$(a, b)_{bf}^\sigma$	$(a, b)_{fit}^\sigma$	$\frac{\Delta_x}{x}$
PL1	(0.953,0.010)	(0.959,0.013)	(0.928,3.688)	(1.000,-0.073)	(0.593,0.354)	(0.616,0.355)	0.004
PL2	(0.914,-0.008)	(0.873,-0.024)	(1.013,-0.836)	(0.989,0.292)	(0.689,0.299)	(0.643,0.341)	0.002
PL3	(0.880,-0.052)	(0.937,-0.013)	(0.965,1.729)	(1.008,-0.513)	(0.683,0.340)	(0.664,0.352)	0.003
PL4	(0.946,0.024)	(0.964,0.024)	(0.995,-0.076)	(1.086,-4.905)	(0.614,0.364)	(0.585,0.380)	0.006
PL5	(0.916,-0.030)	(0.962,0.004)	(1.033,-2.067)	(0.828,9.095)	(0.716,0.333)	(0.679,0.356)	0.005

Table 5.1: Slope a and zero point b of the fitted vs. input parameters for both the best fit and median values (labelled with subscripts bf and fit , respectively). The superscript denotes the parameter fitted with (τ, α_0, σ) referring to $(\alpha_\tau, \alpha_0, \sigma_{int})$, respectively. $\frac{\Delta_x}{x}$ is the bias for each efficiency function considered. (Table from Dainotti, Del Vecchio, Nagataki, and Capozziello (2015b).)

Id	$(a, b)_{bf}^{\tau}$	$(a, b)_{fit}^{\tau}$	$(a, b)_{bf}^{\alpha_0}$	$(a, b)_{fit}^{\alpha_0}$	$(a, b)_{bf}^{\sigma}$	$(a, b)_{fit}^{\sigma}$	$\frac{\Delta_x}{x}$
PoL1	(0.950,0.020)	(0.928,0.011)	(1.099,-5.545)	(1.178,-9.935)	(0.647,0.350)	(0.673,0.349)	0.004
PoL2	(1.095,0.128)	(1.075,0.105)	(1.030,-1.662)	(1.023,-1.278)	(0.681,0.337)	(0.625,0.372)	0.0008
PoL3	(0.984,0.063)	(0.936,0.015)	(0.711,15.258)	(0.988,0.376)	(0.741,0.289)	(0.685,0.336)	0.007
PoL4	(0.870,-0.025)	(0.969,0.052)	(0.730,14.103)	(0.734,13.872)	(0.630,0.351)	(0.582,0.381)	0.009
PoL5	(1.004,0.069)	(0.972,0.030)	(0.963,11.772)	(1.002,-0.374)	(0.581,0.384)	(0.549,0.402)	0.18

Table 5.2: Same as Table 5.1 but for the polynomial \mathcal{E}_λ model. (Table from Dainotti, Del Vecchio, Nagataki, and Capozziello (2015b).)

CHAPTER 6

Study of the decaying part of the X-ray afterglow

6.1 Preface

In this Chapter, the analysis of the GRB afterglow phase is focused on the investigation of the light curve temporal decay parameter $\alpha_{X,a}$. This quantity is considered to carry information about GRB interaction with the external medium during the afterglow phase.

In the work presented below $\alpha_{X,a}$ and its correlation with $L_{X,a}$ are investigated, as different structures of the GRB external medium can lead to various values of $\alpha_{X,a}$ in the afterglow light curve. Therefore, this study is intended to reveal eventual correlations between the GRB afterglow parameters and the ambient medium created in the GRB pre-explosion phase.

As a result of the analysis, following the work presented by Phillips (1993) for SNe Ia¹, a correlation between $\alpha_{X,a}$ and $\log(L_{X,a}/L_{\text{LT}})$ was discovered, and it is used to propose a model for correcting GRB luminosity and improve the LT correlation. This is a small step towards the GRB standardization.

The following Chapter of the thesis is quoted from the article Del Vecchio, Dainotti & Ostrowski, ApJ, Volume 828, 36, (2016). In this paper, the thesis author was the leading author. She performed all presented analyses and prepared a first draft of the paper. She was also co-editing it after discussions with the co-authors and the referee reviewing the paper for the journal.

¹Who presented a correlation between the maximum brightness of SNe Ia and their light curve decay rate in the optical B band after 15 days. This correlation, known as Phillips correlation, became very important for using SNe Ia as cosmological standard candles.

Abstract

In this work we study the distribution of temporal power-law decay indices, $\alpha_{X,a}$, in the Gamma Ray Burst (GRB) afterglow phase, fitted for 176 GRBs (139 long GRBs, 12 short GRBs *with extended emission* and 25 X-ray Flashes (XRFs)) with known redshifts. These indices are compared with the temporal decay index, α_W , derived with the light curve fitting using the W07 model. This model fitting yields similar distributions of α_W to the fitted $\alpha_{X,a}$, but for individual bursts a difference can be significant. Analysis of $(\alpha_{X,a}, L_{X,a})$ distribution, where $L_{X,a}$ is the characteristic luminosity at the end of the plateau, reveals only a weak correlation of these quantities. However, we discovered a significant regular trend when studying GRB $\alpha_{X,a}$ values along the Dainotti et al. (2008) correlation between $L_{X,a}$ and the end time of the plateau emission in the rest-frame, $T_{X,a}^*$, hereafter LT correlation. We note a systematic variation of the $\alpha_{X,a}$ parameter distribution with luminosity for any selected $T_{X,a}^*$. We analyse this systematics with respect to the fitted LT correlation line, expecting that the presented trend may allow to constrain the GRB physical models. We also attempted to use the derived correlation of $\alpha_{X,a}(T_{X,a})$ versus $L_{X,a}(T_{X,a})$ to diminish the luminosity scatter related to the variations of $\alpha_{X,a}$ along the LT distribution, a step forward in the effort of standardizing GRBs. A proposed toy model accounting for this systematics applied to the analysed GRB distribution results in a slight increase of the LT correlation coefficient.

6.2 Introduction

Gamma Ray Bursts (GRBs) with their powerful emission processes are observed up to high redshifts, $z > 9$ (Cucchiara et al., 2011). A significant progress in studying GRB observations has been the advent of Swift satellite (Gehrels et al., 2004), which has revealed a more complex behaviour of the light curves (O'Brien et al., 2006; Nousek et al., 2006; Zhang et al., 2006a; Sakamoto et al., 2007) than in the past. There are several emission models proposed in the literature providing predictions for characteristic GRB light curve features. Well known is the model of Mészáros (1998); Mészáros and Rees (1999); Mészáros (2006), consisting of jet internal shocks generating the GRB prompt phase emission and external shocks of the GRB expanding fireball generating the afterglow emission.

In the present paper we study distributions of the GRB afterglow parameters versus light curve temporal decay indices $\alpha_{X,a}$, for the power-law decay observed in the afterglow phase, with the X-ray luminosity $L_{X,a}$. We analyse an extended sample of 176 GRBs with known redshifts observed by Swift from January 2005 to July 2014. In the presented analysis we use the LT correlation (Dainotti et al., 2008), updated in Dainotti et al. (2010, 2011a, 2013b, 2015b), between the derived characteristic afterglow plateau luminosity, $L_{X,a}$, and time, $T_{X,a}^*$ (an index * indicates the GRB rest-frame quantity). An attempt to study similar afterglow properties was presented by Gendre et al. (2008). They analysed the “late” light

curve properties at the time of 1 day after the burst to reveal existence of grouping the GRB luminosities into two groups which also differ in their redshift distributions. In their study they noted correlations among some GRB parameters, in particular a non-trivial distribution of X-ray spectral indices versus the light curve temporal decay indices, but no dependence of these indices on the GRB luminosity. In addition, correlations among prompt-afterglow parameters have been studied by Dainotti et al. (2011b, 2015a), Margutti et al. (2013) and Grupe et al. (2013).

Importance of the present study results also from the fact that the afterglow LT correlation has already been the object of theoretical modelling either via accretion (Kumar et al., 2008; Lindner et al., 2010; Cannizzo and Gehrels, 2009; Cannizzo et al., 2011), via a magnetar model (Dall’Osso et al., 2011; Bernardini et al., 2011; Rowlinson and O’Brien, 2012; Rowlinson et al., 2013, 2014; Rea et al., 2015) or energy injection (Sultana et al., 2013; Leventis et al., 2014; van Eerten, 2014a,b) and there were attempts to apply it as a cosmological tool (Cardone et al., 2009, 2010; Dainotti et al., 2013a; Postnikov et al., 2014). Here, we extend the LT correlation study looking into its possible dependence on the additional physical parameter $\alpha_{X,a}$ characterizing the afterglow light curve.

Below, in Section 6.3 we introduce the data set analysed in this study. In Section 6.4 we describe the performed observational data analysis and the derived distributions of decay indices $\alpha_{X,a}$. The analysis reveals a weak correlation for $\alpha_{X,a}$ and $L_{X,a}$, but a significant systematic trend along the correlated $(L_{X,a}, T_{X,a}^*)$ distribution. In Section 6.5 we present final discussion and conclusions. We shortly consider physical interpretation of the $\alpha_{X,a}$ distribution. Then, we preliminary explore a new possibility of using GRBs as cosmological standard candles, illustrated with a proposed toy model involving scaling GRB afterglow luminosity to the selected standard α_0 .

The fitted slopes and normalization parameters of the correlations presented in this paper are derived using the D’Agostini (2005) method. The Λ CDM cosmology applied here uses the parameters $H_0 = 71 \text{ km s}^{-1} \text{ Mpc}^{-1}$, $\Omega_\Lambda = 0.73$ and $\Omega_M = 0.27$.

6.3 Data Sample

Below, we analyse distribution of afterglow light curve decay indices, $\alpha_{X,a}$, for the data set of 176 GRBs with known redshifts, observed by Swift from January 2005 to July 2014. Within this sample we consider separately subsamples of 139 long GRBs, 25 X-ray Flashes (XRFs)², 12 short GRBs with extended emission. The sample of 164 long GRBs and XRFs is also considered together as a single sample.

²XRFs are bursts of high energy emission similar to long GRBs, but with a spectral peak energy one order of magnitude smaller than in the long GRBs and with fluence greater in the X-rays than in the gamma ray band. Sometimes XRFs are considered to be misaligned long GRBs (Ioka and Nakamura, 2001; Yamazaki et al., 2002) and it is why we also analyze both these samples together.

As described in Dainotti et al. (2013b), all the analysed light curves were fitted using an analytic functional form proposed by W07. The considered sample was chosen from all Swift GRBs with known redshifts by selecting only those events which allowed a reliable afterglow fitting. The fits provided physical parameters for the GRB afterglows, including its characteristic luminosity and time, $L_{X,a}$ and $T_{X,a}^*$, at the end of the afterglow plateau phase, and the power-law temporal decay index, α_W , for the afterglow decaying phase³. The fitted indices α_W are influenced by the requirement of the best global light curve fitting for the considered analytic model. Therefore, we decided to apply a different procedure for the derivation of the temporal decay index $\alpha_{X,a}$ to be used in the following analysis, intended to provide a more accurate fit of the light curve power-law decay part immediately after the plateau. In each GRB we selected the afterglow light curve section with a power-law and we performed the χ^2 fitting of $\alpha_{X,a}$ in such a range, as presented in Appendix A including a set of figures for all GRBs showing the performed fits and providing the fitting parameters in the table. We compared these parameters with those by Evans et al. (2009) and the ones quoted in the Swift Burst Analyser (http://www.swift.ac.uk/burst_analyser/), having nearly the same $\alpha_{X,a}$ values in the majority of cases. However, also significant differences are found in individual cases due to the different time ranges considered for the fits.

The applied procedure allowed to remove all clear deviations of the power-law from the fitting due to flares and non-uniformities in the observational data. In the case of a break in the decaying part of the light curve, a value of $\alpha_{X,a}$ was fitted to the brighter/earlier part of the light curve. We have to note that in some rare cases it was impossible to decide if the first part of the light curve can be considered the decaying part, or still a steep plateau phase, and the presented fits can be disputed. We decided to use all derived data in the analysis and correlations studied in this paper, leaving possibility of some particular data selection and/or rejecting some events from the analysis to the future study.

Comparison of the $\alpha_{X,a}$ and α_W distributions in Fig. 6.3.1 shows that both measured decay indices have similar distributions, but differences for individual fitted values can be significant. The parameters of the Gaussian fits for both presented distributions are: a mean value $\mu(\alpha_{X,a}) = 1.40$ with standard deviation $\sigma(\alpha_{X,a}) = 0.46$ for our power-law fitting compared to $\mu(\alpha_W) = 1.45$ and $\sigma(\alpha_W) = 0.45$ for the Willingale model fitting. The P-value of the T-test between these two distributions is 0.89, indicating no statistically significant differences between the two distributions.

6.4 Analysis of the afterglow decay light curves

By adopting the analysed subsample of long GRBs+XRFs, systematic trends in the $(\log L_{X,a}, \alpha_{X,a})$ distribution can be studied. As presented in Fig. 6.4.1, there is an indication that these

³These data are available upon request from M.G. Dainotti.

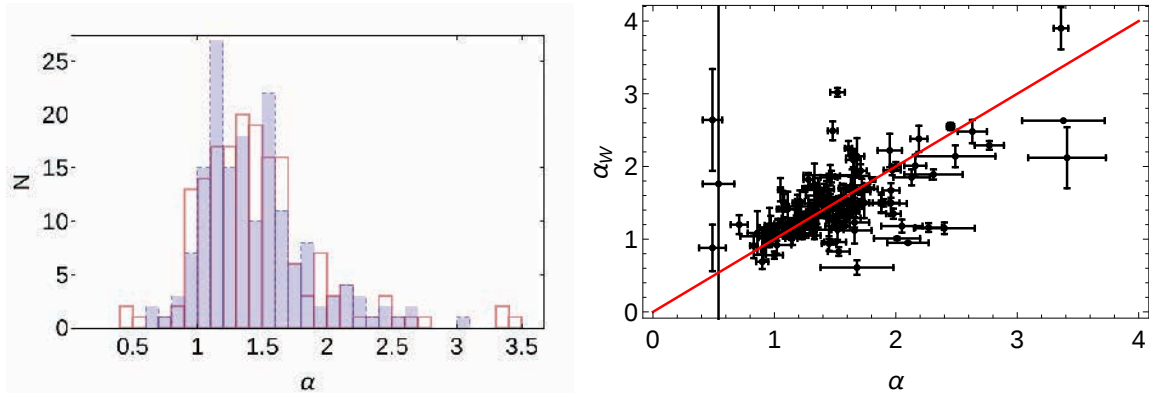


Figure 6.3.1: Comparison of the derived indices $\alpha_{X,a}$ and α_W . Left panel: histograms of fitted $\alpha_{X,a}$ (solid red line) and α_W (shaded area). Right panel: the α_W versus $\alpha_{X,a}$ distribution. The red line $\alpha_{X,a} = \alpha_W$ is provided for reference. (Figure from Del Vecchio, Dainotti, and Ostrowski (2016).)

quantities are (weakly) correlated. However, scatter of points around the correlation line is substantial and the derived Spearman (Spearman, 1904) correlation coefficient $\rho = 0.17$ is small. The fitted correlation line is $\log L_{X,a} = 0.30 \alpha_{X,a} + 47.20$, showing that *on average* faster light curve decay seems to occur for GRBs with higher luminosities. However, here we stress again, the trend is weak in this highly scattered distribution. The same analysis using the long GRBs subsample only leads to a slightly weaker correlation with $\rho = 0.14$ and $P = 10^{-4}$.

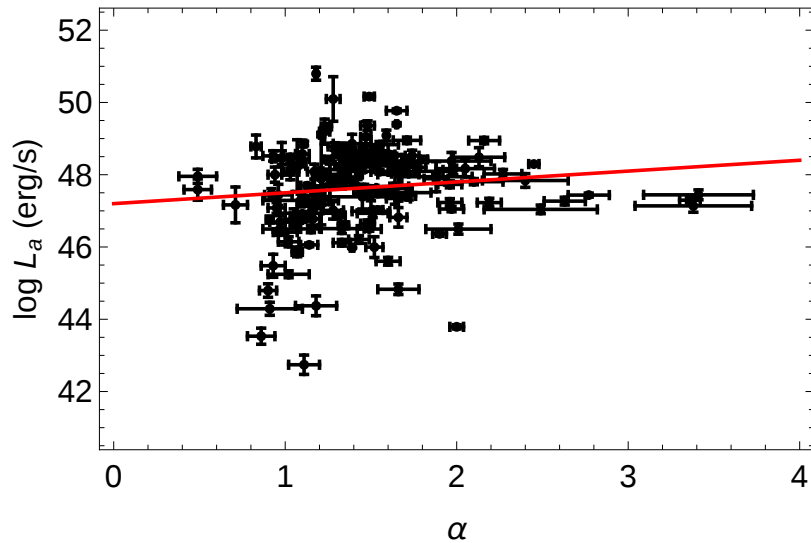


Figure 6.4.1: Distribution of $\log L_{X,a}$ versus $\alpha_{X,a}$ for the long GRBs+XRFs subsample. The line presents a fitted weak correlation. (Figure from Del Vecchio, Dainotti, and Ostrowski (2016).)

It should be noted that the large scatter of the GRB luminosity distribution cannot be due only to the fitting method used for its derivation. Significant contribution to this scatter must result from the very nature of the GRB sources, possibly modified by the explosion

geometry.

In the attempt to evaluate the trend in Fig. 6.4.1 we decided to compare distributions of $\alpha_{X,a}$ plotted for three luminosity ranges with equal numbers of GRBs: a low luminosity range – $\log L_{X,a} < 47.25$, a medium range – $47.25 < \log L_{X,a} < 48.2$, and a high range – $\log L_{X,a} > 48.2$. Normalized cumulative distributions function CDF ($CDF(x) \equiv \sum_0^x (1/N)$, where summing includes all GRBs with $\alpha_{X,a} < x$ and N is the number of GRBs in the considered sample) approximates the cumulative probability function in the $\alpha_{X,a}$ space. Below, in Fig. 6.4.2 we present these functions in the 3 analysed luminosity ranges for the whole GRBs sample, as well as for long GRBs, short GRBs and XRFs subsamples. Comparison of the red and blue CDF distributions presented in Fig. 6.4.2 convincingly (maybe less convincingly for the short subsample) supports the existence of the $(\log L_{X,a}, \alpha_{X,a})$ correlation. The same systematics for all analysed GRB samples with lower luminosity events show tendency to slower light curve decay. The most luminous GRBs (blue lines) seem to grow faster to unity with their smaller $\alpha_{X,a}$ scatter. This result is also confirmed by the Kolmogorov-Smirnov (KS) test. The test applied for low (red line) and high (blue line) luminosity GRB distributions along the $\alpha_{X,a}$ coordinate (Fig. 6.4.3) shows that it is highly unlikely, with $P = 0.01$, that both distributions are drawn randomly from the same population. As regards the XRFs and short GRBs subsamples, the available number of elements is too low for establishing reliable statistical results, however the distributions of brighter GRBs seem to show the same tendency to be centered at higher $\alpha_{X,a}$ values than the dimmer ones.

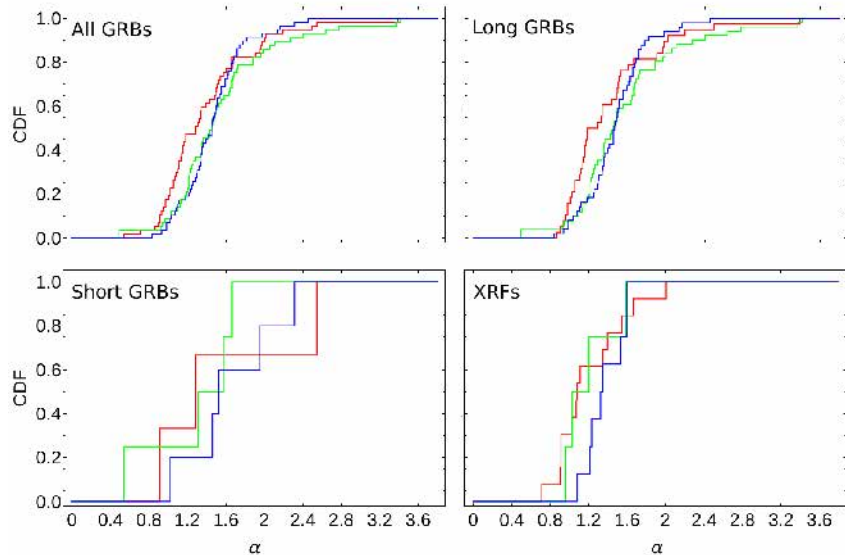


Figure 6.4.2: Normalized cumulative distribution functions, CDF , versus $\alpha_{X,a}$ for the analysed GRB subsamples in 3 considered luminosity ranges: $\log L_{X,a} < 47.25$ (red), $47.25 < \log L_{X,a} < 48.2$ (green) and $\log L_{X,a} > 48.2$ (blue). (Figure from Del Vecchio, Dainotti, and Ostrowski (2016).)

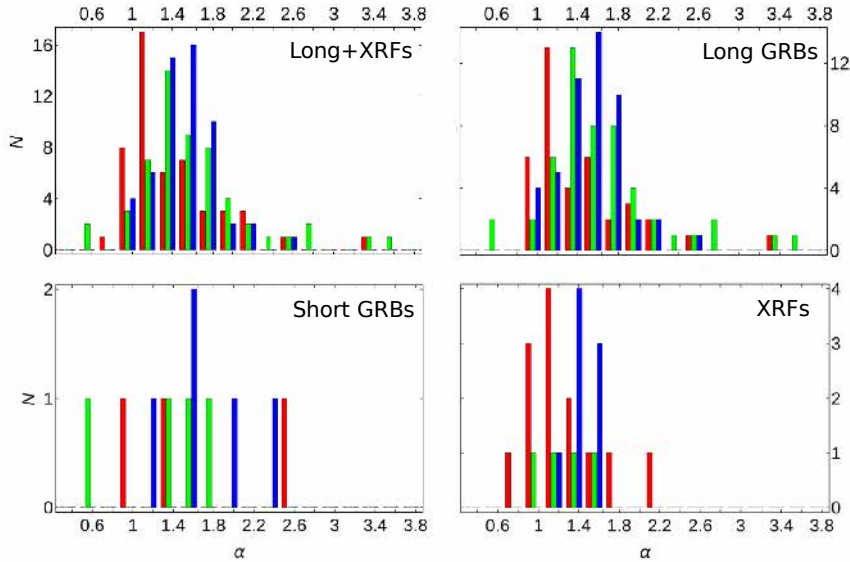


Figure 6.4.3: GRB distributions of $\alpha_{X,a}$ for the analysed subsamples in 3 considered luminosity ranges: $\log L_{X,a} < 47.25$ (red), $47.25 < \log L_{X,a} < 48.2$ (green) and $\log L_{X,a} > 48.2$ (blue). In each $\Delta\alpha_{X,a}$ bin the data for the different luminosity ranges are plotted as (shifted within the considered bin) separate colour bars. (Figure from Del Vecchio, Dainotti, and Ostrowski (2016).)

There is no well understood universal recipe yet for differentiating the physical properties of the GRB source from observational data, but the existence of $\log L_{X,a}$ versus $\log T_{X,a}^*$ correlation reflects the presence of \sim uniformly varying properties of GRB progenitor in the plateau phase. If these properties would be the GRB progenitor mass and/or its angular momentum, then different external medium profiles could be expected around the exploding massive star, where the afterglow related shock propagates. Therefore, it may be expected to detect more clear dependence between the afterglow luminosity and the $\alpha_{X,a}$ index for GRBs analysed within a limited range of $T_{X,a}^*$. To proceed, in analogy to the above analysis for selected luminosity ranges, we study relative distributions of GRB subsamples along the LT distribution in three ranges of the decay index: the “slowly” decaying light curves with $0.53 < \alpha_{X,a} < 1.23$, the “intermediate” ones with $1.23 < \alpha_{X,a} < 1.54$ and the “fast” decaying light curves with $1.54 < \alpha_{X,a} < 3.41$. With such selection each subsample has the same size.

Inspection of Fig. 6.4.4, presenting the considered long GRBs+XRFs $\alpha_{X,a}$ -subsamples distributed along the LT correlation line, clearly reveals separation among these distributions. This behaviour is also well visible in the normalized cumulative distribution functions plotted in Fig. 6.4.5. In particular, in Fig. 6.4.5 the considered samples (all, long GRBs and long GRBs+XRFs) are presented with respect to the ratio of the GRB afterglow luminosity $L_{X,a}(T_{X,a}^*)$ to the respective luminosity $L_{LT}(T_{X,a}^*)$ at the fitted correlation line: in the logarithmic scale $\log(L_{X,a}/L_{LT}) = \log L_{X,a} - \log L_{LT}$. A significant trend between the relative luminosity, $\log(L_{X,a}/L_{LT})$, and $\alpha_{X,a}$ is visible in Fig. 6.4.6, leading, e.g. to negligible

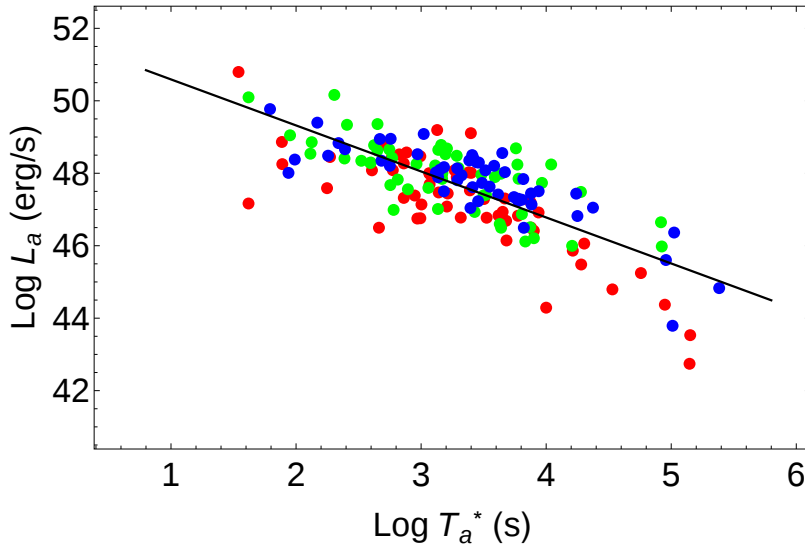


Figure 6.4.4: Distribution of the long GRBs+XRFs subsample on the $(\log L_{X,a}, \log T_{X,a}^*)$ plane for the three selected $\alpha_{X,a}$ subsamples: $0.53 < \alpha_{X,a} < 1.23$ (red), $1.23 < \alpha_{X,a} < 1.54$ (green) and $1.54 < \alpha_{X,a} < 3.41$ (blue). The black line represents the LT correlation line fitted for all presented GRBs. (Figure from Del Vecchio, Dainotti, and Ostrowski (2016).)

KS probability, $P = 1.4 \times 10^{-6}$, that the low and high $\alpha_{X,a}$ subsamples are randomly drawn from a single GRB population.

In Fig. 6.4.7 we present the distribution of $\log(L_{X,a}/L_{LT})$ versus the $\alpha_{X,a}$ index for the long GRBs+XRFs subsample. A linear fit for this distribution is

$$\log L_{X,a} - \log L_{LT} = (0.49 \pm 0.17) \alpha_{X,a} - (0.70 \pm 0.25) , \quad (6.1)$$

with Spearman correlation coefficient $\rho = 0.36$, and the probability for random occurrence $P = 10^{-10}$. Using the long GRB subsample only, the correlation has a slightly smaller slope (0.42) with $\rho = 0.36$ and $P = 7.7 \times 10^{-10}$. This correlation shows the observed tendency – with respect to the LT correlation line – for higher afterglow luminosity to have steeper light curve decay.

To better evaluate the errors of the parameters fitted for the analysed GRB sample, we decided to perform an additional statistical analysis using the Monte Carlo modelling of the data with $3 \cdot 10^4$ simulations in each case. For each GRB we consider parameters $L_{X,a}$, $T_{X,a}^*$, and $\alpha_{X,a}$ to have Gaussian distributions around the fitted values, with the distribution width given by the respective 1σ uncertainty. Then, we randomly selected from the considered GRB sample - using a bootstrap procedure - the samples to be analysed, where each GRB parameter was drawn from the respective Gaussian distribution. For each randomly created data sample we derived the correlation coefficient and the correlation slope by fitting the respective correlation $\log(L_{X,a}/L_{LT})$ vs. $\alpha_{X,a}$. As presented in the upper panels of Fig.

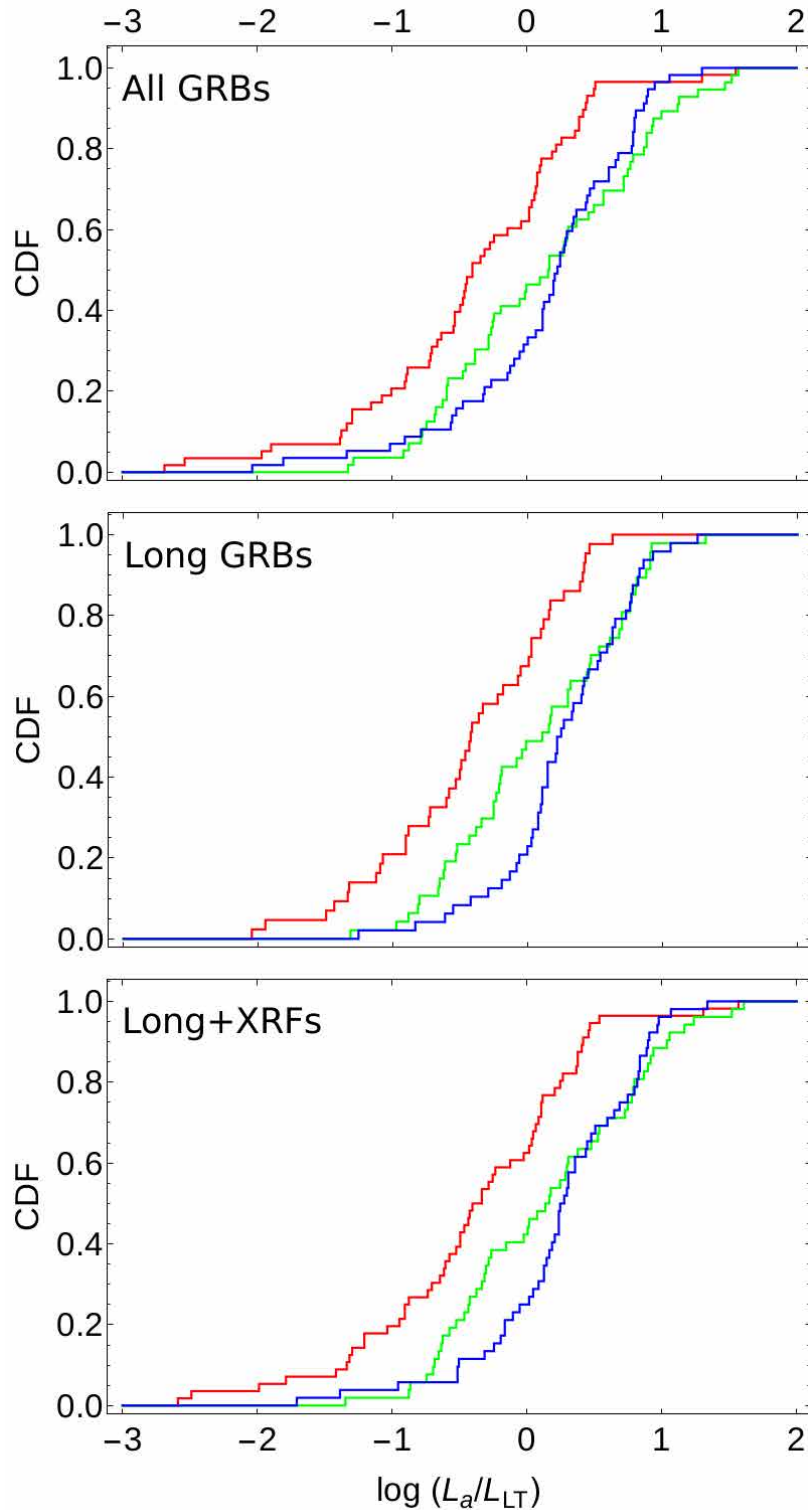


Figure 6.4.5: Normalized cumulative distributions function CDF versus $\log(L_{X,a}/L_{LT})$ for the analysed GRB subsamples in 3 considered α ranges: $0.53 < \alpha_{X,a} < 1.23$ (red), $1.23 < \alpha_{X,a} < 1.54$ (green) and $1.54 < \alpha_{X,a} < 3.41$ (blue). (Figure from Del Vecchio, Dainotti, and Ostrowski (2016).)

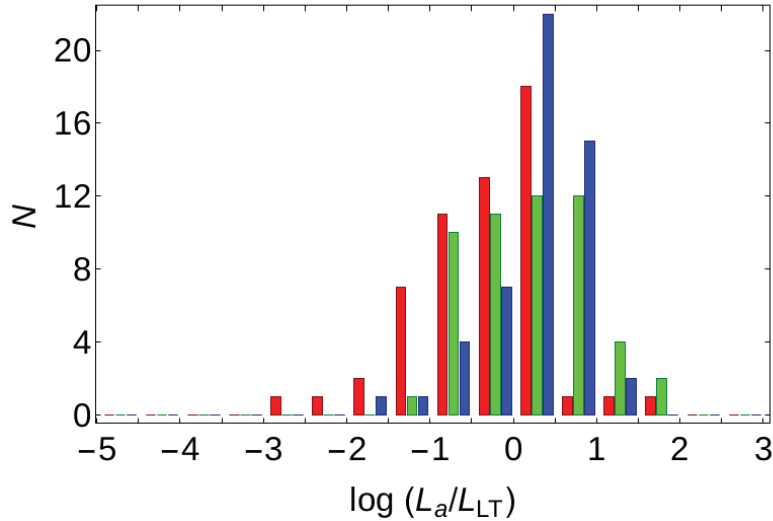


Figure 6.4.6: Distributions of $\log(L_{X,a}/L_{LT})$ for the long GRBs+XRFs subsamples, for the three $\alpha_{X,a}$ ranges: $0.53 < \alpha_{X,a} < 1.23$ (red), $1.23 < \alpha_{X,a} < 1.54$ (green) and $1.54 < \alpha_{X,a} < 3.41$ (blue). (Figure from Del Vecchio, Dainotti, and Ostrowski (2016).)

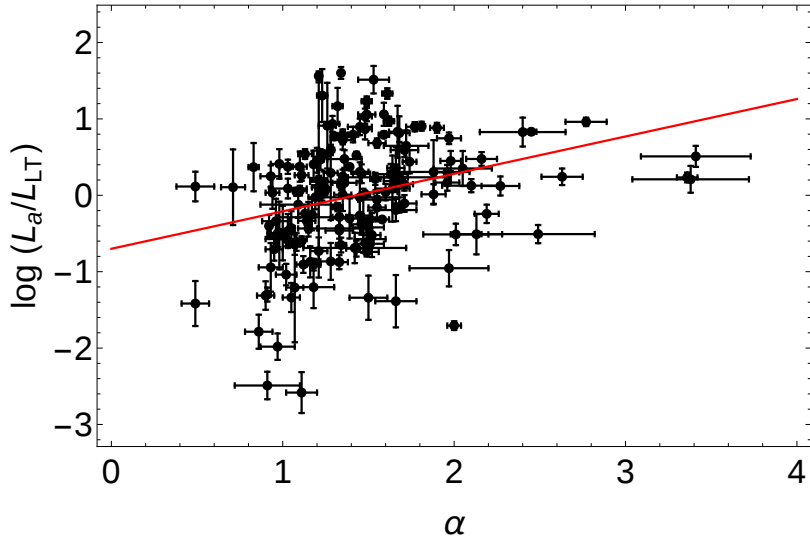


Figure 6.4.7: Distribution of the long GRBs+XRFs subsample on the $(\alpha_{X,a}, \log(L_{X,a}/L_{LT}))$ plane. The red line presents the fitted correlation. (Figure from Del Vecchio, Dainotti, and Ostrowski (2016).)

6.4.8, the simulations fully confirm reality of the derived correlation. We find that within the measurement errors existing correlation coefficient should be approximately between $0.2 < \rho < 0.5$ (mean value 0.35) and the fitted $\log(L_{X,a}/L_{LT})$ vs. $\alpha_{X,a}$ correlation should have an inclination $0.3 < a < 0.5$ (mean value 0.41), in agreement with the fitted errors in Equation 6.1.

Using similar simulations as above, it can also be independently checked the possibility of randomly obtaining the studied $\log(L_{X,a}/L_{LT})$ vs. $\alpha_{X,a}$ correlation if no systematic correlation of $\alpha_{X,a}$ in respect to $L_{X,a}$ and $T_{X,a}^*$ exists. We performed such analysis by randomly drawing samples using the procedure above, again within the bootstrap scheme, but with separately drawing pairs of parameters $L_{X,a}$ and $T_{X,a}^*$ from the GRB sample, and the $\alpha_{X,a}$ values from the sample of these values for the considered GRBs. Such procedure removes any correlation between $\alpha_{X,a}$ and other GRB parameters in the sample and shows that the possibility of randomly obtaining the correlation coefficient found in the real data is negligible (Fig. 6.4.8, lower panels).

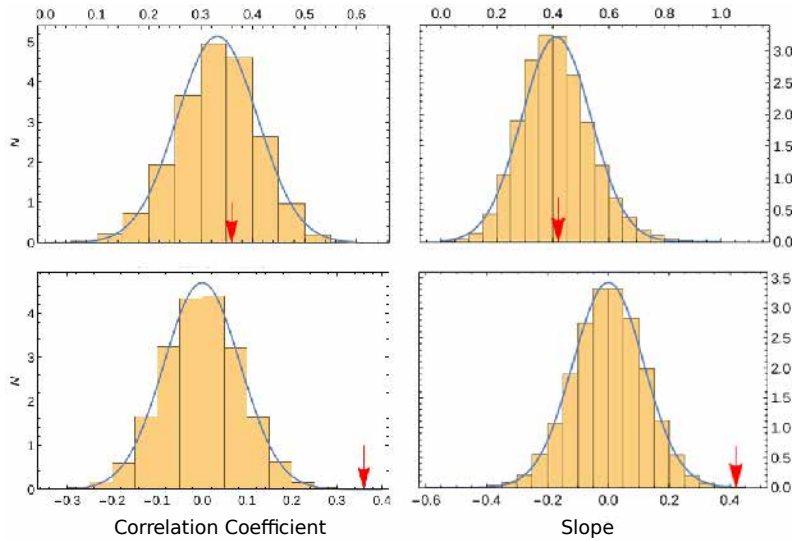


Figure 6.4.8: The results of the Monte Carlo simulations for the long subsample: the normalized distributions of the correlation coefficient ρ and the slope a of the $\log(L_{X,a}/L_{LT})$ vs. $\alpha_{X,a}$ correlation for bootstrapped simulations including random data scatter within the measurement error ranges (upper panels) and the analogous distributions with the $\alpha_{X,a}$ parameters separately randomly drawn from the sample (lower panels). With red arrows we indicated values obtained in the above analysis of the original data. (Figure from Del Vecchio, Dainotti, and Ostrowski (2016).)

6.5 Final discussion and Conclusions

Analysis of the fitted afterglow power-law temporal decay indices for the subsample of long GRBs+XRFs reveals a weak trend towards a steeper decay phase for higher afterglow luminosity $L_{X,a}$. The trend turns into a significant correlation if we consider GRB afterglow luminosity scaled to the one expected from the fitted LT correlation, for a given GRB

afterglow plateau end time $T_{X,a}^*$. As different $T_{X,a}^*$ values result from varying properties of the GRB sources, the present analysis can be used to get new insight into physical nature of such sources.

6.5.1 Theoretical models

It is worth noting the attempts in the literature to provide physical interpretation of $\log L_{X,a}$ versus $\alpha_{X,a}$ relation. We can refer to such model presented by Hascoët et al. (2014) (see also Genet et al. (2007)) in order to relate the considered $\alpha_{X,a}$ parameter to the microphysics of the reverse shock emission. In the model of Hascoët et al. the energy deposition rate, \dot{E}_T , in the GRB afterglow, varied in time “ t ” with a power-law dependence on the Lorentz gamma factor, $\Gamma(t)$:

$$\dot{E}_T(\Gamma(t)) = \begin{cases} \dot{E}_* \left(\frac{\Gamma(t)}{\Gamma_*} \right)^{-q} & \text{for } \Gamma(t) > \Gamma_* \\ \dot{E}_* \left(\frac{\Gamma(t)}{\Gamma_*} \right)^{q'} & \text{for } \Gamma(t) < \Gamma_* \end{cases} \quad (6.2)$$

where the energy scale \dot{E}_* is determined by the total energy injected in the afterglow phase; q and q' are the power-law indices for the time dependence of the energy injection rate. In this model the q parameter constraints the shape of the plateau phase, while q' carries information about the light curve temporal decay index after the plateau. The characteristic value of Γ_* sets the duration of the plateau. With the assumed power-law radial distribution of the medium surrounding the GRB progenitor, the Lorentz factor evolves as

$$\Gamma(t) = \Gamma_* \left(\frac{t}{T_{X,a}^*} \right)^{-\gamma}, \quad (6.3)$$

where, e.g., $\gamma = 3/8$ for a uniform medium and $\gamma = 1/4$ for a stellar wind. Hascoët et al. derived the light curve temporal decay indices before (α_1) and after (α_2) the break at the end of the plateau phase as

$$\begin{cases} \alpha_1 = \gamma q - 1 \\ \alpha_2 = -\gamma q' - 1 \end{cases} \quad (6.4)$$

so that the flat plateau phase should be present for $q \approx 1/\gamma$, i.e. close to $q = 8/3$ in the uniform medium and $q = 4$ in the wind case. In the presented example Hascoët et al. (2014) considered the temporal decay index after the plateau $\alpha_2 = -1.5$, leading to $q' = 1/(2\gamma)$ and the parameters of the central engine energy deposition in the late afterglow stage $q' = 4/3$ and 2, for the uniform medium and the wind case, respectively. It should be noted that this

example uses the α_2 value very close to the mean value of our distribution, $\alpha_{mean} = 1.4 \pm 0.3$, as visible in the left panel of Fig. 6.3.1.

We should remark here that the observed large scatter in the $\alpha_{X,a}$ distribution seems to be difficult to be explained only by variations of the source radial density profile, influencing the shock propagation. Therefore, we consider the present discussion only as an example of the study based on the $\alpha_{X,a}$ parameter measurements.

6.5.2 GRB standardization

As the second aspect of the present study, we consider a possible usage of the measured afterglow light curve $\alpha_{X,a}$ for physically differentiating the observed GRBs. E.g., the revealed $\log(L_{X,a}/LLT)$ versus $\alpha_{X,a}$ correlation can be used to search for the procedure which could enable the standardization of GRBs and eventually to reveal a new cosmological standard candle. As an *illustrative toy model*, for such approach we introduce a procedure for GRBs resembling the one used for the standardization of SN Ia light curves by using the so-called Phillips correlation between the peak magnitude and the “stretching parameter” (Phillips, 1993). In an attempt to scale GRBs with different temporal decay indices $\alpha_{X,a}$ to the standard source properties, we define the standard GRB as the one characterized by the value of the temporal decay index $\alpha_0 = 1.4$, approximately the mean value of the distribution presented in Fig. 6.3.1. Further, we postulate that the expected “standardized” GRB luminosity, $L_{a,0}$, can be derived using its measured decay index $\alpha_{X,a}$ and by scaling it to α_0 using Equation 6.1:

$$\log L_{a,0} = \log L_{X,a} + 0.49 (\alpha_0 - \alpha_{X,a}) . \quad (6.5)$$

This procedure applied for all the events in the analysed subsample of long GRBs+XRFs results in only a slight increase in the LT correlation coefficient absolute value, from $\rho = -0.72$ for the original $(\log L_{X,a}, \log T_{X,a}^*)$ data to $\rho_0 = -0.76$ for the modified distribution $(\log L_{a,0}, \log T_{X,a}^*)$. When using the long GRBs subsample only the increase in the correlation coefficient is even smaller. This increase in the correlation coefficient is obtained by the fits for quite different shapes of the afterglow light curves and thus different quality of available GRB parameters $L_{X,a}$, $T_{X,a}^*$ and $\alpha_{X,a}$. More detailed analysis of this standardization procedure, with careful consideration of the afterglow light curves for the selected events, is in progress now.

CHAPTER 7

Summary and final remarks

After a general overview of the correlations between the prompt-afterglow parameters in Chapters 3 and 4, the analysis of the afterglow phase was presented. The main aim of the work described in Chapter 5 was to test new methods for analysing the selection effects present in the LT correlation. This is a very important issue to be studied because reliable results in the analysis of GRB correlations are obtained only with taking correctly the biases into account. Indeed, a proper investigation of the GRB correlations (Amati et al., 2002; Ghirlanda et al., 2004b; Dainotti et al., 2018; Dainotti and Del Vecchio, 2017) can possibly give the valuable tools for the cosmological use of GRBs as distance indicators. For example, a significant result was obtained by Schaefer (2007) who had built a GRB Hubble diagram (HD) using five correlations among physical parameters of the prompt emission phase. However, the error bars on the distance moduli were larger in comparison to the errors obtained from SNe Ia analysis (Betoule et al., 2014; Calcino and Davis, 2017). Nevertheless, an analysis of the correlations among afterglow physical parameters could lead to a more precise HD, as already shown by Cardone et al. (2010). Another study of the cosmological parameters using the correlations among physical parameters of the GRB prompt phase was presented by Amati and Della Valle (2013), but the errors in the derived matter density and the dark energy density obtained in this work are still larger than those calculated using the Planck mission data (Planck Collaboration et al., 2016).

In the work described in Chapter 5, another particular aspect of the LT correlation (Dainotti et al., 2008, 2010) was studied in detail: the consequences of the selection biases affecting time and luminosity measurements. Assuming an unknown efficiency function for the detector, the correlation between the SFR and the GFR was analysed, as well as the redshift evolution of GRB luminosity and timescales. Several proposed shapes of the SFR were considered to find the one which best fits the data, and several functional forms were assumed for the efficiency function of the detector, giving interesting results. Simulating selection cuts on both luminosity and time measurements, the parameters of the LT correlation obtained appear to be compatible with those already known in the literature (Dainotti et al., 2013b). Therefore, it is important to consider properly the limitations of the detectors used for observations and the selections made on the data sample.

In the study shown in Chapter 6 a new approach was proposed to analyse the afterglow phase of the GRBs. The method, investigating the $\alpha_{X,a}$ parameter to find a common feature of at least a subsample of GRBs, allows for an approach resembling the usage of the Phillips correlation for SNe Ia. To explore such link between SNe and GRBs, Cano (2014) and Li and Hjorth (2014) studied several optical light curves of GRBs associated with SNe, and they found a correlation between peak luminosity and decay rate of the light curve of the elements in their sample.

Another important aspect considered here is the jet emission and its interaction with the external medium that several studies attempted to model (Panaitescu et al., 1997; Panaitescu, 2009). For example, Hascoët et al. (2014) analysed the afterglow phase using two interpretations: one in the forward shock (FS) scenario and the other in the reverse shock (RS) scenario. The model applying the RS gave results more compatible with the observed GRB light curves. Additionally, one may note that their average decay index after the end of the plateau phase is equal within the errors to the one found in the work presented here (even if a large data scatter is present), showing that their model can be an acceptable physical explanation for the $\log(L_{X,a}/L_{LT}) - \alpha_{X,a}$ correlation.

In the statistical analysis of the $\alpha_{X,a}$ parameter presented in Chapter 6, a correlation between the afterglow luminosity and $\alpha_{X,a}$ was found. For investigating the afterglow phase in more detail, it is relevant to consider a new quantity, the relative luminosity $\log(L_{X,a}/L_{LT})$, namely the ratio of the afterglow luminosity at the end of the plateau phase to the luminosity value of the LT correlation best fit line at the same time. This relative luminosity was studied as a function of $\alpha_{X,a}$; as a result, a significant systematic effect was found of GRBs with higher luminosity decaying faster. This can be due to a difference in the external medium or in the acceleration process of the two groups of GRBs. In addition, this new parameter was employed to standardize the GRB emission. A new general luminosity indicator was built taking into account the average value of $\alpha_{X,a}$ found in this work and the correlation between the relative luminosity and $\alpha_{X,a}$. The new LT correlation resulting from this new luminosity has a higher Spearman correlation coefficient than the one of the original LT correlation, leading to a tighter correlation.

In any case the results of the work presented here are not definitive, and require much further effort to standardize GRB phenomena by considering different physical parameters and to use finally GRBs as cosmological distance indicators. The outcomes of this analysis seem to point out that a wider multi-wavelength analysis needs to be involved to obtain more robust results, although the complete multi-wavelength coverage for all GRBs is difficult to obtain at the moment. In the research plans of the thesis author the simultaneous analysis of the GRB X-ray and optical data is considered in this respect, but this work is at an initial phase now. On the other hand, a review of the currently known correlations, derived for highly scattered distributions of GRB parameters, does not provide convincing support to believe that the final success is granted in that matter.

Bibliography

- B. P. Abbott, R. Abbott, T. D. Abbott, M. R. Abernathy, F. Acernese, K. Ackley, C. Adams, T. Adams, P. Addesso, R. X. Adhikari, and et al. Observation of Gravitational Waves from a Binary Black Hole Merger. *Physical Review Letters*, 116(6):061102, February 2016a. doi: 10.1103/PhysRevLett.116.061102.
- B. P. Abbott, R. Abbott, T. D. Abbott, M. R. Abernathy, F. Acernese, K. Ackley, C. Adams, T. Adams, P. Addesso, R. X. Adhikari, and et al. Observation of Gravitational Waves from a Binary Black Hole Merger. *Physical Review Letters*, 116(6):061102, February 2016b. doi: 10.1103/PhysRevLett.116.061102.
- B. P. Abbott, R. Abbott, T. D. Abbott, F. Acernese, K. Ackley, C. Adams, T. Adams, P. Addesso, R. X. Adhikari, V. B. Adya, and et al. A gravitational-wave standard siren measurement of the Hubble constant. *Nature*, 551:85–88, November 2017a. doi: 10.1038/nature24471.
- B. P. Abbott, R. Abbott, T. D. Abbott, F. Acernese, K. Ackley, C. Adams, T. Adams, P. Addesso, R. X. Adhikari, V. B. Adya, and et al. Gravitational Waves and Gamma-Rays from a Binary Neutron Star Merger: GW170817 and GRB 170817A. *ApJ*, 848:L13, October 2017b. doi: 10.3847/2041-8213/aa920c.
- A. A. Abdo, M. Ackermann, M. Ajello, K. Asano, W. B. Atwood, M. Axelsson, L. Baldini, J. Ballet, G. Barbiellini, M. G. Baring, and et al. Fermi Observations of GRB 090902B: A Distinct Spectral Component in the Prompt and Delayed Emission. *ApJ*, 706:L138–L144, November 2009a. doi: 10.1088/0004-637X/706/1/L138.
- A. A. Abdo, M. Ackermann, M. Arimoto, K. Asano, W. B. Atwood, M. Axelsson, L. Baldini, J. Ballet, D. L. Band, G. Barbiellini, and et al. Fermi Observations of High-Energy Gamma-Ray Emission from GRB 080916C. *Science*, 323:1688, March 2009b. doi: 10.1126/science.1169101.
- M. Ackermann, K. Asano, W. B. Atwood, M. Axelsson, L. Baldini, J. Ballet, G. Barbiellini, M. G. Baring, D. Bastieri, K. Bechtol, and et al. Fermi Observations of GRB 090510: A Short-Hard Gamma-ray Burst with an Additional, Hard Power-law Component from 10 keV TO GeV Energies. *ApJ*, 716:1178–1190, June 2010. doi: 10.1088/0004-637X/716/2/1178.
- M. Ackermann, M. Ajello, K. Asano, M. Axelsson, L. Baldini, J. Ballet, G. Barbiellini,

- M. G. Baring, D. Bastieri, K. Bechtol, and et al. Detection of a Spectral Break in the Extra Hard Component of GRB 090926A. *ApJ*, 729:114, March 2011. doi: 10.1088/0004-637X/729/2/114.
- M. Ackermann, M. Ajello, A. Allafort, W. B. Atwood, L. Baldini, J. Ballet, G. Barbiellini, D. Bastieri, K. Bechtol, A. Belfiore, and et al. The First Fermi-LAT Catalog of Sources above 10 GeV. *ApJS*, 209:34, December 2013. doi: 10.1088/0067-0049/209/2/34.
- P. C. Agrawal. Astrosat: The First Indian Astronomy Satellite with Multiwavelength Capability. *International Cosmic Ray Conference*, 4:171, 2005.
- L. Amati. Intrinsic spectra and energetics of cosmological Gamma-Ray Bursts. *Chinese Journal of Astronomy and Astrophysics Supplement*, 3:455–460, December 2003. doi: 10.1088/1009-9271/3/S1/455.
- L. Amati. The $E_{p,i}$ - E_{iso} correlation in gamma-ray bursts: updated observational status, re-analysis and main implications. *MNRAS*, 372:233–245, October 2006. doi: 10.1111/j.1365-2966.2006.10840.x.
- L. Amati. COSMOLOGY WITH THE $E_{p,i}$ - E_{iso} CORRELATION OF GAMMA-RAY BURSTS. *International Journal of Modern Physics Conference Series*, 12:19–27, March 2012. doi: 10.1142/S2010194512006228.
- L. Amati and M. Della Valle. Measuring Cosmological Parameters with Gamma Ray Bursts. *International Journal of Modern Physics D*, 22:1330028, December 2013. doi: 10.1142/S0218271813300280.
- L. Amati, F. Frontera, M. Tavani, J. J. M. in't Zand, A. Antonelli, E. Costa, M. Feroci, C. Guidorzi, J. Heise, N. Masetti, E. Montanari, L. Nicastro, E. Palazzi, E. Pian, L. Piro, and P. Soffitta. Intrinsic spectra and energetics of BeppoSAX Gamma-Ray Bursts with known redshifts. *A&A*, 390:81–89, July 2002. doi: 10.1051/0004-6361:20020722.
- L. Amati, M. Della Valle, F. Frontera, D. Malesani, C. Guidorzi, E. Montanari, and E. Pian. On the consistency of peculiar GRBs 060218 and 060614 with the $E_{p,i}$ - E_{iso} correlation. *A&A*, 463:913–919, March 2007. doi: 10.1051/0004-6361:20065994.
- L. Amati, C. Guidorzi, F. Frontera, M. Della Valle, F. Finelli, R. Landi, and E. Montanari. Measuring the cosmological parameters with the $E_{p,i}$ - E_{iso} correlation of gamma-ray bursts. *MNRAS*, 391:577–584, December 2008. doi: 10.1111/j.1365-2966.2008.13943.x.
- L. Amati, F. Frontera, and C. Guidorzi. Extremely energetic Fermi gamma-ray bursts obey spectral energy correlations. *A&A*, 508:173–180, December 2009. doi: 10.1051/0004-6361/200912788.
- L. Amati, F. Frontera, and C. Guidorzi. Extremely energetic Fermi gamma-ray bursts obey spectral energy correlations. *A&A*, October 2017.

- S. Andreon. In *Astrostatistical Challenges for the New Astronomy*. pages 41–62, 2013. doi: 10.1007/978-1-4614-3508-2_3.
- J.-L. Atteia. A simple empirical redshift indicator for gamma-ray bursts. *A&A*, 407:L1–L4, August 2003. doi: 10.1051/0004-6361:20030958.
- W. Baade and F. Zwicky. On Super-novae. *Proceedings of the National Academy of Science*, 20:254–259, May 1934. doi: 10.1073/pnas.20.5.254.
- L. G. Balazs, A. Meszaros, and I. Horvath. Anisotropy of the sky distribution of gamma-ray bursts. *A&A*, 339:1–6, November 1998.
- D. Band, J. Matteson, L. Ford, B. Schaefer, D. Palmer, B. Teegarden, T. Cline, M. Briggs, W. Paciesas, G. Pendleton, G. Fishman, C. Kouveliotou, C. Meegan, R. Wilson, and P. Lestrade. BATSE observations of gamma-ray burst spectra. I - Spectral diversity. *ApJ*, 413:281–292, August 1993. doi: 10.1086/172995.
- R. Barkana and A. Loeb. Gamma-Ray Bursts versus Quasars: Ly α Signatures of Reionization versus Cosmological Infall. *ApJ*, 601:64–77, January 2004. doi: 10.1086/380435.
- C. Barraud, J.-F. Olive, J. P. Lestrade, J.-L. Atteia, K. Hurley, G. Ricker, D. Q. Lamb, N. Kawai, M. Boer, J.-P. Dezelay, G. Pizzichini, R. Vanderspek, G. Crew, J. Doty, G. Monnelly, J. Villasenor, N. Butler, A. Levine, A. Yoshida, Y. Shirasaki, T. Sakamoto, T. Tamagawa, K. Torii, M. Matsuoka, E. E. Fenimore, M. Galassi, T. Tavenner, T. Q. Donaghy, C. Graziani, and J. G. Jernigan. Spectral analysis of 35 GRBs/XRFs observed with HETE-2/FREGATE. *A&A*, 400:1021–1030, March 2003. doi: 10.1051/0004-6361:20030074.
- S. D. Barthelmy, G. Chincarini, D. N. Burrows, N. Gehrels, S. Covino, A. Moretti, P. Romano, P. T. O'Brien, C. L. Sarazin, C. Kouveliotou, M. Goad, S. Vaughan, G. Tagliaferri, B. Zhang, L. A. Antonelli, S. Campana, J. R. Cummings, P. D'Avanzo, M. B. Davies, P. Giommi, D. Grupe, Y. Kaneko, J. A. Kennea, A. King, S. Kobayashi, A. Melandri, P. Meszaros, J. A. Nousek, S. Patel, T. Sakamoto, and R. A. M. J. Wijers. An origin for short γ -ray bursts unassociated with current star formation. *Nature*, 438:994–996, December 2005. doi: 10.1038/nature04392.
- R. Basak and A. R. Rao. Correlation between the Isotropic Energy and the Peak Energy at Zero Fluence for the Individual Pulses of Gamma-Ray Bursts: Toward a Universal Physical Correlation for the Prompt Emission. *ApJ*, 749:132, April 2012. doi: 10.1088/0004-637X/749/2/132.
- R. Basak and A. R. Rao. Pulse-wise Amati correlation in Fermi gamma-ray bursts. *MNRAS*, 436:3082–3088, December 2013. doi: 10.1093/mnras/stt1790.
- L. Bassani, G. Malaguti, E. Jourdain, J. P. Roques, and W. N. Johnson. Detection of soft

- gamma-ray emission from the Seyfert 2 galaxy NGC 4507 by the OSSE telescope. *ApJ*, 444:L73–L76, May 1995. doi: 10.1086/187863.
- A. Begue & Pe'er. Poynting-flux-dominated Jets Challenged by their Photospheric Emission. *ApJ*, 802:134,141, April 2015. doi: 10.1088/0004-637X/802/2/134.
- A. M. Beloborodov. Collisional mechanism for gamma-ray burst emission. *MNRAS*, 407: 1033–1047, September 2010. doi: 10.1111/j.1365-2966.2010.16770.x.
- A. M. Beloborodov. Radiative Transfer in Ultrarelativistic Outflows. *ApJ*, 737:68, August 2011. doi: 10.1088/0004-637X/737/2/68.
- A. M. Beloborodov and P. Mészáros. Photospheric Emission of Gamma-Ray Bursts. *Space Sci. Rev.*, 207:87–110, July 2017. doi: 10.1007/s11214-017-0348-6.
- E. Berger. The Prompt Gamma-Ray and Afterglow Energies of Short-Duration Gamma-Ray Bursts. *ApJ*, 670:1254–1259, December 2007. doi: 10.1086/522195.
- E. Berger. Short-Duration Gamma-Ray Bursts. *ARA&A*, 52:43–105, August 2014a. doi: 10.1146/annurev-astro-081913-035926.
- E. Berger. Short-Duration Gamma-Ray Bursts. *ARA&A*, 52:43–105, August 2014b. doi: 10.1146/annurev-astro-081913-035926.
- M. G. Bernardini, C. L. Bianco, L. Caito, P. Chardonnet, A. Corsi, M. G. Dainotti, F. Fraschetti, R. Guida, R. Ruffini, and S. S. Xue. GRB970228 as a prototype for short GRBs with afterglow. *Nuovo Cimento B Serie*, 121:1439–1440, December 2006. doi: 10.1393/ncb/i2007-10283-0.
- M. G. Bernardini, C. L. Bianco, L. Caito, M. G. Dainotti, R. Guida, and R. Ruffini. GRB 970228 and a class of GRBs with an initial spikelike emission. *A&A*, 474:L13–L16, October 2007. doi: 10.1051/0004-6361:20078300.
- M. G. Bernardini, R. Margutti, G. Chincarini, C. Guidorzi, and J. Mao. Gamma-ray burst long lasting X-ray flaring activity. *A&A*, 526:A27, February 2011. doi: 10.1051/0004-6361/201015703.
- M. G. Bernardini, R. Margutti, E. Zaninoni, and G. Chincarini. A universal scaling for short and long gamma-ray bursts: $E_{X,iso} - E_{iso} - E_{pk}$. *MNRAS*, 425:1199–1204, September 2012a. doi: 10.1111/j.1365-2966.2012.21487.x.
- M. G. Bernardini, R. Margutti, E. Zaninoni, and G. Chincarini. A universal scaling for short and long gamma-ray bursts: $E_{X,iso} - E_{iso} - E_{pk}$. *MNRAS*, 425:1199–1204, September 2012b. doi: 10.1111/j.1365-2966.2012.21487.x.
- A. Bernui, I. S. Ferreira, and C. A. Wuensche. On the Large-Scale Angular Distribution of Short Gamma-Ray Bursts. *ApJ*, 673:968–971, February 2008. doi: 10.1086/524678.

- M. Betoule, R. Kessler, J. Guy, J. Mosher, D. Hardin, R. Biswas, P. Astier, P. El-Hage, M. Konig, S. Kuhlmann, J. Marriner, R. Pain, N. Regnault, C. Balland, B. A. Bassett, P. J. Brown, H. Campbell, R. G. Carlberg, F. Cellier-Holzem, D. Cinabro, A. Conley, C. B. D'Andrea, D. L. DePoy, M. Doi, R. S. Ellis, S. Fabbro, A. V. Filippenko, R. J. Foley, J. A. Frieman, D. Fouchez, L. Galbany, A. Goobar, R. R. Gupta, G. J. Hill, R. Hlozek, C. J. Hogan, I. M. Hook, D. A. Howell, S. W. Jha, L. Le Guillou, G. Leloudas, C. Lidman, J. L. Marshall, A. Möller, A. M. Mourão, J. Neveu, R. Nichol, M. D. Olmstead, N. Palanque-Delabrouille, S. Perlmutter, J. L. Prieto, C. J. Pritchett, M. Richmond, A. G. Riess, V. Ruhlmann-Kleider, M. Sako, K. Schahmaneche, D. P. Schneider, M. Smith, J. Sollerman, M. Sullivan, N. A. Walton, and C. J. Wheeler. Improved cosmological constraints from a joint analysis of the SDSS-II and SNLS supernova samples. *A&A*, 568: A22, August 2014. doi: [10.1051/0004-6361/201423413](https://doi.org/10.1051/0004-6361/201423413).
- P. R. Bevington and D. K. Robinson. *Data reduction and error analysis for the physical sciences*. McGraw-Hill, 2003.
- R. D. Blandford and C. F. McKee. Fluid dynamics of relativistic blast waves. *Physics of Fluids*, 19:1130–1138, August 1976. doi: [10.1063/1.861619](https://doi.org/10.1063/1.861619).
- R. D. Blandford and R. L. Znajek. Electromagnetic extraction of energy from Kerr black holes. *MNRAS*, 179:433–456, May 1977.
- J. S. Bloom, D. A. Frail, and R. Sari. The Prompt Energy Release of Gamma-Ray Bursts using a Cosmological k-Correction. *AJ*, 121:2879–2888, June 2001. doi: [10.1086/321093](https://doi.org/10.1086/321093).
- G. Boella, R. C. Butler, G. C. Perola, L. Piro, L. Scarsi, and J. A. M. Bleeker. BeppoSAX, the wide band mission for X-ray astronomy. *A&AS*, 122, April 1997. doi: [10.1051/aas:1997136](https://doi.org/10.1051/aas:1997136).
- M. Boér and B. Gendre. Evidences for two Gamma-Ray Burst afterglow emission regimes. *A&A*, 361:L21–L24, September 2000.
- L. Borgonovo and F. Ryde. On the Hardness-Intensity Correlation in Gamma-Ray Burst Pulses. *ApJ*, 548:770–786, February 2001. doi: [10.1086/319008](https://doi.org/10.1086/319008).
- M. Böttcher and C. L. Fryer. X-Ray Spectral Features from Gamma-Ray Bursts: Predictions of Progenitor Models. *ApJ*, 547:338–344, January 2001. doi: [10.1086/318346](https://doi.org/10.1086/318346).
- Ž. Bošnjak and F. Daigne. Spectral evolution in gamma-ray bursts: Predictions of the internal shock model and comparison to observations. *A&A*, 568:A45, August 2014. doi: [10.1051/0004-6361/201322341](https://doi.org/10.1051/0004-6361/201322341).
- M. S. Briggs, W. S. Paciesas, G. N. Pendleton, C. A. Meegan, G. J. Fishman, J. M. Horack, M. N. Brock, C. Kouveliotou, D. H. Hartmann, and J. Hakkila. BATSE Observations of the Large-Scale Isotropy of Gamma-Ray Bursts. *ApJ*, 459:40, March 1996. doi: [10.1086/176867](https://doi.org/10.1086/176867).

- V. Bromm and A. Loeb. High-Redshift Gamma-Ray Bursts from Population III Progenitors. *ApJ*, 642:382–388, May 2006. doi: 10.1086/500799.
- J.M. Burgess. The Rest-Frame Golenetskii Correlation via a Hierarchical Bayesian Analysis. *MNRAS*, December 2015.
- D. N. Burrows, P. Romano, A. Falcone, S. Kobayashi, B. Zhang, A. Moretti, P. T. O’Brien, M. R. Goad, S. Campana, K. L. Page, L. Angelini, S. Barthelmy, A. P. Beardmore, M. Capalbi, G. Chincarini, J. Cummings, G. Cusumano, D. Fox, P. Giommi, J. E. Hill, J. A. Kennea, H. Krimm, V. Mangano, F. Marshall, P. Mészáros, D. C. Morris, J. A. Nousek, J. P. Osborne, C. Pagani, M. Perri, G. Tagliaferri, A. A. Wells, S. Woosley, and N. Gehrels. Bright X-ray Flares in Gamma-Ray Burst Afterglows. *Science*, 309:1833–1835, September 2005. doi: 10.1126/science.1116168.
- N. R. Butler, J. S. Bloom, and D. Poznanski. The Cosmic Rate, Luminosity Function, and Intrinsic Correlations of Long Gamma-Ray Bursts. *ApJ*, 711:495–516, March 2010. doi: 10.1088/0004-637X/711/1/495.
- L. Caito, M. G. Bernardini, C. L. Bianco, M. G. Dainotti, R. Guida, and R. Ruffini. GRB060614: a “fake” short GRB from a merging binary system. *A&A*, 498:501–507, May 2009. doi: 10.1051/0004-6361/200810676.
- J. Calcino and T. Davis. The need for accurate redshifts in supernova cosmology. *Journal of Cosmology and Astroparticle Physics*, 1:038, January 2017. doi: 10.1088/1475-7516/2017/01/038.
- J. K. Cannizzo and N. Gehrels. A New Paradigm for Gamma-ray Bursts: Long-term Accretion Rate Modulation by an External Accretion Disk. *ApJ*, 700:1047–1058, August 2009. doi: 10.1088/0004-637X/700/2/1047.
- J. K. Cannizzo, E. Troja, and N. Gehrels. Fall-back Disks in Long and Short Gamma-Ray Bursts. *ApJ*, 734:35, June 2011. doi: 10.1088/0004-637X/734/1/35.
- Z. Cano. Gamma-Ray Burst Supernovae as Standardizable Candles. *ApJ*, 794:121, October 2014. doi: 10.1088/0004-637X/794/2/121.
- Z. Cano, A. de Ugarte Postigo, A. Pozanenko, N. Butler, C. C. Thöne, C. Guidorzi, T. Krühler, J. Gorosabel, P. Jakobsson, G. Leloudas, D. Malesani, J. Hjorth, A. Melandri, C. Mundell, K. Wiersema, P. D’Avanzo, S. Schulze, A. Gomboc, A. Johansson, W. Zheng, D. A. Kann, F. Knust, K. Varela, C. W. Akerlof, J. Bloom, O. Burkhanov, E. Cooke, J. A. de Diego, G. Dhungana, C. Farina, F. V. Ferrante, H. A. Flewelling, O. D. Fox, J. Fynbo, N. Gehrels, L. Georgiev, J. J. González, J. Greiner, T. Güver, O. Hartoog, N. Hatch, M. Jelinek, R. Kehoe, S. Klose, E. Klunko, D. Kopač, A. Kutyrev, Y. Krugly, W. H. Lee, A. Levan, V. Linkov, A. Matkin, N. Minikulov, I. Molotov, J. X. Prochaska, M. G. Richer, C. G. Román-Zúñiga, V. Rumyantsev, R. Sánchez-Ramírez, I. Steele, N. R. Tanvir, A. Volnova,

- A. M. Watson, D. Xu, and F. Yuan. A trio of gamma-ray burst supernovae: GRB 120729A, GRB 130215A/SN 2013ez, and GRB 130831A/SN 2013fu. *A&A*, 568:A19, August 2014. doi: 10.1051/0004-6361/201423920.
- Z. Cano, L. Izzo, A. de Ugarte Postigo, C. C. Thöne, T. Krühler, K. E. Heintz, D. Malesani, S. Geier, C. Fuentes, T.-W. Chen, S. Covino, V. D'Elia, J. P. U. Fynbo, P. Goldoni, A. Gomboc, J. Hjorth, P. Jakobsson, D. A. Kann, B. Milvang-Jensen, G. Pugliese, R. Sánchez-Ramírez, S. Schulze, J. Sollerman, N. R. Tanvir, and K. Wiersema. GRB 161219B/SN 2016jca: A low-redshift gamma-ray burst supernova powered by radioactive heating. *A&A*, 605:A107, September 2017. doi: 10.1051/0004-6361/201731005.
- S. Capozziello and L. Izzo. Cosmography by gamma ray bursts. *A&A*, 490:31–36, October 2008. doi: 10.1051/0004-6361:200810337.
- V. F. Cardone, S. Capozziello, and M. G. Dainotti. An updated gamma-ray bursts Hubble diagram. *MNRAS*, 400:775–790, December 2009. doi: 10.1111/j.1365-2966.2009.15456.x.
- V. F. Cardone, M. G. Dainotti, S. Capozziello, and R. Willingale. Constraining cosmological parameters by gamma-ray burst X-ray afterglow light curves. *MNRAS*, 408:1181–1186, October 2010. doi: 10.1111/j.1365-2966.2010.17197.x.
- J. Carson. GLAST: physics goals and instrument status. In F. Halzen, A. Karle, and T. Montaruli, editors, *Journal of Physics Conference Series*, volume 60 of *Journal of Physics Conference Series*, pages 115–118, March 2007. doi: 10.1088/1742-6596/60/1/020.
- G. Cavallo and M. J. Rees. A qualitative study of cosmic fireballs and gamma-ray bursts. *MNRAS*, 183:359–365, May 1978a. doi: 10.1093/mnras/183.3.359.
- G. Cavallo and M. J. Rees. A qualitative study of cosmic fireballs and gamma-ray bursts. *MNRAS*, 183:359–365, May 1978b. doi: 10.1093/mnras/183.3.359.
- C. Ceccobello and P. Kumar. Inverse-Compton drag on a highly magnetized GRB jet in stellar envelope. *MNRAS*, 449:2566–2575, May 2015. doi: 10.1093/mnras/stv457.
- S. B. Cenko, J. Kelemen, F. A. Harrison, D. B. Fox, S. R. Kulkarni, M. M. Kasliwal, E. O. Ofek, A. Rau, A. Gal-Yam, D. A. Frail, and D.-S. Moon. Dark Bursts in the Swift Era: The Palomar 60 Inch-Swift Early Optical Afterglow Catalog. *ApJ*, 693:1484–1493, March 2009. doi: 10.1088/0004-637X/693/2/1484.
- M. Chevallier and D. Polarski. Accelerating Universes with Scaling Dark Matter. *International Journal of Modern Physics D*, 10:213–223, 2001. doi: 10.1142/S0218271801000822.
- G. Chincarini, A. Moretti, P. Romano, A. D. Falcone, D. Morris, J. Racusin, S. Campana, S. Covino, C. Guidorzi, G. Tagliaferri, D. N. Burrows, C. Pagani, M. Stroh, D. Grupe, M. Capalbi, G. Cusumano, N. Gehrels, P. Giommi, V. La Parola, V. Mangano, T. Mineo, J. A. Nousek, P. T. O'Brien, K. L. Page, M. Perri, E. Troja, R. Willingale, and B. Zhang.

- The First Survey of X-Ray Flares from Gamma-Ray Bursts Observed by Swift: Temporal Properties and Morphology. *ApJ*, 671:1903–1920, December 2007. doi: 10.1086/521591.
- A. C. Collazzi, B. E. Schaefer, and J. A. Moree. The Total Errors in Measuring E_{peak} for Gamma-ray Bursts. *ApJ*, 729:89, March 2011. doi: 10.1088/0004-637X/729/2/89.
- V. Connaughton, E. Burns, A. Goldstein, L. Blackburn, M. S. Briggs, B.-B. Zhang, J. Camp, N. Christensen, C. M. Hui, P. Jenke, T. Littenberg, J. E. McEnery, J. Racusin, P. Shawhan, L. Singer, J. Veitch, C. A. Wilson-Hodge, P. N. Bhat, E. Bissaldi, W. Cleveland, G. Fitzpatrick, M. M. Giles, M. H. Gibby, A. von Kienlin, R. M. Kippen, S. McBreen, B. Mailyan, C. A. Meegan, W. S. Paciesas, R. D. Preece, O. J. Roberts, L. Sparke, M. Stanbro, K. Toelge, and P. Veres. Fermi GBM Observations of LIGO Gravitational-wave Event GW150914. *ApJ*, 826:L6, July 2016. doi: 10.3847/2041-8205/826/1/L6.
- B. Cordier, J. Wei, and J.L. et al. Atteia. The SVOM gamma-ray burst mission. *Proceedings of the conference Swift: 10 Years of Discovery*, January 2015.
- E. Costa, F. Frontera, J. Heise, M. Feroci, J. in't Zand, F. Fiore, M. N. Cinti, D. Dal Fiume, L. Nicastro, M. Orlandini, E. Palazzi, M. Rapisarda, G. Zavattini, R. Jager, A. Parmar, A. Owens, S. Molendi, G. Cusumano, M. C. Maccarone, S. Giarrusso, A. Coletta, L. A. Antonelli, P. Giommi, J. M. Muller, L. Piro, and R. C. Butler. Discovery of an X-ray afterglow associated with the γ -ray burst of 28 February 1997. *Nature*, 387:783–785, June 1997. doi: 10.1038/42885.
- A. Cucchiara, A. J. Levan, D. B. Fox, N. R. Tanvir, T. N. Ukwatta, E. Berger, T. Krühler, A. Küpcü Yoldaş, X. F. Wu, K. Toma, J. Greiner, F. E. Olivares, A. Rowlinson, L. Amati, T. Sakamoto, K. Roth, A. Stephens, A. Fritz, J. P. U. Fynbo, J. Hjorth, D. Malesani, P. Jakobsson, K. Wiersema, P. T. O'Brien, A. M. Soderberg, R. J. Foley, A. S. Fruchter, J. Rhoads, R. E. Rutledge, B. P. Schmidt, M. A. Dopita, P. Podsiadlowski, R. Willingale, C. Wolf, S. R. Kulkarni, and P. D'Avanzo. A Photometric Redshift of $z \sim 9.4$ for GRB 090429B. *ApJ*, 736:7, July 2011. doi: 10.1088/0004-637X/736/1/7.
- G. D'Agostini. Fits, and especially linear fits, with errors on both axes, extra variance of the data points and other complications. *ArXiv Physics e-prints*, November 2005.
- Z. G. Dai and T. Lu. Gamma-ray burst afterglows and evolution of postburst fireballs with energy injection from strongly magnetic millisecond pulsars. *A&A*, 333:L87–L90, May 1998.
- Z. G. Dai, E. W. Liang, and D. Xu. Constraining Ω_M and Dark Energy with Gamma-Ray Bursts. *ApJ*, 612:L101–L104, September 2004. doi: 10.1086/424694.
- F. Daigne and R. Mochkovitch. Gamma-ray bursts from internal shocks in a relativistic wind: temporal and spectral properties. *MNRAS*, 296:275–286, May 1998. doi: 10.1046/j.1365-8711.1998.01305.x.

- F. Daigne and R. Mochkovitch. The physics of pulses in gamma-ray bursts: emission processes, temporal profiles and time-lags. *MNRAS*, 342:587–592, June 2003. doi: 10.1046/j.1365-8711.2003.06575.x.
- M. Dainotti, V. Petrosian, R. Willingale, P. O’Brien, M. Ostrowski, and S. Nagataki. Luminosity-time and luminosity-luminosity correlations for GRB prompt and afterglow plateau emissions. *MNRAS*, 451:3898–3908, August 2015a. doi: 10.1093/mnras/stv1229.
- M. G. Dainotti and R. Del Vecchio. Gamma Ray Burst afterglow and prompt-afterglow relations: An overview. *New A Rev.*, 77:23–61, April 2017. doi: 10.1016/j.newar.2017.04.001.
- M. G. Dainotti, M. G. Bernardini, C. L. Bianco, L. Caito, R. Guida, and R. Ruffini. GRB 060218 and GRBs associated with supernovae Ib/c. *A&A*, 471:L29–L32, August 2007. doi: 10.1051/0004-6361:20078068.
- M. G. Dainotti, V. F. Cardone, and S. Capozziello. A time-luminosity correlation for γ -ray bursts in the X-rays. *MNRAS*, 391:L79–L83, November 2008. doi: 10.1111/j.1745-3933.2008.00560.x.
- M. G. Dainotti, R. Willingale, S. Capozziello, V. Fabrizio Cardone, and M. Ostrowski. Discovery of a Tight Correlation for Gamma-ray Burst Afterglows with "Canonical" Light Curves. *ApJ*, 722:L215–L219, October 2010. doi: 10.1088/2041-8205/722/2/L215.
- M. G. Dainotti, V. Fabrizio Cardone, S. Capozziello, M. Ostrowski, and R. Willingale. Study of Possible Systematics in the $L^*_X-T^*_a$ Correlation of Gamma-ray Bursts. *ApJ*, 730:135, April 2011a. doi: 10.1088/0004-637X/730/2/135.
- M. G. Dainotti, M. Ostrowski, and R. Willingale. Towards a standard gamma-ray burst: tight correlations between the prompt and the afterglow plateau phase emission. *MNRAS*, 418:2202–2206, December 2011b. doi: 10.1111/j.1365-2966.2011.19433.x.
- M. G. Dainotti, V. F. Cardone, E. Piedipalumbo, and S. Capozziello. Slope evolution of GRB correlations and cosmology. *MNRAS*, 436:82–88, November 2013a. doi: 10.1093/mnras/stt1516.
- M. G. Dainotti, V. Petrosian, J. Singal, and M. Ostrowski. Determination of the Intrinsic Luminosity Time Correlation in the X-Ray Afterglows of Gamma-Ray Bursts. *ApJ*, 774:157, September 2013b. doi: 10.1088/0004-637X/774/2/157.
- M. G. Dainotti, R. Del Vecchio, S. Nagataki, and S. Capozziello. Selection Effects in Gamma-Ray Burst Correlations: Consequences on the Ratio between Gamma-Ray Burst and Star Formation Rates. *ApJ*, 800:31, February 2015b. doi: 10.1088/0004-637X/800/1/31.
- M. G. Dainotti, S. Postnikov, X. Hernandez, and M. Ostrowski. A Fundamental Plane for Long Gamma-Ray Bursts with X-Ray Plateaus. *ApJ*, 825:L20, July 2016. doi: 10.3847/2041-8205/825/2/L20.

- M. G. Dainotti, X. Hernandez, S. Postnikov, S. Nagataki, P. O'brien, R. Willingale, and S. Striegel. A Study of the Gamma-Ray Burst Fundamental Plane. *ApJ*, 848:88, October 2017a. doi: 10.3847/1538-4357/aa8a6b.
- M. G. Dainotti, S. Nagataki, K. Maeda, S. Postnikov, and E. Pian. A study of gamma ray bursts with afterglow plateau phases associated with supernovae. *A&A*, 600:A98, April 2017b. doi: 10.1051/0004-6361/201628384.
- M. G. Dainotti, R. Del Vecchio, and M. Tarnopolski. Gamma-Ray Burst Prompt Correlations. *Advances in Astronomy*, 2018:4969503, 2018. doi: 10.1155/2018/4969503.
- V. D'Alessio and L. Piro. General properties of X-Ray Riches and X-Ray Flashes in comparison with Gamma-Ray Bursts. *Nuovo Cimento C Geophysics Space Physics C*, 28: 497, July 2005. doi: 10.1393/ncc/i2005-10092-6.
- S. Dall'Osso, G. Stratta, D. Guetta, S. Covino, G. De Cesare, and L. Stella. Gamma-ray bursts afterglows with energy injection from a spinning down neutron star. *A&A*, 526: A121, February 2011. doi: 10.1051/0004-6361/201014168.
- P. D'Avanzo, R. Salvaterra, B. Sbarufatti, L. Nava, A. Melandri, M. G. Bernardini, S. Campana, S. Covino, D. Fugazza, G. Ghirlanda, G. Ghisellini, V. L. Parola, M. Perri, S. D. Vergani, and G. Tagliaferri. A complete sample of bright Swift Gamma-ray bursts: X-ray afterglow luminosity and its correlation with the prompt emission. *MNRAS*, 425:506–513, September 2012. doi: 10.1111/j.1365-2966.2012.21489.x.
- T. M. Davis, E. Mörtsell, J. Sollerman, A. C. Becker, S. Blondin, P. Challis, A. Clocchiatti, A. V. Filippenko, R. J. Foley, P. M. Garnavich, S. Jha, K. Krisciunas, R. P. Kirshner, B. Leibundgut, W. Li, T. Matheson, G. Miknaitis, G. Pignata, A. Rest, A. G. Riess, B. P. Schmidt, R. C. Smith, J. Spyromilio, C. W. Stubbs, N. B. Suntzeff, J. L. Tonry, W. M. Wood-Vasey, and A. Zenteno. Scrutinizing Exotic Cosmological Models Using ESSENCE Supernova Data Combined with Other Cosmological Probes. *ApJ*, 666:716–725, September 2007. doi: 10.1086/519988.
- R. S. de Souza, N. Yoshida, and K. Ioka. Populations III.1 and III.2 gamma-ray bursts: constraints on the event rate for future radio and X-ray surveys. *A&A*, 533:A32, September 2011. doi: 10.1051/0004-6361/201117242.
- H. Dekker, S. D'Odorico, A. Kaufer, B. Delabre, and H. Kotzlowski. Design, construction, and performance of UVES, the echelle spectrograph for the UT2 Kueyen Telescope at the ESO Paranal Observatory. In M. Iye and A. F. Moorwood, editors, *Optical and IR Telescope Instrumentation and Detectors*, volume 4008 of Proc. SPIE, pages 534–545, August 2000. doi: 10.1117/12.395512.
- R. Del Vecchio, M. G. Dainotti, and M. Ostrowski. Study of GRB Light-curve Decay Indices in the Afterglow Phase. *ApJ*, 828:36, September 2016. doi: 10.3847/0004-637X/828/1/36.

- M. Della Valle and M. Livio. On the progenitors of type IA supernovae in early-type and late-type galaxies. *ApJ*, 423:L31–L33, March 1994. doi: 10.1086/187228.
- M. Della Valle, D. Malesani, S. Benetti, G. Chincarini, L. Stella, and G. Tagliaferri. Supernova 2005nc and GRB 050525A. *IAU Circ.*, 8696:1, March 2006.
- M. Demianski, E. Piedipalumbo, D. Sawant, and L. Amati. Cosmology with gamma-ray bursts. I. The Hubble diagram through the calibrated $E_{p,I}$ - E_{iso} correlation. *A&A*, 598: A112, February 2017. doi: 10.1051/0004-6361/201628909.
- J. Deng, P. A. Mazzali, K. Maeda, and K. Nomoto. The type Ic hypernova SN 2002ap. *Nuclear Physics A*, 718:569–571, May 2003. doi: 10.1016/S0375-9474(03)00855-8.
- C. D. Dermer. Rapid X-Ray Declines and Plateaus in Swift GRB Light Curves Explained by a Highly Radiative Blast Wave. *ApJ*, 664:384–396, July 2007. doi: 10.1086/518996.
- P. C. Duffell and A. I. MacFadyen. From Engine to Afterglow: Collapsars Naturally Produce Top-heavy Jets and Early-time Plateaus in Gamma-Ray Burst Afterglows. *ApJ*, 806:205, June 2015. doi: 10.1088/0004-637X/806/2/205.
- R. C. Duncan and C. Thompson. Formation of very strongly magnetized neutron stars - Implications for gamma-ray bursts. *ApJ*, 392:L9–L13, June 1992. doi: 10.1086/186413.
- B. Efron and V. Petrosian. A simple test of independence for truncated data with applications to redshift surveys. *ApJ*, 399:345–352, November 1992. doi: 10.1086/171931.
- B. Efron and V. Petrosian. Testing Isotropy versus Clustering of Gamma-Ray Bursts. *ApJ*, 449:216, August 1995. doi: 10.1086/176048.
- D. Eichler, M. Livio, T. Piran, and D. N. Schramm. Nucleosynthesis, neutrino bursts and gamma-rays from coalescing neutron stars. *Nature*, 340:126–128, July 1989. doi: 10.1038/340126a0.
- P. A. Evans, A. P. Beardmore, K. L. Page, J. P. Osborne, P. T. O’Brien, R. Willingale, R. L. C. Starling, D. N. Burrows, O. Godet, L. Vetere, J. Racusin, M. R. Goad, K. Wiersema, L. Angelini, M. Capalbi, G. Chincarini, N. Gehrels, J. A. Kennea, R. Margutti, D. C. Morris, C. J. Mountford, C. Pagani, M. Perri, P. Romano, and N. Tanvir. Methods and results of an automatic analysis of a complete sample of Swift-XRT observations of GRBs. *MNRAS*, 397:1177–1201, August 2009. doi: 10.1111/j.1365-2966.2009.14913.x.
- P. A. Evans, R. Willingale, J. P. Osborne, P. T. O’Brien, N. R. Tanvir, D. D. Frederiks, V. D. Pal’shin, D. S. Svinkin, A. Lien, J. Cummings, S. Xiong, B.-B. Zhang, D. Götz, V. Savchenko, H. Negoro, S. Nakahira, K. Suzuki, K. Wiersema, R. L. C. Starling, A. J. Castro-Tirado, A. P. Beardmore, R. Sánchez-Ramírez, J. Gorosabel, S. Jeong, J. A. Kennea, D. N. Burrows, and N. Gehrels. GRB 130925A: an ultralong gamma ray burst with a dust-echo afterglow, and implications for the origin of the ultralong GRBs. *MNRAS*, 444:250–267, October 2014. doi: 10.1093/mnras/stu1459.

- P. A. Evans, J. A. Kennea, S. D. Barthelmy, A. P. Beardmore, D. N. Burrows, S. Campana, S. B. Cenko, N. Gehrels, P. Giommi, C. Gronwall, F. E. Marshall, D. Malesani, C. B. Markwardt, B. Mingo, J. A. Nousek, P. T. O'Brien, J. P. Osborne, C. Pagani, K. L. Page, D. M. Palmer, M. Perri, J. L. Racusin, M. H. Siegel, B. Sbarufatti, and G. Tagliaferri. Swift follow-up of the Gravitational Wave source GW150914. *MNRAS*, April 2016. doi: 10.1093/mnrasl/slw065.
- Y.-Z. Fan. The spectrum of γ -ray burst: a clue. *MNRAS*, 403:483–490, March 2010. doi: 10.1111/j.1365-2966.2009.16134.x.
- E. E. Fenimore and E. Ramirez-Ruiz. Redshifts For 220 BATSE Gamma-Ray Bursts Determined by Variability and the Cosmological Consequences. *ArXiv Astrophysics e-prints*, April 2000.
- E. E. Fenimore, J. J. M. in 't Zand, J. P. Norris, J. T. Bonnell, and R. J. Nemiroff. Gamma-Ray Burst Peak Duration as a Function of Energy. *ApJ*, 448:L101, August 1995. doi: 10.1086/309603.
- E. E. Fenimore, C. D. Madras, and S. Nayakshin. Expanding Relativistic Shells and Gamma-Ray Burst Temporal Structure. *ApJ*, 473:998, December 1996. doi: 10.1086/178210.
- A. V. Filippenko. Supernova 1987K - Type II in youth, type Ib in old age. *AJ*, 96:1941–1948, December 1988. doi: 10.1086/114940.
- A. V. Filippenko. Supernovae and Their Massive Star Progenitors. In R. Humphreys and K. Stanek, editors, *The Fate of the Most Massive Stars*, volume 332 of *Astronomical Society of the Pacific Conference Series*, page 34, September 2005.
- M. Fink, W. Hillebrandt, and F. K. Röpke. Double-detonation supernovae of sub-Chandrasekhar mass white dwarfs. *A&A*, 476:1133–1143, December 2007. doi: 10.1051/0004-6361:20078438.
- C. Firmani, G. Ghisellini, G. Ghirlanda, and V. Avila-Reese. A new method optimized to use gamma-ray bursts as cosmic rulers. *MNRAS*, 360:L1–L5, June 2005. doi: 10.1111/j.1745-3933.2005.00023.x.
- C. Firmani, G. Ghisellini, V. Avila-Reese, and G. Ghirlanda. Discovery of a tight correlation among the prompt emission properties of long gamma-ray bursts. *MNRAS*, 370:185–197, July 2006. doi: 10.1111/j.1365-2966.2006.10445.x.
- C. Firmani, V. Avila-Reese, G. Ghisellini, and G. Ghirlanda. Long Gamma-Ray Burst prompt emission properties as a cosmological tool. *Rev. Mexicana Astron. Astrofis.*, 43: 203–216, April 2007.
- G. J. Fishman and C. A. Meegan. Gamma-Ray Bursts. *ARA&A*, 33:415–458, 1995. doi: 10.1146/annurev.aa.33.090195.002215.

- G. J. Fishman, C. A. Meegan, R. B. Wilson, M. N. Brock, J. M. Horack, C. Kouveliotou, S. Howard, W. S. Paciesas, M. S. Briggs, G. N. Pendleton, T. M. Koshut, R. S. Mallozzi, M. Stollberg, and J. P. Lestrade. The first BATSE gamma-ray burst catalog. *ApJS*, 92: 229–283, May 1994. doi: 10.1086/191968.
- D. B. Fox, D. A. Frail, P. A. Price, S. R. Kulkarni, E. Berger, T. Piran, A. M. Soderberg, S. B. Cenko, P. B. Cameron, A. Gal-Yam, M. M. Kasliwal, D.-S. Moon, F. A. Harrison, E. Nakar, B. P. Schmidt, B. Penprase, R. A. Chevalier, P. Kumar, K. Roth, D. Watson, B. L. Lee, S. Shectman, M. M. Phillips, M. Roth, P. J. McCarthy, M. Rauch, L. Cowie, B. A. Peterson, J. Rich, N. Kawai, K. Aoki, G. Kosugi, T. Totani, H.-S. Park, A. MacFadyen, and K. C. Hurley. The afterglow of GRB 050709 and the nature of the short-hard γ -ray bursts. *Nature*, 437:845–850, October 2005. doi: 10.1038/nature04189.
- D. A. Frail, S. R. Kulkarni, R. Sari, S. G. Djorgovski, J. S. Bloom, T. J. Galama, D. E. Reichart, E. Berger, F. A. Harrison, P. A. Price, S. A. Yost, A. Diercks, R. W. Goodrich, and F. Chaffee. Beaming in Gamma-Ray Bursts: Evidence for a Standard Energy Reservoir. *ApJ*, 562:L55–L58, November 2001. doi: 10.1086/338119.
- D. L. Freedman and E. Waxman. On the Energy of Gamma-Ray Bursts. *ApJ*, 547:922–928, February 2001. doi: 10.1086/318386.
- F. Frontera, L. Amati, E. Costa, J. M. Muller, E. Pian, L. Piro, P. Soffitta, M. Tavani, A. Castro-Tirado, D. Dal Fiume, M. Feroci, J. Heise, N. Masetti, L. Nicastro, M. Orlandini, E. Palazzi, and R. Sari. Prompt and Delayed Emission Properties of Gamma-Ray Bursts Observed with BeppoSAX. *ApJS*, 127:59–78, March 2000. doi: 10.1086/313316.
- F. Frontera, L. Amati, C. Guidorzi, R. Landi, and J. in't Zand. Broadband Time-resolved $E_{p,i} - L_{iso}$ Correlation in Gamma-Ray Bursts. *ApJ*, 754:138, August 2012. doi: 10.1088/0004-637X/754/2/138.
- F. Frontera, L. Amati, R. Farinelli, S. Dichiara, C. Guidorzi, R. Landi, and L. Titarchuk. Possible physical explanation of the intrinsic $E_{p,i}$ –”intensity” correlation commonly used to ”standardize” GRBs. *International Journal of Modern Physics D*, 25:1630014, March 2016. doi: 10.1142/S0218271816300147.
- A. Fruchter. Gamma-Ray Bursts and their Host Environments. HST Proposal, July 2000.
- C. L. Fryer, S. E. Woosley, and D. H. Hartmann. Formation Rates of Black Hole Accretion Disk Gamma-Ray Bursts. *ApJ*, 526:152–177, November 1999a. doi: 10.1086/307992.
- C. L. Fryer, S. E. Woosley, M. Herant, and M. B. Davies. Merging White Dwarf/Black Hole Binaries and Gamma-Ray Bursts. *ApJ*, 520:650–660, August 1999b. doi: 10.1086/307467.
- J. P. U. Fynbo, D. Watson, C. C. Thöne, J. Sollerman, J. S. Bloom, T. M. Davis, J. Hjorth, P. Jakobsson, U. G. Jørgensen, J. F. Graham, A. S. Fruchter, D. Bersier, L. Kewley, A. Cassan, J. M. Castro Cerón, S. Foley, J. Gorosabel, T. C. Hinse, K. D. Horne, B. L.

Jensen, S. Klose, D. Kocevski, J.-B. Marquette, D. Perley, E. Ramirez-Ruiz, M. D. Stritzinger, P. M. Vreeswijk, R. A. M. Wijers, K. G. Woller, D. Xu, and M. Zub. No supernovae associated with two long-duration γ -ray bursts. *Nature*, 444:1047–1049, December 2006. doi: 10.1038/nature05375.

T. J. Galama, P. M. Vreeswijk, J. van Paradijs, C. Kouveliotou, T. Augusteijn, H. Böhnhardt, J. P. Brewer, V. Doublier, J.-F. Gonzalez, B. Leibundgut, C. Lidman, O. R. Hainaut, F. Patat, J. Heise, J. in't Zand, K. Hurley, P. J. Groot, R. G. Strom, P. A. Mazzali, K. Iwamoto, K. Nomoto, H. Umeda, T. Nakamura, T. R. Young, T. Suzuki, T. Shigeyama, T. Koshut, M. Kippen, C. Robinson, P. de Wildt, R. A. M. J. Wijers, N. Tanvir, J. Greiner, E. Pian, E. Palazzi, F. Frontera, N. Masetti, L. Nicastro, M. Feroci, E. Costa, L. Piro, B. A. Peterson, C. Tinney, B. Boyle, R. Cannon, R. Stathakis, E. Sadler, M. C. Begam, and P. Ianna. An unusual supernova in the error box of the γ -ray burst of 25 April 1998. *Nature*, 395:670–672, October 1998. doi: 10.1038/27150.

N. Gehrels and S. Razzaque. Gamma-ray bursts in the Swift-Fermi era. *Frontiers of Physics*, 8:661–678, December 2013. doi: 10.1007/s11467-013-0282-3.

N. Gehrels, G. Chincarini, P. Giommi, K. O. Mason, J. A. Nousek, A. A. Wells, N. E. White, S. D. Barthelmy, D. N. Burrows, L. R. Cominsky, K. C. Hurley, F. E. Marshall, P. Mészáros, P. W. A. Roming, L. Angelini, L. M. Barbier, T. Belloni, S. Campana, P. A. Caraveo, M. M. Chester, O. Citterio, T. L. Cline, M. S. Cropper, J. R. Cummings, A. J. Dean, E. D. Feigelson, E. E. Fenimore, D. A. Frail, A. S. Fruchter, G. P. Garmire, K. Gendreau, G. Ghisellini, J. Greiner, J. E. Hill, S. D. Hunsberger, H. A. Krimm, S. R. Kulkarni, P. Kumar, F. Lebrun, N. M. Lloyd-Ronning, C. B. Markwardt, B. J. Mattson, R. F. Mushotzky, J. P. Norris, J. Osborne, B. Paczynski, D. M. Palmer, H.-S. Park, A. M. Parsons, J. Paul, M. J. Rees, C. S. Reynolds, J. E. Rhoads, T. P. Sasseen, B. E. Schaefer, A. T. Short, A. P. Smale, I. A. Smith, L. Stella, G. Tagliaferri, T. Takahashi, M. Tashiro, L. K. Townsley, J. Tueller, M. J. L. Turner, M. Vietri, W. Voges, M. J. Ward, R. Willingale, F. M. Zerbi, and W. W. Zhang. The Swift Gamma-Ray Burst Mission. *ApJ*, 611:1005–1020, August 2004. doi: 10.1086/422091.

N. Gehrels, J. P. Norris, S. D. Barthelmy, J. Granot, Y. Kaneko, C. Kouveliotou, C. B. Markwardt, P. Mészáros, E. Nakar, J. A. Nousek, P. T. O'Brien, M. Page, D. M. Palmer, A. M. Parsons, P. W. A. Roming, T. Sakamoto, C. L. Sarazin, P. Schady, M. Stamatikos, and S. E. Woosley. A new γ -ray burst classification scheme from GRB060614. *Nature*, 444:1044–1046, December 2006. doi: 10.1038/nature05376.

N. Gehrels, S. D. Barthelmy, D. N. Burrows, J. K. Cannizzo, G. Chincarini, E. Fenimore, C. Kouveliotou, P. O'Brien, D. M. Palmer, J. Racusin, P. W. A. Roming, T. Sakamoto, J. Tueller, R. A. M. J. Wijers, and B. Zhang. Correlations of Prompt and Afterglow Emission in Swift Long and Short Gamma-Ray Bursts. *ApJ*, 689:1161–1172, December 2008. doi: 10.1086/592766.

- N. Gehrels, E. Ramirez-Ruiz, and D. B. Fox. Gamma-Ray Bursts in the Swift Era. *ARA&A*, 47:567–617, September 2009. doi: 10.1146/annurev.astro.46.060407.145147.
- Neil Gehrels. Short GRB Prompt and Afterglow Correlations. 2007. URL :<https://ntrs.nasa.gov/archive/nasa/casi.ntrs.nasa.gov/20080045485.pdf>.
- B. Gendre, A. Galli, and M. Boér. X-Ray Afterglow Light Curves: Toward A Standard Candle? *ApJ*, 683:620–629, August 2008. doi: 10.1086/589805.
- F. Genet and J. Granot. Realistic analytic model for the prompt and high-latitude emission in GRBs. *MNRAS*, 399:1328–1346, November 2009. doi: 10.1111/j.1365-2966.2009.15355.x.
- F. Genet, F. Daigne, and R. Mochkovitch. Can the early X-ray afterglow of gamma-ray bursts be explained by a contribution from the reverse shock? *MNRAS*, 381:732–740, October 2007. doi: 10.1111/j.1365-2966.2007.12243.x.
- G. Ghirlanda. Advances on GRB as cosmological tools. In G. Giobbi, A. Tornambe, G. Raimondo, M. Limongi, L. A. Antonelli, N. Menci, and E. Brocato, editors, *American Institute of Physics Conference Series*, volume 1111 of *American Institute of Physics Conference Series*, pages 579–586, May 2009. doi: 10.1063/1.3141613.
- G. Ghirlanda, A. Celotti, and G. Ghisellini. Extremely hard GRB spectra prune down the forest of emission models. *A&A*, 406:879–892, August 2003. doi: 10.1051/0004-6361:20030803.
- G. Ghirlanda, G. Ghisellini, and A. Celotti. The spectra of short gamma-ray bursts. *A&A*, 422:L55–L58, July 2004a. doi: 10.1051/0004-6361:20048008.
- G. Ghirlanda, G. Ghisellini, and D. Lazzati. The Collimation-corrected Gamma-Ray Burst Energies Correlate with the Peak Energy of Their νF_ν Spectrum. *ApJ*, 616:331–338, November 2004b. doi: 10.1086/424913.
- G. Ghirlanda, G. Ghisellini, and C. Firmani. Probing the existence of the E_{peak} - E_{iso} correlation in long gamma ray bursts. *MNRAS*, 361:L10–L14, July 2005a. doi: 10.1111/j.1745-3933.2005.00053.x.
- G. Ghirlanda, G. Ghisellini, C. Firmani, A. Celotti, and Z. Bosnjak. The peak luminosity-peak energy correlation in gamma-ray bursts. *MNRAS*, 360:L45–L49, June 2005b. doi: 10.1111/j.1745-3933.2005.00043.x.
- G. Ghirlanda, G. Ghisellini, and C. Firmani. Gamma-ray bursts as standard candles to constrain the cosmological parameters. *New Journal of Physics*, 8:123, July 2006. doi: 10.1088/1367-2630/8/7/123.
- G. Ghirlanda, L. Nava, G. Ghisellini, and C. Firmani. Confirming the γ -ray burst spectral-energy correlations in the era of multiple time breaks. *A&A*, 466:127–136, April 2007. doi: 10.1051/0004-6361:20077119.

- G. Ghirlanda, L. Nava, G. Ghisellini, C. Firmani, and J. I. Cabrera. The E_{peak} - E_{iso} plane of long gamma-ray bursts and selection effects. *MNRAS*, 387:319–330, June 2008. doi: 10.1111/j.1365-2966.2008.13232.x.
- G. Ghirlanda, L. Nava, G. Ghisellini, A. Celotti, and C. Firmani. Short versus long gamma-ray bursts: spectra, energetics, and luminosities. *A&A*, 496:585–595, March 2009. doi: 10.1051/0004-6361/200811209.
- G. Ghirlanda, L. Nava, and G. Ghisellini. Spectral-luminosity relation within individual Fermi gamma rays bursts. *A&A*, 511:A43, February 2010. doi: 10.1051/0004-6361/200913134.
- G. Ghirlanda, G. Ghisellini, L. Nava, and D. Burlon. Spectral evolution of Fermi/GBM short gamma-ray bursts. *MNRAS*, 410:L47–L51, January 2011. doi: 10.1111/j.1745-3933.2010.00977.x.
- G. Ghirlanda, G. Ghisellini, R. Salvaterra, L. Nava, D. Burlon, G. Tagliaferri, S. Campana, P. D’Avanzo, and A. Melandri. The faster the narrower: characteristic bulk velocities and jet opening angles of gamma-ray bursts. *MNRAS*, 428:1410–1423, January 2013. doi: 10.1093/mnras/sts128.
- G. Ghisellini, M. Nardini, G. Ghirlanda, and A. Celotti. A unifying view of gamma-ray burst afterglows. *MNRAS*, 393:253–271, February 2009. doi: 10.1111/j.1365-2966.2008.14214.x.
- D. Giannios. Prompt emission spectra from the photosphere of a GRB. *A&A*, 457:763–770, October 2006. doi: 10.1051/0004-6361:20065000.
- D. Giannios. Prompt GRB emission from gradual energy dissipation. *A&A*, 480:305–312, March 2008. doi: 10.1051/0004-6361:20079085.
- A. Goldstein, R. D. Preece, and M. S. Briggs. A New Discriminator for Gamma-ray Burst Classification: The E_{peak} -fluence Energy Ratio. *ApJ*, 721:1329–1332, October 2010. doi: 10.1088/0004-637X/721/2/1329.
- A. Goldstein, V. Connaughton, M. S. Briggs, and E. Burns. Estimating Long GRB Jet Opening Angles and Rest-frame Energetics. *ApJ*, 818:18, February 2016. doi: 10.3847/0004-637X/818/1/18.
- S. V. Golenetskii, E. P. Mazets, R. L. Aptekar, and V. N. Ilinskii. Correlation between luminosity and temperature in gamma-ray burst sources. *Nature*, 306:451–453, December 1983. doi: 10.1038/306451a0.
- Golkhou, V. Zach, and N. Butler. Uncovering the Intrinsic Variability of Gamma-Ray Bursts. *ApJ*, 787:90–99, May 2014. doi: 10.1088/0004-637X/787/1/90.
- Golkhou, V. Zach, N. Butler, J. Littlejohns, and M. Owen. The Energy Dependence of GRB Minimum Variability Timescales. *ApJ*, 811:93–104, January 2015. doi: 10.1088/0004-637X/811/2/93.

- B. Gompertz and A. Fruchter. Magnetars in Ultra-Long Gamma-Ray Bursts and GRB 111209A. *ApJ*, 839:49, April 2017. doi: 10.3847/1538-4357/aa6629.
- B. P. Gompertz, P. T. O'Brien, G. A. Wynn, and A. Rowlinson. Can magnetar spin-down power extended emission in some short GRBs? *MNRAS*, 431:1745–1751, May 2013. doi: 10.1093/mnras/stt293.
- M. M. González, B. L. Dingus, Y. Kaneko, R. D. Preece, C. D. Dermer, and M. S. Briggs. A γ -ray burst with a high-energy spectral component inconsistent with the synchrotron shock model. *Nature*, 424:749–751, August 2003. doi: 10.1038/nature01869.
- J. Goodman. Are gamma-ray bursts optically thick? *ApJ*, 308:L47–L50, September 1986. doi: 10.1086/184741.
- D. Gotz. INTEGRAL Results on Gamma-Ray Bursts. *ArXiv e-prints*, February 2013.
- J. Granot, T. Piran, and R. Sari. Images and Spectra from the Interior of a Relativistic Fireball. *ApJ*, 513:679–689, March 1999. doi: 10.1086/306884.
- J. Greiner, W. Bornemann, C. Clemens, M. Deuter, G. Hasinger, M. Honsberg, H. Huber, S. Huber, M. Krauss, T. Krühler, A. Küpcü Yoldaş, H. Mayer-Hasselwander, B. Mican, N. Primak, F. Schrey, I. Steiner, G. Szokoly, C. C. Thöne, A. Yoldaş, S. Klose, U. Laux, and J. Winkler. GROND a 7-Channel Imager. *PASP*, 120:405, April 2008. doi: 10.1086/587032.
- J. Greiner, P. A. Mazzali, D. A. Kann, T. Krühler, E. Pian, S. Prentice, F. Olivares E., A. Rossi, S. Klose, S. Taubenberger, F. Knust, P. M. J. Afonso, C. Ashall, J. Bolmer, C. Delvaux, R. Diehl, J. Elliott, R. Filgas, J. P. U. Fynbo, J. F. Graham, A. N. Guelbenzu, S. Kobayashi, G. Leloudas, S. Savaglio, P. Schady, S. Schmidl, T. Schweyer, V. Sudilovsky, M. Tanga, A. C. Updike, H. van Eerten, and K. Varela. A very luminous magnetar-powered supernova associated with an ultra-long γ -ray burst. *Nature*, 523:189–192, July 2015. doi: 10.1038/nature14579.
- P. J. Groot, T. J. Galama, J. van Paradijs, and C. Kouveliotou. Optical afterglow of a gamma-ray burst: GRB 970228. *IEEE Spectrum*, 14:8–11, June 1997.
- D. Grupe, J. A. Nousek, P. Veres, B.-B. Zhang, and N. Gehrels. Evidence for New Relations between Gamma-Ray Burst Prompt and X-Ray Afterglow Emission from 9 Years of Swift. *ApJS*, 209:20, December 2013. doi: 10.1088/0067-0049/209/2/20.
- D. Guetta. Short GRBs: Rates and luminosity function implications. *Nuovo Cimento B Serie*, 121:1061–1066, October 2006. doi: 10.1393/ncb/i2007-10061-0.
- R. Guida, M. G. Bernardini, C. L. Bianco, L. Caito, M. G. Dainotti, and R. Ruffini. The Amati relation in the “fireshell” model. *A&A*, 487:L37–L40, August 2008. doi: 10.1051/0004-6361:200810338.
- C. Guidorzi, F. Frontera, E. Montanari, F. Rossi, L. Amati, A. Gomboc, K. Hurley, and

- C. G. Mundell. The gamma-ray burst variability-peak luminosity correlation: new results. MNRAS, 363:315–325, October 2005. doi: 10.1111/j.1365-2966.2005.09450.x.
- C. Guidorzi, F. Frontera, E. Montanari, F. Rossi, L. Amati, A. Gomboc, and C. G. Mundell. The slope of the gamma-ray burst variability/peak luminosity correlation. MNRAS, 371: 843–851, September 2006. doi: 10.1111/j.1365-2966.2006.10717.x.
- S. Guiriec, M. S. Briggs, V. Connaughthon, E. Kara, F. Daigne, C. Kouveliotou, A. J. van der Horst, W. Paciesas, C. A. Meegan, P. N. Bhat, S. Foley, E. Bissaldi, M. Burgess, V. Chaplin, R. Diehl, G. Fishman, M. Gibby, M. M. Giles, A. Goldstein, J. Greiner, D. Gruber, A. von Kienlin, M. Kippen, S. McBreen, R. Preece, A. Rau, D. Tierney, and C. Wilson-Hodge. Time-resolved Spectroscopy of the Three Brightest and Hardest Short Gamma-ray Bursts Observed with the Fermi Gamma-ray Burst Monitor. ApJ, 725: 225–241, December 2010. doi: 10.1088/0004-637X/725/1/225.
- S. Guiriec, V. Connaughton, M. S. Briggs, M. Burgess, F. Ryde, F. Daigne, P. Mészáros, A. Goldstein, J. McEnery, N. Omodei, P. N. Bhat, E. Bissaldi, A. Camero-Arranz, V. Chaplin, R. Diehl, G. Fishman, S. Foley, M. Gibby, M. M. Giles, J. Greiner, D. Gruber, A. von Kienlin, M. Kippen, C. Kouveliotou, S. McBreen, C. A. Meegan, W. Paciesas, R. Preece, A. Rau, D. Tierney, A. J. van der Horst, and C. Wilson-Hodge. Detection of a Thermal Spectral Component in the Prompt Emission of GRB 100724B. ApJ, 727:L33, February 2011. doi: 10.1088/2041-8205/727/2/L33.
- S. Guiriec, F. Daigne, R. Hascoët, G. Vianello, F. Ryde, R. Mochkovitch, C. Kouveliotou, S. Xiong, P. N. Bhat, S. Foley, D. Gruber, J. M. Burgess, S. McGlynn, J. McEnery, and N. Gehrels. Evidence for a Photospheric Component in the Prompt Emission of the Short GRB 120323A and Its Effects on the GRB Hardness-Luminosity Relation. ApJ, 770:32, June 2013. doi: 10.1088/0004-637X/770/1/32.
- S. Guiriec, C. Kouveliotou, F. Daigne, B. Zhang, R. Hascoët, R. S. Nemmen, D. J. Thompson, P. N. Bhat, N. Gehrels, M. M. Gonzalez, Y. Kaneko, J. McEnery, R. Mochkovitch, J. L. Racusin, F. Ryde, J. R. Sacahui, and A. M. Ünsal. Toward a Better Understanding of the GRB Phenomenon: a New Model for GRB Prompt Emission and its Effects on the New L_i^{NT} - $E_{peak,i}^{rest,NT}$ Relation. ApJ, 807:148, July 2015a. doi: 10.1088/0004-637X/807/2/148.
- S. Guiriec, R. Mochkovitch, T. Piran, F. Daigne, C. Kouveliotou, J. Racusin, N. Gehrels, and J. McEnery. GRB 131014A: A Laboratory for Studying the Thermal-like and Non-thermal Emissions in Gamma-Ray Bursts, and the New $L^{nTh,i}$ - $E^{nTh,rest}_{peak,i}$ Relation. ApJ, 814: 10, November 2015b. doi: 10.1088/0004-637X/814/1/10.
- S. Guiriec, M. M. Gonzalez, J. R. Sacahui, C. Kouveliotou, N. Gehrels, and J. McEnery. CGRO/BATSE Data Support the New Paradigm for GRB Prompt Emission and the New

- L_i^{nTh} - $E_{peak,i}^{nTh,rest}$ Relation. ApJ, 819:79, March 2016. doi: 10.3847/0004-637X/819/1/79.
- S. et al. Guiriec. A Unified Model for GRB Prompt Emission from Optical to $\hat{\gamma}$ -Rays: Exploring GRBs as Standard Candles . ApJ, 831:1, November 2016. doi: 10.3847/2041-8205/831/1/L8.
- C. J. Hailey, H. An, K. L. Blaedel, N. F. Brejnholt, F. E. Christensen, W. W. Craig, T. A. Decker, M. Doll, J. Gum, J. E. Koglin, C. P. Jensen, L. Hale, K. Mori, M. J. Pivovaroff, M. Sharpe, M. Stern, G. Tajiri, and W. W. Zhang. The Nuclear Spectroscopic Telescope Array (NuSTAR): optics overview and current status. In *Space Telescopes and Instrumentation 2010: Ultraviolet to Gamma Ray*, volume 7732 of Proc. SPIE, page 77320T, July 2010. doi: 10.1117/12.857654.
- J. Hakkila and R. D. Preece. Gamma-Ray Burst Pulse Shapes: Evidence for Embedded Shock Signatures? ApJ, 783:88, March 2014. doi: 10.1088/0004-637X/783/2/88.
- J. Hakkila, T. W. Giblin, J. P. Norris, P. C. Fragile, and J. T. Bonnell. Correlations between Lag, Luminosity, and Duration in Gamma-Ray Burst Pulses. ApJ, 677:L81, April 2008. doi: 10.1086/588094.
- M. Hamuy. Observed and Physical Properties of Core-Collapse Supernovae. ApJ, 582: 905–914, January 2003. doi: 10.1086/344689.
- D. H. Hartmann. Theoretical models for gamma-ray bursts. A&AS, 120:31–41, November 1996.
- D. H. Hartmann and S. E. Woosley. Models for classical gamma-ray bursts. *Advances in Space Research*, 15, May 1995. doi: 10.1016/0273-1177(94)00055-6.
- R. Hascoët, F. Daigne, and R. Mochkovitch. Prompt thermal emission in gamma-ray bursts. A&A, 551:A124, March 2013. doi: 10.1051/0004-6361/201220023.
- R. Hascoët, F. Daigne, and R. Mochkovitch. The prompt-early afterglow connection in gamma-ray bursts: implications for the early afterglow physics. MNRAS, 442:20–27, July 2014. doi: 10.1093/mnras/stu750.
- J. Heise, J. I. Zand, R. M. Kippen, and P. M. Woods. X-Ray Flashes and X-Ray Rich Gamma Ray Bursts. In E. Costa, F. Frontera, and J. Hjorth, editors, *Gamma-ray Bursts in the Afterglow Era*, page 16, 2001. doi: 10.1007/10853853__4.
- V. Heussaff, J.-L. Atteia, and Y. Zolnierowski. The E_{peak} - E_{iso} relation revisited with Fermi GRBs. Resolving a long-standing debate? A&A, 557:A100, September 2013. doi: 10.1051/0004-6361/201321528.
- J. Hjorth, J. Sollerman, P. Møller, J. P. U. Fynbo, S. E. Woosley, C. Kouveliotou, N. R. Tanvir, J. Greiner, M. I. Andersen, A. J. Castro-Tirado, J. M. Castro Cerón, A. S. Fruchter,

- J. Gorosabel, P. Jakobsson, L. Kaper, S. Klose, N. Masetti, H. Pedersen, K. Pedersen, E. Pian, E. Palazzi, J. E. Rhoads, E. Rol, E. P. J. van den Heuvel, P. M. Vreeswijk, D. Watson, and R. A. M. J. Wijers. A very energetic supernova associated with the γ -ray burst of 29 March 2003. *Nature*, 423:847–850, June 2003. doi: 10.1038/nature01750.
- D. E. Holz and S. A. Hughes. Using Gravitational-Wave Standard Sirens. *ApJ*, 629:15–22, August 2005. doi: 10.1086/431341.
- I. Horváth. A Third Class of Gamma-Ray Bursts? *ApJ*, 508:757–759, December 1998. doi: 10.1086/306416.
- I. Horváth. A further study of the BATSE Gamma-Ray Burst duration distribution. *A&A*, 392:791–793, September 2002. doi: 10.1051/0004-6361:20020808.
- I. Horváth. Classification of BeppoSAX’s gamma-ray bursts. *Ap&SS*, 323:83–86, September 2009. doi: 10.1007/s10509-009-0039-1.
- I. Horváth, L. G. Balázs, Z. Bagoly, F. Ryde, and A. Mészáros. A new definition of the intermediate group of gamma-ray bursts. *A&A*, 447:23–30, February 2006. doi: 10.1051/0004-6361:20041129.
- I. Horváth, L. G. Balázs, Z. Bagoly, and P. Veres. Classification of Swift’s gamma-ray bursts. *A&A*, 489:L1–L4, October 2008. doi: 10.1051/0004-6361:200810269.
- I. Horváth, Z. Bagoly, L. G. Balázs, A. de Ugarte Postigo, P. Veres, and A. Mészáros. Detailed Classification of Swift’s Gamma-ray Bursts. *ApJ*, 713:552–557, April 2010. doi: 10.1088/0004-637X/713/1/552.
- D. Huja, A. Mészáros, and J. Řípa. A comparison of the gamma-ray bursts detected by BATSE and Swift. *A&A*, 504:67–71, September 2009. doi: 10.1051/0004-6361/200809802.
- S. Inoue, K. Omukai, and B. Ciardi. The radio to infrared emission of very high redshift gamma-ray bursts: probing early star formation through molecular and atomic absorption lines. *MNRAS*, 380:1715–1728, October 2007. doi: 10.1111/j.1365-2966.2007.12234.x.
- K. Ioka and P. Mészáros. Radio Afterglows of Gamma-Ray Bursts and Hypernovae at High Redshift and Their Potential for 21 Centimeter Absorption Studies. *ApJ*, 619:684–696, February 2005. doi: 10.1086/426785.
- K. Ioka and T. Nakamura. Peak Luminosity-Spectral Lag Relation Caused by the Viewing Angle of the Collimated Gamma-Ray Bursts. *ApJ*, 554:L163–L167, June 2001. doi: 10.1086/321717.
- H. Ito, S. Nagataki, M. Ono, S.-H. Lee, J. Mao, S. Yamada, A. Pe’er, A. Mizuta, and S. Harikae. Photospheric Emission from Stratified Jets. *ApJ*, 777:62, November 2013. doi: 10.1088/0004-637X/777/1/62.

- H. Ito, S. Nagataki, J. Matsumoto, S.-H. Lee, A. Tolstov, J. Mao, M. Dainotti, and A. Mizuta. Spectral and Polarization Properties of Photospheric Emission from Stratified Jets. *ApJ*, 789:159, July 2014. doi: 10.1088/0004-637X/789/2/159.
- P. Jakobsson, J. Hjorth, J. P. U. Fynbo, D. Watson, K. Pedersen, G. Björnsson, and J. Gorosabel. Swift Identification of Dark Gamma-Ray Bursts. *ApJ*, 617:L21–L24, December 2004. doi: 10.1086/427089.
- P. A. James and J. P. Anderson. The H α Galaxy Survey . III. Constraints on supernova progenitors from spatial correlations with H α emission. *A&A*, 453:57–65, July 2006. doi: 10.1051/0004-6361:20054509.
- F. Jansen, D. Lumb, B. Altieri, J. Clavel, M. Ehle, C. Erd, C. Gabriel, M. Guainazzi, P. Gondoin, R. Much, R. Munoz, M. Santos, N. Schartel, D. Texier, and G. Vacanti. XMM-Newton observatory. I. The spacecraft and operations. *A&A*, 365:L1–L6, January 2001. doi: 10.1051/0004-6361:20000036.
- A. Jerkstrand, F. X. Timmes, G. Magkotsios, S. A. Sim, C. Fransson, J. Spyromilio, B. Müller, A. Heger, J. Sollerman, and S. J. Smartt. Constraints on Explosive Silicon Burning in Core-collapse Supernovae from Measured Ni/Fe Ratios. *ApJ*, 807:110, July 2015. doi: 10.1088/0004-637X/807/1/110.
- Y. Kaneko, E. Ramirez-Ruiz, J. Granot, C. Kouveliotou, S. E. Woosley, S. K. Patel, E. Rol, J. J. M. in 't Zand, A. J. van der Horst, R. A. M. J. Wijers, and R. Strom. Prompt and Afterglow Emission Properties of Gamma-Ray Bursts with Spectroscopically Identified Supernovae. *ApJ*, 654:385–402, January 2007. doi: 10.1086/508324.
- D. A. Kann, S. Klose, B. Zhang, D. Malesani, E. Nakar, A. Pozanenko, A. C. Wilson, N. R. Butler, P. Jakobsson, S. Schulze, M. Andreev, L. A. Antonelli, I. F. Bikmaev, V. Biryukov, M. Böttcher, R. A. Burenin, J. M. Castro Cerón, A. J. Castro-Tirado, G. Chincarini, B. E. Cobb, S. Covino, P. D'Avanzo, V. D'Elia, M. Della Valle, A. de Ugarte Postigo, Y. Efimov, P. Ferrero, D. Fugazza, J. P. U. Fynbo, M. Gålfalk, F. Grundahl, J. Gorosabel, S. Gupta, S. Guziy, B. Hafizov, J. Hjorth, K. Holhjem, M. Ibrahimov, M. Im, G. L. Israel, M. Jelínek, B. L. Jensen, R. Karimov, I. M. Khamitov, Ü. Kiziloğlu, E. Klunko, P. Kubánek, A. S. Kutyrev, P. Laursen, A. J. Levan, F. Mannucci, C. M. Martin, A. Mescheryakov, N. Mirabal, J. P. Norris, J.-E. Ovaldsen, D. Paraficz, E. Pavlenko, S. Piranomonte, A. Rossi, V. Rumyantsev, R. Salinas, A. Sergeev, D. Sharapov, J. Sollerman, B. Stecklum, L. Stella, G. Tagliaferri, N. R. Tanvir, J. Telting, V. Testa, A. C. Updike, A. Volnova, D. Watson, K. Wiersema, and D. Xu. The Afterglows of Swift-era Gamma-ray Bursts. I. Comparing pre-Swift and Swift-era Long/Soft (Type II) GRB Optical Afterglows. *ApJ*, 720:1513–1558, September 2010. doi: 10.1088/0004-637X/720/2/1513.
- J. I. Katz. Yet Another Model of Gamma-Ray Bursts. *ApJ*, 490:633–641, December 1997. doi: 10.1086/304896.

- D. Kazanas, J. L. Racusin, J. Sultana, and A. Mastichiadis. The Statistics of the Prompt-to-Afterglow GRB Flux Ratios and the Supercritical Pile GRB Model. *ArXiv e-prints*, January 2015.
- M. G. Kendall. A new measure of rank correlation. *Biometrika*, 30(1-2):81–93, 1938. doi: 10.1093/biomet/30.1-2.81. URL <http://biomet.oxfordjournals.org/content/30/1-2/81.short>.
- R. P. Kerr. Gravitational Field of a Spinning Mass as an Example of Algebraically Special Metrics. *Physical Review Letters*, 11:237–238, September 1963. doi: 10.1103/PhysRevLett.11.237.
- R. M. Kippen, P. M. Woods, J. Heise, J. I. Zand, R. D. Preece, and M. S. Briggs. BATSE Observations of Fast X-Ray Transients Detected by BeppoSAX-WFC. In E. Costa, F. Frontera, and J. Hjorth, editors, *Gamma-ray Bursts in the Afterglow Era*, page 22, 2001. doi: 10.1007/10853853__5.
- M. D. Kistler, H. Yüksel, J. F. Beacom, A. M. Hopkins, and J. S. B. Wyithe. The Star Formation Rate in the Reionization Era as Indicated by Gamma-Ray Bursts. *ApJ*, 705:L104–L108, November 2009. doi: 10.1088/0004-637X/705/2/L104.
- M. D. Kistler, H. Yuksel, and A. M. Hopkins. The Cosmic Star Formation Rate from the Faintest Galaxies in the Unobservable Universe. *ArXiv e-prints*, May 2013.
- R. W. Klebesadel, I. B. Strong, and R. A. Olson. Observations of Gamma-Ray Bursts of Cosmic Origin. *ApJ*, 182:L85, June 1973. doi: 10.1086/181225.
- S. Kobayashi, T. Piran, and R. Sari. Can Internal Shocks Produce the Variability in Gamma-Ray Bursts? *ApJ*, 490:92, November 1997. doi: 10.1086/512791.
- D. Kocevski and E. Liang. The Connection between Spectral Evolution and Gamma-Ray Burst Lag. *ApJ*, 594:385–389, September 2003. doi: 10.1086/376868.
- Y. Kodama, D. Yonetoku, T. Murakami, S. Tanabe, R. Tsutsui, and T. Nakamura. Gamma-ray bursts in $1.8 < z < 5.6$ suggest that the time variation of the dark energy is small. *MNRAS*, 391:L1–L4, November 2008. doi: 10.1111/j.1745-3933.2008.00508.x.
- C. Koen and A. Bere. On multiple classes of gamma-ray bursts, as deduced from autocorrelation functions or bivariate duration/hardness ratio distributions. *MNRAS*, 420:405–415, February 2012. doi: 10.1111/j.1365-2966.2011.20045.x.
- E. Komatsu, K. M. Smith, J. Dunkley, C. L. Bennett, B. Gold, G. Hinshaw, N. Jarosik, D. Larson, M. R. Nolta, L. Page, D. N. Spergel, M. Halpern, R. S. Hill, A. Kogut, M. Limon, S. S. Meyer, N. Odegard, G. S. Tucker, J. L. Weiland, E. Wollack, and E. L. Wright. Seven-year Wilkinson Microwave Anisotropy Probe (WMAP) Observations: Cosmological Interpretation. *ApJS*, 192:18, February 2011. doi: 10.1088/0067-0049/192/2/18.

- C. Kouveliotou, C. A. Meegan, G. J. Fishman, N. P. Bhat, M. S. Briggs, T. M. Koshut, W. S. Paciesas, and G. N. Pendleton. Identification of two classes of gamma-ray bursts. *ApJ*, 413:L101–L104, August 1993. doi: 10.1086/186969.
- P. Kumar and T. Piran. Some Observational Consequences of Gamma-Ray Burst Shock Models. *ApJ*, 532:286–293, March 2000. doi: 10.1086/308537.
- P. Kumar and B. Zhang. The physics of gamma-ray bursts and relativistic jets. *Phys. Rep.*, 561:1–109, February 2015. doi: 10.1016/j.physrep.2014.09.008.
- P. Kumar, R. Narayan, and J. L. Johnson. Properties of Gamma-Ray Burst Progenitor Stars. *Science*, 321:376–, July 2008. doi: 10.1126/science.1159003.
- D. Q. Lamb, T. Q. Donaghy, and C. Graziani. A unified jet model of X-ray flashes and γ -ray bursts. *New A Rev.*, 48:459–464, April 2004. doi: 10.1016/j.newar.2003.12.030.
- T. Laskar, E. Berger, N. Tanvir, B. A. Zauderer, R. Margutti, A. Levan, D. Perley, W.-f. Fong, K. Wiersema, K. Menten, and M. Hrudkova. GRB 120521C at $z \sim 6$ and the Properties of High-redshift γ -Ray Bursts. *ApJ*, 781:1, January 2014. doi: 10.1088/0004-637X/781/1/1.
- T. Laskar, E. Berger, R. Margutti, D. Perley, B. A. Zauderer, R. Sari, and W.-f. Fong. Energy Injection in Gamma-Ray Burst Afterglows. *ApJ*, 814:1, November 2015. doi: 10.1088/0004-637X/814/1/1.
- D. Lazzati and M. C. Begelman. Non-thermal Emission from the Photospheres of Gamma-ray Burst Outflows. I. High-Frequency Tails. *ApJ*, 725:1137–1145, December 2010. doi: 10.1088/0004-637X/725/1/1137.
- D. Lazzati, S. Campana, and G. Ghisellini. Iron line in the afterglow: a key to unveil gamma-ray burst progenitors. *MNRAS*, 304:L31–L35, April 1999. doi: 10.1046/j.1365-8711.1999.02517.x.
- T. Le and C. D. Dermer. On the Redshift Distribution of Gamma-Ray Bursts in the Swift Era. *ApJ*, 661:394–415, May 2007. doi: 10.1086/513460.
- A. Lee, E. D. Bloom, and V. Petrosian. Properties of Gamma-Ray Burst Time Profiles Using Pulse Decomposition Analysis. *ApJS*, 131:1–19, November 2000. doi: 10.1086/317364.
- T. T. Lee and V. Petrosian. Distributions of Peak Flux and Duration for Gamma-Ray Bursts. *ApJ*, 470:479, October 1996. doi: 10.1086/177879.
- W. H. Lei, D. X. Wang, L. Zhang, Z. M. Gan, Y. C. Zou, and Y. Xie. Magnetically Torqued Neutrino-dominated Accretion Flows for Gamma-ray Bursts. *ApJ*, 700:1970–1976, August 2009. doi: 10.1088/0004-637X/700/2/1970.
- A. J. Levan, P. Jakobsson, C. Hurkett, N. R. Tanvir, J. Gorosabel, P. Vreeswijk, E. Rol, R. Chapman, N. Gehrels, P. T. O'Brien, J. P. Osborne, R. S. Priddey, C. Kouveliotou, R. Starling, D. vanden Berk, and K. Wiersema. A case of mistaken identity? GRB060912A

and the nature of the long-short GRB divide. MNRAS, 378:1439–1446, July 2007. doi: 10.1111/j.1365-2966.2007.11879.x.

- A. J. Levan, N. R. Tanvir, R. L. C. Starling, K. Wiersema, K. L. Page, D. A. Perley, S. Schulze, G. A. Wynn, R. Chornock, J. Hjorth, S. B. Cenko, A. S. Fruchter, P. T. O’Brien, G. C. Brown, R. L. Tunnicliffe, D. Malesani, P. Jakobsson, D. Watson, E. Berger, D. Bersier, B. E. Cobb, S. Covino, A. Cucchiara, A. de Ugarte Postigo, D. B. Fox, A. Gal-Yam, P. Goldoni, J. Gorosabel, L. Kaper, T. Krühler, R. Karjalainen, J. P. Osborne, E. Pian, R. Sánchez-Ramírez, B. Schmidt, I. Skillen, G. Tagliaferri, C. Thöne, O. Vaduvescu, R. A. M. J. Wijers, and B. A. Zauderer. A New Population of Ultra-long Duration Gamma-Ray Bursts. ApJ, 781:13, January 2014. doi: 10.1088/0004-637X/781/1/13.
- K. Leventis, R. A. M. J. Wijers, and A. J. van der Horst. The plateau phase of gamma-ray burst afterglows in the thick-shell scenario. MNRAS, 437:2448–2460, January 2014. doi: 10.1093/mnras/stt2055.
- L. Li, E.-W. Liang, Q.-W. Tang, J.-M. Chen, S.-Q. Xi, H.-J. Lü, H. Gao, B. Zhang, J. Zhang, S.-X. Yi, R.-J. Lu, L.-Z. Lü, and J.-Y. Wei. A Comprehensive Study of Gamma-Ray Burst Optical Emission. I. Flares and Early Shallow-decay Component. ApJ, 758:27, October 2012. doi: 10.1088/0004-637X/758/1/27.
- L.-X. Li. Star formation history up to $z = 7.4$: implications for gamma-ray bursts and cosmic metallicity evolution. MNRAS, 388:1487–1500, August 2008. doi: 10.1111/j.1365-2966.2008.13488.x.
- L.-X. Li and B. Paczyński. Improved correlation between the variability and peak luminosity of gamma-ray bursts. MNRAS, 366:219–226, February 2006. doi: 10.1111/j.1365-2966.2005.09836.x.
- W. Li, J. Leaman, R. Chornock, A. V. Filippenko, D. Poznanski, M. Ganeshalingam, X. Wang, M. Modjaz, S. Jha, R. J. Foley, and N. Smith. Nearby supernova rates from the Lick Observatory Supernova Search - II. The observed luminosity functions and fractions of supernovae in a complete sample. MNRAS, 412:1441–1472, April 2011. doi: 10.1111/j.1365-2966.2011.18160.x.
- X. Li and J. Hjorth. Light Curve Properties of Supernovae Associated With Gamma-ray Bursts. *ArXiv e-prints*, July 2014.
- X. Li, F.-W. Zhang, Q. Yuan, Z.-P. Jin, Y.-Z. Fan, S.-M. Liu, and D.-M. Wei. Implications of the Tentative Association between GW150914 and a Fermi-GBM Transient. ApJ, 827:L16, August 2016. doi: 10.3847/2041-8205/827/1/L16.
- E. Liang and V. Kargatis. Dependence of the spectral evolution of γ -ray bursts on their photon fluence. Nature, 381:49–51, May 1996. doi: 10.1038/381049a0.
- E. Liang and B. Zhang. Model-independent Multivariable Gamma-Ray Burst Luminosity

- Indicator and Its Possible Cosmological Implications. *ApJ*, 633:611–623, November 2005. doi: 10.1086/491594.
- E. Liang and B. Zhang. Identification of Two Categories of Optically Bright Gamma-Ray Bursts. *ApJ*, 638:L67–L70, February 2006a. doi: 10.1086/501049.
- E. Liang and B. Zhang. Calibration of gamma-ray burst luminosity indicators. *MNRAS*, 369:L37–L41, June 2006b. doi: 10.1111/j.1745-3933.2006.00169.x.
- E. W. Liang, Z. G. Dai, and X. F. Wu. The Luminosity- E_p Relation within Gamma-Ray Bursts and the Implications for Fireball Models. *ApJ*, 606:L29–L32, May 2004. doi: 10.1086/421047.
- E.-W. Liang, B.-B. Zhang, and B. Zhang. A Comprehensive Analysis of Swift XRT Data. II. Diverse Physical Origins of the Shallow Decay Segment. *ApJ*, 670:565–583, November 2007. doi: 10.1086/521870.
- E.-W. Liang, S.-X. Yi, J. Zhang, H.-J. Lü, B.-B. Zhang, and B. Zhang. Constraining Gamma-ray Burst Initial Lorentz Factor with the Afterglow Onset Feature and Discovery of a Tight Γ_0 - $E_{gamma,iso}$ Correlation. *ApJ*, 725:2209–2224, December 2010. doi: 10.1088/0004-637X/725/2/2209.
- N. Liang, W. K. Xiao, Y. Liu, and S. N. Zhang. A Cosmology-Independent Calibration of Gamma-Ray Burst Luminosity Relations and the Hubble Diagram. *ApJ*, 685:354–360, September 2008. doi: 10.1086/590903.
- H.-N. Lin, X. Li, S. Wang, and Z. Chang. Are long gamma-ray bursts standard candles? *MNRAS*, 453:128–132, October 2015. doi: 10.1093/mnras/stv1624.
- H.-N. Lin, X. Li, and Z. Chang. Model-independent distance calibration of high-redshift gamma-ray bursts and constrain on the Λ CDM model. *MNRAS*, 455:2131–2138, January 2016a. doi: 10.1093/mnras/stv2471.
- H.-N. Lin, X. Li, and Z. Chang. Effect of GRB spectra on the empirical luminosity correlations and the GRB Hubble diagram. *MNRAS*, April 2016b. doi: 10.1093/mnras/stw817.
- C. C. Lindner, M. Milosavljević, S. M. Couch, and P. Kumar. Collapsar Accretion and the Gamma-Ray Burst X-Ray Light Curve. *ApJ*, 713:800–815, April 2010. doi: 10.1088/0004-637X/713/2/800.
- Y. Lithwick and R. Sari. Lower Limits on Lorentz Factors in Gamma-Ray Bursts. *ApJ*, 555: 540–545, July 2001a. doi: 10.1086/321455.
- Y. Lithwick and R. Sari. Lower Limits on Lorentz Factors in Gamma-Ray Bursts. *ApJ*, 555: 540–545, July 2001b. doi: 10.1086/321455.
- O. M. Littlejohns and N. R. Butler. Investigating signatures of cosmological time dilation

- in duration measures of prompt gamma-ray burst light curves. MNRAS, 444:3948–3960, November 2014. doi: 10.1093/mnras/stu1767.
- O. M. Littlejohns, N. R. Tanvir, R. Willingale, P. A. Evans, P. T. O’Brien, and A. J. Levan. Are gamma-ray bursts the same at high redshift and low redshift? MNRAS, 436:3640–3655, December 2013. doi: 10.1093/mnras/stt1841.
- R.-Y. Liu, X.-Y. Wang, and X.-F. Wu. Interpretation of the Unprecedentedly Long-lived High-energy Emission of GRB 130427A. ApJ, 773:L20, August 2013. doi: 10.1088/2041-8205/773/2/L20.
- N. M. Lloyd and V. Petrosian. Distribution of Spectral Characteristics and the Cosmological Evolution of Gamma-Ray Bursts. ApJ, 511:550–561, February 1999. doi: 10.1086/306719.
- N. M. Lloyd, V. Petrosian, and R. S. Mallozzi. Cosmological versus Intrinsic: The Correlation between Intensity and the Peak of the νF Spectrum of Gamma-Ray Bursts. ApJ, 534: 227–238, May 2000a. doi: 10.1086/308742.
- N. M. Lloyd, V. Petrosian, and R. D. Preece. Synchrotron emission as the source of GRB spectra, Part II: Observations. In R. M. Kippen, R. S. Mallozzi, and G. J. Fishman, editors, *Gamma-ray Bursts, 5th Huntsville Symposium*, volume 526 of *American Institute of Physics Conference Series*, pages 155–159, September 2000b. doi: 10.1063/1.1361525.
- N. M. Lloyd-Ronning and V. Petrosian. Interpreting the Behavior of Time-resolved Gamma-Ray Burst Spectra. ApJ, 565:182–194, January 2002. doi: 10.1086/324484.
- N. M. Lloyd-Ronning and E. Ramirez-Ruiz. On the Spectral Energy Dependence of Gamma-Ray Burst Variability. ApJ, 576:101–106, September 2002. doi: 10.1086/341723.
- A. Loeb. Electromagnetic Counterparts to Black Hole Mergers Detected by LIGO. ApJ, 819:L21, March 2016. doi: 10.3847/2041-8205/819/2/L21.
- F. Longo, M. Tavani, G. Barbiellini, A. Argan, M. Bassett, F. Boffelli, A. Bulgarelli, P. Caraveo, P. Cattaneo, A. Chen, E. Costa, E. Del Monte, G. Di Cocco, G. di Persio, I. Donnarumma, M. Feroci, M. Fiorini, L. Foggetta, T. Froysland, M. Frutti, F. Fuschino, M. Galli, F. Gianotti, A. Giuliani, C. Labanti, I. Lapshov, F. Lazzarotto, F. Liello, P. Lipari, M. Marisaldi, M. Mastropietro, E. Mattaini, F. Mauri, S. Mereghetti, E. Morelli, A. Morselli, L. Pacciani, A. Pellizzoni, F. Perotti, P. Picozza, C. Pittori, C. Pontoni, G. Porrovecchio, M. Prest, M. Rapisarda, E. Rossi, A. Rubini, P. Soffitta, A. Traci, M. Trifoglio, A. Trois, E. Vallazza, S. Vercellone, and D. Zanello. The AGILE Mission and Gamma-Ray Bursts. In M. Axelsson and F. Ryde, editors, *Gamma-Ray Bursts: Prospects for GLAST*, volume 906 of *American Institute of Physics Conference Series*, pages 147–155, May 2007. doi: 10.1063/1.2737416.
- H.-J. Lü and B. Zhang. A Test of the Millisecond Magnetar Central Engine Model of Gamma-Ray Bursts with Swift Data. ApJ, 785:74, April 2014. doi: 10.1088/0004-637X/785/1/74.

- J. Lü, Y.-C. Zou, W.-H. Lei, B. Zhang, Q. Wu, D.-X. Wang, E.-W. Liang, and H.-J. Lü. Lorentz-factor-Isotropic-luminosity/Energy Correlations of Gamma-Ray Bursts and Their Interpretation. *ApJ*, 751:49, May 2012a. doi: 10.1088/0004-637X/751/1/49.
- J. Lü, Y.-C. Zou, W.-H. Lei, B. Zhang, Q. Wu, D.-X. Wang, E.-W. Liang, and H.-J. Lü. Lorentz-factor-Isotropic-luminosity/Energy Correlations of Gamma-Ray Bursts and Their Interpretation. *ApJ*, 751:49, May 2012b. doi: 10.1088/0004-637X/751/1/49.
- R. Lu and E. Liang. Luminosity-peak energy relation in the decay phases of gamma-ray burst pulses. *Science China Physics, Mechanics, and Astronomy*, 53:163–170, January 2010. doi: 10.1007/s11433-010-0086-1.
- R.-J. Lu, J.-J. Wei, E.-W. Liang, B.-B. Zhang, H.-J. Lü, L.-Z. Lü, W.-H. Lei, and B. Zhang. A Comprehensive Analysis of Fermi Gamma-Ray Burst Data. II. E_p Evolution Patterns and Implications for the Observed Spectrum-Luminosity Relations. *ApJ*, 756:112, September 2012. doi: 10.1088/0004-637X/756/2/112.
- R. Lunnan, R. Chornock, E. Berger, T. Laskar, W. Fong, A. Rest, N. E. Sanders, P. M. Challis, M. R. Drout, R. J. Foley, M. E. Huber, R. P. Kirshner, C. Leibler, G. H. Marion, M. McCrum, D. Milisavljevic, G. Narayan, D. Scolnic, S. J. Smartt, K. W. Smith, A. M. Soderberg, J. L. Tonry, W. S. Burgett, K. C. Chambers, H. Flewelling, K. W. Hodapp, N. Kaiser, E. A. Magnier, P. A. Price, and R. J. Wainscoat. Hydrogen-poor Superluminous Supernovae and Long-duration Gamma-Ray Bursts Have Similar Host Galaxies. *ApJ*, 787:138, June 2014. doi: 10.1088/0004-637X/787/2/138.
- N. Lyons, P. T. O’Brien, B. Zhang, R. Willingale, E. Troja, and R. L. C. Starling. Can X-ray emission powered by a spinning-down magnetar explain some gamma-ray burst light-curve features? *MNRAS*, 402:705–712, February 2010. doi: 10.1111/j.1365-2966.2009.15538.x.
- A. I. MacFadyen. The collapsar model for gamma-ray bursts. In H.-Y. Chang, C.-H. Lee, M. Rho, and I. Yi, editors, *Explosive Phenomena in Astrophysical Compact Objects*, volume 556 of *American Institute of Physics Conference Series*, pages 313–323, March 2001. doi: 10.1063/1.1368288.
- A. I. MacFadyen and S. E. Woosley. Collapsars: Gamma-Ray Bursts and Explosions in “Failed Supernovae”. *ApJ*, 524:262–289, October 1999. doi: 10.1086/307790.
- A. I. MacFadyen, S. E. Woosley, and A. Heger. Supernovae, Jets, and Collapsars. *ApJ*, 550:410–425, March 2001. doi: 10.1086/319698.
- M. Magliocchetti, G. Ghirlanda, and A. Celotti. Evidence for anisotropy in the distribution of short-lived gamma-ray bursts. *MNRAS*, 343:255–258, July 2003. doi: 10.1046/j.1365-8711.2003.06657.x.
- D. Malesani, G. Tagliaferri, G. Chincarini, S. Covino, M. Della Valle, D. Fugazza, P. A. Mazzali, F. M. Zerbi, P. D’Avanzo, S. Kalogerakos, A. Simoncelli, L. A. Antonelli, L. Burderi,

- S. Campana, A. Cucchiara, F. Fiore, G. Ghirlanda, P. Goldoni, D. Götz, S. Mereghetti, I. F. Mirabel, P. Romano, L. Stella, T. Minezaki, Y. Yoshii, and K. Nomoto. SN 2003lw and GRB 031203: A Bright Supernova for a Faint Gamma-Ray Burst. *ApJ*, 609:L5–L8, July 2004. doi: 10.1086/422684.
- R. S. Mallozzi, W. S. Paciesas, G. N. Pendleton, M. S. Briggs, R. D. Preece, C. A. Meegan, and G. J. Fishman. The nu F nu Peak Energy Distributions of Gamma-Ray Bursts Observed by BATSE. *ApJ*, 454:597, December 1995. doi: 10.1086/176513.
- A. et al. Mandel. TYPE Ia SUPERNOVA LIGHT CURVE INFERENCE: HIERARCHICAL MODELS in the OPTICAL and NEAR-INFRARED . *ApJ*, 731:2, 2011. doi: 10.1088/0004-637X/731/2/120.
- K. S. Mandel, W. M. Wood-Vasey, A. S. Friedman, and R. P. Kirshner. Type Ia Supernova Light-Curve Inference: Hierarchical Bayesian Analysis in the Near-Infrared. *ApJ*, 704: 629–651, October 2009. doi: 10.1088/0004-637X/704/1/629.
- V. Mangano, B. Sbarufatti, and G. Stratta. Extending the plateau luminosity-duration anticorrelation. *Memorie della Societa Astronomica Italiana Supplementi*, 21:143, 2012.
- S. Mao and I. Yi. Relativistic beaming and gamma-ray bursts. *ApJ*, 424:L131–L134, April 1994. doi: 10.1086/187292.
- M.C. March, R. Trotta, and P. et al. Berkes. Improved Constraints on Cosmological Parameters From Type Ia Supernova Data. *MNRAS*, 418:4, December 2011. doi: 10.1111/j.1365-2966.2011.19584.x.
- R. Margutti, C. Guidorzi, G. Chincarini, M. G. Bernardini, F. Genet, J. Mao, and F. Pasotti. Lag-luminosity relation in γ -ray burst X-ray flares: a direct link to the prompt emission. *MNRAS*, 406:2149–2167, August 2010. doi: 10.1111/j.1365-2966.2010.16824.x.
- R. Margutti, E. Zaninoni, M. G. Bernardini, G. Chincarini, F. Pasotti, C. Guidorzi, L. Angelini, D. N. Burrows, M. Capalbi, P. A. Evans, N. Gehrels, J. Kennea, V. Mangano, A. Moretti, J. Nousek, J. P. Osborne, K. L. Page, M. Perri, J. Racusin, P. Romano, B. Sbarufatti, S. Stafford, and M. Stamatikos. The prompt-afterglow connection in gamma-ray bursts: a comprehensive statistical analysis of Swift X-ray light curves. *MNRAS*, 428: 729–742, January 2013. doi: 10.1093/mnras/sts066.
- A. Maxham and B. Zhang. Modeling Gamma-Ray Burst X-Ray Flares Within the Internal Shock Model. *ApJ*, 707:1623–1633, December 2009. doi: 10.1088/0004-637X/707/2/1623.
- E. P. Mazets, S. V. Golenetskii, V. N. Ilinskii, V. N. Panov, R. L. Aptekar, I. A. Gurian, M. P. Proskura, I. A. Sokolov, Z. I. Sokolova, and T. V. Kharitonova. Catalog of cosmic gamma-ray bursts from the KONUS experiment data. I. *Ap&SS*, 80:3–83, November 1981. doi: 10.1007/BF00649140.

- C. A. Meegan, G. J. Fishman, R. B. Wilson, J. M. Horack, M. N. Brock, W. S. Paciesas, G. N. Pendleton, and C. Kouveliotou. Spatial distribution of gamma-ray bursts observed by BATSE. *Nature*, 355:143–145, January 1992. doi: 10.1038/355143a0.
- A. Melandri, C. G. Mundell, S. Kobayashi, C. Guidorzi, A. Gomboc, I. A. Steele, R. J. Smith, D. Bersier, C. J. Mottram, D. Carter, M. F. Bode, P. T. O’Brien, N. R. Tanvir, E. Rol, and R. Chapman. The Early-Time Optical Properties of Gamma-Ray Burst Afterglows. *ApJ*, 686:1209–1230, October 2008. doi: 10.1086/591243.
- A. Melandri, S. Covino, D. Rogantini, R. Salvaterra, B. Sbarufatti, M. G. Bernardini, S. Campana, P. D’Avanzo, V. D’Elia, D. Fugazza, G. Ghirlanda, G. Ghisellini, L. Nava, S. D. Vergani, and G. Tagliaferri. Optical and X-ray rest-frame light curves of the BAT6 sample. *A&A*, 565:A72, May 2014. doi: 10.1051/0004-6361/201323361.
- S. Mendoza, J. C. Hidalgo, D. Olvera, and J. I. Cabrera. Internal shocks in relativistic jets with time-dependent sources. *MNRAS*, 395:1403–1408, May 2009. doi: 10.1111/j.1365-2966.2009.14483.x.
- A. Mészáros and J. Štoček. Anisotropy in the angular distribution of the long gamma-ray bursts? *A&A*, 403:443–448, May 2003. doi: 10.1051/0004-6361:20030328.
- A. Mészáros, Z. Bagoly, I. Horváth, L. G. Balázs, and R. Vavrek. A Remarkable Angular Distribution of the Intermediate Subclass of Gamma-Ray Bursts. *ApJ*, 539:98–101, August 2000a. doi: 10.1086/309193.
- A. Mészáros, Z. Bagoly, and R. Vavrek. On the existence of the intrinsic anisotropies in the angular distributions of gamma-ray bursts. *A&A*, 354:1–6, February 2000b.
- A. Mészáros, L. G. Balázs, Z. Bagoly, and P. Veres. Impact on Cosmology of the Celestial Anisotropy of the Short Gamma-Ray Bursts. *Baltic Astronomy*, 18:293–296, 2009.
- P. Mészáros. Theoretical models of gamma-ray bursts. In C. A. Meegan, R. D. Preece, and T. M. Koshut, editors, *Gamma-Ray Bursts, 4th Huntsville Symposium*, volume 428 of *American Institute of Physics Conference Series*, pages 647–656, May 1998. doi: 10.1063/1.55394.
- P. Mészáros. Theories of Gamma-Ray Bursts. *ARA&A*, 40:137–169, 2002. doi: 10.1146/annurev.astro.40.060401.093821.
- P. Mészáros. Gamma-ray bursts. *Reports on Progress in Physics*, 69:2259–2321, August 2006. doi: 10.1088/0034-4885/69/8/R01.
- P. Mészáros and M. J. Rees. Poynting Jets from Black Holes and Cosmological Gamma-Ray Bursts. *ApJ*, 482:L29–L32, June 1997a. doi: 10.1086/310692.
- P. Mészáros and M. J. Rees. Optical and Long-Wavelength Afterglow from Gamma-Ray Bursts. *ApJ*, 476:232–237, February 1997b.

- P. Mészáros and M. J. Rees. GRB 990123: reverse and internal shock flashes and late afterglow behaviour. *MNRAS*, 306:L39–L43, July 1999. doi: 10.1046/j.1365-8711.1999.02800.x.
- P. Mészáros and M. J. Rees. Collapsar Jets, Bubbles, and Fe Lines. *ApJ*, 556:L37–L40, July 2001. doi: 10.1086/322934.
- P. Mészáros and M J. Rees. Gamma-ray bursts. In A. Ashtekar, B. Berger, J. Isenberg, and M. A. H MacCallum, editors, *General Relativity and Gravitation: A Centennial Perspective*, Cambridge Univ. Press, Cambridge, pages 148–161, June 2015.
- B. D. Metzger, D. Giannios, T. A. Thompson, N. Bucciantini, and E. Quataert. The protomagnetar model for gamma-ray bursts. *MNRAS*, 413:2031–2056, May 2011. doi: 10.1111/j.1365-2966.2011.18280.x.
- M. R. Metzger, S. G. Djorgovski, S. R. Kulkarni, C. C. Steidel, K. L. Adelberger, D. A. Frail, E. Costa, and F. Frontera. Spectral constraints on the redshift of the optical counterpart to the γ -ray burst of 8 May 1997. *Nature*, 387:878–880, June 1997. doi: 10.1038/43132.
- J. Miralda-Escudé. Small-Angle Scattering of X-Rays from Extragalactic Sources by Dust in Intervening Galaxies. *ApJ*, 512:21–24, February 1999. doi: 10.1086/306767.
- R. Mochkovitch and L. Nava. The $E_p - E_{iso}$ relation and the internal shock model. *A&A*, 577:A31, May 2015. doi: 10.1051/0004-6361/201424490.
- B. J. Morsony, J. C. Workman, and D. M. Ryan. Modeling the Afterglow of the Possible Fermi-GBM event Associated with GW150914. *ApJ*, 825:L24, July 2016. doi: 10.3847/2041-8205/825/2/L24.
- S. Mukherjee, E. D. Feigelson, G. Jogesh Babu, F. Murtagh, C. Fraley, and A. Raftery. Three Types of Gamma-Ray Bursts. *ApJ*, 508:314–327, November 1998. doi: 10.1086/306386.
- E. Nakar. Short-hard gamma-ray bursts. *Phys. Rep.*, 442:166–236, April 2007a. doi: 10.1016/j.physrep.2007.02.005.
- E. Nakar. Short-hard gamma-ray bursts. *Phys. Rep.*, 442:166–236, April 2007b. doi: 10.1016/j.physrep.2007.02.005.
- E. Nakar and T. Piran. Time-scales in long gamma-ray bursts. *MNRAS*, 331:40–44, March 2002. doi: 10.1046/j.1365-8711.2002.05158.x.
- E. Nakar and T. Piran. Outliers to the peak energy-isotropic energy relation in gamma-ray bursts. *MNRAS*, 360:L73–L76, June 2005. doi: 10.1111/j.1745-3933.2005.00049.x.
- D. Nakauchi, K. Kashiyama, Y. Suwa, and T. Nakamura. Blue Supergiant Model for Ultra-long Gamma-Ray Burst with Superluminous-supernova-like Bump. *ApJ*, 778:67, November 2013. doi: 10.1088/0004-637X/778/1/67.
- P. J. Napier, A. R. Thompson, and R. D. Ekers. The Very Large Array - Design and

- performance of a modern synthesis radio telescope. *IEEE Proceedings*, 71:1295–1320, November 1983.
- R. Narayan, B. Paczynski, and T. Piran. Gamma-ray bursts as the death throes of massive binary stars. *ApJ*, 395:L83–L86, August 1992a. doi: 10.1086/186493.
- R. Narayan, B. Paczynski, and T. Piran. Gamma-ray bursts as the death throes of massive binary stars. *ApJ*, 395:L83–L86, August 1992b. doi: 10.1086/186493.
- R. Narayan, T. Piran, and P. Kumar. Accretion Models of Gamma-Ray Bursts. *ApJ*, 557: 949–957, August 2001. doi: 10.1086/322267.
- P. Narayana Bhat, C. A. Meegan, A. von Kienlin, W. S. Paciesas, M. S. Briggs, J. M. Burgess, E. Burns, V. Chaplin, W. H. Cleveland, A. C. Collazzi, V. Connaughton, A. M. Diekmann, G. Fitzpatrick, M. H. Gibby, M. M. Giles, A. M. Goldstein, J. Greiner, P. A. Jenke, R. M. Kippen, C. Kouveliotou, B. Mailyan, S. McBreen, V. Pelassa, R. D. Preece, O. J. Roberts, L. S. Sparke, M. Stanbro, P. Veres, C. A. Wilson-Hodge, S. Xiong, G. Younes, H.-F. Yu, and B. Zhang. The Third Fermi GBM Gamma-Ray Burst Catalog: The First Six Years. *ApJS*, 223:28, April 2016. doi: 10.3847/0067-0049/223/2/28.
- M. Nardini, G. Ghisellini, G. Ghirlanda, F. Tavecchio, C. Firmani, and D. Lazzati. Clustering of the optical-afterglow luminosities of long gamma-ray bursts. *A&A*, 451:821–833, June 2006. doi: 10.1051/0004-6361:20054085.
- M. Nardini, G. Ghisellini, and G. Ghirlanda. Optical afterglow luminosities in the Swift epoch: confirming clustering and bimodality. *MNRAS*, 386:L87–L91, May 2008a. doi: 10.1111/j.1745-3933.2008.00467.x.
- M. Nardini, G. Ghisellini, and G. Ghirlanda. Optical afterglows of gamma-ray bursts: a bimodal distribution? *MNRAS*, 383:1049–1057, January 2008b. doi: 10.1111/j.1365-2966.2007.12588.x.
- L. Nava, G. Ghisellini, G. Ghirlanda, F. Tavecchio, and C. Firmani. On the interpretation of spectral-energy correlations in long gamma-ray bursts. *A&A*, 450:471–481, May 2006. doi: 10.1051/0004-6361:20054211.
- L. Nava, R. Salvaterra, G. Ghirlanda, G. Ghisellini, S. Campana, S. Covino, G. Cusumano, P. D’Avanzo, V. D’Elia, D. Fugazza, A. Melandri, B. Sbarufatti, S. D. Vergani, and G. Tagliaferri. A complete sample of bright Swift long gamma-ray bursts: testing the spectral-energy correlations. *MNRAS*, 421:1256–1264, April 2012. doi: 10.1111/j.1365-2966.2011.20394.x.
- E. T. Newman, E. Couch, K. Chinnapared, A. Exton, A. Prakash, and R. Torrence. Metric of a Rotating, Charged Mass. *Journal of Mathematical Physics*, 6:918–919, June 1965. doi: 10.1063/1.1704351.

- D. Nielsen, A. Guffanti, and A. et al. Sarkar. Marginal evidence for cosmic acceleration from Type Ia supernovae. *ApJ*, 355:96:6, October 2016. doi: 10.1038/srep35596.
- K. Nomoto, K. Maeda, T. Nakamura, K. Iwamoto, T. Suzuki, P. A. Mazzali, M. Turatto, I. J. Danziger, and F. Patat. Properties of hypernovae: SNe 1997ef, 1998bw, and 1997cy. In R. M. Kippen, R. S. Mallozzi, and G. J. Fishman, editors, *Gamma-ray Bursts, 5th Huntsville Symposium*, volume 526 of *American Institute of Physics Conference Series*, pages 622–627, September 2000. doi: 10.1063/1.1361611.
- J. P. Norris and J. T. Bonnell. Short Gamma-Ray Bursts with Extended Emission. *ApJ*, 643:266–275, May 2006. doi: 10.1086/502796.
- J. P. Norris, R. J. Nemiroff, J. T. Bonnell, J. D. Scargle, C. Kouveliotou, W. S. Paciesas, C. A. Meegan, and G. J. Fishman. Attributes of Pulses in Long Bright Gamma-Ray Bursts. *ApJ*, 459:393, March 1996a. doi: 10.1086/176902.
- J. P. Norris, R. J. Nemiroff, J. T. Bonnell, J. D. Scargle, C. Kouveliotou, W. S. Paciesas, C. A. Meegan, and G. J. Fishman. Attributes of Pulses in Long Bright Gamma-Ray Bursts. *ApJ*, 459:393, March 1996b. doi: 10.1086/176902.
- J. P. Norris, G. F. Marani, and J. T. Bonnell. Connection between Energy-dependent Lags and Peak Luminosity in Gamma-Ray Bursts. *ApJ*, 534:248–257, May 2000. doi: 10.1086/308725.
- J. P. Norris, N. Gehrels, and J. D. Scargle. Threshold for Extended Emission in Short Gamma-ray Bursts. *ApJ*, 717:411–419, July 2010. doi: 10.1088/0004-637X/717/1/411.
- J. A. Nousek, C. Kouveliotou, D. Grupe, K. L. Page, J. Granot, E. Ramirez-Ruiz, S. K. Patel, D. N. Burrows, V. Mangano, S. Barthelmy, A. P. Beardmore, S. Campana, M. Capalbi, G. Chincarini, G. Cusumano, A. D. Falcone, N. Gehrels, P. Giommi, M. R. Goad, O. Godet, C. P. Hurkett, J. A. Kennea, A. Moretti, P. T. O’Brien, J. P. Osborne, P. Romano, G. Tagliaferri, and A. A. Wells. Evidence for a Canonical Gamma-Ray Burst Afterglow Light Curve in the Swift XRT Data. *ApJ*, 642:389–400, May 2006. doi: 10.1086/500724.
- M. Nysewander, A. S. Fruchter, and A. Pe’er. A Comparison of the Afterglows of Short- and Long-duration Gamma-ray Bursts. *ApJ*, 701:824–836, August 2009. doi: 10.1088/0004-637X/701/1/824.
- S. R. Oates, M. J. Page, P. Schady, M. de Pasquale, T. S. Koch, A. A. Breeveld, P. J. Brown, M. M. Chester, S. T. Holland, E. A. Hoversten, N. P. M. Kuin, F. E. Marshall, P. W. A. Roming, M. Still, D. E. vanden Berk, S. Zane, and J. A. Nousek. A statistical study of gamma-ray burst afterglows measured by the Swift Ultraviolet Optical Telescope. *MNRAS*, 395:490–503, May 2009. doi: 10.1111/j.1365-2966.2009.14544.x.
- S. R. Oates, M. J. Page, M. De Pasquale, P. Schady, A. A. Breeveld, S. T. Holland, N. P. M. Kuin, and F. E. Marshall. A correlation between the intrinsic brightness and average

- decay rate of Swift/UVOT gamma-ray burst optical/ultraviolet light curves. MNRAS, 426:L86–L90, October 2012. doi: 10.1111/j.1745-3933.2012.01331.x.
- S. R. Oates, J. L. Racusin, M. De Pasquale, M. J. Page, A. J. Castro-Tirado, J. Gorosabel, P. J. Smith, A. A. Breeveld, and N. P. M. Kuin. Exploring the canonical behaviour of long gamma-ray bursts using an intrinsic multiwavelength afterglow correlation. MNRAS, 453:4121–4135, November 2015. doi: 10.1093/mnras/stv1956.
- P. T. O’Brien and R. Willingale. Using Swift observations of prompt and afterglow emission to classify GRBs. *Royal Society of London Philosophical Transactions Series A*, 365: 1179–1188, May 2007. doi: 10.1098/rsta.2006.1984.
- P. T. O’Brien, R. Willingale, J. Osborne, M. R. Goad, K. L. Page, S. Vaughan, E. Rol, A. Beardmore, O. Godet, C. P. Hurkett, A. Wells, B. Zhang, S. Kobayashi, D. N. Burrows, J. A. Nousek, J. A. Kennea, A. Falcone, D. Grupe, N. Gehrels, S. Barthelmy, J. Cannizzo, J. Cummings, J. E. Hill, H. Krimm, G. Chincarini, G. Tagliaferri, S. Campana, A. Moretti, P. Giommi, M. Perri, V. Mangano, and V. LaParola. The Early X-Ray Emission from GRBs. ApJ, 647:1213–1237, August 2006. doi: 10.1086/505457.
- R. Ouyed and J. Staff. Quark-novae in neutron star - white dwarf binaries: a model for luminous (spin-down powered) sub-Chandrasekhar-mass Type Ia supernovae? *Research in Astronomy and Astrophysics*, 13:435–464, April 2013. doi: 10.1088/1674-4527/13/4/006.
- B. Paczynski. Gamma-ray bursters at cosmological distances. ApJ, 308:L43–L46, September 1986. doi: 10.1086/184740.
- B. Paczynski. Super-Eddington winds from neutron stars. ApJ, 363:218–226, November 1990. doi: 10.1086/169332.
- B. Paczynski. On the Galactic origin of gamma-ray bursts. Acta Astron., 41:157–166, 1991a.
- B. Paczynski. Cosmological gamma-ray bursts. Acta Astron., 41:257–267, 1991b.
- B. Paczyński. Are Gamma-Ray Bursts in Star-Forming Regions? ApJ, 494:L45–L48, February 1998. doi: 10.1086/311148.
- D. N. Page and K. S. Thorne. Disk-Accretion onto a Black Hole. Time-Averaged Structure of Accretion Disk. ApJ, 191:499–506, July 1974. doi: 10.1086/152990.
- A. Panaiteescu. An external-shock origin of the relation for gamma-ray bursts. MNRAS, 393: 1010–1015, March 2009. doi: 10.1111/j.1365-2966.2008.14240.x.
- A. Panaiteescu and P. Kumar. Analytic Light Curves of Gamma-Ray Burst Afterglows: Homogeneous versus Wind External Media. ApJ, 543:66–76, November 2000. doi: 10.1086/317090.
- A. Panaiteescu and P. Kumar. Properties of Relativistic Jets in Gamma-Ray Burst Afterglows. ApJ, 571:779–789, June 2002. doi: 10.1086/340094.

- A. Panaiteescu and W. T. Vestrand. Taxonomy of gamma-ray burst optical light curves: identification of a salient class of early afterglows. *MNRAS*, 387:497–504, June 2008. doi: 10.1111/j.1365-2966.2008.13231.x.
- A. Panaiteescu and W. T. Vestrand. Optical afterglows of gamma-ray bursts: peaks, plateaus and possibilities. *MNRAS*, 414:3537–3546, July 2011. doi: 10.1111/j.1365-2966.2011.18653.x.
- A. Panaiteescu, L. Wen, P. Laguna, and P. Mészáros. Impact of Relativistic Fireballs on External Matter: Numerical Models of Cosmological Gamma-Ray Bursts. *ApJ*, 482: 942–950, June 1997. doi: 10.1086/304185.
- A. Panaiteescu, M. Spada, and P. Mészáros. Power Density Spectra of Gamma-Ray Bursts in the Internal Shock Model. *ApJ*, 522:L105–L108, September 1999. doi: 10.1086/312230.
- A. Panaiteescu, P. Mészáros, D. Burrows, J. Nousek, N. Gehrels, P. O’Brien, and R. Willingale. Evidence for chromatic X-ray light-curve breaks in Swift gamma-ray burst afterglows and their theoretical implications. *MNRAS*, 369:2059–2064, July 2006. doi: 10.1111/j.1365-2966.2006.10453.x.
- A. Panaiteescu, W. T. Vestrand, and P. Woźniak. An external-shock model for gamma-ray burst afterglow 130427A. *MNRAS*, 436:3106–3111, December 2013. doi: 10.1093/mnras/stt1792.
- A. Pe’er. Temporal Evolution of Thermal Emission from Relativistically Expanding Plasma. *ApJ*, 682:463–473, July 2008. doi: 10.1086/588136.
- A. Pe’er. Physics of Gamma-Ray Bursts Prompt Emission. *Advances in Astronomy*, 2015: 907321, 2015. doi: 10.1155/2015/907321.
- A. Pe’er. Theory of Photospheric Emission in Gamma-Ray Bursts. In K. Rosquist, editor, *Thirteenth Marcel Grossmann Meeting: On Recent Developments in Theoretical and Experimental General Relativity, Astrophysics and Relativistic Field Theories*, pages 1745–1747, January 2015. doi: 10.1142/9789814623995_0271.
- Z. Y. Peng, Y. Yin, T. F. Yi, Y. Y. Bao, and H. Wu. A comprehensive comparative study of temporal properties between X-ray flares and GRB pulses. *Ap&SS*, 355:95–103, January 2015. doi: 10.1007/s10509-014-2149-7.
- D. A. Perley, N. R. Tanvir, J. Hjorth, T. Laskar, E. Berger, R. Chary, A. de Ugarte Postigo, J. P. U. Fynbo, T. Krühler, A. J. Levan, M. J. Michałowski, and S. Schulze. The Swift GRB Host Galaxy Legacy Survey. II. Rest-frame Near-IR Luminosity Distribution and Evidence for a Near-solar Metallicity Threshold. *ApJ*, 817:8, January 2016. doi: 10.3847/0004-637X/817/1/8.
- S. Perlmutter. Supernovae, Dark Energy, and the Accelerating Universe. *Physics Today*, 56 (4):53–62, April 2003. doi: 10.1063/1.1580050.

- S. Perlmutter, G. Aldering, M. della Valle, S. Deustua, R. S. Ellis, S. Fabbro, A. Fruchter, G. Goldhaber, D. E. Groom, I. M. Hook, A. G. Kim, M. Y. Kim, R. A. Knop, C. Lidman, R. G. McMahon, P. Nugent, R. Pain, N. Panagia, C. R. Pennypacker, P. Ruiz-Lapuente, B. Schaefer, and N. Walton. Discovery of a supernova explosion at half the age of the universe. *Nature*, 391:51, January 1998. doi: 10.1038/34124.
- R. Perna, P. J. Armitage, and B. Zhang. Flares in Long and Short Gamma-Ray Bursts: A Common Origin in a Hyperaccreting Accretion Disk. *ApJ*, 636:L29–L32, January 2006. doi: 10.1086/499775.
- R. Perna, D. Lazzati, and B. Giacomazzo. Short Gamma-Ray Bursts from the Merger of Two Black Holes. *ApJ*, 821:L18, April 2016. doi: 10.3847/2041-8205/821/1/L18.
- J. H. Petersen, K. K. Holst, and E. Budtz-Jørgensen. Correcting a Statistical Artifact in the Estimation of the Hubble Constant Based on Type Ia Supernovae Results in a Change in Estimate of 1.2%. *ApJ*, 723:966–968, November 2010. doi: 10.1088/0004-637X/723/1/966.
- V. Petrosian, A. Bouvier, and F. Ryde. Gamma-Ray Bursts as Cosmological Tools. *ArXiv e-prints*, September 2009.
- Vahe Petrosian, Jack Singal, and Lukasz Stawarz. Luminosity correlations, luminosity evolutions, and radio loudness of agns from multiwavelength observations. In *Mult wavelength AGN Surveys and Studies*, volume 9 of *Proceedings of the International Astronomical Union*, pages 172–172, 10 2013. doi: 10.1017/S174392131400369X. URL http://journals.cambridge.org/article_S174392131400369X.
- M. M. Phillips. The absolute magnitudes of Type IA supernovae. *ApJ*, 413:L105–L108, August 1993. doi: 10.1086/186970.
- T. Piran. Gamma-ray bursts and the fireball model. *Phys. Rep.*, 314:575–667, June 1999. doi: 10.1016/S0370-1573(98)00127-6.
- T. Piran. The physics of gamma-ray bursts. *Reviews of Modern Physics*, 76:1143–1210, October 2004. doi: 10.1103/RevModPhys.76.1143.
- T. Piran, E. Nakar, P. Mazzali, and E. Pian. Relativistic Jets in Core Collapse Supernovae. *ArXiv e-prints*, April 2017.
- L. Piro, G. Garmire, M. Garcia, G. Stratta, E. Costa, M. Feroci, P. Mészáros, M. Vietri, H. Bradt, D. Frail, F. Frontera, J. Halpern, J. Heise, K. Hurley, N. Kawai, R. M. Kippen, F. Marshall, T. Murakami, V. V. Sokolov, T. Takeshima, and A. Yoshida. Observation of X-ray Lines from a Gamma-Ray Burst (GRB991216): Evidence of Moving Ejecta from the Progenitor. *Science*, 290:955–958, November 2000. doi: 10.1126/science.290.5493.955.
- Planck Collaboration, P. A. R. Ade, N. Aghanim, M. Arnaud, M. Ashdown, J. Aumont, C. Baccigalupi, A. J. Banday, R. B. Barreiro, J. G. Bartlett, and et al. Planck 2015 results.

- XIII. Cosmological parameters. *A&A*, 594:A13, September 2016. doi: 10.1051/0004-6361/201525830.
- A. Pontzen, A. Deason, F. Governato, M. Pettini, J. Wadsley, T. Quinn, A. Brooks, J. Bellovary, and J. P. U. Fynbo. The nature of HIabsorbers in gamma-ray burst afterglows: clues from hydrodynamic simulations. *MNRAS*, 402:1523–1535, March 2010. doi: 10.1111/j.1365-2966.2009.16017.x.
- C. Porciani and P. Madau. On the Association of Gamma-Ray Bursts with Massive Stars: Implications for Number Counts and Lensing Statistics. *ApJ*, 548:522–531, February 2001. doi: 10.1086/319027.
- S. Postnikov, M. G. Dainotti, X. Hernandez, and S. Capozziello. Nonparametric Study of the Evolution of the Cosmological Equation of State with SNeIa, BAO, and High-redshift GRBs. *ApJ*, 783:126, March 2014. doi: 10.1088/0004-637X/783/2/126.
- R. D. Preece, M. S. Briggs, R. S. Mallozzi, G. N. Pendleton, W. S. Paciesas, and D. L. Band. The BATSE Gamma-Ray Burst Spectral Catalog. I. High Time Resolution Spectroscopy of Bright Bursts Using High Energy Resolution Data. *ApJS*, 126:19–36, January 2000. doi: 10.1086/313289.
- D. Proga and B. Zhang. The late time evolution of gamma-ray bursts: ending hyperaccretion and producing flares. *MNRAS*, 370:L61–L65, July 2006. doi: 10.1111/j.1745-3933.2006.00189.x.
- S. Qi and T. Lu. A New Luminosity Relation for Gamma-ray Bursts and its Implication. *ApJ*, 717:1274–1278, July 2010. doi: 10.1088/0004-637X/717/2/1274.
- Y.-P. Qin and Z.-F. Chen. Statistical classification of gamma-ray bursts based on the Amati relation. *MNRAS*, 430:163–173, March 2013. doi: 10.1093/mnras/sts547.
- Y.-P. Qin, G.-Z. Xie, S.-J. Xue, E.-W. Liang, X.-T. Zheng, and D.-C. Mei. The Hardness-Duration Correlation in the Two Classes of Gamma-Ray Bursts. *PASJ*, 52:759, October 2000. doi: 10.1093/pasj/52.5.759.
- F. Quilligan, B. McBreen, L. Hanlon, S. McBreen, K. J. Hurley, and D. Watson. Temporal properties of gamma ray bursts as signatures of jets from the central engine. *A&A*, 385:377–398, April 2002. doi: 10.1051/0004-6361:20020038.
- J. L. Racusin, S. R. Oates, P. Schady, D. N. Burrows, M. de Pasquale, D. Donato, N. Gehrels, S. Koch, J. McEnery, T. Piran, P. Roming, T. Sakamoto, C. Swenson, E. Troja, V. Vasileiou, F. Virgili, D. Wanderman, and B. Zhang. Fermi and Swift Gamma-ray Burst Afterglow Population Studies. *ApJ*, 738:138, September 2011. doi: 10.1088/0004-637X/738/2/138.
- J. L. Racusin, S. R. Oates, M. de Pasquale, and D. Kocevski. A Correlation between the Intrinsic Brightness and Average Decay Rate of Gamma-Ray Burst X-Ray Afterglow Light Curves. *ApJ*, 826:45, July 2016. doi: 10.3847/0004-637X/826/1/45.

- E. Ramirez-Ruiz. Photospheric signatures imprinted on the γ -ray burst spectra. MNRAS, 363:L61–L65, October 2005. doi: 10.1111/j.1745-3933.2005.00089.x.
- N. Rea, M. Gullón, J. A. Pons, R. Perna, M. G. Dainotti, J. A. Miralles, and D. F. Torres. Constraining the GRB-Magnetar Model by Means of the Galactic Pulsar Population. ApJ, 813:92, November 2015. doi: 10.1088/0004-637X/813/2/92.
- M. J. Rees and P. Meszaros. Relativistic fireballs - Energy conversion and time-scales. MNRAS, 258:41P–43P, September 1992.
- M. J. Rees and P. Meszaros. Unsteady outflow models for cosmological gamma-ray bursts. ApJ, 430:L93–L96, August 1994. doi: 10.1086/187446.
- M. J. Rees and P. Mészáros. Refreshed Shocks and Afterglow Longevity in Gamma-Ray Bursts. ApJ, 496:L1–L4, March 1998. doi: 10.1086/311244.
- M. J. Rees and P. Mészáros. Dissipative Photosphere Models of Gamma-Ray Bursts and X-Ray Flashes. ApJ, 628:847–852, August 2005. doi: 10.1086/430818.
- J. N. Reeves, D. Watson, J. P. Osborne, K. A. Pounds, P. T. O'Brien, A. D. T. Short, M. J. L. Turner, M. G. Watson, K. O. Mason, M. Ehle, and N. Schartel. The signature of supernova ejecta in the X-ray afterglow of the γ -ray burst 011211. Nature, 416:512–515, April 2002. doi: 10.1038/416512a.
- D. E. Reichart and M. C. Nysewander. GRB Variability-Luminosity Correlation Confirmed. *ArXiv Astrophysics e-prints*, August 2005.
- D. E. Reichart, D. Q. Lamb, E. E. Fenimore, E. Ramirez-Ruiz, T. L. Cline, and K. Hurley. A Possible Cepheid-like Luminosity Estimator for the Long Gamma-Ray Bursts. ApJ, 552:57–71, May 2001. doi: 10.1086/320434.
- D.E. et al. Reichart. A Bayesian Inference Analysis of the X-Ray Cluster Luminosity-Temperature Relation. ApJ, 516:1, 1999. doi: 10.1086/307105.
- J. E. Rhoads. How to Tell a Jet from a Balloon: A Proposed Test for Beaming in Gamma-Ray Bursts. ApJ, 487:L1–L4, September 1997. doi: 10.1086/310876.
- J. E. Rhoads. The Dynamics and Light Curves of Beamed Gamma-Ray Burst Afterglows. ApJ, 525:737–749, November 1999. doi: 10.1086/307907.
- A. G. Riess, A. V. Filippenko, P. Challis, A. Clocchiatti, A. Diercks, P. M. Garnavich, R. L. Gilliland, C. J. Hogan, S. Jha, R. P. Kirshner, B. Leibundgut, M. M. Phillips, D. Reiss, B. P. Schmidt, R. A. Schommer, R. C. Smith, J. Spyromilio, C. Stubbs, N. B. Suntzeff, and J. Tonry. Observational Evidence from Supernovae for an Accelerating Universe and a Cosmological Constant. AJ, 116:1009–1038, September 1998. doi: 10.1086/300499.
- A. G. Riess, L.-G. Strolger, J. Tonry, S. Casertano, H. C. Ferguson, B. Mobasher, P. Challis, A. V. Filippenko, S. Jha, W. Li, R. Chornock, R. P. Kirshner, B. Leibundgut, M. Dickinson,

- M. Livio, M. Giavalisco, C. C. Steidel, T. Benítez, and Z. Tsvetanov. Type Ia Supernova Discoveries at $z > 1$ from the Hubble Space Telescope: Evidence for Past Deceleration and Constraints on Dark Energy Evolution. *ApJ*, 607:665–687, June 2004. doi: 10.1086/383612.
- A. G. Riess, L. Macri, S. Casertano, M. Sosey, H. Lampeitl, H. C. Ferguson, A. V. Filippenko, S. W. Jha, W. Li, R. Chornock, and D. Sarkar. A Redetermination of the Hubble Constant with the Hubble Space Telescope from a Differential Distance Ladder. *ApJ*, 699:539–563, July 2009. doi: 10.1088/0004-637X/699/1/539.
- A. G. Riess, L. M. Macri, S. L. Hoffmann, D. Scolnic, S. Casertano, A. V. Filippenko, B. E. Tucker, M. J. Reid, D. O. Jones, J. M. Silverman, R. Chornock, P. Challis, W. Yuan, P. J. Brown, and R. J. Foley. A 2.4% Determination of the Local Value of the Hubble Constant. *ApJ*, 826:56, July 2016. doi: 10.3847/0004-637X/826/1/56.
- D. Rizzuto, C. Guidorzi, P. Romano, S. Covino, S. Campana, M. Capalbi, G. Chincarini, G. Cusumano, D. Fugazza, V. Mangano, A. Moretti, M. Perri, and G. Tagliaferri. Testing the gamma-ray burst variability/peak luminosity correlation on a Swift homogeneous sample. *MNRAS*, 379:619–628, August 2007. doi: 10.1111/j.1365-2966.2007.11880.x.
- B. E. Robertson and R. S. Ellis. Connecting the Gamma Ray Burst Rate and the Cosmic Star Formation History: Implications for Reionization and Galaxy Evolution. *ApJ*, 744:95, January 2012. doi: 10.1088/0004-637X/744/2/95.
- S. A. Rodney, A. G. Riess, D. M. Scolnic, D. O. Jones, S. Hemmati, A. Molino, C. McCully, B. Mobasher, L.-G. Strolger, O. Graur, B. Hayden, and S. Casertano. Two SNe Ia at Redshift ~ 2 : Improved Classification and Redshift Determination with Medium-band Infrared Imaging. *AJ*, 150:156, November 2015. doi: 10.1088/0004-6256/150/5/156.
- A. Rowlinson and P. O’Brien. Energy injection in short GRBs and the role of magnetars. In *Gamma-Ray Bursts 2012 Conference (GRB 2012)*, 2012.
- A. Rowlinson, P. T. O’Brien, and N. R. Tanvir. The unusual X-ray emission of the short Swift GRB 090515: Evidence for the formation of a magnetar? In J. E. McEnery, J. L. Racusin, and N. Gehrels, editors, *American Institute of Physics Conference Series*, volume 1358 of *American Institute of Physics Conference Series*, pages 195–198, August 2011. doi: 10.1063/1.3621770.
- A. Rowlinson, P. T. O’Brien, B. D. Metzger, N. R. Tanvir, and A. J. Levan. Signatures of magnetar central engines in short GRB light curves. *MNRAS*, 430:1061–1087, April 2013. doi: 10.1093/mnras/sts683.
- A. Rowlinson, B. P. Gompertz, M. Dainotti, P. T. O’Brien, R. A. M. J. Wijers, and A. J. van der Horst. Constraining properties of GRB magnetar central engines using the observed plateau luminosity and duration correlation. *MNRAS*, 443:1779–1787, September 2014. doi: 10.1093/mnras/stu1277.

- A. Roychoudhury, S. K. Sarkar, and A. Bhadra. Spectral Lag Features of GRB 060814 from Swift BAT and Suzaku Observations. *ApJ*, 782:105, February 2014. doi: 10.1088/0004-637X/782/2/105.
- D. Rubin, G. Aldering, and K. et al. Barbary. UNITY: Confronting Supernova Cosmology's Statistical and Systematic Uncertainties in a Unified Bayesian Framework. *ApJ*, 813:2, November 2015. doi: 10.1088/0004-637X/813/2/137.
- M. Ruderman and K. S. Cheng. Evolution of a short-period gamma-ray pulsar family - Crab, Vela. COS B source, gamma-ray burst source. *ApJ*, 335:306–318, December 1988. doi: 10.1086/166929.
- R. Ruffini, J. D. Salmonson, J. R. Wilson, and S.-S. Xue. On the pair electromagnetic pulse of a black hole with electromagnetic structure. *A&A*, 350:334–343, October 1999.
- R. Ruffini, M. Muccino, C. L. Bianco, M. Enderli, L. Izzo, M. Kovacevic, A. V. Penacchioni, G. B. Pisani, J. A. Rueda, and Y. Wang. On binary-driven hypernovae and their nested late X-ray emission. *A&A*, 565:L10, May 2014. doi: 10.1051/0004-6361/201423812.
- R. Ruffini, J. A. Rueda, M. Muccino, Y. Aimuratov, L. M. Becerra, C. L. Bianco, M. Kovacevic, R. Moradi, F. G. Oliveira, G. B. Pisani, and Y. Wang. On the Classification of GRBs and Their Occurrence Rates. *ApJ*, 832:136, December 2016. doi: 10.3847/0004-637X/832/2/136.
- G. Ryan, H. van Eerten, A. MacFadyen, and B.-B. Zhang. Gamma-Ray Bursts are Observed Off-axis. *ApJ*, 799:3, January 2015. doi: 10.1088/0004-637X/799/1/3.
- F. Ryde. Is Thermal Emission in Gamma-Ray Bursts Ubiquitous? *ApJ*, 625:L95–L98, June 2005. doi: 10.1086/431239.
- F. Ryde and V. Petrosian. Gamma-Ray Burst Spectra and Light Curves as Signatures of a Relativistically Expanding Plasma. *ApJ*, 578:290–303, October 2002. doi: 10.1086/342271.
- F. Ryde and R. Svensson. On the Variety of the Spectral and Temporal Behavior of Long Gamma-Ray Burst Pulses. *ApJ*, 566:210–228, February 2002. doi: 10.1086/337962.
- F. Ryde, C.-I. Björnsson, Y. Kaneko, P. Mészáros, R. Preece, and M. Battelino. Gamma-Ray Burst Spectral Correlations: Photospheric and Injection Effects. *ApJ*, 652:1400–1415, December 2006. doi: 10.1086/508410.
- T. Sakamoto, D. Q. Lamb, C. Graziani, T. Q. Donaghy, M. Suzuki, G. Ricker, J.-L. Atteia, N. Kawai, A. Yoshida, Y. Shirasaki, T. Tamagawa, K. Torii, M. Matsuoka, E. E. Fenimore, M. Galassi, T. Tavener, J. Doty, R. Vanderspek, G. B. Crew, J. Villasenor, N. Butler, G. Prigozhin, J. G. Jernigan, C. Barraud, M. Boer, J.-P. Dezelaly, J.-F. Olive, K. Hurley, A. Levine, G. Monnelly, F. Martel, E. Morgan, S. E. Woosley, T. Cline, J. Braga, R. Manchanda, G. Pizzichini, K. Takagishi, and M. Yamauchi. High Energy Transient

- Explorer 2 Observations of the Extremely Soft X-Ray Flash XRF 020903. *ApJ*, 602: 875–885, February 2004. doi: 10.1086/381232.
- T. Sakamoto, D. Q. Lamb, N. Kawai, A. Yoshida, C. Graziani, E. E. Fenimore, T. Q. Donaghy, M. Matsuoka, M. Suzuki, G. Ricker, J.-L. Atteia, Y. Shirasaki, T. Tamagawa, K. Torii, M. Galassi, J. Doty, R. Vanderspek, G. B. Crew, J. Villasenor, N. Butler, G. Prigozhin, J. G. Jernigan, C. Barraud, M. Boer, J.-P. Dezalay, J.-F. Olive, K. Hurley, A. Levine, G. Monnelly, F. Martel, E. Morgan, S. E. Woosley, T. Cline, J. Braga, R. Manchanda, G. Pizzichini, K. Takagishi, and M. Yamauchi. Global Characteristics of X-Ray Flashes and X-Ray-Rich Gamma-Ray Bursts Observed by HETE-2. *ApJ*, 629:311–327, August 2005. doi: 10.1086/431235.
- T. Sakamoto, J. E. Hill, R. Yamazaki, L. Angelini, H. A. Krimm, G. Sato, S. Swindell, K. Takami, and J. P. Osborne. Evidence of Exponential Decay Emission in the Swift Gamma-Ray Bursts. *ApJ*, 669:1115–1129, November 2007. doi: 10.1086/521640.
- M. Sako, F. A. Harrison, and R. E. Rutledge. A Search for Discrete X-Ray Spectral Features in a Sample of Bright γ -Ray Burst Afterglows. *ApJ*, 623:973–999, April 2005. doi: 10.1086/425644.
- J. D. Salmonson. On the Kinematic Origin of the Luminosity-Pulse Lag Relationship in Gamma-Ray Bursts. *ApJ*, 544:L115–L117, December 2000. doi: 10.1086/317305.
- J. D. Salmonson and T. J. Galama. Discovery of a Tight Correlation between Pulse Lag/Luminosity and Jet-Break Times: A Connection between Gamma-Ray Bursts and Afterglow Properties. *ApJ*, 569:682–688, April 2002. doi: 10.1086/339391.
- R. Salvaterra. High redshift Gamma-Ray Bursts. *Journal of High Energy Astrophysics*, 7: 35–43, September 2015. doi: 10.1016/j.jheap.2015.03.001.
- R. Sari and P. Mészáros. Impulsive and Varying Injection in Gamma-Ray Burst Afterglows. *ApJ*, 535:L33–L37, May 2000. doi: 10.1086/312689.
- R. Sari and T. Piran. Variability in Gamma-Ray Bursts: A Clue. *ApJ*, 485:270–273, August 1997. doi: 10.1086/304428.
- R. Sari and T. Piran. GRB 990123: The Optical Flash and the Fireball Model. *ApJ*, 517: L109–L112, June 1999. doi: 10.1086/312039.
- R. Sari, T. Piran, and J. P. Halpern. Jets in Gamma-Ray Bursts. *ApJ*, 519:L17–L20, July 1999. doi: 10.1086/312109.
- V. Savchenko, C. Ferrigno, S. Mereghetti, L. Natalucci, A. Bazzano, E. Bozzo, S. Brandt, T. J.-L. Courvoisier, R. Diehl, L. Hanlon, A. von Kienlin, E. Kuulkers, P. Laurent, F. Lebrun, J. P. Roques, P. Ubertini, and G. Weidenspointner. INTEGRAL Upper Limits on Gamma-Ray Emission Associated with the Gravitational Wave Event GW150914. *ApJ*, 820:L36, April 2016. doi: 10.3847/2041-8205/820/2/L36.

- P. Schady, K. O. Mason, M. J. Page, M. de Pasquale, D. C. Morris, P. Romano, P. W. A. Roming, S. Immler, and D. E. vanden Berk. Dust and gas in the local environments of gamma-ray bursts. *MNRAS*, 377:273–284, May 2007. doi: 10.1111/j.1365-2966.2007.11592.x.
- B. Schaefer. Four luminosity indicators for gamma-ray bursts. In *34th COSPAR Scientific Assembly*, volume 34 of *COSPAR Meeting*, page 1141, 2002.
- B. E. Schaefer. Gamma-Ray Burst Hubble Diagram to $z=4.5$. *ApJ*, 583:L67–L70, February 2003a. doi: 10.1086/368104.
- B. E. Schaefer. Explaining the Gamma-Ray Burst E_{peak} Distribution. *ApJ*, 583:L71–L74, February 2003b. doi: 10.1086/368106.
- B. E. Schaefer. Explaining the Gamma-Ray Burst Lag/Luminosity Relation. *ApJ*, 602:306–311, February 2004. doi: 10.1086/380898.
- B. E. Schaefer. The Hubble Diagram to Redshift > 6 from 69 Gamma-Ray Bursts. *ApJ*, 660:16–46, May 2007. doi: 10.1086/511742.
- B. E. Schaefer, M. Deng, and D. L. Band. Redshifts and Luminosities for 112 Gamma-Ray Bursts. *ApJ*, 563:L123–L127, December 2001. doi: 10.1086/338651.
- B. E. Schaefer. Gamma-ray bursts: The brightest explosions in the universe, 2002.
- S. Schulze, D. Malesani, A. Cucchiara, N. R. Tanvir, T. Krühler, A. de Ugarte Postigo, G. Leloudas, J. Lyman, D. Bersier, K. Wiersema, D. A. Perley, P. Schady, J. Gorosabel, J. P. Anderson, A. J. Castro-Tirado, S. B. Cenko, A. De Cia, L. E. Ellerbroek, J. P. U. Fynbo, J. Greiner, J. Hjorth, D. A. Kann, L. Kaper, S. Klose, A. J. Levan, S. Martín, P. T. O’Brien, K. L. Page, G. Pignata, S. Rapaport, R. Sánchez-Ramírez, J. Sollerman, I. A. Smith, M. Sparre, C. C. Thöne, D. J. Watson, D. Xu, F. E. Bauer, M. Bayliss, G. Björnsson, M. Bremer, Z. Cano, S. Covino, V. D’Elia, D. A. Frail, S. Geier, P. Goldoni, O. E. Hartoog, P. Jakobsson, H. Korhonen, K. Y. Lee, B. Milvang-Jensen, M. Nardini, A. Nicuesa Guelbenzu, M. Oguri, S. B. Pandey, G. Petitpas, A. Rossi, A. Sandberg, S. Schmidl, G. Tagliaferri, R. P. J. Tilanus, J. M. Winters, D. Wright, and E. Wuyts. GRB 120422A/SN 2012bz: Bridging the gap between low- and high-luminosity gamma-ray bursts. *A&A*, 566:A102, June 2014. doi: 10.1051/0004-6361/201423387.
- B. F. Schutz. Determining the Hubble constant from gravitational wave observations. *Nature*, 323:310, September 1986. doi: 10.1038/323310a0.
- B. F. Schutz. Lighthouses of Gravitational Wave Astronomy. In M. Gilfanov, R. Sunyeav, and E. Churazov, editors, *Lighthouses of the Universe: The Most Luminous Celestial Objects and Their Use for Cosmology*, page 207, 2002. doi: 10.1007/10856495_29.
- L. Shao and Z. G. Dai. Behavior of X-Ray Dust Scattering and Implications for X-Ray Afterglows of Gamma-Ray Bursts. *ApJ*, 660:1319–1325, May 2007. doi: 10.1086/513139.

- L. Shao, Z. G. Dai, and N. Mirabal. Echo Emission from Dust Scattering and X-Ray Afterglows of Gamma-Ray Bursts. *ApJ*, 675:507–518, March 2008. doi: 10.1086/527047.
- H. et al. Shariff. BAHAMAS: New SNIa Analysis Reveals Inconsistencies with Standard Cosmology . *ApJ*, 827:1, 2016.
- A. Shemi and T. Piran. The appearance of cosmic fireballs. *ApJ*, 365:L55–L58, December 1990. doi: 10.1086/185887.
- R.-F. Shen, R. Willingale, P. Kumar, P. T. O'Brien, and P. A. Evans. The dust scattering model cannot explain the shallow X-ray decay in GRB afterglows. *MNRAS*, 393:598–606, February 2009. doi: 10.1111/j.1365-2966.2008.14223.x.
- Y. Shirasaki, N. Kawai, A. Yoshida, T. Tamagawa, K. Torii, T. Sakamoto, M. Matsuoka, E. E. Fenimore, M. C. Galassi, D. Q. Lamb, C. Graziani, T. Q. Donaghy, R. K. Vanderspek, M. Yamauchi, K. Tagagishi, and I. Hatsukade. In-orbit performance of wide-field x-ray monitor on HETE-2. In J. E. Truemper and H. D. Tananbaum, editors, *X-Ray and Gamma-Ray Telescopes and Instruments for Astronomy.*, volume 4851 of Proc. SPIE, pages 1310–1319, March 2003. doi: 10.1117/12.461414.
- S. J. Smartt, P. M. Vreeswijk, E. Ramirez-Ruiz, G. F. Gilmore, W. P. S. Meikle, A. M. N. Ferguson, and J. H. Knapen. On the Progenitor of the Type Ic Supernova 2002ap. *ApJ*, 572:L147–L151, June 2002. doi: 10.1086/341747.
- M. V. Smolsky and V. V. Usov. Relativistic Beam–Magnetic Barrier Collision and Nonthermal Radiation of Cosmological γ -Ray Bursters. *ApJ*, 461:858, April 1996. doi: 10.1086/177107.
- M. Sparre, J. Sollerman, J. P. U. Fynbo, D. Malesani, P. Goldoni, A. de Ugarte Postigo, S. Covino, V. D'Elia, H. Flores, F. Hammer, J. Hjorth, P. Jakobsson, L. Kaper, G. Leloudas, A. J. Levan, B. Milvang-Jensen, S. Schulze, G. Tagliaferri, N. R. Tanvir, D. J. Watson, K. Wiersema, and R. A. M. J. Wijers. Spectroscopic Evidence for SN 2010ma Associated with GRB 101219B. *ApJ*, 735:L24, July 2011. doi: 10.1088/2041-8205/735/1/L24.
- C. Spearman. The proof and measurement of association between two things. *The American Journal of Psychology*, 15(1):72–101, 1904. ISSN 00029556. URL <http://www.jstor.org/stable/1412159>.
- K. Z. Stanek, P. M. Garnavich, J. Kaluzny, W. Pych, and I. Thompson. BVRI Observations of the Optical Afterglow of GRB 990510. *ApJ*, 522:L39–L42, September 1999. doi: 10.1086/312219.
- B. E. Stern and R. Svensson. Evidence for "Chain Reaction" in the Time Profiles of Gamma-Ray Bursts. *ApJ*, 469:L109, October 1996. doi: 10.1086/310267.
- D. Stern, R. Jimenez, L. Verde, S. A. Stanford, and M. Kamionkowski. Cosmic Chronometers: Constraining the Equation of State of Dark Energy. II. A Spectroscopic Catalog of

Red Galaxies in Galaxy Clusters. *ApJS*, 188:280–289, May 2010. doi: 10.1088/0067-0049/188/1/280.

- G. Stratta, S. Basa, N. Butler, J. L. Atteia, B. Gendre, A. Pé langeon, F. Malacrino, Y. Mellier, D. A. Kann, S. Klose, A. Zeh, N. Masetti, E. Palazzi, J. Gorosabel, A. J. Castro-Tirado, A. de Ugarte Postigo, M. Jelinek, J. Cepa, H. Castañeda, D. Martínez-Delgado, M. Boér, J. Braga, G. Crew, T. Q. Donaghy, J.-P. Dezalay, J. Doty, E. E. Fenimore, M. Galassi, C. Graziani, J. G. Jernigan, N. Kawai, D. Q. Lamb, A. Levine, R. K. Manchanda, F. Martel, M. Matsuoka, Y. Nakagawa, J.-F. Olive, G. Pizzichini, G. Prigozhin, G. Ricker, T. Sakamoto, Y. Shirasaki, S. Sugita, M. Suzuki, K. Takagishi, T. Tamagawa, R. Vanderspek, J. Villasenor, S. E. Woosley, M. Yamauchi, and A. Yoshida. X-ray flashes or soft gamma-ray bursts?. The case of the likely distant XRF 040912. *A&A*, 461:485–492, January 2007. doi: 10.1051/0004-6361:20065831.
- G. Stratta, D. Guetta, V. D’Elia, M. Perri, S. Covino, and L. Stella. Evidence for an anticorrelation between the duration of the shallow decay phase of GRB X-ray afterglows and redshift. *A&A*, 494:L9–L12, February 2009. doi: 10.1051/0004-6361:200811335.
- G. Stratta, B. Gendre, J. L. Atteia, M. Boér, D. M. Coward, M. De Pasquale, E. Howell, A. Klotz, S. Oates, and L. Piro. The Ultra-long GRB 111209A. II. Prompt to Afterglow and Afterglow Properties. *ApJ*, 779:66, December 2013. doi: 10.1088/0004-637X/779/1/66.
- T. E. Strohmayer, E. E. Fenimore, T. Murakami, and A. Yoshida. X-Ray Spectral Characteristics of GINGA Gamma-Ray Bursts. *ApJ*, 500:873–887, June 1998. doi: 10.1086/305735.
- J. Sultana, D. Kazanas, and K. Fukumura. Luminosity Correlations for Gamma-Ray Bursts and Implications for Their Prompt and Afterglow Emission Mechanisms. *ApJ*, 758:32, October 2012. doi: 10.1088/0004-637X/758/1/32.
- J. Sultana, D. Kazanas, and A. Mastichiadis. The Supercritical Pile Gamma-Ray Burst Model: The GRB Afterglow Steep Decline and Plateau Phase. *ApJ*, 779:16, December 2013. doi: 10.1088/0004-637X/779/1/16.
- N. Suzuki, D. Rubin, C. Lidman, G. Aldering, R. Amanullah, K. Barbary, L. F. Barrientos, J. Botyanszki, M. Brodwin, N. Connolly, K. S. Dawson, A. Dey, M. Doi, M. Donahue, S. Deustua, P. Eisenhardt, E. Ellingson, L. Faccioli, V. Fadeyev, H. K. Fakhouri, A. S. Fruchter, D. G. Gilbank, M. D. Gladders, G. Goldhaber, A. H. Gonzalez, A. Goobar, A. Gude, T. Hattori, H. Hoekstra, E. Hsiao, X. Huang, Y. Ihara, M. J. Jee, D. Johnston, N. Kashikawa, B. Koester, K. Konishi, M. Kowalski, E. V. Linder, L. Lubin, J. Melbourne, J. Meyers, T. Morokuma, F. Munshi, C. Mullis, T. Oda, N. Panagia, S. Perlmutter, M. Postman, T. Pritchard, J. Rhodes, P. Ripoche, P. Rosati, D. J. Schlegel, A. Spadafora, S. A. Stanford, V. Stanishev, D. Stern, M. Strovink, N. Takanashi, K. Tokita, M. Wagner, L. Wang, N. Yasuda, H. K. C. Yee, and T. Supernova Cosmology Project. The Hubble Space Telescope Cluster Supernova Survey. V. Improving the Dark-energy Constraints

- above $z > 1$ and Building an Early-type-hosted Supernova Sample. *ApJ*, 746:85, February 2012. doi: 10.1088/0004-637X/746/1/85.
- R. Svensson. Electron-Positron Pair Equilibria in Relativistic Plasmas. *ApJ*, 258:335, July 1982. doi: 10.1086/160082.
- M. Tarnopolski. Testing the anisotropy in the angular distribution of Fermi/GBM gamma-ray bursts. *MNRAS*, 472:4819–4831, December 2017. doi: 10.1093/mnras/stx2356.
- B. J. Teegarden and S. J. Sturner. INTEGRAL Observations of Gamma-Ray Bursts. In *AAS/High Energy Astrophysics Division #4*, volume 31 of *Bulletin of the American Astronomical Society*, page 717, April 1999.
- M. Tegmark, D. H. Hartmann, M. S. Briggs, and C. A. Meegan. The Angular Power Spectrum of BATSE 3B Gamma-Ray Bursts. *ApJ*, 468:214, September 1996. doi: 10.1086/177684.
- C. Thompson. A Model of Gamma-Ray Bursts. *MNRAS*, 270:480, October 1994. doi: 10.1093/mnras/270.3.480.
- K. S. Thorne. Disk-Accretion onto a Black Hole. II. Evolution of the Hole. *ApJ*, 191:507–520, July 1974. doi: 10.1086/152991.
- K. S. Thorne, R. H. Price, and D. A. MacDonald. *Black holes: The membrane paradigm*. 1986.
- A. Tiengo, S. Mereghetti, G. Ghisellini, E. Rossi, G. Ghirlanda, and N. Schartel. The X-ray afterglow of GRB 030329. *A&A*, 409:983–987, October 2003. doi: 10.1051/0004-6361:20031127.
- L. Titarchuk, R. Farinelli, F. Frontera, and L. Amati. An Upscattering Spectral Formation Model for the Prompt Emission of Gamma-Ray Bursts. *ApJ*, 752:116, June 2012. doi: 10.1088/0004-637X/752/2/116.
- T. Totani. Cosmological Gamma-Ray Bursts and Evolution of Galaxies. *ApJ*, 486:L71–L74, September 1997. doi: 10.1086/310853.
- V. L. Toy, S. B. Cenko, J. M. Silverman, N. R. Butler, A. Cucchiara, A. M. Watson, D. Bersier, D. A. Perley, R. Margutti, E. Bellm, J. S. Bloom, Y. Cao, J. I. Capone, K. Clubb, A. Corsi, A. De Cia, J. A. de Diego, A. V. Filippenko, O. D. Fox, A. Gal-Yam, N. Gehrels, L. Georgiev, J. J. González, M. M. Kasliwal, P. L. Kelly, S. R. Kulkarni, A. S. Kutyrev, W. H. Lee, J. X. Prochaska, E. Ramirez-Ruiz, M. G. Richer, C. Román-Zúñiga, L. Singer, D. Stern, E. Troja, and S. Veilleux. Optical and Near-infrared Observations of SN 2013dx Associated with GRB 130702A. *ApJ*, 818:79, February 2016. doi: 10.3847/0004-637X/818/1/79.
- E. Troja, G. Cusumano, P. T. O'Brien, B. Zhang, B. Sbarufatti, V. Mangano, R. Willingale, G. Chincarini, J. P. Osborne, F. E. Marshall, D. N. Burrows, S. Campana, N. Gehrels, C. Guidorzi, H. A. Krimm, V. La Parola, E. W. Liang, T. Mineo, A. Moretti, K. L. Page,

- P. Romano, G. Tagliaferri, B. B. Zhang, M. J. Page, and P. Schady. Swift Observations of GRB 070110: An Extraordinary X-Ray Afterglow Powered by the Central Engine. *ApJ*, 665:599–607, August 2007. doi: 10.1086/519450.
- E. Troja, T. Sakamoto, S. B. Cenko, A. Lien, N. Gehrels, A. J. Castro-Tirado, R. Ricci, J. Capone, V. Toy, A. Kutyrev, N. Kawai, A. Cucchiara, A. Fruchter, J. Gorosabel, S. Jeong, A. Levan, D. Perley, R. Sanchez-Ramirez, N. Tanvir, and S. Veilleux. An Achromatic Break in the Afterglow of the Short GRB 140903A: Evidence for a Narrow Jet. *ApJ*, 827:102, August 2016. doi: 10.3847/0004-637X/827/2/102.
- E. Troja, L. Piro, H. van Eerten, R. T. Wollaeger, M. Im, O. D. Fox, N. R. Butler, S. B. Cenko, T. Sakamoto, C. L. Fryer, R. Ricci, A. Lien, R. E. Ryan, O. Korobkin, S.-K. Lee, J. M. Burgess, W. H. Lee, A. M. Watson, C. Choi, S. Covino, P. D’Avanzo, C. J. Fontes, J. B. González, H. G. Khandrika, J. Kim, S.-L. Kim, C.-U. Lee, H. M. Lee, A. Kutyrev, G. Lim, R. Sánchez-Ramírez, S. Veilleux, M. H. Wieringa, and Y. Yoon. The X-ray counterpart to the gravitational-wave event GW170817. *Nature*, 551:71–74, November 2017. doi: 10.1038/nature24290.
- R. Tsutsui, T. Nakamura, D. Yonetoku, T. Murakami, S. Tanabe, and Y. Kodama. Redshift Dependent Lag-Luminosity Relation in 565 BASTE Gamma Ray Bursts. In M. Galassi, D. Palmer, and E. Fenimore, editors, *American Institute of Physics Conference Series*, volume 1000 of *American Institute of Physics Conference Series*, pages 28–31, May 2008. doi: 10.1063/1.2943466.
- R. Tsutsui, T. Nakamura, D. Yonetoku, T. Murakami, Y. Kodama, and K. Takahashi. Cosmological constraints from calibrated Yonetoku and Amati relation suggest fundamental plane of gamma-ray bursts. *J. Cosmology Astropart. Phys.*, 8:015, August 2009a. doi: 10.1088/1475-7516/2009/08/015.
- R. Tsutsui, T. Nakamura, D. Yonetoku, T. Murakami, S. Tanabe, Y. Kodama, and K. Takahashi. Constraints on w_0 and w_a of dark energy from high-redshift gamma-ray bursts. *MNRAS*, 394:L31–L35, March 2009b. doi: 10.1111/j.1745-3933.2008.00604.x.
- R. Tsutsui, T. Nakamura, D. Yonetoku, T. Murakami, and K. Takahashi. Intrinsic Dispersion of Correlations among E_p , L_p , and E_{iso} of Gamma Ray Bursts depends on the quality of Data Set. *ArXiv e-prints*, December 2010.
- R. Tsutsui, D. Yonetoku, T. Nakamura, K. Takahashi, and Y. Morihara. Possible existence of the E_p - L_p and E_p - E_{iso} correlations for short gamma-ray bursts with a factor 5-100 dimmer than those for long gamma-ray bursts. *MNRAS*, 431:1398–1404, May 2013. doi: 10.1093/mnras/stt262.
- Z. L. Uhm and B. Zhang. Toward an Understanding of GRB Prompt Emission Mechanism. I. The Origin of Spectral Lags. *ApJ*, 825:97, July 2016. doi: 10.3847/0004-637X/825/2/97.

- T. N. Ukwatta, M. Stamatikos, K. S. Dhuga, T. Sakamoto, S. D. Barthelmy, A. Eskandarian, N. Gehrels, L. C. Maximon, J. P. Norris, and W. C. Parke. Spectral Lags and the Lag-Luminosity Relation: An Investigation with Swift BAT Gamma-ray Bursts. *ApJ*, 711: 1073–1086, March 2010. doi: 10.1088/0004-637X/711/2/1073.
- T. N. Ukwatta, K. S. Dhuga, M. Stamatikos, C. D. Dermer, T. Sakamoto, E. Sonbas, W. C. Parke, L. C. Maximon, J. T. Linnemann, P. N. Bhat, A. Eskandarian, N. Gehrels, A. U. Abeysekara, K. Tollefson, and J. P. Norris. The lag-luminosity relation in the GRB source frame: an investigation with Swift BAT bursts. *MNRAS*, 419:614–623, January 2012. doi: 10.1111/j.1365-2966.2011.19723.x.
- Y. Urata, R. Yamazaki, T. Sakamoto, K. Huang, W. Zheng, G. Sato, T. Aoki, J. Deng, K. Ioka, W. Ip, K. S. Kawabata, Y. Lee, X. Liping, H. Mito, T. Miyata, Y. Nakada, T. Ohsugi, Y. Qiu, T. Soyano, K. Tarusawa, M. Tashiro, M. Uemura, J. Wei, and T. Yamashita. Testing the External-Shock Model of Gamma-Ray Bursts Using the Late-Time Simultaneous Optical and X-Ray Afterglows. *ApJ*, 668:L95–L98, October 2007. doi: 10.1086/522930.
- V. V. Usov. Millisecond pulsars with extremely strong magnetic fields as a cosmological source of gamma-ray bursts. *Nature*, 357:472–474, June 1992. doi: 10.1038/357472a0.
- V. V. Usov. On the Nature of Nonthermal Radiation from Cosmological Gamma-Ray Bursters. *MNRAS*, 267:1035, April 1994. doi: 10.1093/mnras/267.4.1035.
- J. Řípa and A. Shafieloo. Testing the Isotropic Universe Using the Gamma-Ray Burst Data of Fermi/GBM. *ApJ*, 851:15, December 2017. doi: 10.3847/1538-4357/aa9708.
- J. Řípa, A. Mészáros, C. Wigger, D. Huja, R. Hudec, and W. Hajdas. Search for gamma-ray burst classes with the RHESSI satellite. *A&A*, 498:399–406, May 2009. doi: 10.1051/0004-6361/200810913.
- S. D. Van Dyk, W. Li, and A. V. Filippenko. A Search for Core-Collapse Supernova Progenitors in Hubble Space Telescope Images. *PASP*, 115:1–20, January 2003. doi: 10.1086/345748.
- H. van Eerten. Self-similar relativistic blast waves with energy injection. *MNRAS*, 442: 3495–3510, August 2014a. doi: 10.1093/mnras/stu1025.
- H. J. van Eerten. Gamma-ray burst afterglow plateau break time-luminosity correlations favour thick shell models over thin shell models. *MNRAS*, 445:2414–2423, December 2014b. doi: 10.1093/mnras/stu1921.
- R. Vavrek, L. G. Balázs, A. Mészáros, I. Horváth, and Z. Bagoly. Testing the randomness in the sky-distribution of gamma-ray bursts. *MNRAS*, 391:1741–1748, December 2008. doi: 10.1111/j.1365-2966.2008.13635.x.

- P. Veres, Z. Bagoly, I. Horváth, A. Mészáros, and L. G. Balázs. A Distinct Peak-flux Distribution of the Third Class of Gamma-ray Bursts: A Possible Signature of X-ray Flashes? *ApJ*, 725:1955–1964, December 2010. doi: 10.1088/0004-637X/725/2/1955.
- G Vereshchagin. Pair plasma and Gamma-Ray Bursts. *PhD thesis, University La Sapienza, Rome*, 2008.
- M. Vietri and L. Stella. A Gamma-Ray Burst Model with Small Baryon Contamination. *ApJ*, 507:L45–L48, November 1998. doi: 10.1086/311674.
- F. J. Virgili, C. G. Mundell, V. Pal’shin, C. Guidorzi, R. Margutti, A. Melandri, R. Harrison, S. Kobayashi, R. Chornock, A. Henden, A. C. Updike, S. B. Cenko, N. R. Tanvir, I. A. Steele, A. Cucchiara, A. Gomboc, A. Levan, Z. Cano, C. J. Mottram, N. R. Clay, D. Bersier, D. Kopač, J. Japelj, A. V. Filippenko, W. Li, D. Svinkin, S. Golenetskii, D. H. Hartmann, P. A. Milne, G. Williams, P. T. O’Brien, D. B. Fox, and E. Berger. GRB 091024A and the Nature of Ultra-long Gamma-Ray Bursts. *ApJ*, 778:54, November 2013. doi: 10.1088/0004-637X/778/1/54.
- V. Vitagliano, J.-Q. Xia, S. Liberati, and M. Viel. High-redshift cosmography. *J. Cosmology Astropart. Phys.*, 3:005, March 2010. doi: 10.1088/1475-7516/2010/03/005.
- I. Vurm and A. M. Beloborodov. Radiative Transfer Models for Gamma-Ray Bursts. *ApJ*, 831:175, November 2016. doi: 10.3847/0004-637X/831/2/175.
- F. Y. Wang and Z. G. Dai. High-redshift star formation rate up to $z \sim 8.3$ derived from gamma-ray bursts and influence of background cosmology. *MNRAS*, 400:L10–L14, November 2009. doi: 10.1111/j.1745-3933.2009.00751.x.
- F. Y. Wang, Z. G. Dai, and S. Qi. Probing the cosmographic parameters to distinguish between dark energy and modified gravity models. *A&A*, 507:53–59, November 2009. doi: 10.1051/0004-6361/200911998.
- F.-Y. Wang, S. Qi, and Z.-G. Dai. The updated luminosity correlations of gamma-ray bursts and cosmological implications. *MNRAS*, 415:3423–3433, August 2011. doi: 10.1111/j.1365-2966.2011.18961.x.
- F. Y. Wang, Z. G. Dai, and E. W. Liang. Gamma-ray burst cosmology. *New A Rev.*, 67: 1–17, August 2015. doi: 10.1016/j.newar.2015.03.001.
- D. Watson, J. N. Reeves, J. Hjorth, P. Jakobsson, and K. Pedersen. Delayed Soft X-Ray Emission Lines in the Afterglow of GRB 030227. *ApJ*, 595:L29–L32, September 2003. doi: 10.1086/378790.
- D. Watson, J. Hjorth, P. Jakobsson, K. Pedersen, S. Patel, and C. Kouveliotou. Massive star-formation rates of γ -ray burst host galaxies: An unobscured view in X-rays. *A&A*, 425:L33–L36, October 2004. doi: 10.1051/0004-6361:200400058.

- E. Waxman. γ -Ray Burst Afterglow: Confirming the Cosmological Fireball Model. *ApJ*, 489:L33–L36, November 1997. doi: 10.1086/310960.
- H. Wei and S.-N. Zhang. Reconstructing the cosmic expansion history up to redshift $z=6.29$ with the calibrated gamma-ray bursts. *European Physical Journal C*, 63:139–147, September 2009. doi: 10.1140/epjc/s10052-009-1086-z.
- D. H. Weinberg, M. J. Mortonson, D. J. Eisenstein, C. Hirata, A. G. Riess, and E. Rozo. Observational probes of cosmic acceleration. *Phys. Rep.*, 530:87–255, September 2013. doi: 10.1016/j.physrep.2013.05.001.
- R. A. M. J. Wijers and T. J. Galama. Physical Parameters of GRB 970508 and GRB 971214 from Their Afterglow Synchrotron Emission. *ApJ*, 523:177–186, September 1999. doi: 10.1086/307705.
- R. A. M. J. Wijers, M. J. Rees, and P. Meszaros. Shocked by GRB 970228: the afterglow of a cosmological fireball. *MNRAS*, 288:L51–L56, July 1997.
- R. Willingale, P. T. O'Brien, J. P. Osborne, O. Godet, K. L. Page, M. R. Goad, D. N. Burrows, B. Zhang, E. Rol, N. Gehrels, and G. Chincarini. Testing the Standard Fireball Model of Gamma-Ray Bursts Using Late X-Ray Afterglows Measured by Swift. *ApJ*, 662:1093–1110, June 2007. doi: 10.1086/517989.
- R. Willingale, F. Genet, J. Granot, and P. T. O'Brien. The spectral-temporal properties of the prompt pulses and rapid decay phase of gamma-ray bursts. *MNRAS*, 403:1296–1316, April 2010. doi: 10.1111/j.1365-2966.2009.16187.x.
- S. E. Woosley. Gamma-ray bursts from stellar mass accretion disks around black holes. *ApJ*, 405:273–277, March 1993. doi: 10.1086/172359.
- S. E. Woosley and J. S. Bloom. The Supernova Gamma-Ray Burst Connection. *ARA&A*, 44:507–556, September 2006a. doi: 10.1146/annurev.astro.43.072103.150558.
- S. E. Woosley and J. S. Bloom. The Supernova Gamma-Ray Burst Connection. *ARA&A*, 44:507–556, September 2006b. doi: 10.1146/annurev.astro.43.072103.150558.
- X.-F. Wu, S.-J. Hou, and W.-H. Lei. Giant X-Ray Bump in GRB 121027A: Evidence for Fall-back Disk Accretion. *ApJ*, 767:L36, April 2013. doi: 10.1088/2041-8205/767/2/L36.
- L. Xiao and B. E. Schaefer. Estimating Redshifts for Long Gamma-Ray Bursts. *ApJ*, 707:387–403, December 2009. doi: 10.1088/0004-637X/707/1/387.
- L.-P. Xin, Y.-Z. Wang, T.-T. Lin, E.-W. Liang, H.-J. Lü, S.-Q. Zhong, Y. Urata, X.-H. Zhao, C. Wu, J.-Y. Wei, K.-Y. Huang, Y.-L. Qiu, and J.-S. Deng. Multi-wavelength Observations of GRB 111228A and Implications for the Fireball and its Environment. *ApJ*, 817:152, February 2016. doi: 10.3847/0004-637X/817/2/152.

- D. Xu, Z. G. Dai, and E. W. Liang. Can Gamma-Ray Bursts Be Used to Measure Cosmology? A Further Analysis. *ApJ*, 633:603–610, November 2005. doi: 10.1086/466509.
- R. Yamazaki. Prior Emission Model for X-ray Plateau Phase of Gamma-Ray Burst Afterglows. *ApJ*, 690:L118–L121, January 2009. doi: 10.1088/0004-637X/690/2/L118.
- R. Yamazaki, K. Ioka, and T. Nakamura. X-Ray Flashes from Off-Axis Gamma-Ray Bursts. *ApJ*, 571:L31–L35, May 2002. doi: 10.1086/341225.
- R. Yamazaki, D. Yonetoku, and T. Nakamura. An Off-Axis Jet Model For GRB 980425 and Low-Energy Gamma-Ray Bursts. *ApJ*, 594:L79–L82, September 2003. doi: 10.1086/378736.
- S. X. Yi, Z. G. Dai, X. F. Wu, and F. Y. Wang. X-Ray Afterglow Plateaus of Long Gamma-Ray Bursts: Further Evidence for Millisecond Magnetars. *ArXiv e-prints*, January 2014.
- T.-F. Yi, G.-Z. Xie, and F.-W. Zhang. A Close Correlation between the Spectral Lags and Redshifts of Gamma-Ray Bursts. *Chinese J. Astron. Astrophys.*, 8:81–86, February 2008. doi: 10.1088/1009-9271/8/1/08.
- D. Yonetoku, T. Murakami, T. Nakamura, R. Yamazaki, A. K. Inoue, and K. Ioka. Gamma-Ray Burst Formation Rate Inferred from the Spectral Peak Energy-Peak Luminosity Relation. *ApJ*, 609:935–951, July 2004. doi: 10.1086/421285.
- D. Yonetoku, T. Murakami, R. Tsutsui, T. Nakamura, Y. Morihara, and K. Takahashi. Possible Origins of Dispersion of the Peak Energy-Brightness Correlations of Gamma-Ray Bursts. *PASJ*, 62:1495–, December 2010. doi: 10.1093/pasj/62.6.1495.
- D. Yonetoku, T. Nakamura, T. Sawano, K. Takahashi, and A. Toyano. Short Gamma-Ray Burst Formation Rate from BATSE Data Using E_p - L_p Correlation and the Minimum Gravitational-wave Event Rate of a Coalescing Compact Binary. *ApJ*, 789:65, July 2014. doi: 10.1088/0004-637X/789/1/65.
- Y.-W. Yu, J.-P. Zhu, S.-Z. Li, H.-J. Lü, and Y.-C. Zou. A Statistical Study of Superluminous Supernovae Using the Magnetar Engine Model and Implications for Their Connection with Gamma-Ray Bursts and Hypernovae. *ApJ*, 840:12, May 2017. doi: 10.3847/1538-4357/aa6c27.
- E. Zaninoni, M. G. Bernardini, R. Margutti, S. Oates, and G. Chincarini. Gamma-ray burst optical light-curve zoo: comparison with X-ray observations. *A&A*, 557:A12, September 2013. doi: 10.1051/0004-6361/201321221.
- B. Zhang. Gamma-Ray Bursts in the Swift Era. *Chinese J. Astron. Astrophys.*, 7:1–50, February 2007. doi: 10.1088/1009-9271/7/1/01.
- B. Zhang. Open questions in GRB physics. *Comptes Rendus Physique*, 12:206–225, April 2011. doi: 10.1016/j.crhy.2011.03.004.

- B. Zhang and S. Kobayashi. Gamma-Ray Burst Early Afterglows: Reverse Shock Emission from an Arbitrarily Magnetized Ejecta. *ApJ*, 628:315–334, July 2005. doi: 10.1086/429787.
- B. Zhang and P. Mészáros. Gamma-Ray Burst Afterglow with Continuous Energy Injection: Signature of a Highly Magnetized Millisecond Pulsar. *ApJ*, 552:L35–L38, May 2001. doi: 10.1086/320255.
- B. Zhang and P. Mészáros. An Analysis of Gamma-Ray Burst Spectral Break Models. *ApJ*, 581:1236–1247, December 2002. doi: 10.1086/344338.
- B. Zhang and A. Pe'er. Evidence of an Initially Magnetically Dominated Outflow in GRB 080916C. *ApJ*, 700:L65–L68, August 2009. doi: 10.1088/0004-637X/700/2/L65.
- B. Zhang and H. Yan. The Internal-collision-induced Magnetic Reconnection and Turbulence (ICMART) Model of Gamma-ray Bursts. *ApJ*, 726:90, January 2011. doi: 10.1088/0004-637X/726/2/90.
- B. Zhang, X. Dai, N. M. Lloyd-Ronning, and P. Mészáros. Quasi-universal Gaussian Jets: A Unified Picture for Gamma-Ray Bursts and X-Ray Flashes. *ApJ*, 601:L119–L122, February 2004. doi: 10.1086/382132.
- B. Zhang, Y. Z. Fan, J. Dyks, S. Kobayashi, P. Mészáros, D. N. Burrows, J. A. Nousek, and N. Gehrels. Physical Processes Shaping Gamma-Ray Burst X-Ray Afterglow Light Curves: Theoretical Implications from the Swift X-Ray Telescope Observations. *ApJ*, 642:354–370, May 2006a. doi: 10.1086/500723.
- B. Zhang, E. Liang, K. L. Page, D. Grupe, B.-B. Zhang, S. D. Barthelmy, D. N. Burrows, S. Campana, G. Chincarini, N. Gehrels, S. Kobayashi, P. Mészáros, A. Moretti, J. A. Nousek, P. T. O'Brien, J. P. Osborne, P. W. A. Roming, T. Sakamoto, P. Schady, and R. Willingale. GRB Radiative Efficiencies Derived from the Swift Data: GRBs versus XRFs, Long versus Short. *ApJ*, 655:989–1001, February 2007a. doi: 10.1086/510110.
- B. Zhang, B.-B. Zhang, F. J. Virgili, E.-W. Liang, D. A. Kann, X.-F. Wu, D. Proga, H.-J. Lv, K. Toma, P. Mészáros, D. N. Burrows, P. W. A. Roming, and N. Gehrels. Discerning the Physical Origins of Cosmological Gamma-ray Bursts Based on Multiple Observational Criteria: The Cases of $z = 6.7$ GRB 080913, $z = 8.2$ GRB 090423, and Some Short/Hard GRBs. *ApJ*, 703:1696–1724, October 2009. doi: 10.1088/0004-637X/703/2/1696.
- B.-B. Zhang, E.-W. Liang, and B. Zhang. A Comprehensive Analysis of Swift XRT Data. I. Apparent Spectral Evolution of Gamma-Ray Burst X-Ray Tails. *ApJ*, 666:1002–1011, September 2007b. doi: 10.1086/519548.
- W. Zhang, S. E. Woosley, and A. I. MacFadyen. Relativistic Jets in Collapsars. *ApJ*, 586: 356–371, March 2003. doi: 10.1086/367609.
- Z. Zhang, G. Z. Xie, J. G. Deng, and W. Jin. Revisiting the characteristics of the spectral lags

- in short gamma-ray bursts. *MNRAS*, 373:729–732, December 2006b. doi: 10.1111/j.1365-2966.2006.11058.x.
- H. Zitouni, N. Guessoum, W. J. Azzam, and R. Mochkovitch. Statistical study of observed and intrinsic durations among BATSE and Swift/BAT GRBs. *Ap&SS*, 357:7, May 2015. doi: 10.1007/s10509-015-2311-x.
- Y.-C. Zou and T. Piran. Lorentz factor constraint from the very early external shock of the gamma-ray burst ejecta. *MNRAS*, 402:1854–1862, March 2010. doi: 10.1111/j.1365-2966.2009.15863.x.

APPENDIX

A

Fits of the decay indices $\alpha_{X,a}$ for the GRB afterglow light curves

A.1 The fitted values

Table A.1a presents the Swift GRB sample analysed in Del Vecchio et al. (2016). In the successive columns there are displayed: a reference name of GRB, a value of the X-ray afterglow decay index, $\alpha_{X,a}$, with respective fitting errors, $\Delta\alpha_{X,a}$, and logarithms of the starting and final time of the fit, T_1 and T_2 , respectively. The last column presents the type of the GRB: long - L, short - S, X-ray Flashes – XRF.

GRB	$\alpha_{X,a}$	$\pm\Delta\alpha_{X,a}$	$\log T_1$	$\log T_2$	Type
050315	1.26	± 0.05	4.80	5.87	L
050318	1.28	± 0.04	3.50	4.50	L
050319	1.53	± 0.09	4.50	5.73	L(XRF)
050401	1.35	± 0.07	3.70	5.74	L
050416A	0.91	± 0.02	3.60	6.38	L(XRF)
050505	1.67	± 0.05	4.50	6.02	L
050525A	1.49	± 0.03	3.77	5.59	L
050603	1.66	± 0.05	4.54	5.76	L
050730	2.45	± 0.03	4.00	5.15	L
050802	1.59	± 0.03	3.46	5.00	L(XRF)
050820A	1.21	± 0.01	3.67	6.35	L(XRF)
050824	1.02	± 0.12	5.32	6.31	L(XRF)
050904	1.68	± 0.30	2.82	3.22	L
050922C	1.20	± 0.01	2.07	4.98	L(XRF)
051016B	1.33	± 0.05	4.52	6.05	L
051109A	1.22	± 0.02	3.75	6.18	L
051109B	1.07	± 0.09	3.76	4.89	L

Table A.1a: Table describing the results of the afterglow decay index fit for the GRB sample analysed in Del Vecchio et al. (2016).

GRB	$\alpha_{X,a}$	$\pm\Delta\alpha_{X,a}$	$\log T_1$	$\log T_2$	Type
051221A	1.25	± 0.05	4.40	5.74	S
060115	1.46	± 0.06	4.59	5.30	L
060124	1.34	± 0.01	4.06	6.29	L(XRF)
060206	1.22	± 0.04	3.72	5.97	L(XRF)
060210	1.32	± 0.03	4.52	5.93	L(XRF)
060218	1.26	± 0.08	4.98	5.99	L(XRF)
060223A	1.97	± 0.23	3.72	4.31	L
060418	1.71	± 0.07	3.63	5.33	L
060502A	1.10	± 0.04	4.58	6.20	L
060510B	0.71	± 0.07	3.74	5.18	L(XRF)
060512	1.16	± 0.04	3.58	5.44	L
060522	1.35	± 0.05	3.74	5.60	L
060526	1.03	± 0.05	3.71	5.28	L(XRF)
060604	1.23	± 0.04	4.43	5.88	L
060605	1.98	± 0.06	3.99	4.86	L
060607A	3.36	± 0.06	4.05	4.95	L
060614	2.00	± 0.04	4.99	6.24	L(XRF)
060707	2.40	± 0.25	5.88	6.29	L
060714	1.23	± 0.03	3.74	5.80	L
060729	1.35	± 0.02	5.00	6.20	L(XRF)
060814	1.28	± 0.02	4.05	6.12	L
060904B	1.34	± 0.03	3.57	5.59	L(XRF)
060906	1.63	± 0.10	4.06	5.41	L
060908	1.51	± 0.04	2.98	4.67	L
060912A	1.05	± 0.05	3.72	5.64	L
060926	1.17	± 0.04	2.64	4.71	L
060927	1.45	± 0.06	3.56	5.00	L
061007	1.67	± 0.01	2.00	4.99	L
061110A	1.18	± 0.12	5.09	5.87	L
061121	1.43	± 0.01	4.02	6.32	L
061201	1.95	± 0.10	3.75	5.08	S
061222A	1.62	± 0.03	4.80	6.19	L
070110	1.07	± 0.05	4.89	6.34	L
070208	1.72	± 0.12	4.01	4.64	L
070306	1.97	± 0.07	4.79	5.91	L
070318	2.01	± 0.19	5.17	5.90	L
070508	1.67	± 0.03	4.22	5.81	L

Table A.1b: Continuation of Table A.1a.

GRB	$\alpha_{X,a}$	$\pm\Delta\alpha_{X,a}$	$\log T_1$	$\log T_2$	Type
070518	0.93	± 0.07	4.26	6.17	L
070521	2.27	± 0.11	4.38	5.43	L
070529	1.33	± 0.04	3.65	5.23	L
070714B	1.45	± 0.16	3.20	4.25	L
070721B	2.19	± 0.07	4.01	5.14	L
070724A	2.54	± 0.04	4.66	5.11	S
070802	1.09	± 0.22	4.01	5.51	L
070809	0.91	± 0.19	3.85	4.82	S(XRF)
070810A	1.33	± 0.08	3.58	4.54	L
071020	1.11	± 0.01	2.02	6.12	L
071031	0.96	± 0.08	3.78	5.18	L(XRF)
071117	0.97	± 0.06	3.48	4.79	L
080310	1.66	± 0.07	4.24	5.56	L
080319B	1.78	± 0.01	3.01	4.35	L(XRF)
080319C	1.60	± 0.07	4.46	5.54	L
080411	1.35	± 0.03	5.01	6.74	L
080430	1.14	± 0.05	5.12	6.46	L
080603B	0.83	± 0.03	2.41	4.08	L
080607	1.71	± 0.03	3.63	5.43	L
080710	1.43	± 0.06	4.02	5.74	L
080721	1.49	± 0.03	4.52	6.12	L
080810	1.42	± 0.03	3.58	5.08	L
080916A	1.26	± 0.05	4.61	6.17	L(XRF)
080928	1.71	± 0.05	4.00	5.34	L
081007	1.21	± 0.03	4.40	6.19	L(XRF)
081008	1.96	± 0.07	4.22	5.46	L
081028	2.77	± 0.12	4.79	5.40	L
081029	2.63	± 0.12	4.30	4.96	L
081203A	1.74	± 0.04	3.62	5.53	L
081221	1.16	± 0.03	4.03	5.41	L
081222	1.65	± 0.06	4.62	5.85	L
090102	1.44	± 0.03	3.44	5.30	L
090205	2.05	± 0.17	4.26	5.02	L
090418	1.47	± 0.03	3.63	5.64	L
090423	1.45	± 0.05	4.01	5.50	L
090424	1.11	± 0.01	3.74	6.00	L(XRF)
090426	1.02	± 0.04	2.54	5.69	S

Table A.1c: Continuation of Table A.1a.

GRB	$\alpha_{X,a}$	$\pm\Delta\alpha_{X,a}$	$\log T_1$	$\log T_2$	Type
090429B	1.39	± 0.11	3.63	5.11	L
090510	2.31	± 0.24	3.72	4.31	S
090516	1.77	± 0.05	4.22	5.45	L
090519	1.50	± 0.11	3.25	4.21	L
090529	1.52	± 0.05	5.25	5.89	L
090618	1.58	± 0.04	5.00	6.46	L(XRF)
090812	1.36	± 0.07	4.08	5.29	L
090927	1.15	± 0.06	4.14	5.84	L
091020	1.34	± 0.02	3.69	5.99	L
091029	1.13	± 0.04	4.54	6.27	L
091109A	1.03	± 0.04	3.63	5.57	L
091127	1.54	± 0.03	5.03	6.64	L(XRF)
091208B	1.13	± 0.04	4.01	5.57	L
100219A	3.38	± 0.34	4.45	5.07	L
100316B	> 1.28	± 0.06	3.00	4.69	L
100418A	1.66	± 0.12	5.18	6.32	L(XRF)
100425A	0.95	± 0.05	4.02	5.70	L
100513A	0.93	± 0.06	3.71	5.52	L
100621A	1.48	± 0.03	4.80	6.25	L
100724A	1.57	± 0.11	3.74	4.84	S
100728A	1.35	± 0.01	2.85	5.78	L
100814A	1.90	± 0.04	5.01	6.22	L
100816A	1.02	± 0.06	4.04	5.73	L
100901A	1.49	± 0.05	5.01	6.19	L
100906A	1.55	± 0.05	3.68	5.08	L
101219B	0.90	± 0.05	4.81	5.74	L(XRF)
110106B	1.49	± 0.07	4.85	5.73	L
110213A	1.81	± 0.02	3.77	5.68	L
110422A	1.54	± 0.02	3.82	5.44	L
110503A	1.55	± 0.11	5.18	5.97	L
110715A	1.50	± 0.09	5.03	5.93	L
110731A	1.18	± 0.01	2.00	5.81	L
110808A	1.00	± 0.07	4.60	5.84	L
110818A	1.88	± 0.21	4.52	5.19	L
111008A	1.29	± 0.04	4.07	5.66	L
111123A	1.72	± 0.13	4.54	5.26	L
111209A	1.52	± 0.06	5.04	6.17	S

Table A.1d: Continuation of Table A.1a.

GRB	$\alpha_{X,a}$	$\pm\Delta\alpha_{X,a}$	$\log T_1$	$\log T_2$	Type
111228A	1.32	± 0.03	4.62	6.19	L
120118B	0.94	± 0.04	3.73	5.88	L
120327A	1.46	± 0.05	3.66	5.16	L
120404A	1.88	± 0.07	3.68	5.10	L
120422A	0.86	± 0.08	5.25	6.19	L
120521C	1.45	± 0.26	4.07	4.62	L
120724A	0.49	± 0.08	2.86	4.38	L
120729A	2.49	± 0.33	4.01	4.35	L
120802A	0.49	± 0.11	3.62	4.24	L
120811C	1.03	± 0.11	4.06	4.99	L
120907A	1.12	± 0.04	4.03	5.45	L
120922A	1.10	± 0.04	4.05	5.87	L
121024A	1.21	± 0.04	3.59	5.63	L
121027A	1.48	± 0.04	5.14	6.42	L
121128A	1.71	± 0.08	3.84	4.85	L
121211A	1.33	± 0.13	4.60	5.56	L
121229A	0.54	± 0.13	3.72	5.34	S
130408A	3.41	± 0.32	4.43	4.90	L
130418A	1.51	± 0.08	3.57	5.61	L
130420A	1.21	± 0.05	4.82	6.11	L
130505A	1.61	± 0.03	4.86	6.30	L
130511A	1.66	± 0.12	3.87	4.54	L
130514A	1.21	± 0.05	3.81	5.50	L
130603B	1.66	± 0.14	4.00	4.68	S
130604A	1.95	± 0.04	1.95	3.71	L
130606A	1.68	± 0.06	4.05	5.38	L
130831A	1.01	± 0.06	4.00	5.01	L
130925A	1.31	± 0.02	5.52	7.10	S
131004A	1.46	± 0.22	3.67	4.36	S
131030A	1.25	± 0.02	4.00	6.22	L
131105A	1.19	± 0.04	4.07	5.86	L
131117A	0.98	± 0.04	3.63	5.23	L
140206A	1.45	± 0.07	5.10	6.12	L
140213A	1.96	± 0.07	5.00	6.00	L
140419A	1.48	± 0.04	4.54	5.94	L
140423A	1.36	± 0.10	4.52	5.68	L
140430A	1.15	± 0.18	4.52	5.06	L

Table A.1e: Continuation of Table A.1a.

GRB	$\alpha_{X,a}$	$\pm\Delta\alpha_{X,a}$	$\log T_1$	$\log T_2$	Type
140506A	0.92	± 0.01	2.84	6.32	L
140509A	2.16	± 0.20	4.23	4.87	L
140512A	1.81	± 0.19	5.03	5.42	L
140515A	0.98	± 0.05	3.73	5.00	L
140614A	1.64	± 0.10	3.87	5.09	L
140629A	1.49	± 0.05	3.63	4.84	L
140710A	0.97	± 0.10	3.62	4.99	L

Table A.1f: Continuation of Table A.1a.

A.2 Illustrations of performed fits

The X-ray light curves for the GRB sample analysed in Del Vecchio et al. (2016) are presented with fits indicated by red lines in Figures A.2.1–A.2.172. The data presented on the plots were registered by the XRT and the BAT instruments on board of the Swift satellite¹. For each GRB, the figure caption provides the identification number of the event and a value of the fitted decay index. The time range for each fit is provided in Table A.1a.

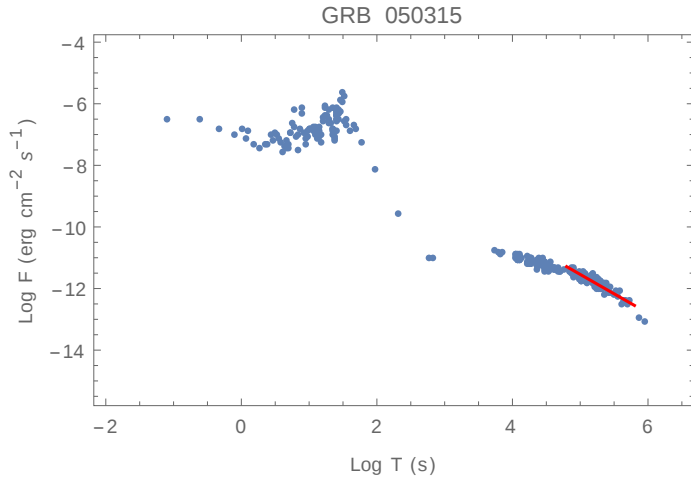


Figure A.2.1: GRB 050315: $\alpha_{X,a} = 1.26$.

¹http://swift.gsfc.nasa.gov/archive/grb_table/

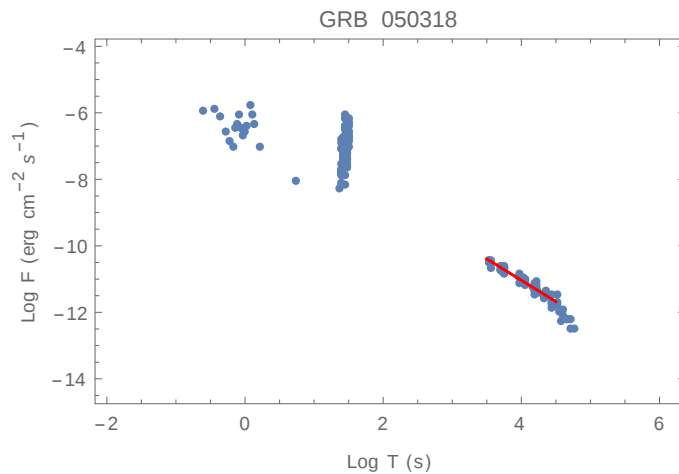


Figure A.2.2: GRB 050318: $\alpha_{X,a} = 1.28$.

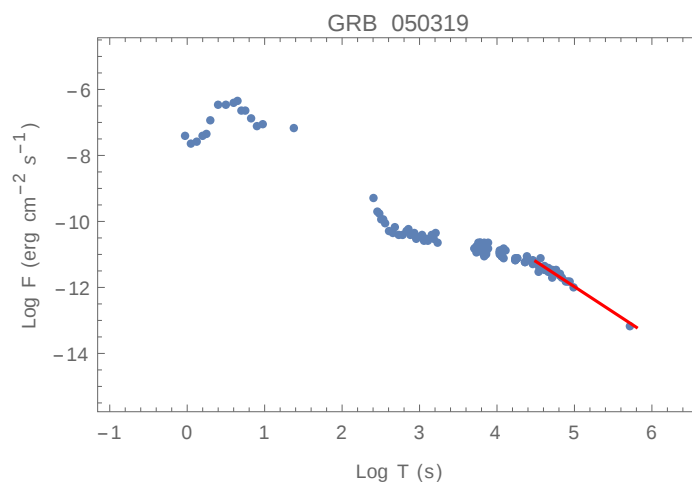


Figure A.2.3: GRB 050319: $\alpha_{X,a} = 1.53$.

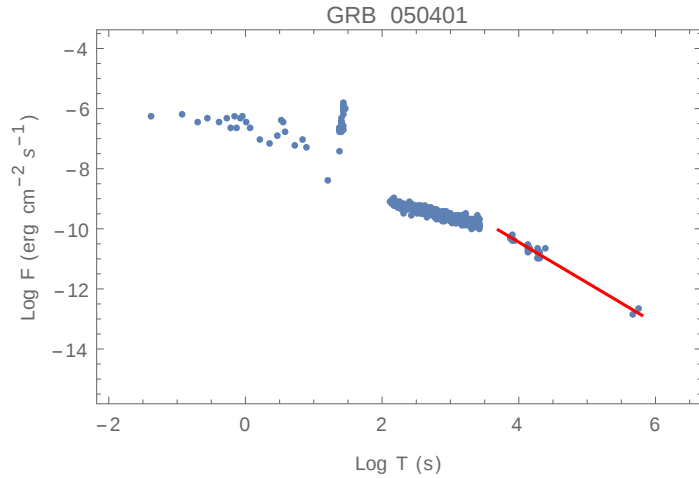


Figure A.2.4: GRB 050401: $\alpha_{X,a} = 1.35$.

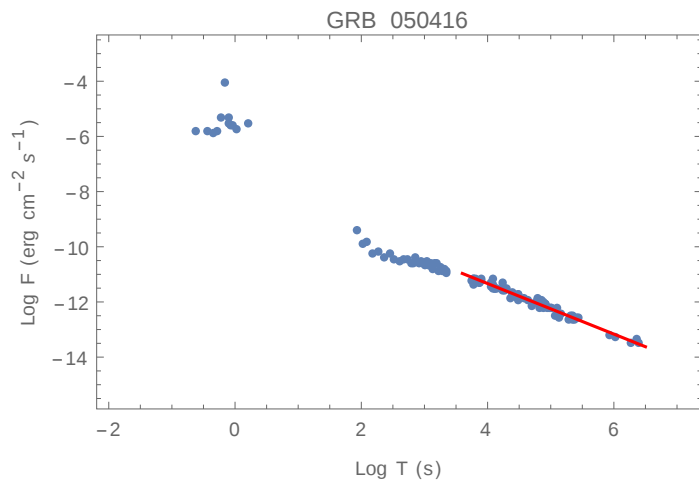


Figure A.2.5: GRB 050416A: $\alpha_{X,a} = 0.91$.

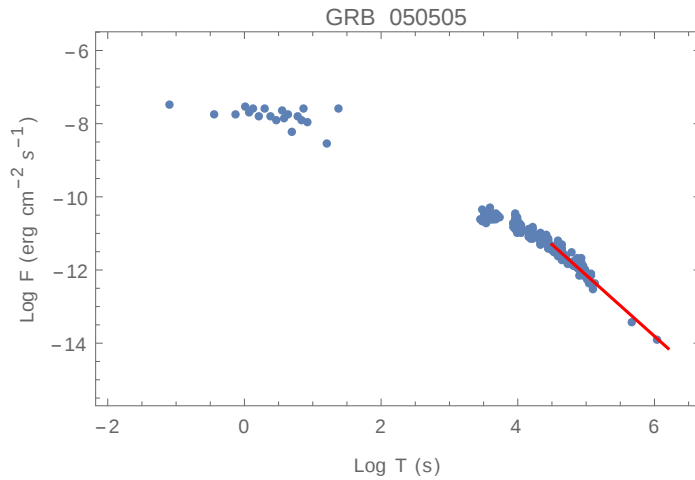


Figure A.2.6: GRB 050505: $\alpha_{X,a} = 1.67$.

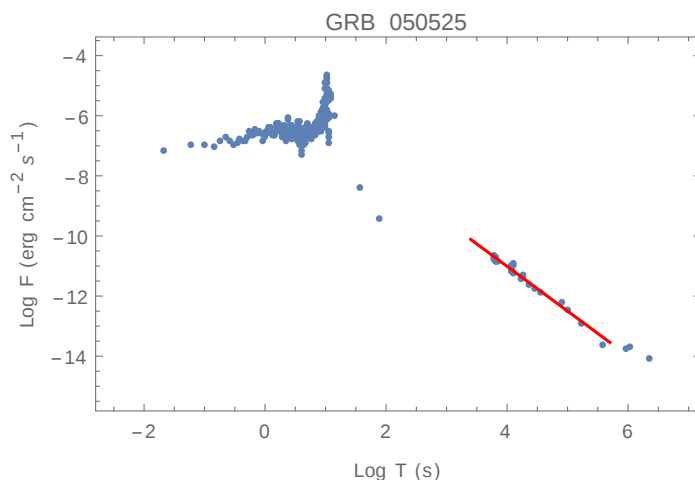


Figure A.2.7: GRB 050525A: $\alpha_{X,a} = 1.49$.

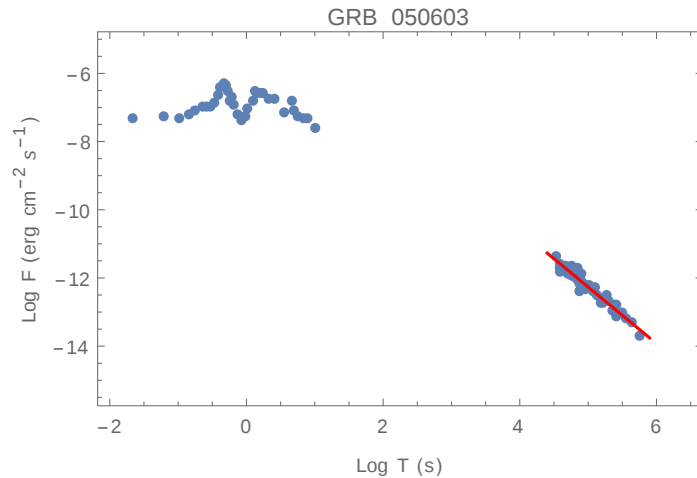


Figure A.2.8: GRB 050603: $\alpha_{X,a} = 1.66$.

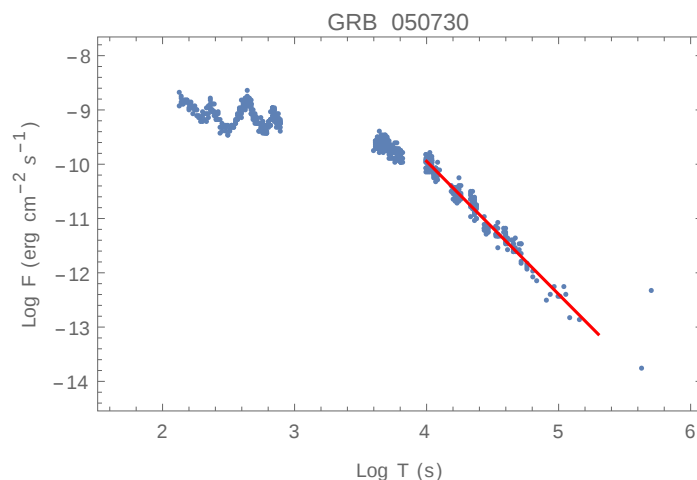


Figure A.2.9: GRB 050730: $\alpha_{X,a} = 2.45$.

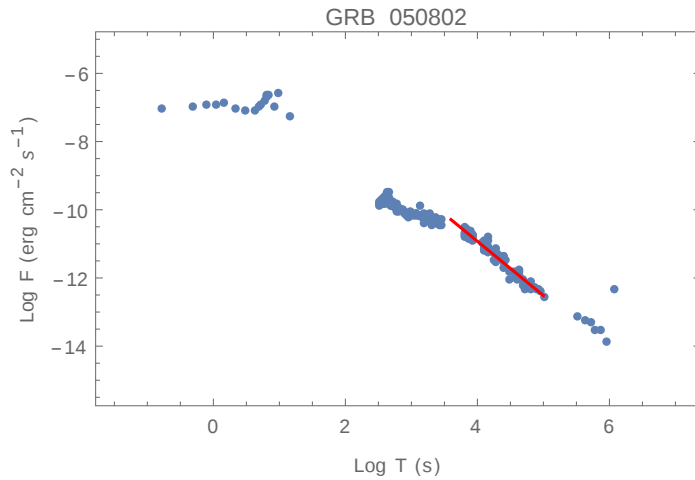


Figure A.2.10: GRB 050802: $\alpha_{X,a} = 1.59$.

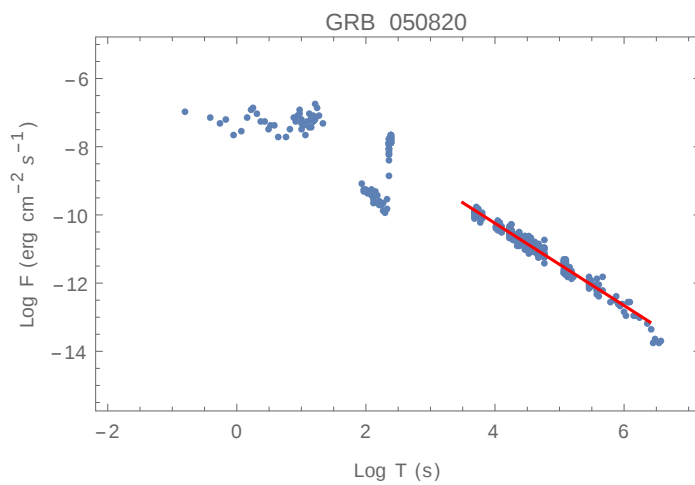


Figure A.2.11: GRB 050820A: $\alpha_{X,a} = 1.21$.

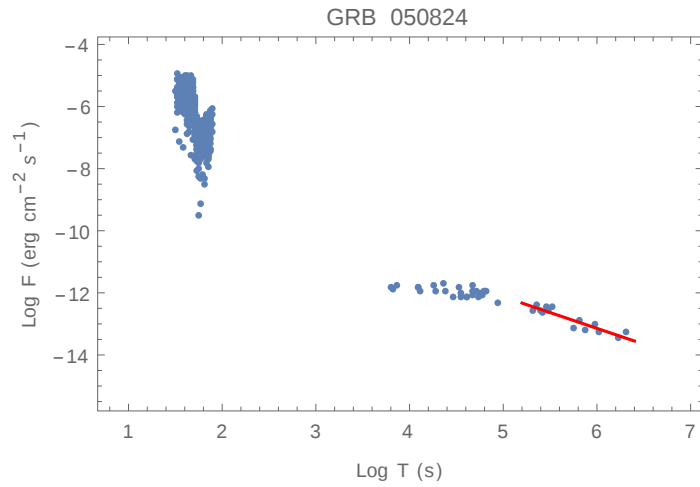


Figure A.2.12: GRB 050824: $\alpha_{X,a} = 1.02$.

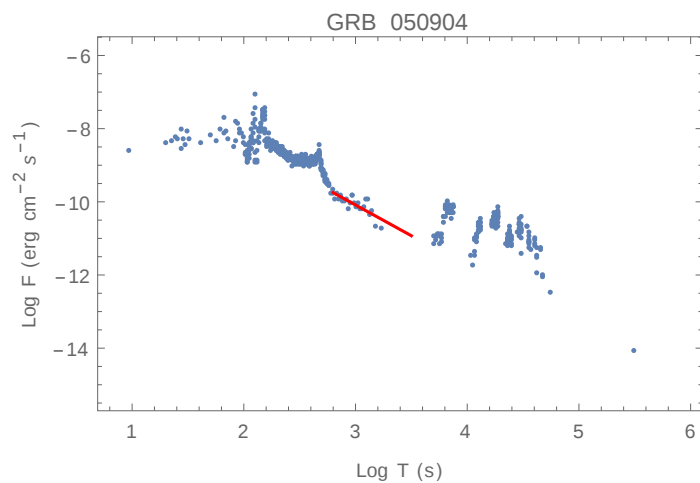


Figure A.2.13: GRB 050904: $\alpha_{X,a} = 1.68$.

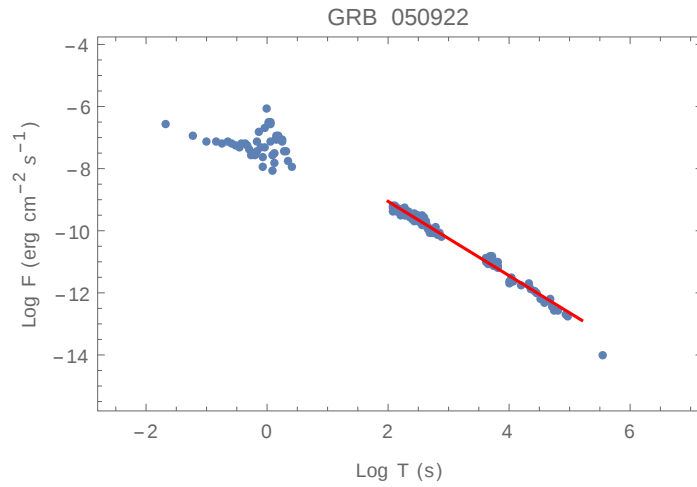


Figure A.2.14: GRB 050922C: $\alpha_{X,a} = 1.20$.

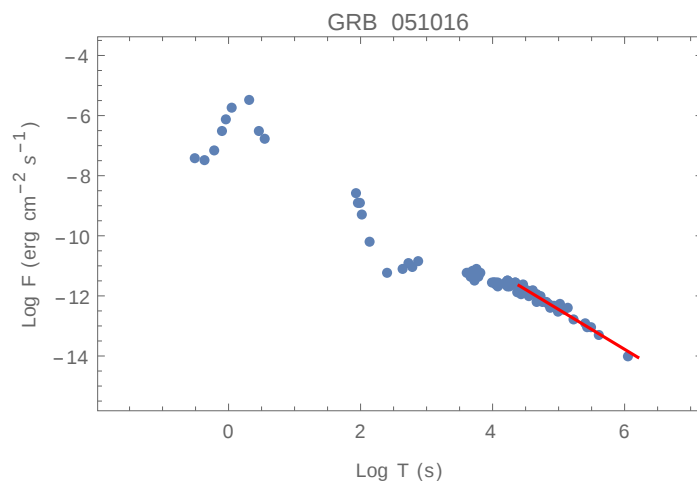


Figure A.2.15: GRB 051016B: $\alpha_{X,a} = 1.33$.

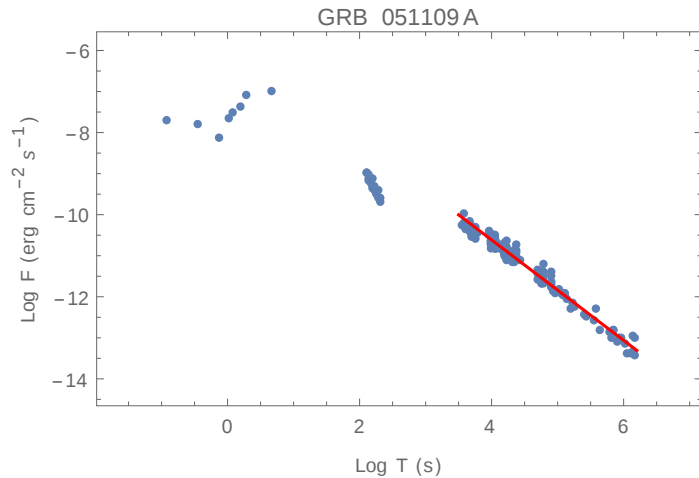


Figure A.2.16: GRB 051109A: $\alpha_{X,a} = 1.22$.

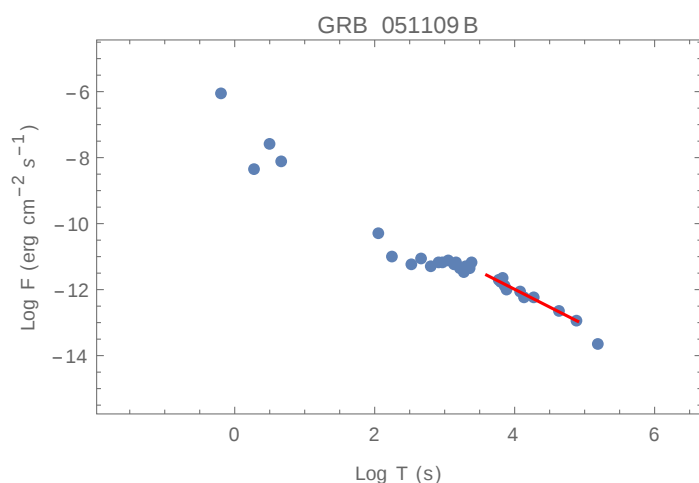


Figure A.2.17: GRB 051109B: $\alpha_{X,a} = 1.07$.

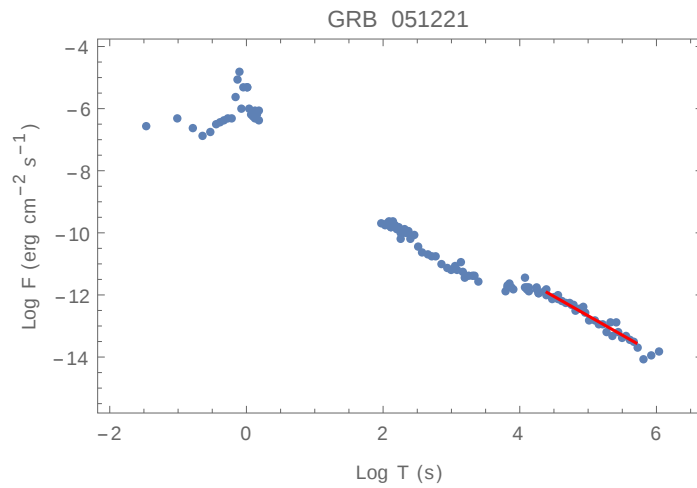


Figure A.2.18: GRB 051221A: $\alpha_{X,a} = 1.25$.

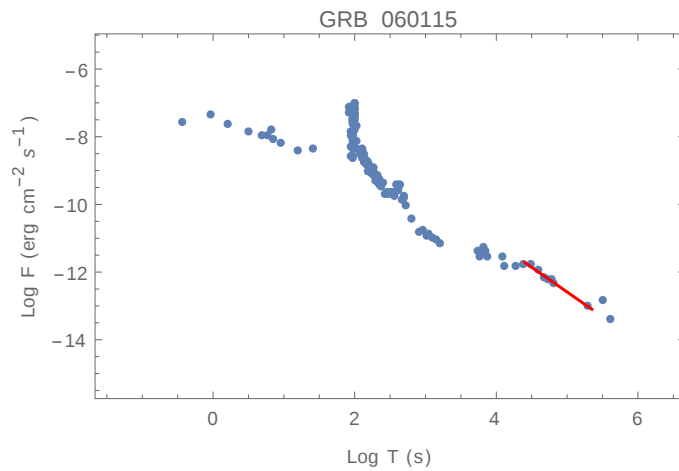


Figure A.2.19: GRB 060115: $\alpha_{X,a} = 1.46$.

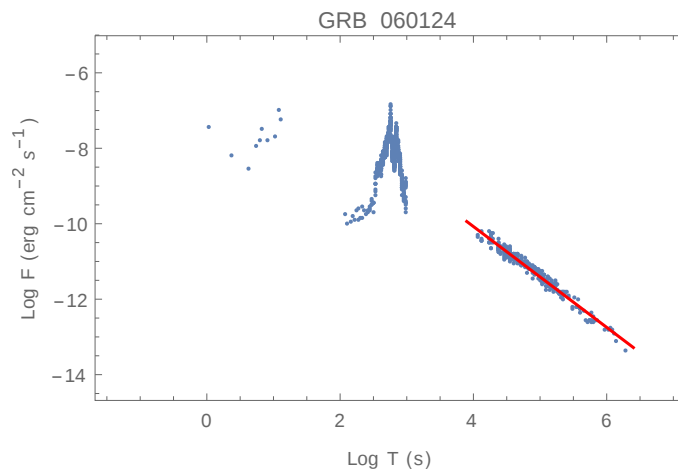


Figure A.2.20: GRB 060124: $\alpha_{X,a} = 1.34$.

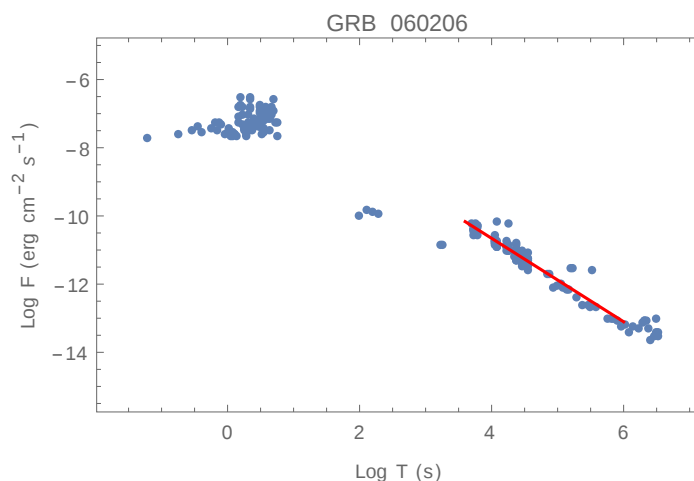


Figure A.2.21: GRB 060206: $\alpha_{X,a} = 1.22$.

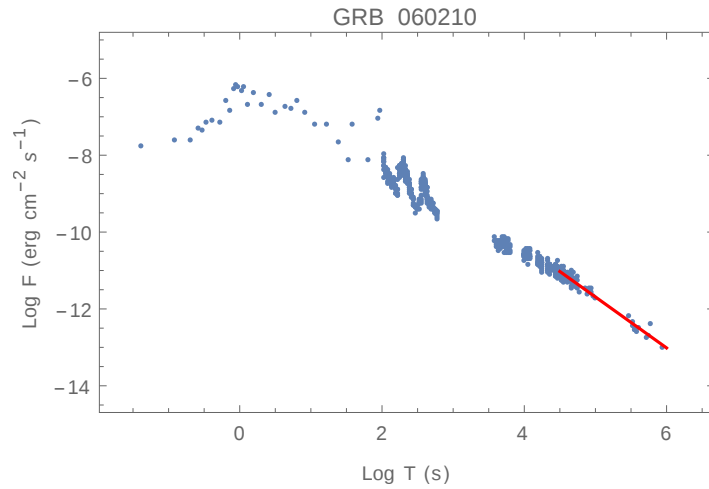


Figure A.2.22: GRB 060210: $\alpha_{X,a} = 1.32$.

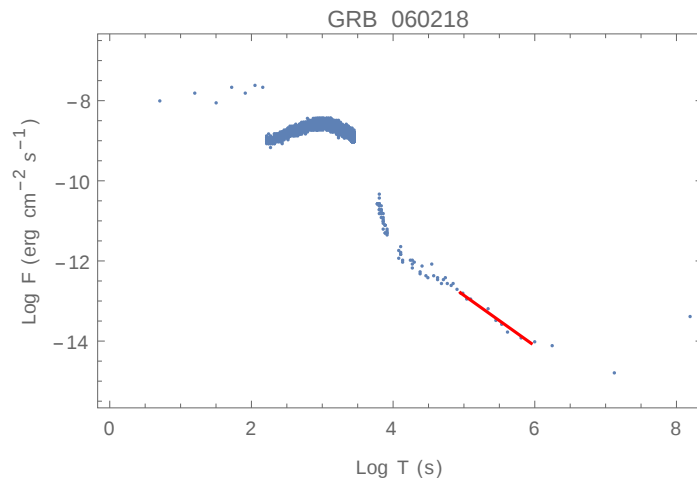


Figure A.2.23: GRB 060218: $\alpha_{X,a} = 1.26$.

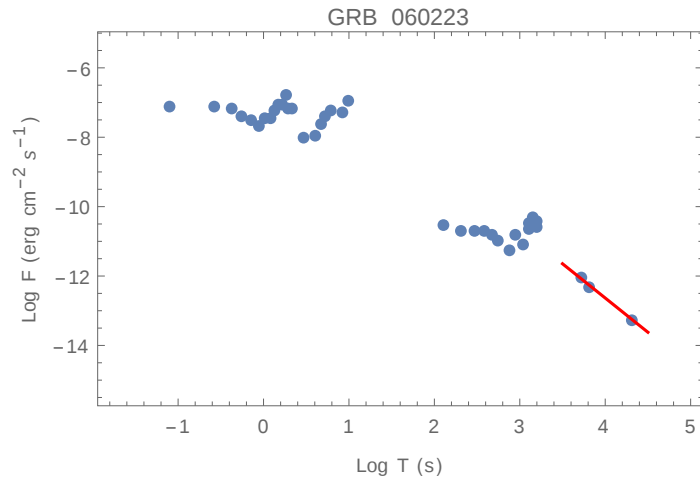


Figure A.2.24: GRB 060223A: $\alpha_{X,a} = 1.97$.

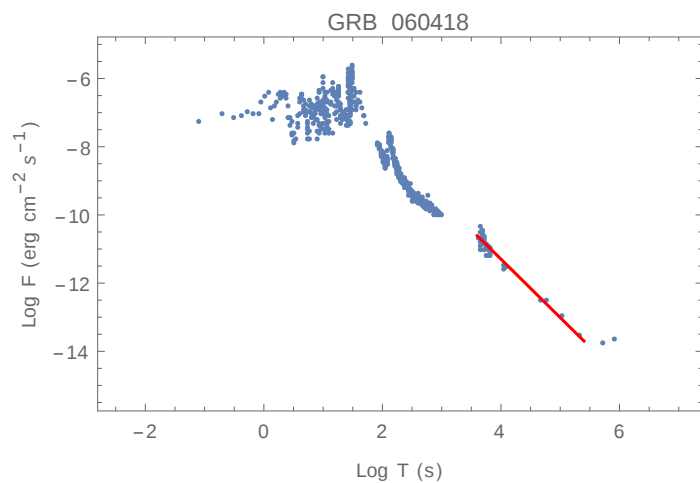


Figure A.2.25: GRB 060418: $\alpha_{X,a} = 1.71$.

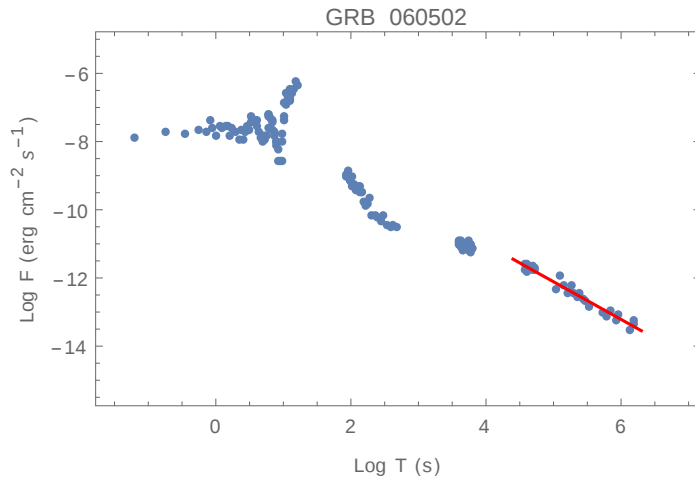


Figure A.2.26: GRB 060502A: $\alpha_{X,a} = 1.10$.

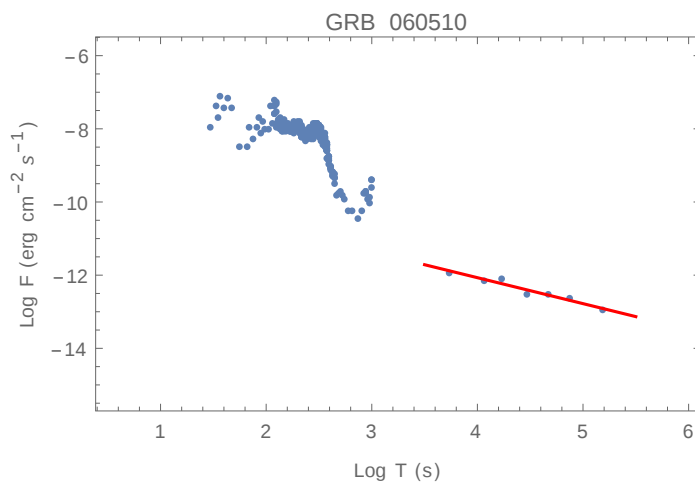


Figure A.2.27: GRB 060510B: $\alpha_{X,a} = 0.71$.

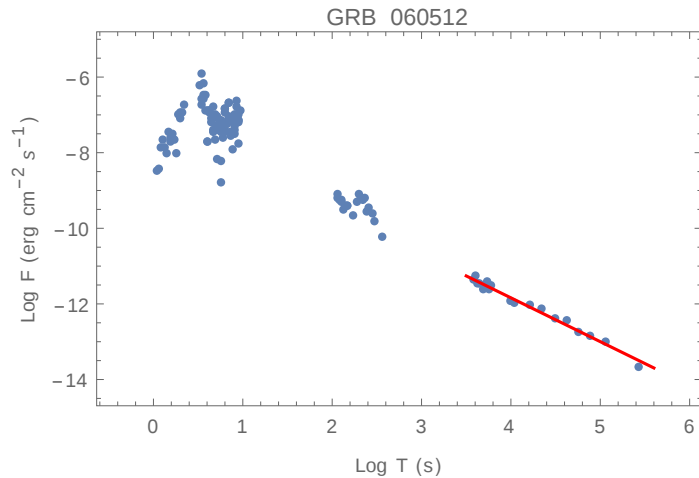


Figure A.2.28: GRB 060512: $\alpha_{X,a} = 1.16$.

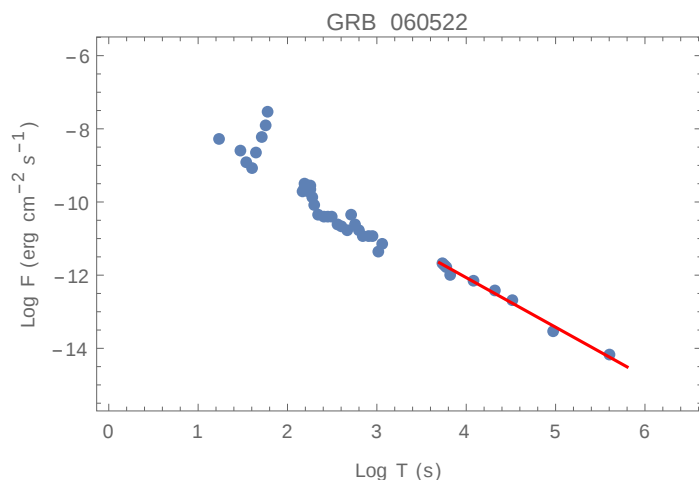


Figure A.2.29: GRB 060522: $\alpha_{X,a} = 1.35$.

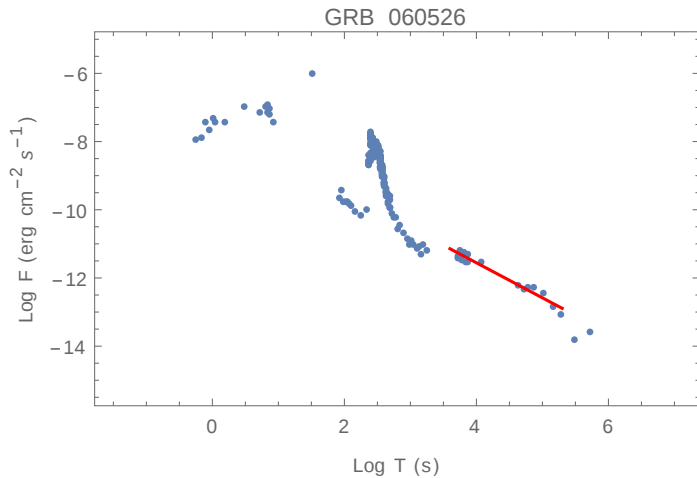


Figure A.2.30: GRB 060526: $\alpha_{X,a} = 1.03$.

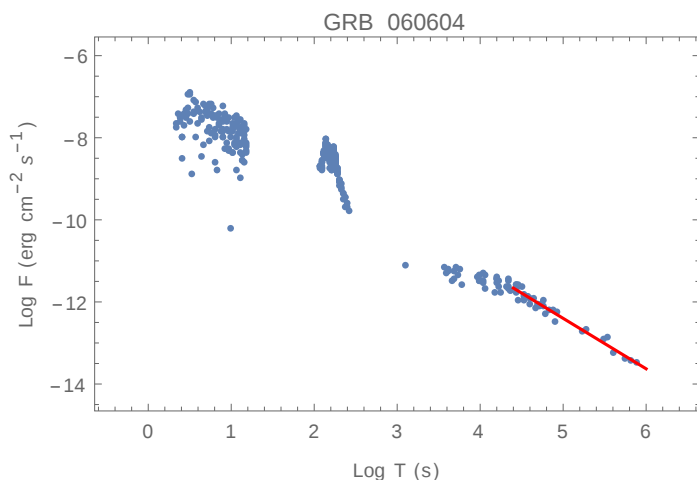


Figure A.2.31: GRB 060604: $\alpha_{X,a} = 1.23$.

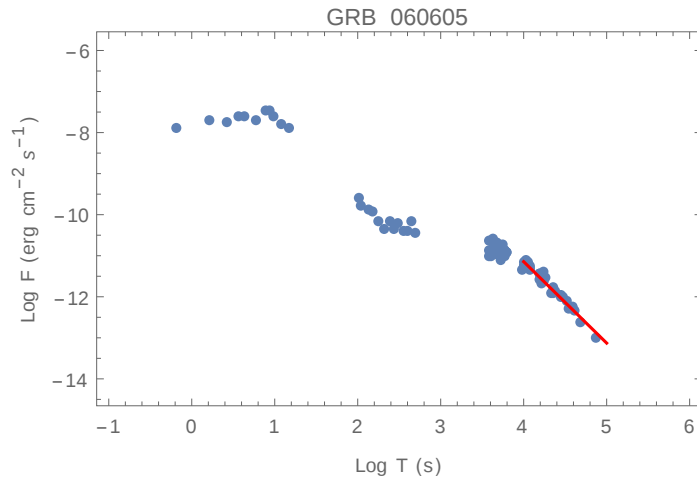


Figure A.2.32: GRB 060605: $\alpha_{X,a} = 1.98$.

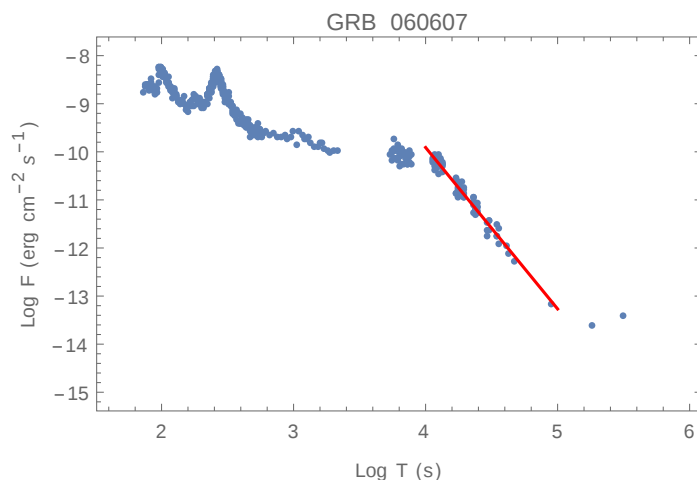


Figure A.2.33: GRB 060607A: $\alpha_{X,a} = 3.36$.

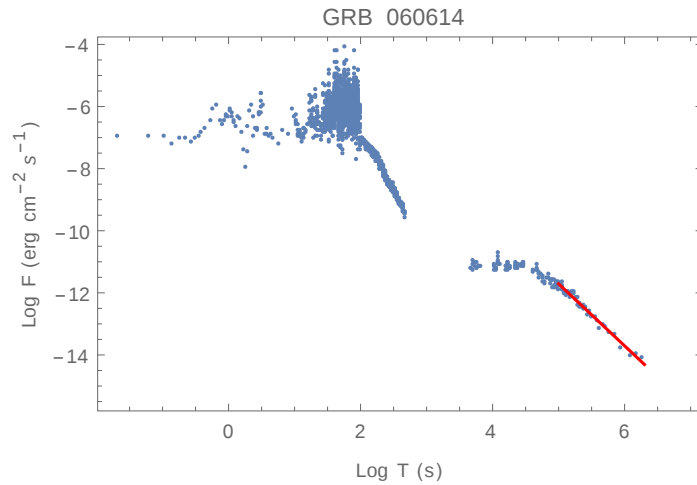


Figure A.2.34: GRB 060614: $\alpha_{X,a} = 2.00$.

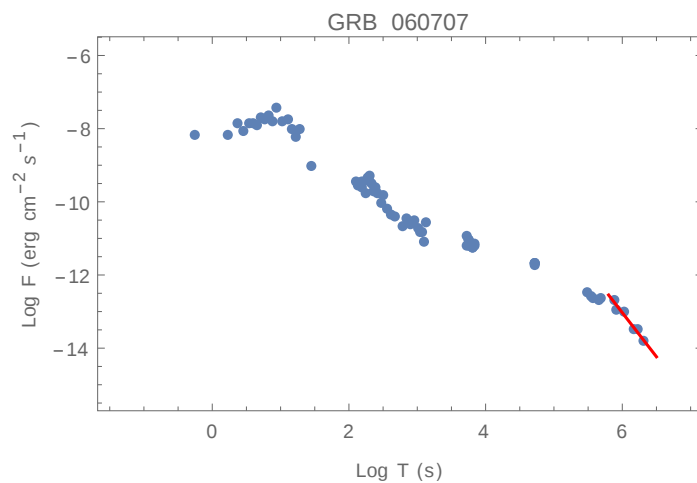


Figure A.2.35: GRB 060707: $\alpha_{X,a} = 2.40$.

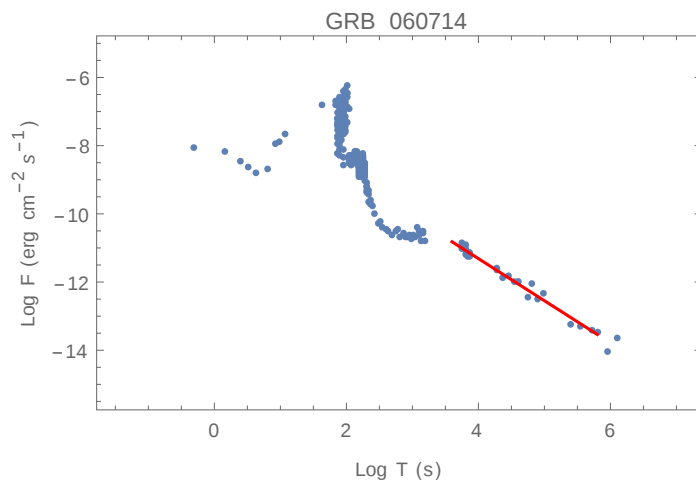


Figure A.2.36: GRB 060714: $\alpha_{X,a} = 1.23$.

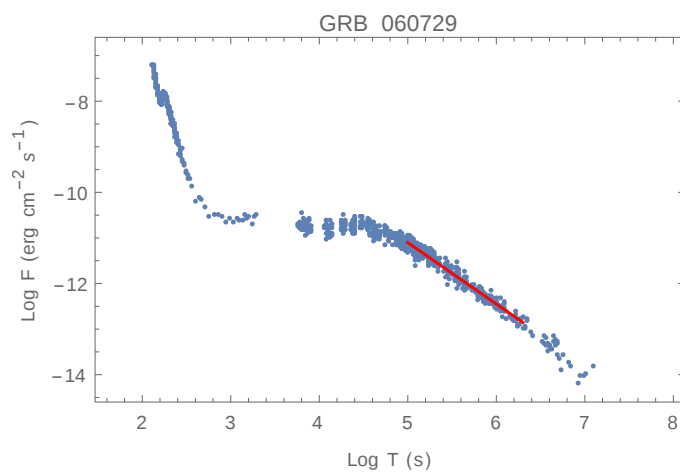


Figure A.2.37: GRB 060729: $\alpha_{X,a} = 1.35$.

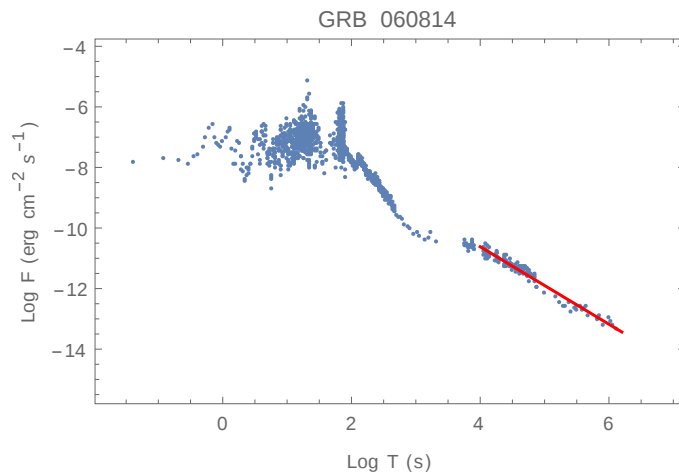


Figure A.2.38: GRB 060814: $\alpha_{X,a} = 1.28$.

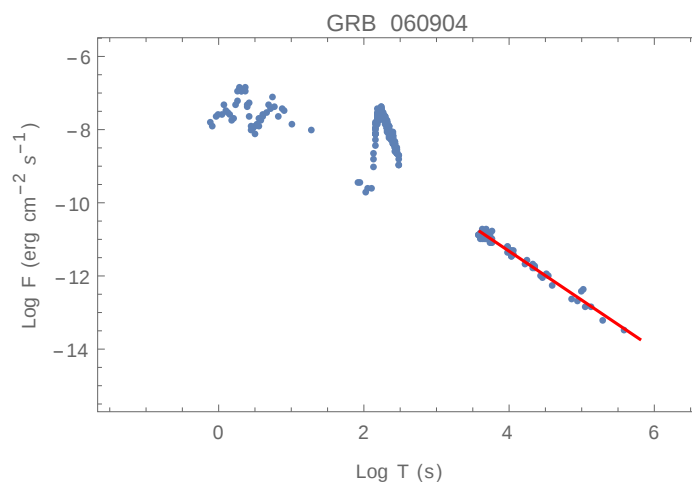


Figure A.2.39: GRB 060904B: $\alpha_{X,a} = 1.34$.

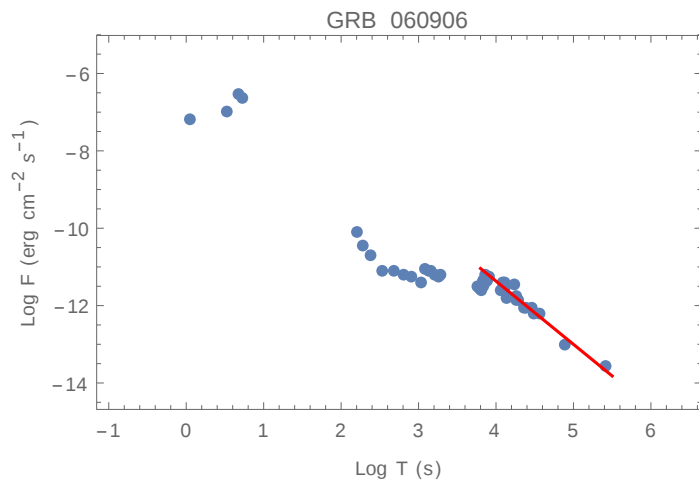


Figure A.2.40: GRB 060906: $\alpha_{X,a} = 1.63$.

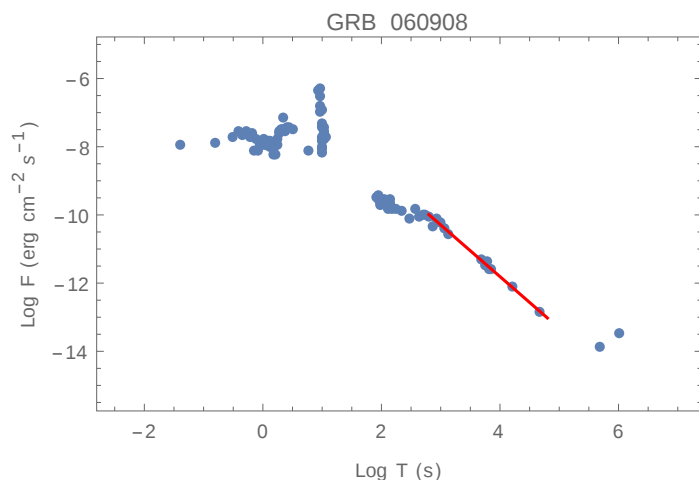


Figure A.2.41: GRB 060908: $\alpha_{X,a} = 1.51$.

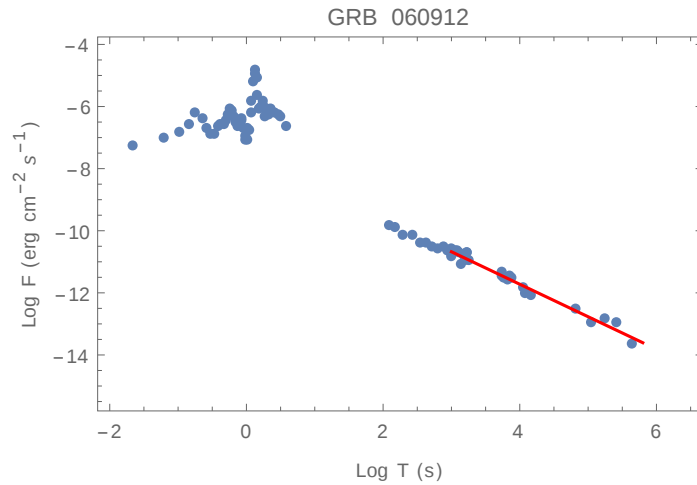


Figure A.2.42: GRB 060912A: $\alpha_{X,a} = 1.05$.

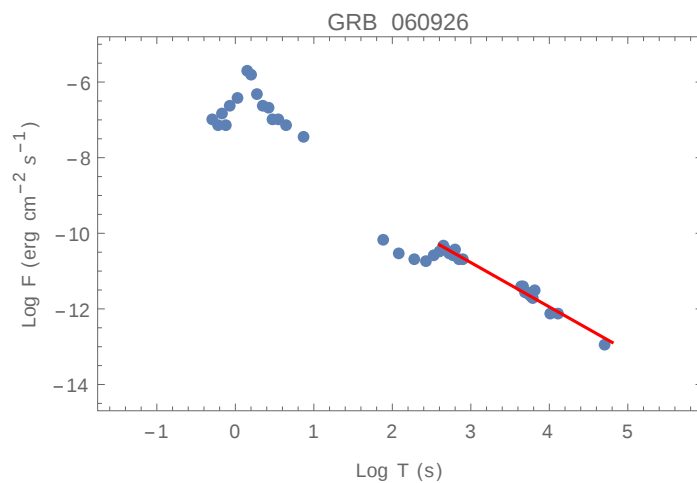


Figure A.2.43: GRB 060926: $\alpha_{X,a} = 2.26$.

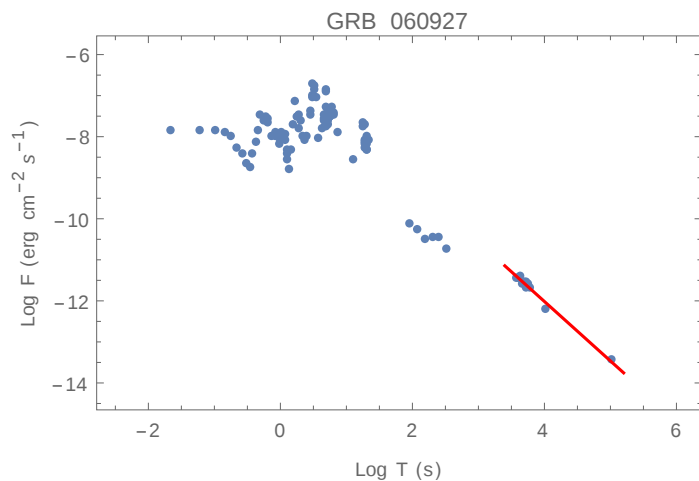


Figure A.2.44: GRB 060927: $\alpha_{X,a} = 1.45$.

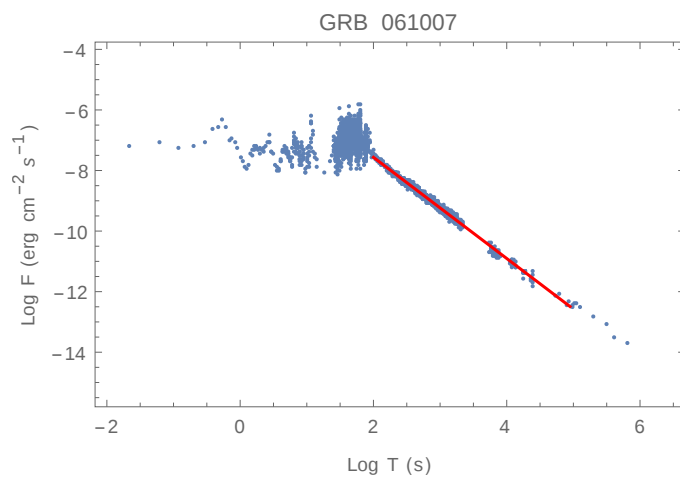


Figure A.2.45: GRB 061007: $\alpha_{X,a} = 1.67$.

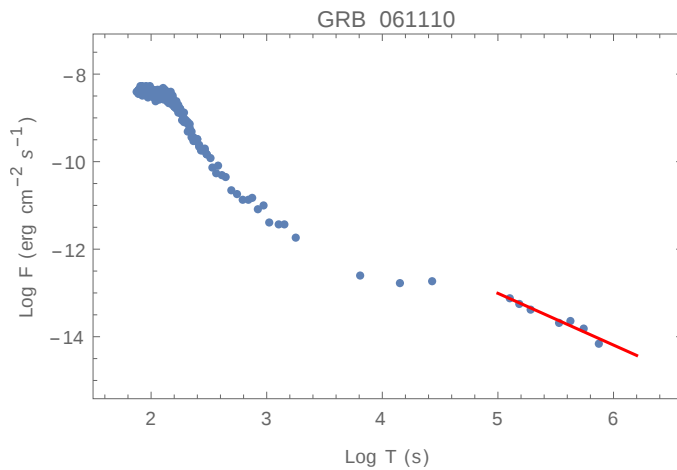


Figure A.2.46: GRB 061110A: $\alpha_{X,a} = 1.18$.

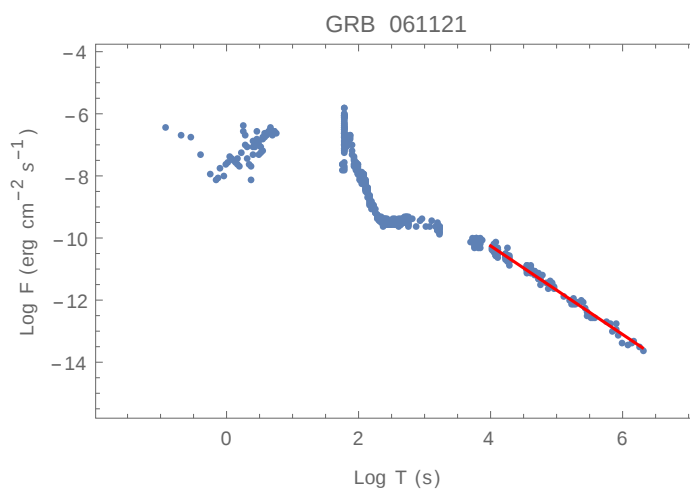


Figure A.2.47: GRB 061121: $\alpha_{X,a} = 1.43$.

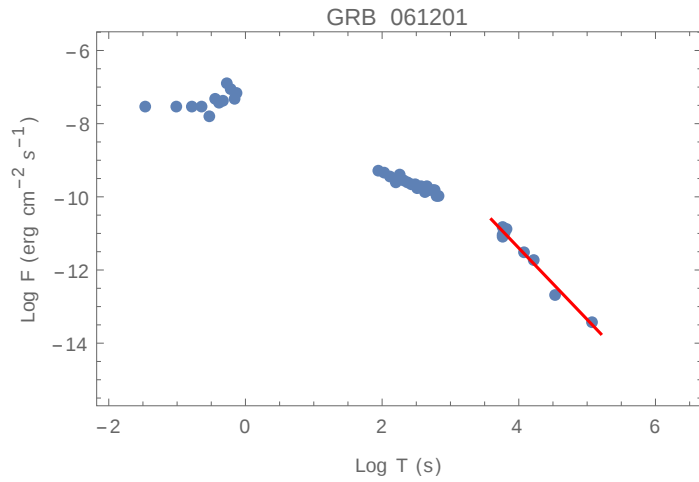


Figure A.2.48: GRB 061201: $\alpha_{X,a} = 1.95$.

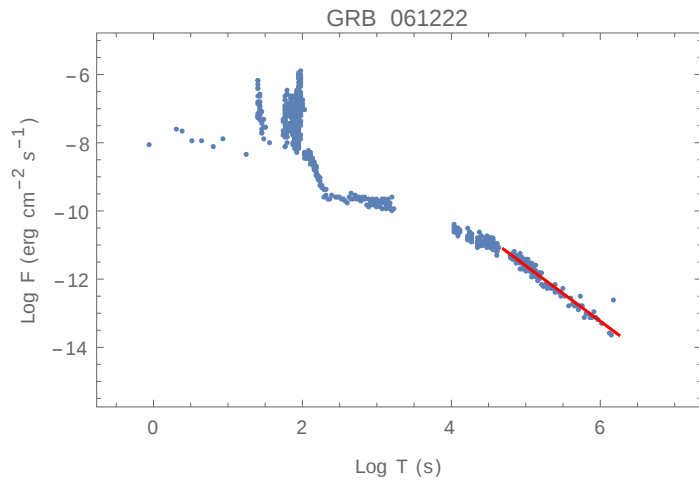


Figure A.2.49: GRB 061222A: $\alpha_{X,a} = 1.62$.

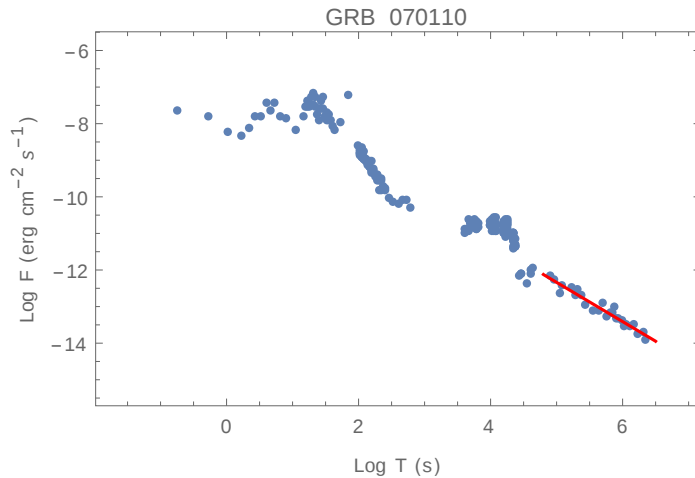


Figure A.2.50: GRB 070110: $\alpha_{X,a} = 1.07$.

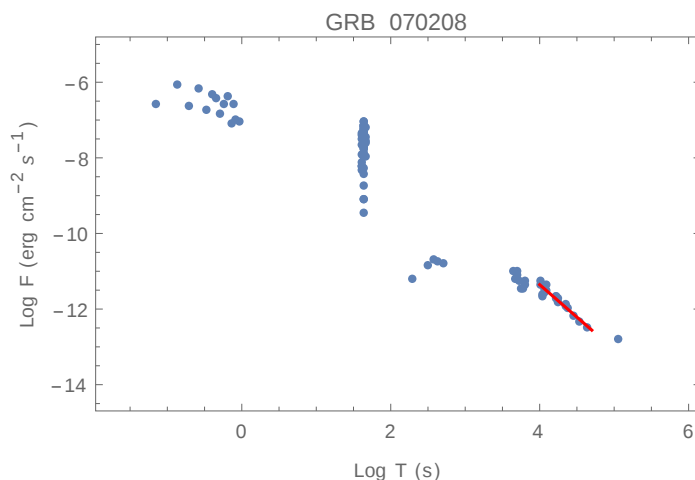


Figure A.2.51: GRB 070208: $\alpha_{X,a} = 1.72$.

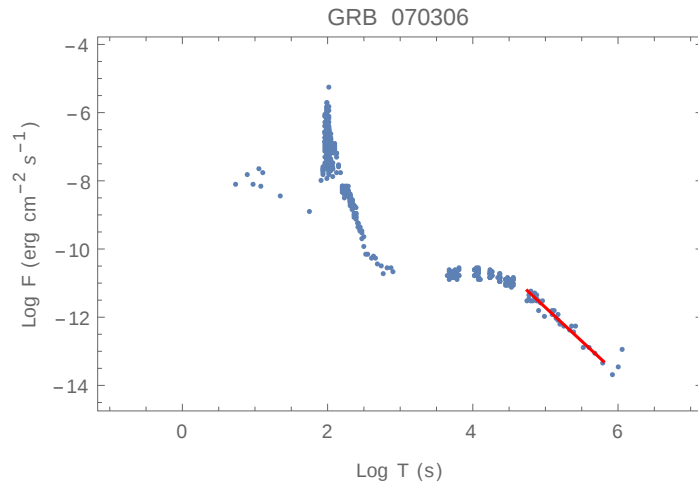


Figure A.2.52: GRB 070306: $\alpha_{X,a} = 1.97$.

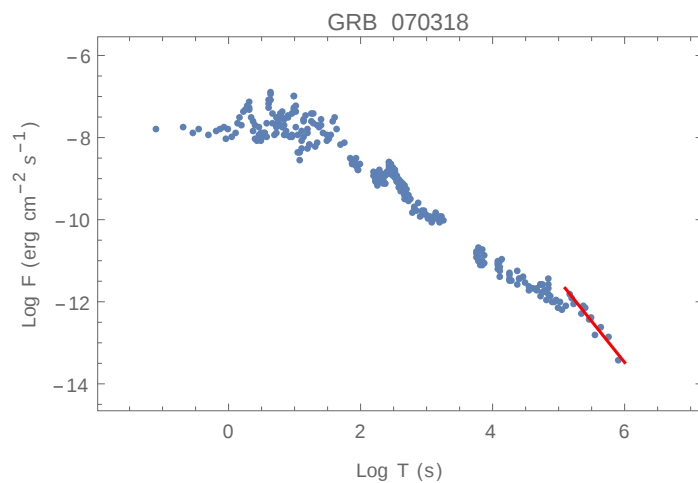


Figure A.2.53: GRB 070318: $\alpha_{X,a} = 2.01$.

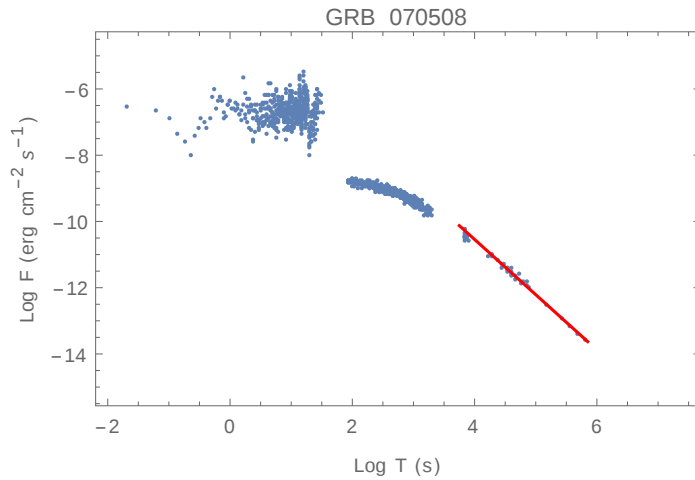


Figure A.2.54: GRB 070508: $\alpha_{X,a} = 1.67$.

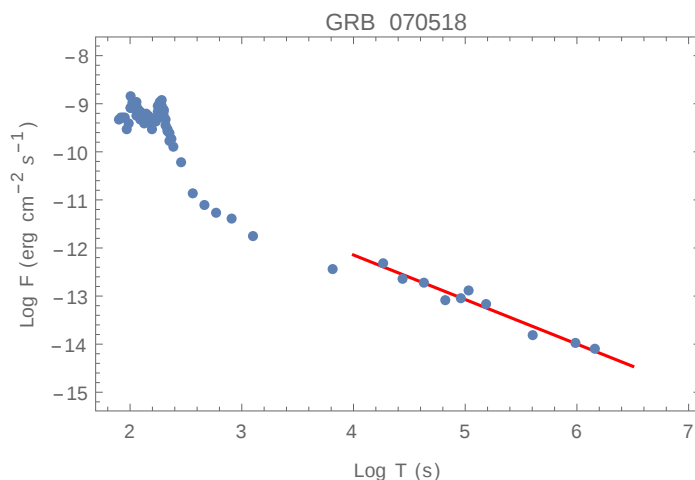


Figure A.2.55: GRB 070518: $\alpha_{X,a} = 0.93$.

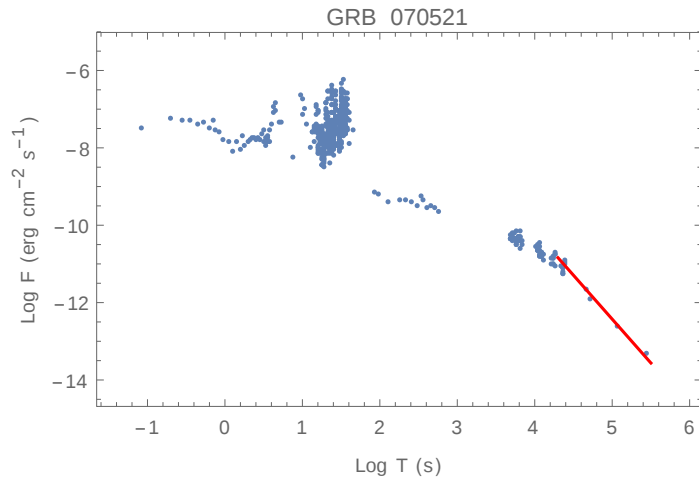


Figure A.2.56: GRB 070521: $\alpha_{X,a} = 2.27$.

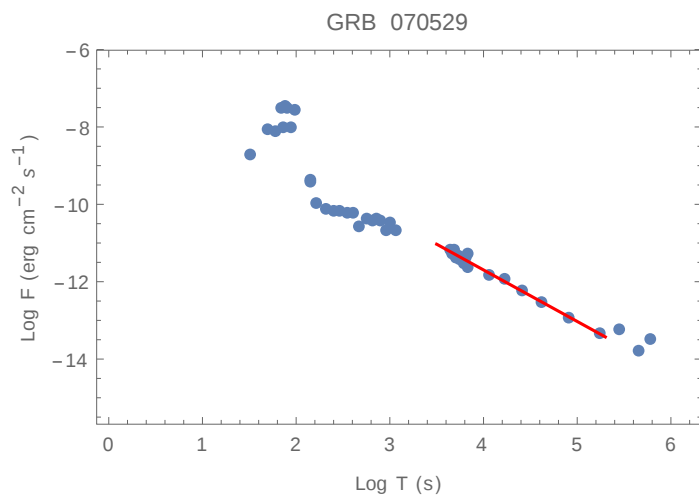


Figure A.2.57: GRB 070529: $\alpha_{X,a} = 1.33$.

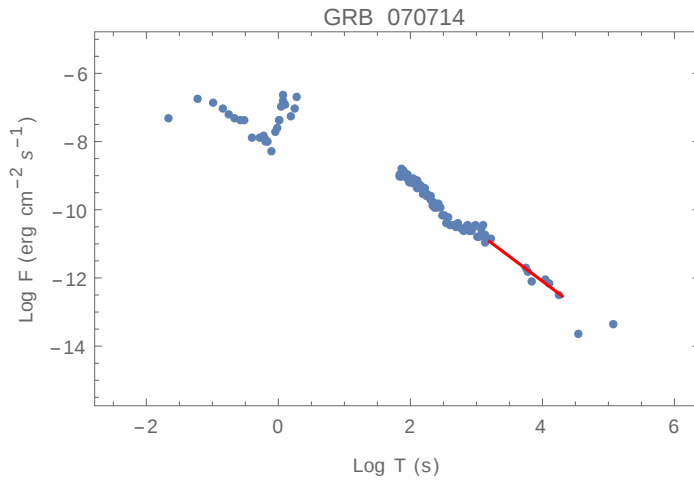


Figure A.2.58: GRB 070714B: $\alpha_{X,a} = 1.45$.

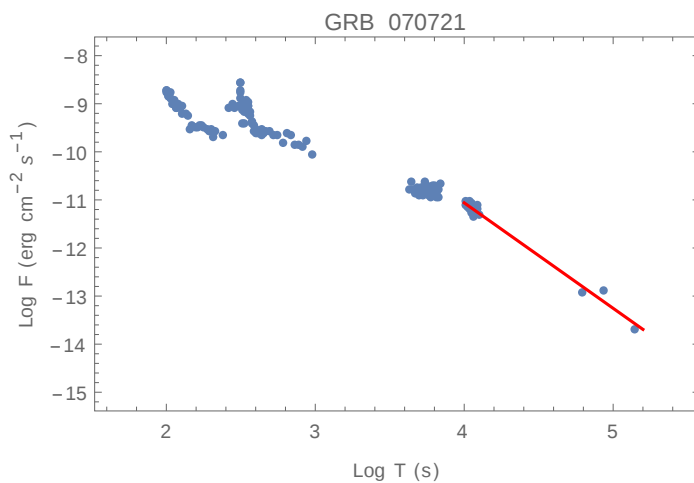


Figure A.2.59: GRB 070721B: $\alpha_{X,a} = 2.19$.

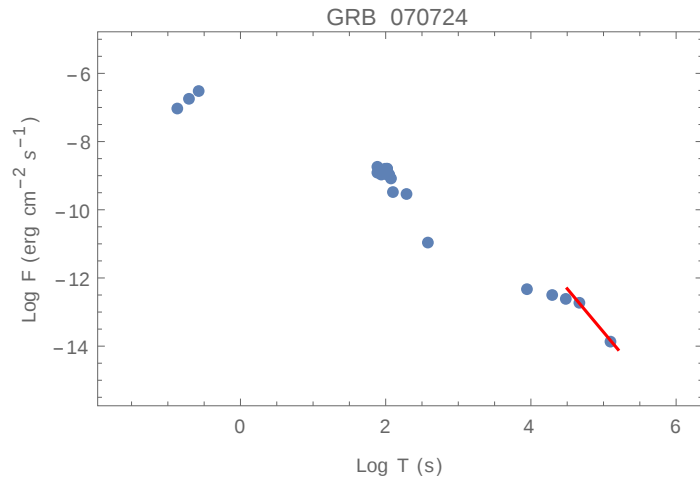


Figure A.2.60: GRB 070724A: $\alpha_{X,a} = 2.54$.

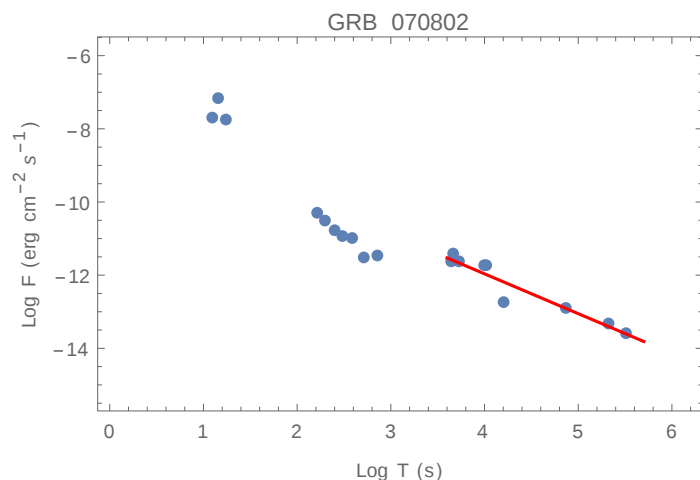


Figure A.2.61: GRB 070802: $\alpha_{X,a} = 1.09$.

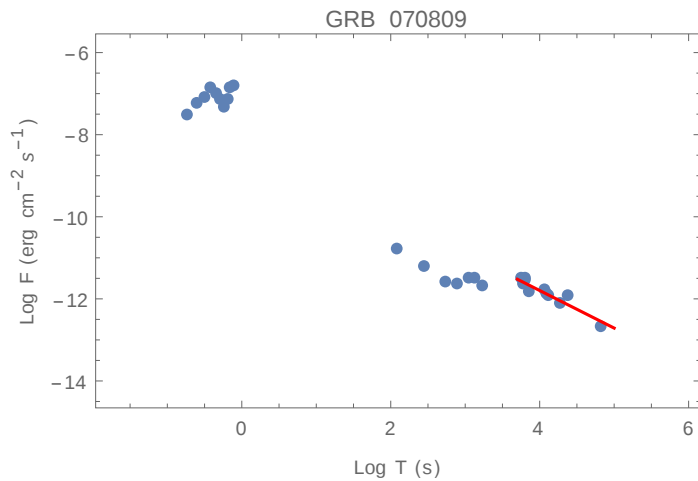


Figure A.2.62: GRB 070809: $\alpha_{X,a} = 0.91$.

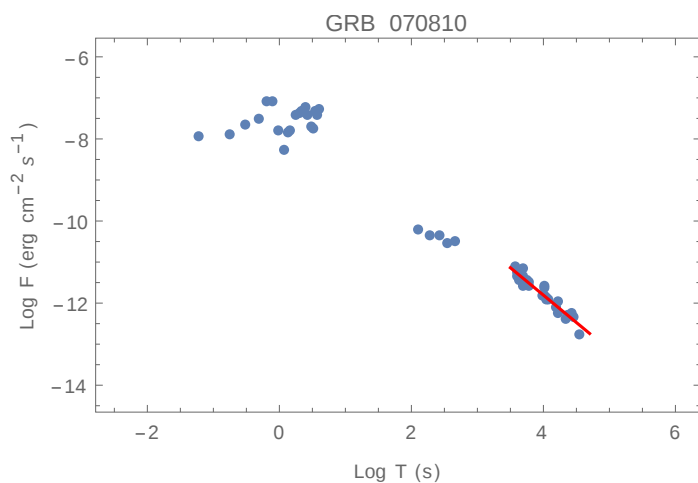


Figure A.2.63: GRB 070810A: $\alpha_{X,a} = 1.33$.

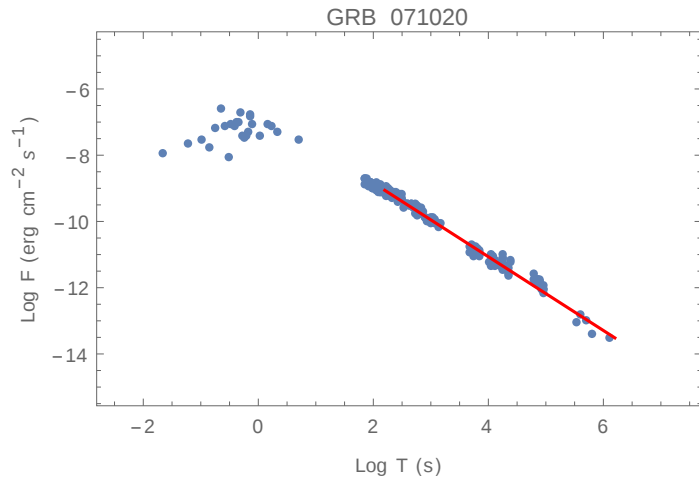


Figure A.2.64: GRB 071020: $\alpha_{X,a} = 1.11$.

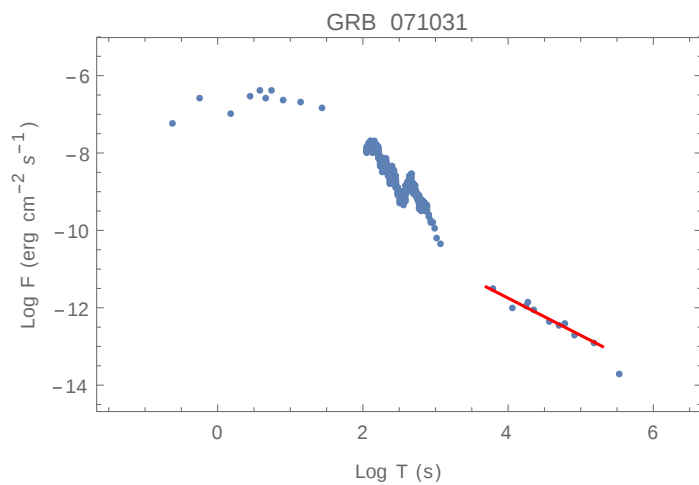


Figure A.2.65: GRB 071031: $\alpha_{X,a} = 0.96$.

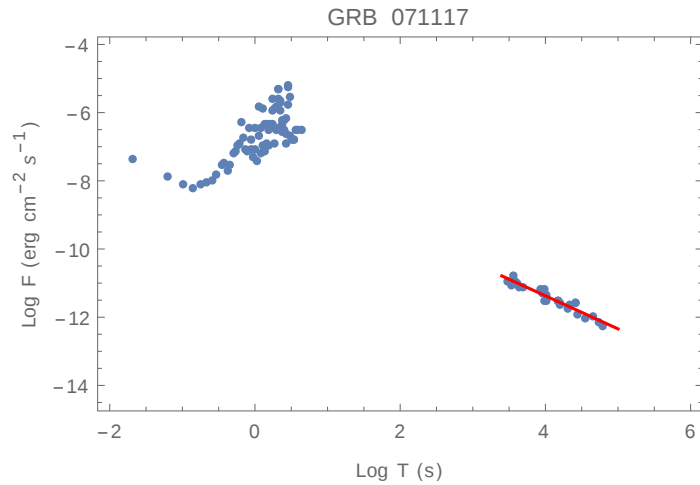


Figure A.2.66: GRB 071117: $\alpha_{X,a} = 0.97$.

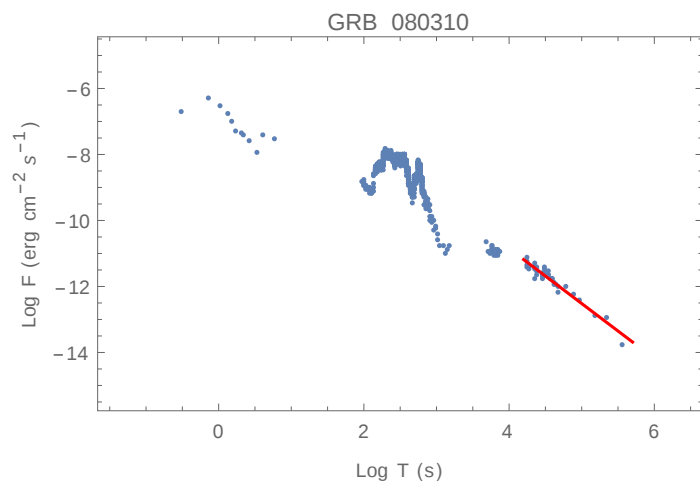


Figure A.2.67: GRB 080310: $\alpha_{X,a} = 1.66$.

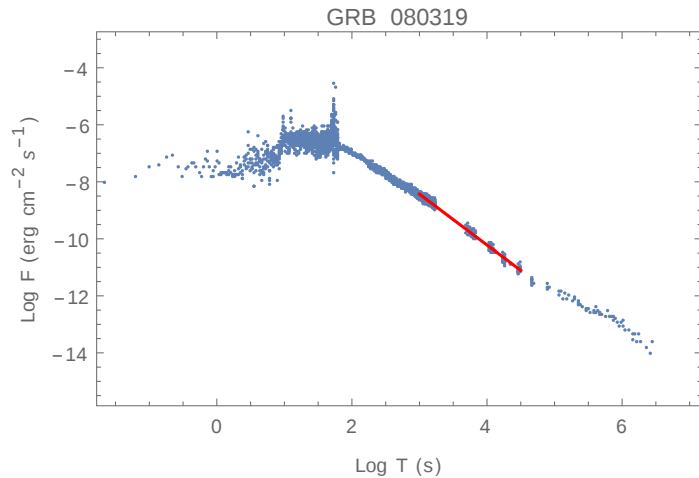


Figure A.2.68: GRB 080319B: $\alpha_{X,a} = 1.78$.

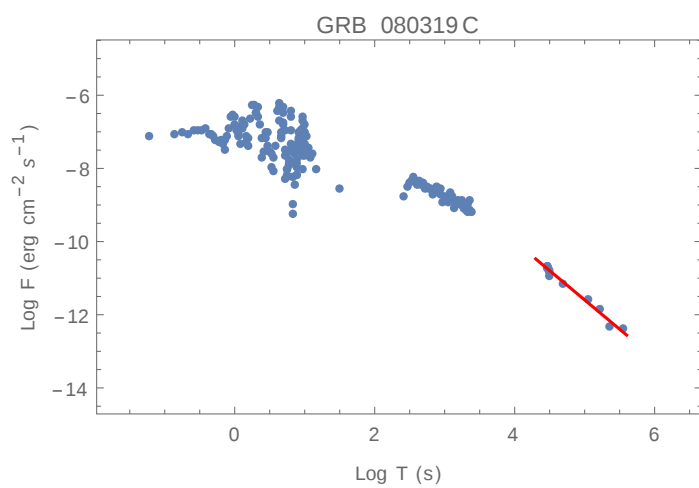


Figure A.2.69: GRB 080319C: $\alpha_{X,a} = 1.60$.

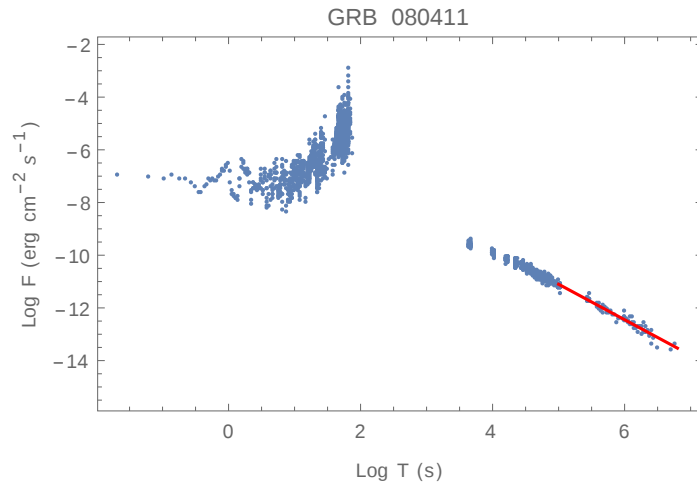


Figure A.2.70: GRB 080411: $\alpha_{X,a} = 1.35$.

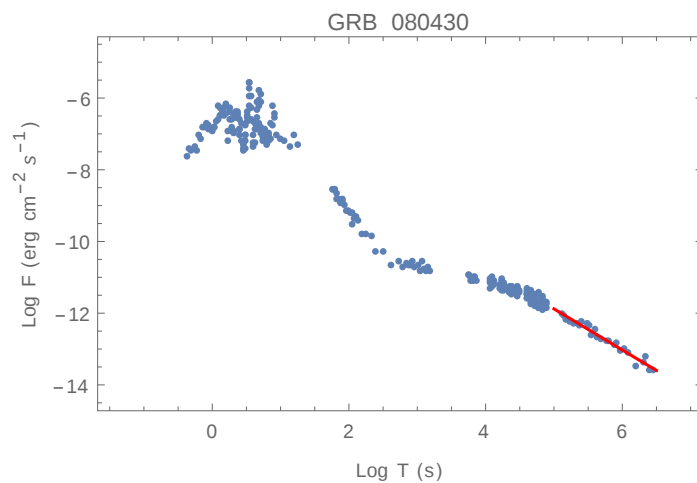


Figure A.2.71: GRB 080430: $\alpha_{X,a} = 1.14$.

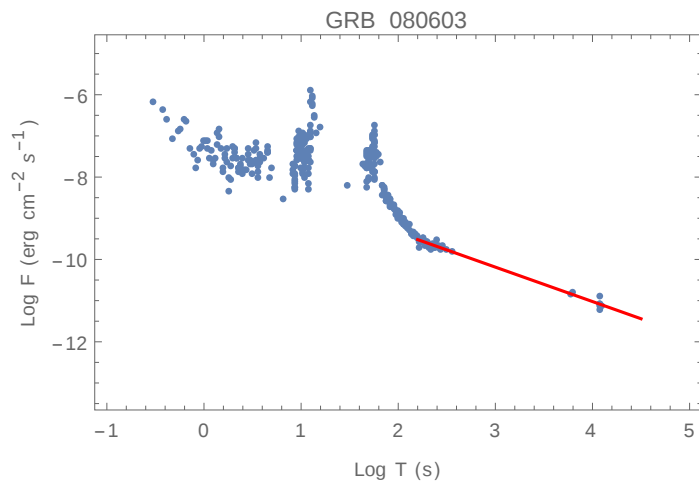


Figure A.2.72: GRB 080603B: $\alpha_{X,a} = 0.83$.

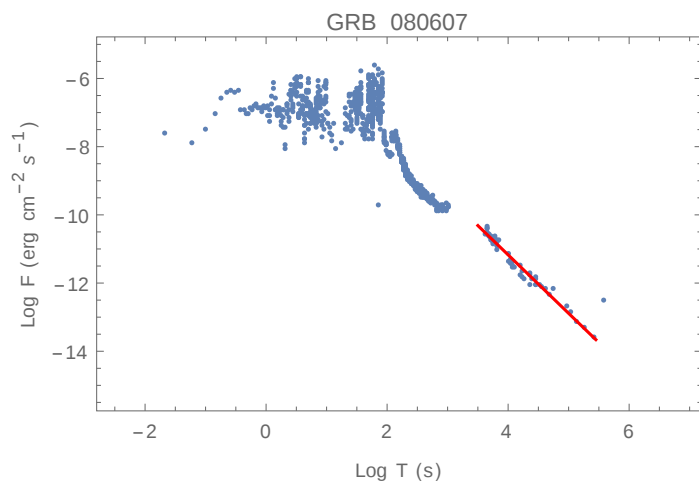


Figure A.2.73: GRB 080607: $\alpha_{X,a} = 1.71$.

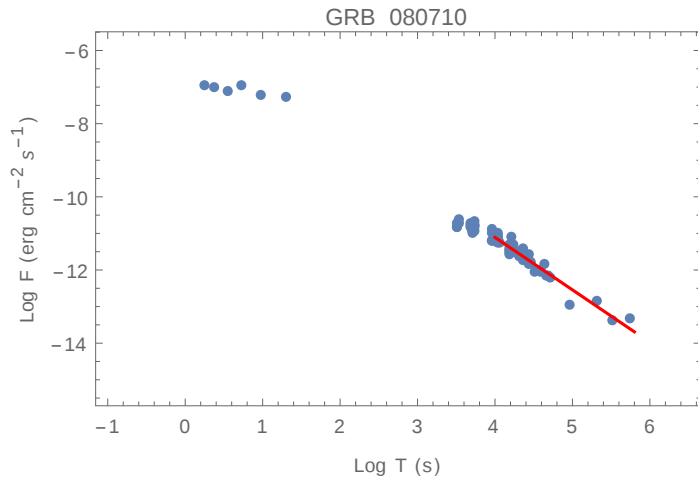


Figure A.2.74: GRB 080710: $\alpha_{X,a} = 1.43$.

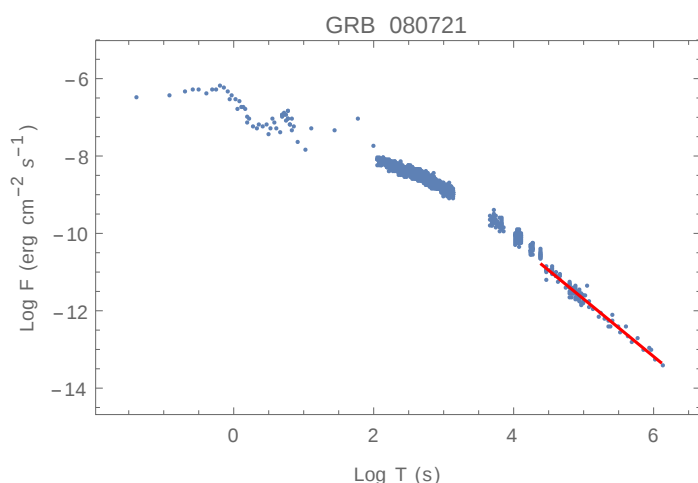


Figure A.2.75: GRB 080721: $\alpha_{X,a} = 1.49$.

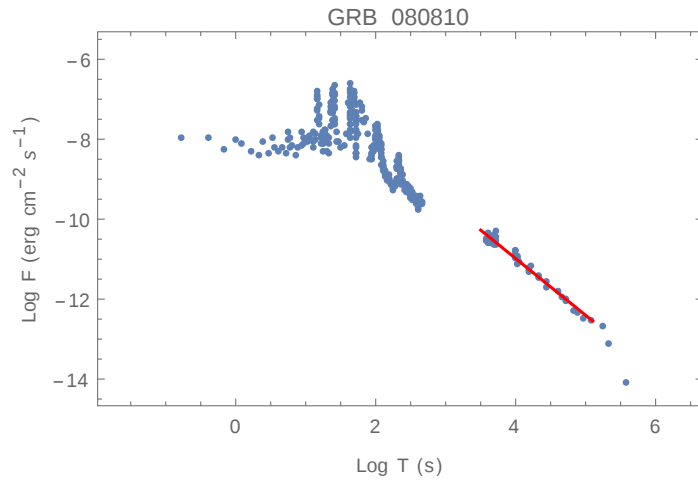


Figure A.2.76: GRB 080810: $\alpha_{X,a} = 1.42$.

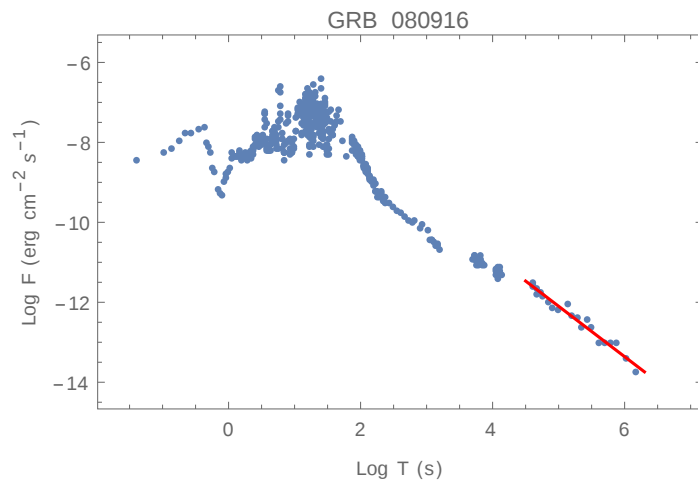


Figure A.2.77: GRB 080916A: $\alpha_{X,a} = 1.26$.

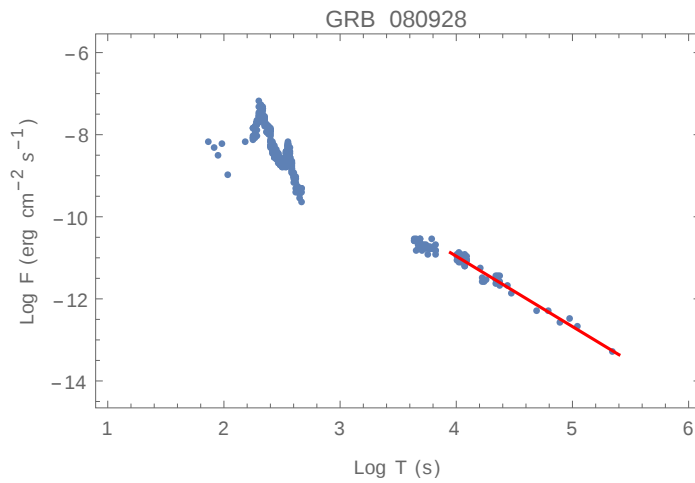


Figure A.2.78: GRB 080928: $\alpha_{X,a} = 1.71$.

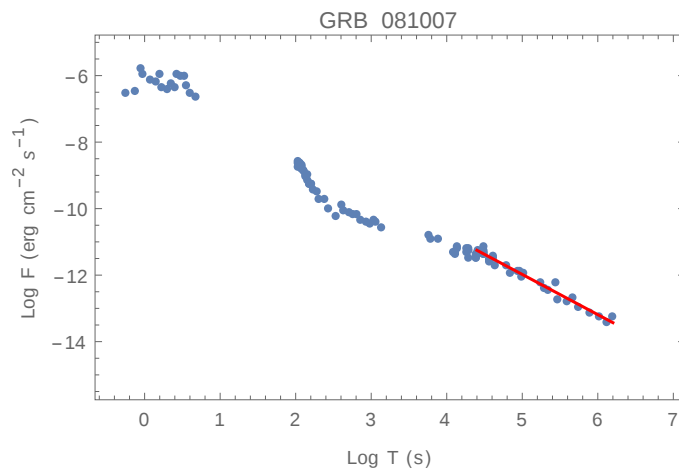


Figure A.2.79: GRB 081007: $\alpha_{X,a} = 1.21$.

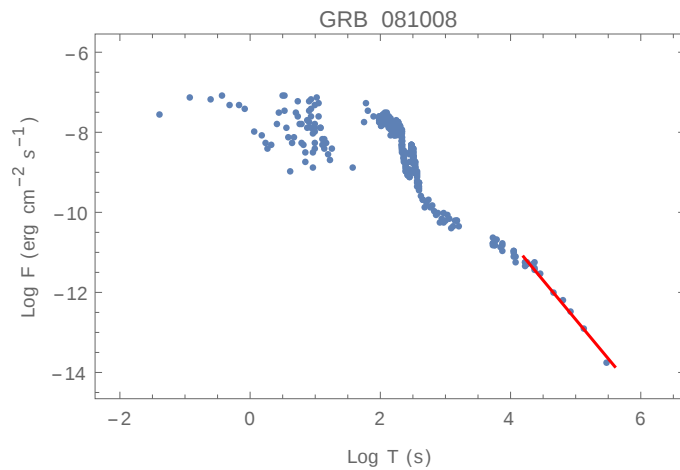


Figure A.2.80: GRB 081008: $\alpha_{X,a} = 1.96$.

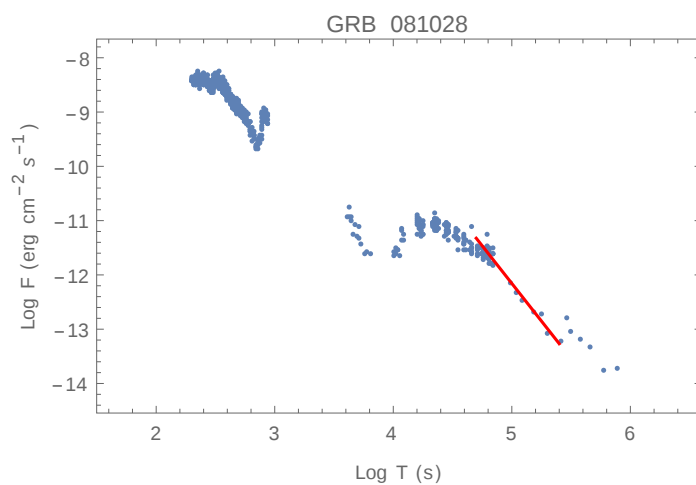


Figure A.2.81: GRB 081028: $\alpha_{X,a} = 2.77$.

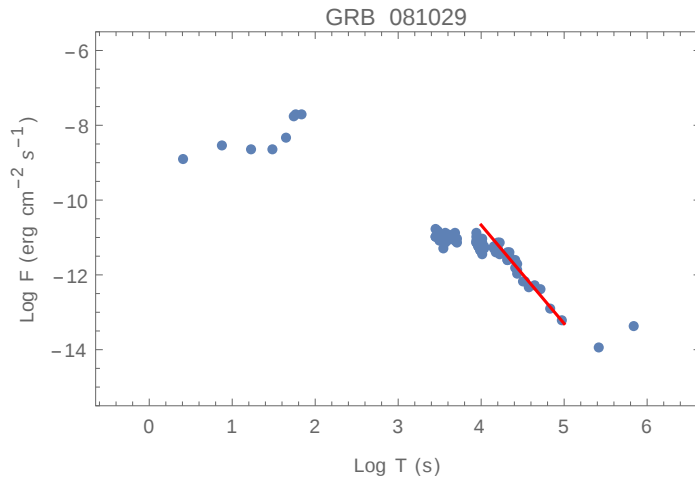


Figure A.2.82: GRB 081029: $\alpha_{X,a} = 2.63$.

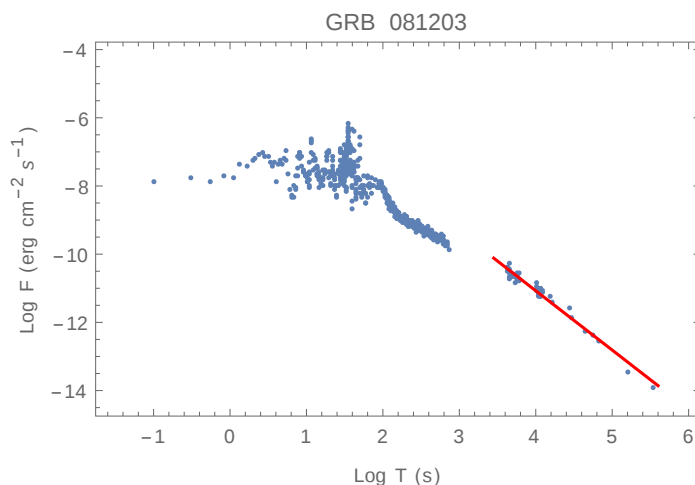


Figure A.2.83: GRB 081203A: $\alpha_{X,a} = 1.74$.

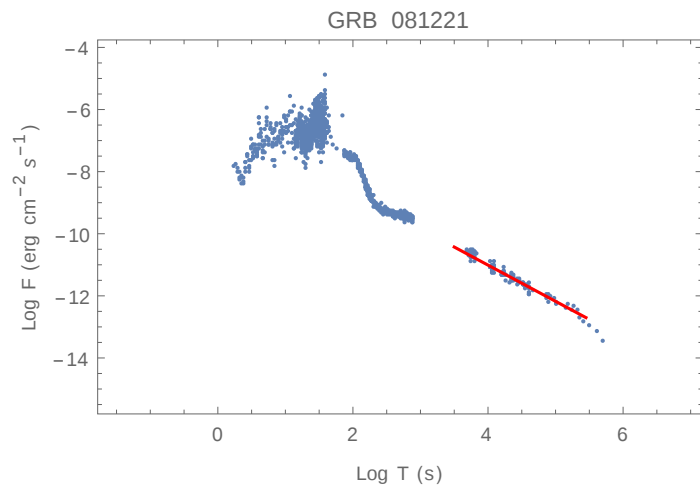


Figure A.2.84: GRB 081221: $\alpha_{X,a} = 1.16$.

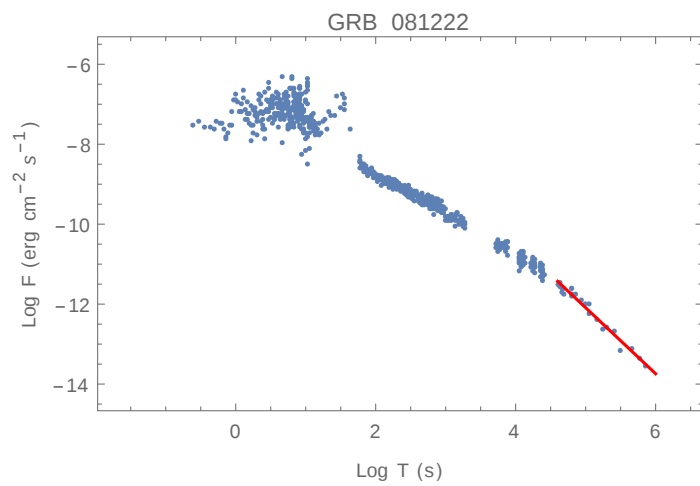


Figure A.2.85: GRB 081222: $\alpha_{X,a} = 1.65$.

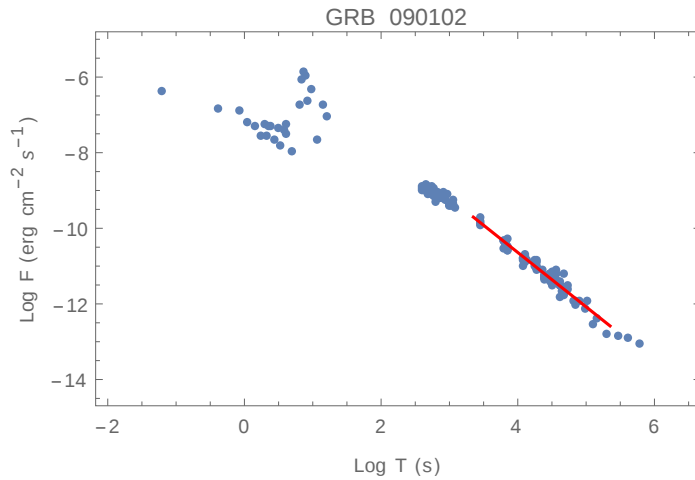


Figure A.2.86: GRB 090102: $\alpha_{X,a} = 1.44$.

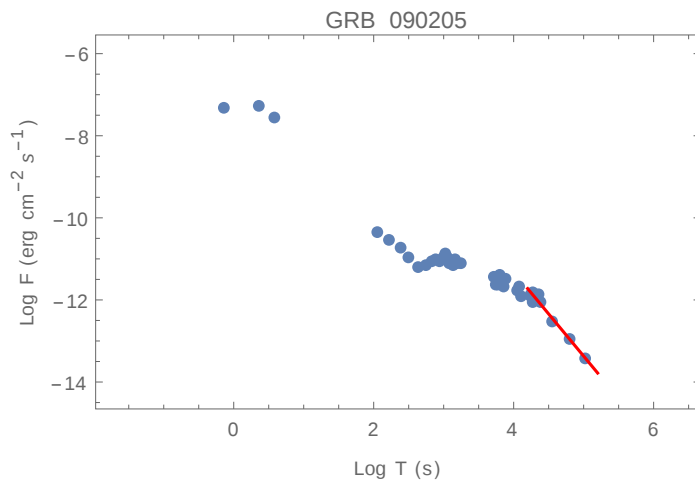


Figure A.2.87: GRB 090205: $\alpha_{X,a} = 2.05$.

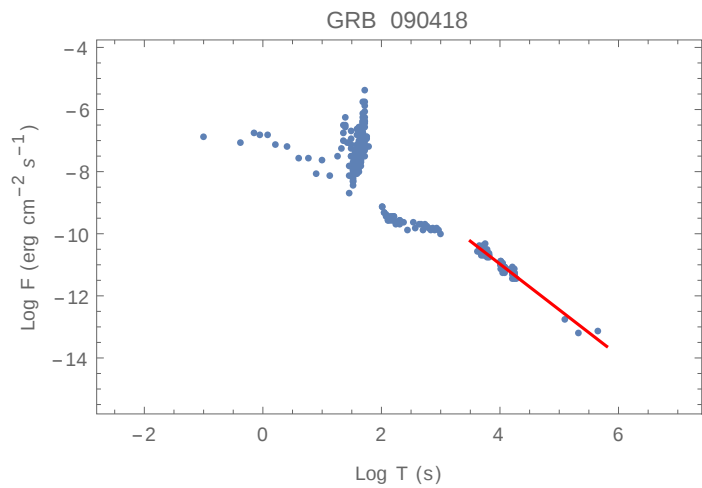


Figure A.2.88: GRB 090418: $\alpha_{X,a} = 1.47$.

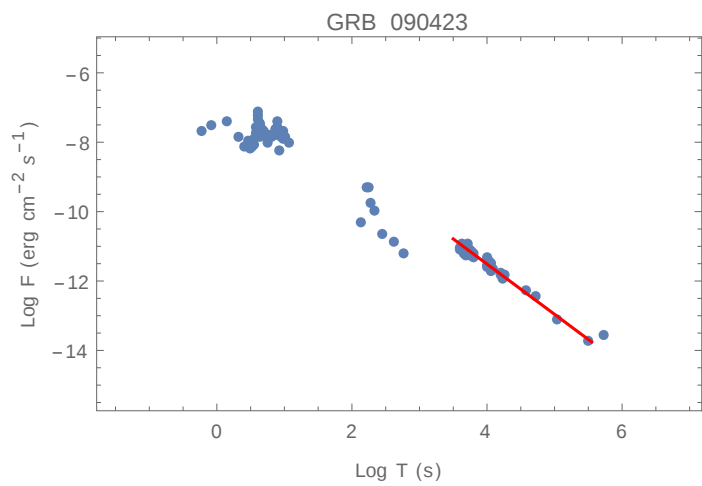


Figure A.2.89: GRB 090423: $\alpha_{X,a} = 1.45$.

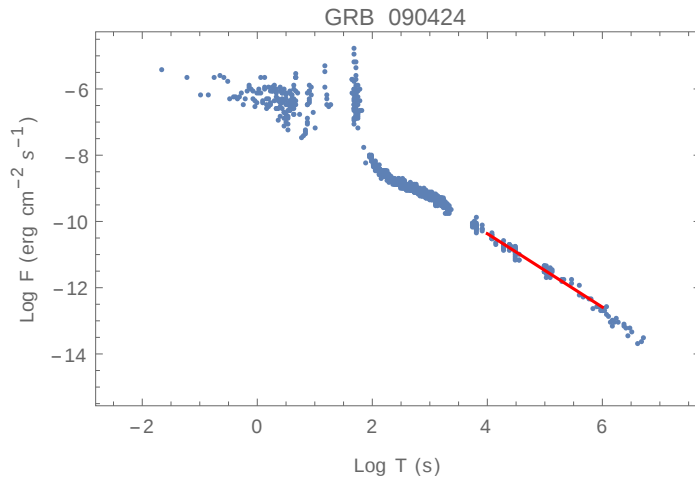


Figure A.2.90: GRB 090424: $\alpha_{X,a} = 1.11$.

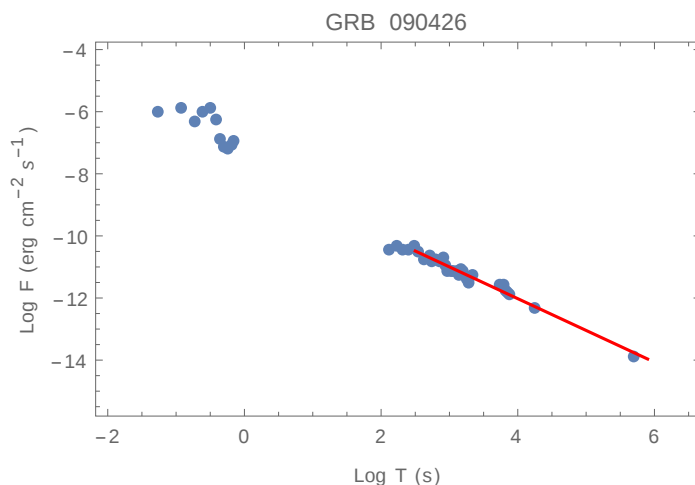


Figure A.2.91: GRB 090426: $\alpha_{X,a} = 1.02$.

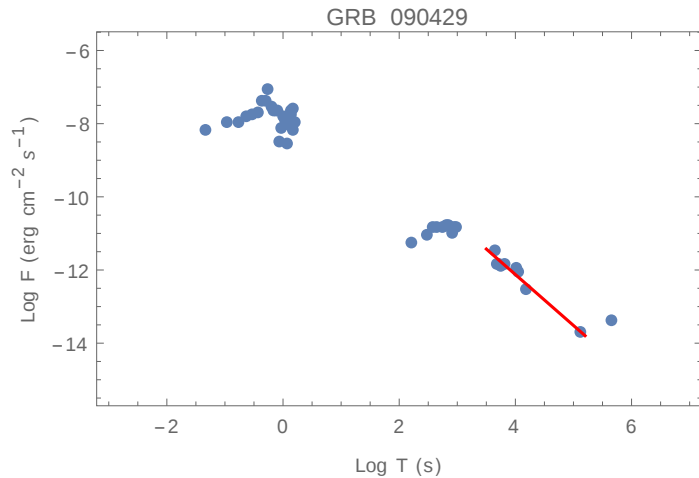


Figure A.2.92: GRB 090429B: $\alpha_{X,a} = 1.39$.

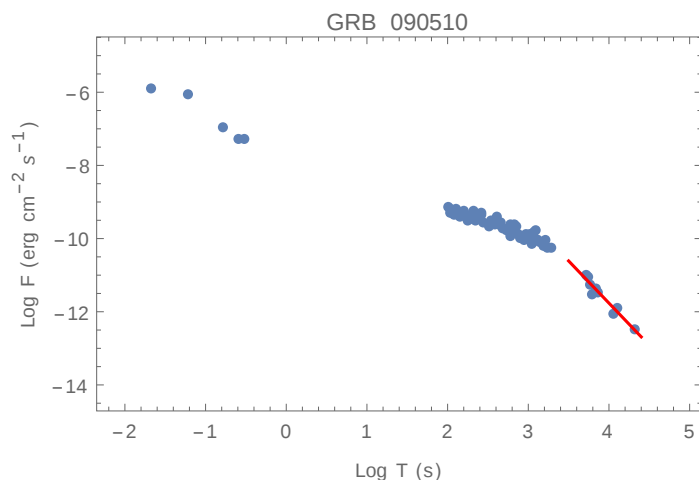


Figure A.2.93: GRB 090510: $\alpha_{X,a} = 2.31$.

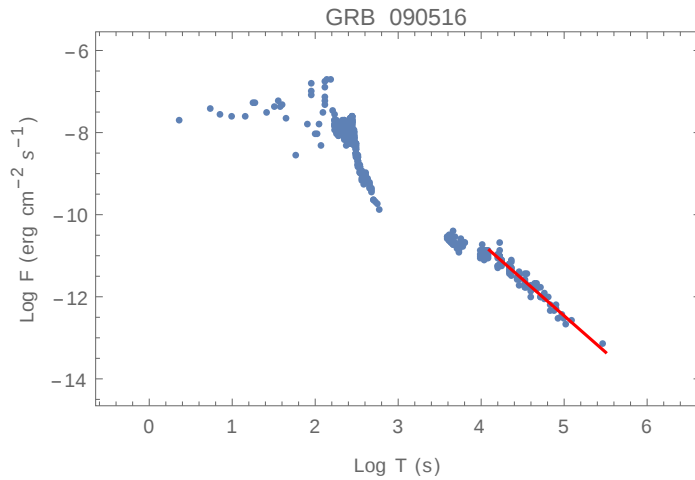


Figure A.2.94: GRB 090516: $\alpha_{X,a} = 1.77$.

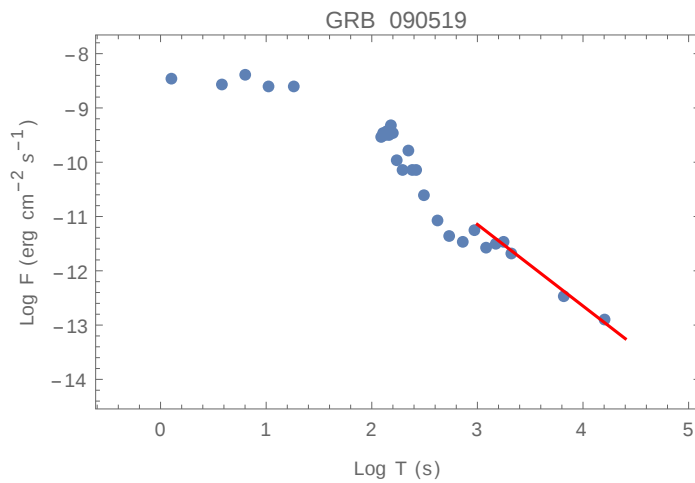


Figure A.2.95: GRB 090519: $\alpha_{X,a} = 1.50$.

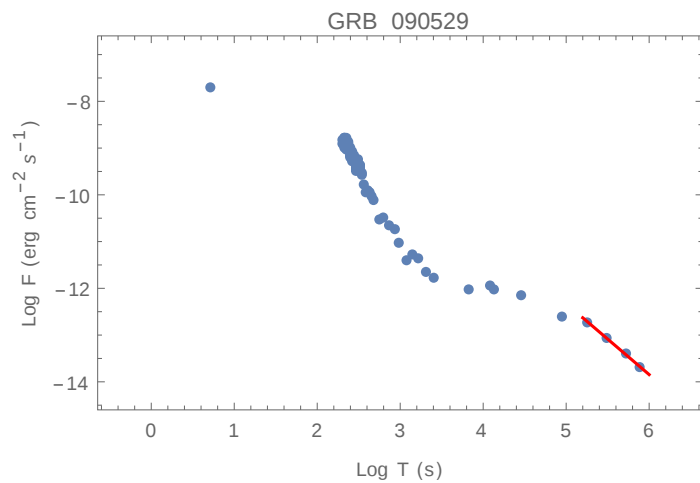


Figure A.2.96: GRB 090529: $\alpha_{X,a} = 1.52$.

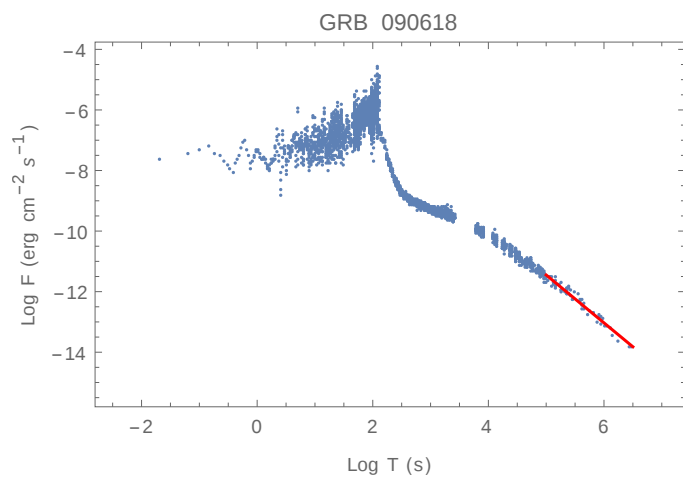


Figure A.2.97: GRB 090618: $\alpha_{X,a} = 1.58$.

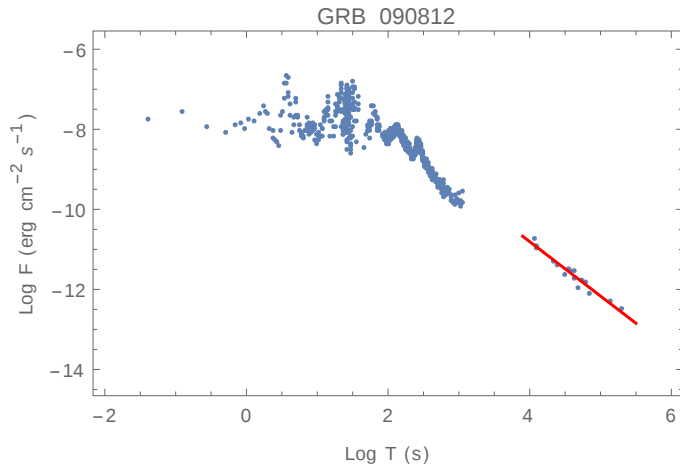


Figure A.2.98: GRB 090812: $\alpha_{X,a} = 1.36$.

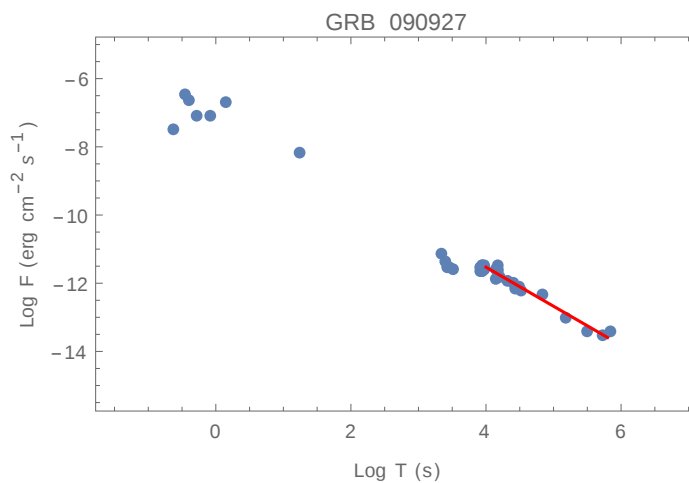


Figure A.2.99: GRB 090927: $\alpha_{X,a} = 1.15$.

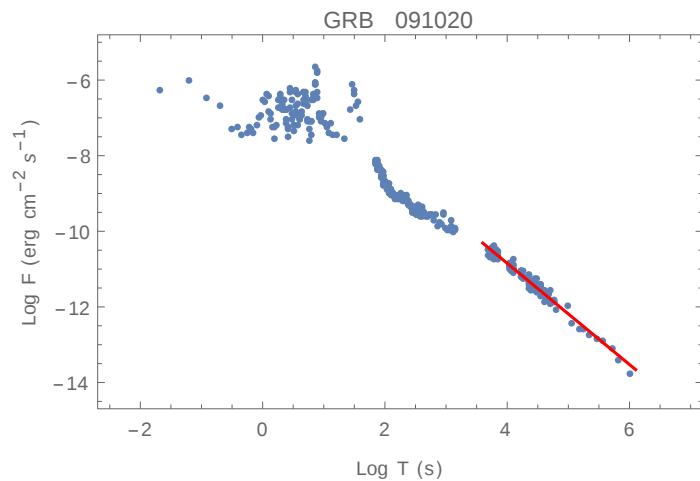


Figure A.2.100: GRB 091020: $\alpha_{X,a} = 1.34$.

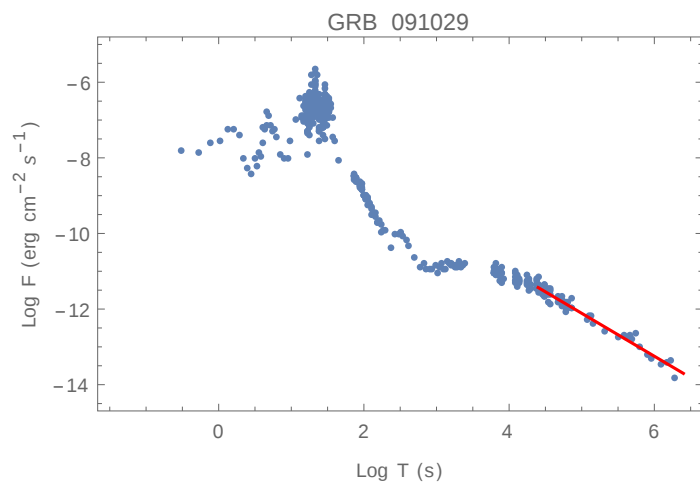


Figure A.2.101: GRB 091029: $\alpha_{X,a} = 1.13$.

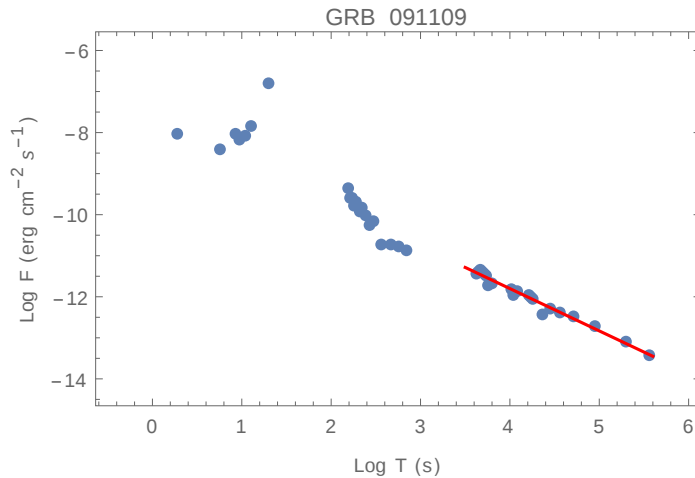


Figure A.2.102: GRB 091109A: $\alpha_{X,a} = 1.03$.

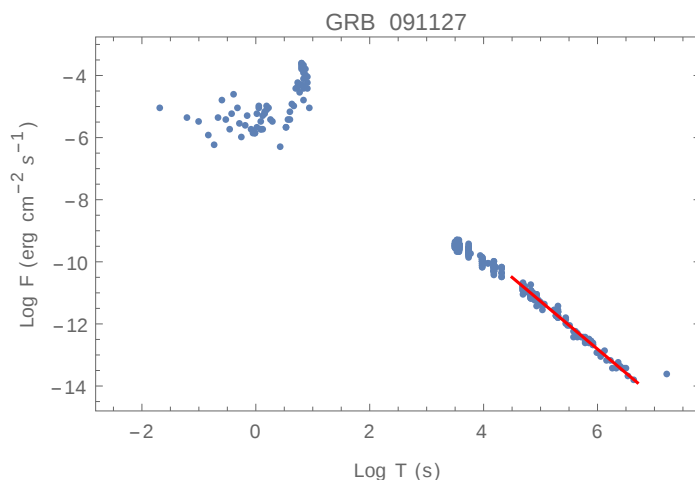


Figure A.2.103: GRB 091127: $\alpha_{X,a} = 1.54$.

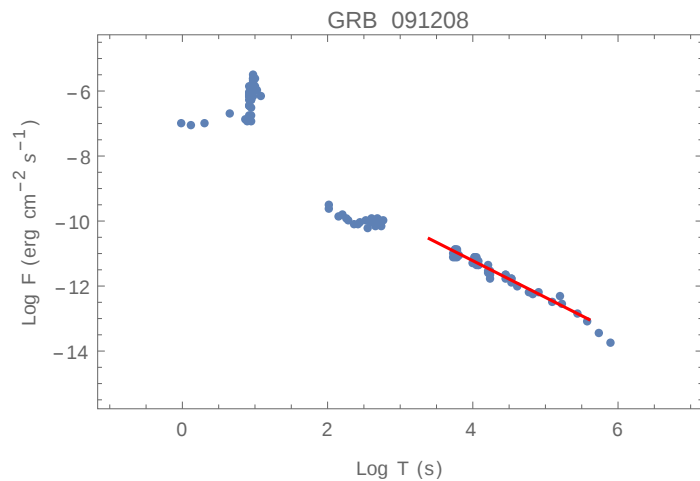


Figure A.2.104: GRB 091208B: $\alpha_{X,a} = 1.13$.

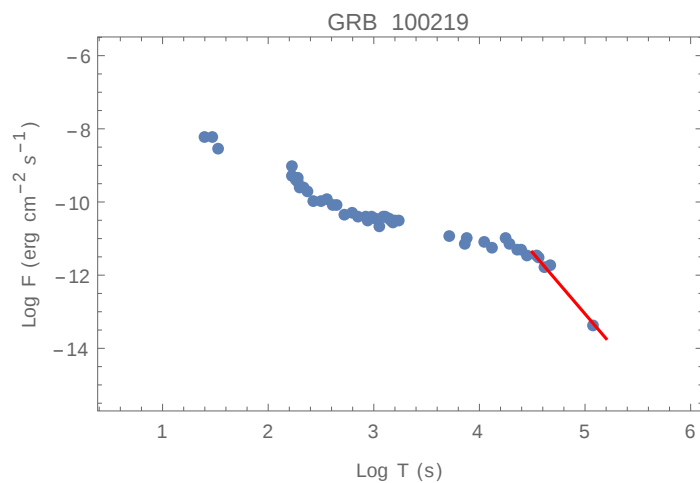


Figure A.2.105: GRB 100219A: $\alpha_{X,a} = 3.38$.

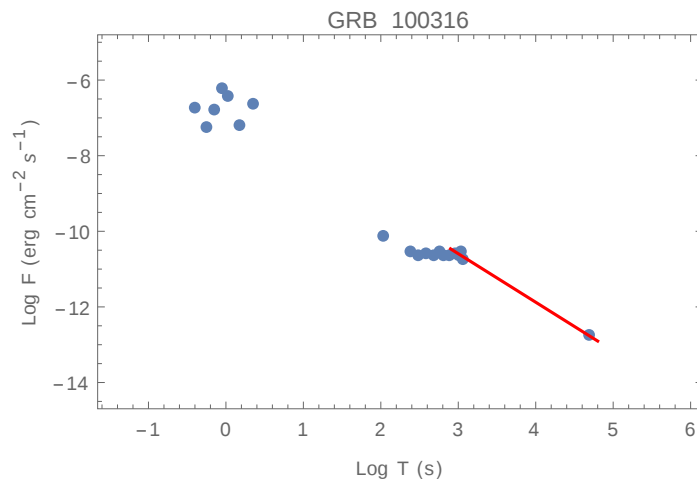


Figure A.2.106: GRB 100316B: $\alpha_{X,a} = 1.28$.

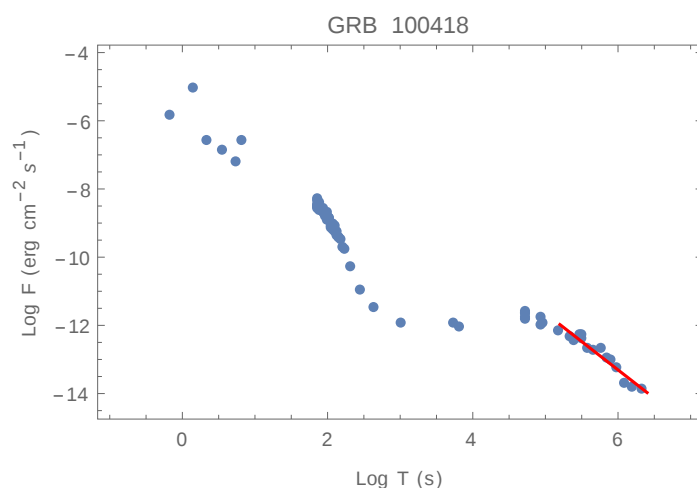


Figure A.2.107: GRB 100418A: $\alpha_{X,a} = 1.66$.

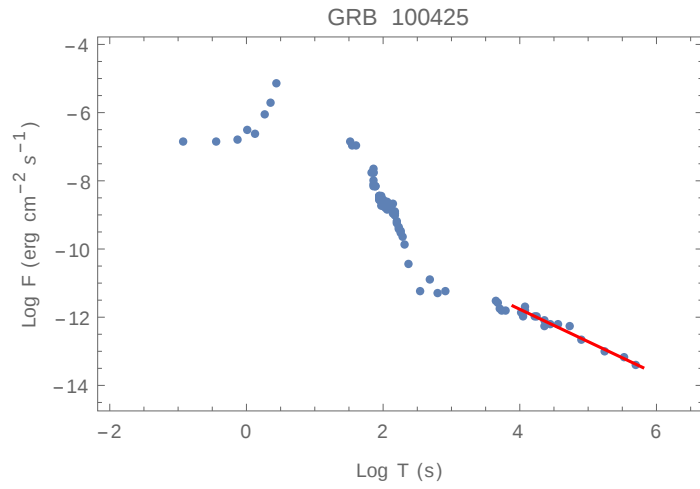


Figure A.2.108: GRB 100425A: $\alpha_{X,a} = 0.95$.

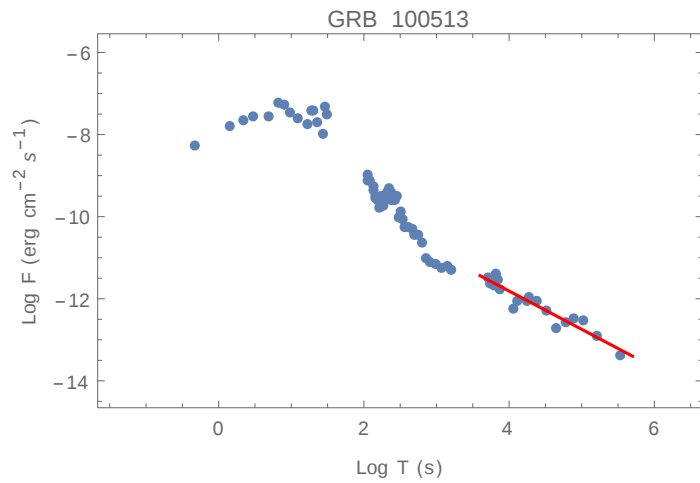


Figure A.2.109: GRB 100513A: $\alpha_{X,a} = 0.93$.

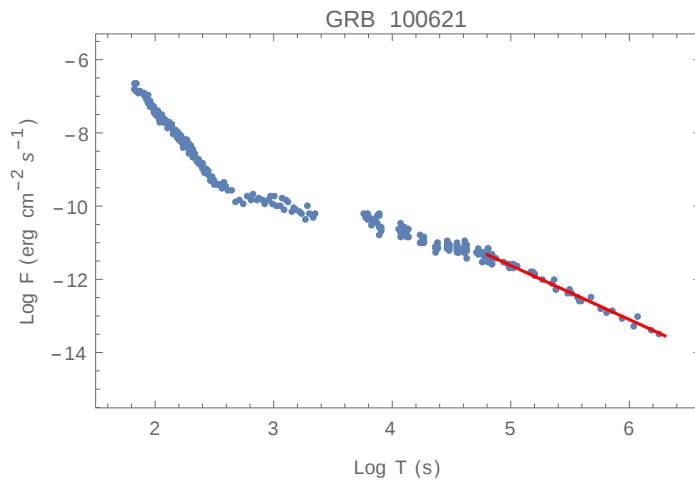


Figure A.2.110: GRB100621A: $\alpha_{X,a} = 1.48$.

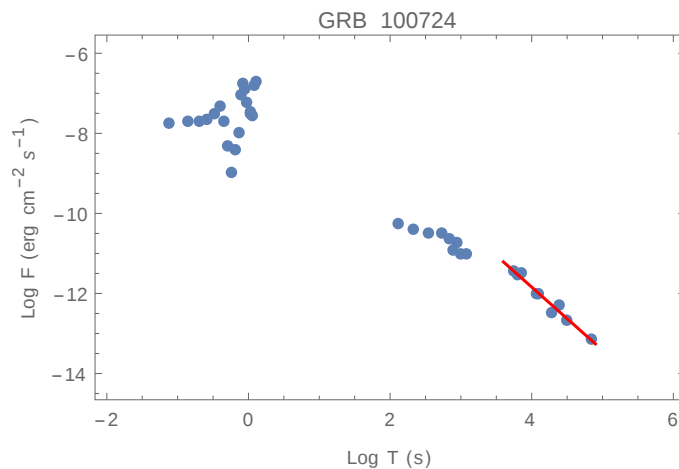


Figure A.2.111: GRB 100724A: $\alpha_{X,a} = 1.57$.

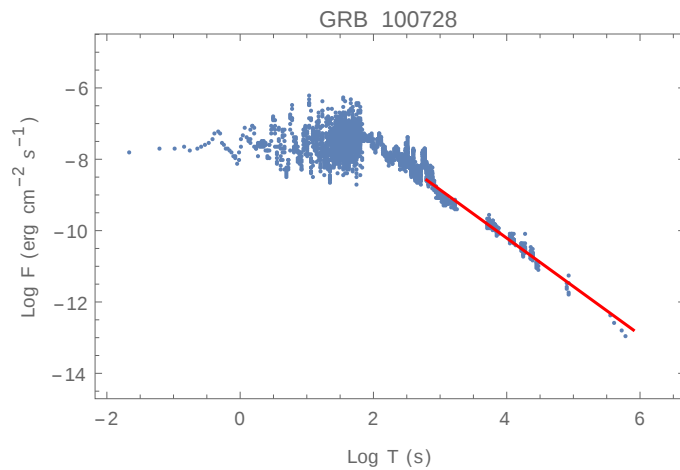


Figure A.2.112: GRB 100728A: $\alpha_{X,a} = 1.35$.

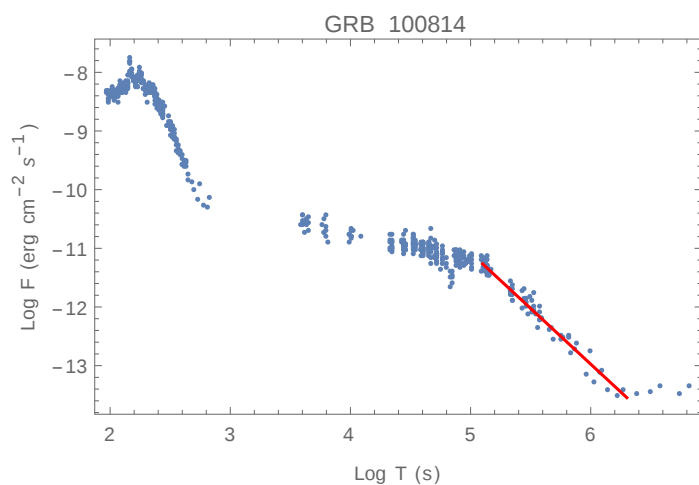


Figure A.2.113: GRB 100814A: $\alpha_{X,a} = 1.90$.

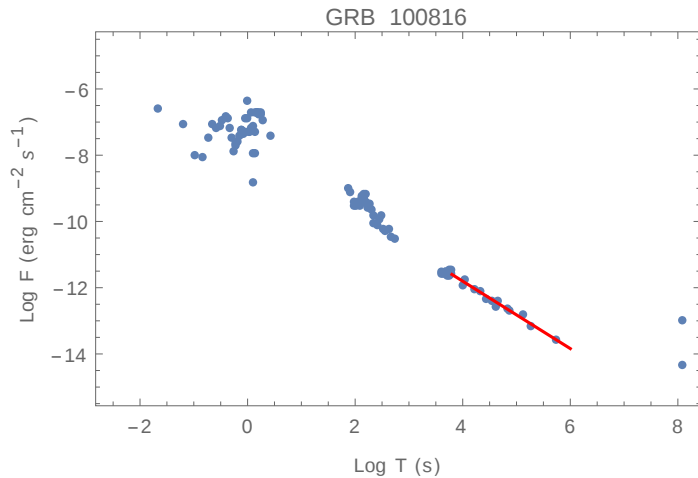


Figure A.2.114: GRB 100816A: $\alpha_{X,a} = 1.02$.

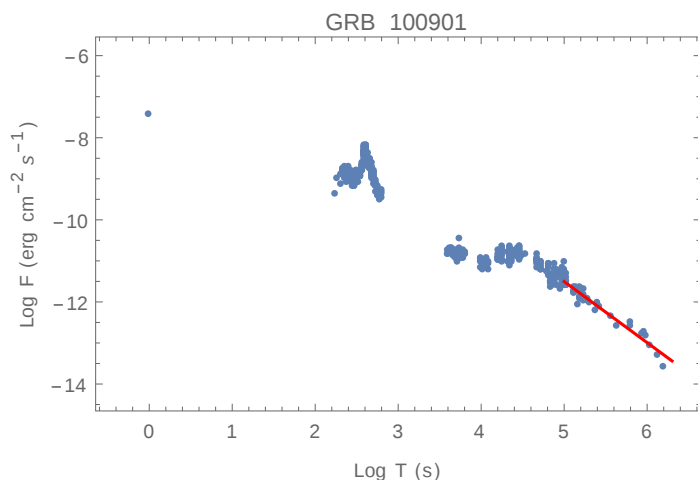


Figure A.2.115: GRB 100901A: $\alpha_{X,a} = 1.49$.

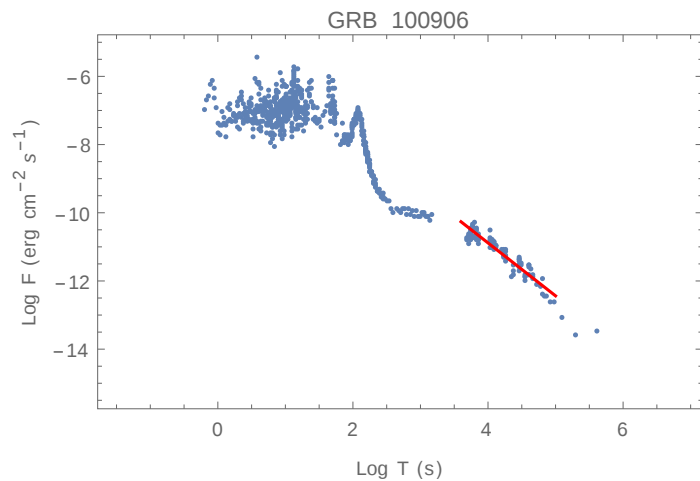


Figure A.2.116: GRB 100906A: $\alpha_{X,a} = 1.55$.

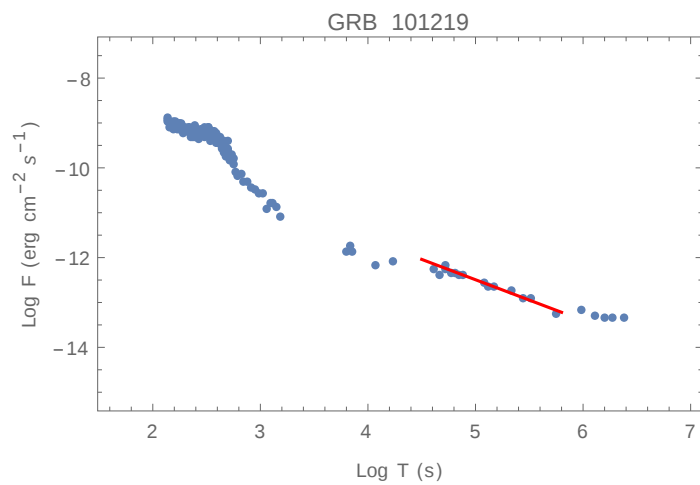


Figure A.2.117: GRB 101219B: $\alpha_{X,a} = 0.90$.

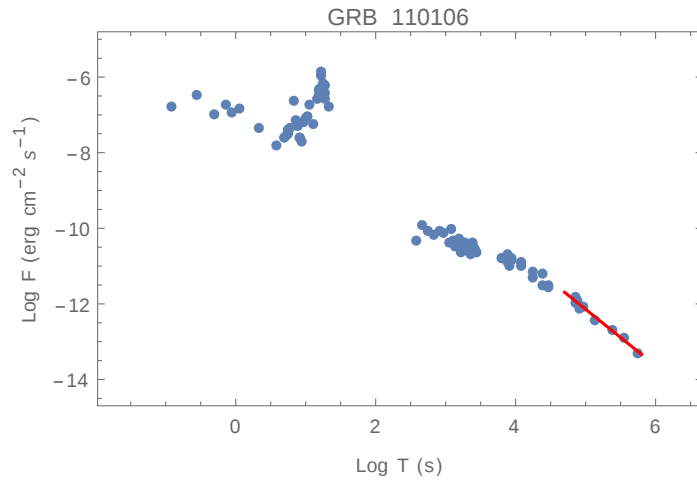


Figure A.2.118: GRB 110106B: $\alpha_{X,a} = 1.49$.

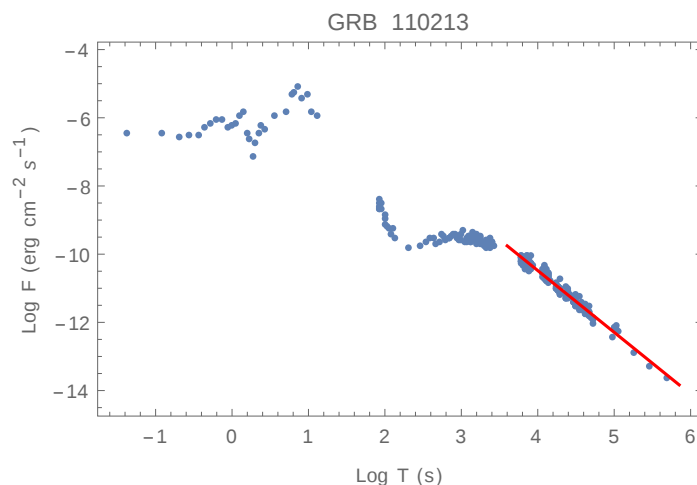


Figure A.2.119: GRB 110213A: $\alpha_{X,a} = 1.81$.

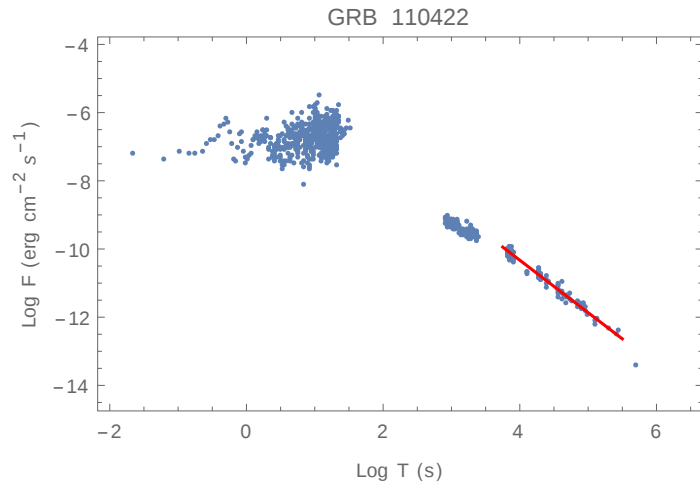


Figure A.2.120: GRB 110422A: $\alpha_{X,a} = 1.54$.

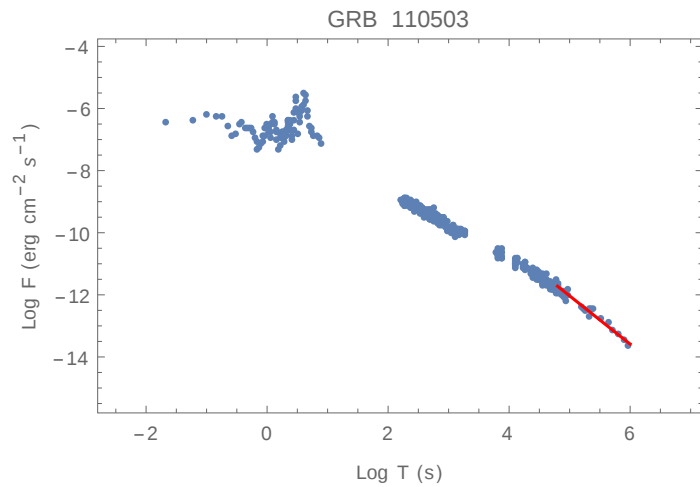


Figure A.2.121: GRB 110503A: $\alpha_{X,a} = 1.55$.

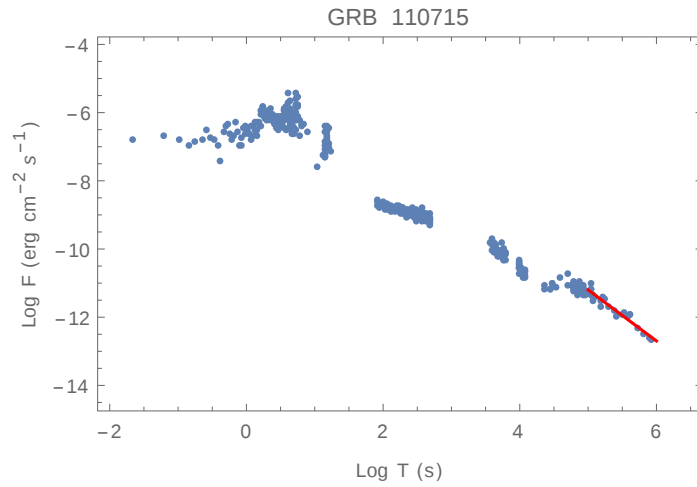


Figure A.2.122: GRB 110715A: $\alpha_{X,a} = 1.50$.

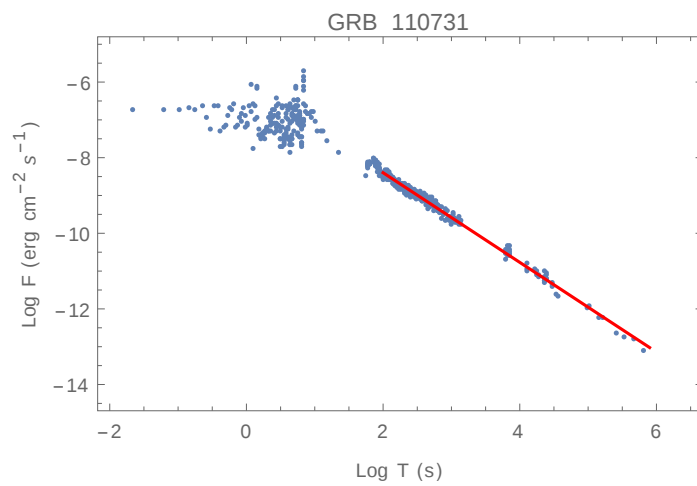


Figure A.2.123: GRB 110731A: $\alpha_{X,a} = 1.18$.

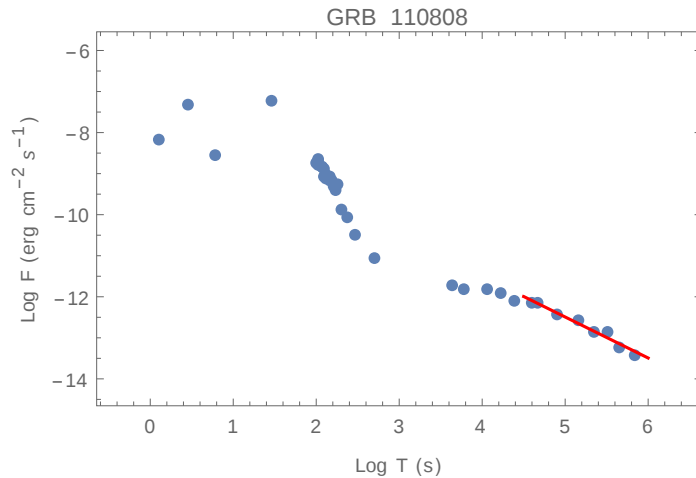


Figure A.2.124: GRB 110808A: $\alpha_{X,a} = 1.00$.

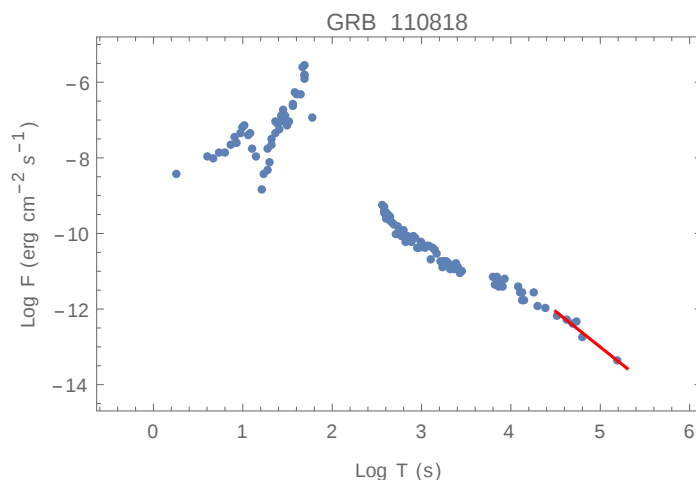


Figure A.2.125: GRB 110818A: $\alpha_{X,a} = 1.88$.

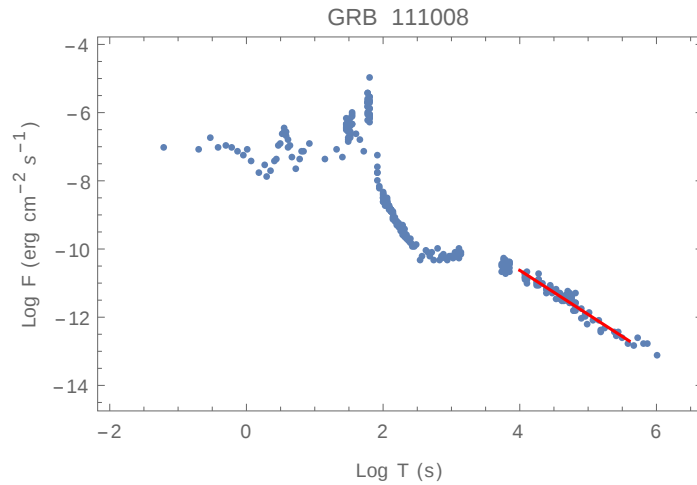


Figure A.2.126: GRB 111008A: $\alpha_{X,a} = 1.29$.

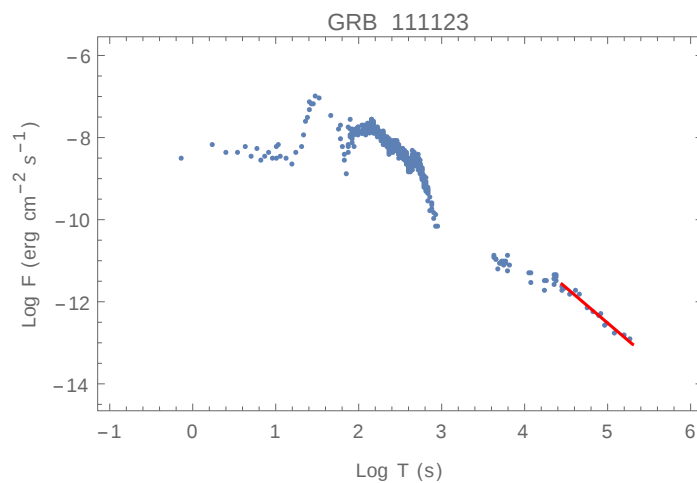


Figure A.2.127: GRB 111123A: $\alpha_{X,a} = 1.72$.

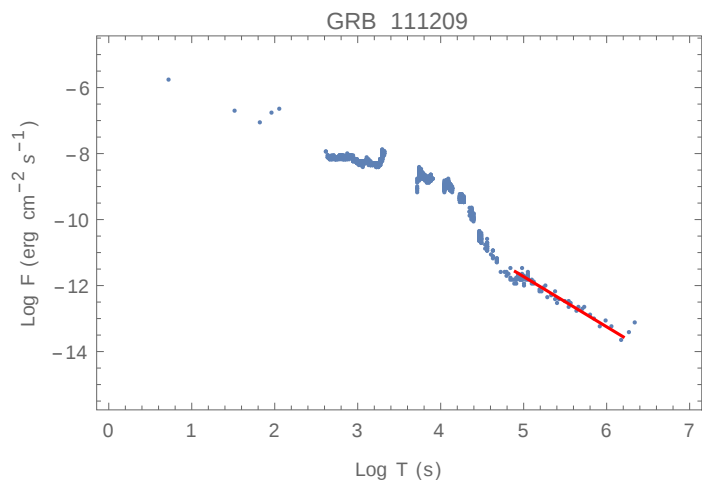


Figure A.2.128: GRB 111209A: $\alpha_{X,a} = 1.52$.

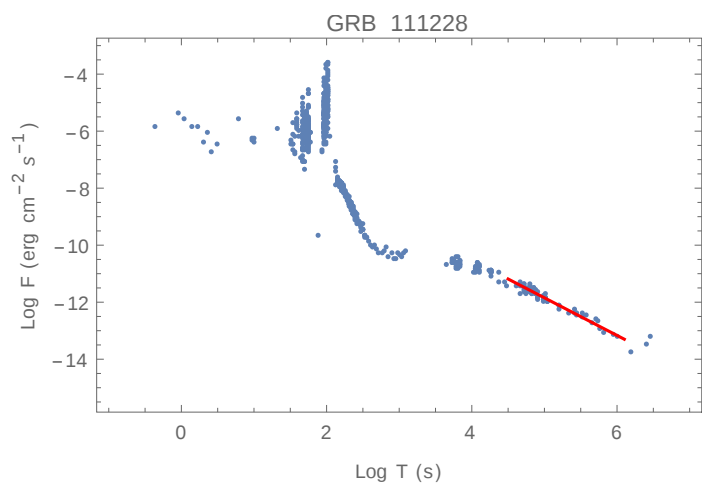


Figure A.2.129: GRB 111228A: $\alpha_{X,a} = 1.32$.

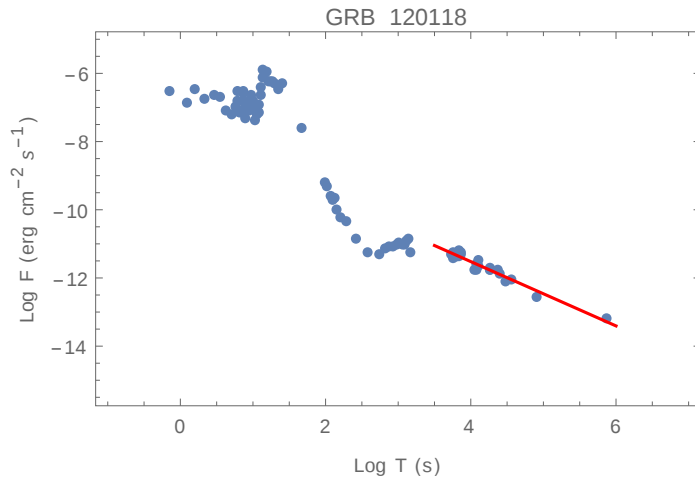


Figure A.2.130: GRB 120118B: $\alpha_{X,a} = 0.94$.

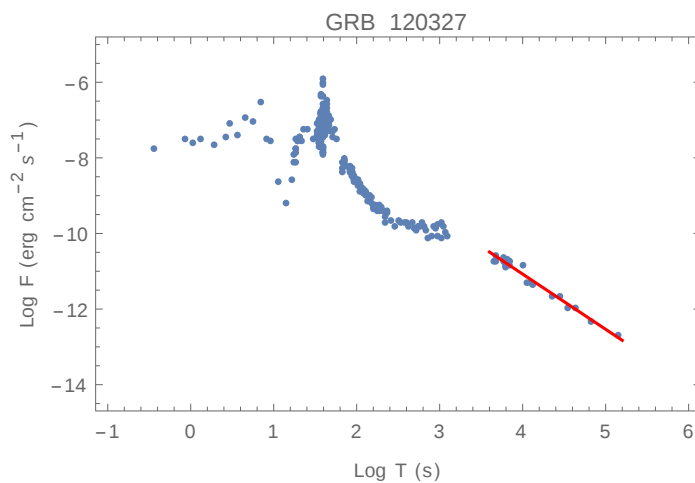


Figure A.2.131: GRB 120327A: $\alpha_{X,a} = 1.46$.

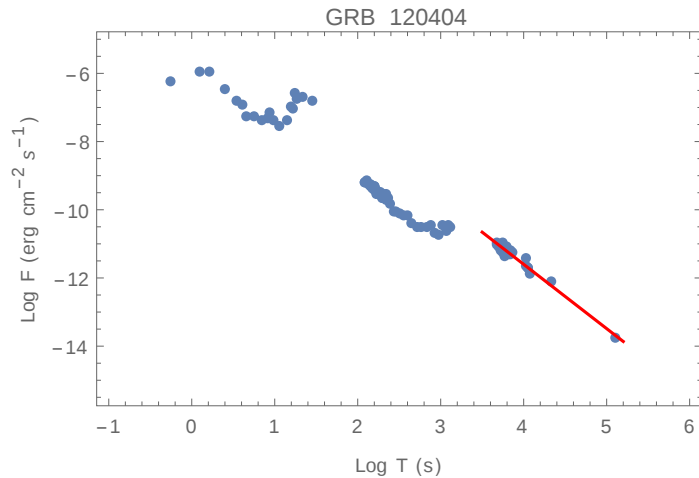


Figure A.2.132: GRB 120404A: $\alpha_{X,a} = 1.88$.

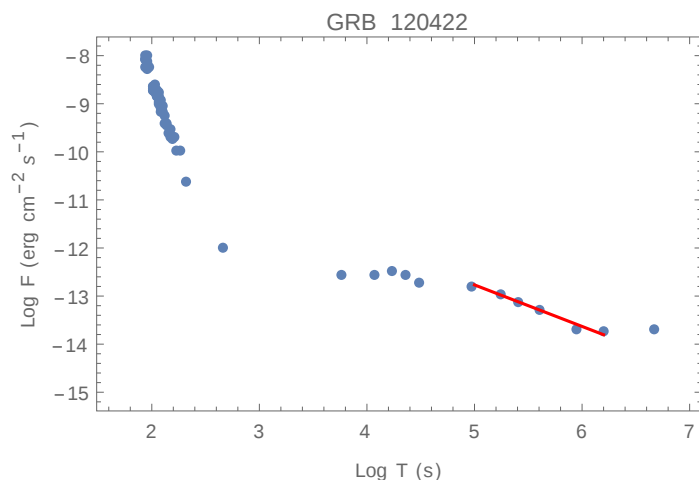


Figure A.2.133: GRB 120422A: $\alpha_{X,a} = 0.86$.

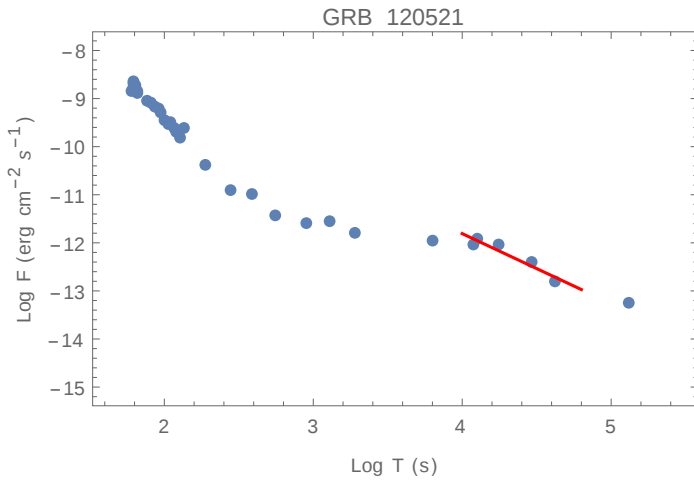


Figure A.2.134: GRB 120521C: $\alpha_{X,a} = 1.45$.

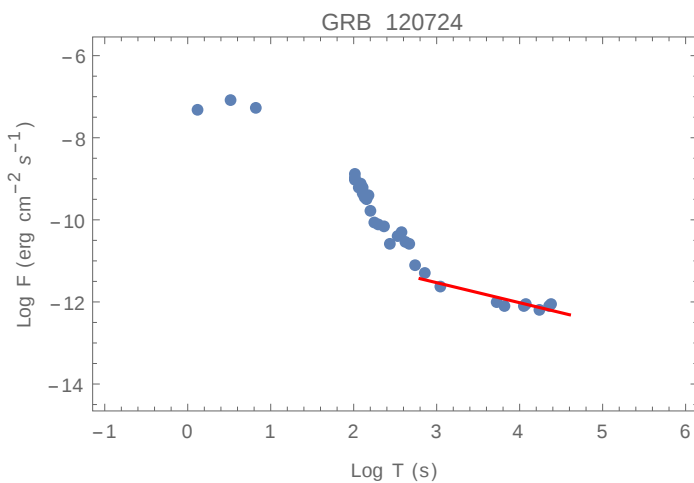


Figure A.2.135: GRB 120724A: $\alpha_{X,a} = 0.49$.

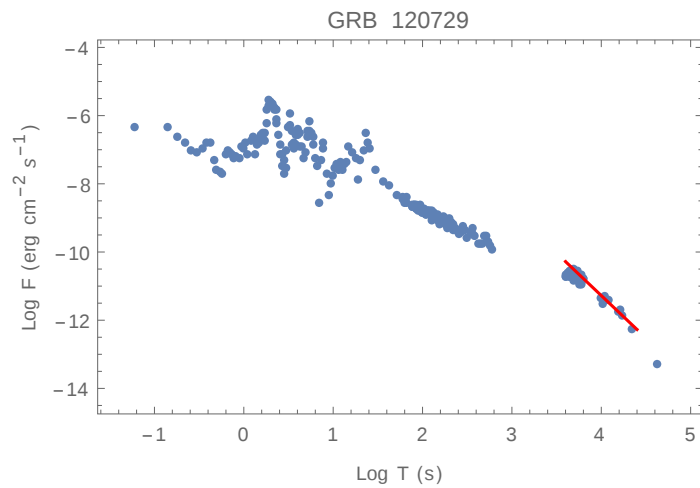


Figure A.2.136: GRB 120729A: $\alpha_{X,a} = 2.49$.

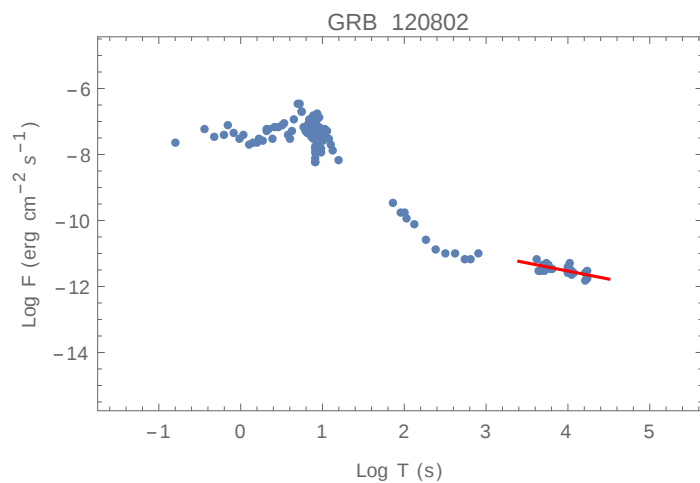


Figure A.2.137: GRB 120802A: $\alpha_{X,a} = 0.49$.

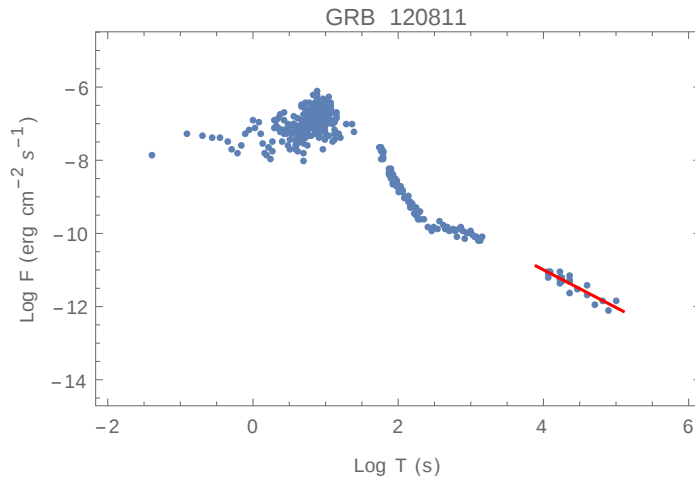


Figure A.2.138: GRB 120811C: $\alpha_{X,a} = 1.03$.

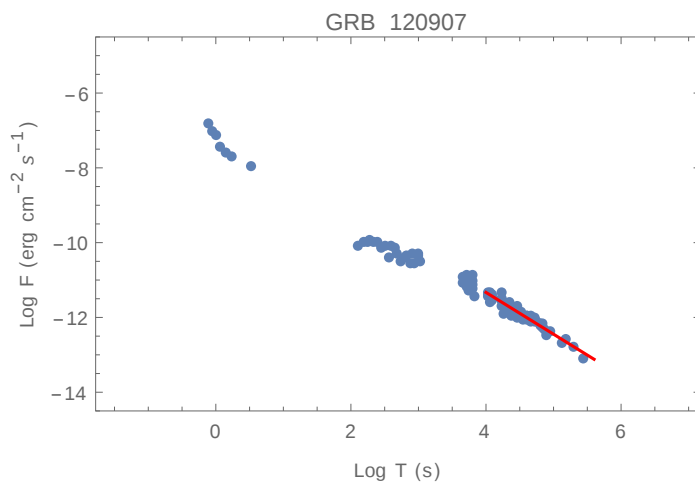


Figure A.2.139: GRB 120907A: $\alpha_{X,a} = 1.12$.

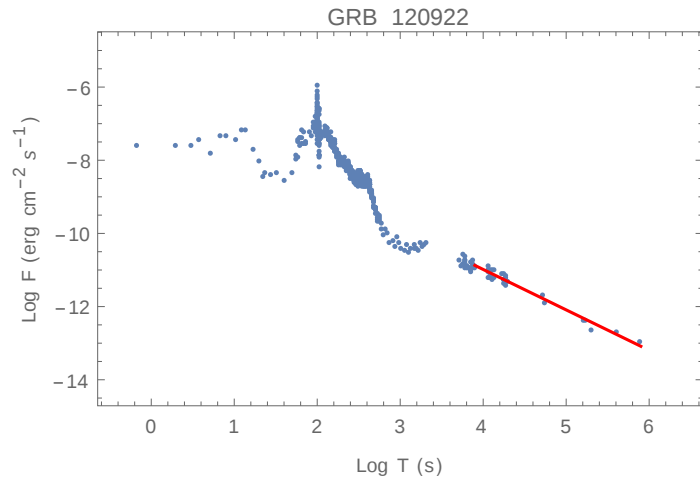


Figure A.2.140: GRB 120922A: $\alpha_{X,a} = 1.10$.

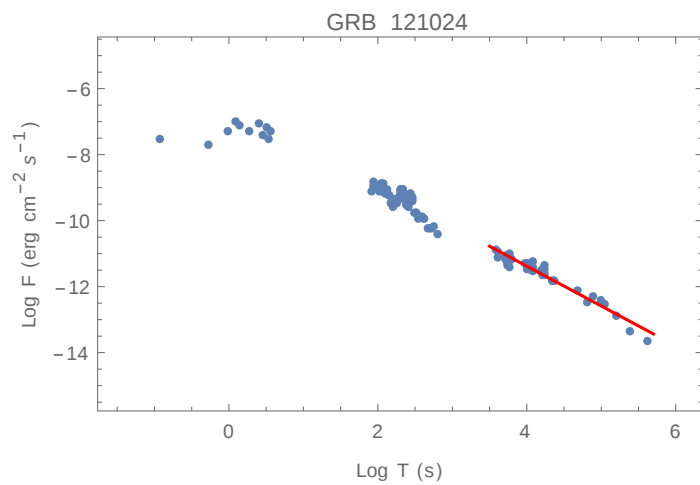


Figure A.2.141: GRB 121024A: $\alpha_{X,a} = 1.21$.

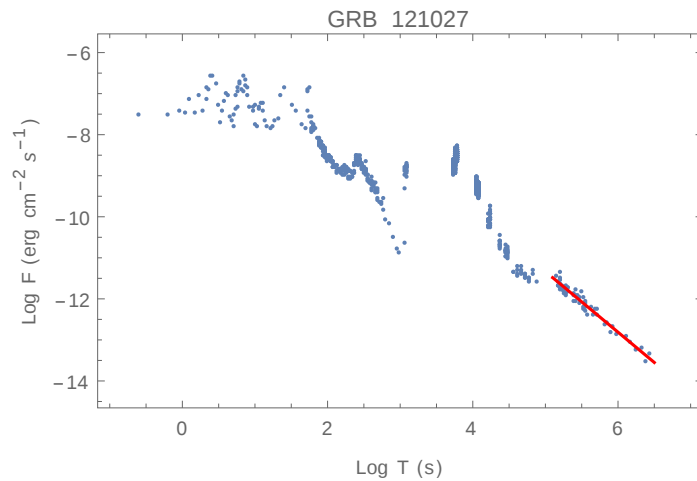


Figure A.2.142: GRB 121027A: $\alpha_{X,a} = 1.48$.

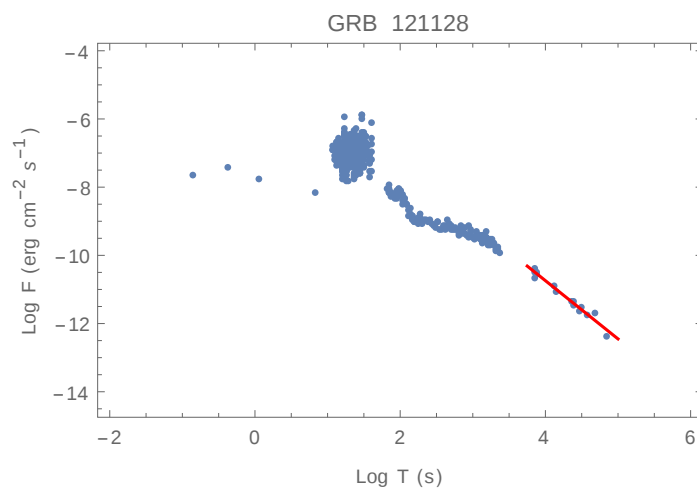


Figure A.2.143: GRB 121128A: $\alpha_{X,a} = 1.71$.

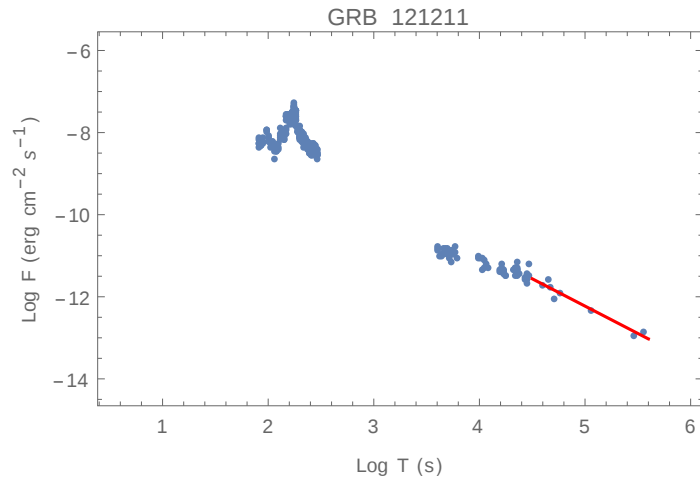


Figure A.2.144: GRB 121211A: $\alpha_{X,a} = 1.33$.

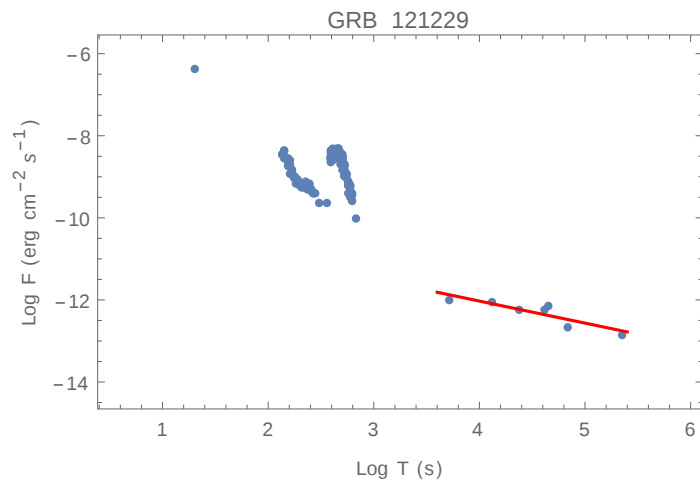


Figure A.2.145: GRB 121229A: $\alpha_{X,a} = 0.54$.

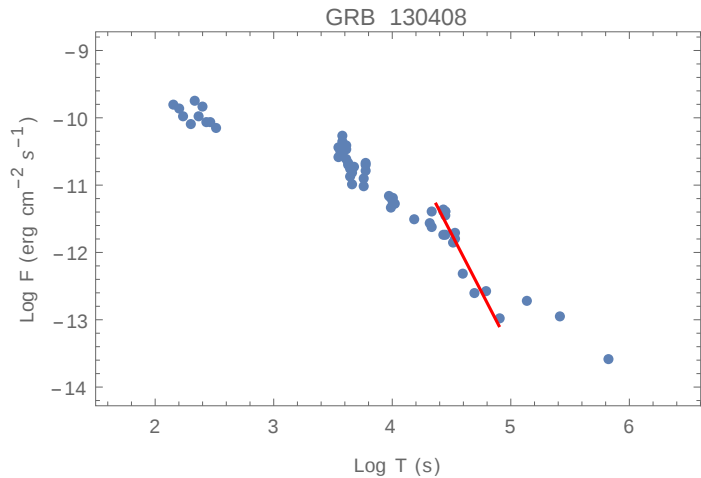


Figure A.2.146: GRB 130408A: $\alpha_{X,a} = 3.41$.

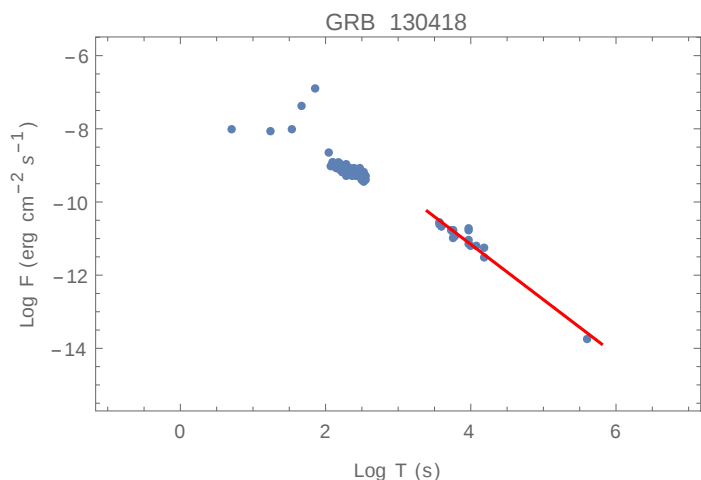


Figure A.2.147: GRB 130418A: $\alpha_{X,a} = 1.51$.

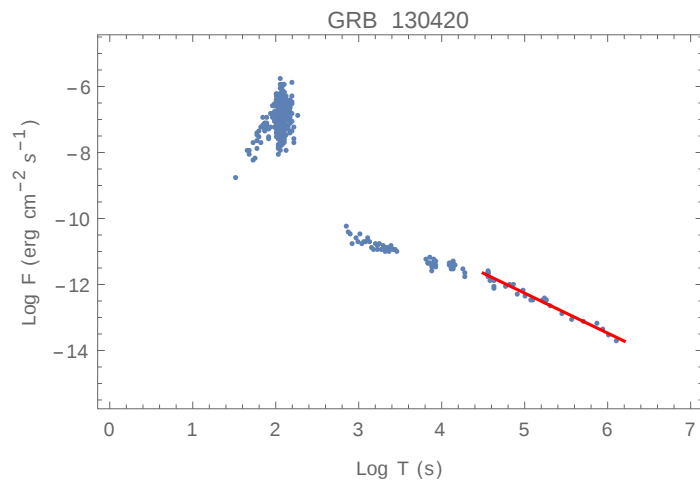


Figure A.2.148: GRB 130420A: $\alpha_{X,a} = 1.21$.

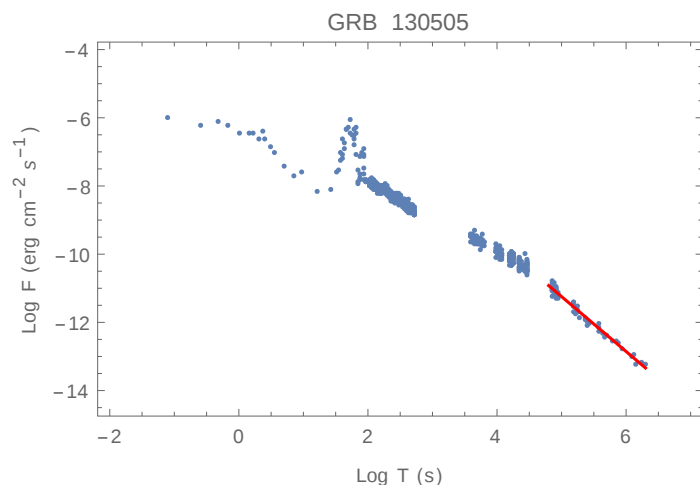


Figure A.2.149: GRB 130505A: $\alpha_{X,a} = 1.61$.

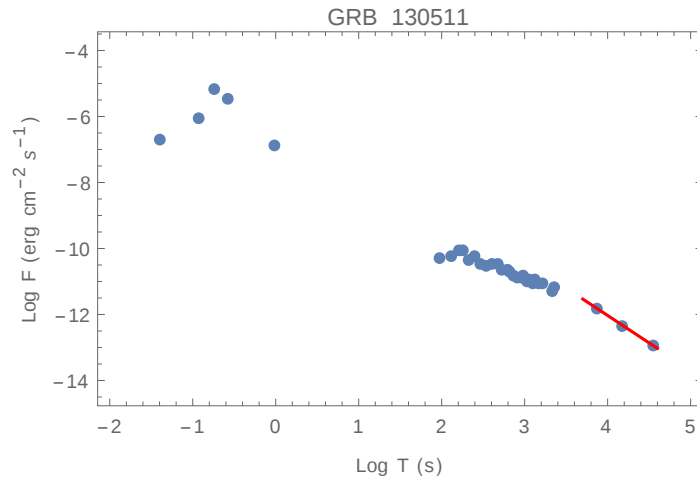


Figure A.2.150: GRB 130511A: $\alpha_{X,a} = 1.66$.

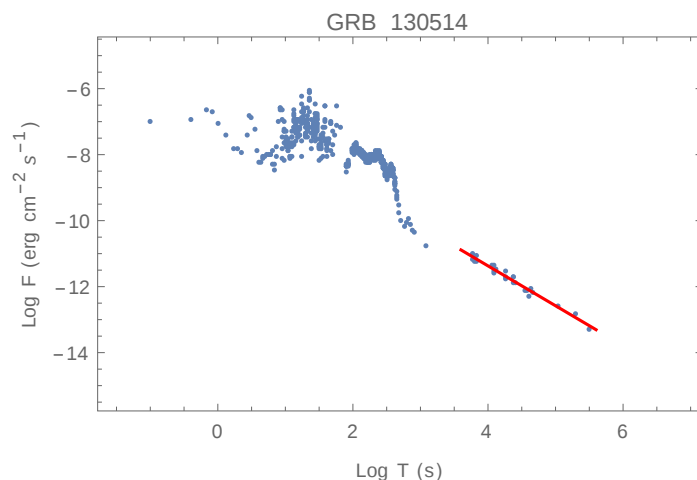


Figure A.2.151: GRB 130514A: $\alpha_{X,a} = 1.21$.

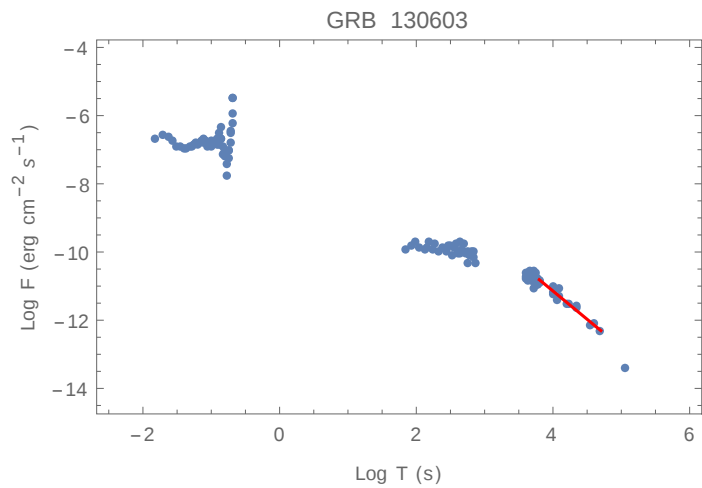


Figure A.2.152: GRB 130603B: $\alpha_{X,a} = 1.66$.

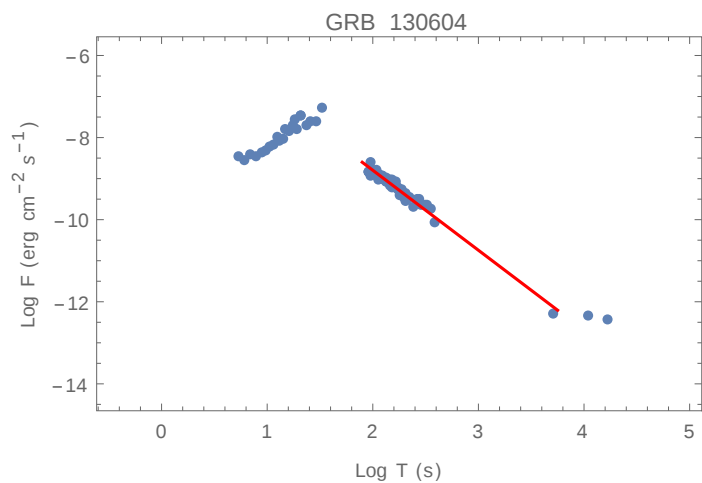


Figure A.2.153: GRB 130604A: $\alpha_{X,a} = 1.95$.

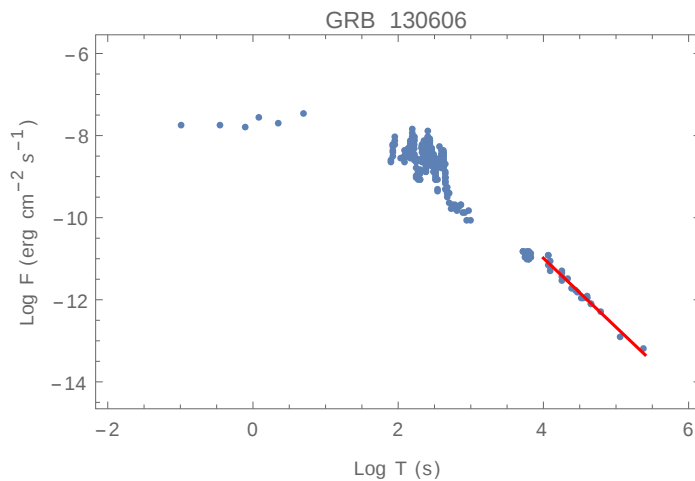


Figure A.2.154: GRB 130606A: $\alpha_{X,a} = 1.68$.

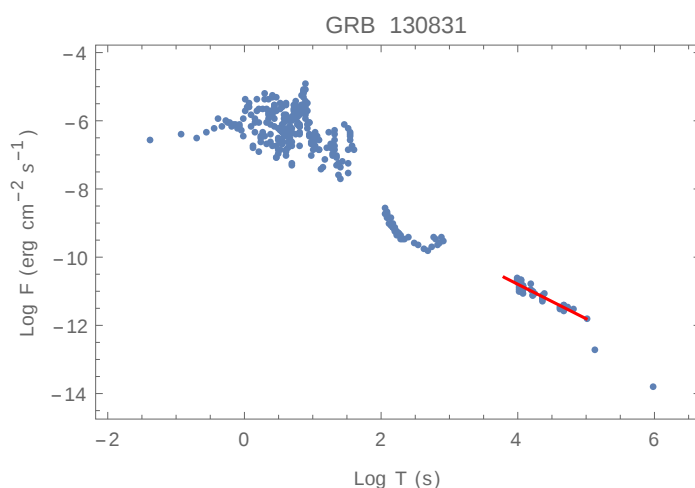


Figure A.2.155: GRB 130831A: $\alpha_{X,a} = 1.01$.

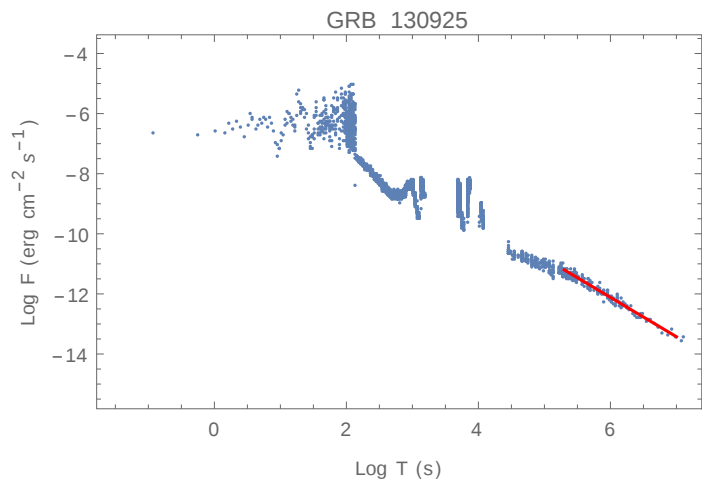


Figure A.2.156: GRB 130925A: $\alpha_{X,a} = 1.31$.

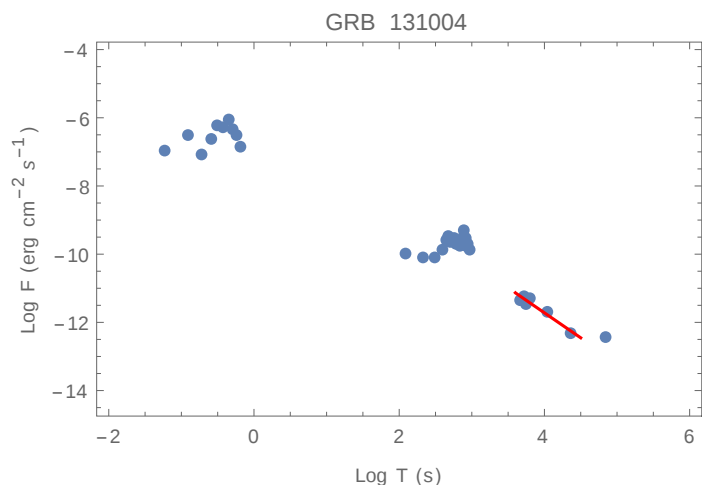


Figure A.2.157: GRB 131004A: $\alpha_{X,a} = 1.46$.

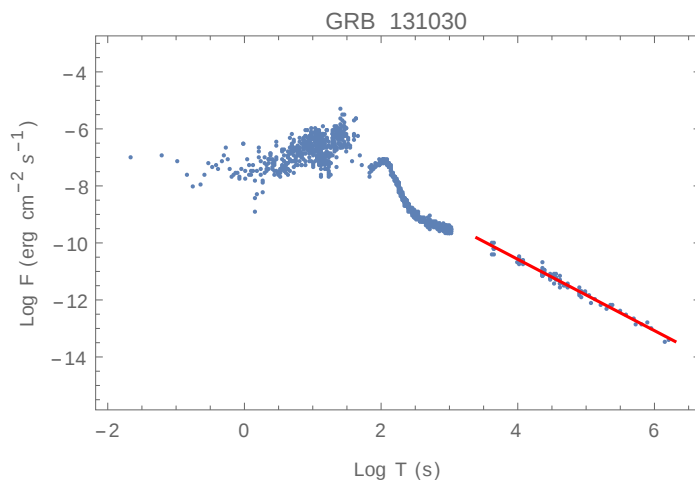


Figure A.2.158: GRB 131030A: $\alpha_{X,a} = 1.25$.

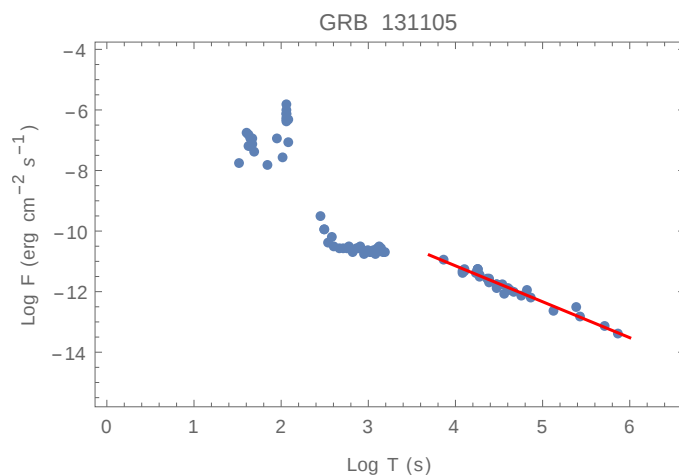


Figure A.2.159: GRB 131105A: $\alpha_{X,a} = 1.19$.

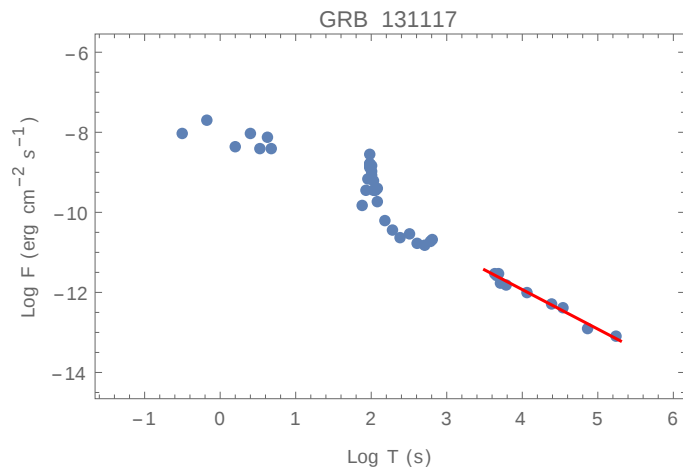


Figure A.2.160: GRB 131117A: $\alpha_{X,a} = 0.98$.

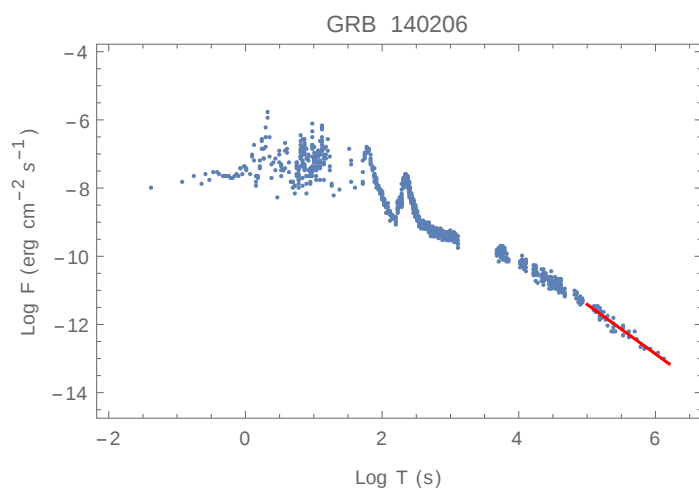


Figure A.2.161: GRB 140206A: $\alpha_{X,a} = 1.45$.

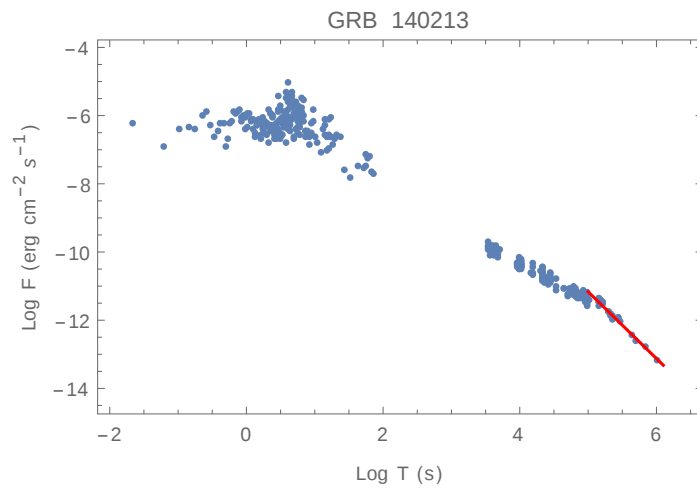


Figure A.2.162: GRB 140213A: $\alpha_{X,a} = 1.96$.

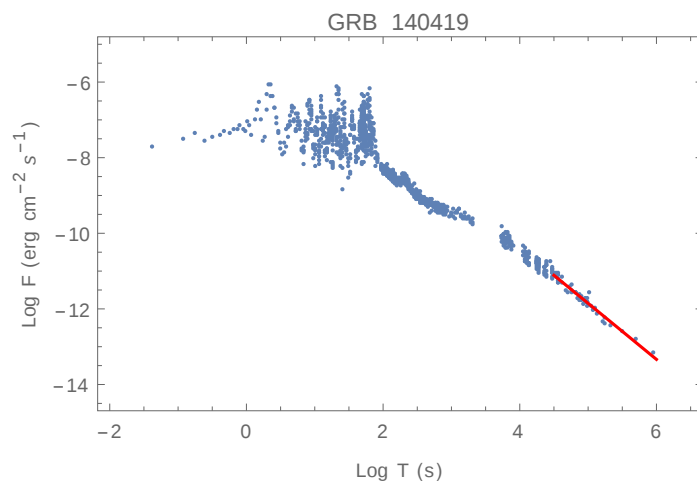


Figure A.2.163: GRB 140419A: $\alpha_{X,a} = 1.48$.

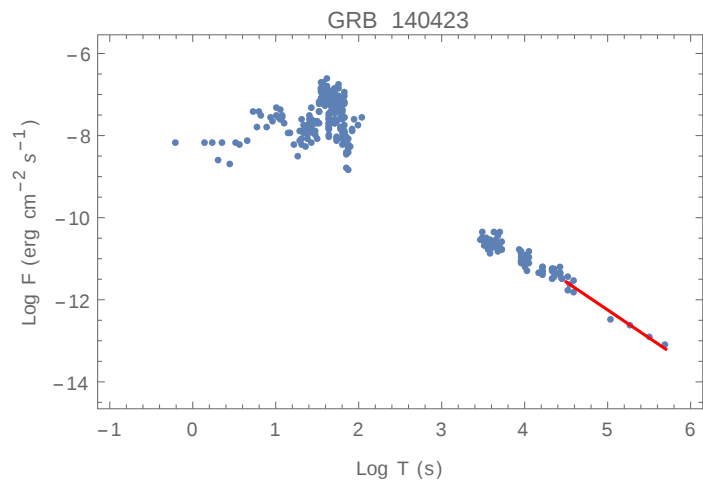


Figure A.2.164: GRB 140423A: $\alpha_{X,a} = 1.36$.

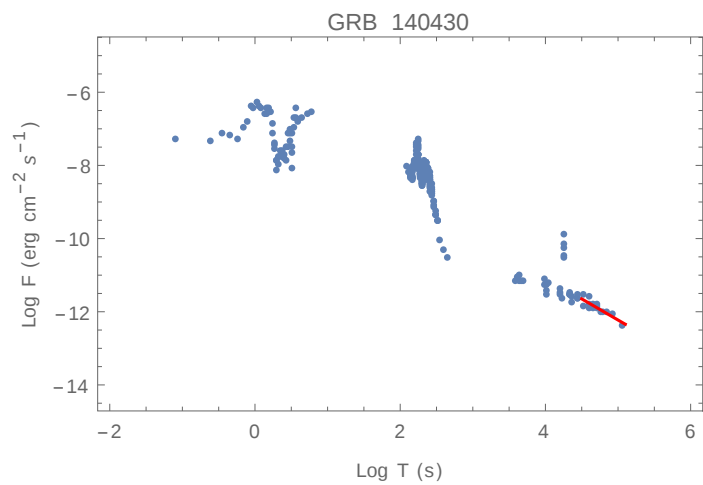


Figure A.2.165: GRB 140430A: $\alpha_{X,a} = 1.15$.

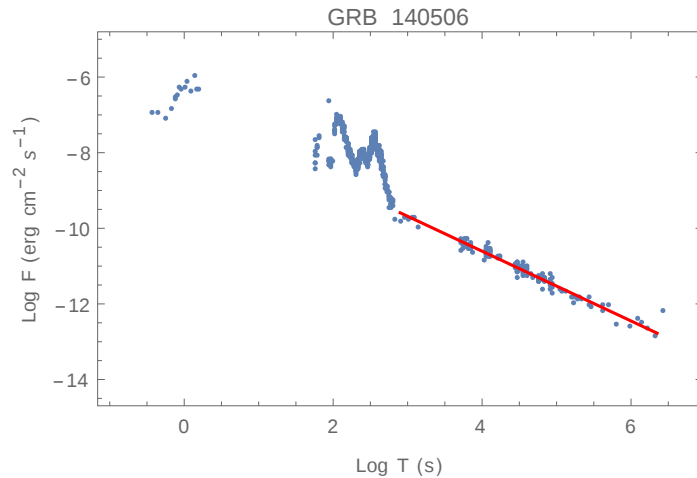


Figure A.2.166: GRB 140506A: $\alpha_{X,a} = 0.92$.

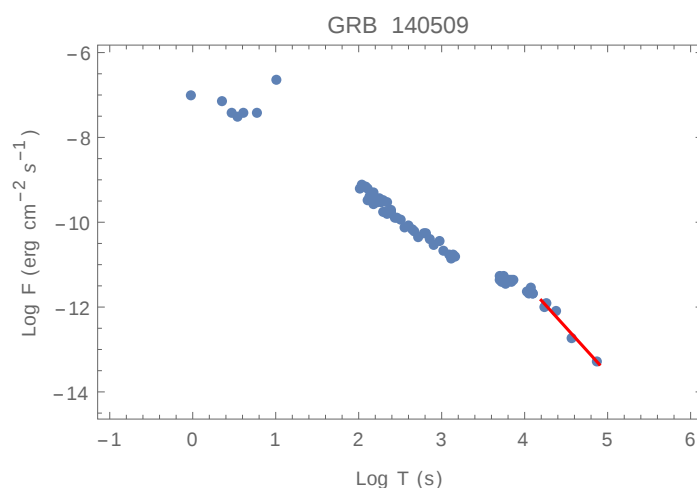


Figure A.2.167: GRB 140509A: $\alpha_{X,a} = 2.16$.

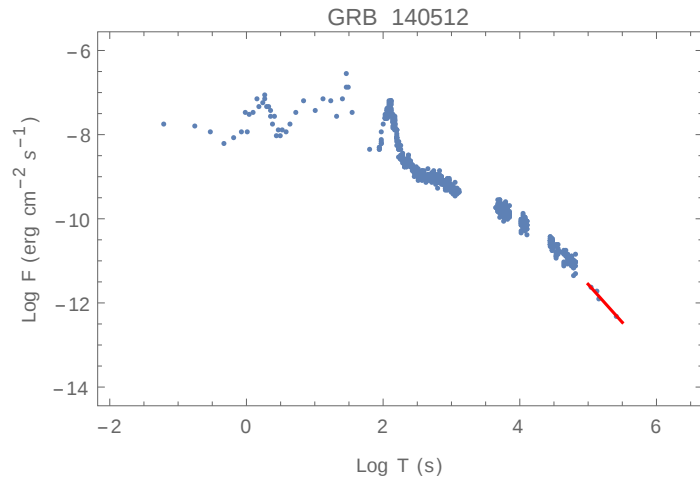


Figure A.2.168: GRB 140512A: $\alpha_{X,a} = 1.81$.

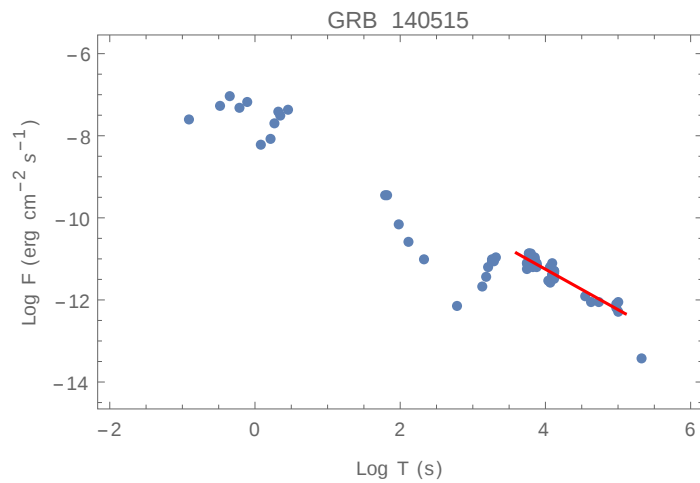


Figure A.2.169: GRB 140515A: $\alpha_{X,a} = 0.98$.

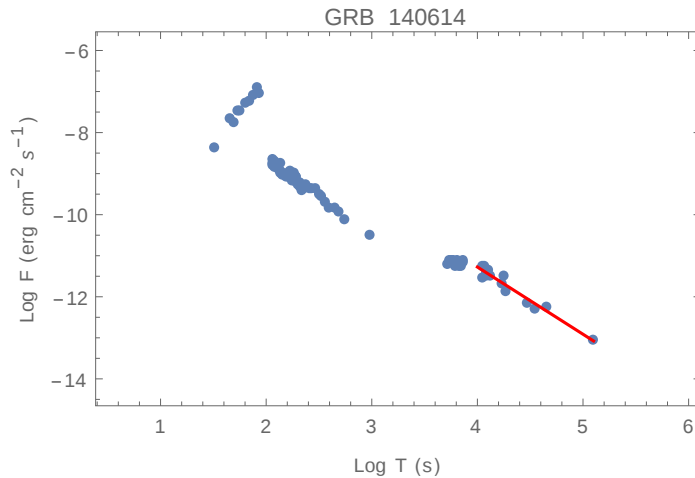


Figure A.2.170: GRB 140614A: $\alpha_{X,a} = 1.64$.

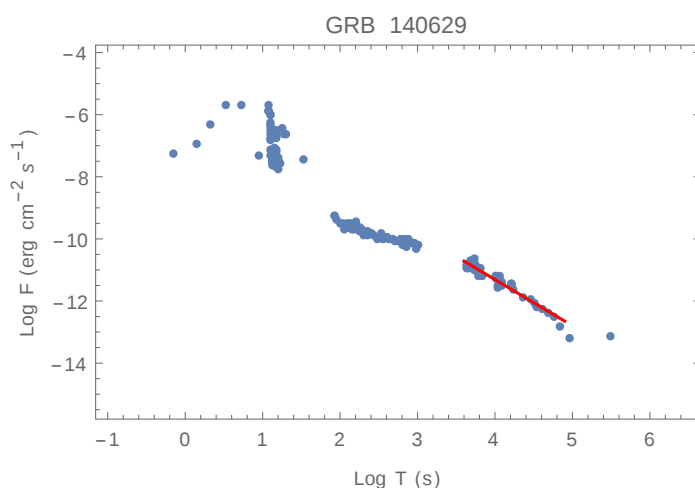


Figure A.2.171: GRB 140629A: $\alpha_{X,a} = 1.49$.

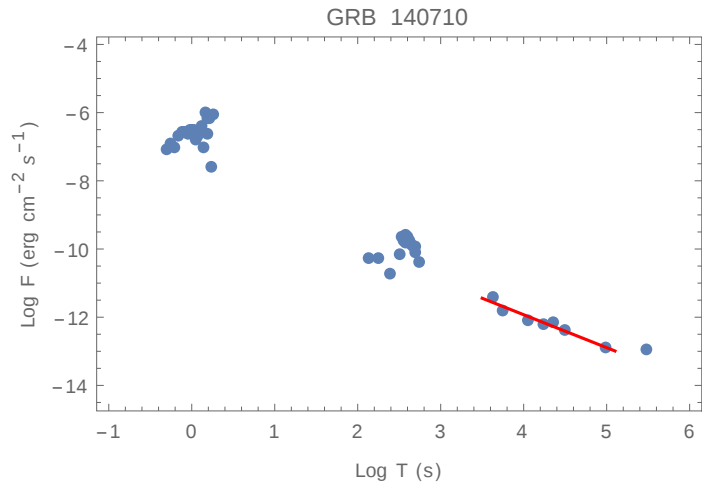


Figure A.2.172: GRB 140710A: $\alpha_{X,a} = 0.97$.

The Swift mission

The data used in the work presented here were collected from the Swift catalogue¹. The Swift spacecraft (see Fig. B.1.1) is a space mission dedicated to GRB observations. It was launched at the end of 2004 and planned to work for only two years. Nevertheless, due to the outstanding results obtained from the mission, it was prolonged and it is still running.

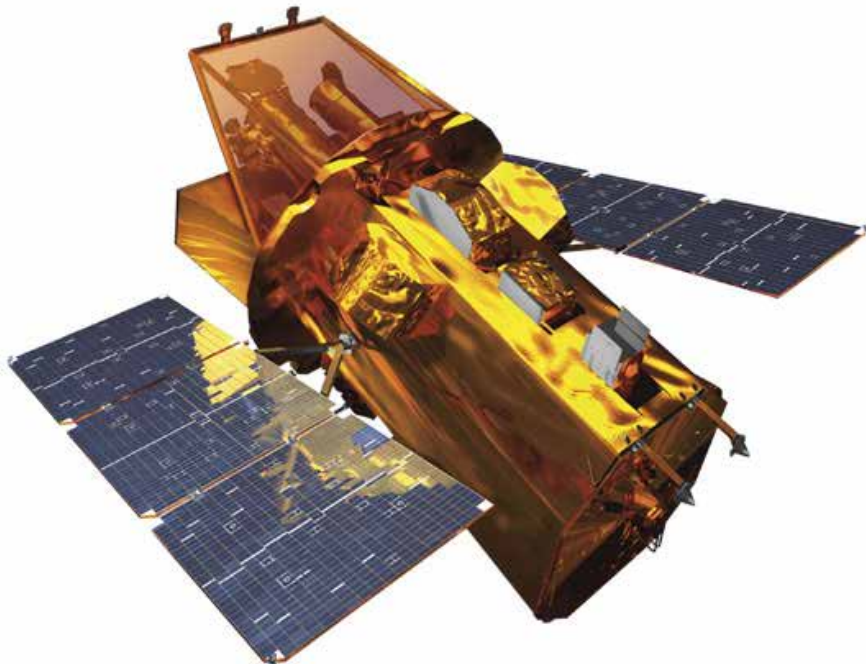


Figure B.1.1: A drawing of the Swift satellite from <http://swift.sonoma.edu/resources/multimedia/images/>.

The Swift observatory is composed of three instruments:

- The Burst Alert Telescope (BAT): a hard X-ray detector working in the energy range 15–100 keV with a wide field of view (Fig. B.1.2, technical specifications in Table B.1).

¹http://www.swift.ac.uk/burst_analyser/

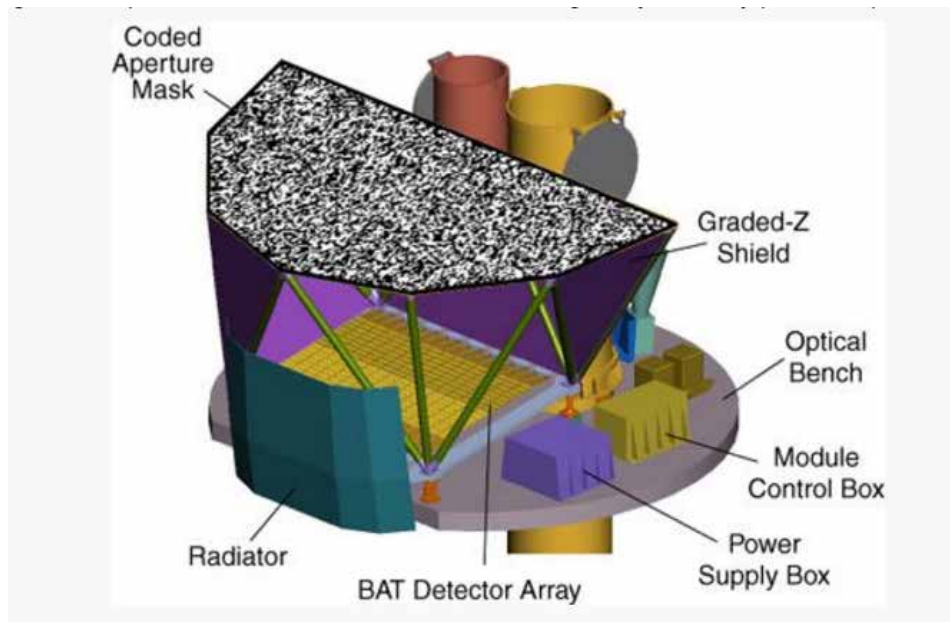


Figure B.1.2: Plot displaying the BAT instrument from the Swift website (https://swift.gsfc.nasa.gov/about_swift/bat_desc.html).

- The X-ray Telescope (XRT): a CCD spectrometer running in the energy range 0.3–10 keV (Fig. B.1.3, technical specifications in Table B.2).
- The Ultraviolet/Optical Telescope (UVOT): a CCD optical detector operating in the range 170–650 nanometers (Fig. B.1.4, technical specifications in Table B.3).

XRT has two operating modes. The first one is the Windowed Timing mode (WT), used for one-dimensional imaging with 1.7 millisecond time resolution and full energy resolution (the full width at half maximum (FWHM) was 145 eV measured at 5.895 keV at the moment of the launch). The second one is the Photon Counting mode (PC), used for two-dimensional imaging with 2.5 second time resolution and full energy resolution. Data from the Swift satellite are used in the study presented here especially for the availability of and precision in redshift measurements of this space mission. In Tables B.1, B.2 and B.3 the technical specifications of the instruments on board of the Swift satellite are presented.

In addition, for the redshift measurements the Swift satellite uses the grism on the UVOT instrument to compute the shift of the Lyman-alpha line². The accuracy of the measured redshift is around 0.1, even at redshift higher than 2. Finally, from the Swift Burst Analyser³ it is possible to obtain the GRB light curves with different time binning modes: constant time bin modes (64 ms, 1 s, and 10 s) and time bin modes defined by a certain value of

²https://swift.gsfc.nasa.gov/about_swift/redshift.html.

³http://www.swift.ac.uk/burst_analyser

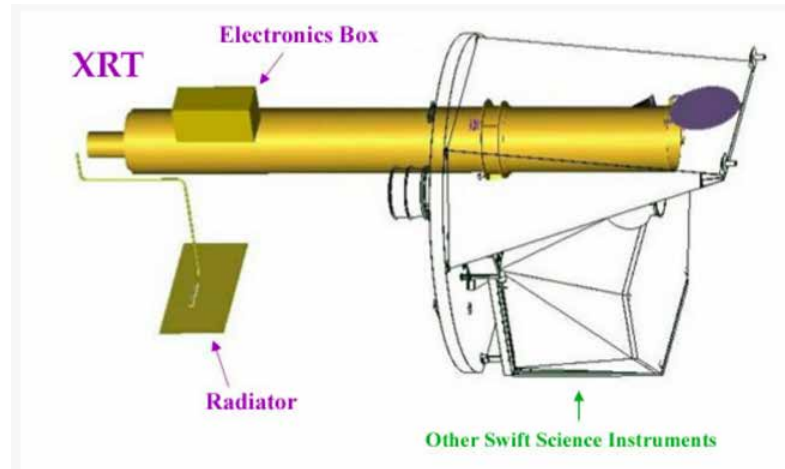


Figure B.1.3: Plot displaying the XRT instrument from the Swift website (https://swift.gsfc.nasa.gov/about_swift/xrt_desc.html).

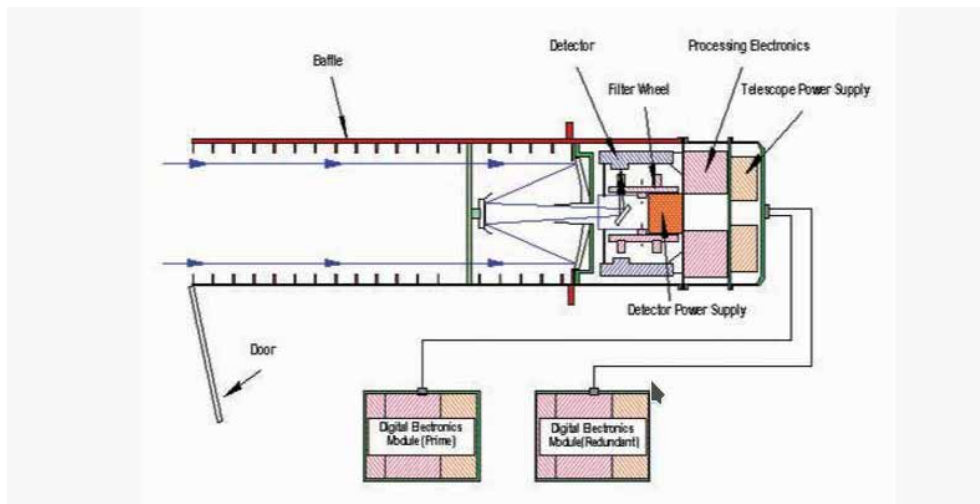


Figure B.1.4: Plot displaying the UVOT instrument from the Swift website (https://swift.gsfc.nasa.gov/about_swift/uvot_desc.html).

BAT instrument parameters	
Property	Description
Aperture	Coded mask
Detecting area	5200 cm ²
Detector	CdZnTe
Detector operation	Photon counting
Field of view	1.4 sr (partially coded)
Detection elements	256 modules of 128 elements
Detector size	4 mm × 4 mm × 2 mm
Telescope PSF	17 arcmin
Energy range	15-150 keV

Table B.1: Technical specifications of the BAT instrument on board of Swift satellite from the Swift website (https://swift.gsfc.nasa.gov/about_swift/bat_desc.html).

XRT instrument parameters	
Property	Description
Telescope	JET-X Wolter I
Focal length	3.5 m
Effective area	110 cm ² @ 1.5 keV
Telescope PSF	18 arcsec HPD @ 1.5 keV
Detector	EEV CCD-22, 600×600 pixels
Detector operation	Imaging, timing and photon counting
Detector element	40×40 micron pixels
Pixel scale	2.36 micron/pixel
Energy range	0.2-10 keV
Sensitivity	4×10^{-14} erg cm ² s ⁻¹ in 10^4 s for known sources 1×10^{-13} erg cm ² s ⁻¹ in 10^4 s for blind searches

Table B.2: Technical specifications of the XRT instrument on board of Swift satellite from the Swift website (https://swift.gsfc.nasa.gov/about_swift/xrt_desc.html).

UVOT instrument parameters	
Property	Description
Telescope	Modified Ritchey-Chrétien
Focal ratio	12.7
Detector	Intensified CCD
Detector operation	Photon counting
Field of view	17×17 arcmin
Detection element	2048×2048 pixels
Telescope PSF	2.5 arcsec @ 350 nm
Wavelength range	170-650 nm
Filters	7
Sensitivity	B=22.3 in white light in 1000 s
Pixel scale	0.502 arcsec
Brightness limit	V=7.4 mag
Camera speed	11 ms

Table B.3: Technical specifications of the UVOT instrument on board of Swift satellite from the Swift website (https://swift.gsfc.nasa.gov/about_swift/uvot_desc.html).

the signal to noise ratio (SNR 4, SNR 5, SNR 6, SNR 7)⁴. In the work presented here, the default time binning mode for the light curves is SNR5.

⁴http://www.swift.ac.uk/burst_analyser/docs.php

APPENDIX C

Published papers used in this work

Review Article

Gamma-Ray Burst Prompt Correlations

M. G. Dainotti^{1,2,3}, R. Del Vecchio,³ and M. Tarnopolski³

¹*Physics Department, Stanford University, Via Pueblo Mall 382, Stanford, CA, USA*

²*INAF, Istituto di Astrofisica Spaziale e Fisica Cosmica, Via Gobetti 101, 40129 Bologna, Italy*

³*Astronomical Observatory, Jagiellonian University, Orla 171, 30-244 Kraków, Poland*

Correspondence should be addressed to M. G. Dainotti; mdainott@stanford.edu

Received 25 May 2016; Accepted 27 November 2016; Published 24 January 2018

Academic Editor: Alberto J. Castro-Tirado

Copyright © 2018 M. G. Dainotti et al. This is an open access article distributed under the Creative Commons Attribution License, which permits unrestricted use, distribution, and reproduction in any medium, provided the original work is properly cited.

The mechanism responsible for the prompt emission of gamma-ray bursts (GRBs) is still a debated issue. The prompt phase-related GRB correlations can allow discriminating among the most plausible theoretical models explaining this emission. We present an overview of the observational two-parameter correlations, their physical interpretations, and their use as redshift estimators and possibly as cosmological tools. The nowadays challenge is to make GRBs, the farthest stellar-scaled objects observed (up to redshift $z = 9.4$), standard candles through well established and robust correlations. However, GRBs spanning several orders of magnitude in their energetics are far from being standard candles. We describe the advances in the prompt correlation research in the past decades, with particular focus paid to the discoveries in the last 20 years.

1. Introduction

Gamma-ray bursts (GRBs) are highly energetic events with the total isotropic energy released of the order of 10^{48} – 10^{55} erg (for recent reviews, see [1–6]). GRBs were discovered by military satellites *Vela* in late 1960s and were recognized early to be of extrasolar origin [7]. A bimodal structure (reported first by Mazets et al. [8]) in the duration distribution of GRBs detected by the Burst and Transient Source Experiment (BATSE) onboard the *Compton Gamma-Ray Observatory* (CGRO) [9], based on which GRBs are nowadays commonly classified into short (with durations $T_{90} < 2$ s, SGRBs) and long (with $T_{90} > 2$ s, LGRBs), was found [10]. BATSE observations allowed also confirming the hypothesis of Klebesadel et al. [7] that GRBs are of extragalactic origin due to isotropic angular distribution in the sky combined with the fact that they exhibited an intensity distribution that deviated strongly from the $-3/2$ power law [9, 11–14]. This was later corroborated by establishing the first redshift measurement, taken for GRB970508, which with $0.835 < z \leq 2.3$ was placed at a cosmological distance of at least 2.9 Gpc [15]. Despite initial isotropy, SGRBs were shown to be distributed anisotropically on the sky, while LGRBs are distributed isotropically [16–23]. Cosmological conse-

quences of the anisotropic celestial distribution of SGRBs were discussed lately by Mészáros et al. [24] and Mészáros and Rees [6]. Finally, the progenitors of LGRBs are associated with supernovae (SNe) [25–29] related to collapse of massive stars. Progenitors of SGRBs are thought to be neutron star–black hole (NS–BH) or NS–NS mergers [12, 30–32], and no connection between SGRBs and SNe has been proven [33].

While the recent first direct detection of gravitational waves (GW), termed GW150914, by the Laser Interferometer Gravitational Wave Observatory (LIGO) [34], interpreted as a merger of two stellar-mass BHs with masses $36^{+5}_{-4} M_{\odot}$ and $29^{+4}_{-4} M_{\odot}$, is by itself a discovery of prime importance, it becomes especially interesting in light of the finding of Connaughton et al. [35] who reported a weak transient source lasting 1 s and detected by *Fermi*/GBM [36] only 0.4 s after the GW150914, termed GW150914-GBM. Its false alarm probability is estimated to be 0.0022. The fluence in the energy band 1 keV–10 MeV is computed to be $1.8^{+1.5}_{-1.0} \times 10^{49}$ erg s $^{-1}$. While these GW and GRB events are consistent in direction, its connection is tentative due to relatively large uncertainties in their localization. This association is unexpected as SGRBs have been thought to originate from NS–NS or NS–BH mergers. Moreover, neither *INTEGRAL* [37] nor *Swift* [38] detected any signals that could be ascribed

to a GRB. Even if it turns out that it is only a chance coincidence [39], it has already triggered scenarios explaining how a BH–BH merger can become a GRB; for example, the nascent BH could generate a GRB via accretion of a mass $\approx 10^{-5} M_{\odot}$ [40], indicating its location in a dense medium (see also [41]), or two high-mass, low-metallicity stars could undergo an SN explosion, and the matter ejected from the last exploding star can form—after some time—an accretion disk producing an SGRB [42]. Also the possible detection of an afterglow that can be visible many months after the event [43] could shed light on the nature of the GW and SGRB association.

From a phenomenological point of view, a GRB is composed of the prompt emission, which consists of high-energy photons such as γ -rays and hard X-rays, and the afterglow emission, that is, a long lasting multiwavelength emission (X-ray, optical, and sometimes also radio), which follows the prompt phase. The first afterglow observation (for GRB970228) was due to the *BeppoSAX* satellite [44, 45]. Another class, besides SGRBs and LGRBs, that is, intermediate in duration, was proposed to be present in univariate duration distributions [46–51], as well as in higher dimensional parameter spaces [51–56]. On the other hand, this elusive intermediate class might be a statistical feature that can be explained by modeling the duration distribution with skewed distributions, instead of the commonly applied standard Gaussians [57–61]. Additionally, GRB classification was shown to be detector-dependent [1, 62, 63]. Moreover, a subclass classification of LGRBs was proposed [64], and Norris and Bonnell [65] discovered the existence of an intermediate class or SGRBs with extended emission, that show mixed properties between SGRBs and LGRBs. GRBs with very long durations (ultralong GRBs, with $T_{90} > 1000$ s) are statistically different than regular (i.e., with $T_{90} < 500$ s) LGRBs [66] and hence might form a different class (see also [67–70]). Another relevant classification appears related to the spectral features distinguishing normal GRBs from X-ray flashes (XRFs). The XRFs [71, 72] are extragalactic transient X-ray sources with spatial distribution and spectral and temporal characteristics similar to LGRBs. The remarkable property that distinguishes XRFs from GRBs is that their νF_{ν} prompt emission spectrum peaks at energies which are observed to be typically an order of magnitude lower than the observed peak energies of GRBs. XRFs are empirically defined by a greater fluence (time-integrated flux) in the X-ray band (2–30 keV) than in the γ -ray band (30–400 keV). This classification is also relevant for the investigation of GRB correlations since some of them become stronger or weaker by introducing different GRB categories. Grupe et al. [73], using 754 *Swift* GRBs, performed an exhaustive analysis of several correlations as well as the GRB redshift distribution, discovering that the bright bursts are more common in the high- z (i.e., $z \gtrsim 3$) than in the local universe.

This classification has further enhanced the knowledge of the progenitor system from which GRBs originate. It was soon after their discovery that LGRBs were thought to originate from distant star-forming galaxies. Since then, LGRBs have been firmly associated with powerful core-collapse SNe and the association seems solid. Nevertheless,

there have been puzzling cases of LGRBs that were not associated with bright SNe [74, 75]. This implies that it is possible to observe GRBs without an associated bright SNe or there are other progenitors for LGRBs than core-collapse of massive stars. Another relevant uncertainty concerning the progenitor systems for LGRBs is the role of metallicity Z . In the collapsar model [27], LGRBs are only formed by massive stars with Z/Z_{\odot} below ≈ 0.1 –0.3. However, several GRBs have been located in very metal-rich systems [76] and it is an important goal to understand whether there are other ways to form LGRBs than through the collapsar scenario [77]. One of the models used to explain the GRB phenomenon is the “fireball” model [78–80] in which a compact central engine (either the collapsed core of a massive star or the merger product of an NS–NS binary) launches a highly relativistic, jetted electron-positron-baryon plasma. Interactions of blobs within the jet are believed to produce the prompt emission. Instead, the interaction of the jet with the ambient material causes the afterglow phase. However, problems in explaining the light curves within this model have been shown by Willingale et al. [81]. Specifically, for $\approx 50\%$ of GRBs, the observed afterglows are in agreement with the model, but for the rest the temporal and spectral indices do not conform and suggest a continued late energy injection. Melandri et al. [82] performed a multiwavelength analysis and found that the forward shock (FS) model does not explain almost 50% of the examined GRBs, even after taking into account energy injection. Rykoff et al. [83] showed that the fireball model does not model correctly early afterglows. Reference [84] analysed the prompt and afterglow light curves and pointed out that some GRBs required energy injection to explain the outflows. The crisis of the standard fireball models appeared when *Swift* [85] observations revealed a more complex behaviour of the light curves than observed in the past [86–88] and pointed out that GRBs often follow “canonical” light curves [89]. Therefore, the discovery of correlations among relevant physical parameters in the prompt phase is very important in this context in order to use them as possible model discriminators. In fact, many theoretical models have been presented in the literature in order to explain the wide variety of observations, but each model has some advantages as well as drawbacks, and the use of the phenomenological correlations can boost the understanding of the mechanism responsible for the prompt emission. Moreover, given the much larger (compared to SNe) redshift range over which GRBs can be observed, it is tempting to include them as cosmological probes, extending the redshift range by almost an order of magnitude further than the available SNe Ia. GRBs are observed up to redshift $z = 9.4$ [90], much more distant than SNe Ia, observed up to $z = 2.26$ [91], and therefore they can help to understand the nature of dark energy and determine the evolution of its equation of state at very high z . However, contrary to SNe Ia, which originate from white dwarves reaching the Chandrasekhar limit and always releasing the same amount of energy, GRBs cannot yet be considered standard candles with their (isotropic-equivalent) energies spanning 8 orders of magnitude (see also [92] and references therein). Therefore, finding universal relations among observable properties can help to standardize their

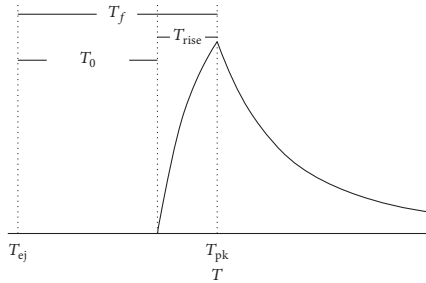


FIGURE 1: A sketch of the pulse displaying T_{ej} and T_{peak} (denoted by T_{pk} here) and the quantities T_f and $T_0 = T_f - T_{rise}$. (Figure after Willingale et al. [108]; see Figure 1 therein.)

energetics and/or luminosities. They can serve as a tracer of the history of the cosmic star formation rate [93–97] and provide invaluable information on the physics in the intergalactic medium [98–100]. This is the reason why the study of GRB correlations is so relevant for understanding the GRB emission mechanism, for finding a good distance indicator, and for exploring the high-redshift universe [101].

This paper is organized in the following manner. In Section 2, we explain the nomenclature and definitions adopted in this work, and in Section 3 we analyse the correlations between various prompt parameters. We summarize in Section 4.

2. Notations and Nomenclature

For clarity we report a summary of the nomenclature adopted in the review. L , F , E , S , and T indicate the luminosity, the energy flux, the energy, the fluence, and the timescale, respectively, which can be measured in several wavelengths. More specifically,

- (i) T_{90} is the time interval in which 90% of the GRB's fluence is accumulated, starting from the time at which 5% of the total fluence was detected [10];
- (ii) T_{50} is defined, similar to T_{90} , as the time interval from 25% to 75% of the total detected fluence;
- (iii) T_{45} is the time spanned by the brightest 45% of the total counts detected above background [102];
- (iv) T_{peak} is the time at which the pulse (i.e., a sharp rise and a slower, smooth decay [103–106]) in the prompt light curve peaks (see Figure 1);
- (v) T_{break} is the time of a power law break in the afterglow light curve [107, 108], that is, the time when the afterglow brightness has a power law decline that suddenly steepens due to the slowing down of the jet until the relativistic beaming angle roughly equals the jet-opening angle θ_{jet} [109];
- (vi) τ_{lag} and τ_{RT} are the difference of arrival times to the observer of the high-energy photons and low energy photons defined between 25–50 keV and

100–300 keV energy band and the shortest time over which the light curve increases by 50% of the peak flux of the pulse;

- (vii) T_p is the end time prompt phase at which the exponential decay switches to a power law, which is usually followed by a shallow decay called the plateau phase, and T_a is the time at the end of this plateau phase [81];
- (viii) T_p is the pulse width since the burst trigger at the time T_{ej} of the ejecta;
- (ix) E_{peak} , E_{iso} , E_γ , and E_{prompt} are the peak energy, that is, the energy at the peak of the γF_γ spectrum [110], the total isotropic energy emitted during the whole burst (e.g., [111]), the total energy corrected for the beaming factor [the latter two are connected via $E_\gamma = (1 - \cos \theta_{jet}) E_{iso}$], and the isotropic energy emitted in the prompt phase, respectively;
- (x) F_{peak} , F_{tot} are the peak and the total fluxes, respectively [112];
- (xi) L_a , $L_{X,p}$, and L_f are the luminosities respective to T_a , T_p (specified in the X-ray band), and T_f ;
- (xii) L is the observed luminosity, and specifically L_{peak} and L_{iso} are the peak luminosity (i.e., the luminosity at the pulse peak, [113]) and the total isotropic luminosity, both in a given energy band. More precisely, L_{peak} is defined as follows:

$$L_{peak} = 4\pi D_L(z, \Omega_M, \Omega_\Lambda)^2 F_{peak}, \quad (1)$$

with $D_L(z, \Omega_M, \Omega_\Lambda)$ the luminosity distance given by

$$D_L(z, \Omega_M, \Omega_\Lambda) = \frac{c(1+z)}{H_0} \int_0^z \frac{dz'}{\sqrt{\Omega_M(1+z')^3 + \Omega_\Lambda}}, \quad (2)$$

where Ω_M and Ω_Λ are the matter and dark energy density parameters, H_0 is the present-day Hubble constant, and z is the redshift. Similarly, L_{iso} is given by

$$L_{iso} = 4\pi D_L(z, \Omega_M, \Omega_\Lambda)^2 F_{tot}; \quad (3)$$

- (xiii) S_γ , S_{obs} , S_{tot} indicate the prompt fluence in the whole gamma band (i.e., from a few hundred keV to a few MeV), the observed fluence in the range 50–300 keV, and the total fluence in the 20 keV–1.5 MeV energy band;
- (xiv) V is the variability of the GRB's light curve. It is computed by taking the difference between the observed light curve and its smoothed version, squaring this difference, summing these squared differences over time intervals, and appropriately normalizing the resulting sum [102]. Different smoothing filters may be applied (see also [114] for a different approach). V_f denotes the variability for a certain fraction of the smoothing timescale in the light curve.

Most of the quantities described above are given in the observer frame, except for E_{iso} , E_{prompt} , L_{peak} , and L_{iso} , which are already defined in the rest frame. With the upper index “ $*$ ” we explicitly denote the observables in the GRB rest frame. The rest frame times are the observed times divided by

$$N_E(E) = A_{\text{norm}} \times \begin{cases} \left(\frac{E}{100 \text{ keV}} \right)^{\alpha} \exp \left(-\frac{E}{E_0} \right), & E \leq (\alpha - \beta) E_0, \\ \left[\frac{(\alpha - \beta) E_0}{100 \text{ keV}} \right]^{\alpha-\beta} \left(\frac{E}{100 \text{ keV}} \right)^{\beta} \exp(\alpha - \beta), & E \geq (\alpha - \beta) E_0, \end{cases} \quad (4)$$

where A_{norm} is the normalization. Here, α and β are the low- and high-energy indices of the Band function, respectively. $N_E(E)$ is in units of photons $\text{cm}^{-2} \text{s}^{-1} \text{keV}^{-1}$. For the cases $\beta < -2$ and $\alpha > -2$, E_{peak} can be derived as $E_{\text{peak}} = (2 + \alpha) E_0$, which corresponds to the energy at the maximum flux in the νF_ν spectra [115, 116].

The Pearson correlation coefficient [117, 118] is denoted by r , the Spearman correlation coefficient [119] is denoted by ρ , and the p value (a probability that a correlation is drawn by chance) is denoted by P .

Finally, we mostly deal with correlations of the form $y = ax + b$. However, when the intercept b is neglected in the text, but its value is nonnegligible (or not known due to lacking in the original paper), we use the notation $y \sim ax$ to emphasize the slope.

3. The Prompt Correlations

Several physical relations between relevant quantities in GRBs were found since the 1990s. In each paragraph below, we follow the discovery of the correlation with the definition of the quantities, the discussions presented in literature, and their physical interpretation.

3.1. The $L_{\text{peak}}\text{-}\tau_{\text{lag}}$ Correlation

3.1.1. Literature Overview. Liang and Kargatis [120], using 34 bright GRBs detected by BATSE, found that E_{peak} depends linearly on the previous flux emitted by the pulse, that is, that the rate of change of E_{peak} is proportional to the instantaneous luminosity. Quantitatively

$$\frac{L_{\text{peak}}}{N} = -\frac{dE_{\text{peak}}}{dt}, \quad (5)$$

where N is a normalization constant expressing the luminosity for each pulse within a burst, and L_{peak} was calculated from the observed flux via (1).

The $L_{\text{peak}}\text{-}\tau_{\text{lag}}$ correlation was introduced for the first time by Norris et al. [113] who examined a sample of 174 GRBs detected by BATSE, among which 6 GRBs had an established redshift and those were used to find an anticorrelation

the cosmic time expansion; for example the rest frame time in the prompt phase is denoted by $T_p^* = T_p/(1 + z)$. The energetics are transformed differently, for example, $E_{\text{peak}}^* = E_{\text{peak}}(1 + z)$.

The Band function [115] is a commonly applied phenomenological spectral profile, such that

between L_{peak} and τ_{lag} in the form of the following (see Figure 2(a)):

$$\log L_{\text{peak}} = 55.11 - 1.14 \log \tau_{\text{lag}}^*, \quad (6)$$

with L_{peak} , in units of $10^{53} \text{ erg s}^{-1}$, computed in the 50–300 keV range, and τ_{lag}^* is measured in seconds. A remarkably consistent relation was found by Schaefer et al. [121], who used a sample of 112 BATSE GRBs and reported that

$$\log L_{\text{peak}} = 52.46 - (1.14 \pm 0.20) \log \tau_{\text{lag}}, \quad (7)$$

being in perfect agreement with the result of Norris et al. [113]. Here, L_{peak} is in units of $10^{51} \text{ erg s}^{-1}$ and τ_{lag} in seconds. This relation has been confirmed by several studies (e.g., [122–124]).

Schaefer [125] showed that the $L_{\text{peak}}\text{-}\tau_{\text{lag}}$ relation is a consequence of the Liang and Kargatis [120] empirical relation from (5), and he derived this dependence to be of the form $\log L_{\text{peak}} \sim -\log \tau_{\text{lag}}$. This correlation was useful in the investigation of Kocevski and Liang [126], who used a sample of 19 BATSE GRBs and the $L_{\text{peak}}\text{-}\tau_{\text{lag}}$ relation from [121] to infer their pseudoredshifts. Their approach was to vary the guessed z until it allowed matching the luminosity distance D_L measured with the GRB's energy flux and D_L that can be calculated from the guessed redshift within a flat Λ CDM model, until the agreement among the two converged to within 10^{-3} . Next, the rate of E_{peak} decay, as in [120], was measured. Finally, Kocevski and Liang [126] showed that the L_{peak} is directly related to the GRB's spectral evolution. However, Hakkila et al. [127] found a different slope, -0.62 ± 0.04 and argued that the $L_{\text{peak}}\text{-}\tau_{\text{lag}}$ relation is a pulse rather than a burst property; that is, each pulse is characterized by its own τ_{lag} distinct for various pulses within a GRB.

Tsutsui et al. [128], using pseudoredshifts estimated via the Yonetoku relation (see Section 3.6.2) for 565 BATSE GRBs, found that the $L_{\text{peak}}\text{-}\tau_{\text{lag}}$ relation has a ρ of only 0.38 (see Figure 2(b)). However, assuming that the luminosity is a function of both the redshift and the lag, a new redshift-dependent $L_{\text{peak}}\text{-}\tau_{\text{lag}}$ relation was found as

$$\log L_{\text{peak}} = 50.88 + 2.53 \log(1 + z) - 0.282 \log \tau_{\text{lag}}, \quad (8)$$

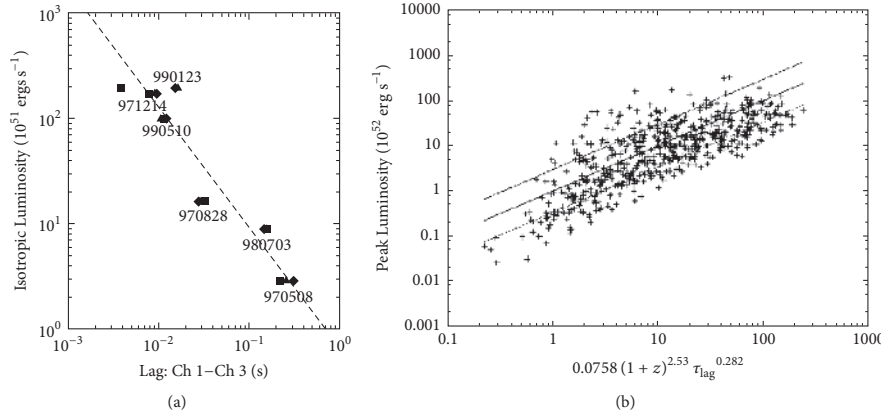


FIGURE 2: (a) L_{peak} versus τ_{lag}^* distribution for six GRBs with measured redshifts. The dashed line represents the power law fit to the lag times for ranges consisting of count rates larger than $0.1 \times \text{peak intensity}$ (squares), yielding $\log L_{\text{peak}} \sim -1.14 \log(\tau_{\text{lag}}^*/0.01 \text{ s})$. The lag time is computed using channel 1 (25–50 keV) and channel 3 (100–300 keV) of the BATSE instrument. (Figure after Norris et al. [113]; see Figure 6 therein. © AAS. Reproduced with permission.) (b) The $L_{\text{peak}}-\tau_{\text{lag}}$ distribution in the $\log L_{\text{peak}}$ versus $\sim 2.53 \log(1+z) - 0.282 \log \tau_{\text{lag}}$ plane. The correlation coefficient is $\rho = 0.77$, $P = 7.9 \times 10^{-75}$. The solid line represents the best-fit line and two dashed lines delineate 1σ deviation. (Figure after Tsutsui et al. [128]; see Figure 4 therein. Copyright © 2008 AIP Publishing.)

with L_{peak} in units of $10^{50} \text{ erg s}^{-1}$, τ_{lag} in seconds, $\rho = 0.77$ and $P = 7.9 \times 10^{-75}$. Although the spectral lag is computed from two channels of BATSE, this new $L_{\text{peak}}-\tau_{\text{lag}}$ relation suggests that a future lag-luminosity relation defined within the *Swift* data should also depend on the redshift.

Afterwards, Sultana et al. [129] presented a relation between the z - and k -corrected τ_{lag} for the *Swift* energy bands 50–100 keV and 100–200 keV, and L_{peak} , for a subset of 12 *Swift* long GRBs. The z -correction takes into account the time dilatation effect by multiplying the observed lag by $(1+z)^{-1}$ to translate it into the rest frame. The k -correction takes into account a similar effect caused by energy bands being different in the observer and rest frames via multiplication by $(1+z)^{0.33}$ [130]. The net corrected τ_{lag}^* is thence $(1+z)^{-0.67} \tau_{\text{lag}}$. In addition, Sultana et al. [129] demonstrated that this correlation in the prompt phase can be extrapolated into the $L_a-T_a^*$ relation [131–134]. Sultana et al. [129] found the following (Note that Sultana et al. [129] used L_{iso} to denote the peak isotropic luminosity.):

$$\begin{aligned} \log L_{\text{peak}} &= (54.87 \pm 0.29) \\ &\quad - (1.19 \pm 0.17) \log [(1+z)^{-0.67} \tau_{\text{lag}}], \quad (9) \\ \log L_a &= (51.57 \pm 0.10) - (1.10 \pm 0.03) \log T_a^*, \end{aligned}$$

with τ_{lag} in ms, T_a^* in seconds, and L in erg s^{-1} . The correlation coefficient is significant for these two relations ($\rho = -0.65$ for the $L_{\text{peak}}-\tau_{\text{lag}}$ and $\rho = -0.88$ for the $L_a-T_a^*$ relations) and has surprisingly similar best-fit power law indices (-1.19 ± 0.17 and -1.10 ± 0.03 , resp.). Although τ_{lag} and T_a^* represent different GRB time variables, it appears distinctly that the $L_{\text{peak}}-\tau_{\text{lag}}$ relation extrapolates into $L_a-T_a^*$ for timescales

$\tau_{\text{lag}} \approx T_a^*$. A discussion and comparison of this extrapolation with the L_f-T_f relation are extensively presented in [135].

Ukwatta et al. [136] confirmed that there is a correlation between L_{peak}^* and the z - and k -corrected τ_{lag} among 31 GRBs observed by *Swift*, with $r = -0.68$, $P = 7 \times 10^{-2}$ and the slope equal to -1.4 ± 0.3 , hence confirming the $L_{\text{peak}}-\tau_{\text{lag}}$ relation, although with a large scatter. This was followed by another confirmation of this correlation [137] with the use of 43 *Swift* GRBs with known redshift, which yielded $r = -0.82$, $P = 5.5 \times 10^{-5}$, and a slope of -1.2 ± 0.2 , being consistent with the previous results.

Finally, Margutti et al. [138] established that the X-ray flares obey the same $L_{\text{peak}}-\tau_{\text{lag}}^*$ relation (in the rest frame energy band 0.3–10 keV) as GRBs and proposed that their underlying mechanism is similar.

3.1.2. Physical Interpretation of the $L_{\text{peak}}-\tau_{\text{lag}}$ Relation. The physical assumption on which the work by Norris et al. [113] was based is that the initial mechanism for the energy formation affects the development of the pulse much more than dissipation. From the study of several pulses in bright, long BATSE GRBs, it was claimed that, for pulses with precisely defined shape, the rise-to-decay ratio is ≤ 1 . In addition, when the ratio diminishes, pulses show a tendency to be broader and weaker.

Salmonson [122] proposed that the $L_{\text{peak}}-\tau_{\text{lag}}$ relation arises from an entirely kinematic effect. In this scenario, an emitting region with constant (among the bursts) luminosity is the source of the GRB's radiation. He also claimed that variations in the line-of-sight velocity should affect the observed luminosity proportionally to the Lorentz factor of the jet's expansion, $\Gamma = [1 - (v/c)^2]^{-1/2}$ (where v is the relative velocity

between the inertial reference frames and c is the speed of light), while the apparent τ_{lag} is proportional to $1/\Gamma$. The variations in the velocity among the lines of sight is a result of the jet's expansion velocity combined with the cosmological expansion. The differences of luminosity and lag between different bursts are due to the different velocities of the individual emitting regions. In this case, the luminosity is expected to be proportional to $1/\tau_{\text{lag}}$, which is consistent with the observed relation. This explanation, however, requires the comoving luminosity to be nearly constant among the bursts, which is a very strong condition to be fulfilled. Moreover, this scenario has several other problems (as pointed out by Schaefer [125]):

- (1) It requires the Lorentz factor and luminosity to have the same range of variation. However, the observed L_{peak} span more than three orders of magnitude (e.g., [121]), while the Lorentz factors span less than one order of magnitude (i.e., a factor of 5) [139].
- (2) It follows that the observed luminosity should be linearly dependent on the jet's Lorentz factor, yet this claim is not justified. In fact, a number of corrections are to be taken into account, leading to a significantly nonlinear dependence. The forward motion of the jet introduces by itself an additional quadratic dependence [140].

Ioka and Nakamura [141] proposed another interpretation for the $L_{\text{peak}}-\tau_{\text{lag}}$ correlation. From their analysis, a model in which the peak luminosity depends on the viewing angle is elaborated: the viewing angle is the off-axis angular position from which the observer examines the emission. Indeed, it is found that a high-luminosity peak in GRBs with brief spectral lag is due to an emitted jet with a smaller viewing angle than a fainter peak with extended lag. It is also claimed that the viewing angle can have implications on other correlations, such as the luminosity-variability relation presented in Section 3.2. As an additional result from this study, it was pointed out that XRFs can be seen as GRBs detected from large angles with high spectral lag and small variability.

On the other hand, regarding the jet angle distributions, Liang et al. [142] found an anticorrelation between the jet-opening angle and the isotropic kinetic energy among 179 X-ray GRB light curves and the afterglow data of 57 GRBs. Assuming that the GRB rate follows the star formation rate, and, after a careful consideration of selection effects, Lü et al. [143] found in a sample of 77 GRBs an anticorrelation between the jet-opening angle θ_{jet} and the redshift in the following form:

$$\log \theta_{\text{jet}} = (-0.90 \pm 0.09) - (0.94 \pm 0.19) \log(1+z), \quad (10)$$

with $\rho = 0.55$ and $P < 10^{-4}$. Using a mock sample and bootstrap technique, they showed that the observed $\theta_{\text{jet}}-z$ relation is most likely due to instrumental selection effects. Moreover, they argued that while other types of relation, for example, $\tau_{\text{lag}}-z$ [144] or the redshift dependence of the shallow decay in X-ray afterglows by Stratta et al. [145], might have connections with the jet geometry, they are also likely

to stem from observational biases or sample selection effects. Also, Ryan et al. [146] investigated the jet-opening angle properties using a sample of 226 *Swift*/XRT GRBs with known redshift. They found that most of the observed afterglows were observed off-axis; hence the expected behaviour of the afterglow light curves can be significantly affected by the viewing angle.

Zhang et al. [33] argued, on the basis of the kinematic model, that the origin of the $L_{\text{peak}}-\tau_{\text{lag}}$ relation is due to a more intrinsic $L_{\text{peak}}-V$ relation (see Section 3.2). They also gave an interpretation of the latter relation within the internal shock model (see Section 3.2.2). Recently, Uhm and Zhang [147] constructed a model based on the synchrotron radiation mechanism that explains the physical origin of the spectral lags and is consistent with observations.

Another explanation for the origin of the $L_{\text{peak}}-\tau_{\text{lag}}$ relation, given by Sultana et al. [129], involves only kinematic effects. In this case, L_{peak} and τ_{lag} depend on the quantity:

$$D = \frac{1}{\Gamma(1 - \beta_0 \cos \theta)(1+z)}, \quad (11)$$

depicting the Doppler factor of a jet at a viewing angle θ and with velocity $\beta_0 \equiv v/c$ at redshift z . In this study there is no reference to the masses and forces involved and, as a consequence of the Doppler effect, the factor D associates the GRB rest frame timescale τ with the observed time t in the following way:

$$t = \frac{\tau}{D}. \quad (12)$$

Therefore, considering a decay timescale $\Delta\tau$ in the GRB rest frame, (12) in the observer frame will give $\Delta t = \Delta\tau/D$. Furthermore, taking into account a spectrum given by $\Phi(E) \propto E^{-\alpha}$, the peak luminosity (as already pointed out by Salmonson [122]) can be computed as

$$L_{\text{peak}} \propto D^\alpha, \quad (13)$$

with $\alpha \approx 1$. In such a way, (12) and (13) allow retrieving the observed $L_{\text{peak}}-\tau_{\text{lag}}$ relation. Finally, the analogous correlation coefficients and best-fit slopes of the $L_{\text{peak}}-\tau_{\text{lag}}$ and $L_a-T_a^*$ correlations obtained by Sultana et al. [129] seem to hint toward a similar origin for these two relations.

3.2. The $L_{\text{peak}}-V$ Correlation. The first correlation between L_{peak} and V was discovered by Fenimore and Ramirez-Ruiz [148] and was given as

$$\log L_{\text{peak}} = 56.49 + 3.35 \log V, \quad (14)$$

with L_{peak} measured in erg s^{-1} . Here, the luminosity is per steradian in a specified (rest frame) energy bandpass (50–300 keV), averaged over 256 ms. First, seven BATSE GRBs with a measured redshift were used to calibrate the $L_{\text{peak}}-V$ relation. Next, the obtained relationship was applied to 220 bright BATSE GRBs in order to obtain the luminosities and distances and to infer that the GRB formation rate scales as $(1+z)^{3.3 \pm 0.3}$. Finally, the authors emphasized the need of confirmation of the proposed $L_{\text{peak}}-V$ relation.

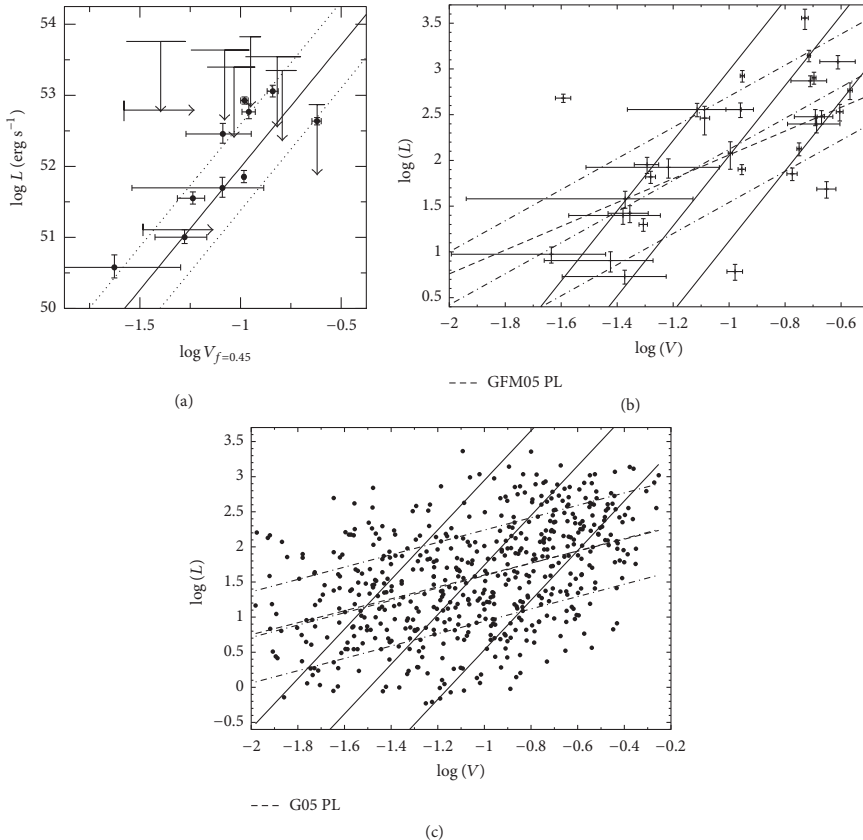


FIGURE 3: (a) The variabilities $V_{f=0.45}$ and peak luminosities L_{peak} of the data set, excluding GRB980425. In this case, $V_{f=0.45}$ indicates the variabilities for the 45% smoothing timescale of the light curve. The solid and dotted lines are the best-fit line and 1σ deviation, respectively, in $\log L_{\text{peak}} - \log V_{f=0.45}$ plane. (Figure after Reichart et al. [102]; see Figure 9 therein.) @ AAS. Reproduced with permission.) (b) The $\log L_{\text{peak}} - \log V$ plane for the sample of 32 GRBs with measured redshift. The best-fit lines and 1σ deviations are also displayed: solid lines are computed with the Reichart et al. [102] method, dashed-dotted lines with the D'Agostini [153] method, and the dashed lines are recovered by Guidorzi et al. [149]. (Figure after Guidorzi et al. [151]; see Figure 1 therein.) (c) $\log L_{\text{peak}} - \log V_f$ relation for the set of 551 BATSE GRBs. The best-fit lines and 1σ regions are also shown, the solid lines are fitted with the Reichart et al. [102] method, the dashed-dotted lines with the D'Agostini [153] method, and the dashed lines are recovered by Guidorzi et al. [149]. (Figure after Guidorzi et al. [151]; see Figure 2 therein.)

3.2.1. Literature Overview. Reichart et al. [102] used a total of 20 GRBs observed by CGRO/BATSE (13 bursts), the KONUS/Wind (5 bursts), the Ulysses/GRB (1 burst), and the NEAR/XGRS (1 burst), finding

$$\log L_{\text{peak}} \sim (3.3^{+1.1}_{-0.9}) \log V, \quad (15)$$

with $\rho = 0.8$ and $P = 1.4 \times 10^{-4}$ (see Figure 3(a)); L_{peak} was computed in the 50–300 keV observer-frame energy band, which corresponds roughly to the range 100–1000 keV in the rest frame for $z \approx 1$ –2, typical for GRBs in the sample examined. The distribution of the sample's bursts in the

$\log L_{\text{peak}} - \log V_f$ plane appears to be well modeled by the following parameterization:

$$\log V_f(L) = \log \bar{V}_f + b + m(\log L_{\text{peak}} - \log \bar{L}_{\text{peak}}), \quad (16)$$

where $b = 0.013^{+0.075}_{-0.092}$ is the intercept of the line, $m = 0.302^{+0.112}_{-0.075}$ is its slope, and \bar{V}_f and \bar{L}_{peak} are the median values of V_f and L_{peak} for the bursts in the sample for which spectroscopic redshifts, peak fluxes, and 64 ms or better resolution light curves are available.

Later, Guidorzi et al. [149] updated the sample to 32 GRBs detected by different satellites, that is, BeppoSAX, CGRO/BATSE, HETE-2, and KONUS (see Figure 3(b)). The

existence of a correlation was confirmed, but they found a dramatically different relationship with respect to the original one:

$$\log L_{\text{peak}} = 3.36_{-0.43}^{+0.89} + 1.30_{-0.44}^{+0.84} \log V, \quad (17)$$

with $\rho = 0.625$ and $P = 10^{-4}$, and L_{peak} in units of $10^{50} \text{ erg s}^{-1}$.

However, Reichart and Nysewander [150] using the same sample claimed that this result was the outcome of an improper statistical methodology and confirmed the previous work of Reichart et al. [102]. Indeed, they showed that the difference among their results and the ones from Guidorzi et al. [149] was due to the fact that the variance of the sample in the fit in [149] was not taken into account. They used an updated data set, finding that the fit was well described by the slope $m = 3.4_{-0.6}^{+0.9}$, with a sample variance $\sigma_V = 0.2 \pm 0.04$.

Subsequently, Guidorzi et al. [151], using a sample of 551 BATSE GRBs with pseudoredshifts derived using the $L_{\text{peak}}-\tau_{\text{lag}}$ relation [152], tested the $L_{\text{peak}}-V$ correlation (see Figure 3(c)). They also calculated the slope of the correlation of the samples using the methods implemented by Reichart et al. [102] and D'Agostini [153]. The former method provided a value of the slope in the $L_{\text{peak}}-V$ correlation consistent with respect to the previous works:

$$\log L_{\text{peak}} \sim 3.5_{-0.4}^{+0.6} \log V. \quad (18)$$

Instead, the slope for this sample using the latter method is much lower than the value in [102]:

$$\log L_{\text{peak}} \sim 0.88_{-0.13}^{+0.12} \log V. \quad (19)$$

The latter slope m is consistent with the results obtained by Guidorzi et al. [149], but inconsistent with the results derived by Reichart and Nysewander [150].

Afterwards, Rizzuto et al. [154] tested this correlation with a sample of 36 LGRBs detected by *Swift* in the 15–350 keV energy range and known redshifts. The sample consisted of bright GRBs with $L_{\text{peak}} > 5 \times 10^{50} \text{ erg s}^{-1}$ within 100–1000 keV energy range. In their study, they adopted two definitions of variability, presented by Reichart et al. [102], called V_R , and by Li and Paczyński [114], hereafter V_{LP} . V_R and V_{LP} differ from each other with a different smoothing filter which, in the second case, selects only high-frequency variability. Finally, Rizzuto et al. [154] confirmed the correlation and its intrinsic dispersion around the best-fitting power law given by

$$\log L_{\text{peak}} \sim (2.3 \pm 0.17) \log V_{LP}, \quad (20)$$

with $\rho = 0.758$ and $P = 0.011$, and

$$\log L_{\text{peak}} \sim (1.7 \pm 0.4) \log V_R, \quad (21)$$

with $\sigma_{\log L} = 0.58_{-0.12}^{+0.15}$, $\rho = 0.115$, and $P = 0.506$. Six low-luminosity GRBs (i.e., GRB050223, GRB050416A, GRB050803, GRB051016B, GRB060614, and GRB060729), out of a total of 36 in the sample, are outliers of the correlation, showing values of V_R higher than expected. Thus, the correlation is not valid for low-luminosity GRBs.

As is visible from this discussion, the scatter in this relation is not negligible, thus making it less reliable than the previously discussed ones. However, investigating the physical explanation of this correlation is worth being depicted for further developments.

3.2.2. Physical Interpretation of the $L_{\text{peak}}-V$ Relation. We here briefly describe the internal and external shock model [80, 155], in which the GRB is caused by emission from a relativistic, expanding baryonic shell with a Lorentz bulk factor Γ . Let there be a spherical section with an opening angle θ_{jet} . In general, θ_{jet} can be greater than Γ^{-1} , but the observer can detect radiation coming only from the angular region with size $\approx \Gamma^{-1}$. An external shock is formed when the expanding shell collides with the external medium. In general, there might be more than one shell, and the internal shock takes place when a faster shell reaches a slower one. In both cases one distinguishes an FS, when the shock propagates into the external shell or the external medium, and a reverse shock (RS), when it propagates into the inner shell.

Fenimore and Ramirez-Ruiz [148] pointed out that the underlying cause of the $L_{\text{peak}}-V$ relation is unclear. In the context of the internal shock model, larger initial Γ factors tend to produce more efficient collisions. After changing some quantities such as the Γ factors, the ambient density, and/or the initial mass of the shells, the observed variability values are not recovered. Therefore, the central engine seems to play a relevant role in the explanation for the observed $L_{\text{peak}}-V$ correlation. In fact, this correlation was also explored within the context of a model in which the GRB variability is due to a change in the jet-opening angles and narrower jets have faster outflows [156]. As a result, this model predicts bright luminosities, small pulse lags, and large variability as well as an early jet break time for on-axis observed bursts. On the other hand, dimmer luminosities, longer pulse lags, flatter bursts, and later jet break times will cause larger viewing angles.

Guidorzi et al. [151] gave an interpretation for the smaller value of the correlation in the context of the jet-emission scenario where a stronger dependence of Γ of the expanding shells on the jet-opening angle is expected. However, Schaefer [157] attributed the origin of the $L_{\text{peak}}-V$ relation to be based on relativistically shocked jets. Indeed, V and L_{peak} are both functions of Γ , where L_{peak} is proportional to a high power of Γ , as was already demonstrated in the context of the $L_{\text{peak}}-\tau_{\text{lag}}$ relation (see Section 3.1.2), and hence fast rise times and short pulse durations imply high variability.

3.3. The $L_{\text{iso}}-\tau_{\text{RT}}$ Correlation and Its Physical Interpretation. Schaefer [158] predicted that τ_{RT} should be connected with L_{iso} in a following manner:

$$L_{\text{iso}} \propto \tau_{\text{RT}}^{-N/2}, \quad (22)$$

with the exponent $N \approx 3$ (see also Schaefer [157, 158]). Therefore, fast rises indicate high luminosities and slow rises low luminosities. τ_{RT} can be directly connected to the physics of the shocked jet. Indeed, for a sudden collision of a material within a jet (with the shock creating an individual pulse

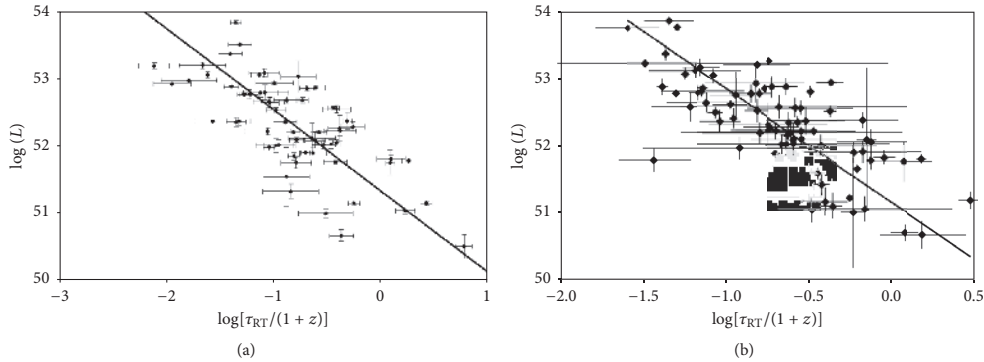


FIGURE 4: (a) The $\log L_{\text{iso}}$ - $\log \tau_{\text{RT}}^*$ relation with the best-fit line displayed. The errors are given by the 1σ confidence interval. (Figure after Schaefer [157]; see Figure 5 therein. @ AAS. Reproduced with permission.) (b) The $\log L_{\text{iso}}$ - $\log \tau_{\text{RT}}^*$ correlation with the best fit line. (Figure after Xiao and Schaefer [159]; see Figure 3 therein. @ AAS. Reproduced with permission.)

in the GRB light curve), τ_{RT} will be determined as the maximum delay between the arrival time of photons from the center of the visible region versus their arrival time from its edge.

The angular opening of the emitted jet, usually associated with Γ , could cause this delay leading to a relation $\tau_{\text{RT}} \propto \Gamma^{-2}$. The radius at which the material is shocked affects the proportionality constant, and the minimum radius under which the material cannot radiate efficiently anymore should be the same for each GRB [139]. In addition, a large scatter is expected depending on the distance from which the collisions are observed.

With both τ_{RT} and L_{iso} being functions of Γ , Schaefer [157] confirmed that $\log L_{\text{iso}}$ should be $\sim -N/2 \log \tau_{\text{RT}}$. From 69 GRBs detected by BATSE and *Swift*, the following relation was obtained:

$$\log L_{\text{iso}} = 53.54 - 1.21 \log \tau_{\text{RT}}^*, \quad (23)$$

with L_{iso} in erg s^{-1} and τ_{RT}^* measured in seconds. The 1σ uncertainties in the intercept and slope are $\sigma_a = 0.06$ and $\sigma_b = 0.06$ (see Figure 4(a)). The uncertainty in the log of the burst luminosity is

$$\begin{aligned} \sigma_{\log L_{\text{iso}}}^2 &= \sigma_a^2 + \left[\sigma_b \log \frac{\tau_{\text{RT}}^*}{0.1 \text{ s}} \right]^2 + \left(\frac{0.43 b \sigma_{\text{RT}}}{\tau_{\text{RT}}} \right)^2 \\ &\quad + \sigma_{\text{RT,sys}}^2, \end{aligned} \quad (24)$$

where Schaefer [157] takes into account the extra scatter, σ_{sys} . When $\sigma_{\text{RT,sys}} = 0.47$, χ^2 of the best-fit line is unity.

Xiao and Schaefer [159] explained in detail the procedure of how they calculated τ_{RT} using 107 GRBs with known spectroscopic redshift observed by BATSE, HETE, KONUS, and *Swift* (see Figure 4(b)), taking into account also the Poissonian noise. Their analysis yielded

$$\log L_{\text{iso}} = 53.84 - 1.70 \log \tau_{\text{RT}}^*, \quad (25)$$

with the same units as in (23). As a consequence, the flattening of the light curve before computing the rise time is an important step. The problem is that the flattening should be done carefully, in fact if the light curve is flattened too much, a rise time comparable with the smoothing-time bin is obtained, while if it is flattened not enough, the Poissonian noise dominates the apparent fastest rise time, giving a too small rise time. Therefore, for some of the dimmest bursts, the Poissonian-noise dominant region and the smoothing-effect dominant region can coincide, thus not yielding τ_{RT} values for the weakest bursts. Finally, the physical interpretation of this correlation is given by Schaefer [157]. It is shown that the fastest rise in a light curve is related to the Lorentz factor Γ simply due to the geometrical rise time for a region subtending an angle of $1/\Gamma$, assuming that the minimum radius for which the optical depth of the jet material is of order of unity remains constant. The luminosity of the burst is also a power law of Γ , which scales as Γ^N for $3 < N < 5$. Therefore, the $\tau_{\text{RT}}-\Gamma$ and the $L_{\text{iso}}-\Gamma$ relations together yield the observed $L_{\text{iso}}-\tau_{\text{RT}}$ relation.

3.4. The Γ_0 - E_{prompt} and Γ_0 - L_{iso} Correlations and Their Physical Interpretation. Freedman and Waxman [160] in their analysis of the GRB emission, considering a relativistic velocity for the fireball, showed that the radiation detected by an observer is within an opening angle $\approx 1/\Gamma(t)$. Hence, the total fireball energy E should be interpreted as the energy that the fireball would have carried if this is assumed spherically symmetric. In particular, it was claimed that the afterglow flux measurements in X-rays gave a strong evaluation for the fireball energy per unit solid angle represented by $\epsilon_e = \xi_e E/4\pi$, within the observable opening angle $1/\Gamma(t)$, where ξ_e is the electron energy fraction. It was found that

$$\Gamma(t) = 10.6 \left(\frac{1+z}{2} \right)^{3/8} \left(\frac{E_{\text{prompt}}}{n_0} \right)^{1/8} t^{-3/8}, \quad (26)$$

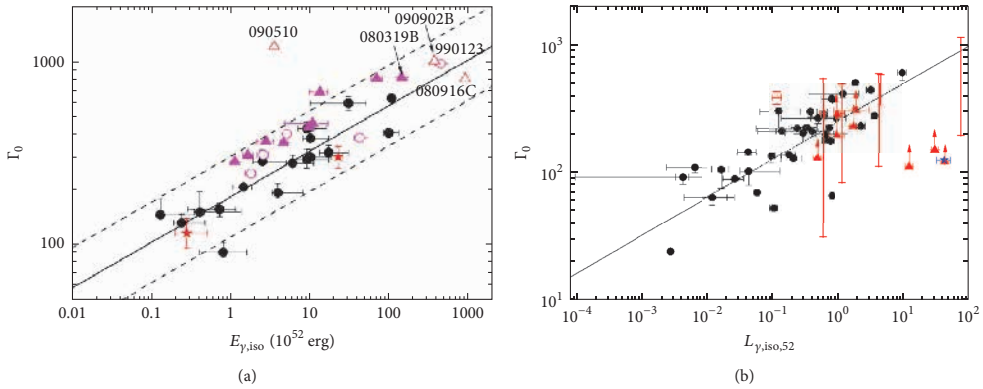


FIGURE 5: (a) $\log \Gamma_0$ - $\log E_{\text{prompt}}$ relation with the addition of GRBs with an onset trend in the X-ray band (GRBs 070208 and 080319C; red stars), Γ_0 computed by RS peaks or probable afterglow peaks (pink open circles), lower values of Γ_0 obtained from single power law decay light curves (pink solid triangles), and strong lower values of Γ_0 for *Fermi*/LAT GRBs 080916C, 090902B, and 090510 (red open triangles) calculated from opacity limits with *Fermi*/LAT observations. The solid line indicates the best fit of the Γ_0 - E_{prompt} relation, $\log \Gamma_0 = 2.26 + 0.25 \log E_{\text{prompt}}$. The two dashed lines represent the 2σ deviation, where the standard deviation of the ratio $\Gamma_0/E_{\text{prompt}}^{0.25}$ for the data sample is $\sigma = 0.11$. (Figure after Liang et al. [164]; see Figure 8 therein. @ AAS. Reproduced with permission.) (b) $\log \Gamma_0$ versus $\log L_{\text{iso}}$ distribution. The best-fit line is given by $\log \Gamma_0 \approx 2.40 + 0.30 \log L_{\text{iso}}$ with $r = 0.79$. The triangles represent the bursts with only lower values and the star indicates the only short burst in the sample, GRB090510. (Figure after Lü et al. [143]; see Figure 2 therein. @ AAS. Reproduced with permission.)

where E_{prompt} is in units of 10^{53} erg, n_0 is the uniform ambient density of the expanding fireball in units of cm^{-3} , and t is the time of the fireball expansion in days. Finally, it was pointed out that ξ_e from the afterglow observations should be close to equipartition, namely, $\xi_e \approx 1/3$. For example, for GRB970508, it was found that $\xi_e \approx 0.2$ [161–163]. A similar conclusion, that is, that it is also close to equipartition, could be drawn for GRB971214; however Wijers and Galama [162] proposed another interpretation for this GRB's data, demanding $\xi_e \approx 1$.

Liang et al. [164] selected from the *Swift* catalogue 20 optical and 12 X-ray GRBs showing the onset of the afterglow shaped by the deceleration of the fireball due to the circumburst medium. The optically selected GRBs were used to fit a linear relation in the $\log \Gamma_0$ - $\log E_{\text{prompt}}$ plane, where Γ_0 is the initial Lorentz factor of the fireball and E_{prompt} is in units of 10^{52} erg (see Figure 5(a)). The best-fit line of the Γ_0 - E_{prompt} relation is given by

$$\log \Gamma_0 = (2.26 \pm 0.03) + (0.25 \pm 0.03) \log E_{\text{prompt}}, \quad (27)$$

with $\rho = 0.89$, $P < 10^{-4}$, and $\sigma = 0.11$ which can be measured with the deviation of the ratio $\Gamma_0/E_{\text{prompt}}^{0.25}$. It was found that most of the GRBs with a lower limit of Γ_0 are enclosed within the 2σ region represented by the dashed lines in Figure 5(a), and it was pointed out that GRBs with a tentative Γ_0 derived from RS peaks or the afterglow peaks, as well as those which lower limits of Γ_0 were derived from light curves with a single power law, are systematically above the best-fit line. The lower values of Γ_0 , obtained from a set of optical afterglow light curves with a decaying trend since the start of the detection, were compatible with this correlation.

Later, this correlation was verified by Ghirlanda et al. [165] and Lü et al. [143]. Ghirlanda et al. [165], studying the spectral evolution of 13 SGRBs detected by *Fermi*/GBM, investigated spectra resolved in the 8 keV–35 MeV energy range, and confirmed the results of Liang et al. [164].

Lü et al. [143] enlarged this sample reaching a total of 51 GRBs with spectroscopically confirmed redshifts and engaged three methods to constrain Γ_0 : (1) the afterglow onset method [166] which considers T_{peak} of the early afterglow light curve as the deceleration time of the external FS; (2) the pair opacity constraint method [167] which requires that the observed high-energy γ -rays (i.e., those in the GeV range) are optically thin to electron-positron pair production, thus leading to a lower limit on Γ_0 of the emitting region; (3) the early external forward emission method [168] where an upper limit of Γ_0 can be derived from the quiescent periods between the prompt emission pulses, in which the signal of external shock has to go down the instrument thresholds. Considering some aspects of the external shock emission, the Γ_0 - E_{prompt} correlation was statistically reanalysed using 38 GRBs with Γ_0 calculated using method (1) (as the other two provide only a range of the Lorentz factors, not a definite value), finding

$$\log \Gamma_0 = (1.96 \pm 0.002) + (0.29 \pm 0.002) \log E_{\text{prompt}}, \quad (28)$$

with $r = 0.67$, and E_{prompt} in units of 10^{52} erg. In addition, applying the beaming correction, a relation between Γ_0 and L_{iso} , using the same sample (see Figure 5(b)), was found to be

$$\log \Gamma_0 = (2.40 \pm 0.002) + (0.30 \pm 0.002) \log L_{\text{iso}}, \quad (29)$$

with $r = 0.79$ and L_{iso} in units of $10^{52} \text{ erg s}^{-1}$.

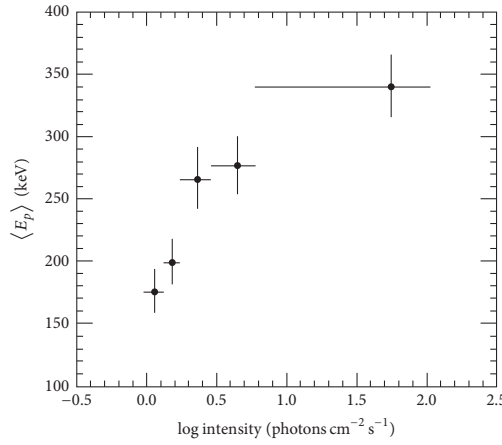


FIGURE 6: The average νF_ν peak energies as a function of intensity for five groups of GRB spectra. The vertical bars represent 1σ estimated error in the mean, where the peak energy distributions were assumed to be approximately Gaussian in logarithm of energy. The horizontal bars mark the bin widths. (Figure after Mallozzi et al. [110]; see Figure 2 therein. @ AAS. Reproduced with permission.)

Regarding the physical interpretation, Liang et al. [164] claimed that this correlation clearly shows the association of E_{prompt} with Γ_0 angular structure, and this result yielded another evidence for the fireball deceleration model. Instead, Lü et al. [143] found that this relation is well explained by a neutrino-annihilation-powered jet during the emission, indicating a high accretion rate and not very fast BH spin. Besides, evidence for a jet dominated by a magnetic field have already been presented [169–171]. From the studies of the BH central engine models it was also indicated that magnetic fields are a fundamental feature [172]. Nevertheless, the baryon loading mechanism in a strongly magnetized jet is more complex, and it has still to be fully investigated.

3.5. Correlations between the Energetics and the Peak Energy

3.5.1. The $\langle E_{\text{peak}} \rangle$ - F_{peak} and the $E_{\text{peak}}\text{-}S_{\text{tot}}$ Correlations. Mallozzi et al. [110] analysed 399 GRBs observed by BATSE and discovered a correlation between the logarithmic average peak energies $\langle E_{\text{peak}} \rangle$ and F_{peak} . Choosing as a selection criterion for the bursts $F_{\text{peak}} \geq 1 \text{ ph cm}^{-2} \text{ s}^{-1}$, they derived F_{peak} from the count rate data in 256 ms time bins in the energy band 50–300 keV and used the F_{peak} distribution derived from the Comptonized photon model (the differential photon number flux per unit energy):

$$\frac{dN}{dE} = Ae^{-E(2+\beta_S)/E_{\text{peak}}} \left(\frac{E}{E_{\text{piv}}}\right)^{\beta_S}, \quad (30)$$

with A the normalization, β_S the spectral index, and $E_{\text{piv}} = 100 \text{ keV}$. Then, they grouped the sample into 5 different width F_{peak} bins of about 80 events each (see Figure 6). The bursts

were ranked such that group 1 had the lowest peak flux values and group 5 had the highest values. They found a correlation with $\rho = 0.90$ and $P = 0.04$. Lower intensity GRBs exhibited a lower $\langle E_{\text{peak}} \rangle$.

Later, Lloyd et al. [173] examined the $E_{\text{peak}}\text{-}S_{\text{tot}}$ correlation with 1000 simulated bursts in the same energy range as Mallozzi et al. [110] and found a strong correlation between E_{peak} and S_{tot} (see Figure 7(a)). The relation between the two variables was as follows:

$$\log E_{\text{peak}} \sim 0.29 \log S_{\text{tot}}, \quad (31)$$

with the Kendall correlation coefficient [174] $\tau = 0.80$ and $P = 10^{-13}$. In addition, they compared it to the $E_{\text{peak}}\text{-}F_{\text{peak}}$ relation (see Figure 7(b)). This relation was for the whole spectral sample and consistent with earlier results [110, 175]. However, they selected a subsample composed of only the most luminous GRBs, because spectral parameters obtained from bursts near the detector threshold are not robust. Therefore, to better understand the selection effects relevant to E_{peak} and burst strength, they considered the following selection criteria: $F_{\text{peak}} \geq 3 \text{ ph cm}^{-2} \text{ s}^{-1}$, $S_{\text{obs}} \geq 10^{-6} \text{ erg cm}^{-2}$, and $S_{\text{tot}} \geq 5 \times 10^{-6} \text{ erg cm}^{-2}$. Due to the sensitivity over a certain energy band of all the detectors, especially BATSE, and to some restrictions to the trigger, the selection effects are inevitable. However, the subsample of the most luminous GRBs presents a weak $E_{\text{peak}}\text{-}F_{\text{peak}}$ correlation. Instead, a tight $E_{\text{peak}}\text{-}S_{\text{tot}}$ correlation was found for the whole sample as well as the subsample of the brightest GRBs. Lloyd et al. [173] paid more attention to the $E_{\text{peak}}\text{-}S_{\text{tot}}$ correlation for the brightest GRBs because it is easier to deal with the truncation effects in this case, and the cosmological interpretation is simpler.

This correlation has been the basis for the investigation of the Amati relation (see Section 3.5.2) and the Ghirlanda relation (see Section 3.5.3). Lloyd et al. [173] concluded that “the observed correlation can be explained by cosmological expansion alone if the total radiated energy (in the γ -ray range) is constant.” In fact, their finding does not depend on the GRB rate density or on the distribution of other parameters. However, the data from GRBs with known redshift are incompatible with a narrow distribution of radiated energy or luminosity.

Following a different approach, Goldstein et al. [176] pointed out that the ratio $E_{\text{peak}}/S_{\text{tot}}$ can serve as an indicator of the ratio of the energy at which most of the γ -rays are radiated to the total energy and claimed that the $E_{\text{peak}}\text{-}S_{\text{tot}}$ relation is a significant tool for classifying LGRBs and SGRBs. The fluence indicates the duration of the burst without providing a biased value of T_{90} and $E_{\text{peak}}/S_{\text{tot}}$ displays, as a spectral hardness ratio, an increased hardness for SGRBs in respect to LGRBs, in agreement with [10]. This correlation is quite interesting, since the energy ratio, being dependent only on the square of the luminosity distance, gets rid of the cosmological dependence for the considered quantities. Therefore, it was evaluated that the energy ratio could be used as a GRB classifier.

Later, Lu et al. [177], with the results of time-resolved spectral analysis, computed the $E_{\text{peak}}\text{-}S_{\text{tot}}$ relation for 51 LGRBs and 11 bright SGRBs observed with *Fermi*/GBM. For

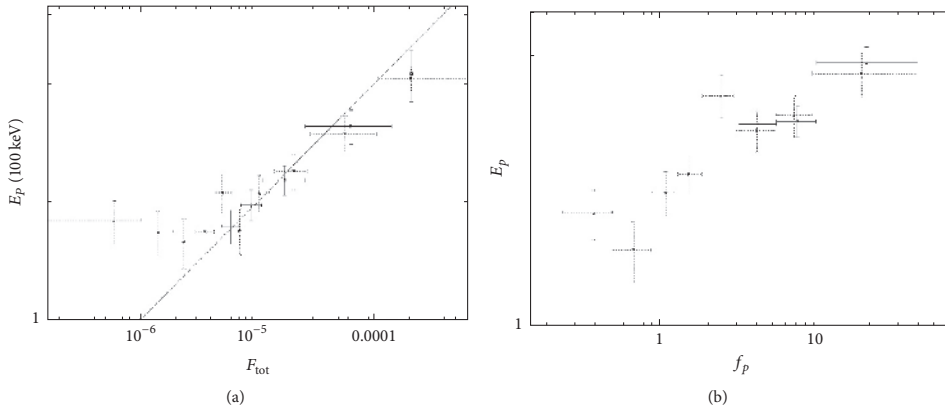


FIGURE 7: E_{peak} versus (a) S_{tot} and (b) F_{peak} distributions for the complete (dashed elements) and sub (solid elements) spectral sample. The flux suggests a tight correlation at low values, but not for the most luminous GRBs. The solid line represents a least squares fit compatible with the correlation computed by statistical methods. (Figures after Lloyd et al. [173]; see Figure 3 therein. @ AAS. Reproduced with permission.)

each GRB, they fitted a simple power law function. They measured its scatter with the distance of the data points from the best-fit line. The measured scatter of the $E_{\text{peak}}-S_{\text{tot}}$ relation is 0.17 ± 0.08 . This result was reported for the first time by Golenetskii et al. [178] and later confirmed by Borgonovo and Ryde [179]; Ghirlanda et al. [180]; Guiriec et al. [181]; Ghirlanda et al. [165].

3.5.2. The $E_{\text{peak}}-E_{\text{iso}}$ Correlation. Evidence for a correlation between E_{peak} and S_{tot} was first found by Lloyd and Petrosian [182] and Lloyd et al. [183] based on 46 BATSE events, but this relation was in the observer frame due to the paucity of the data with precise redshift measurement, as was shown in previous paragraphs. Evidence for a stronger correlation between E_{peak} and E_{iso} , also called the Amati relation, was reported by Amati et al. [111] based on a limited sample of 12 GRBs with known redshifts (9 with firm redshift and 3 with plausible values) detected by *BeppoSAX*. They found that

$$\log E_{\text{peak}} \sim (0.52 \pm 0.06) \log E_{\text{iso}}, \quad (32)$$

with $r = 0.949$, $P = 0.005$, and E_{iso} calculated as

$$E_{\text{iso}} = 4\pi D_L(z, \Omega_M, \Omega_\Lambda)^2 S_{\text{tot}} (1+z)^{-2}. \quad (33)$$

Regarding the methodology considered, instead of fitting the observed spectra, as done, for example, by Bloom et al. [184], the GRB spectra were blue-shifted to the rest frames to obtain their intrinsic form. Then, the total emitted energy is calculated by integrating the Band et al. [115] spectral model in $1-10^4$ keV energy band and scaling for the luminosity distance. This was computed employing a flat Friedmann-Lemaitre-Robertson-Walker cosmological model with $H_0 = 65 \text{ km s}^{-1} \text{ Mpc}^{-1}$, $\Omega_M = 0.3$, $\Omega_\Lambda = 0.7$ and taking into account both the cosmological time dilation and spectral redshift.

Amati et al. [185] enlarged the set of Amati et al. [111] by including 20 GRBs from *BeppoSAX* with known redshift for which new spectral data (*BeppoSAX* events) or published best-fitting spectral parameters (BATSE and *HETE-2* events) were accessible. The relation was found to be

$$\log E_{\text{peak}} = (2.07 \pm 0.03) + (0.35 \pm 0.06) \log E_{\text{iso}}, \quad (34)$$

with $r = 0.92$, $P = 1.1 \times 10^{-8}$, E_{peak} in keV and E_{iso} in units of 10^{52} erg. Therefore, its statistical significance increased, providing a correlation coefficient comparable to that obtained by Amati et al. [111], but based on a larger set.

Based on *HETE-2* measurements, Lamb et al. [186] and Sakamoto et al. [187] verified the previous results and considered also XRFs, finding out that the Amati relation remains valid over three orders of magnitude in E_{peak} and five orders of magnitude in E_{iso} . The increasing amount of GRBs with measured redshift allowed verifying this relation and strengthen its validity, as found by Ghirlanda et al. [188] with 29 events ($r = 0.803$ and $P = 7.6 \times 10^{-7}$; see Figure 9(a)).

Ghirlanda et al. [189] verified the $E_{\text{peak}}-E_{\text{iso}}$ correlation among LGRBs considering a set of 442 BATSE GRBs with measured E_{peak} and with pseudoredshifts computed via the $L_{\text{peak}}-\tau_{\text{lag}}$ correlation. It was shown that the scatter of the sample around the best-fitting line is comparable with that of another set composed of 27 GRBs with measured spectroscopic redshifts. This is because the weights of the outliers were marginal. It was noted that the relation for the 442 BATSE GRBs has a slope slightly smaller (0.47) than the one obtained for the 27 GRBs with measured spectroscopic redshifts (0.56).

Afterwards, Amati [190] (see Figures 8(a) and 8(c)) updated the study of the $E_{\text{peak}}-E_{\text{iso}}$ correlation considering a sample of 41 LGRBs/XRFs with firm values of z and E_{peak} , 12 GRBs with uncertain z and/or E_{peak} , 2 SGRBs with certain values of z and E_{peak} , and the subenergetic events

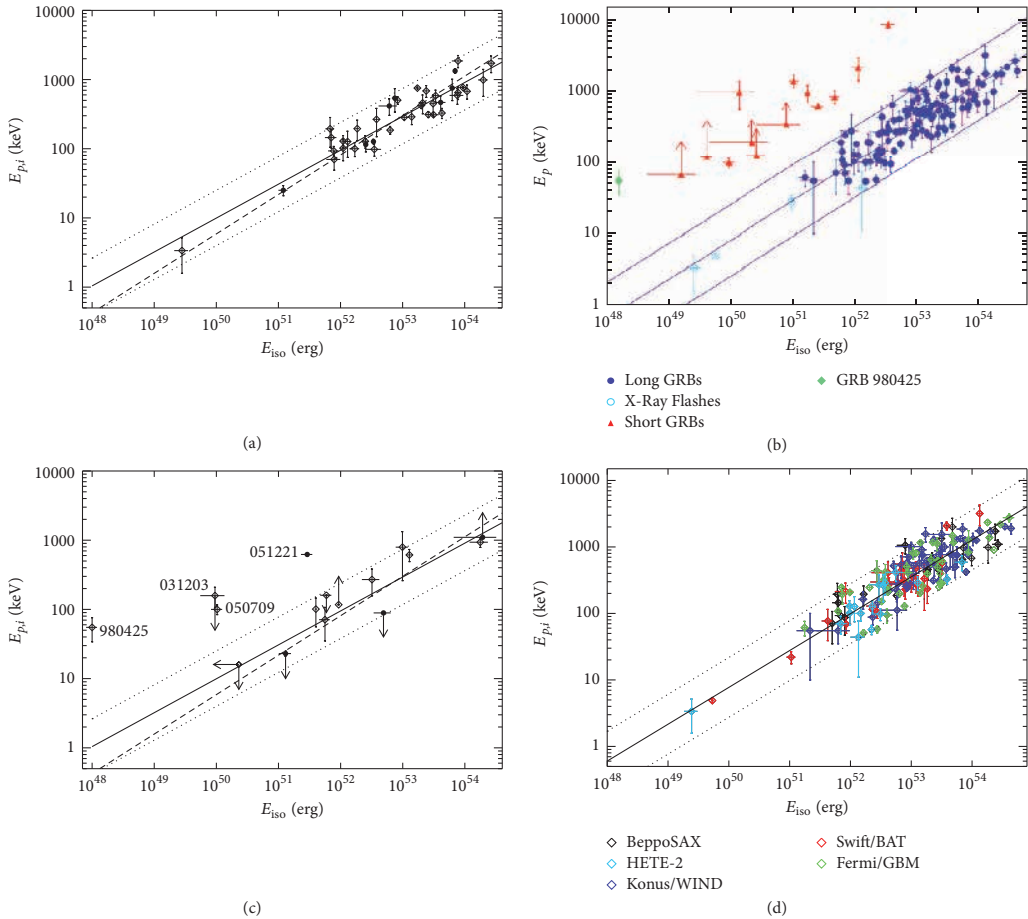


FIGURE 8: (a) $E_{\text{peak}} - E_{\text{iso}}$ distribution for 41 GRBs/XRFs with measured redshifts and E_{peak} values. Filled circles indicate *Swift* GRBs. The solid line represents the best-fit line $\log E_{\text{peak}} = 1.98 + 0.49 \log E_{\text{iso}}$; the dotted lines show the region within a vertical logarithmic deviation of 0.4. The dashed line represents the best-fit line $\log E_{\text{peak}} = 1.89 + 0.57 \log E_{\text{iso}}$ computed without taking into account the sample variance. (Figure after Amati [190]; see Figure 2 therein.) (b) The distribution of the sample in the $E_{\text{peak}} - E_{\text{iso}}$ plane. The lines indicate the best-fit line and the $\pm 2\sigma$ confidence region for LGRBs and XRFs. (Figure after Amati [193]; see Figure 4 therein. Copyright @ 2012 World Scientific Publishing Company.) (c) $E_{\text{peak}} - E_{\text{iso}}$ distribution of 12 GRBs with uncertain values of z and/or E_{peak} for the subenergetic event GRB980425 and for the two SGRBs 050709 and 051221. Filled circles represent *Swift* GRBs. The solid line is the best-fit line $\log E_{\text{peak}} = 1.98 + 0.49 \log E_{\text{iso}}$; the dotted lines mark the region within a vertical deviation in logarithmic scale of 0.4. The dashed line is the best-fit line $\log E_{\text{peak}} = 1.89 + 0.57 \log E_{\text{iso}}$ computed without taking into account the sample variance. (Figure after Amati [190]; see Figure 3 therein.) (d) The $E_{\text{peak}} - E_{\text{iso}}$ distribution for the LGRBs. The black line represents the best-fit line and, for each point, the color indicates the instrument which performed the spectral measurement. (Figure after Amati and Valle [197]; see Figure 4 therein. Copyright @ 2013 World Scientific Publishing Company.)

GRB980425/SN1998bw and GRB031203/SN2003lw. The different sets are displayed in Figure 8(b). Taking into account also the sample variance, it was found that

$$\log E_{\text{peak}} = 1.98^{+0.05}_{-0.04} + (0.49^{+0.06}_{-0.05}) \log E_{\text{iso}}, \quad (35)$$

with $\rho = 0.89$, $P = 7 \times 10^{-15}$, and units being the same as in (34). Moreover, subenergetic GRBs (980425 and possibly

031203) and SGRBs were incompatible with the $E_{\text{peak}} - E_{\text{iso}}$ relation, suggesting that it can be an important tool for distinguishing different classes of GRBs. Indeed, the increasing number of GRBs with measured z and E_{peak} can provide the most reliable evidence for the existence of two or more subclasses of outliers for the $E_{\text{peak}} - E_{\text{iso}}$ relation. Moreover, the relation is valid also for the particular subenergetic event

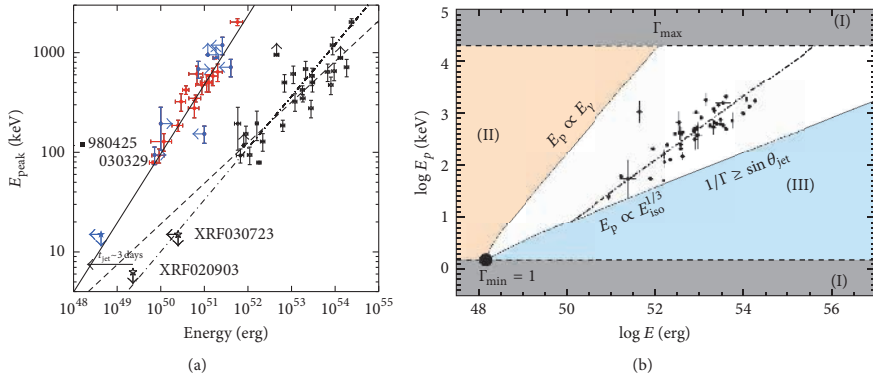


FIGURE 9: (a) E_{peak}^* - E_{γ} relation for GRBs with known redshift. The filled circles represent E_{γ} for the events where a jet break was detected. Grey symbols indicate lower/upper limits. The solid line represents the best fit, that is, $\log E_{\text{peak}} \sim 53.68 + 0.7 \log E_{\gamma}$. Open circles denote E_{iso} for the GRBs. The dashed line represents the best fit to these points and the dash-dotted line is the relation shown by Amati et al. [111]. (Figure after Ghirlanda et al. [188]; see Figure 1 therein. @ AAS. Reproduced with permission.) (b) Rest frame plane of GRB energy. The large black dot indicates that all simulated GRBs were assigned $E_{\text{peak}}^* = 1.5 \text{ keV}$ and $E_{\gamma}^* = 1.5 \times 10^{48} \text{ erg}$. Since $\Gamma > 1$ but less than 8000, regions (I) are forbidden. Since for all the simulated GRBs $\theta_{\text{jet}} \leq 90^\circ$, they cannot stay in region (II). When Γ is small, the beaming cone turns out to be larger than the jet. Therefore, the isotropic-equivalent energy is given by $\log E_{\text{iso}} = \log E_{\gamma} + \log(1 + \beta_0) + 2 \log \Gamma$, lower than the energy computed by $\log E_{\text{iso}} = \log E_{\gamma} - \log(1 - \cos \theta_{\text{jet}})$. This brings in a constraint, $\log E_{\text{peak}} \sim 1/3 \times \log E_{\text{iso}}$, and GRBs cannot lie to the right of this constraint. Hence, region (III) is not allowed. The black dots indicate the actual GRBs of the *Swift* sample. The fit to the *Swift* sample is displayed as the dot-dashed line. (Figure after Ghirlanda et al. [209]; see Figure 1 therein.)

GRB060218. Finally, the normalization considered by Amati [190] is consistent with those obtained by other instruments.

Ghirlanda et al. [191] confirmed the E_{peak}^* - E_{iso} correlation for softer events (XRFs). The sample consisted of 76 GRBs observed by several satellites, mainly *HETE-2*, *KONUS/Wind*, *Swift*, and *Fermi/GBM*. The most important outcome is a tight correlation with no new outliers (with respect to the classical GRB980425 and GRB031203) in the E_{peak}^* - E_{iso} plane. The obtained relation was

$$\log E_{\text{peak}} \sim (0.54 \pm 0.01) \log E_{\text{iso}}. \quad (36)$$

Amati et al. [192] studied 95 *Fermi* GRBs with measured z and obtained an updated E_{peak}^* - E_{iso} relation, which read

$$\log E_{\text{peak}} \sim 0.57 \log E_{\text{iso}}, \quad (37)$$

with $\rho = 0.88$ and $P < 10^{-3}$. In particular, they investigated two GRBs (080916C and 090323) with very energetic prompt emission and found that they follow the E_{peak}^* - E_{iso} relation well. On the other hand, an SGRB, 090510, also a very luminous and energetic event, was found not to obey the relation. Hence, Amati et al. [192] proposed that the correlation might serve as a discriminating factor among high-energetic GRBs. In addition, they claimed that the physics of the radiation process for really luminous and energetic GRBs is identical to that for average-luminous and soft-dim long events (XRFs), because all these groups follow the Amati relation.

Later, Amati [193] provided an update of the analysis by Amati et al. [194] with a larger sample of 120 GRBs (see

Figure 8(b)) finding it to be consistent with the following relation:

$$\log E_{\text{peak}} = 2 + 0.5 \log E_{\text{iso}}. \quad (38)$$

with units the same as in (34) and (35). Afterwards, Qin and Chen [195] analysed a sample of 153 GRBs with measured z , E_{peak} , E_{iso} , and T_{90} , observed by various instruments up to 2012 May. The distribution of the logarithmic deviation of E_{peak} from the Amati relation displayed a clear bimodality which was well represented by a mixture of two Gaussian distributions. Moreover, it was suggested to use the logarithmic deviation of the E_{peak} value for distinguishing GRBs in the E_{peak} versus E_{iso} plane. This procedure separated GRBs into two classes: the Amati type bursts, which follow the Amati relation, and the non-Amati type bursts, which do not follow it. For the Amati type bursts it was found that

$$\log E_{\text{peak}} = (2.06 \pm 0.16) + (0.51 \pm 0.12) \log E_{\text{iso}}, \quad (39)$$

with $r = 0.83$ and $P < 10^{-36}$, while, for non-Amati bursts,

$$\log E_{\text{peak}} = (3.16 \pm 0.65) + (0.39 \pm 0.33) \log E_{\text{iso}}, \quad (40)$$

with $r = 0.91$ and $P < 10^{-7}$. In both relations E_{peak} is in keV, and E_{iso} is in units of 10^{52} erg .

In addition, it was pointed out that almost all Amati type bursts are LGRBs at higher energies, as opposed to non-Amati type bursts which are mostly SGRBs. An improvement to this classification procedure is that the two types of GRBs are clearly separated; hence different GRBs can be easily classified.

Heussaff et al. [196], applying particular selection criteria for the duration and the spectral indices, obtained a set of *Fermi* GRBs and analysed their locations in the $E_{\text{peak}}\text{-}E_{\text{iso}}$ plane. The sample, composed of 43 GRBs with known redshifts, yielded the following relation:

$$\log E_{\text{peak}} = 2.07 + 0.49 \log E_{\text{iso}}, \quad (41)$$

with $\rho = 0.70$, $P = 1.7 \times 10^{-7}$, and the same units as in previous relations of this type.

Amati and Della Valle [197] pointed out that an enlarged sample of 156 LGRBs with known z and E_{peak} also follows the Amati relation with a slope ≈ 0.5 (see Figure 8(d)). Additionally, Basak and Rao [198] showed that a time-resolved Amati relation also holds within each single GRB with normalization and slope consistent with those obtained with time-averaged spectra and energetics/luminosity and is even better than the time-integrated relation [199]. Time-resolved E_{peak} and E_{iso} are obtained at different times during the prompt phase (see also [177, 180, 200] and Section 3.6).

3.5.3. The $E_{\text{peak}}\text{-}E_{\gamma}$ Correlation. The $E_{\text{peak}}\text{-}E_{\gamma}$ relation (also called the Ghirlanda relation) was first discovered by Ghirlanda et al. [188], who used 40 GRBs with z and E_{peak} known at their time of writing. Considering the time T_{break} , its value can be used to deduce E_{γ} from E_{iso} . Indeed, even if only a little less than half of the bursts have observed jet breaks (47%), from [107] we know that

$$\theta_{\text{jet}} = 0.161 \left(\frac{T_{\text{break}}}{1+z} \right)^{3/8} (n\eta_{\gamma} E_{\text{iso}})^{1/8}, \quad (42)$$

where T_{break} is measured in days, n is the density of the circumburst medium in particles per cm^3 , η_{γ} is the radiative efficiency, and E_{iso} is in units of 10^{52} erg. Here, θ_{jet} is in degrees and it is the angular radius (the half opening angle) subtended by the jet. For GRBs with no measured n , the median value $n = 3 \text{ cm}^{-3}$ of the distribution of the computed densities, extending between 1 and 10 cm^{-3} , was considered [139, 201–203].

Later, Liang and Zhang [204] using a sample of 15 GRBs with measured z , E_{peak} and T_{break} , considered a purely phenomenological T_{break}^* of the optical afterglow light curves, thus avoiding the assumption of any theoretical model, contrary to what was done by Ghirlanda et al. [188]. The functional form of this correlation is given by:

$$\begin{aligned} \log E_{\gamma} = & (0.85 \pm 0.21) + (1.94 \pm 0.17) \log E_{\text{peak}}^* \\ & - (1.24 \pm 0.23) \log T_{\text{break}}^*, \end{aligned} \quad (43)$$

where E_{γ} is in units of 10^{52} erg, E_{peak}^* in units of 100 keV, T_{break}^* is measured in days, and $\rho = 0.96$ and $P < 10^{-4}$.

Nava et al. [205] found that the Ghirlanda relation, assuming a wind-like circumburst medium, is as strong as the one considering a homogeneous medium. They analysed the discrepancy between the correlations in the observed and in the comoving frame (with Lorentz factor identical to the fireball's one). Since both E_{peak} and E_{γ} transform in the

same way, the wind-like Ghirlanda relation remains linear also in the comoving frame, no matter what the Lorentz factor's distribution is. The wind-like relation corresponds to bursts with the same number of photons emitted. Instead, for the homogeneous density medium scenario, it is common to consider a tight relation between the Lorentz factor and the total energy, thus limiting the emission models of the prompt radiation. Using 18 GRBs with firm z , E_{peak} , and T_{break} , Nava et al. [205] found for the homogeneous density case

$$\begin{aligned} \log \frac{E_{\text{peak}}^*}{100 \text{ keV}} = & 0.45^{+0.02}_{-0.03} \\ & + (0.69 \pm 0.04) \log \frac{E_{\gamma}}{2.72 \times 10^{52} \text{ erg}}, \end{aligned} \quad (44)$$

with $\rho = 0.93$ and $P = 2.3 \times 10^{-8}$. Instead, for the wind case

$$\begin{aligned} \log \frac{E_{\text{peak}}^*}{100 \text{ keV}} = & 0.48^{+0.02}_{-0.03} \\ & + (1.03 \pm 0.06) \log \frac{E_{\gamma}}{2.2 \times 10^{50} \text{ erg}}, \end{aligned} \quad (45)$$

with $\rho = 0.92$ and $P = 6.9 \times 10^{-8}$.

Ghirlanda et al. [206] tested the $E_{\text{peak}}\text{-}E_{\gamma}$ correlation using 33 GRBs (16 new bursts detected by *Swift* with firm z and E_{peak} up to December 2006, and 17 pre-*Swift* GRBs). They claimed that, for computing T_{break} , the following is required:

- (1) The detection of the jet break should be in the optical.
- (2) The optical light curve should continue up to a time longer than the T_{break} .
- (3) The host galaxy flux and the flux from a probable SN should be removed.
- (4) The break should not depend on the frequency in the optical, and a coincident break in the X-ray light curve is not necessary, because the flux in X-rays could be controlled by another feature.
- (5) The considered T_{break} should be different from the one at the end of the plateau emission (the time T_a in [81]); otherwise the feature affecting the X-ray flux is also influencing the optical one.

Therefore, considering all these restrictions, the sample was reduced to 16 GRBs, all compatible with the following $E_{\text{peak}}\text{-}E_{\gamma}$ relation:

$$\begin{aligned} \log \frac{E_{\text{peak}}}{100 \text{ keV}} = & (0.48 \pm 0.02) \\ & + (0.70 \pm 0.04) \log \frac{E_{\gamma}}{4.4 \times 10^{50} \text{ erg}}. \end{aligned} \quad (46)$$

No outliers were detected. Therefore, the reduced scatter of the $E_{\text{peak}}\text{-}E_{\gamma}$ relation corroborates the use of GRBs as standardizable candles.

3.5.4. Physical Interpretation of the Energetics versus Peak Energy Relations. Lloyd et al. [173] investigated the physical explanation of the $E_{\text{peak}}\text{-}S_{\text{tot}}$ correlation assuming the emission process to be a synchrotron radiation from internal and external shocks. Indeed, they claimed that this correlation is easily obtained considering a thin synchrotron radiation by a power law distribution of electrons with Γ larger than some minimum threshold value, Γ_m . Moreover, the internal shock model illustrates the tight $E_{\text{peak}}\text{-}S_{\text{tot}}$ relation and the emitted energy better than the external shock model.

Lloyd-Ronning and Petrosian [207] pointed out that the GRB particle acceleration is not a well analysed issue. Generally, the main hypothesis is that the emitted particles are accelerated via recurrent scatterings through the (internal) shocks. They found that the recurrent crossings of the shock come from a power law distribution of the particles with a precise index, providing a large energy synchrotron photon index. Moreover, the connection between E_{peak} and the photon flux can be justified by the variation of the magnetic field or electron energy in the emission events. Finally, they claimed that, in the majority of GRBs, the acceleration of particles is not an isotropic mechanism but occurs along the magnetic field lines.

Amati et al. [111] confirmed the findings of Lloyd et al. [183] that the $\log E_{\text{peak}} \sim 0.5 \log E_{\text{iso}}$ relation is obtained assuming an optically thin synchrotron shock model. This model considers electrons following the $N(\Gamma) = N_0 \Gamma^{-P}$ distribution for $\Gamma > \Gamma_m$ with Γ_m , GRB duration, and N_0 constant in each GRB. However, the above assumptions are not fully justifiable. In fact the duration is different in each GRB and E_{iso} might be smaller in the case of beamed emission.

Amati [190] pointed out the impact that the correlation has on the modeling of the prompt emission and on the possible unification of the two classes of GRBs and XRFs. In addition, this correlation is often applied for checking GRB synthesis models (e.g., [208, 209]).

In every model, E_{peak} and E_{iso} depend on Γ , and the $E_{\text{peak}}\text{-}E_{\text{iso}}$ relation can help to relate the parameters of the synchrotron shock model and inverse-Compton model [203, 208]. Specifically, Zhang and Mészáros [208] and Rees and Mészáros [210] found that, for an electron distribution given by a power law and produced by an internal shock in a fireball with velocity Γ , the peak energy is given as

$$\log E_{\text{peak}}^* \sim -2 \log \Gamma + 0.5 \log L - \log t_v, \quad (47)$$

where L is the total fireball luminosity and t_v is the variability timescale. However, to recover the $E_{\text{peak}}\text{-}E_{\text{iso}}$ relation from this relation, Γ and t_v should be similar for each GRB, a condition that cannot be easily supported. A further issue arises when one considers that $L \propto \Gamma^N$, with N between 2 and 3 in different models [203, 208, 211]. An explanation could be that direct or Comptonized thermal radiation from the fireball photosphere [208, 210–219] can affect significantly the GRB prompt emission. This can be a good interpretation of the really energetic spectra presented for many events [220–222] and the flat shape in GRB average spectra. In such cases, E_{peak} depends on the peak temperature $T_{bb,\text{peak}}$ of photons distributed as by a blackbody, and therefore it is associated

with the luminosity or emitted energy. For Comptonized radiation from the photosphere the relations are

$$\log E_{\text{peak}} \sim \log \Gamma + \log T_{bb,\text{peak}} \sim 2 \log \Gamma - 0.25 \log L \quad (48)$$

or

$$\begin{aligned} \log E_{\text{peak}} &\sim \log \Gamma + \log T_{bb,\text{peak}} \\ &\sim -0.5 \log r_0 + 0.25 \log L, \end{aligned} \quad (49)$$

where r_0 is a particular distance between the central engine and the energy radiating area, such that the Lorentz factor evolves as $\Gamma \approx r/r_0$ up to some saturation radius r_s [210]. As suggested by Rees and Mészáros [210], in this scenario the $E_{\text{peak}}\text{-}E_{\text{iso}}$ relation could be recovered for particular physical cases just underneath the photosphere, though it would rely on an undefined number of unknown parameters.

Also for high-energetic GRBs (i.e., $E_{\text{iso}} \approx 10^{55}$ erg) the nonthermal synchrotron emission model can explain the $E_{\text{peak}}\text{-}E_{\text{iso}}$ correlation. This can be possible by considering either the minimum Lorentz factor and the normalization of the power law distribution of the emitting electrons constant in each GRB or constraints on the slope of the relation between Γ and the luminosity [183, 208].

Panaiteescu [223] used 76 GRBs with measured redshifts to analyse the case in which the $E_{\text{peak}}\text{-}E_{\text{iso}}$ relation for LGRBs is due to the external shock generated by a relativistic outflow interacting with the ambient medium. He considered the effect of each parameter defining the $E_{\text{peak}}\text{-}E_{\text{iso}}$ relation on the radial distribution of the external medium density and pointed out that the $\log E_{\text{peak}} \sim 0.5 \log E_{\text{iso}}$ relation is recovered if the external medium is radially stratified. For some combinations of radiative (synchrotron or inverse-Compton) and dissipation (such as RS or FS) mechanisms, it is concluded that the external medium requires a particle density distributed distinctly from R^{-2} , with R being the distance at which the GRB radiation is generated. This tendency should be commonly associated with uniform mass-loss rate and final velocity.

Mochkovitch and Nava [224] checked whether the $E_{\text{peak}}\text{-}E_{\text{iso}}$ relation can be recovered in a case when the prompt emission is due to internal shocks, or alternatively if the correlation can give some limits for the internal shock scenario defined through the impact of only two shells. Simulated GRB samples were obtained considering different model parameter distributions, such as the emitted power in the relativistic emission and Γ . Simulated $E_{\text{peak}}\text{-}E_{\text{iso}}$ distributions were plotted for each case and analysed together with the observed relation (based on 58 GRBs). The sample contained only luminous *Swift* GRBs with $F_{\text{peak}} > 2.6 \text{ ph cm}^{-2} \text{ s}^{-1}$ in the 15–150 keV energy band. In conclusion, a correspondence between the model and data was found, but exclusively if the following restrictions for the dynamics of the emission and for the dispersion of the energy are assumed:

- (1) The majority of the dispersed energy should be radiated in few electrons.
- (2) The spread between the highest and the lowest Lorentz factor should be small.

- (3) If the mean Lorentz factor grows as $\bar{\Gamma} \propto \dot{E}^{1/2}$ (where \dot{E} is the rate of injected energy, or mean emitted power, in the relativistic outflow), the $E_{\text{peak}}-E_{\text{iso}}$ relation is not retrieved and E_{peak} is diminishing with larger E_{iso} . However, the $E_{\text{peak}}-E_{\text{iso}}$ relation can be regained if $\bar{\Gamma} \propto \dot{E}^{1/2}$ is a lower constraint for a particular \dot{E} .
- (4) When the timescale or the width of the variability of the Lorentz factor is associated with $\bar{\Gamma}$, $E_{\text{peak}}-E_{\text{iso}}$ relation is recovered.

For the Ghirlanda relation [188], with the assumption that the line of sight is within the jet angle, the $E_{\text{peak}}-E_{\gamma}$ relation indicates its invariance when moving from the rest frame to the comoving frame. As a result, the number of radiated photons in each GRBs is comparable and should be about 10^{57} . The last characteristic could be important for understanding the dynamics of GRBs and the radiative mechanisms (see also Figure 9(b)).

Collazzi et al. [225] found that the mean E_{peak}^* is near to 511 keV, the electron rest-mass energy $m_e c^2$. Therefore, it is claimed that the tight shape of the E_{peak} distribution does not stem only from selection effects. No studied mechanism can drive this effect; however, with the E_{peak}^* compatible with the effective temperature of the γ -ray radiating area, the almost constant temperature needs some mechanism similar to a thermostat, keeping the temperature at a steady value. It was suggested that such a mechanism could be an electron-positron annihilation.

Ghirlanda et al. [209], using a simulated sample, analysed if different intrinsic distributions of Γ and θ_{jet} can replicate a grid of observational constraints. With the assumption that, in the comoving frame each GRB has similar E_{peak} and E_{γ} , it was found that the distributions of Γ and θ_{jet} cannot be power laws. Instead, the highest concordance between simulation and data is given by log-normal distributions and a connection between their maxima, like $\theta_{\text{jet,max}}^{2.5} \Gamma_{\text{max}} = \text{const}$. In this work θ_{jet} and Γ are important quantities for the calculation of the GRB energetics. Indeed, from a sample of ≈ 30 GRBs with known θ_{jet} or Γ it was found that the E_{γ} distribution is centered at $10^{50}-10^{51}$ erg and it is tightly related to E_{peak} . It was obtained that

$$\log E_{\text{peak}} \sim \log \frac{E_{\gamma}}{5 - 2\beta_0}. \quad (50)$$

Present values of Γ and θ_{jet} rely on incomplete data sets and their distributions could be affected by biases. Nevertheless, Ghirlanda et al. [209] claimed that greater values of Γ are related to smaller θ_{jet} values; that is, the faster a GRB, the narrower its jet.

Furthermore, GRBs fulfilling the condition $\sin \theta_{\text{jet}} < 1/T$ might not display any jet break in the afterglow light curve, and Ghirlanda et al. [209] predicted that this group should comprise $\approx 6\%$ of the on-axis GRBs. Finally, their work is crucial as it allowed finding that the local rate of GRBs is $\approx 0.3\%$ of the local SNe Ib/c rate and $\approx 4.3\%$ of the local hypernovae(i.e., SNe Ib/c with wide-lines) rate.

3.6. Correlations between the Luminosity and the Peak Energy

3.6.1. The $L_{\text{iso}}-E_{\text{peak}}$ Correlation. The $L_{\text{iso}}-E_{\text{peak}}$ relation was discovered by Schaefer [203] who used 84 GRBs with known E_{peak} from the BATSE catalogue [121] and 20 GRBs with luminosities based on optically measured redshift [111, 226]. It was found that (see Figure 10) for the 20 GRBs

$$\log E_{\text{peak}} \sim (0.38 \pm 0.11) \log L_{\text{iso}}, \quad (51)$$

with $r = 0.90$ and $P = 3 \times 10^{-8}$, and among the 84 GRBs the relation was

$$\log E_{\text{peak}} \sim (0.36 \pm 0.03) \log L_{\text{iso}}. \quad (52)$$

The underlying idea is that L_{iso} varies as a power of Γ , as we have already discussed in Section 3.1.2, and E_{peak} also varies as some other power of Γ , so that E_{peak} and L_{iso} will be correlated to each other through their dependence on Γ . For the general case where the luminosity varies as Γ^N and E_{peak} varies as Γ^M , and therefore $\log E_{\text{peak}}$ will vary as $(M + 1)/N \times \log L_{\text{iso}}$.

Frontera et al. [200], using a sample of 9 GRBs detected simultaneously with the Wide Field Camera (WFC) on board the *BeppeSAX* satellite and by the BATSE instrument, reported the results of a systematic study of the broadband (2–2000 keV) time-resolved prompt emission spectra. However, only 4 of those GRBs (970111, 980329, 990123, 990510) were bright enough to allow a fine time-resolved spectral analysis, resulting in a total of 40 spectra. Finally, the study of the time-resolved dependence (see also the end of Section 3.5.2) of E_{peak} on the corresponding L_{iso} was possible for two bursts with known redshift (i.e., 990123 and 990510) and found using the least squares method (see Figure 11):

$$\log E_{\text{peak}}^* \sim (0.66 \pm 0.03) \log L_{\text{iso}}, \quad (53)$$

with $\rho = 0.94$ and $P = 1.57 \times 10^{-13}$.

Afterwards, Nava et al. [227], using a sample of 46 *Swift* GRBs with measured z and E_{peak} , found a strong $L_{\text{iso}}-E_{\text{peak}}$ correlation, with a functional form of

$$\log E_{\text{peak}}^* = -(25.33 \pm 3.26) + (0.53 \pm 0.06) \log L_{\text{iso}}, \quad (54)$$

with $\rho = 0.65$ and $P = 10^{-6}$; E_{peak} is in keV and L_{iso} is in units of 10^{51} erg s $^{-1}$. Furthermore, using 12 GRBs with only an upper limit on z (3 events) or no redshift at all (3 events), or with a lower limit on E_{peak} (3 events) or no estimate at all (3 events), they found that these bursts also obey the obtained $L_{\text{iso}}-E_{\text{peak}}$ relation.

3.6.2. The $L_{\text{peak}}-E_{\text{peak}}$ Correlation. It was also found that the Amati relation holds even if E_{iso} is substituted with L_{iso} and L_{peak} , which is not surprising given that these “energy indicators” are strongly correlated. To this end, the Yonetoku correlation ([116], see Figure 12(a)) relates E_{peak} with L_{peak} . The relation was obtained employing 11 GRBs with known redshifts detected by BATSE, together with *BeppeSAX* GRBs from [111]. This relation uses L_{peak} of the burst instead of L_{iso} ,

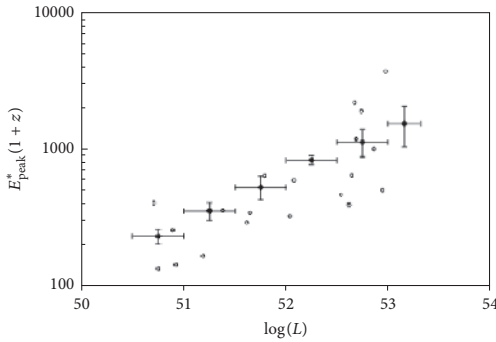


FIGURE 10: Direct fit of $\log L_{\text{iso}} - \log E_{\text{peak}}$ data. This is shown here for two independent data sets for which the luminosities are derived by two independent methods. The first data set consists of 20 bursts with spectroscopically measured redshifts (the open circles). The second one is for 84 bursts (whose binned values are shown as filled diamonds, and the horizontal bars are the bin widths) whose luminosity (and then redshift) were determined with the spectral lag and variability light curve parameters. Both data sets show a highly significant and similar power law relations. (Figure after Schaefer [203]; see Figure 3 therein. @ AAS. Reproduced with permission.)

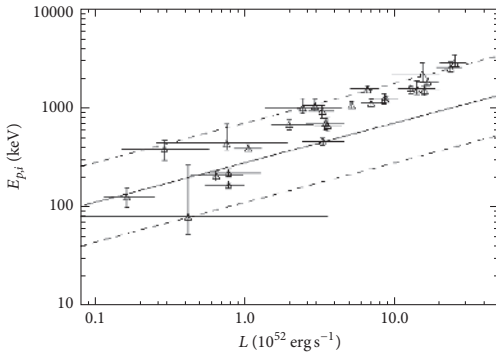


FIGURE 11: E_{peak}^* versus L_{iso} , obtained from data for GRBs 990123 and 990510. The solid line is the best-fit power law. (Figure after Frontera et al. [200]; see Figure 6 therein. @ AAS. Reproduced with permission.)

and it is tighter than previous prompt correlations. The best-fit line is given by

$$\log L_{\text{peak}} \sim (2.0 \pm 0.2) \log E_{\text{peak}}^*, \quad (55)$$

with $r = 0.958$, $P = 5.31 \times 10^{-9}$, and the uncertainties are 1 σ error. This relation agrees well with the standard synchrotron model [183, 208]. Finally, it has been used to estimate pseudoredshifts of 689 BATSE LGRBs with unknown distances and to derive their formation rate as a function of z .

Ghirlanda et al. [228] selected 36 bright SGRBs detected by BATSE, with an F_{peak} on the 64 ms timescale in the

50–300 keV energy range exceeding $10 \text{ ph cm}^{-2} \text{ s}^{-1}$. In 7 cases, the signal-to-noise-ratio was too low to reliably constrain the spectral best-fit parameters. One case yielded missing data. Hence, the sample consisted of 28 events. Due to unknown redshifts, E_{peak}^* , E_{iso} , and L_{peak} were expressed as functions of the redshift in the range $z \in [0.001, 10]$. It was found that SGRBs are unlikely to obey the Amati relation, $E_{\text{iso}} - E_{\text{peak}}^*$, but the results were consistent with the $L_{\text{peak}} - E_{\text{peak}}^*$ relation of Yonetoku et al. [116]. Hence, assuming that this relation indeed holds for SGRBs, their pseudoredshifts were estimated and found to have a similar distribution as LGRBs, with a slightly smaller average redshift.

Afterwards, Yonetoku et al. [229] investigated the prompt emission of 101 GRBs with measured redshifts and a reported F_{peak} detected until the end of 2009. The sample comes from events detected in a number of independent missions: the satellites used for this purpose are *KONUS*, *Swift*, *HXD-WAM*, and *RHESSI*. Using this data set, the $E_{\text{peak}} - L_{\text{peak}}$ correlation was revised, and its functional form could be written as

$$\begin{aligned} \log L_{\text{peak}} &= (52.43 \pm 0.037) \\ &+ (1.60 \pm 0.082) \log E_{\text{peak}}^*, \end{aligned} \quad (56)$$

with $r = 0.889$ for 99 degrees of freedom and an associated $P = 2.18 \times 10^{-35}$; L_{peak} is expressed in erg s^{-1} and E_{peak}^* in units of 355 keV. To provide reference to previous works, the 1–10⁴ keV energy band in the GRB rest frame was used to calculate the bolometric energy and L_{peak} . Finally, it was demonstrated that this relation is intrinsic to GRBs and affected by the truncation effects imposed by the detector threshold.

Lu and Liang [230], using time-resolved spectral data for a sample of 30 pulses in 27 bright GRBs detected by BATSE, investigated the $L_{\text{peak}} - E_{\text{peak}}$ relation in the decay phases of these pulses (see Figure 12(b)). Quite all of the pulses followed a narrow $L_{\text{peak}} - E_{\text{peak}}$ relation given by

$$\log L_{\text{peak}} \sim (1.42 \pm 0.03) \log E_{\text{peak}}^*, \quad (57)$$

with $r = 0.91$ and $P < 10^{-4}$, but the power law index varied. The statistical or observational effects could not account for the large scatter of the power law index, and it was suggested to be an intrinsic feature, indicating that no relation common for all GRB pulses $L_{\text{peak}} - E_{\text{peak}}$ would be expected. However, in the light of *Fermi* observations that revealed deviations from the Band function ([181, 231–234]; see also [235]), it was proposed recently that the GRB spectra should be modeled not with the Band function itself (constituting a nonthermal component), but with additional blackbody (BB, thermal) and power law (PL, nonthermal) components [216, 218, 219, 236]. The nonthermal component was well described within the context of synchrotron radiation from particles in the jet, while the thermal component was interpreted by the emission from the jet photosphere. The PL component was claimed to originate most likely from the inverse-Compton process. The results point toward a universal relation between L_{peak} and E_{peak}^* related to the nonthermal components.

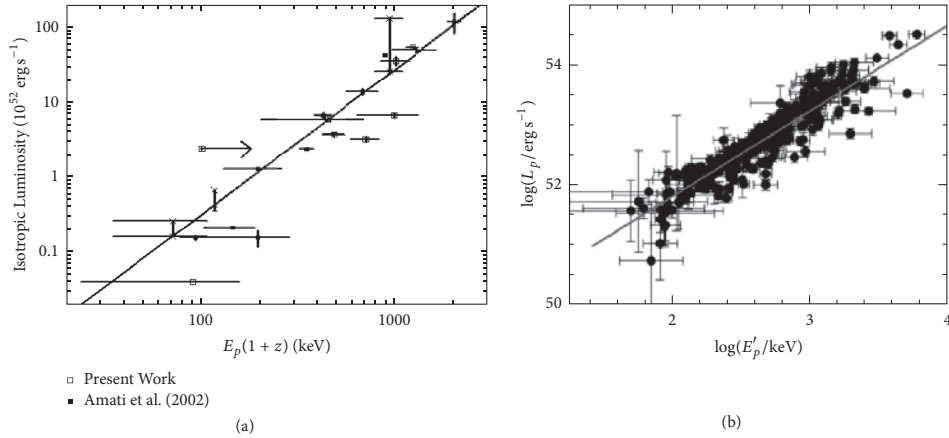


FIGURE 12: (a) The $\log L_{\text{peak}}$ - $\log E_{\text{peak}}$ relation. The open squares mark the BATSE data. *BeppeSAX* events, which are converted into the energy range of 30–10000 keV, are shown as filled squares and the cross points. The solid line indicates the best-fit line. (Figure after Yonetoku et al. [116]; see Figure 1 therein. @ AAS. Reproduced with permission.) (b) $\log L_{\text{peak}}$ versus $\log E_{\text{peak}}$ for 276 time-resolved spectra within the decay pulses for the sample. The solid line stands for the best fit to the data. (Figure after Lu and Liang [230]; see Figure 4 therein. Copyright @ 2010 Springer.)

Tsutsui et al. [237] analysed 13 SGRB candidates (i.e., an SGRB with $T_{90}^* < 2$ s), from among which they selected 8 events considering them as secure ones. An SGRB candidate is regarded as a misguided SGRB if it is located within the $3\sigma_{\text{int}}$ dispersion region from the best-fit E_{peak}^* - E_{iso} function of the correlation for LGRBs, while the others are regarded as secure SGRBs. The relation obtained with secure GRBs is the following:

$$\log L_{\text{peak}} = (52.29 \pm 0.066) + (1.59 \pm 0.11) \log E_{\text{peak}}^*, \quad (58)$$

with $r = 0.98$ and $P = 1.5 \times 10^{-5}$, where E_{peak}^* (in units of 774.5 keV) is from the time-integrated spectrum, while L_{peak} (in erg s^{-1}) was taken as the luminosity integrated for 64 ms at the peak considering the shorter duration of SGRBs. Application of this relation to 71 bright BATSE SGRBs resulted in pseudoredshifts distributed in the range $z \in [0.097, 2.258]$, with $\langle z \rangle = 1.05$, which is apparently lower than $\langle z \rangle = 2.2$ for LGRBs. Finally, Yonetoku et al. [238], using 72 SGRBs with well determined spectral features as observed by BATSE, determined their pseudoredshifts and luminosities by employing the L_{peak}^* - E_{peak} correlation for SGRBs found by Tsutsui et al. [237]. It was found that the obtained redshift distribution for $z \leq 1$ was in agreement with that of 22 *Swift* SGRBs, indicating the reliability of the redshift determination via the E_{peak}^* - L_{peak} relation.

3.6.3. Physical Interpretation of the Luminosity versus Peak Energy Relations. As pointed out by Schaefer et al. [121] and Schaefer [203], E_{peak} and L_{iso} are correlated because of their dependence on Γ . The L_{iso}^* - E_{peak} relation could shed light on the structure of the ultrarelativistic outflow, the

shock acceleration, and the magnetic field generation [239]. However, since only few SGRBs are included in the samples used, the correlations and interpretations are currently only applicable to LGRBs.

Schaefer et al. [121] and Schaefer [203] claimed that the values of E_{peak} are approximately constant for all the bursts with $z \geq 5$. However, with the launch of the *Swift* satellite in the end of 2004 the hunt for “standard candles” via a number of GRB correlations is still ongoing. Thus, the great challenge is to find universal constancy in some GRB parameters, despite the substantial diversity exhibited by their light curves. If this goal is achieved, GRBs might prove to be a useful cosmological tool [240].

Liang et al. [241] defined a parameter $\omega = (L_{\text{iso}}/10^{52} \text{ erg s}^{-1})^{0.5}/(E_{\text{peak}}/200 \text{ keV})$ and discussed possible implications of the E_{peak}^* - L_{iso} relation for the fireball models. They found that ω is limited to the range ≈ 0.1 –1. They constrained some parameters, such as the combined internal shock parameter, ζ_i , for the internal as well as external shock models, with an assumption of uncorrelated model parameters. Their distributions suggest that the production of prompt γ -rays within internal shocks dominated by kinetic energy is in agreement with the standard internal shock model. Similarly in case when the γ -rays come from external shocks dominated by magnetic dissipation. These results imply that both models can provide a physical interpretation of the $L_{\text{iso}} \propto E_{\text{peak}}^2$ relation as well as the parameter ω .

To explain the origin of this correlation, Mendoza et al. [242] considered simple laws of mass and linear momentum conservation on the emission surface to give a full description of the working surface flow parameterized by the initial velocity and mass injection rate. They assumed a source-ejecting matter in a preferred direction x with

a velocity $v(t)$ and a mass ejection rate $\dot{m}(t)$, both dependent on time t as measured from the jet's source; that is, they studied the case of a uniform release of mass and the luminosity was measured considering simple periodic oscillations of the particle velocity, a common assumption in the internal shock model scenario.

Due to the presence of a velocity shear with a considerable variation in Γ at the boundary of the spine and sheath region, a fraction of the injected photons is accelerated via a Fermi-like acceleration mechanism such that a high-energy power law tail is formed in the resultant spectrum. Ito et al. [243] showed in particular that if a velocity shear with a considerable variance in Γ is present, the high-energy part of the observed GRB photon spectrum can be explained by this photon acceleration mechanism. The accelerated photons may also account for the origin of the extra hard power law component above the bump of the thermal-like peak seen in some peculiar GRBs (090510, 090902B, 090926A). It was demonstrated that time-integrated spectra can also reproduce the low energy spectra of GRBs consistently due to a multitemperature effect when time evolution of the outflow is considered.

Regarding the Yonetoku relation, its implications are related to the GRB formation rate and the luminosity function of GRBs. In fact, the analysis of Yonetoku et al. [116] showed that the existence of the luminosity evolution of GRBs, assuming as a function a simple power law dependence on the redshift, such as $g(z) = (1 + z)^{1.85}$, may indicate the evolution of GRB progenitor itself (mass) or the jet evolution. To study the evolution of jet-opening angle they considered two assumptions: either the maximum jet-opening angle decreases or the total jet energy increases. In the former case, the GRB formation rate obtained may be an underestimation since the chance probability of observing the high-redshift GRBs will decrease. If so, the evolution of the ratio of the GRB formation rate to the star formation rate becomes more rapid. On the other hand, in the latter case, GRB formation rate provides a reasonable estimate.

Recently Frontera et al. [244], building on the spectral model of the prompt emission of Titarchuk et al. [245], gave a physical interpretation of the origin of the time-resolved $L_{\text{iso}}\text{-}E_{\text{peak}}$ relation. The model consists of an expanding plasma shell, result of the star explosion, and a thermal bath of soft photons. Frontera et al. [244] showed analytically that in the asymptotic case of the optical depth $\tau \gg 1$ the relation $\log L_{\text{iso}}\text{-}\log E_{\text{peak}}$ indeed has a slope of $1/2$. This, in turn, is evidence for the physical origin of the Amati relation (see Section 3.5.2).

3.7. Comparisons between $E_{\text{peak}}\text{-}E_{\text{iso}}$ and $E_{\text{peak}}\text{-}L_{\text{peak}}$ Correlation. For a more complete dissertation we compare the $E_{\text{peak}}\text{-}E_{\text{iso}}$ correlation with the $E_{\text{peak}}\text{-}L_{\text{peak}}$ correlation. To this end, Ghirlanda et al. [246] derived the $E_{\text{peak}}\text{-}L_{\text{peak}}$ relation with a sample of 22 GRBs with known z and well determined spectral properties. This relation has a slope of 0.51, similar to the one proposed by Yonetoku et al. [116] with 12 GRBs, although its scatter is much larger than the one originally found.

Tsutsui et al. [247] investigated these two relations using only data from the prompt phase of 33 low-redshift GRBs with $z \leq 1.6$. In both cases the correlation coefficient was high, but a significant scatter was also present. Next, a partial linear correlation degree, which is the degree of association between two random variables, was found to be $\rho_{L_{\text{peak}}, E_{\text{iso}}, E_{\text{peak}}} = 0.38$. Here, $\rho_{1,2,3}$ means the correlation coefficient between the first and the second parameter after fixing the third parameter. This fact indicates that two distance indicators may be independent from each other even if they are characterized by the same physical quantity, E_{peak} , and similar quantities, L_{peak} and E_{iso} . To correct the large dispersion of the Yonetoku correlation, Tsutsui et al. [247] introduced a luminosity time constant T_L defined by $T_L = E_{\text{iso}}/L_{\text{peak}}$ as a third parameter and a new correlation was established in the following form:

$$\begin{aligned} \log L_{\text{peak}} = & (-3.87 \pm 0.19) + (1.82 \pm 0.08) \log E_{\text{peak}} \\ & - (0.34 \pm 0.09) \log T_L, \end{aligned} \quad (59)$$

with $r = 0.94$ and $P = 10^{-10}$. Here, L_{peak} is in units of $10^{52} \text{ ergs}^{-1}$, E_{peak} is in keV, and T_L in seconds. In this way the systematic errors were reduced by about 40%, and the plane represented by this correlation might be regarded as a “fundamental plane” of GRBs.

Later, Tsutsui et al. [248] reconsidered the correlations among E_{peak} , L_{peak} , and E_{iso} , using the database constructed by Yonetoku et al. [229], which consisted of 109 GRBs with known redshifts, and E_{peak} , L_{peak} , and E_{iso} well determined. The events are divided into two groups by their data quality. One (gold data set) consisted of GRBs with E_{peak} determined by the Band function with four free parameters. GRBs in the other group (bronze data set) had relatively poor energy spectra so that their E_{peak} were determined by the Band function with three free parameters (i.e., one spectral index was fixed) or by the cut-off power law (CPL) model with three free parameters. Using only the gold data set, the intrinsic dispersion, σ_{int} , in $\log L_{\text{peak}}$, is 0.13 for the $E_{\text{peak}}\text{-}T_L\text{-}L_{\text{peak}}$ correlation and 0.22 for the $E_{\text{peak}}\text{-}L_{\text{peak}}$ correlation. In addition, GRBs in the bronze data set had systematically larger E_{peak} than expected by the correlations constructed with the gold data set. This indicates that the quality of the sample is an important issue for the scatter of correlations among E_{peak} , L_{peak} , and E_{iso} .

The difference between the $E_{\text{peak}}\text{-}L_{\text{peak}}$ correlation for LGRBs from [180] and the one from [229] is due to the presence of GRB060218. In the former, it was considered an ordinary LGRB, while, in the latter, it was considered an outlier by a statistical argument. Because GRB060218 is located far from the $L_{\text{peak}}\text{-}E_{\text{peak}}$ correlation in [229] (more than 8σ), it makes the best-fit line much steeper.

Regarding the high-energetic GRBs, Ghirlanda et al. [180] considered 13 GRBs detected by *Fermi* up to the end of July 2009 and with known redshift. They found a tight relation:

$$\log E_{\text{peak}}^* \sim 0.4 \log L_{\text{iso}}, \quad (60)$$

with a scatter of $\sigma = 0.26$. A similarly tight relation exists between E_{peak}^* and E_{iso} :

$$\log E_{\text{peak}}^* \sim 0.5 \log E_{\text{iso}}. \quad (61)$$

The time-integrated spectra of 8 *Fermi* GRBs with measured redshift were consistent with both the $E_{\text{peak}}\text{-}E_{\text{iso}}$ and the $E_{\text{peak}}\text{-}L_{\text{iso}}$ correlations defined by 100 pre-*Fermi* bursts.

Regarding the study of SGRBs within the context of these two correlations, Tsutsui et al. [237] used 8 SGRBs out of 13 SGRB candidates to check whether the $E_{\text{peak}}\text{-}E_{\text{iso}}$ and $E_{\text{peak}}\text{-}L_{\text{peak}}$ correlations exist for SGRBs as well. It was found that the $E_{\text{peak}}\text{-}E_{\text{iso}}$ correlation seemed to hold in the following form:

$$\log E_{\text{iso}} = (51.42 \pm 0.15) + (1.58 \pm 0.28) \log E_{\text{peak}}^*, \quad (62)$$

with $r = 0.91$, $P = 1.5 \times 10^{-3}$, E_{iso} in erg s^{-1} and E_{peak}^* in units of 774.5 keV . They also found that the $E_{\text{peak}}\text{-}L_{\text{peak}}$ correlation with a functional form as in (58) is tighter than the $E_{\text{peak}}\text{-}E_{\text{iso}}$ one. Both correlations for SGRBs indicate that they are less luminous than LGRBs, for the same E_{peak} , by factors ≈ 100 (for $E_{\text{peak}}\text{-}E_{\text{iso}}$) and ≈ 5 (for $E_{\text{peak}}\text{-}L_{\text{peak}}$). It was the first time that the existence of distinct $E_{\text{peak}}\text{-}E_{\text{iso}}$ and $E_{\text{peak}}\text{-}L_{\text{peak}}$ correlations for SGRBs was argued.

3.8. The $L_{X,p}\text{-}T_p^*$ Correlation and Its Physical Interpretation. Using data gathered by *Swift*, Willingale et al. [81] proposed a unique phenomenological function to estimate some relevant parameters of both the prompt and afterglow emission. Both components are well fitted by the same functional form:

$$f_i(t) = \begin{cases} F_i e^{\alpha_i(1-t/T_i)} e^{-t_i/t}, & t < T_i, \\ F_i \left(\frac{t}{T_i}\right)^{-\alpha_i} e^{-t_i/t}, & t \geq T_i. \end{cases} \quad (63)$$

The index i can take the values p or a to indicate the prompt and afterglow, respectively. The complete light curve, $f_{\text{tot}}(t) = f_p(t) + f_a(t)$, is described by two sets of four parameters each: $\{T_i, F_i, \alpha_i, t_i\}$, where α_i is the temporal power law decay index, the time t_i is the initial rise timescale, F_i is the flux, and T_i is the break time. Figure 13 schematically illustrates this function.

Following the same approach as adopted in [131], Qi and Lu [249] investigated the prompt emission properties of 107 GRB light curves detected by the XRT instrument onboard the *Swift* satellite in the X-ray energy band (0.3–10 keV). They found that there is a correlation between $L_{X,p}$ and T_p^* . Among the 107 GRBs, they used only 47, because some of the events did not have a firm redshift and some did not present reliable spectral parameters in the prompt decay phase. Among the 47 GRBs, only 37 had $T_p^* > 2$ s, and 3 of them had $T_p^* > 100$ s.

The functional form for this correlation could be written in the following way:

$$\log L_{X,p} = a + b \log T_p^*, \quad (64)$$

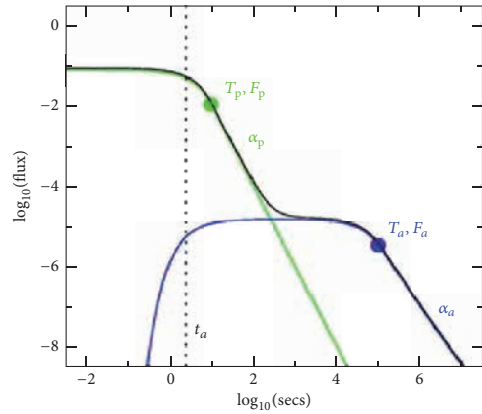


FIGURE 13: Functional form of the decay and the fitted parameters. The prompt component (green curve) has no rise because time zero is set at the peak. The afterglow component (blue curve) rises at time T_a as shown. (Figure after Willingale et al. [81]; see Figure 1 therein. © AAS. Reproduced with permission.)

where $L_{X,p}$ is in erg s^{-1} and T_p^* is in seconds. The fits were performed via the D'Agostini [153] fitting method applied to the following data sets:

- (1) The total sample of 47 GRBs (see Figure 14(a))
- (2) 37 GRBs with $T_p^* > 2$ s (see Figure 14(b))
- (3) 34 GRBs with $2 \text{ s} < T_p^* < 100$ s (see Figure 14(c))

The results of these fittings turned out to give different forms of (64). In case (1), $a = 50.91 \pm 0.23$ and $b = -0.89 \pm 0.19$ were obtained. The slope b is different in cases (2) and (3), $b = -1.73$ and $b = -0.74$, respectively. The best fit with the smallest σ_{int} comes from case (3). Remarkably, in this case the slope b is close to the slope $(-0.74^{+0.20}_{-0.19})$ of a similar $\log L_X\text{-}\log T_p^*$ relation [131].

Qi and Lu [249] noticed a broken linear relation of the $L_{X,p}\text{-}T_p^*$ correlation. More specifically, an evidence of curvature appears in Figure 14(b). One can see, from Figure 14(a), that if the best-fit line is extended to the range of $T_p^* < 2$ s, all the GRBs with $T_p^* < 2$ s are located below this line. However, the small sample of GRBs used in their analysis is still not sufficient to conclude whether the change in the slope is real or just a selection bias caused by outliers. If there is a change in the slope this may suggest that GRBs could be classified into two groups, long and short, based on their values of T_p^* instead of T_{90} , since T_p^* is an estimate of the GRB duration based on temporal features of the light curves and T_{90} is a measure based on the energy. This idea has actually been proposed for the first time by O'Brien and Willingale [250]. It is worth noting that while T_{90} and T_p are both estimates of the GRB duration, the correlation does not hold if T_p is replaced with T_{90} . For an analysis of an extended sample and comparison of T_{45} versus T_p also, see [251].

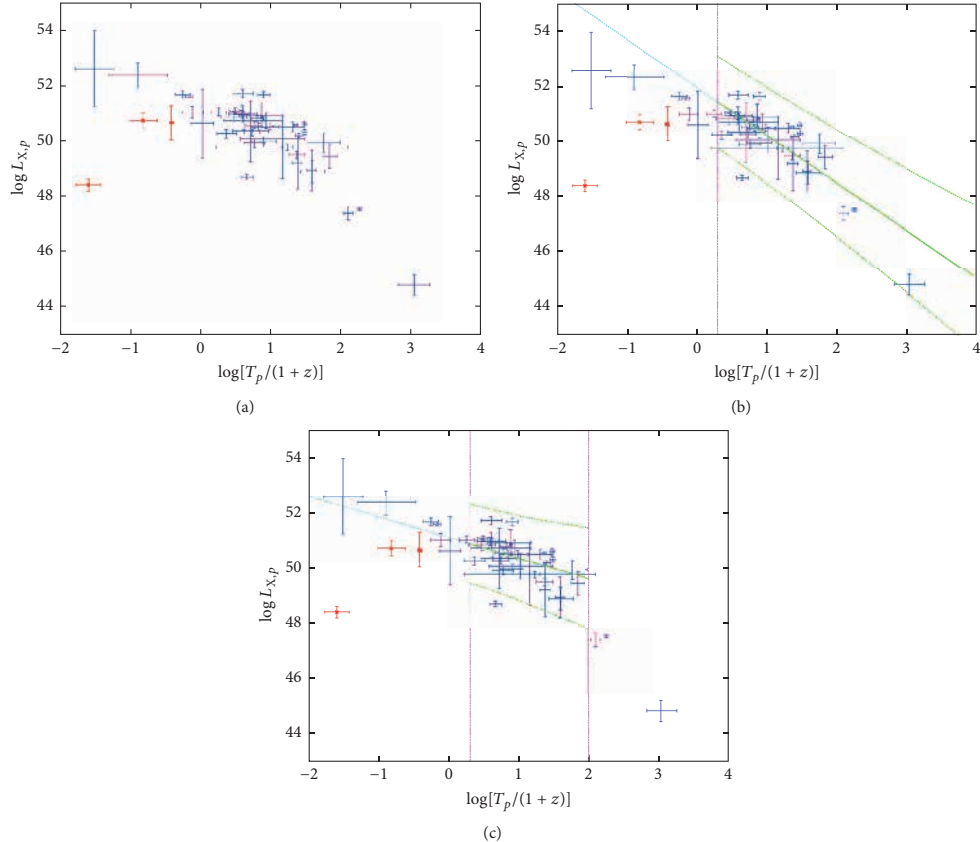


FIGURE 14: (a) $\log L_{X,p}$ (in erg s^{-1}) versus $\log T_p^*$ (in s) for the whole sample of 47 GRBs. The red dots represent SGRBs (i.e., $T_{90} < 2$ s). (Figure after Qi and Lu [249]; see Figure 1 therein. @ AAS. Reproduced with permission.) (b) Best fit of the $\log L_{X,p}$ (in erg s^{-1}) versus $\log T_p^*$ (in s) relation following equation (64) and the corresponding 2σ confidence region. Only GRBs with $T_p^* > 2$ s are included in the fit. (Figure after Qi and Lu [249]; see Figure 2 therein. @ AAS. Reproduced with permission.) (c) Best fit of the $\log L_{X,p}$ (in erg s^{-1}) versus $\log T_p^*$ (in s) relation following equation (64) and the corresponding 2σ confidence region. In this case only the 34 GRBs with $2 < T_p^* < 100$ s are included in the fit. (Figure after Qi and Lu [249]; see Figure 3 therein. @ AAS. Reproduced with permission.)

Regarding the physical interpretation, the change of the slope in the $L_{X,p}$ - T_p^* relation at different values of T_p^* in [249] can be due to the presence of few GRBs with a large T_p^* , but it might also be due to different emission mechanisms. Unfortunately, the paucity of the sample prevents putting forward any conclusion due to the presence of (potential) outliers in the data set. A more detailed analysis is necessary to further validate this correlation and better understand its physical interpretation.

3.9. The L_f - T_f Correlation and Its Physical Interpretation. In most GRBs a rapid decay phase (RDP) soon after the prompt emission is observed [89], and this RDP appears to continue

smoothly after the prompt, in terms of both temporal and spectral variations [86]. This indicates that the RDP could be the prompt emission's tail and a number of models have been proposed to take it into account (see [88]), in particular the high latitude emission (HLE). This model states that once the prompt emission from a spherical shell turns off at some radius, then the photons reach the observer from angles apparently larger (relative to the line of sight) due to the added path length caused by the curvature of the emitting region. The Doppler factor of these late-arriving photons is smaller.

A successful attempt to individually fit all the distinct pulses in the prompt phase and in the late X-ray flares observed by the complete *Swift*/BAT + XRT light curves has been performed by Willingale et al. [108] using a physically

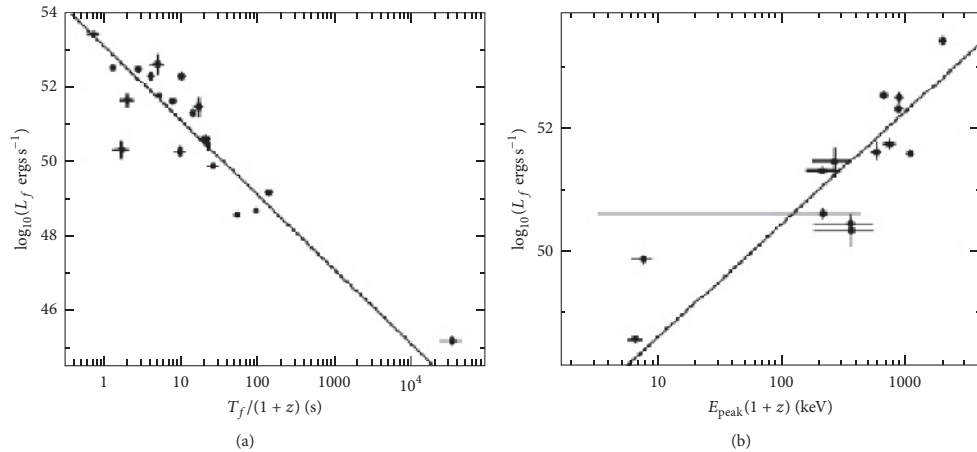


FIGURE 15: (a) L_f (in erg s^{-1}) versus T_f^* . (b) L_f (in erg s^{-1}) versus E_{peak} . (Figures after Willingale et al. [108]; see Figure 16 therein.)

motivated pulse profile. This fitting is an improved procedure compared to the Willingale et al. [81] one. The pulse profile has the following functional form:

$$P = \left\{ \left[\min \left(\frac{T - T_{\text{ej}}}{T_f}, 1 \right)^{\alpha+2} - \left(\frac{T_f - T_{\text{rise}}}{T_f} \right)^{\alpha+2} \right] \cdot \left[1 - \left(\frac{T_f - T_{\text{rise}}}{T_f} \right)^{\alpha+2} \right]^{-1} \right\} \left(\frac{T - T_{\text{ej}}}{T_f} \right)^{-1}, \quad (65)$$

where $T_0 = T_f - T_{\text{rise}}$ (with T_{rise} the rise time of the pulse) is the arrival time of the first photon emitted from the shell. It is assumed here that the emission comes from an ultrarelativistic thin shell spreading over a finite range of radii along the line of sight, in the observer frame measured with respect to the ejection time, T_{ej} . From these assumptions it is possible to model the rise of the pulse through α , T_{rise} , and T_f (see also Figure 1).

The combination of the pulse profile function $P(t, T_f, T_{\text{rise}})$ and the blue shift of the spectral profile $B(x)$ produces the rise and fall of the pulse. $B(x)$ is approximated with the Band function in the following form:

$$B(x) = B_{\text{norm}} \times \begin{cases} x^{(\alpha-1)} e^{-x}, & x \leq \alpha - \beta, \\ x^{(\beta-1)} (\alpha - \beta)^{(\alpha-\beta)} e^{-(\alpha-\beta)}, & x > \alpha - \beta, \end{cases} \quad (66)$$

where $x = (E/E_f)[(T - T_{\text{ej}})/T_f]^{-1}$, with E_f being the energy at the spectral break, and B_{norm} is the normalization.

Using this motivated pulse profile, Willingale et al. [108] found that, within a sample of 12 GRBs observed by *Swift* in

the BAT and XRT energy bands, L_f is anticorrelated with T_f^* in the following way:

$$\log L_f \sim -(2.0 \pm 0.2) \log T_f^*. \quad (67)$$

Therefore, high-luminosity pulses occur shortly after ejection, while low-luminosity pulses appear at later time (see Figure 15(a)). Moreover, Willingale et al. [108] also found a correlation between L_f and E_{peak} as shown in Figure 15(b). This is in agreement with the known correlation between L_{peak} for the whole burst and E_{peak} of the spectrum during the time T_{90} [116, 237]; for comparison with the $L_{\text{peak}}-E_{\text{peak}}$ correlation, see also Section 3.6.2.

In the 12 light curves considered by Willingale et al. [108], 49 pulses were analysed. Although several pulses with a hard peak could not be correctly fitted, the overall fitting to the RDP was satisfactory and the HLE model was shown to be able to take into account phase of the GRB emission. However, it is worth mentioning the hard pulse in GRB061121 which requires a spectral index $\beta_S = 2.4$, larger than the value expected for synchrotron emission, that is, $\beta_S = 1$.

Lee et al. [252] and Quilligan et al. [253] discussed analogous correlations, although these authors considered the width of a pulse rather than T_f , which is in fact closely correlated with pulse width. Many authors afterwards [254–264] have used the motivated pulse profile of Willingale et al. [108] for various studies on the prompt emission properties of the pulses.

Regarding the physical interpretation, in [108], the flux density of each prompt emission pulse is depicted by an analytical expression derived under the assumption that the radiation comes from a thin shell, as we have already described. The decay after the peak involves the HLE [265] along the considered shell which is delayed and modified with a different Doppler factor due to the curvature of the surface [266, 267].

4. Summary

In this work we have reviewed the bivariate correlations among a number of GRB prompt phase parameters and their characteristics. It is important to mention that several of these correlations have the problem of double truncation which affects the parameters. Some relations have also been tested to prove their intrinsic nature like the $E_{\text{peak}}\text{-}S_{\text{tot}}$, $E_{\text{peak}}\text{-}E_{\text{iso}}$, and $L_{\text{peak}}\text{-}E_{\text{peak}}$ relations. For the others, we are not aware of their intrinsic forms and consequently how far the use of the observed relations can influence the evaluation of the theoretical models and the “best” cosmological settings. Therefore, the evaluation of the intrinsic correlations is crucial for the determination of the most plausible model to explain the prompt emission. In fact, though there are several theoretical interpretations describing each correlation, in many cases more than one is viable, thus showing that the emission processes that rule GRBs still need to be further investigated. These correlations might also serve as discriminating factors among different GRB classes, as several of them hold different forms for SGRBs and LGRBs, hence providing insight into the generating mechanisms. Hopefully those correlations could lead to new standard candles allowing exploring the high-redshift universe.

Conflicts of Interest

The authors declare that they have no conflicts of interest.

Acknowledgments

M. Tarnopolski acknowledges support in a form of a special scholarship of Marian Smoluchowski Scientific Consortium “Matter-Energy-Future” from KNOW funding, Grant no. KNOW/48/SS/PC/2015. The work of R. Del Vecchio was supported by the Polish National Science Centre through Grant DEC-2012/04/A/ST9/00083.

References

- [1] E. Nakar, “Short-hard gamma-ray bursts,” *Physics Reports*, vol. 442, no. 1–6, pp. 166–236, 2007.
- [2] B. Zhang, “Open questions in GRB physics,” *Comptes Rendus Physique*, vol. 12, no. 3, pp. 206–225, 2011.
- [3] N. Gehrels and S. Razzaque, “ γ -ray bursts in the swift-Fermi era,” *Frontiers of Physics*, vol. 8, no. 6, pp. 661–678, 2013.
- [4] E. Berger, “Short-duration gamma-ray bursts,” *Annual Review of Astronomy and Astrophysics*, vol. 52, no. 1, pp. 43–105, 2014.
- [5] P. Kumar and B. Zhang, “The physics of gamma-ray bursts and relativistic jets,” *Physics Reports*, vol. 561, pp. 1–109, 2015.
- [6] P. Mészáros and M. J. Rees, “Gamma-ray bursts,” *General Relativity and Gravitation*.
- [7] R. W. Klebesadel, I. B. Strong, and R. A. Olson, “Observations of gamma-ray bursts of cosmic origin,” *The Astrophysical Journal*, vol. 182, pp. L85–L88, 1973.
- [8] E. P. Mazets, S. V. Golenetskii, V. N. Il'inskii et al., “Catalog of cosmic gamma-ray bursts from the KONUS experiment data—parts I and II,” *Astrophysics and Space Science*, vol. 80, no. 1, pp. 3–83, 1981.
- [9] C. Meegan, G. Fishman, R. Wilson et al., “The spatial distribution of gamma-ray bursts observed by BATSE,” in *Proceedings of the Compton Gamma-Ray Observatory*, pp. 681–685, USA.
- [10] C. Kouveliotou, C. A. Meegan, G. J. Fishman et al., “Identification of two classes of gamma-ray bursts,” *The Astrophysical Journal*, vol. 413, no. 2, pp. 101–104, 1993.
- [11] B. Paczynski, “On the Galactic origin of gamma-ray bursts,” *Acta Astron*, vol. 348, pp. 485–494, 1990.
- [12] B. Paczynski, “Cosmological gamma-ray bursts,” *Acta Astronomica*, vol. 41:0, pp. 257–267, 1991.
- [13] G. J. Fishman, “ γ -ray bursts,” *Annual Review of Astronomy and Astrophysics*, vol. 33, no. 1, pp. 415–458.
- [14] M. S. Briggs, W. S. Paciesas, G. N. Pendleton et al., “BATSE observations of the large-scale isotropy of gamma-ray bursts,” *The Astrophysical Journal*, vol. 459, p. 40, 1996.
- [15] M. R. Metzger, S. G. Djorgovski, S. R. Kulkarni et al., “Spectral constraints on the redshift of the optical counterpart to the γ -ray burst of 8 May 1997,” *Nature*, vol. 387, no. 6636, pp. 878–880, 1997.
- [16] L. G. Balazs, A. Meszaros, and I. Horvath, “Anisotropy of the sky distribution of gamma-ray bursts,” p. 339, 0 1–6, 339, November 1998.
- [17] A. Mészáros, Z. Bagoly, I. Horváth, L. G. Balázs, and R. Vavrek, “A remarkable angular distribution of the intermediate subclass of gamma-ray bursts,” *The Astrophysical Journal*, vol. 539, no. 1, pp. 98–101, 2000.
- [18] A. Mészáros, Z. Bagoly, and R. Vavrek, “On the existence of the intrinsic anisotropies in the angular distributions of gamma-ray bursts,” *Astronomy & Astrophysics*, vol. 354, no. 1, pp. 1–6, 2000.
- [19] A. Mészáros and J. Štöček, “Anisotropy in the angular distribution of the long gamma-ray bursts?” *Astronomy & Astrophysics*, vol. 403, no. 2, pp. 443–448, 2003.
- [20] M. Magliocchetti, G. Ghirlanda, and A. Celotti, “Evidence for anisotropy in the distribution of short-lived gamma-ray bursts,” *Monthly Notices of the Royal Astronomical Society*, vol. 343, no. 1, pp. 255–258, 2003.
- [21] A. Bernui, I. S. Ferreira, and C. A. Wuensche, “On the large-scale angular distribution of short gamma-ray bursts,” *The Astrophysical Journal*, vol. 673, no. 2, pp. 968–971, 2008.
- [22] R. Vavrek, L. G. Balázs, A. Mészáros, I. Horváth, and Z. Bagoly, “Testing the randomness in the sky-distribution of gamma-ray bursts,” *Monthly Notices of the Royal Astronomical Society*, vol. 391, no. 4, pp. 1741–1748, 2008.
- [23] M. Tarnopolski, “Testing the anisotropy in the angular distribution of Fermi/GBM gamma-ray bursts,” *Monthly Notices of the Royal Astronomical Society*, vol. 472, no. 4, pp. 4819–4831, 2017.
- [24] A. Mészáros, L. G. Balázs, Z. Bagoly, and P. Veres, “Impact on cosmology of the celestial anisotropy of the short gamma-ray bursts,” *Baltic Astronomy*, vol. 18, no. 3–4, pp. 293–296, 2009.
- [25] J. Hjorth, J. Sollerman, P. Möller et al., “A very energetic supernova associated with the γ -ray burst of 29 March 2003,” *Nature*, vol. 423, no. 6942, pp. 847–850, 2003.
- [26] D. Malesani, G. Tagliaferri, G. Chincarini et al., “SN 2003lw and GRB 031203: a bright supernova for a faint gamma-ray burst,” *The Astrophysical Journal*, vol. 609, no. 1, pp. L5–L8, 2004.
- [27] S. E. Woosley and J. S. Bloom, “The supernova-gamma-ray burst connection,” *Annual Review of Astronomy and Astrophysics*, vol. 44, pp. 507–556, 2006.
- [28] M. Sparre, J. Sollerman, J. P. U. Fynbo et al., “Spectroscopic evidence for SN 2010ma associated with GRB 101219B,” *The Astrophysical Journal Letters*, vol. 735, no. 1, p. L24, 2011.

- [29] S. Schulze, D. Malesani, A. Cucchiara et al., “GRB 120422A/SN 2012bz: bridging the gap between low- and high-luminosity gamma-ray bursts,” *Astronomy & Astrophysics*, vol. 566, article A102, 2014.
- [30] D. Eichler, M. Livio, T. Piran, and D. N. Schramm, “Nucleosynthesis, neutrino bursts and γ -rays from coalescing neutron stars,” *Nature*, vol. 340, no. 6229, pp. 126–128, 1989.
- [31] R. Narayan, B. Paczyński, and T. Piran, “Gamma-ray bursts as the death throes of massive binary stars,” *The Astrophysical Journal*, vol. 395, no. 2, pp. 83–86, 1992.
- [32] E. Nakar and T. Piran, “Outliers to the peak energy-isotropic energy relation in gamma-ray bursts,” *Monthly Notices of the Royal Astronomical Society*, vol. 360, no. 1, pp. L73–L76, 2005.
- [33] B. Zhang, B.-B. Zhang, F. J. Virgili et al., “Discerning the physical origins of cosmological gamma-ray bursts based on multiple observational criteria: the cases of $z = 6.7$ GRB 080913, $z = 8.2$ GRB 090423, and some short/hard GRBs,” *The Astrophysical Journal*, vol. 703, no. 2, pp. 1696–1724, 2009.
- [34] B. P. Abbott, R. Abbott, T. D. Abbott et al., “Observation of gravitational waves from a binary black hole merger,” *Physical Review Letters*, vol. 116, no. 6, 061102, 16 pages, 2016.
- [35] V. Connaughton, E. Burns, A. Goldstein et al., “Fermi GBM observations of ligo gravitational-wave event GW150914,” *The Astrophysical Journal Letters*, vol. 826, no. 1, article no. L6, 2016.
- [36] P. N. Bhat, C. A. Meegan, A. Von Kienlin et al., “The third fermi gbm gamma-ray burst catalog: the first six years,” *The Astrophysical Journal Supplement Series*, vol. 223, no. 2, article no. 28, 2016.
- [37] V. Savchenko, C. Ferrigno, S. Mereghetti et al., “Integral upper limits on gamma-ray emission associated with the gravitational wave event gw150914,” *The Astrophysical Journal Letters*, vol. 820, no. 2, article no. L36, 2016.
- [38] P. A. Evans, J. A. Kennea, S. D. Barthelmy et al., “Swift follow-up of the gravitational wave source GW150914,” *MNRAS Letters*, vol. 460, no. 1, pp. L40–L44, 2016.
- [39] M. Lyutikov, “Fermi GBM signal contemporaneous with GW150914—an unlikely association”
- [40] X. Li, F.-W. Zhang, Q. Yuan et al., “Implications of the tentative association between gw150914 and a fermi-gbm transient,” *The Astrophysical Journal Letters*, vol. 827, no. 1, article no. L16, 2016.
- [41] A. Loeb, “Electromagnetic counterparts to black hole mergers detected by ligo,” *The Astrophysical Journal Letters*, vol. 819, no. 2, article no. L21, 2016.
- [42] R. Perna, D. Lazzati, and B. Giacomazzo, “Short gamma-ray bursts from the merger of two black holes,” *The Astrophysical Journal Letters*, vol. 821, no. 1, article no. L18, 2016.
- [43] B. J. Morsony, J. C. Workman, and D. M. Ryan, “Modeling the afterglow of the possible Fermi-GBM event associated with GW150914,” *The Astrophysical Journal Letters*, vol. 825, no. 2, article no. L24, 2016.
- [44] E. Costa, F. Frontera, J. Heise et al., “Discovery of an X-ray afterglow associated with the γ -ray burst of 28 February 1997,” *Nature*, vol. 387, no. 6635, pp. 783–785, 1997.
- [45] J. van Paradijs, P. J. Groot, T. Galama et al., “Transient optical emission from the error box of the γ -ray burst of 28 february 1997,” *Nature*, vol. 386, no. 6626, pp. 686–689, 1997.
- [46] I. Horváth, “A third class of gamma-ray bursts?” *The Astrophysical Journal*, vol. 508, no. 2, pp. 757–759, 1998.
- [47] I. Horváth, “A further study of the BATSE Gamma-Ray Burst duration distribution,” *Astronomy & Astrophysics*, vol. 392, no. 3, pp. 791–793, 2002.
- [48] I. Horváth, L. G. Balázsz, Z. Bagoly, and P. Veres, “Classification of Swift’s gamma-ray bursts,” *Astronomy & Astrophysics*, vol. 489, no. 1, pp. L1–L4, 2008.
- [49] I. Horváth, “Classification of BeppoSAX’s gamma-ray bursts,” *Astrophysics and Space Science*, vol. 323, no. 1, pp. 83–86, 2009.
- [50] D. Huja, A. Mészáros, and J. Řípa, “A comparison of the gamma-ray bursts detected by BATSE and Swift,” *Astronomy & Astrophysics*, vol. 504, no. 1, pp. 67–71, 2009.
- [51] J. Řípa, A. Mészáros, C. Wigger, D. Huja, R. Hudec, and W. Hajdas, “Search for gamma-ray burst classes with the RHESSI satellite,” *Astronomy & Astrophysics*, vol. 498, no. 2, pp. 399–406, 2009.
- [52] S. Mukherjee, E. D. Feigelson, G. J. Babu, F. Murtagh, C. Fraley, and A. Raftery, “Three types of gamma-ray bursts,” *The Astrophysical Journal*, vol. 508, no. 1, pp. 314–327, 1998.
- [53] I. Horváth, L. G. Balázsz, Z. Bagoly, F. Ryde, and A. Mészáros, “A new definition of the intermediate group of gamma-ray bursts,” *Astronomy & Astrophysics*, vol. 447, no. 1, pp. 23–30, 2006.
- [54] I. Horváth, Z. Bagoly, L. G. Balázsz, A. De Ugarte Postigo, P. Veres, and A. Mészáros, “Detailed classification of swift’s gamma-ray bursts,” *The Astrophysical Journal*, vol. 713, no. 1, pp. 552–557, 2010.
- [55] P. Veres, Z. Bagoly, I. Horváth, A. Mészáros, and L. G. Balázsz, “A distinct peak-flux distribution of the third class of gamma-ray bursts: a possible signature of X-ray flashes?” *The Astrophysical Journal*, vol. 725, no. 2, pp. 1955–1964, 2010.
- [56] C. Koen and A. Bere, “On multiple classes of gamma-ray bursts, as deduced from autocorrelation functions or bivariate duration/hardness ratio distributions,” *Monthly Notices of the Royal Astronomical Society*, vol. 420, no. 1, pp. 405–415, 2012.
- [57] H. Zitouni, N. Guessoum, W. J. Azzam, and R. Mochkovitch, “Statistical study of observed and intrinsic durations among BATSE and Swift/BAT GRBs,” *Astrophysics and Space Science*, vol. 357, no. 1, 2015.
- [58] M. Tarnopolski, “Analysis of Fermi gamma-ray burst duration distribution,” *Astronomy and Astrophysics*, vol. 581, 2015.
- [59] M. Tarnopolski, “Analysis of gamma-ray burst duration distribution using mixtures of skewed distributions,” *Monthly Notices of the Royal Astronomical Society*, vol. 458, no. 2, pp. 2024–2031, 2016.
- [60] M. Tarnopolski, “Analysis of the observed and intrinsic durations of gamma-ray bursts with known redshift,” *Astrophysics and Space Science*, vol. 361, no. 3, article no. 125, 2016.
- [61] M. Tarnopolski, “Analysis of the observed and intrinsic durations of Swift/BAT gamma-ray bursts,” *New Astronomy*, vol. 46, pp. 54–59, 2016.
- [62] O. Bromberg, E. Nakar, T. Piran, and R. Sari, “Short versus long and collapsars versus non-collapsars: a quantitative classification of gamma-ray bursts,” *The Astrophysical Journal*, vol. 764, no. 2, article 179, 2013.
- [63] M. Tarnopolski, “On the limit between short and long GRBs,” *Astrophysics and Space Science*, vol. 359, no. 1, 2015.
- [64] H. Gao, Y. Lu, and S. N. Zhang, “A new class of γ -ray bursts from stellar disruptions by intermediate-mass black holes,” *The Astrophysical Journal*, vol. 717, no. 1, pp. 268–276, 2010.
- [65] J. P. Norris and J. T. Bonnell, “Short gamma-ray bursts with extended emission,” *The Astrophysical Journal*, vol. 643, no. 1, article 266, 2006.
- [66] M. Boer, B. Gendre, and G. Stratta, “Are ultra-long gamma-ray bursts different?” *The Astrophysical Journal*, vol. 800, no. 1, article no. 16, 2015.

- [67] F. J. Virgili, C. G. Mundell, V. Pal'Shin et al., "GRB 091024A and the nature of ultra-long gamma-ray bursts," *The Astrophysical Journal*, vol. 778, no. 1, article 54, 2013.
- [68] B.-B. Zhang, B. Zhang, K. Murase, V. Connaughton, and M. S. Briggs, "How long does a burst burst?" *The Astrophysical Journal*, vol. 787, no. 1, article 66, 2014.
- [69] A. J. Levan, N. R. Tanvir, R. L. C. Starling et al., "A new population of ultra-long duration gamma-ray bursts," *The Astrophysical Journal*, vol. 781, no. 1, article 13, 2014.
- [70] A. J. Levan, "Swift discoveries of new populations of extremely long duration high energy transient," *Journal of High Energy Astrophysics*, vol. 7, pp. 44–55, 2015.
- [71] J. Heise, J. I. Zand, R. M. Kippen, and P. M. Woods, "X-ray flashes and X-ray rich gamma ray bursts," *Gamma-Ray Bursts in the Afterglow Era*, pp. 16–21, 2001.
- [72] R. M. Kippen, P. M. Woods, J. Heise, J. I. Zand, R. D. Preece, and M. S. Briggs, "BATSE observations of fast X-ray transients detected by BeppoSAX-WFC," in *Gamma-ray Bursts in the Afterglow Era*, E. Costa, F. Frontera, and J. Hjorth, Eds., p. 22, 2001.
- [73] D. Grupe, J. A. Nousek, P. Veres, B.-B. Zhang, and N. Gehrels, "Evidence for new relations between gamma-ray burst prompt and x-ray afterglow emission from 9 years of swift," *The Astrophysical Journal Supplement Series*, vol. 209, no. 2, article no. 20, 2013.
- [74] J. P. U. Fynbo, D. Watson, C. C. Thöne et al., "No supernovae associated with two long-duration γ -ray bursts," *Nature*, vol. 444, no. 7122, pp. 1047–1049, 2006.
- [75] M. Della Valle, D. Malesani, J. S. Bloom et al., "Hypernova signatures in the late rebrightening of GRB 050525A," *The Astrophysical Journal Letters*, vol. 642, no. 2, pp. L103–L106, 2006.
- [76] D. A. Perley, N. R. Tanvir, J. Hjorth et al., "The swift GRB host galaxy legacy survey. ii. rest-frame near-ir luminosity distribution and evidence for a near-solar metallicity threshold," *The Astrophysical Journal*, vol. 817, no. 1, article no. 8, 2016.
- [77] J. Greiner, P. A. Mazzali, and D. A. Kann, "A very luminous magnetar-powered supernova associated with an ultra-long γ -ray burst," *Nature*, vol. 523, no. 7559, pp. 189–192, 2015.
- [78] R. A. M. J. Wijers, M. J. Rees, and P. Mészáros, "Shocked by GRB 970228: the afterglow of a cosmological fireball," *Monthly Notices of the Royal Astronomical Society*, vol. 288, no. 4, pp. L51–L56, 1997.
- [79] P. Mészáros, "Theoretical models of gamma-ray bursts," in *Proceedings of the Gamma-Ray BURSTS*, pp. 647–656, Huntsville, Alabama (USA).
- [80] P. Mészáros, "Gamma-ray bursts," *Reports on Progress in Physics*.
- [81] R. Willingale, P. T. O'Brien, J. P. Osborne et al., "Testing the standard fireball model of gamma-ray bursts using late X-ray afterglows measured by Swift," *The Astrophysical Journal*, vol. 662, no. 2 I, pp. 1093–1110, 2007.
- [82] A. Melandri, C. G. Mundell, S. Kobayashi et al., "The early-time optical properties of gamma-ray burst afterglows," *The Astrophysical Journal*, vol. 686, no. 2, pp. 1209–1230, 2008.
- [83] E. S. Rykoff, F. Aharonian, and C. W. Akerlof, "Looking into the fireball: Rotse-III and Swift observations of early gamma-ray burst afterglows," *The Astrophysical Journal*, vol. 702, no. 1, p. 489, 2009.
- [84] S. R. Oates, M. J. Page, P. Schady et al., "A statistical comparison of the optical/UV and X-ray afterglows of gamma-ray bursts using the swift ultraviolet optical and X-ray telescopes," *Monthly Notices of the Royal Astronomical Society*, vol. 412, no. 1, pp. 561–579, 2011.
- [85] N. Gehrels, G. Chincarini, P. Giommi et al., "The swift gamma-ray burst mission," *The Astrophysical Journal*, vol. 611, pp. 1005–1020, August 2004.
- [86] P. T. O'Brien, R. Willingale, J. Osborne et al., "The early X-ray emission from GRBs," *The Astrophysical Journal Letters*, vol. 647, no. 2, pp. L123–L127, 2006.
- [87] T. Sakamoto, J. E. Hill, R. Yamazaki et al., "Evidence of exponential decay emission in the gamma-ray bursts," *The Astrophysical Journal*, vol. 669, no. 2, pp. 1115–1129, 2007.
- [88] B.-B. Zhang, E. N.-W. Liang, and B. Zhang, "A comprehensive analysis of Swift XRT data. I. Apparent spectral evolution of gamma-ray burst X-ray tails," *The Astrophysical Journal*, vol. 666, no. 2 I, pp. 1002–1011, 2007.
- [89] J. A. Nousek, C. Kouveliotou, and D. Grupe, "Evidence for a canonical gamma-ray burst afterglow light curve in the Swift XRT Data," *The Astrophysical Journal*, vol. 642, no. 1, pp. 389–400, 2006.
- [90] A. Cucchiara, A. J. Levan, D. B. Fox et al., "A photometric redshift of $z \sim 9.4$ for GRB 090429B," *The Astrophysical Journal*, vol. 736, no. 1, article 7, 2011.
- [91] S. A. Rodney, A. G. Riess, D. M. Scolnic et al., "Erratum: Two SNe Ia at redshift ~ 2 : Improved classification and redshift determination with medium-band infrared imaging," *The Astronomical Journal*, vol. 151, no. 2, 2016.
- [92] H. Lin, X. Li, S. Wang, and Z. Chang, "Are long gamma-ray bursts standard candles?" *Monthly Notices of the Royal Astronomical Society*, vol. 453, no. 1, pp. 128–132, 2015.
- [93] T. Totani, "Cosmological gamma-ray bursts and evolution of galaxies," *The Astrophysical Journal*, vol. 486, no. 2, pp. L71–L74.
- [94] C. Porciani and P. Madau, "On the association of gamma-ray bursts with massive stars: Implications for number counts and lensing statistics," *The Astrophysical Journal*, vol. 548, no. 2, pp. 522–531, 2001.
- [95] V. Bromm and A. Loeb, "High-redshift γ -ray bursts from population III progenitors," *The Astrophysical Journal*, vol. 642, no. 1 I, pp. 382–388, 2006.
- [96] M. D. Kistler, H. Yüksel, J. F. Beacom, A. M. Hopkins, and J. S. B. Wyithe, "The star formation rate in the reionization era as indicated by gamma-ray bursts," *The Astrophysical Journal*, vol. 705, no. 2, pp. L104–L108, 2009.
- [97] R. S. De Souza, N. Yoshida, and K. Ioka, "Populations III.1 and III.2 gamma-ray bursts: constraints on the event rate for future radio and X-ray surveys," *Astronomy & Astrophysics*, vol. 533, article A32, 2011.
- [98] R. Barkana and A. Loeb, "Gamma-ray bursts versus quasars: Ly α signatures of reionization versus cosmological infall," *The Astrophysical Journal*, vol. 601, no. 1 I, pp. 64–77, 2004.
- [99] K. Ioka and P. Mészáros, "Radio afterglows of gamma-ray bursts and hypernovae at high redshift and their potential for 21 centimeter absorption studies," *The Astrophysical Journal*, vol. 619, no. 2, pp. 684–696, 2005.
- [100] S. Inoue, K. Omukai, and B. Ciardi, "The radio to infrared emission of very high redshift gamma-ray bursts: probing early star formation through molecular and atomic absorption lines," *Monthly Notices of the Royal Astronomical Society*, vol. 380, no. 4, pp. 1715–1728, 2007.
- [101] R. Salvaterra, "High redshift gamma-ray bursts," *Journal of High Energy Astrophysics*, vol. 7, pp. 35–43, 2015.
- [102] D. E. Reichart, D. Q. Lamb, E. E. Fenimore, E. Ramirez-Ruiz, T. L. Cline, and K. Hurley, "A possible cepheid-like luminosity estimator for the long gamma-ray bursts," *The Astrophysical Journal*, vol. 552, no. 1, pp. 57–71, 2001.

- [103] G. J. Fishman, C. A. Meegan, R. B. Wilson et al., "The first batse gamma-ray burst catalog," *The Astrophysical Journal Supplement Series*, vol. 92, no. 1, pp. 229–283, 1994.
- [104] J. P. Norris, R. J. Nemiroff, and J. T. Bonnell, "Attributes of pulses in long bright gamma-ray bursts," *The Astrophysical Journal*, vol. 459, p. 393, 1996.
- [105] B. E. Stern and R. Svensson, "Evidence for "chain reaction" in the time profiles of gamma-ray bursts," *The Astrophysical Journal*, vol. 469, no. 2, pp. L109–L113.
- [106] F. Ryde and R. Svensson, "On the variety of the spectral and temporal behavior of long gamma-ray burst pulses," *The Astrophysical Journal*, vol. 566, no. 1 I, pp. 210–228, 2002.
- [107] R. Sari, T. Piran, and J. P. Halpern, "Jets in gamma-ray bursts," *The Astrophysical Journal Letters*, vol. 519, no. 1, pp. L17–L20, 1999.
- [108] R. Willingale, F. Genet, J. Granot, and P. T. O'Brien, "The spectral-temporal properties of the prompt pulses and rapid decay phase of gamma-ray bursts," *Monthly Notices of the Royal Astronomical Society*, vol. 403, no. 3, pp. 1296–1316, 2010.
- [109] J. E. Rhoads, "How to tell a jet from a balloon: a proposed test for beaming in gamma-ray bursts," *The Astrophysical Journal Letters*, vol. 487, no. 1, p. L1, 1997.
- [110] R. S. Mallozzi, W. S. Paciesas, G. N. Pendleton et al., "The nu F nu Peak Energy Distributions of Gamma-Ray Bursts Observed by BATSE," *The Astrophysical Journal*, vol. 454, p. 597, 1995.
- [111] L. Amati, F. Frontera, M. Tavani et al., "Intrinsic spectra and energetics of BeppoSAX gamma-ray bursts with known redshifts," *Astronomy & Astrophysics*, vol. 390, no. 1, pp. 81–89, 2002.
- [112] T. T. Lee and V. Petrosian, "Distributions of peak flux and duration for gamma-ray bursts," *The Astrophysical Journal*, vol. 470, p. 479, 1996.
- [113] J. P. Norris, G. F. Marani, and J. T. Bonnell, "Connection between energy-dependent lags and peak luminosity in gamma-ray bursts," *The Astrophysical Journal*, vol. 534, no. 1, pp. 248–257, 2000.
- [114] L. Li and B. Paczynski, "Improved correlation between the variability and peak luminosity of gamma-ray bursts," *Monthly Notices of the Royal Astronomical Society*, vol. 366, no. 1, pp. 219–226, 2006.
- [115] D. Band, J. Matteson, L. Ford et al., "BATSE observations of gamma-ray burst spectra. I. Spectral diversity," *The Astrophysical Journal Letters*, vol. 413, no. 1, pp. 281–292, 1993.
- [116] D. Yonetoku, T. Murakami, T. Nakamura, R. Yamazaki, A. K. Inoue, and K. Ioka, "Gamma-ray burst formation rate inferred from the spectral peak energy-peak luminosity relation," *The Astrophysical Journal*, vol. 609, no. 2, pp. 935–951, 2004.
- [117] M. G. Kendall and A. Stuart, *The Advanced Theory of Statistics*, vol. 2 of *Inference and Relationship*, Macmillan, New York, NY, USA, 1973.
- [118] P. R. Bevington and D. K. Robinson, *Data Reduction and Error Analysis for the Physical Sciences*, McGraw-Hill, Boston, Mass, USA, 2nd edition, 1992.
- [119] C. Spearman, "The proof and measurement of association between two things," *The American Journal of Psychology*, vol. 15, no. 1, p. 72, 1904.
- [120] E. Liang and V. Kargatis, "Dependence of the spectral evolution of γ -ray bursts on their photon fluence," *Nature*, vol. 381, no. 6577, pp. 49–51, 1996.
- [121] B. E. Schaefer, M. Deng, and D. L. Band, "Redshifts and luminosities for 112 gamma-ray bursts," *The Astrophysical Journal*, vol. 563, no. 2, pp. L123–L127, 2001.
- [122] J. D. Salmonson, "On the kinematic origin of the luminosity-pulse lag relationship in gamma-ray bursts," *The Astrophysical Journal*, vol. 544, no. 2, pp. L115–L117, 2000.
- [123] F. Daigne and R. Mochkovitch, "The physics of pulses in gamma-ray bursts: Emission processes, temporal profiles and time-lags," *Monthly Notices of the Royal Astronomical Society*, vol. 342, no. 2, pp. 587–592, 2003.
- [124] Z. Zhang, G. Z. Xie, J. G. Deng, and W. Jin, "Revisiting the characteristics of the spectral lags in short gamma-ray bursts," *Monthly Notices of the Royal Astronomical Society*, vol. 373, no. 2, pp. 729–732, 2006.
- [125] B. E. Schaefer, "Explaining the gamma-ray burst lag/luminosity relation," *The Astrophysical Journal*, vol. 602, no. 1, pp. 306–311, 2004.
- [126] D. Kocevski and E. Liang, "The connection between spectral evolution and gamma-ray burst lag," *The Astrophysical Journal*, vol. 594, no. 1, pp. 385–389, 2003.
- [127] J. Hakkila, T. W. Giblin, J. P. Norris, P. C. Fragile, and J. T. Bonnell, "Correlations between lag, luminosity, and duration in gamma-ray burst pulses," *The Astrophysical Journal*, vol. 677, no. 2, pp. L81–L84, 2008.
- [128] R. Tsutsui, T. Nakamura, D. Yonetoku, T. Murakami, S. Tanabe, and Y. Kodama, "Redshift dependent lag-luminosity relation in 565 baste gamma ray bursts," in *Proceedings of the Santa Fe Conference on Gamma-Ray Bursts 2007, GRB 2007*, pp. 28–31, USA, November 2007.
- [129] J. Sultana, D. Kazanas, and K. Fukumura, "Luminosity correlations for gamma-ray bursts and implications for their prompt and afterglow emission mechanisms," *The Astrophysical Journal*, vol. 758, no. 1, p. 32, 2012.
- [130] N. Gehrels, J. P. Norris, S. D. Barthelmy et al., "A new γ -ray burst classification scheme from GRB 060614," *Nature*, vol. 444, no. 7122, pp. 1044–1046, 2006.
- [131] M. G. Dainotti, V. F. Cardone, and S. Capozziello, "A time-luminosity correlation for γ -ray bursts in the X-rays," *Monthly Notices of the Royal Astronomical Society*, vol. 391, no. 1, pp. L79–L83, 2008.
- [132] M. G. Dainotti, R. Willingale, S. Capozziello, V. F. Cardone, and M. Ostrowski, "Discovery of a tight correlation for gamma-ray burst afterglows with "canonical" light curves," *The Astrophysical Journal*, vol. 722, no. 2, pp. L215–L219, 2010.
- [133] M. G. Dainotti, V. F. Cardone, S. Capozziello, M. Ostrowski, and R. Willingale, "Study of possible systematics in the L_X^* - T_a correlation of gamma-ray bursts," *The Astrophysical Journal*, vol. 730, no. 2, article no. 135, 2011.
- [134] M. G. Dainotti, V. F. Cardone, E. Piedipalumbo, and S. Capozziello, "Slope evolution of GRB correlations and cosmology," *Monthly Notices of the Royal Astronomical Society*, vol. 436, no. 1, pp. 82–88, 2013.
- [135] M. Dainotti, V. Petrosian, R. Willingale, P. O'Brien, M. Ostrowski, and S. Nagataki, "Luminosity-time and luminosity-luminosity correlations for GRB prompt and afterglow plateau emissions," *Monthly Notices of the Royal Astronomical Society*, vol. 451, no. 4, pp. 3898–3908, 2015.
- [136] T. N. Ukwatta, M. Stamatikos, K. S. Dhuga et al., "Spectral lags and the lag-luminosity relation: an investigation with swift bat gamma-ray bursts," *The Astrophysical Journal Letters*, vol. 711, no. 2, pp. 1073–1086, 2010.
- [137] T. N. Ukwatta, K. S. Dhuga, M. Stamatikos et al., "The lag-luminosity relation in the GRB source frame: An investigation with Swift BAT bursts," *Monthly Notices of the Royal Astronomical Society*, vol. 419, no. 1, pp. 614–623, 2012.

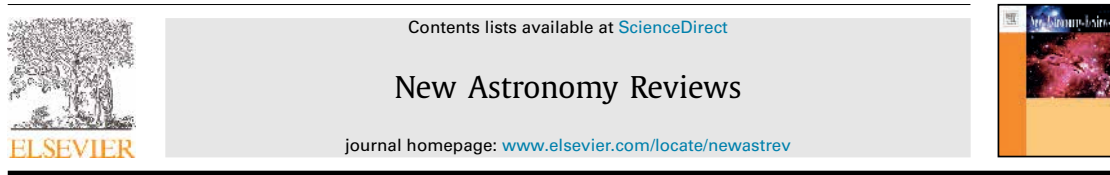
- [138] R. Margutti, C. Guidorzi, G. Chincarini et al., "Lag-luminosity relation in γ -ray burst X-ray flares: a direct link to the prompt emission," *Monthly Notices of the Royal Astronomical Society*, vol. 406, no. 4, pp. 2149–2167, 2010.
- [139] A. Panaiteescu and P. Kumar, "Properties of relativistic jets in gamma-ray burst afterglows," *The Astrophysical Journal Letters*, vol. 571, no. 2, pp. 779–789, 2002.
- [140] E. E. Fenimore, C. D. Madras, and S. Nayakshin, "Expanding relativistic shells and gamma-ray burst temporal structure," *The Astrophysical Journal*, vol. 473, no. 2, pp. 998–1012, 1996.
- [141] K. Ioka and T. Nakamura, "Peak luminosity-spectral lag relation caused by the viewing angle of the collimated gamma-ray bursts," *The Astrophysical Journal Letters*, vol. 554, no. 2, pp. L163–L167, 2001.
- [142] E.-W. Liang, J. L. Racusin, B. Zhang, B.-B. Zhang, and D. N. Burrows, "A comprehensive analysis of Swift XRT data. III. Jet break candidates in X-ray and optical afterglow light curves," *The Astrophysical Journal*, vol. 675, no. 1, pp. 528–552, 2008.
- [143] J. Lü, Y.-C. Zou, W.-H. Lei et al., "Lorentz-factor-isotropic-luminosity/energy correlations of gamma-ray bursts and their interpretation," *The Astrophysical Journal*, vol. 751, no. 1, article no. 49, 2012.
- [144] T.-F. Yi, G.-Z. Xie, and F.-W. Zhang, "A close correlation between the spectral lags and redshifts of gamma-ray bursts," *Chinese Journal of Astronomy and Astrophysics*, vol. 8, no. 1, pp. 81–86, 2008.
- [145] G. Stratta, D. Guetta, V. D'Elia, M. Perri, S. Covino, and L. Stella, "Evidence for an anticorrelation between the duration of the shallow decay phase of GRB X-ray afterglows and redshift," *Astronomy & Astrophysics*, vol. 494, no. 2, p. -L12, 2009.
- [146] G. Ryan, H. van Eerten, A. MacFadyen, and B.-B. Zhang, "Gamma-ray bursts are observed off-axis," *The Astrophysical Journal*, vol. 799, no. 1, article 3, 2015.
- [147] Z. L. Uhm and B. Zhang, "Toward an understanding of GRB prompt emission mechanism. I. the origin of spectral lags," *The Astrophysical Journal*, vol. 825, no. 2, article no. 97, 2016.
- [148] E. E. Fenimore and E. Ramirez-Ruiz, "Redshifts For 220 BATSE γ -Ray Bursts Determined by Variability and the Cosmological Consequences".
- [149] C. Guidorzi, F. Frontera, E. Montanari et al., "The gamma-ray burst variability-peak luminosity correlation: New results," *Monthly Notices of the Royal Astronomical Society*, vol. 363, no. 1, pp. 315–325, 2005.
- [150] D. E. Reichart and M. C. Nysewander, "GRB Variability-Luminosity Correlation Confirmed," *ArXiv Astrophysics e-prints*, August 2005.
- [151] C. Guidorzi, F. Frontera, E. Montanari et al., "The slope of the gamma-ray burst variability/peak luminosity correlation," *Monthly Notices of the Royal Astronomical Society*, vol. 371, no. 2, pp. 843–851, 2006.
- [152] C. Guidorzi, "Testing the gamma-ray burst variability/peak luminosity correlation using the pseudo-redshifts of a large sample of BATSE gamma-ray bursts," *Monthly Notices of the Royal Astronomical Society*, vol. 364, no. 1, pp. 163–168, 2005.
- [153] G. D'Agostini, "Fits, and especially linear fits, with errors on both axes," *Extra Variance of The Data Points And Other Complications. Arxiv Physics E-Prints*, November 2005.
- [154] D. Rizzuto, C. Guidorzi, P. Romano et al., "Testing the gamma-ray burst variability/peak luminosity correlation on a Swift homogeneous sample," *Monthly Notices of the Royal Astronomical Society*, vol. 379, no. 2, pp. 619–628, 2007.
- [155] T. Piran, "The physics of gamma-ray bursts," *Reviews of Modern Physics*, vol. 76, no. 4, pp. 1143–1210, 2004.
- [156] J. D. Salmonson and T. J. Galama, "Discovery of a tight correlation between pulse LAG/luminosity and jet-break times: A connection between gamma-ray bursts and afterglow properties," *The Astrophysical Journal*, vol. 569, no. 2 I, pp. 682–688, 2002.
- [157] B. E. Schaefer, "The Hubble Diagram to Redshift $>$ from 69," *Gamma-Ray Bursts*, vol. 660:0, Article ID 511742, pp. 16–46, May 2007.
- [158] B. Schaefer, "Four luminosity indicators for gamma-ray bursts," in *Proceedings of the COSPAR Scientific Assembly, volume 34 of COSPAR Meeting*, p. 1141, Houston, Texas, USA, Oct 2002.
- [159] L. Xiao and B. E. Schaefer, "Estimating redshifts for long gamma-ray bursts," *The Astrophysical Journal*, vol. 707, no. 1, pp. 387–403, 2009.
- [160] D. L. Freedman and E. Waxman, "On the energy of gamma-ray bursts," *The Astrophysical Journal*, vol. 547, no. 2, pp. 922–928, 2001.
- [161] E. Waxman, " γ -Ray burst afterglow: confirming the cosmological fireball model," *The Astrophysical Journal*, vol. 489, no. 1, pp. L33–L36.
- [162] R. A. M. J. Wijers and T. J. Galama, "Physical parameters of GRB 970508 and GRB 971214 from their afterglow synchrotron emission," *The Astrophysical Journal*, vol. 523, no. 1, pp. 177–186, 1999.
- [163] J. Granot, T. Piran, and R. Sari, "Images and spectra from the interior of a relativistic fireball," *The Astrophysical Journal*, vol. 513, no. 2, pp. 679–689, 1999.
- [164] E.-W. Liang, S.-X. Yi, J. Zhang, H.-J. Lü, and B.-B. Zhang, "Constraining gamma-ray burst initial lorentz factor with the afterglow onset feature and discovery of a tight Γ_0 - $E_{\text{gamma,iso}}$ Correlation," *The Astrophysical Journal*, vol. 725, pp. 2209–2224, 2010.
- [165] G. Ghirlanda, G. Ghisellini, L. Nava, and D. Burlon, "Spectral evolution of Fermi/GBM short gamma-ray bursts," *Monthly Notices of the Royal Astronomical Society*, vol. 410, no. 1, pp. L47–L51, 2011.
- [166] R. Sari and T. Piran, "GRB 990123: the optical flash and the fireball model," *The Astrophysical Journal*, vol. 517, no. 2, pp. L109–L112, 1999.
- [167] Y. Lithwick and R. Sari, "Lower limits on Lorentz factors in gamma-ray bursts," *The Astrophysical Journal Letters*, vol. 555, no. 1, pp. 540–545, 2001.
- [168] Y.-C. Zou and T. Piran, "Lorentz factor constraint from the very early external shock of the gamma-ray burst ejecta," *Monthly Notices of the Royal Astronomical Society*, vol. 402, no. 3, pp. 1854–1862, 2010.
- [169] B. Zhang and A. Pe'er, "Evidence of an initially magnetically dominated outflow in GRB 080916C," *The Astrophysical Journal Letters*, vol. 700, no. 2, pp. L65–L68, 2009.
- [170] Y. Fan, "The spectrum of γ -ray burst: a clue," *Monthly Notices of the Royal Astronomical Society*, vol. 403, no. 1, pp. 483–490, 2010.
- [171] B. Zhang and H. Yan, "The internal-collision-induced magnetic reconnection and turbulence (ICMART) model of gamma-ray bursts," *The Astrophysical Journal*, vol. 726, no. 2, p. 90, 2011.
- [172] W. H. Lei, D. X. Wang, L. Zhang, Z. M. Gan, Y. C. Zou, and Y. Xie, "Magnetically torqued neutrino-dominated accretion flows for gamma-ray bursts," *The Astrophysical Journal*, vol. 700, no. 2, pp. 1970–1976, 2009.
- [173] N. M. Lloyd, V. Petrosian, and R. S. Mallozzi, "Cosmological versus Intrinsic: The Correlation between Intensity and the Peak of the $\nu F(\nu)$," *The Astrophysical Journal*, vol. 534, no. 1, pp. 227–238, 2000.

- [174] M. G. Kendall, "A New Measure of Rank Correlation," *Biometrika*, vol. 30, no. 1-2, p. 81, 1938.
- [175] R. S. Mallozzi, G. N. Pendleton, W. S. Paciesas, R. D. Preece, and M. S. Briggs, "Gamma-ray burst spectra and the hardness-intensity correlation," in *Proceedings of the GAMMA-RAY BURSTS*, vol. 428, pp. 273–277, Huntsville, Alabama (USA).
- [176] A. Goldstein, R. D. Preece, and M. S. Briggs, "A new discriminator for gamma-ray burst classification: The E_{peak} -fluence energy ratio," *The Astrophysical Journal*, vol. 721, no. 2, pp. 1329–1332, 2010.
- [177] R.-J. Lu, J.-J. Wei, E.-W. Liang et al., "A comprehensive analysis of fermi gamma-ray burst data. II. E_p evolution patterns and implications for the observed spectrum-luminosity relations," *The Astrophysical Journal*, vol. 756, no. 2, article no. 112, 2012.
- [178] S. V. Golenetskii, E. P. Mazets, R. L. Aptekar, and V. N. Ilyinskii, "Correlation between luminosity and temperature in γ -ray burst sources," *Nature*, vol. 306, no. 5942, pp. 451–453, 1983.
- [179] L. Borgonovo and F. Ryde, "On the hardness-intensity correlation in gamma-ray burst pulses," *The Astrophysical Journal*, vol. 548, no. 2, pp. 770–786, 2001.
- [180] G. Ghirlanda, L. Nava, and G. Ghisellini, "Spectral-luminosity relation within individual Fermi gamma rays bursts," *Astronomy & Astrophysics*, vol. 511, no. 1, article A43, 2010.
- [181] S. Guiriec, M. S. Briggs, V. Connaughton et al., "Time-resolved spectroscopy of the three brightest and hardest short gamma-ray bursts observed with the fermi gamma-ray burst monitor," *The Astrophysical Journal*, vol. 725, no. 1, pp. 225–241, 2010.
- [182] N. M. Lloyd and V. Petrosian, "Distribution of spectral characteristics and the cosmological evolution of gamma-ray bursts," *The Astrophysical Journal*, vol. 511, no. 2, pp. 550–561, 1999.
- [183] N. M. Lloyd, V. Petrosian, and R. D. Preece, "Synchrotron emission as the source of GRB spectra, Part II: Observations," in *Proceedings of the The fifth huntsville gamma-ray burst symposium*, pp. 155–159, Huntsville, Alabama (USA).
- [184] J. S. Bloom, D. A. Frail, and R. Sari, "The prompt energy release of gamma-ray bursts using a cosmological k-correction," *The Astronomical Journal*, vol. 121, no. 6, pp. 2879–2888, 2001.
- [185] L. Amati, F. Frontera, J. M. Castro Cerón et al., "The Prompt and Afterglow Emission of GRB 001109 Measured by BeppoSAX," in *A Workshop Celebrating the First Year of the HETE Mission American Institute of Physics Conference Series*, J. J. M. and R. K. Ricker, Eds., vol. 662, pp. 387–389, April 2003.
- [186] D. Q. Lamb, T. Q. Donaghy, and C. Graziani, "A unified jet model of X-ray flashes and γ -ray bursts," *New Astronomy Reviews*, vol. 48, no. 5-6, pp. 459–464, 2004.
- [187] T. Sakamoto, D. Q. Lamb, C. Graziani et al., "High energy transient explorer 2 observations of the extremely soft X-ray flash XRF 020903," *The Astrophysical Journal*, vol. 602, no. 2, pp. 875–885, 2004.
- [188] G. Ghirlanda, G. Ghisellini, and D. Lazzati, "The collimation-corrected gamma-ray burst energies correlate with the peak energy of their vF_v spectrum," *The Astrophysical Journal*, vol. 616, no. 1, pp. 331–338, 2004.
- [189] G. Ghirlanda, G. Ghisellini, and C. Firmani, "Probing the existence of the $E_{\text{peak}}\text{-}E_{\text{iso}}$ correlation in long gamma ray bursts," *Monthly Notices of the Royal Astronomical Society*, vol. 361, no. 1, pp. L10–L14, 2005.
- [190] L. Amati, "The $E_{\text{p},i}\text{-}E_{\text{iso}}$ correlation in gamma-ray bursts: updated observational status, re-analysis and main implications," *Monthly Notices of the Royal Astronomical Society*, vol. 372, no. 1, pp. 233–245, 2006.
- [191] G. Ghirlanda, L. Nava, G. Ghisellini, C. Firmani, and J. I. Cabrera, "The $E_{\text{peak}}\text{-}E_{\text{iso}}$ plane of long gamma-ray bursts and selection effects," *Monthly Notices of the Royal Astronomical Society*, vol. 387, no. 1, pp. 319–330, 2008.
- [192] L. Amati, F. Frontera, and C. Guidorzi, "Extremely energetic Fermi gamma-ray bursts obey spectral energy correlations," *Astronomy & Astrophysics*, vol. 508, no. 1, pp. 173–180, 2009.
- [193] L. Amati, "Cosmology with the $E_{\text{p},i}\text{-}E_{\text{iso}}$ correlation of gamma-ray bursts," *International Journal of Modern Physics: Conference Series*, vol. 12, pp. 19–27, 2012.
- [194] L. Amati, C. Guidorzi, F. Frontera et al., "Measuring the cosmological parameters with the $E_{\text{p},i}\text{-}E_{\text{iso}}$ correlation of gamma-ray bursts," *Monthly Notices of the Royal Astronomical Society*, vol. 391, no. 2, pp. 577–584, 2008.
- [195] Y.-P. Qin and Z.-F. Chen, "Statistical classification of gamma-ray bursts based on the amati relation," *Monthly Notices of the Royal Astronomical Society*, vol. 430, no. 1, pp. 163–173, 2013.
- [196] V. Heussaff, J.-L. Atteia, and Y. Zolnierowski, "The $E_{\text{peak}}\text{-}E_{\text{iso}}$ relation revisited with fermi GRBs: resolving a long-standing debate?" *Astronomy & Astrophysics*, vol. 557, article 100, 2013.
- [197] L. Amati and M. Della Valle, "Measuring cosmological parameters with gamma ray bursts," *International Journal of Modern Physics D*, vol. 22, no. 14, Article ID 1330028, 2013.
- [198] R. Basak and A. R. Rao, "Erratum: Correlation between the isotropic energy and the peak energy at zero fluence for the individual pulses of gamma-ray bursts: Toward a universal physical correlation for the prompt emission," *The Astrophysical Journal*, vol. 754, no. 1, article no. 79, 2012.
- [199] R. Basak and A. R. Rao, "Pulse-wise Amati correlation in Fermi gamma-ray bursts," *Monthly Notices of the Royal Astronomical Society*, vol. 436, no. 4, pp. 3082–3088, 2013.
- [200] F. Frontera, L. Amati, C. Guidorzi, R. Landi, and J. In'T Zand, "Erratum: Broadband time-resolved $E_{\text{p},i}\text{-}L_{\text{iso}}$ correlation in γ -ray bursts (Astrophysical Journal (2012) 754 (138))," *The Astrophysical Journal*, vol. 757, no. 1, article no. 107, 2012.
- [201] D. A. Frail, S. R. Kulkarni, R. Sari et al., "The radio afterglow from grb 980519: a test of the jet and circumstellar models," *The Astrophysical Journal*, vol. 534, no. 2, pp. 559–564, 2000.
- [202] S. A. Yost, D. A. Frail, F. A. Harrison et al., "The broadband afterglow of GRB 980329," *The Astrophysical Journal*, vol. 577, no. 1, pp. 155–163, 2002.
- [203] B. E. Schaefer, "Explaining the gamma-ray burst E_{peak} distribution," *The Astrophysical Journal*, vol. 583, no. 2, pp. L71–L74, 2003.
- [204] E. Liang and B. Zhang, "Model-independent multivariable gamma-ray burst luminosity indicator and its possible cosmological implications," *The Astrophysical Journal*, vol. 633, no. 2, pp. 611–623, 2005.
- [205] L. Nava, G. Ghisellini, G. Ghirlanda, F. Tavecchio, and C. Firmani, "On the interpretation of spectral-energy correlations in long gamma-ray bursts," *Astronomy & Astrophysics*, vol. 450, no. 2, pp. 471–481, 2006.
- [206] G. Ghirlanda, L. Nava, G. Ghisellini, and C. Firmani, "Confirming the γ -ray burst spectral-energy correlations in the era of multiple time breaks," *Astronomy & Astrophysics*, vol. 466, no. 1, pp. 127–136, 2007.
- [207] N. M. Lloyd-Ronning and V. Petrosian, "Interpreting the behavior of time-resolved gamma-ray burst spectra," *The Astrophysical Journal Letters*, vol. 565, no. 1, pp. 182–194, 2002.
- [208] B. Zhang and P. Mészáros, "An analysis of gamma-ray burst spectral break models," *The Astrophysical Journal*, vol. 581, no. 2, pp. 1236–1247, 2002.

- [209] G. Ghirlanda, G. Ghisellini, R. Salvaterra et al., "The faster the narrower: Characteristic bulk velocities and jet opening angles of gamma-ray bursts," *Monthly Notices of the Royal Astronomical Society*, vol. 428, no. 2, pp. 1410–1423, 2013.
- [210] M. J. Rees and P. Mészáros, "Dissipative photosphere models of gamma-ray bursts and X-ray flashes," *The Astrophysical Journal*, vol. 628, no. 2, p. 847, 2005.
- [211] E. Ramirez-Ruiz, "Photospheric signatures imprinted on the γ -ray burst spectra," *Monthly Notices of the Royal Astronomical Society*, vol. 363, no. 1, pp. L61–L65, 2005.
- [212] F. Ryde, "Is thermal emission in gamma-ray bursts ubiquitous?" *The Astrophysical Journal Letters*, vol. 625, no. 2, pp. L95–L98, 2005.
- [213] A. M. Beloborodov, "Collisional mechanism for gamma-ray burst emission," *Monthly Notices of the Royal Astronomical Society*, vol. 407, no. 2, pp. 1033–1047, 2010.
- [214] S. Guiriec, V. Connaughton, M. S. Briggs et al., "Detection of a thermal spectral component in the prompt emission of GRB 100724B," *The Astrophysical Journal Letters*, vol. 727, no. 2, article L33, 2011.
- [215] R. Hascoët, F. Daigne, and R. Mochkovitch, "Prompt thermal emission in gamma-ray bursts," *Astronomy & Astrophysics*, vol. 551, article A124, 2013.
- [216] S. Guiriec, F. Daigne, R. Hascoët et al., "Evidence for a photospheric component in the prompt emission of the short GRB 120323a and its effects on the GRB hardness-luminosity relation," *The Astrophysical Journal*, vol. 770, no. 1, article 32, 2013.
- [217] I. Vurm and A. M. Beloborodov, "Radiative transfer models for gamma-ray bursts," *The Astrophysical Journal*, vol. 831, no. 2, article no. 175, 2016.
- [218] S. Guiriec, C. Kouveliotou, F. Daigne et al., "Toward a better understanding of the grb phenomenon: a new model for grb prompt emission and its effects on the new $L_i^{NT} - E_{peak,i}^{nth,rest}$ relation," *The Astrophysical Journal*, vol. 807, no. 2, article no. 148, 2015.
- [219] S. Guiriec, R. Mochkovitch, T. Piran et al., "GRB 131014A: A laboratory for studying the thermal-like and non-thermal emissions in gamma-ray bursts, and the new $L_i^{nth} - E_i^{nth,rest}$ relation," *The Astrophysical Journal*, vol. 814, no. 1, article no. 10, 2015.
- [220] F. Frontera, L. Amati, E. Costa et al., "Prompt and delayed emission properties of γ -ray bursts observed with *BeppeSAX*," *The Astrophysical Journal*, vol. 127, no. 1, pp. 59–78, 2000.
- [221] R. D. Preece, M. S. Briggs, R. S. Mallozzi, G. N. Pendleton, W. S. Paciesas, and D. L. Band, "The BATSE gamma-ray Burst spectral catalog. I. High time resolution spectroscopy of bright Bursts using high energy resolution data," *The Astrophysical Journal*, vol. 126, no. 1, pp. 19–36, 2000.
- [222] G. Ghirlanda, A. Celotti, and G. Ghisellini, "Extremely hard GRB spectra prune down the forest of emission models," *Astronomy & Astrophysics*, vol. 406, no. 3, pp. 879–892, 2003.
- [223] A. Panaiteescu, "An external-shock origin of the relation for gamma-ray bursts," *Monthly Notices of the Royal Astronomical Society*, vol. 393, no. 3, pp. 1010–1015, March 2009.
- [224] R. Mochkovitch and L. Nava, "The $E_p - E_{iso}$ relation and the internal shock model. Δp ," *Astronomy and Astrophysics*, vol. 557, pp. 10–1051, May 2015.
- [225] A. C. Collazzi, B. E. Schaefer, and J. A. Moree, "The total errors in measuring E_{peak} for γ -ray bursts," *The Astrophysical Journal*, vol. 729, no. 2, article 89, 2011.
- [226] B. E. Schaefer, "Gamma-ray burst Hubble diagram to $z = 4.5$," *The Astrophysical Journal Letters*, vol. 583, no. 2, pp. L67–L70, 2003.
- [227] L. Nava, R. Salvaterra, G. Ghirlanda et al., "A complete sample of bright Swift long gamma-ray bursts: testing the spectral-energy correlations," *Monthly Notices of the Royal Astronomical Society*, vol. 421, no. 2, pp. 1256–1264, 2012.
- [228] G. Ghirlanda, G. Ghisellini, and A. Celotti, "The spectra of short γ -ray bursts," *Astronomy & Astrophysics*, vol. 422, no. 3, pp. L55–L58, 2004.
- [229] D. Yonetoku, T. Murakami, R. Tsutsui, T. Nakamura, Y. Morihara, and K. Takahashi, "Possible origins of dispersion of the peak energy-brightness correlations of gamma-ray bursts," *Publications of the Astronomical Society of Japan*, vol. 62, no. 6, pp. 1495–1507, 2010.
- [230] R. Lu and E. Liang, "Luminosity-peak energy relation in the decay phases of gamma-ray burst pulses," *Science China Physics, Mechanics & Astronomy*, vol. 53, no. 1, pp. 163–170, 2010.
- [231] A. A. Abdo, M. Ackermann, M. Ajello et al., *Fermi Observations of GRB 090902B: A Distinct Spectral Component in the Prompt and Delayed Emission*, 706:0 L138L144, 0 L138–L144, 706, November 2009.
- [232] M. Ackermann, K. Asano, W. B. Atwood et al., *A Short-Hard Gamma-ray Burst with an Additional, Hard Power-law Component from 10 keV TO GeV Energies*, vol. 716:0, 0 1178–1190, 716, June 2010.
- [233] M. Ackermann, M. Ajello, K. Asano et al., *Detection of a Spectral Break in the Extra Hard Component of GRB 090926A*, 0 114, 729, March 2011.
- [234] M. Ackermann, M. Ajello, A. Allafort et al., *The First Fermi-LAT Catalog of Sources above 10 GeV*, 0 34, 209, December.
- [235] H.-N. Lin, X. Li, and Z. Chang, "Effect of gamma-ray burst (GRB) spectra on the empirical luminosity correlations and the GRB Hubble diagram," *Monthly Notices of the Royal Astronomical Society*, vol. 459, no. 3, pp. 2501–2512, 2016.
- [236] S. Guiriec, M. M. Gonzalez, J. R. Sacahui, C. Kouveliotou, N. Gehrels, and J. McEnery, "CGRO/BATSE Data support the new paradigm for GRB prompt emission and the new $L_i^{nth} - E_{peak,i}^{nth,rest}$ relation," *The Astrophysical Journal*, vol. 819, no. 1, article no. 79, 2016.
- [237] R. Tsutsui, D. Yonetoku, T. Nakamura, K. Takahashi, and Y. Morihara, "Possible existence of the $E_p - L_p$ and $E_p - E_{iso}$ correlations for short gamma-ray bursts with a factor 5–100 dimmer than those for long gamma-ray bursts," *Monthly Notices of the Royal Astronomical Society*, vol. 431, no. 2, pp. 1398–1404, 2013.
- [238] D. Yonetoku, T. Nakamura, T. Sawano, K. Takahashi, and A. Toyanago, "Short gamma-ray burst formation rate from batse data using $E_p - L_p$ correlation and the minimum gravitational-wave event rate of a coalescing compact binary," *The Astrophysical Journal*, vol. 789, no. 1, article no. 65, 2014.
- [239] N. M. Lloyd-Ronning and E. Ramirez-Ruiz, "On the spectral energy dependence of gamma-ray burst variability," *The Astrophysical Journal*, vol. 576, no. 1, pp. 101–106, 2002.
- [240] F. Wang, Z. Dai, and E. Liang, "Gamma-ray burst cosmology," *New Astronomy Reviews*, vol. 67, pp. 1–17, 2015.
- [241] E. W. Liang, Z. G. Dai, and X. F. Wu, "The luminosity- E_p relation within gamma-ray bursts and the implications for fireball models," *The Astrophysical Journal*, vol. 606, no. 1, pp. L29–L32, 2004.
- [242] S. Mendoza, J. C. Hidalgo, D. Olvera, and J. I. Cabrera, "Internal shocks in relativistic jets with time-dependent sources," *Monthly Notices of the Royal Astronomical Society*, vol. 395, no. 3, pp. 1403–1408, 2009.

- [243] H. Ito, S. Nagataki, M. Ono et al., “Photospheric emission from stratified jets,” *The Astrophysical Journal*, vol. 777, no. 1, article 62, 2013.
- [244] F. Frontera, L. Amati, R. Farinelli et al., “Possible physical explanation of the intrinsic E_{pi} -“intensity” correlation commonly used to “standardize” GRBs,” *International Journal of Modern Physics D*, vol. 25, no. 5, Article ID 1630014, 2016.
- [245] L. Titarchuk, R. Farinelli, F. Frontera, and L. Amati, “An upscattering spectral formation model for the prompt emission of gamma-ray bursts,” *The Astrophysical Journal*, vol. 752, no. 2, article no. 116, 2012.
- [246] G. Ghirlanda, G. Ghisellini, C. Firmani, A. Celotti, and Z. Bošnjak, “The peak luminosity-peak energy correlation in gamma-ray bursts,” *Monthly Notices of the Royal Astronomical Society*, vol. 360, no. 1, pp. L45–L49, 2005.
- [247] R. Tsutsui, T. Nakamura, D. Yonetoku, T. Murakami, Y. Kodama, and K. Takahashi, “Cosmological constraints from calibrated Yonetoku and Amati relation suggest fundamental plane of gamma-ray bursts,” *Journal of Cosmology and Astroparticle Physics*, vol. 2009, no. 8, article no. 015, 2009.
- [248] R. Tsutsui, T. Nakamura, D. Yonetoku, T. Murakami, and K. Takahashi, “Intrinsic Dispersion of Correlations among Ep, Lp,” and *Eiso of Gamma Ray Bursts depends on the quality of Data Set*. ArXiv e-prints, December 2010.
- [249] S. Qi and T. Lu, “A new luminosity relation for gamma-ray bursts and its implication,” *The Astrophysical Journal*, vol. 717, no. 2, pp. 1274–1278, 2010.
- [250] P. T. O’Brien and R. Willingale, “Using Swift observations of prompt and afterglow emission to classify GRBs,” *Philosophical Transactions of the Royal Society A: Mathematical, Physical & Engineering Sciences*, vol. 365, no. 1854, pp. 1179–1188, 2007.
- [251] M. G. Dainotti, M. Ostrowski, and R. Willingale, “Towards a standard gamma-ray burst: Tight correlations between the prompt and the afterglow plateau phase emission,” *Monthly Notices of the Royal Astronomical Society*, vol. 418, no. 4, pp. 2202–2206, 2011.
- [252] A. Lee, E. D. Bloom, and V. Petrosian, “Properties of Gamma-Ray Burst Time Profiles Using Pulse Decomposition Analysis,” *The Astrophysical Journal*, vol. 131, November 2000.
- [253] F. Quilligan, B. McBreen, L. Hanlon, S. McBreen, K. J. Hurley, and D. Watson, “Temporal properties of gamma ray bursts as signatures of jets from the central engine,” *Astronomy & Astrophysics*, vol. 385, no. 2, pp. 377–398, 2002.
- [254] O. M. Littlejohns, N. R. Tanvir, R. Willingale, P. A. Evans, P. T. O’Brien, and A. J. Levan, “Are gamma-ray bursts the same at high redshift and low redshift?” *Monthly Notices of the Royal Astronomical Society*, vol. 436, no. 4, Article ID stt1841, pp. 3640–3655, 2013.
- [255] Ž. Bošnjak and F. Daigne, “Spectral evolution in gamma-ray bursts: Predictions of the internal shock model and comparison to observations,” *Astronomy & Astrophysics*, vol. 568, article no. A45, 2014.
- [256] P. A. Evans, R. Willingale, J. P. Osborne et al., “GRB 130925A: an ultralong gamma ray burst with a dust-echo afterglow, and implications for the origin of the ultralong GRBs,” *Monthly Notices of the Royal Astronomical Society*, vol. 444, no. 1, pp. 250–267, 2014.
- [257] J. Hakkila and R. D. Preece, “Gamma-ray burst pulse shapes: Evidence for embedded shock signatures?” *The Astrophysical Journal*, vol. 783, no. 2, article no. 88, 2014.
- [258] T. Laskar, E. Berger, N. Tanvir et al., “GRB 120521C at $z \sim 6$ and the properties of high-redshift γ -ray bursts,” *The Astrophysical Journal*, vol. 781, no. 1, article no. 1, 2014.
- [259] O. M. Littlejohns and N. R. Butler, “Investigating signatures of cosmological time dilation in duration measures of prompt gamma-ray burst light curves,” *Monthly Notices of the Royal Astronomical Society*, vol. 444, no. 4, pp. 3948–3960, 2014.
- [260] A. Roychoudhury, S. K. Sarkar, and A. Bhadra, “Spectral lag features of GRB 060814 from swift bat and Suzaku observations,” *The Astrophysical Journal*, vol. 782, no. 2, article no. 105, 2014.
- [261] C. Ceccobello and P. Kumar, “Inverse-Compton drag on a highly magnetized GRB jet in stellar envelope,” *Monthly Notices of the Royal Astronomical Society*, vol. 449, no. 3, pp. 2566–2575, 2015.
- [262] D. Kazanas, J. L. Racusin, J. Sultana, and A. Mastichiadis, “The Statistics of the Prompt-to-Afterglow GRB Flux Ratios and the Supercritical Pile GRB Model.”
- [263] T. Laskar, E. Berger, R. Margutti et al., “Energy injection in gamma-ray burst afterglows,” *The Astrophysical Journal*, vol. 814, no. 1, article no. 1, 2015.
- [264] Z. Y. Peng, Y. Yin, T. F. Yi, Y. Y. Bao, and H. Wu, “A comprehensive comparative study of temporal properties between X-ray flares and GRB pulses,” *Astrophysics and Space Science*, vol. 355, no. 1, pp. 95–103, 2015.
- [265] F. Genet and J. Granot, “Realistic analytic model for the prompt and high-latitude emission in GRBs,” *Monthly Notices of the Royal Astronomical Society*, vol. 399, no. 3, pp. 1328–1346, 2009.
- [266] F. Ryde and V. Petrosian, “Gamma-ray burst spectra and light curves as signatures of a relativistically expanding plasma,” *The Astrophysical Journal*, vol. 578, no. 1 I, pp. 290–303, 2002.
- [267] C. D. Dermer, “Rapid X-ray declines and plateaus in Swift GRB light curves explained by a highly radiative blast wave,” *The Astrophysical Journal*, vol. 664, no. 1 I, pp. 384–396, 2007.

New Astronomy Reviews 77 (2017) 23–61



Gamma Ray Burst afterglow and prompt-afterglow relations: An overview

M.G. Dainotti ^{a,b,c,*}, R. Del Vecchio ^c^a Physics Department, Stanford University, Via Pueblo Mall 382, Stanford, CA, USA^b INAF-Istituto di Astrofisica Spaziale e Fisica cosmica, Via Gobetti 101, Bologna 40129, Italy^c Astronomical Observatory, Jagiellonian University, ul. Orla 171, Kraków 30-244, Poland

ARTICLE INFO

Article history:

Accepted 5 April 2017

Available online 8 April 2017

Keywords:

Gamma rays bursts

Accretion model

LT relation

ABSTRACT

The mechanism responsible for the afterglow emission of Gamma Ray Bursts (GRBs) and its connection to the prompt γ -ray emission is still a debated issue. Relations between intrinsic properties of the prompt or afterglow emission can help to discriminate between plausible theoretical models of GRB production. Here we present an overview of the afterglow and prompt-afterglow two parameter relations, their physical interpretations, their use as redshift estimators and as possible cosmological tools. A similar task has already been correctly achieved for Supernovae (SNe) Ia by using the peak magnitude-stretch relation, known in the literature as the Phillips relation (Phillips 1993). The challenge today is to make GRBs, which are amongst the farthest objects ever observed, standardizable candles as the SNe Ia through well established and robust relations. Thus, the study of relations amongst the observable and physical properties of GRBs is highly relevant together with selection biases in their physical quantities.

Therefore, we describe the state of the art of the existing GRB relations, their possible and debated interpretations in view of the current theoretical models and how relations are corrected for selection biases. We conclude that only after an appropriate evaluation and correction for selection effects can GRB relations be used to discriminate among the theoretical models responsible for the prompt and afterglow emission and to estimate cosmological parameters.

© 2017 Elsevier B.V. All rights reserved.

Contents

1. Introduction	24
2. Notations	25
3. The afterglow relations	26
3.1. The Dainotti relation ($L_X(T_a) - T_{X,a}^*$)	27
3.1.1. Physical interpretation of the Dainotti relation ($L_X(T_a) - T_{X,a}^*$)	29
3.2. The unified $L_X(T_a) - T_{X,a}^*$ and $L_{O,a} - T_{O,a}^*$ relations	31
3.2.1. Physical interpretation of the unified $L_X(T_a) - T_{X,a}^*$ and $L_{O,a} - T_{O,a}^*$ relations	33
3.3. The $L_{O,200s} - \alpha_{O,>200s}$ relation and its physical interpretation	34
4. The prompt-afterglow relations	35
4.1. The $E_{\gamma,afterglow} - E_{X,prompt}$ relation and its physical interpretation	35
4.2. The $L_{X,afterglow} - E_{\gamma,prompt}$ relation and its physical interpretation	37
4.3. The $L_{X,a} - L_{O,a}$ relation and its physical interpretation	38
4.4. The $L_X(T_a) - L_{\gamma,iso}$ relation	40
4.5. The $L_{X,peak} - L_X(T_a)$ relation	43
4.5.1. Physical interpretation of the $L_X(T_a) - L_{\gamma,iso}$ and the $L_{X,peak} - L_X(T_a)$ relations	44
4.6. The $L_{O,peak}^F - T_{O,peak}^{*F}$ relation and its physical interpretation	45

* Corresponding author.

E-mail addresses: mdainotti@stanford.edu (M.G. Dainotti), delvecchioroberta@hotmail.it, mariagiovannadainotti@yahoo.it (R. Del Vecchio).

5.	Selection effects	46
5.1.	Redshift induced relations	47
5.2.	Redshift induced relations through Efron and Petrosian method.	48
5.2.1.	Luminosity evolution	48
5.2.2.	Time Evolution	48
5.3.	Evaluation of the intrinsic slope	49
5.4.	Selection effects for the optical and X-ray luminosities	51
5.5.	Selection effects in the $L_{0,200s} - \alpha_{0,>200s}$ relation.	51
6.	Redshift estimator	51
7.	Cosmology	52
7.1.	The problem of the calibration	52
7.2.	Applications of GRB afterglow relations	53
8.	Summary and discussion	55
9.	Conclusions	58
	Acknowledgments	58
	References	58

1. Introduction

GRBs, amongst the farthest and the most powerful objects ever observed in the Universe, are still a mystery after 50 years from their discovery time by the Vela Satellites (Klebesadel et al., 1973). Phenomenologically, GRBs are traditionally classified in short SGRBs ($T_{90} < 2$ s) and long LGRBs ($T_{90} > 2$ s) (Mazets et al., 1981; Kouveliotou et al., 1993), depending on their duration, where T_{90} is the time in which the 90% (between 5% and 95%) of radiation is emitted in the prompt emission. However, Norris and Bonnell (2006) discovered the existence of an intermediate class (IC), or SGRBs with Extended Emission (SGRBsEE), that shows mixed properties between SGRBs and LGRBs. Another relevant classification related to the spectral features distinguishing normal GRBs from X-ray Flashes (XRFs) appears. The XRFs (Heise et al., 2001; Kippen et al., 2001) are extra-galactic transient X-ray sources with spatial distribution, spectral and temporal characteristics similar to LGRBs. The remarkable property that distinguishes XRFs from GRBs is that their νF_ν prompt emission spectrum peaks at energies typically one order of magnitude lower than the observed peak energies of GRBs. XRFs are empirically defined by a greater fluence (time-integrated flux) in the X-ray band (2–30 keV) than in the gamma-ray band (30–400 keV). This classification is also relevant for the investigation of GRB relations since some of them become stronger or weaker by introducing different GRB categories, see Section 3.1.

One of the historical models used to explain the GRB phenomenon is the “fireball” model (Wijers et al., 1997; Mészáros, 1998, 2006) in which a compact central engine (either the collapsed core of a massive star or the merger product of a neutron star binary) launches a highly relativistic, and jetted electron/positron/baryon plasma. Interactions of blobs within the jet are believed to produce the prompt emission, which consists of high photon energies such as gamma rays and hard X-rays. Instead, the interaction of the jet with the ambient material causes the afterglow phase, namely a long lasting multi-wavelength emission (X-ray, optical and sometimes also radio), which follows the prompt. However, problems in explaining the light curves within this model have been shown by Willingale et al. (2007), hereafter W07. More specifically, for $\sim 50\%$ of GRBs, the observed afterglow is in agreement with the model, but for the rest, the temporal and spectral indices do not conform and are suggestive of continued late energy injection. The difficulty of the standard fireball models appeared when Swift¹ observations had revealed a more complex

behavior of the light curves (O’Brien et al., 2006; Sakamoto et al., 2007; Zhang et al., 2007b) than in the past and pointed out that GRBs often follow “canonical” light curves (Nousek et al., 2006). In fact, the light curves can be divided into two, three and even more segments. The second segment, when it is flat, is called plateau emission. X-ray plateaus can be interpreted as occurring due to an accreting black hole (BH) (Cannizzo and Gehrels, 2009; Cannizzo et al., 2011; Kumar et al., 2008) or a top-heavy jet evolution (Duffell and MacFadyen, 2015). In addition, the fact that a newly born magnetar could be formed either via the collapse of a massive star or during the merger of two neutron stars motivated the interpretation of the X-ray plateaus as resulting from the delayed injection of rotational energy ($\dot{E}_{rot} \sim 10^{50} - 10^{51}$ erg s⁻¹) from a fast spinning magnetar (Usov, 1992; Zhang and Mészáros, 2001; Dall’Osso et al., 2011; Metzger et al., 2011; Rowlinson and O’Brien, 2012; Rowlinson et al., 2014; Rea et al., 2015). These models are summarized in sec. 3.1.1.

Therefore, in this context, the discovery of relations amongst relevant physical parameters between prompt and plateau phases is very important so as to use them as possible model discriminators. In fact, many theoretical models have been presented in the literature to explain the wide variety of observations, but each model has some advantages and drawbacks. The use of the phenomenological relations corrected for selection biases can boost the understanding of the mechanism responsible for such emissions. Moreover, being observed at much larger redshift range than the SNe, it has long been tempting to consider GRBs as useful cosmological probes, extending the redshift range by almost an order of a magnitude further than the available SNe Ia, observed up to $z = 2.26$ (Rodney et al., 2015). Indeed, GRBs are observed up to redshift $z = 9.4$ (Cucchiara et al., 2011), which is much more distant than SNe Ia, and, therefore, they can help to understand the nature of the Dark Energy (DE), which is the main goal of modern cosmology, and determine the evolution of the equation of state (EoS), w , at very high z . So far, the most robust standard candles are the SNe Ia which, by being excellent distance indicators, provide a unique probe for measuring the expansion history of the Universe whose discovery has been awarded the Nobel Prize in 2011 (Riess et al., 1998; Perlmutter et al., 1998). Up-to-date, w has been measured to be -1 within 5% of the Einstein’s cosmological constant, Ω_Λ , the pure vacuum energy. Measurement of the Hubble constant, H_0 , provides another constraint on w when combined with Cosmic Microwave Background Radiation (CMBR) and

¹ The Swift satellite was launched in 2004. With the instruments on board, the Burst Alert Telescope (BAT, divided in four standard channels 15–25; 25–50;

50–100; 100–150 keV), the X-Ray Telescope (XRT, 0.3–10 keV), and the Ultra-Violet/Optical Telescope (UVOT, 170–650 nm), Swift provides a rapid follow-up of the afterglows in several wavelengths with better coverage than previous missions.

Baryon Acoustic Oscillation (BAO) measurements (Weinberg et al., 2013). Therefore, the use of other estimates provided by GRBs would be helpful to confirm further and/or constrain the ranges of values of H_0 . However, different from the SNe Ia, which originate from white dwarves reaching the Chandrasekhar limit and always releasing the same amount of energy, GRBs cannot yet be considered standard candles with their isotropic energies spanning over 8 orders of magnitude. Therefore, finding out universal relations among observable properties can help to standardize their energetics and/or luminosities. It is for this reason that the study of GRB relations is relevant for both understanding the GRB emission mechanism, for finding a good distance indicator and for estimating the cosmological parameters at high z .

Until now, for cosmological purposes, the most used relations are the prompt emission relations: Amati (Amati et al., 2002) and Ghirlanda relations (Ghirlanda et al., 2004). The scatter of these relations is significantly reduced providing constraints on the cosmological parameters, see Ghirlanda et al. (2006) and Ghirlanda (2009) for details. By adopting a maximum likelihood approach which allows for correct quantification of the extrinsic scatter of the relation, Amati et al. (2008) constrained the matter density Ω_M (for a flat Universe) to 0.04–0.40 (68% confidence level, CL), with a best-fit value of $\Omega_M \sim 0.15$, and exclude $\Omega_M = 1$ at $> 99.9\%$ CL. Releasing the assumption of a flat Universe, they found evidence for a low value of Ω_M (0.04–0.50 at 68% CL) as well as a weak dependence of the dispersion of the relation between the prompt peak energy in the vF_v spectrum and the total gamma isotropic energy, $\log E_{\gamma,peak} - \log E_{\gamma,iso}$, on Ω_Λ (with an upper limit of $\Omega_\Lambda \sim 1.15$ at 90% CL). This approach makes no assumptions about the $\log E_{\gamma,peak} - \log E_{\gamma,iso}$ relation and it does not use other calibrators to set the normalization of the relation. Therefore, the treatment of the data is not affected by the so-called circularity problem (to calibrate the GRB luminosity relations for constraining cosmological models a particular cosmological model has to be assumed a priori) and the results are independent of those derived via SNe Ia (or other cosmological probes). Nowadays, the values of the cosmological parameters confirmed by measurements from the Planck Collaboration for the Λ CDM model are $\Omega_M = 0.3089 \pm 0.0062$, $\Omega_\Lambda = 0.6911 \pm 0.0062$, and $H_0 = 67.74 \pm 0.46$ Km s $^{-1}$ Mpc $^{-1}$. For the investigation of the properties of DE, Amati and Della Valle (2013) showed the 68% CL contours in the $\Omega_M - \Omega_\Lambda$ plane obtained by assuming a sample of 250 GRBs expected shortly compared to those from other cosmological probes such as SNe Ia, CMB and Galaxy Clusters.

They obtained the simulated data sets via Monte Carlo techniques by taking into account the slope, normalization, and dispersion of the observed $\log E_{\gamma,peak} - \log E_{\gamma,iso}$ relation, the observed z distribution of GRBs and the distribution of the uncertainties in the measured values of $\log E_{\gamma,peak}$ and $\log E_{\gamma,iso}$. These simulations indicated that with a sample of 250 GRBs, the accuracy in measuring Ω_M would be comparable to that currently provided by SNe data. In addition, they reported the estimates of Ω_M and the parameter of the DE EoS, w_0 , derived from the present and expected future samples. They assumed that the $\log E_{\gamma,peak} - \log E_{\gamma,iso}$ relation is calibrated with a 10% accuracy by using, e.g., the luminosity distances provided by SNe Ia and the self-calibration of the relation with a large enough number of GRBs lying within a narrow range of z ($\Delta z \sim 0.1 - 0.2$). Generally speaking, as the number of GRBs in each redshift bin increases, also the feasibility and accuracy of the self-calibration of GRB relations will improve. For a review on GRB prompt relations, see Dainotti et al. (2016b).

Even though the errors on Ω_M obtained in Amati and Della Valle (2013) may lead to GRBs as promising standard candles, because they are almost comparable with SNe (0.06 for GRBs versus 0.04 for SNe, as provided for the SNe sample by Betoule et al. 2014 and Calcino and Davis 2017), these results

show that Ω_M has an error which is 20 times larger than the value obtained by Planck. Thus, GRBs in a near future can be comparable with SNe Ia, but not likely with Planck. On the other hand, there is discrepancy among the values of H_0 computed by CMB and SNe (Planck Collaboration et al., 2016) and thus adding a new effective cosmological probe as GRBs can help to cast light on this discrepancy and break the degeneracy among several cosmological parameters.

It is clear from this context that selection biases play a major and crucial role even for the close-by probes such as SNe Ia in determining the correct cosmological parameters. This problem is more relevant for GRBs, which are particularly affected by the Malmquist bias effect (Malmquist 1920, Eddington 1940) that favors the brightest objects against faint ones at large distances. Therefore, it is necessary to investigate carefully the problem of selection effects and how to overcome them before using GRB relations as distance estimators, as cosmological probes, and as model discriminators. This is indeed the major aim of this review. Besides, this work is useful, especially for those embarking on the study of GRB relations, because it aims at constituting a brief, but a complete compendium of afterglow and prompt-afterglow relations.

The review is organized as follows: in Section 2, we explain the nomenclature and definitions in all review, in Sections 3 and 4, we analyze the relations between the afterglow parameters and between parameters of both the prompt and afterglow phases. In Section 5, we describe how these relations can be affected by selection biases. In Section 6, we present how to obtain a redshift estimator and in Section 7, we report the use of the Dainotti relation as an example of GRB application as a cosmological tool. Finally, in Section 8, we briefly summarize some findings about the physical models and the cosmological usage of the analyzed relations, while in the last section we draw our conclusions.

2. Notations

For clarity, we report a summary of the nomenclature adopted in the review.

- L , E , F , S , and T indicate the luminosity, the energy, the flux, the fluence and the time which can be observed in several wavelengths, denoted with the first subscript, and at different times or part of the light curve, denoted instead with the second subscript. In addition, with α , β and ν , we represent the temporal and spectral decay indices and the frequencies.

More specifically:

- $T_{X,a}$ and $T_{O,a}$ denote the time in the X-ray at the end of the plateau and the same time, but in the optical wavelength respectively. $F_{X,a}$ are $F_{O,a}$ are their respective fluxes, while $L_{X,a}$ and $L_{O,a}$ are their respective luminosities. An approximation of the energy of the plateau is $E_{X,plateau} = (L_{X,a} \times T_{X,a}^*)$, see the left panel of Fig. 1.
- $T_{O,peak}$ and $T_{X,f}$ are the peak time in the optical and the time since ejection of the pulse. $L_{O,peak}$ and $L_{X,f}$ are their respective luminosities. $F_{O,peak}$ is the respective flux of $T_{O,peak}$.
- $T_{X,peak}$ is the peak time in the X-ray and $F_{X,peak}$ and $L_{X,peak}$ are its flux and luminosity respectively.
- $T_{X,p}$ and $T_{X,t}$ are the time at the end of the prompt emission within the W07 model and the time at which the flat and the step decay behaviors of the light curves join respectively.
- T_{90} and T_{45} are the times in which the 90% (between 5% and 95%) and 45% (between 5% and 50%) of radiation is emitted in the prompt emission respectively.
- τ_{lag} and τ_{RT} are the differences in arrival time to the observer of the high energy photons and low energy photons and the shortest time over which the light curve increases by the 50% of the peak flux of the pulse.

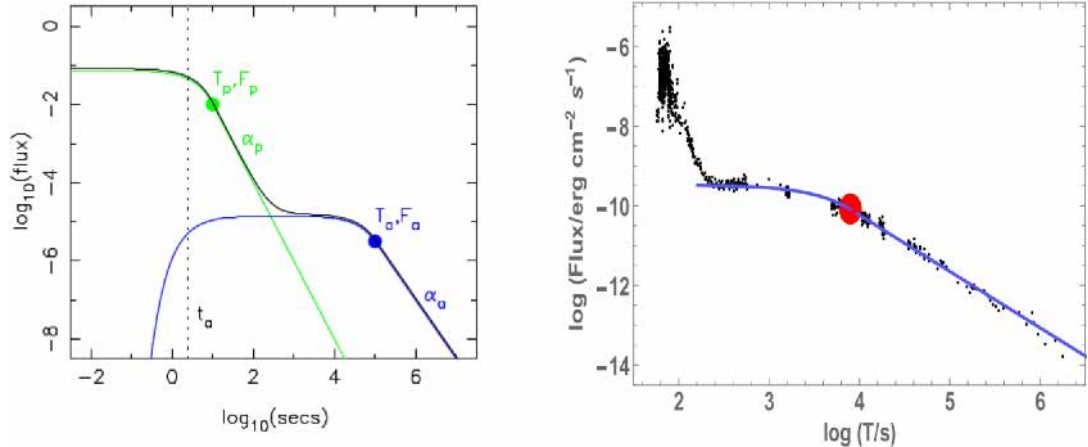


Fig. 1. Left panel: the functional form of the fitting model from Willingale et al. (2007). Right panel: the observed light curve for GRB 061121 with the best-fit W07 model superimposed from Dainotti et al. (2016a). The red dot marks the end of the flat plateau phase in the X-ray afterglow ($T_{X,a}$, $F_{X,a}$). A similar configuration appears in the optical range. (For interpretation of the references to colour in this figure legend, the reader is referred to the web version of this article.)

- $L_{X,200s}, L_{X,10}, L_{X,11}, L_{X,12}, L_{X,1d}$ and $L_{O,200s}, L_{O,10}, L_{O,11}, L_{O,12}, L_{O,1d}$ are the X-ray and optical luminosities at 200 s, at 10, 11, 12 h and at 1 day respectively; $L_{O,100s}, L_{O,1000s}, L_{O,10000s}, L_{O,7}$ are the optical luminosity at 100 s, 1000 s, 10000 s and 7 h; $L_{\gamma,iso}$ and $L_{\nu}(v, T_{X,a})$ are the isotropic prompt emission mean luminosity and the optical or X-ray luminosity of the late prompt emission at the time $T_{X,a}$.
- $F_{X,11}, F_{X,1d}$ and $F_{O,11}, F_{O,1d}$ are the X-ray and optical fluxes at 11 h and at 1 day respectively; $F_{\gamma,prompt}$, $F_{X,afterglow}$ are the gamma-ray flux in the prompt and the X-ray flux in the afterglow respectively. $E_{\gamma,prompt}$ and $E_{X,afterglow}$ are their respective isotropic energies and $L_{\gamma,prompt}$ and $L_{X,afterglow}$ are the respective luminosities. $S_{\gamma,prompt}$ indicates the prompt fluence in the gamma band correspondent to the rest frame isotropic prompt energy $E_{\gamma,prompt}$.
- $E_{O,afterglow}$, $E_{\gamma,iso}$ and $E_{X,f}$ are the optical isotropic energy in the afterglow phase, the total gamma isotropic energy and the prompt emission energy of the pulse.
- $E_{X,corr}$, $E_{\gamma,peak}$ and $E_{\gamma,cor}$ are the isotropic kinetic afterglow energy in X-ray, the prompt peak energy in the vF_v spectrum and the isotropic energy corrected for the beaming factor.
- $\alpha_{X,a}, \alpha_{O,>200s}, \alpha_{X,>200s}, \alpha_{\nu,fl}$ and $\alpha_{\nu,st}$ are the X-ray temporal decay index in the afterglow phase, in the optical after 200 s, in the X-ray after 200 s and the optical or X-ray flat and steep temporal decay indices respectively.
- $\beta_{X,a}, \beta_{O,a}$ and $\beta_{O,>200s}$ are the spectral index of the plateau emission in X-ray, the optical-to-X-ray spectral index for the end time of the plateau and the optical spectral index after 200 s.
- $\nu_X, \nu_O, \nu_C, \nu_m$ are the X-ray and optical frequencies, and the cooling and the peak frequencies of the synchrotron radiation.

All the time quantities described above are given in the observer frame, while with the upper index * we denote in the text the observables in the GRB rest frame. The rest frame times are the observed times divided by the cosmic time expansion, for example, $T_{X,a}^* = T_{X,a}/(1+z)$ denotes the rest frame time at the end of the plateau emission.

In the following table we will give a list of the abbreviations/acronyms used through the text:

Table 1
Table with abbreviations.

Abbreviation	Meaning
DE	Dark Energy
EoS	Equation of State
CL	Confidence Level
IC	Intermediate Class GRB
SGRB	Short GRB
LGRB	Long GRBs
SGRBsEE	Short GRBs with extended emission
XRFs	X-ray Flashes
SNe	Supernovae
BH	Black Hole
z	Redshift
FS	Forward Shock
RS	Reverse Shock
H_0	Hubble constant
Ω_M	Matter density in Λ CDM model
Ω_Λ	Dark Energy density in Λ CDM model
Ω_k	Curvature in Λ CDM model
$\sigma_{\log L_{X,a}}$	Error on the luminosity
$\sigma_{\log T_{X,a}}$	Error on the time
E4	Sample with $\sigma_E = (\sigma_{\log L_{X,a}}^2 + \sigma_{\log T_{X,a}}^2)^{1/2} < 4$
E0095	Sample with $\sigma_E = (\sigma_{\log L_{X,a}}^2 + \sigma_{\log T_{X,a}}^2)^{1/2} < 0.095$
W07	Willingale et al. (2007)
Γ	Lorentz Factor
V	Variability of the GRB light curve
h	Hubble constant divided by 100
w_0, w_a	Coefficients of the DE EoS $w(z) = w_0 + w_a z(1+z)^{-1}$
HD	Hubble Diagram
a	Normalization of the relation
b	Slope of the relation
σ_{int}	Intrinsic scatter of the relation
b_{int}	Intrinsic slope of the relation

3. The afterglow relations

Several relations appeared in literature relating only parameters in the afterglow, such as the $L_X(T_a) - T_{X,a}^*$ relation (Dainotti et al., 2008) and similar ones in the optical and X-ray bands such as the unified $L_X(T_a) - T_{X,a}^*$ and $L_{O,a} - T_{O,a}^*$ (Ghisellini et al., 2009) and the $L_{O,200s} - \alpha_{O,>200s}$ relations (Oates et al., 2012).

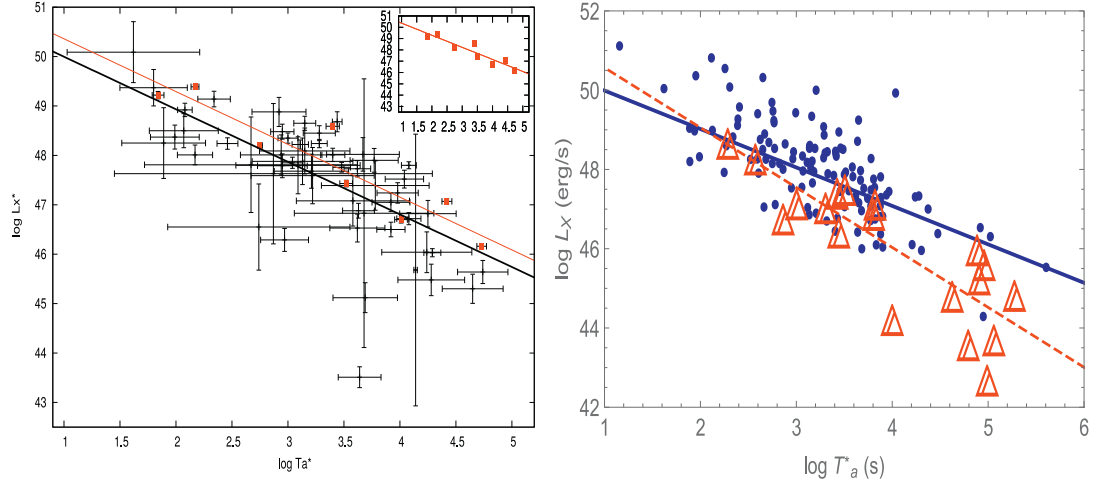


Fig. 2. Left panel: $\log L_{X,a}$ (equivalent to $\log L_X^*$ in this plot) vs. $\log T_{X,a}^*$ for 62 long afterglows with the error energy parameter $\sigma_E < 4$, and the best fitted relation line in black, from Dainotti et al. (2010). The red line fitted to the 8 lowest error (red) points produces an upper envelope of the full data set. The upper envelope points with the best fitted line are separately presented in an inset panel. Right panel: LONG-NO-SNe 128 GRBs (blue points fitted with a solid blue line) and the 19 events from LONG-SNe (red empty triangles) fitted with a red dashed line from Dainotti et al. (2016c). (For interpretation of the references to colour in this figure legend, the reader is referred to the web version of this article.)

3.1. The Dainotti relation ($L_X(T_a) - T_{X,a}^*$)

The first relation to shed light on the plateau properties has been the $L_X(T_a) - T_{X,a}^*$ one, hereafter also referred as LT. The phenomenon is an anti-relation between the X-ray luminosity at the end of the plateau, $L_X(T_a)$, and the time in the X-ray at the end of the plateau, $T_{X,a}^*$, for simplicity of notation we will refer to $L_X(T_a)$ as $L_{X,a}$.

It was discovered by Dainotti et al. (2008) using 33 LGRBs detected by the Swift satellite in the X-ray energy band observed by XRT. Among the 107 GRBs fitted by W07 phenomenological model, shown in the left panel of Fig. 1, only the GRBs that have a good spectral fitting of the plateau and firm determination of z have been chosen. The functional form of the LT relation obtained is the following:

$$\log L_{X,a} = a + b \times \log T_{X,a}^*, \quad (1)$$

with a normalization $a = 48.54$, a slope $b = -0.74^{+0.20}_{-0.19}$, an intrinsic scatter, $\sigma_{int} = 0.43$ and a Spearman correlation coefficient² $\rho = -0.74$. $L_{X,a}$ in the Swift XRT passband, $(E_{min}, E_{max}) = (0.3, 10)$ keV, has been computed from the following equation:

$$L_{X,a}(z) = 4\pi D_L^2(z, \Omega_M, h) F_{X,a} K \quad (2)$$

where $D_L(z, \Omega_M, h)$ represents the GRB luminosity distance for a given z , $F_{X,a}$ indicates the flux in the X-ray at the end of the plateau, and $K = \frac{1}{(1+z)^{(1-\beta_{X,a})}}$ denotes the K-correction for cosmic expansion (Bloom et al., 2001). This anti-relation shows that the shorter the plateau duration, the more luminous the plateau. Since the ratio between the errors on both variables is close to unity, it means that both errors need to be considered and the Marquardt Levenberg algorithm is not the best fitting method to be applied in this circumstance. Therefore, a Bayesian approach (D'Agostini, 2005) needs to be considered. This method takes into

account the errors of both variables and an intrinsic scatter, σ_{int} , of unknown nature. However, the results of both the D'Agostini method and the Marquardt Levenberg algorithm are comparable. Due to the higher accuracy of the first method from now on the authors prefer this technique in their papers. Evidently, the tighter the relation, the better the chances to constrain the cosmological parameters. With this specific challenge in mind, a subsample of bursts has been chosen with particular selection criteria both on luminosity and time, namely $\log L_{X,a} > 45$ and $1 \leq \log T_{X,a}^* \leq 5$. After this selection has been applied, a subsample of 28 LGRBs was obtained with $(a, b, \sigma_{int}) = (48.09, -0.58 \pm 0.18, 0.33)$, thus reducing considerably the scatter.

In agreement with these results, through the analysis of the late prompt phase in optical and X-ray light curves of 33 LGRBs, also Ghisellini et al. (2009) found a common observational model for optical and X-ray light curves with the same value for the slope, $b = -0.58^{+0.18}_{-0.18}$, obtained by Dainotti et al. (2008) when the time is limited between $1 \leq \log T_{X,a}^* \leq 5$.

Instead, Dainotti et al. (2010) from a sample of 62 LGRBs found $b = -1.06^{+0.27}_{-0.28}$, while for the 8 IC GRBs pointed out a much steeper relation ($b = -1.72^{+0.22}_{-0.21}$). Finally, taking into account the errors on luminosity ($\sigma_{\log L_{X,a}}$) and time ($\sigma_{\log T_{X,a}^*}$), the 8 GRBs with the smallest errors were defined as the ones with $\sigma_E = (\sigma_{\log L_{X,a}}^2 + \sigma_{\log T_{X,a}^*}^2)^{1/2} < 0.095$. For this subsample, Dainotti et al. (2010) found a slope $-1.05^{+0.19}_{-0.20}$ see Fig. 2, the right panel of Fig. 3 and Table 2.

Similar to Dainotti et al. (2010), also Bernardini et al. (2012a) and Sultana et al. (2012), with a sample of 64 and 14 LGRBs respectively, found a slope $b \approx -1$, for details see Table 2.

Expanding the sample again to 77 LGRBs, Dainotti et al. (2011a) discovered a relation with $b = -1.20^{+0.27}_{-0.30}$. Later, Mangano et al. (2012), considering in their sample of 50 LGRBs those GRBs with no visible plateau phase and employing a broken power law as a fitting model, found a steeper slope ($b = -1.38^{+0.16}_{-0.16}$). Thus, from all these analyses it is clear that a steepening of the slope has been observed when the sample size is increased.

² A computation of statistical dependence between two variables stating how good the relation between these variables can be represented employing a monotonic function. It assumes a value between -1 and $+1$.

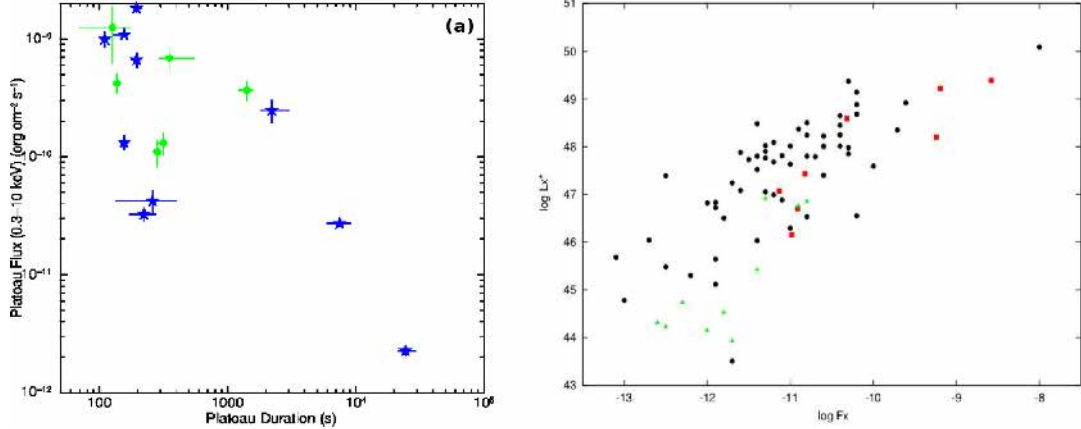


Fig. 3. Left panel: the plateau flux versus the plateau duration for a sample of 22 GRBs from Rowlinson et al. (2013). Blue stars are GRBs with two or more breaks in their light curves, while green circles have one break. Right panel: $\log L_{X,a}$ versus $\log F_{X,a}$ for the full GRB sample from Dainotti et al. (2010). The 8 upper envelope points are shown as red squares, while the IC GRBs are represented by green triangles. (For interpretation of the references to colour in this figure legend, the reader is referred to the web version of this article.)

Table 2

Summary of the LT relation. All the measurements are performed by the Swift XRT Telescope. The first column represents the authors, the second one the number of GRBs in the used sample, the third one the GRB type (S=Short, L=Long, IC=Intermediate), the fourth and the fifth ones are the slope and normalization of the relation and the last two columns are the correlation coefficient and the chance probability, P.

Author	N	Type	Slope	Norm	Corr.coeff.	P
Dainotti et al. (2008)	28	$1 < T_{X,a}^* < 5$	$-0.58^{+0.18}_{-0.18}$	48.09	-0.80	1.6×10^{-7}
Dainotti et al. (2008)	33	All GRBs	$-0.74^{+0.20}_{-0.19}$	48.54	-0.74	10^{-9}
Cardone et al. (2009)	28	L	$-0.58^{+0.18}_{-0.18}$	48.09	-0.74	10^{-9}
Ghisellini et al. (2009)	33	L	$-0.58^{+0.18}_{-0.18}$	48.09	-0.74	10^{-9}
Cardone et al. (2010)	66	L	$-1.04^{+0.23}_{-0.22}$	$50.22^{+0.77}_{-0.76}$	-0.68	7.6×10^{-9}
Dainotti et al. (2010)	62	L	$-1.06^{+0.27}_{-0.28}$	$51.06^{+1.02}_{-1.02}$	-0.76	1.85×10^{-11}
Dainotti et al. (2010)	8	high luminosity	$-1.05^{+0.19}_{-0.20}$	$51.39^{+0.90}_{-0.90}$	-0.93	1.7×10^{-2}
Dainotti et al. (2010)	8	IC	$-1.72^{+0.22}_{-0.21}$	$52.57^{+0.04}_{-0.04}$	-0.66	7.4×10^{-2}
Dainotti et al. (2010a)	77	L	$-1.20^{+0.27}_{-0.30}$	$51.04^{+0.27}_{-0.30}$	-0.69	7.7×10^{-8}
Sultana et al. (2012)	14	L	$-1.10^{+0.03}_{-0.03}$	$51.57^{+0.10}_{-0.10}$	-0.88	10^{-5}
Bernardini et al. (2012)	64	L	$-1.06^{+0.06}_{-0.06}$	51.06	-0.68	7.6×10^{-9}
Mangano et al. (2012)	50	L	$-1.38^{+0.16}_{-0.16}$	$52.2^{+0.06}_{-0.06}$	-0.81	2.4×10^{-10}
Dainotti et al. (2013a)	101	ALL intrinsic	$-1.07^{+0.09}_{-0.14}$	52.94	-0.74	10^{-18}
Dainotti et al. (2013b)	101	All GRBs	$-1.32^{+0.18}_{-0.17}$	$52.8^{+0.9}_{-0.3}$	-0.74	10^{-18}
Dainotti et al. (2013b)	101	without short	$-1.27^{+0.18}_{-0.26}$	52.94	-0.74	10^{-18}
Dainotti et al. (2013b)	101	simulated	$-1.52^{+0.04}_{-0.24}$	$53.27^{+0.54}_{-0.48}$	-0.74	10^{-18}
Postnikov et al. (2014)	101	L ($z < 1.4$)	$-1.51^{+0.26}_{-0.27}$	$53.27^{+0.54}_{-0.48}$	-0.74	10^{-18}
Rowlinson et al. (2014)	159	intrinsic	$-1.07^{+0.09}_{-0.14}$	52.94	-0.74	10^{-18}
Rowlinson et al. (2014)	159	observed	$-1.40^{+0.19}_{-0.19}$	$52.73^{+0.52}_{-0.52}$	-0.74	10^{-18}
Rowlinson et al. (2014)	159	simulated	$-1.30^{+0.03}_{-0.03}$	$52.73^{+0.52}_{-0.52}$	-0.74	10^{-18}
Dainotti et al. (2015)	123	L	$-0.90^{+0.19}_{-0.17}$	$51.14^{+0.58}_{-0.58}$	-0.74	10^{-15}
Dainotti et al. (2016c)	19	L-SNe	$-1.5^{+0.3}_{-0.3}$	$51.85^{+0.94}_{-0.94}$	-0.83	5×10^{-6}

Therefore, before going further with additional analysis, Dainotti et al. (2013a) decided to show how selection biases can influence the slope of the relation. They showed that the steepening of the relation results from selection biases, while the intrinsic slope of the relation is $b = -1.07^{+0.09}_{-0.14}$, see Section 5. Summarizing, Dainotti et al. (2013a) with a sample of 101 GRBs, confirmed the previous results from Dainotti et al. (2010), as well as Rowlinson et al. (2014), with a data set of 159 GRBs.

Dainotti et al. (2015b) also confirmed previous results of Dainotti et al. (2013a) but with a larger sample of 123 LGRBs. All the samples discussed are observed by SWIFT/XRT.

In the context of reducing the scatter of the LT relation, Del Vecchio et al. (2016) investigated the temporal decay indices $\alpha_{X,a}$ after the plateau phase for a sample of 176 GRBs detected by Swift within two different models: a simple power law, considering the decaying phase after the plateau phase, and the W07 one. It is pointed out that the results are independent of the chosen model. It was checked if there are some common characteristics in GRBs phenomena that can allow them to be used as standardizable candles like SNe Ia and to obtain some constraints revealing which is the best physical interpretation describing the plateau emission. The interesting result is that the LT relation for the low

and high luminosity GRBs seems to depend differently on the $\alpha_{X,a}$ parameter, thus possibly implying a diverse density medium.

Continuing the search for a standard set of GRBs, Dainotti et al. (2016c) analyzed 176 GRB afterglow plateaus observed by Swift with known redshifts which revealed that the subsample of LGRBs associated with SNe (LONG-SNe) presents a very high correlation coefficient for the LT relation. They investigated the category of LONG GRBs associated spectroscopically with SNe in order to compare the LT correlation for this sample with the one for LGRBs for which no associated SN has been observed (hereafter LONG-NO-SNe, 128 GRBs). They checked if there is a difference among these subsamples. They adopted first a non-parametric statistical method, the Efron and Petrosian (1992) one, to take into account redshift evolution and check if and how this effect may steepen the slope for the LONG-NO-SNe sample. This procedure is necessary due to the fact that this sample is observed at much higher redshift than the GRB-SNe sample. Therefore, removing selection bias is the first step before any comparison among samples observed at different redshifts could be properly performed. They have demonstrated that there is no evolution for the slope of the LONG-NO-SNe sample and no evolution is expected for the LONG-SNe sample. The difference among the slopes is statistically significant with the probability $P=0.005$ for LONG-SNe. This possibly suggests that the LONG-SNe with firm spectroscopic features of the SNe associated might not require a standard energy reservoir in the plateau phase unlike the LONG-NO-SNe. Therefore, this analysis may open new perspectives in future theoretical investigations of the GRBs with plateau emission and associated with SNe. They also discuss how much this difference can be due to the jet opening angle effect. The difference between the SNe-LONG (A+B) and LONG-NO-SNe sample is only statistically significant at the 10% level when we consider the beaming correction. Thus, one can argue that the difference in slopes can be partially due to the effect of the presence of low luminosity GRBs in the LONG-SNe sample that are not corrected for beaming. However, the beaming corrections are not very accurate due to indeterminate jet opening angles, so the debate remains open and it can only be resolved when we will gather more data.

In Table 2, we report a summary of the parameters a and b with ρ and P for the LT relation. In conclusion, the most reliable parameters for this relation are those from Dainotti et al. (2013a), because they have demonstrated that the intrinsic slope not affected by selection biases is determined to be -1 as computed through the Efron and Petrosian (EP) method.

3.1.1. Physical interpretation of the Dainotti relation ($L_X(T_a) - T_{X,a}^*$)

Here, we revise the theoretical interpretation of the LT relation, which is based mainly on the accretion (Cannizzo and Gehrels, 2009; Cannizzo et al., 2011) and the magnetar models (Zhang and Mészáros, 2001; Dall'Osso et al., 2011; Rowlinson and O'Brien, 2012; Rowlinson et al., 2013, 2014).

The first one states that an accretion disc is created from the motion of the material around the GRB progenitor star collapsing towards its progenitor core. After it is compressed by the gravitational forces, the GRB emission takes place. For LGRBs, the early rate of decline in the initial steep decay phase of the light curve may provide information about the radial density distribution within the progenitor (Kumar et al., 2008).

Cannizzo and Gehrels (2009) predicted a steeper relation slope (-3/2) than the observed one (~ -1), which on the other hand is in good agreement with the prior emission model of Yamazaki (2009).

Later, Cannizzo et al. (2011), using a sample of 62 LGRBs and few SGRBs simulated the fall-back disks surrounding the BH. They found that a circularization radius of the mass around the BH with value $10^{10} - 10^{11}$ cm can give an estimate for the plateau duration

of around 10^4 s for LGRBs maintaining the initial fall back mass at 10^{-4} solar masses (M_\odot), see the left panel of Fig. 4. For SGRBs the radius is estimated to be 10^8 cm. The LT relation provides a lower limit for the accreting mass estimates $\Delta M \approx 10^{-4}$ to $10^{-3} M_\odot$.³ From their results, it was claimed that the LT relation could be obtained if a typical energy reservoir in the fall-back mass is assumed, see the right panel of Fig. 4. However, in their analysis the very steep initial decay following the prompt emission, which have been modeled by Lindner et al. (2010) as fall-back of the progenitor core, is not considered.

Regarding the magnetar model, Zhang and Mészáros (2001) studied the effects of an injecting central engine on the GRB afterglow radiation, concentrating on a strongly magnetized millisecond pulsar. For specific starting values of rotation period and magnetic field of the pulsar, the afterglow light curves should exhibit an achromatic bump lasting from minutes to months, and the observation of such characteristics could set some limits on the progenitor models. More recently, Dall'Osso et al. (2011) investigated the energy evolution in a relativistic shock from a spinning down magnetar in spherical symmetry. With their fit of few observed Swift XRT light curves and the parameters of this model, namely a spin period of (1–3 ms), and high values of magnetic fields ($B \sim 10^{14} - 10^{15}$ G), they managed to well reproduce the properties of the shallow decay phase and the LT relation, see the left panel of Fig. 5.

Afterward, Bernardini et al. (2012a) with a sample of 64 LGRBs confirmed, as previously founded by Dall'Osso et al. (2011), that the shallow decay phase of the GRB light curves and the LT relation can be well explained.

Then, Rowlinson and O'Brien (2012) and Rowlinson et al. (2013) pointed out that energy injection is a fundamental mechanism for describing the plateau emission of both LGRBs and SGRBs. In fact, the remnant of NS-NS mergers can form a magnetar, and indeed the origin of the majority of SGRBs is well explained through the energy injection by a magnetar.

Later, Rowlinson et al. (2014), using 159 GRBs from Swift catalogue, analytically demonstrated that the central engine model accounts for the LT relation assuming that the compact object is injecting energy into the forward shock (FS), a shock driven out into the surrounding circumstellar medium. The luminosity and plateau duration can be computed as follows:

$$\log L_{X,a} \sim \log(B_p^2 P_0^{-4} R^6) \quad (3)$$

and

$$\log T_{X,a}^* = \log(2.05 \times I B_p^{-2} P_0^2 R^{-6}), \quad (4)$$

where $T_{X,a}^*$ is in units of 10^3 s, $L_{X,a}$ is in units of 10^{49} erg s $^{-1}$, I is the moment of inertia in units of 10^{45} g cm 2 , B_p is the magnetic field strength at the poles in units of 10^{15} G, R is the radius of the NS in units of 10^6 cm and P_0 is the initial period of the compact object in milliseconds. Then, substituting the radius from Eq. 4 into Eq. 3, it was derived that:

$$\log(L_{X,a}) \sim \log(10^{52} I^{-1} P_0^{-2}) - \log(T_{X,a}^*). \quad (5)$$

Therefore, an intrinsic relation $\log L_{X,a} \sim -\log T_{X,a}^*$ is confirmed directly from this formulation. Although some magnetar plateaus are inconsistent with energy injection into the FS, Rowlinson et al. (2014) showed that this emission is narrowly beamed and has $\leq 20\%$ efficiency in conversion of rotational

³ This value can be derived considering the total inferred accretion mass $\Delta M/M = \Delta E_X/f^{-1} * \epsilon_{acc} * c^2$ where c is the light speed, f is the X-ray afterglow beaming factor, ϵ_{acc} is the efficiency of the accretion onto the BH and E_X is the observed total energy of the plateau + later decay phases (the integral over time between $T_{X,t}$ and the end of afterglow, see Eq. 2 of W07).

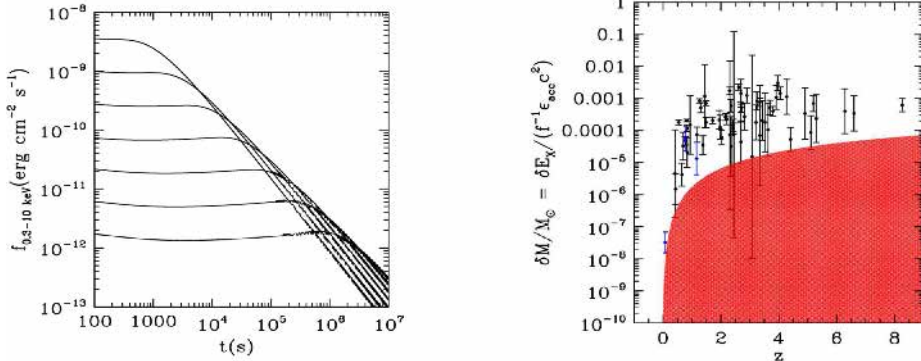


Fig. 4. Left panel: model light curves for LGRB parameters from Cannizzo et al. (2011), keeping the starting fall-back disk mass constant at $10^{-4} M_\odot$ but changing the initial radius and normalization. Right panel: total accretion mass for the plateau + later decay phases of GRBs from Cannizzo et al. (2011), considering 62 LGRBs from Dainotti et al. (2010). The region in red represents a limiting XRT detection flux level $f_{\text{ll}} = 10^{-12} \text{ erg cm}^{-2} \text{ s}^{-1}$ (assuming a plateau duration $t_{\text{pl}} = 10^4 \text{ s}$) in order to study a plateau to sufficient accuracy. A beaming factor $f = 1/300$ and a net efficiency for powering the X-ray flux $\epsilon_{\text{net}} = \epsilon_{\text{acc}} \epsilon_{\text{ex}} = 0.03$ were assumed. (For interpretation of the references to colour in this figure legend, the reader is referred to the web version of this article.)

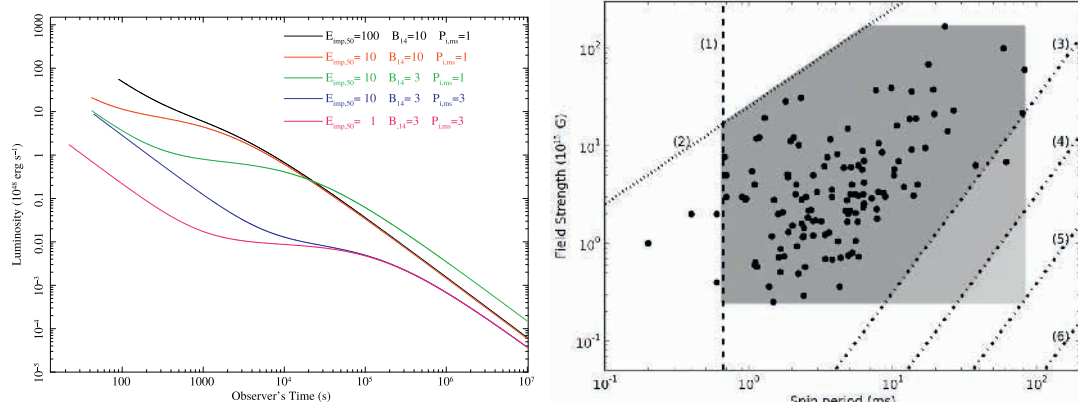


Fig. 5. Left panel: five theoretical light curves obtained by Dall'Osso et al. (2011), changing the initial energy of the afterglow, the dipole magnetic field, B , and the initial spin period of the NS, P . Right panel: the grey shaded areas are the homogeneous distribution of B and P employed to simulate the observable magnetar plateaus from Rowlinson et al. (2014). The upper and lower limits on B and the upper limit on P are computed considering the sample of GRBs fitted with the magnetar model (Lyons et al., 2010; Dall'Osso et al., 2011; Bernardini et al., 2012a; Gompertz et al., 2013; Rowlinson et al., 2013; Yi et al., 2014; Lü and Zhang, 2014). The dashed black vertical line (1) at 0.66 ms is the minimum P allowed. The dotted black line (2) indicates a limit on P and B strengths imposed by the fastest slew time of XRT in their sample in the rest frame of the highest z GRB, as plateaus with durations shorter than the slew time are unobservable. The black dash-dot lines (3–6) are the observational constraints for the dimmest XRT plateau observable assuming the lowest z in the GRB sample. These limits vary as a function of the beaming and efficiency of the magnetar emission: (3) Minimum beaming angle and efficiency (1 degree and 1% respectively), (4) Minimum efficiency (1%) and maximum beaming angle (isotropic), (5) Maximum efficiency (100%) and minimum beaming angle, (6) Maximum efficiency and beaming angle. The observed distributions indicate that the samples have low efficiencies and small beaming angles. (For interpretation of the references to colour in this figure legend, the reader is referred to the web version of this article.)

energy from the compact object into the observed plateau luminosity. In addition, the intrinsic LT relation slope, namely the one where the selection biases are appropriately removed, is explained within the spin-down of a newly formed magnetar at 1σ level, see right panel of Fig. 5. The scatter in the relation is mainly due to the range of the initial spin periods.

After several papers discussing the origin of the LT relation within the context of the magnetar model, very recently a debate has been opened by Rea et al. (2015) on the reliability of this model as the correct interpretation for the X-ray plateaus. Using GRBs with known z detected by Swift from its launch to August 2014, Rea et al. (2015) concluded that the initial magnetic field distribution, used to interpret the GRB X-ray plateaus within the magnetar model does not match the features of GRB-magnetars with the Galactic magnetar population. Therefore, even though

there are large uncertainties in these estimates due to GRB rates, metallicity and star formation, the GRB-magnetar model in its present form is safe only if two kinds of magnetar progenitors are allowed. Namely, the GRB should be different from Galactic magnetar ones (for example for different metallicities) and should be considered supermagnetars (magnetars with an initial magnetic field significantly large). Finally, they set a limit of about ≤ 16 on the number of stable magnetars produced in the Milky Way via a GRB in the past Myr. However, it can be argued that since the rates of Galactic magnetars and GRBs are really different, the number of Galactic magnetars cannot fully describe the origin of GRBs. In fact the Galactic magnetar rate is likely to be greater than 10% than the core collapse SNe rate, while GRB rate is much lower than that. In addition, the number of magnetars in the Milky Way may not be used as a constraint on the GRB rate because the spin-down

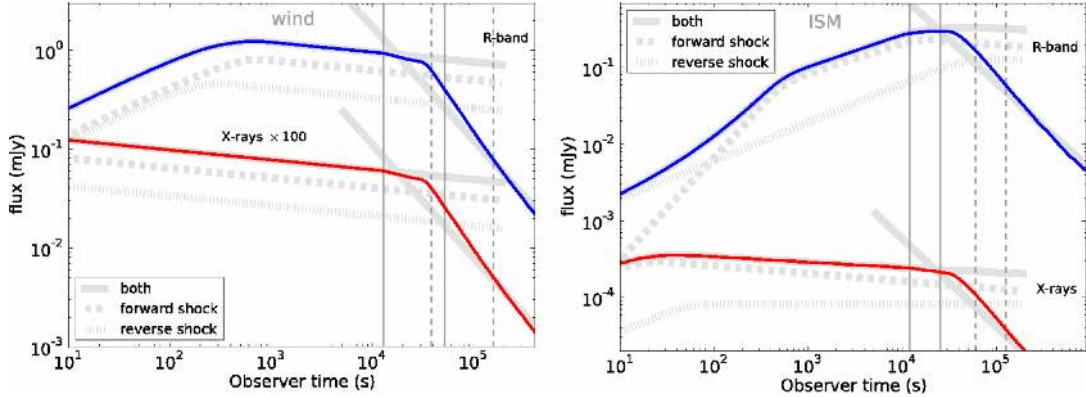


Fig. 6. Optical and X-ray light curves for wind (left panel) and ISM (right plot) scenario's from van Eerten (2014a). Thick light grey curves represent the analytical solutions for prolonged and impulsive energy injection. Thick dashed light grey and the thick dotted light grey curves indicate the forward shock region emission only and the reverse shock region only respectively. The grey vertical lines show (1) the arrival time of emission from the jet back and (2) the arrival time of emission from the jet front. The solid vertical lines indicate arrival times of emission along the jet axis for these two events; the dashed vertical lines express the arrival times of emission from an angle $\theta = 1/\gamma$.

rates of GRB magnetars should be very rapid. Due to the low GRB rate it would not be easy to detect these supermagnetars. Thus, it can be claimed that no conflict stands among this paper and the previous ones.

Still in the context of the energy injection models, van Eerten (2014a) found a relation between the optical flux at the end of the plateau and the time at the end of the plateau itself $f_{0,a} \sim T_{0,a}^{-0.78 \pm 0.08}$ (Panaitescu and Vestrand, 2011; Li et al., 2012) for which observed frame variables were considered. The range of all parameters describing the emission ($E_{\gamma,\text{iso}}$, the fraction of the magnetic energy, ϵ_B , the initial density, n_0) is the principal cause of the scatter in the relation, but it does not affect the slope. Finally, it was claimed that both the wind ($\propto A/r^2$, where A is a constant) and the interstellar medium can reproduce the observed relation within both the reverse shock (RS, a shock driven back into the expanding bubble of the ejecta) and FS scenarios, see Fig. 6.

Considering alternative models explaining the LT relation, Sultana et al. (2013) studied the evolution of the Lorentz gamma factor, $\Gamma = 1/\sqrt{1 - v^2/c^2}$ (where v is the relative velocity between the inertial reference frames and c is the light speed), during the whole duration of the light curves within the context of the Supercritical Pile Model. This model provides an explanation for both the steep-decline and the plateau or the steep-decline and the power law decay phase of the GRB afterglow, as observed in a large number of light curves, and for the LT relation. One of their most important results is that the duration of the plateau in the evolution of Γ becomes shorter with a decreasing value of $M_0 c^2$, where M_0 is the initial rest mass of the flow. This occurrence means that the more luminous the plateau, the shorter its duration and the smaller the $M_0 c^2$, namely the energy.

Instead, in the context of the RS and FS emissions, Leventis et al. (2014), investigating the synchrotron radiation in the thick shell scenario (i.e. when the RS is relativistic), found that this radiation is compatible with the presence of the plateau phase, see the left panel of Fig. 7. In addition, analyzing the $\log F_{X,a} - \log T_{X,a}$ relation in the framework of this model, they arrived at the conclusion that smooth energy injection through the RS is favored respect to the FS, see the right panel of Fig. 7.

van Eerten (2014b), with a simulated sample of GRBs, found out that the observed LT relation rules out basic thin shell models, but not basic thick ones. In fact, in the thick model, the plateau

phase comes from the late central source activity or from additional kinetic energy transfer from slower ejecta which catches up with the blast wave. As a drawback, in this context, it is difficult to distinguish between FS and RS emissions, or homogeneous and stellar wind-type environments.

In the thin shell case, the plateau phase is given by the pre-deceleration emission from a slower component in a two-component or jet-type model, but this scenario is not in agreement with the observed LT relation, see Fig. 8. This, however, does not imply that acceptable fits using a thin shell model are not possible, but further analysis is needed to exclude without any doubts thin shell models. Another model which has not been tested yet on this correlation is the photospheric emission model from stratified jets (Ito et al., 2014).

3.2. The unified $L_X(T_a) - T_{X,a}^*$ and $L_{O,a} - T_{O,a}^*$ relations

In order to describe the unified picture of the X-ray and optical afterglow, it is necessary to introduce relevant features regarding optical luminosities. To this end, Boér and Gendre (2000) studied the afterglow decay index in 8 GRBs in both X-ray and optical wavelengths. In the X-ray, the brightest GRBs had decay indices around 1.6 and the dimmest GRBs had decay indices around 1.11. Instead, they didn't observe this trend for the optical light curves, probably due to the host galaxy absorption.

Later, Nardini et al. (2006) discovered that the monochromatic optical luminosities at 12 h, $L_{O,12}$, of 24 LGRBs cluster at $\log L_{O,12} = 30.65 \text{ erg s}^{-1} \text{ Hz}^{-1}$, with $\sigma_{\text{int}} = 0.28$. The distribution of $L_{O,12}$ is less scattered than the one of $L_{X,12}$, the luminosity at 12 h in the X-ray, and the one of the ratio $L_{O,12}/E_{\gamma,\text{prompt}}$, where $E_{\gamma,\text{prompt}}$ is the rest frame isotropic prompt energy. Three bursts are outliers because they have luminosity which is smaller by a factor ~ 15 . This result suggests the existence of a family of intrinsically optically underluminous dark GRBs, namely GRBs where the optical-to-X-ray spectral index, $\beta_{OX,a}$, is shallower than the X-ray spectral index minus 0.5, $\beta_{X,a} - 0.5$.

Liang and Zhang (2006b) confirmed these results. They found a bimodal distribution of $L_{O,1d}$ using 44 GRBs. Nardini et al. (2008a) also confirmed these findings. They analyzed selection effects present in their observations extending the sample to 55 LGRBs

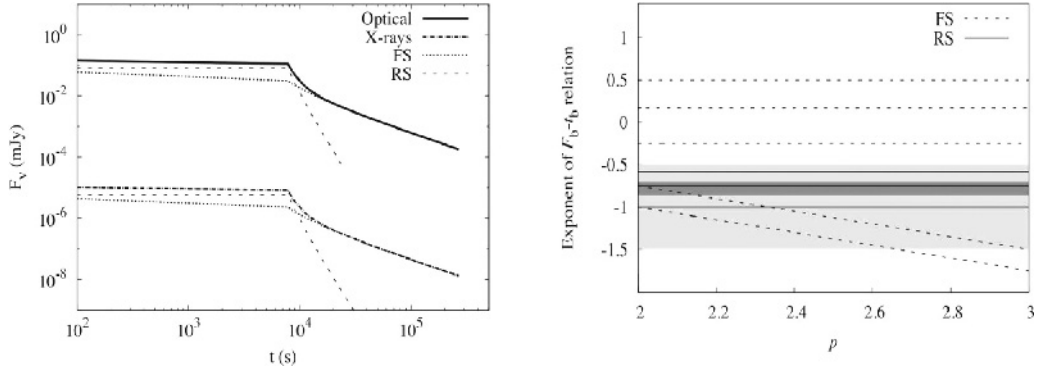


Fig. 7. Left panel: optical and X-ray light curves before and after the injection break from Leventis et al. (2014). The contributions of the FS (dotted line) and RS (dashed line) are shown for both. The considered parameters are \$E = 10^{51}\$ erg, \$n_1 = 50 \text{ cm}^{-3}\$, \$\Delta t = 5 \times 10^3\$ s, \$\eta = 600\$, \$q=0\$, \$\epsilon_e = \epsilon_B = 0.1\$, \$p=2.3\$, \$\theta_j = 90^\circ\$, \$d = 10^{28}\$ cm and \$z = 0.56\$. Right panel: index of the \$F_{0,a} - T_{X,a}\$ relation as a function of the electron distribution index, \$p\$, for the FS and the RS from Leventis et al. (2014). The lightly shaded region includes values allowed by the scaling from Panaitescu and Vestrand (2011), while the darker region indicates the scaling from Li et al. (2012). The five dashed lines show the five possible indices for the FS, while the three solid lines display the three possible (independent of \$p\$) indices for the RS.

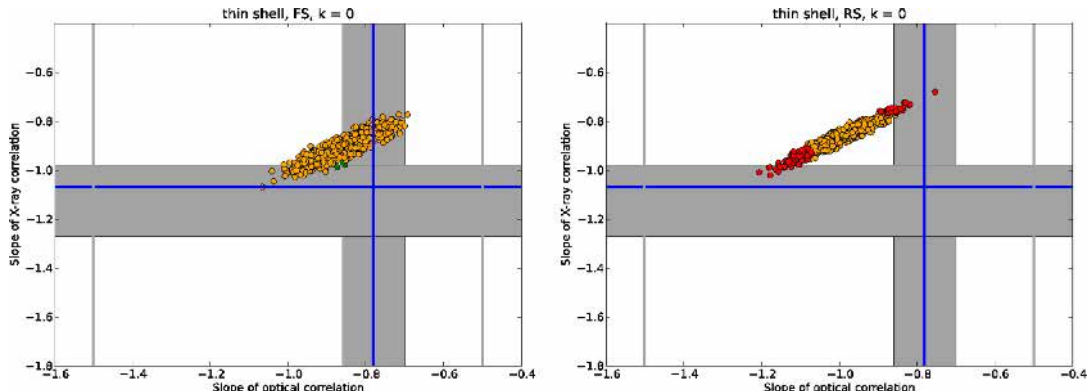


Fig. 8. Comparison of the slopes for 1000 thin shell data set runs and slopes of the observed LT relation in optical (horizontal direction) and the LT relation in X-ray (vertical direction) from van Eerten (2014b) for the FS (left panel) and the RS (right panel) cases. Grey band expresses \$1\sigma\$ errors on the relations, while green dots represent runs consistent at \$1\sigma\$ error bars for both, orange dots are compatible at \$3\sigma\$, but not at \$1\sigma\$ and red dots pass neither test. Vertical grey lines show more scattered LT in optical error bars from Panaitescu and Vestrand (2011). (For interpretation of the references to colour in this figure legend, the reader is referred to the web version of this article.)

with known \$z\$ and rest-frame optical extinction detected by the Swift satellite.

In contrast, Melandri et al. (2008), Oates et al. (2009), Zaninoni et al. (2013) and Melandri et al. (2014) found no bimodality in the distributions of \$L_{0,12}\$, \$L_{0,1d}\$ and \$L_{0,11}\$, investigating samples of 44, 24, 40 and 47 GRBs respectively.

Instead, with the aim of finding a unifying representation of the GRB afterglow phase, Ghisellini et al. (2009) fitted the light curves assuming this functional form:

$$L_L(v, t) = L_L(v, T_{X,a}) \frac{(t/T_{X,t})^{-\alpha_{v,fl}}}{1 + (t/T_{X,t})^{\alpha_{v,st} - \alpha_{v,fl}}} \quad (6)$$

They used a data sample of 33 LGRBs detected by Swift in X-ray (0.3–10 keV) and optical R bands (see the left and middle panels of Fig. 9). Within this approximation, the agreement with data is reasonably good, and they confirmed the X-ray LT relation.

Through their analysis using a data sample of 32 Swift GRBs, Liang et al. (2010) found that the optical peak luminosity, \$L_{0,peak}\$, in the R band in units of \$10^{47} \text{ erg s}^{-1}\$ and the optical peak time, \$T_{0,peak}^*\$, are anti-correlated, see the right panel of Fig. 9, with

a slope \$b = -2.49 \pm 0.39\$ and \$\rho = -0.90\$. They deduced that a fainter bump has its maximum later than brighter ones and it also presents a longer duration.

Panaitescu and Vestrand (2011) showed a similar relation to the one presented in Liang et al. (2010). They found a \$\log L_{0,a} \sim \log T_{0,a}^{-1}\$ anti-relation using 37 Swift GRBs. This result may indicate a unique mechanism for the optical afterglow even though the optical energy has a quite large scatter.

Afterwards, Li et al. (2012) found a relation (see the left panel of Fig. 10) similar to the LT relation, but in the R band. They used 39 GRBs with optical data available in the literature. This relation is between the optical luminosity at the end of the plateau, \$L_{0,a}\$, in units of \$10^{48} \text{ erg s}^{-1}\$ and the optical end of the plateau time, \$\log T_{0,a}^*\$, in the shallow decay phase of the GRB light curves, denoted with the index S. They found a slope \$b = -0.78 \pm 0.08\$, \$\rho = 0.86\$ and \$P < 10^{-4}\$.

\$L_{0,a}^S\$ varies from \$10^{43}\$ to \$10^{47} \text{ erg s}^{-1}\$, and in some GRBs with an early break reaches \$\sim 10^{49} \text{ erg s}^{-1}\$, see the middle panel of Fig. 10. \$T_{0,a}^S\$ spans from tens of seconds to several days after the GRB trigger, with a typical shallow peak time \$T_{0,a}^S\$ of \$\sim 10^4\$ s, see

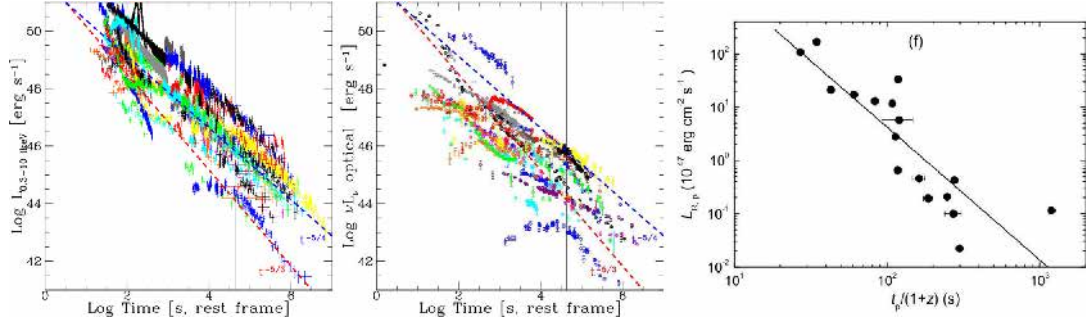


Fig. 9. The light curves of the full sample from Ghisellini et al. (2009) in the X-rays (left panel) and optical (middle panel). The vertical lines represent $\log L_{X,12}$ and $\log L_{O,12}$ in the rest frame respectively. Instead, the dashed lines indicate the $\log t^{-5/4}$ (blue) and the $\log t^{-5/3}$ (red) behaviors. Right panel: relation between $L_{O,\text{peak}}$ (equivalent to $L_{R,p}$ in the picture) and $T_{O,\text{peak}}^*$ of the data set from Liang et al. (2010). Line represents the best fit. (For interpretation of the references to colour in this figure legend, the reader is referred to the web version of this article.)

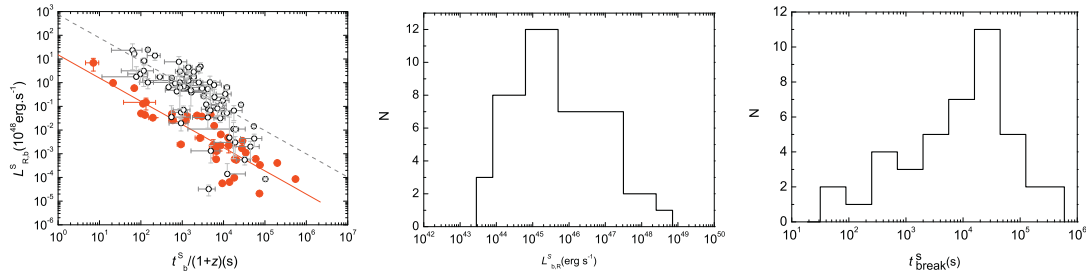


Fig. 10. Left panel: $L_{O,a}^S$ (equivalent to $L_{R,p}^S$ in the picture) as a function of $T_{O,a}^*$ (equivalent to t_b in the picture) from Li et al. (2012). The grey circles represent the X-ray data from Dainotti et al. (2010). Lines correspond to the best fit lines. Middle and Right panels: $L_{O,a}^S$ and $T_{O,a}^*$ distributions for the full GRB data set from Li et al. (2012).

Table 3

Summary of the relations in this section. The first column represents the relation in log scale, the second one the authors, and the third one the number of GRBs in the used sample. Afterwards, the fourth column is the slope of the relation and the last two columns are the correlation coefficient and the chance probability, P.

Correlations	Author	N	Slope	Corr.coeff.	P
$L_{O,\text{peak}} - T_{O,\text{peak}}$	Liang et al. (2010)	32	-2.49 ± 0.39	-0.90	
$L_{O,a} - T_{O,a}$	Panaiteescu & Vestrand (2011)	37	-1		
$L_{O,a}^S - T_{O,a}^*$	Li et al. (2012)	39	-0.78 ± 0.08	0.86	$< 10^{-4}$

the right panel of Fig. 10. By plotting $L_{O,a}$ in units of 10^{48} erg s^{-1} as a function of $T_{O,a}^*$ in the burst frame, they observed that optical data have a similar trend to the X-ray data. In fact, this power law relation, presented in the left panel of Fig. 10, with an index of -0.78 ± 0.08 is similar to that derived for the X-ray flares (see Section 4.6). XRF phenomena are described in Section 1. As a consequence, they recovered the LT relation. In Table 3 a summary of the relations described in this section is displayed.

3.2.1. Physical interpretation of the unified $L_X(T_a) - T_{X,a}^*$ and $L_{O,a} - T_{O,a}^*$ relations

In the unified $L_X(T_a) - T_{X,a}^*$ and $L_{O,a} - T_{O,a}^*$ relations Ghisellini et al. (2009) considered the flux as the sum of synchrotron radiation caused by the standard FS due to the fireball impacting the circumburst medium and of another component may be produced by a long-lived central engine, which resembles mechanisms attributed to a "late prompt". Even if based in part on a phenomenological model, Ghisellini et al. (2009) explained situations in which achromatic and chromatic jet break are either present or not in the observed light curves.

In addition, from their analysis, the decay slope of the late prompt emission results to be $\alpha_{X,a} = -5/4$ (see blue dashed line for X-ray and optical emission in the left and middle panels of Fig. 9 respectively), really close within the errors to the value of the temporal accretion rate of fall-back material (i.e. $\sim \log t^{-5/3}$, see red dashed line for X-ray and for optical emission in the left and middle panels of Fig. 9 respectively). This explains the activity of the central engine for such a long duration. For a similar interpretation within the context of the accretion onto the BH related to LT relation see Section 3.1.1.

Liang et al. (2010) claimed that the external shock model explains well the anti-relation between $L_{O,\text{peak}}$ and $T_{O,\text{peak}}$, because later deceleration time is equivalent to slower ejecta and thus to a less luminous emission.

Furthermore, Panaiteescu and Vestrand (2008) from the analysis of the $\log L_{O,a} - \log T_{O,a}$ relation explained the peaky afterglows (those with $L_{O,a} \propto T_{O,a}^{-1}$) as being a bit outside the cone of view, while the plateau as off-axis events and due to the angular structure of the jet. Later, Panaiteescu and Vestrand (2011) asserted that the double-jet structure of the ejecta is problematic. To overcome

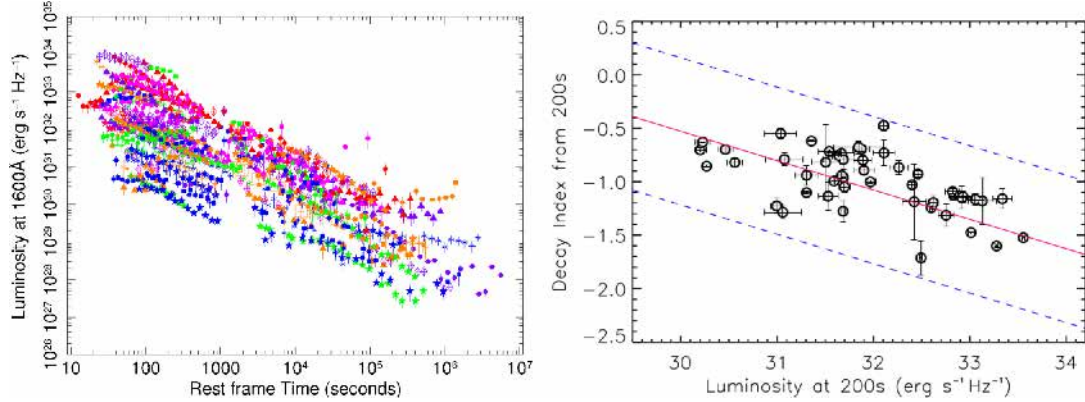


Fig. 11. Left panel: “optical light curves of 56 GRBs from Oates et al. (2012)”. Right panel: “ $\log L_{0,200s}$ vs. $\alpha_{0,>200s}$ from Oates et al. (2012). The red solid line indicates the best fit line and the blue dashed lines show the 3 σ variance”. (For interpretation of the references to colour in this figure legend, the reader is referred to the web version of this article.)

this issue, they suggested a model in which both the peaky and plateau afterglows depend on how much time the central engine allows for the energy injection. More specifically, impulsive ejecta with a narrow range of Γ are responsible for the peaky afterglows, while the plateau afterglows are produced by a distribution of initial Γ which keeps the energy injection till 10^5 s.

Later, Li et al. (2012) pointed out that late GRB central engine activities can account for both optical flares and the optical shallow-decay segments. These activities can be either erratic (for flares) or steady (for internal plateaus). A normal decay follows the external plateaus with $\alpha_{X,a}$ typically around -1 , thus possibly originated by an external shock with the shallow decay segment caused by continuous energy injection into the blast wave (Rees and Mészáros, 1998; Dai and Lu, 1998; Sari and Mészáros, 2000; Zhang and Mészáros, 2001). Instead, the internal plateaus, found first by Troja et al. (2007) in GRB 070110 and later studied statistically by Liang et al. (2007), are followed by a much steeper decay ($\alpha_{X,a}$ steeper than -3), which needs to be powered by internal dissipation of a late outflow. In summary, the afterglow can be interpreted as a mix of internal and external components.

3.3. The $L_{0,200s}$ – $\alpha_{0,>200s}$ relation and its physical interpretation

Oates et al. (2012) discovered a relation between the optical luminosity at 200 s, $\log L_{0,200s}$, and the optical temporal decay index after 200 s, $\alpha_{0,>200s}$, see the right panel of Fig. 11. They used a sample of 48 LGRB afterglow light curves at 1600 Å detected by UVOT on board of the Swift satellite, see the left panel of Fig. 11. The best fit line for this relation is given by:

$$\log L_{0,200s} = (28.08 \pm 0.13) - (3.636 \pm 0.004) \times \alpha_{0,>200s}, \quad (7)$$

with $\rho = -0.58$ and a significance of 99.998% (4.2 σ). This relation means that the brightest GRBs decay faster than the dimmest ones. To obtain the light curves employed for building the relation, they used the criteria from Oates et al. (2009) in order to guarantee that the entire UVOT light curve is not noisy, namely with a high signal to noise (S/N) ratio: the optical/UV light curves must be observed in the V filter of the UVOT with a magnitude ≤ 17.8 , UVOT observations must have begun within the first 400 s after the BAT trigger and the afterglow must have been observed until at least 10^5 s after the trigger. Their results pointed out the dependence of this relation is on the differences in the observing angle and on the rate of the energy release from the central engine.

As a further step, Oates et al. (2015), using the same data set, investigated the same relation both in optical and in X-ray wavelengths in order to make a comparison, and they confirmed previous optical results finding a similar slope for both relations. In addition, they analyzed the connection between the temporal decay indices after 200 s (in X-ray and optical) obtaining as best fit relation $\alpha_{X,>200s} = \alpha_{0,>200s} - 0.25$, see the left panel of Fig. 12. They yielded some similarities between optical and X-ray components of GRBs from these studies. Their results were in disagreement with those previously found by Urata et al. (2007), who investigated the relation between the optical and X-ray temporal decay indices in the normal decay phase derived from the external shock model. In fact, a good fraction of outliers was found in this previous work.

Racusin et al. (2016) studied a similar relation using 237 Swift LGRBs, but in X-ray. For this relation, it was found that slope $b = -0.27 \pm 0.04$ and solid evidence for a strong connection between optical and X-ray components of GRBs was discovered as well. In conclusion, the Monte Carlo simulations and the statistical tests validated the relation between $\log L_{0,200s}$ and $\alpha_{0,>200s}$ by Oates et al. (2012). In addition, it shows a possible connection with its equivalent, the LT relation in X-ray, implying a common physical mechanism. In Table 4 a summary of the relations described in this section is reported.

Regarding the physical interpretation of the $\log L_{0,200s}$ – $\alpha_{0,>200s}$ relation, Oates et al. (2012) explored several scenarios. The first one implies that the relation can be due to the interaction of the jet with the external medium. In a straightforward scenario $\alpha_{0,>200s}$ is not a fixed value and all optical afterglows stem from only one closure relation where $\alpha_{0,>200s}$ and $\beta_{0,>200s}$ are related linearly. Thus a relation between $\log L_{0,200s}$ and $\beta_{0,>200s}$ should naturally appear. Contrary to this expectation, $\alpha_{0,>200s}$ and $\beta_{0,>200s}$ are poorly correlated, see the right panel of Fig. 12, and there is no evidence for the existence of a relation between $\beta_{0,>200s}$ and $\log L_{0,200s}$. Therefore, this scenario cannot be ascribed as the cause of the $\log L_{0,200s}$ – $\alpha_{0,>200s}$ relation.

In the second scenario, they assumed that the $\log L_{0,200s}$ – $\alpha_{0,>200s}$ relation is produced by few closure relations indicated by lines in the right panel of Fig. 12. However, from this picture, the $\alpha_{0,>200s}$ and $\beta_{0,>200s}$ values with similar luminosities do not gather around a particular closure relation, thus also the basic standard model is not a good explanation of the $\log L_{0,200s}$ – $\alpha_{0,>200s}$ relation. As a conclusion, the afterglow model is more complex than it was considered in the past. It is

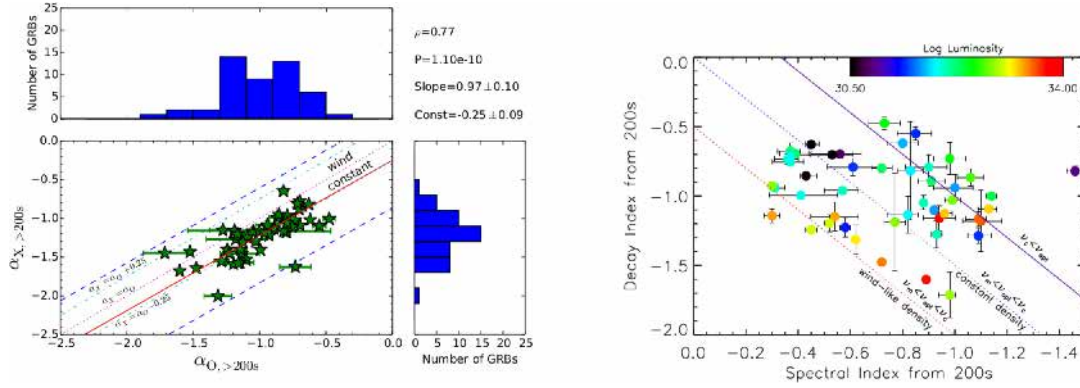


Fig. 12. Left panel: “ $\alpha_{O,>200s}$ and $\alpha_{X,>200s}$ from Oates et al. (2015). The red solid line represents the best fit regression and the blue dashed lines represent 3 times the root mean square (RMS) deviation. The relationships expected between the optical/UV X-ray light curves from the GRB closure relations are also shown. The pink dotted line represents $\alpha_{O,>200s} = \alpha_{X,>200s}$. The light blue dotted-dashed lines represent $\alpha_{X,>200s} = \alpha_{O,>200s} \pm 0.25$. In the top right corner it is given the coefficient ρ with P , and it is provided the best fit slope and constant determined by linear regression”. Right panel: “ $\alpha_{O,>200s}$ and $\beta_{O,>200s}$ for the sample of 48 LGRBs from Oates et al. (2012). The lines represent 3 closure relations and a color scale is used to display the range in $\log L_{0,200s}$ ”. (For interpretation of the references to colour in this figure legend, the reader is referred to the web version of this article.)

Table 4

Summary of the relations in this section. The first column represents the relation in log scale, the second one the authors, and the third one the number of GRBs in the used sample. Afterwards, the fourth and fifth columns are the slope and normalization of the relation and the last two columns are the correlation coefficient and the chance probability, P.

Correlations	Author	N	Slope	Norm	Corr. coeff.	P
$L_{0,200s} - \alpha_{O,>200s}$	Oates et al. (2012)	48	-3.636 ± 0.004	28.08 ± 0.13	-0.58	2×10^{-4}
$L_{0,200s} - \alpha_{O,>200s}$	Oates et al. (2015)	48	-3.636 ± 0.004	28.08 ± 0.13	-0.58	2×10^{-4}
$L_{X,200s} - \alpha_{X,>200s}$	Racusin et al. (2016)	237	-0.27 ± 0.04	-6.99 ± 1.11	0.59	10^{-6}

highly likely that there are physical properties that control the emission mechanism and the decay rate in the afterglow that still need to be investigated.

Therefore, Oates et al. (2012) proposed two additional alternatives. The first is related to some properties of the central engine influencing the rate of energy release so that for fainter afterglows, the energy is released more slowly. Otherwise, the relation can be due to different observing angles where observers at smaller viewing angles see brighter and faster decaying light curves.

As pointed out by Dainotti et al. (2013a), the $\log L_{0,200s} - \alpha_{O,>200s}$ relation is related to the LT one since both show an anti-relation between luminosity and decay rate of the light curve or time. The key point would be to understand how they relate to each other and the possible common physics that eventually drives both of them. To this end, Oates et al. (2015) compared the observed relations with the ones obtained with the simulated sample. The luminosity-decay relationship in the optical/UV is in agreement with that in the X-ray, inferring a common mechanism.

4. The prompt-afterglow relations

As we have discussed in the previous paragraphs, the nature of the plateau and the relations (e.g. the optical one) based on similar physics and directly related to the plateau are still under investigation. For this reason, several models have been proposed. To further enhance its theoretical understanding, it is necessary to evaluate the connection between plateaus and prompt phases. To this end, we hereby review the prompt-afterglow relations, thus helping to establish a more complete picture of the plateau GRB phenomenon.

4.1. The $E_{\gamma,\text{afterglow}} - E_{X,\text{prompt}}$ relation and its physical interpretation

W07 analyzed the relation between the gamma flux in the prompt phase, $F_{\gamma,\text{prompt}}$, and the X-ray flux in the afterglow, $F_{X,\text{afterglow}}$ using 107 Swift GRBs, see the upper left panel of Fig. 13. They calculated $F_{X,\text{afterglow}}$ in the XRT band (0.3–10 keV), while $F_{\gamma,\text{prompt}}$ in the BAT (15–150 keV) plus the XRT (0.3–10 keV) energy band. For GRBs with known redshift, as shown in the upper right panel of Fig. 13, they investigated the prompt isotropic energy, $E_{\gamma,\text{prompt}}$, and the afterglow isotropic energy, $E_{X,\text{afterglow}}$, assuming a cosmology with $H_0 = 71 \text{ km s}^{-1} \text{ Mpc}^{-1}$, $\Omega_\Lambda = 0.73$ and $\Omega_M = 0.27$.

At the same time, Liang et al. (2007) focused on the relation between $E_{\gamma,\text{prompt}}$ and $E_{X,\text{afterglow}}$ using a sample of 53 LGRBs. They pointed out a good relation with $b = 1 \pm 0.16$, see the bottom left panel of Fig. 13.

In agreement with these results, Liang et al. (2010) and Panaiteescu and Vestrand (2011) analyzed this relation, using respectively 32 and 37 GRBs, but considering energy bands different from that used in Liang et al. (2007); they obtained the slopes $b = 0.76 \pm 0.14$ and $b = 1.18$ respectively (see the left and middle panels of Fig. 14).

Rowlinson et al. (2013) and Grupe et al. (2013) confirmed these results, see the left and middle panels of Fig. 15. In fact, they obtained a $E_{\gamma,\text{prompt}} - E_{X,\text{afterglow}}$ relation with slope $b \sim 1$ using 43 SGRBs and 232 GRBs with spectroscopic redshifts detected by Swift respectively.

Finally, Dainotti et al. (2015b) analyzed this relation to find some constraints on the ratio of $E_{X,\text{afterglow}}$ to $E_{\gamma,\text{prompt}}$, considering a sample of 123 LGRBs, see the right panel of Fig. 15.

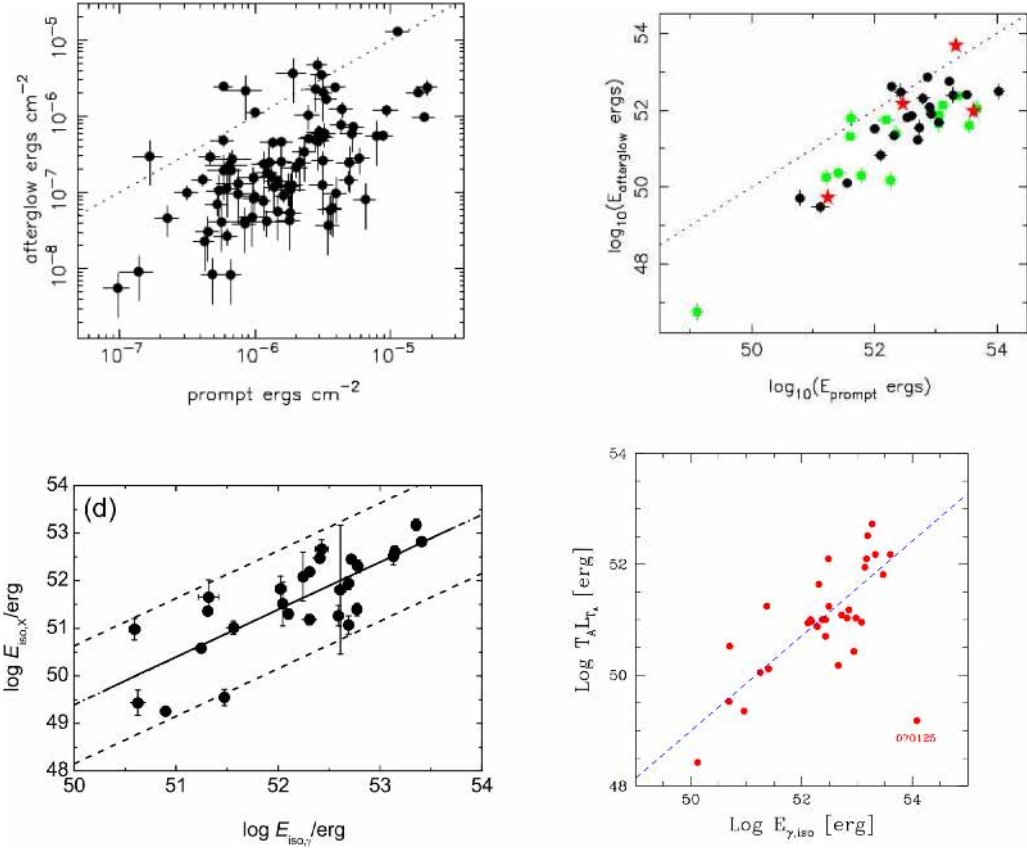


Fig. 13. Upper left panel: the $F_{X,\text{afterglow}}$ in the XRT band (0.3–10 keV) vs. $F_{Y,\text{prompt}}$ computed from the BAT T_{90} flux (15–150 keV) plus the XRT flux (0.3–10 keV) from Willingale et al. (2007). The dotted line represents where $F_{X,\text{afterglow}}$ and $F_{Y,\text{prompt}}$ are identical. Upper right panel: $\log E_{Y,\text{prompt}}$ vs. $\log E_{X,\text{afterglow}}$ from Willingale et al. (2007). Symbols show the position of the afterglow in the $\beta_{X,a} - \alpha_{X,a}$ plane. GRBs that fall in the pre-jet-break region are plotted as dots, those that fall above this in the post-jet-break region are plotted as stars, and those below the pre-jet-break are plotted as squares. The dotted line represents equality between $\log E_{Y,\text{prompt}}$ and $\log E_{X,\text{afterglow}}$. Bottom left panel: the $\log E_{Y,\text{prompt}} - \log E_{X,\text{afterglow}}$ relation ($E_{Y,\text{iso}}$ and $E_{X,\text{iso}}$ respectively in the picture) from Liang et al. (2007). The solid line is the best fit. The dashed line indicates the 2σ area. Bottom right panel: $\log E_{X,\text{plateau}}$ vs. $\log E_{Y,\text{prompt}}$ from Ghisellini et al. (2009). The dashed line represents the least square fit with $\log E_{X,\text{plateau}}$ ($T_a L_t$ in the picture) $\sim 0.86 \times \log E_{Y,\text{prompt}}$ ($E_{Y,\text{iso}}$ in the picture) ($P = 2 \times 10^{-7}$, without the outlier GRB 070125).

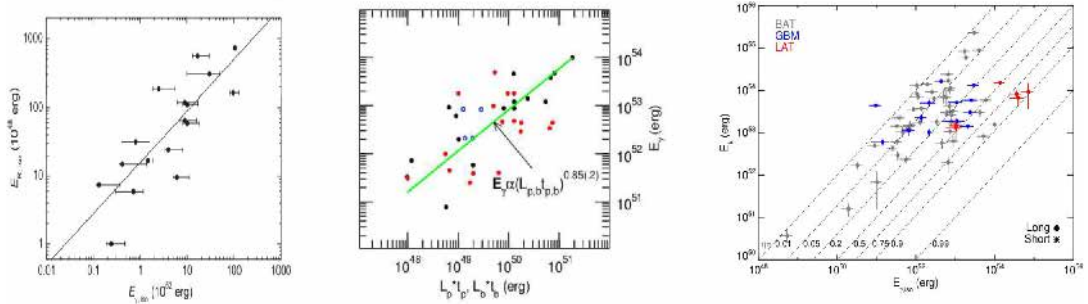


Fig. 14. Left panel: “relation between $E_{Y,\text{prompt}}$ and $E_{X,\text{afterglow}}$ ($E_{Y,\text{iso}}$ and $E_{X,\text{iso}}$ respectively in the picture), for the optically selected sample, from Liang et al. (2010). Line is the best fit”. Middle panel: “relation between $\log E_{Y,\text{prompt}}$ and $\log E_{X,\text{afterglow}}$ ($E_{Y,\text{iso}}$ and $L_p \times t_p$ respectively in the picture) from Panaiteanu and Vestrand (2011). Black symbols are for afterglows with optical peaks, red symbols for optical plateaus, open circles for afterglows of uncertain type. $r(\log E_{X,\text{afterglow}}, \log E_{Y,\text{prompt}}) = 0.66$ for all 37 afterglows. This linear correlation coefficients correspond to a probability $P = 10^{-5.39}$. Right panel: “ $E_{k,\text{eff}}$ as a function of $E_{Y,\text{prompt}}$ ($E_{Y,\text{iso}}$ in the picture), but average $E_{k,\text{eff}}$, and therefore higher values of η than the samples from BAT on board of Swift or GBM on board of Fermi”. (For interpretation of the references to colour in this figure legend, the reader is referred to the web version of this article.)

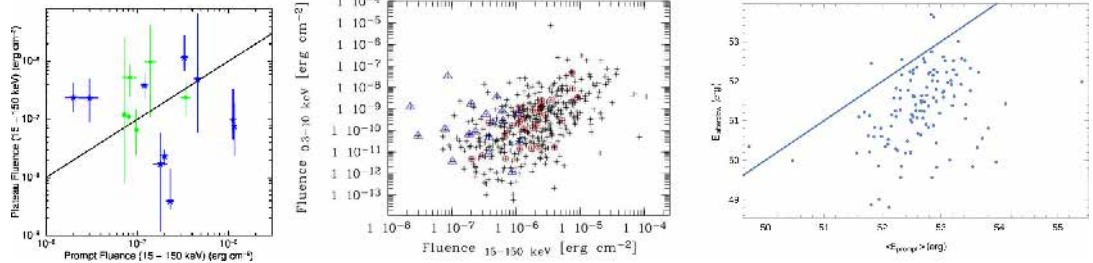


Fig. 15. Left panel: the prompt BAT 15–150 keV fluence vs. the X-ray fluence in the 15–150 keV energy band from Rowlinson et al. (2013). Blue stars are GRBs with 2 or more breaks in their light curves, green circles have 1 break and red triangles have no significant breaks in their light curves. The black line indicates where the shallow decay phase fluence is equal to the prompt fluence. Middle panel: relations of the 0.3–10 keV XRT fluence with fluence in the 15–150 keV BAT band from Grupe et al. (2013). Short bursts are represented with triangles and high-redshift ($z > 3.5$) bursts with circles. Right panel: $\langle \log E_{\gamma, \text{prompt}} \rangle$ vs. $\log E_{X, \text{afterglow}}$ relation from Dainotti et al. (2015b) for 123 LGRBs. The solid line for equal $\log E_{\gamma, \text{prompt}}$ and $\log E_{X, \text{afterglow}}$ is given for reference. (For interpretation of the references to colour in this figure legend, the reader is referred to the web version of this article.)

Instead, Ghisellini et al. (2009), with a sample of 33 LGRBs, considered a similar relation, but assuming the X-ray plateau energy, $E_{X, \text{plateau}}$, as an estimation of $E_{X, \text{afterglow}}$, see the bottom right panel of Fig. 13; they found a slope $b = 0.86$.

In addition, Ghisellini et al. (2009) also investigated the relation between $E_{\gamma, \text{prompt}}$ and the kinetic isotropic energy in the afterglow, $E_{k, \text{aft}}$, with the same sample, finding a relation with $b = 0.42$. Similarly, Racusin et al. (2011) studied the same relation, using 69 GRBs and assuming different efficiencies to find some limits between $E_{k, \text{aft}}$ and $E_{\gamma, \text{prompt}}$, see the right panel of Fig. 14.

This relation was most likely used to study the differences in detection of several instruments and to analyze the transferring process of kinetic energy into the prompt emission in GRBs, making the relation by Racusin et al. (2011) the most reliable one.

To summarize, for comparing the energies in the prompt and the afterglow phases, a $E_{\gamma, \text{prompt}} - E_{X, \text{afterglow}}$ relation was studied by Liang et al. (2007) and confirmed by Rowlinson et al. (2013), Grupe et al. (2013) and Dainotti et al. (2015b). The last study found also some limitations on the ratio among the prompt and the afterglow energies. Furthermore, instead of $E_{X, \text{afterglow}}$, $E_{X, \text{plateau}}$ was considered for the investigation, although this quantity provided similar results to the previous ones (Ghisellini et al., 2009). Finally, the relation between $E_{\gamma, \text{prompt}}$ and $E_{k, \text{aft}}$ was studied by Ghisellini et al. (2009) and confirmed by Racusin et al. (2011), who examined the energy transfer in the prompt phase. These relations are relevant because of their usefulness for investigating the efficiency of the emission processes during the transition from the prompt phase to the afterglow one, and for explaining which the connection between these two emission phases is. As a main result, Ghisellini et al. (2009) and Racusin et al. (2011) claimed that the fraction of kinetic energy transferred from the prompt phase to the afterglow one is around 10%. In particular, Racusin et al. (2011) yielded that this value of the transferred kinetic energy, for BAT-detected GRBs, is in agreement with the analysis by Zhang et al. (2007a) for which the internal shock model well describes this value in the case of a late energy transfer from the fireball to the surrounding medium (Zhang and Kobayashi, 2005).

In Table 5, a summary of the relations described in this section is presented.

As regards the physical interpretation of the $E_{X, \text{afterglow}} - E_{\gamma, \text{prompt}}$ relation, Racusin et al. (2011), estimating the efficiency parameter η for the BAT sample, confirmed the Zhang et al. (2007a) result for which $\sim 57\%$ of BAT bursts have $\eta < 10\%$. However, for the samples from the Gamma Burst Monitor (GBM)

and the Large Area Telescope (LAT), on board the Fermi satellite,⁴ they found that only 25% of the GBM bursts and none of the LAT bursts have $\eta < 10\%$. This implies that Fermi GRBs are more efficient at transferring kinetic energy into prompt radiation.

4.2. The $L_{X, \text{afterglow}} - E_{\gamma, \text{prompt}}$ relation and its physical interpretation

Berger (2007) investigated the prompt and afterglow energies in the observed frame of 16 SGRBs. A large fraction of them (80%) follows a linear relation between the prompt fluence in the gamma band, $S_{\gamma, \text{prompt}}$, in the BAT range and the X-ray flux at 1 day, $F_{X, 1d}$, in the XRT band given by:

$$\log F_{X, 1d} \sim (1.01 \pm 0.09) \times \log S_{\gamma, \text{prompt}}, \quad (8)$$

with $\rho = 0.86$ and $P = 5.3 \times 10^{-5}$. Gehrels et al. (2008) confirmed his results investigating the same relation, but with X-ray fluxes at 11 h, $F_{X, 11}$, see Fig. 16.

Later, Nysewander et al. (2009) considered the relation between $F_{X, 11}$ or the optical flux at 11 h, $F_{O, 11}$, and $E_{\gamma, \text{prompt}}$, finding an almost linear relation, see Fig. 17. They used a data set of 37 SGRBs and 421 LGRBs detected by Swift. Panaiteanu and Vestrand (2011) confirmed, in part, these results. They found a similar relation between $E_{\gamma, \text{prompt}}$ and $F_{O, 11}$ using 37 GRBs, but with a higher slope ($b = 1.67$), see the left panel of Fig. 18.

Kaneko et al. (2007) showed a linear relation $L_{X, 10} \propto E_{\gamma, \text{prompt}}$, where $L_{X, 10}$ is the X-ray luminosity at 10 h calculated in the 2–10 keV energy range, while $E_{\gamma, \text{prompt}}$ in the 20–2000 keV energy range, see the left panel of Fig. 19. This relation compares four long events spectroscopically associated with SNe with “regular” energetic LGRBs ($E_{\gamma, \text{prompt}} \sim 10^{52} - 10^{54}$ erg). The results possibly indicate a common efficiency η for transforming kinetic energy into gamma rays in the prompt phase for both these four events and for “regular” energetic LGRBs.

The same relation has been studied in the context of the low luminosity versus normal luminosity GRBs. Indeed, Amati et al. (2007) found that the relation between $L_{X, 10}$, in the 2–10 keV band, and $E_{\gamma, \text{prompt}}$, in the 1–10000 keV band, becomes stronger ($P \sim 10^{-11}$) including sub-energetic GRBs as GRB 060218,

⁴ The Fermi Gamma ray Space Telescope (FGST), launched in 2008 and still running, is a space observatory being used to perform gamma ray astronomy observations from low Earth orbit. Its main instrument is the Large Area Telescope (LAT), an imaging gamma ray detector, (a pair-conversion instrument) which detects photons with energy from about 20 MeV to 300 GeV with a field of view of about 20% of the sky; it is a sequel to the EGRET instrument on the Compton gamma ray observatory (CGRO). Another instrument aboard Fermi is the Gamma Ray Burst Monitor (GBM), which is used to study prompt GRBs from 8 keV to 30 MeV.

Table 5

Summary of the relations in this section. The first column represents the relation in log scale, the second one the authors, and the third one the number of GRBs in the used sample. Afterwards, the fourth and fifth columns are the slope and normalization of the relation and the last two columns are the correlation coefficient and the chance probability, P.

Correlations	Author	N	Slope	Norm	Corr.coeff.	P
$E_{X,\text{afterglow}} - E_{\gamma,\text{prompt}}$	Liang et al. (2007)	53	$1.00^{+0.16}_{-0.16}$	$-0.50^{+8.10}_{-8.10}$	0.79	$< 10^{-4}$
$E_{X,\text{afterglow}} - E_{\gamma,\text{prompt}}$	Liang et al. (2010)	32	$0.76^{+0.14}_{-0.14}$	$1.30^{+0.10}_{-0.14}$	0.82	$< 10^{-4}$
$E_{X,\text{plateau}} - E_{\gamma,\text{prompt}}$	Panaiteescu & Vestrand (2011)	37	1.18		0.66	$10^{-5.3}$
$E_{k,\text{soft}} - E_{\gamma,\text{prompt}}$	Ghisellini et al. (2009)	33	0.86			2×10^{-7}
$E_{k,\text{soft}} - E_{\gamma,\text{prompt}}$	Ghisellini et al. (2009)	33	0.42			10^{-3}

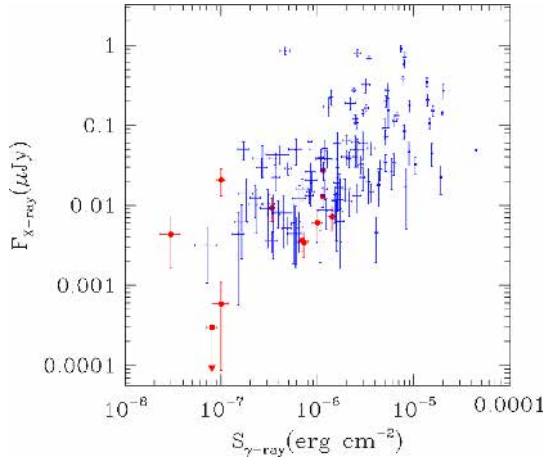


Fig. 16. $F_{X,11} - S_{\gamma,\text{prompt}}$ ($F_{X,\text{ray}}$ and $S_{\gamma,\text{ray}}$ respectively in the picture) relation for Swift SGRBs (in red) and LGRBs (in blue) from Gehrels et al. (2008). The XRT $F_{X,11}$ are computed at 3 keV and the BAT $S_{\gamma,\text{prompt}}$ are detected between 15 and 150 keV (Sakamoto et al., 2008). (For interpretation of the references to colour in this figure legend, the reader is referred to the web version of this article.)

GRB 980425 and GRB 031203, see the middle panel of Fig. 19. Therefore, it is claimed that sub-energetic GRBs are intrinsically faint and are considered to some extent normal cosmological GRBs.

Finally, Berger (2007) also analyzed the relation between the X-ray luminosity at one day, $L_{X,1d}$, and $E_{\gamma,\text{prompt}}$, using 13 SGRBs with measured z . They found a slope $b = 1.13 \pm 0.16$ (see the right panel of Fig. 18).

Liang et al. (2010) confirmed his results in the optical range using a sample of 32 Swift GRBs ($E_{\gamma,\text{prompt}} - L_{O,\text{peak}}$ with $b = 1.40 \pm 0.08$, see the right panel of Fig. 19). In addition, Kann et al. (2010) also confirmed his results with a sample of 76 LGRBs ($E_{\gamma,\text{prompt}} - L_{O,1d}$ with $b = 0.36$, see the left panel of Fig. 20).

Similarly, Dainotti et al. (2011b) analyzed the relation between $\log L_{X,a}$ and $\log E_{\gamma,\text{prompt}}$ using the light curves of 66 LGRBs from the Swift BAT+XRT repository, http://www.swift.ac.uk/burst_analyser/. Their sample has been divided into two subsamples: E4 formed of 62 LGRBs and E0095 consisting of 8 LGRBs, assuming σ_E as a parameter representing the goodness of the fit. For the E4 subsample it was found:

$$\log L_{X,a} = 28.03^{+2.98}_{-2.97} + 0.52^{+0.07}_{-0.06} \times \log E_{\gamma,\text{prompt}}, \quad (9)$$

with $\rho = 0.43$ and $P = 1.4 \times 10^{-5}$, while for the E0095 subsample

$$\log L_{X,a} = 29.82^{+7.11}_{-7.82} + 0.49^{+0.21}_{-0.16} \times \log E_{\gamma,\text{prompt}}, \quad (10)$$

with $\rho = 0.83$ and $P = 3.2 \times 10^{-2}$. Thus, it was concluded that the small error energy sample led to a higher relation and to the existence of a subset of GRBs which can yield a “standardizable candle”. Furthermore, since $\log L_{X,a}$ and $\log T_{X,a}^*$ are strongly correlated, and the slope is roughly -1 , the energy reservoir of the plateau is roughly constant. Since $\log E_{\gamma,\text{peak}}$ and $\log E_{\gamma,\text{prompt}}$ are both linked with $\log L_{X,a}$, then the $\log E_{\gamma,\text{peak}} - \log E_{\gamma,\text{prompt}} - \log E_{X,\text{plateau}}$ relation is straightforward. For its modification taking into account $\log E_{\gamma,\text{iso}}$ of the whole X-ray light curves see Bernardini et al. (2012b). As further confirmations of the $L_{X,a} - E_{\gamma,\text{prompt}}$ relation, D’Avanzo et al. (2012) and Margutti et al. (2013) found a relation between $\log L_{X,a}$ and $E_{\gamma,\text{prompt}}$ with slope $b \sim 1$ and $\rho \approx 0.70$, using 58 and 297 Swift LGRBs respectively.

Furthermore, Berger (2014) studied the relation between the X-ray luminosities at 11 h, $L_{X,11}$, and $E_{\gamma,\text{peak}}$, and the relation between the optical luminosity at 7 h $L_{O,7}$ and $E_{\gamma,\text{peak}}$ for a sample of 70 SGRBs and 73 LGRBs detected mostly by Swift. He found that the observed relations are flatter than the ones simulated by Kann et al. (2010), see the middle and right panels of Fig. 20.

Regarding the relation between $E_{\gamma,\text{prompt}}$ and the optical luminosities, Oates et al. (2015) analyzed the relation between $L_{O,200s}$ or $L_{X,200s}$ and $\log E_{\gamma,\text{prompt}}$ with a sample of 48 LGRBs. They claimed a strong connection between prompt and afterglow phases, see Fig. 21 and Table 6. This relation permits to study some important spectral characteristics of GRBs, the optical and X-ray components of the radiation process and the standard afterglow model. In Table 6, a summary of the relations described in this section is shown.

Regarding the physical interpretation of the $L_{X,\text{afterglow}} - E_{\gamma,\text{prompt}}$ relation, Gehrels et al. (2008) underlined that the optical and X-ray radiation are characterized by $\beta_{OX,a} \approx 0.75$. This value matches the slow cooling case, important at 11 h, when the electron distribution power law index is $p = 2.5$ for $v_m < v_0 < v_X < v_c$.

Oates et al. (2015) pointed out that within the standard afterglow model, the $\log E_{\gamma,\text{prompt}} - (\log L_{O,200s}, \log L_{X,200s})$ relations are expected. However, the slopes of the simulated and observed relations are inconsistent at $> 3 \sigma$ due to values set for the η parameter. If the distribution of the efficiencies is not sufficiently narrow the relation will be more disperse. Thus, the simulations repeated with $\eta = 0.1$ and $\eta = 0.9$ gave, anyway, incompatible results between the simulated and observed slopes at $> 3 \sigma$.

4.3. The $L_{X,a} - L_{O,a}$ relation and its physical interpretation

In the observed frame, Jakobsson et al. (2004) studied the $\log F_{O,11}$ versus $\log F_{X,11}$ distribution, in the optical R band and in the 2–10 keV band respectively, using all known GRBs with a detected X-ray afterglow, see the left panel of Fig. 22. Different from the previous definition of dark bursts (where dark bursts were simply defined as those bursts in which the optical transient is not observed), they defined these bursts as GRBs where

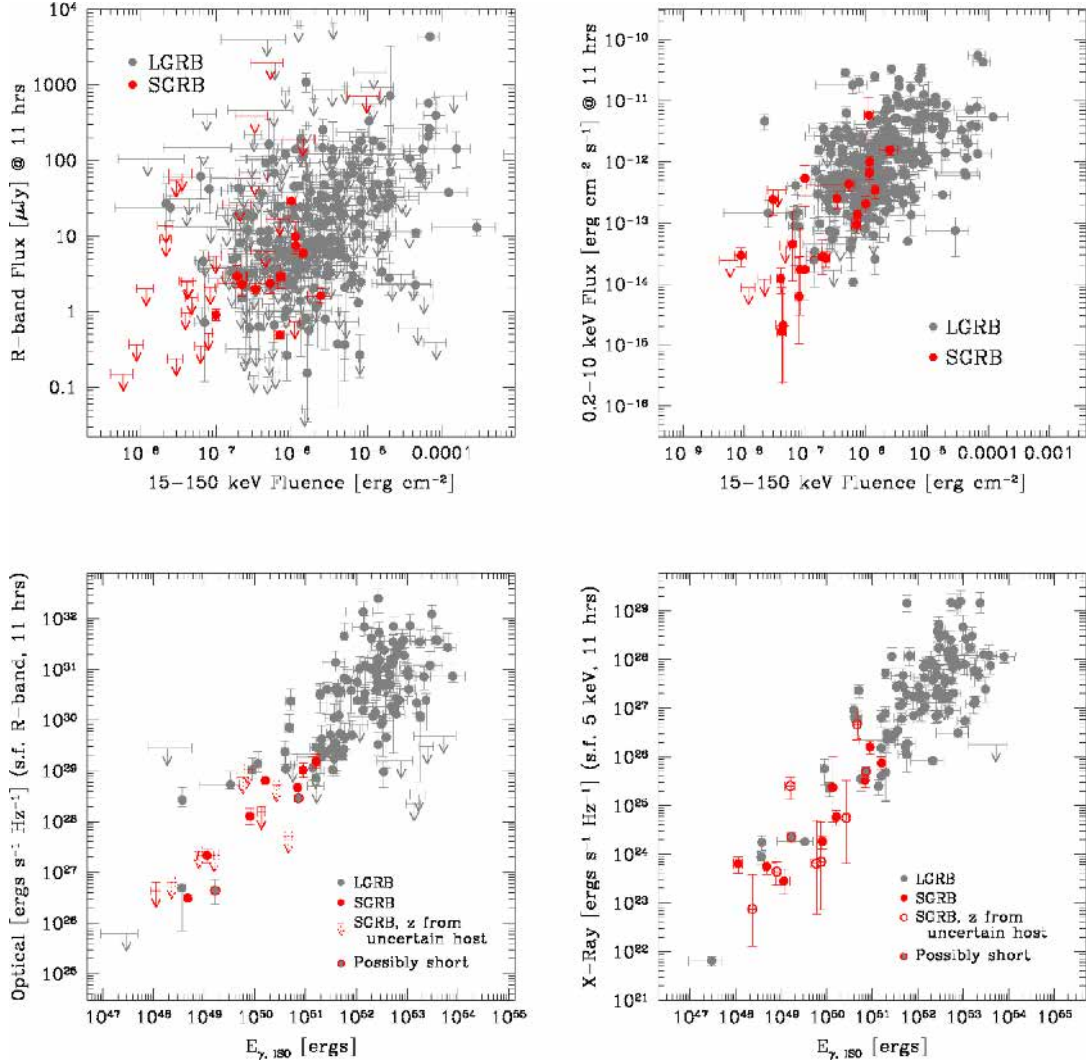


Fig. 17. Upper left panel: “a plot of $F_{0,11}$ (corrected for Galactic extinction) vs. 15–150 keV $S_{\gamma, \text{prompt}}$ for both LGRBs (grey) and SGRBs (red) from Nysewander et al. (2009). Note that below a fluence of 10^{-7} erg cm^{-2} , no optical afterglow of an SGRB has been discovered, while above 10^{-7} , all reasonably deep observing campaigns, but one (GRB 061210) have detected an optical afterglow”. Upper right panel: “a plot of $F_{X,11}$ vs. 15–150 keV $S_{\gamma, \text{prompt}}$ ($E_{\gamma, \text{iso}}$ in the picture) for both LGRBs (grey) and SGRBs (red) from Nysewander et al. (2009)”. Bottom left panel: “a plot of $F_{0,11}$ (corrected for Galactic extinction) vs. $E_{\gamma, \text{prompt}}$ from Nysewander et al. (2009). Dashed upper limits represent SGRBs with a host galaxy determined by XRT error circle only. The classification of GRB 060614 and GRB 060505 is uncertain, therefore, they are labeled as “possibly short””. Bottom right panel: “a plot of $L_{X,11}$ vs. $E_{\gamma, \text{prompt}}$ from Nysewander et al. (2009). The open circles represent SGRBs with a host galaxy determined by XRT error circle only. The classification of GRB 060614 and GRB 060505 is uncertain, therefore, they are labelled as “possibly short”. (For interpretation of the references to colour in this figure legend, the reader is referred to the web version of this article.)

the optical-to-X-ray spectral index, $\beta_{\text{OX},a}$, is shallower than the X-ray spectral index minus 0.5, $\beta_{\text{X},a} - 0.5$. They found out 5 dark bursts among 52 observed by Beppo-SAX.⁵ This analysis aimed

at distinguishing dark GRBs through Swift. Gehrels (2007) and Gehrels et al. (2008) confirmed the results using a data sample of 19 SGRBs and 37 LGRBs + 6 SGRBs respectively, see the middle and

⁵ Beppo-SAX, (1996–2003), was an Italian-Dutch satellite capable of simultaneously observing targets over more than 3 decades of energy, from 0.1 to 600 keV with relatively large area, good (for that time) energy resolution and imaging capabilities (with a spatial resolution of 1 arcmin between 0.1 and 10 keV). The instruments on board Beppo-SAX are Low Energy Concentrator Spectrometer (LECS), Medium Energy Concentrator Spectrometer (MECS), High Pressure Gas Scintillation

Proportional Counter (HPGSPC), Phoswich Detector System (PDS) and Wide Field Camera (WFC, from 2 to 30 keV and from 100 to 600 keV). The first four instruments point to the same direction allowing observations in the broad energy range (0.1–300 keV). With the WFC it was possible to model the afterglow as a simple power law, mainly due to the lack of observations during a certain period in the GRB light curve.

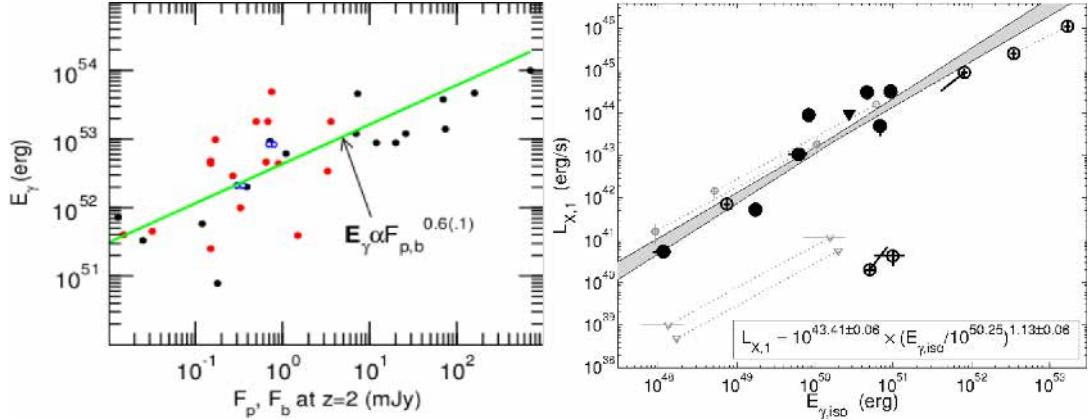


Fig. 18. Left panel: $E_{\gamma, \text{prompt}} - F_{0,a}$ ($E_{\gamma, \text{iso}}$ and F_p respectively in the picture) relation from Panaiteescu and Vestrand (2011). Black symbols are for afterglows with optical peaks, red symbols for optical plateaus, open circles for afterglows of unknown kind. Right panel: $L_{X,11}$ vs. $E_{\gamma, \text{prompt}}$ ($E_{\gamma, \text{iso}}$ in the picture) for the SGRBs with a known z (solid black circles), redshift constraints (open black circles) and without any redshift information (grey symbols connected by dotted lines) from Berger (2007). (For interpretation of the references to colour in this figure legend, the reader is referred to the web version of this article.)

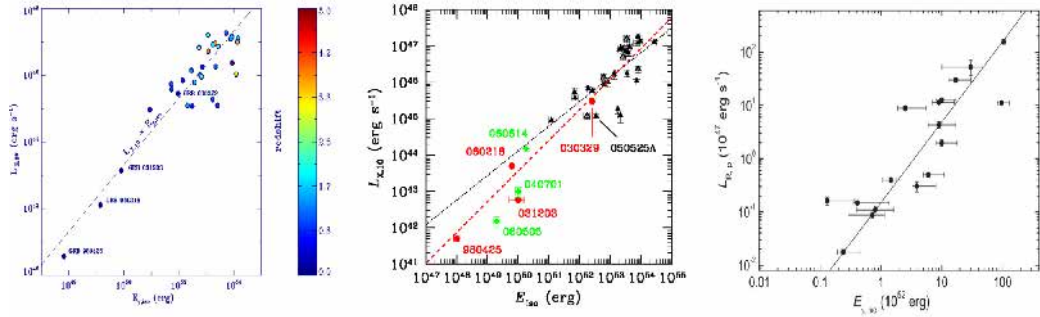


Fig. 19. Left panel: “ $L_{X,10}$ of SN-GRBs (source frame: 2–10 keV) as a function of their $E_{\gamma, \text{prompt}}, E_{\gamma, \text{iso}}$ in the picture, (20–2000 keV) from Kaneko et al. (2007). z for each event is also shown in colour”. Middle panel: “ $L_{X,10}$ (in 2–10 keV range) vs. $E_{\gamma, \text{prompt}}$ ($E_{\gamma, \text{iso}}$ in the picture) for the events included in the sample of Nousek et al. (2006) (triangles) plus the 3 sub-energetic GRB 980425, GRB 031203, GRB 060218, the other GRB/SN event GRB 030329 (circles), and 3 GRBs with known z and deep limits to the peak magnitude of associated SN, XRF 040701, GRB 060505 and GRB 060614 (diamonds) from Amati et al. (2007). Empty triangles indicate those GRBs for which the 1–10000 keV $E_{\gamma, \text{prompt}}$ was computed based on the 100–500 keV $E_{\gamma, \text{prompt}}$ reported by Nousek et al. (2006) by assuming an average spectral index. The plotted lines are the best-fit power laws obtained without (dotted) and with (dashed) sub-energetic GRBs and GRB 030329”. Right panel: “relation between $E_{\gamma, \text{prompt}}$ and $L_{O,\text{peak}}$ ($E_{\gamma, \text{iso}}$ and $L_{R,p}$ respectively in the picture) for the optically selected sample from Liang et al. (2010). Line is the best fit”.

right panels of Fig. 22. In particular, Gehrels et al. (2008) obtained a slope $b = 0.38 \pm 0.03$ for LGRBs and $b = 0.14 \pm 0.45$ for SGRBs.

Instead in the rest-rest frame, Berger (2014) studied the relation between $L_{0,7}$ and $L_{X,11}$ on 70 SGRBs and 73 LGRBs, finding some similarities between SGRBs and LGRBs and a central value $< L_{0,7}/L_{X,11} > \approx 0.08$, see the left panel of Fig. 23.

Oates et al. (2015) improved their study. They analyzed a similar relation with a sample of 48 LGRBs, but using $L_{0,200s}$ and $L_{X,200s}$, see the right panel of Fig. 23. The slope obtained has a value $b = 0.91 \pm 0.22$.

This relation helps to explore the synchrotron spectrum of GRBs and to obtain some constraints on the circumburst medium for both LGRBs and SGRBs. In Table 7 a summary of the relations described in this section is displayed.

Regarding the physical interpretation of the $L_{X,a} - L_{0,a}$ relation, Berger (2014) showed that, in the context of the synchrotron model, the comparison of $L_{0,7}$ and $L_{X,11}$ indicated that usually v_c is near or higher than the X-ray band. Indeed, LGRBs have often

greater circumburst medium densities (about 50 times greater than SGRBs) and therefore $v_c \sim v_X$.

4.4. The $L_X(T_a) - L_{Y,\text{iso}}$ relation

In Dainotti et al. (2011b) the connections between the physical properties of the prompt emission and $\log L_{X,a}$ were analyzed using a sample of 62 Swift LGRBs. A relation was found between $\log L_{X,a}$ in the XRT band and the isotropic prompt luminosity, $\log < L_{Y,\text{iso}} >_{45} \equiv \log(E_{\gamma, \text{prompt}}/T_{45})$, in the BAT energy band, see the left panel of Fig. 24. This relationship can be fitted with the following equation:

$$\log L_{X,a} = 20.58_{-6.73}^{+6.66} + 0.67_{-0.15}^{+0.14} \times \log < L_{Y,\text{iso}} >_{45}, \quad (11)$$

obtaining $\rho = 0.59$ and $P = 7.7 \times 10^{-8}$. In this paper $\log L_{X,a}$ was related to several prompt luminosities defined using different time scales, such as T_{90}, T_{45} (the time in which the 45% between 5%-50% of radiation is emitted in the prompt emission), and $T_{X,p}$

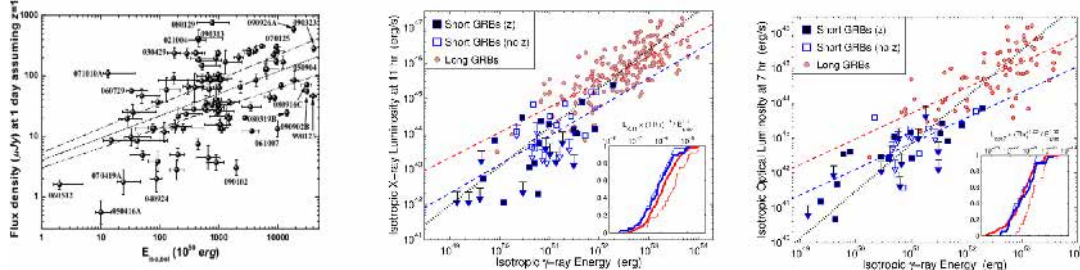


Fig. 20. Left panel: “ $F_{0,1d}$ in the R band plotted against the bolometric $E_{\gamma,\text{prompt}}$ ($E_{\text{iso},\text{bol}}$ in the picture) for all GRBs in the optically selected sample from Kann et al. (2010) (except GRB 991208, which was only discovered after several days, and GRBs 060210, 060607A, 060906 and 080319C, where the follow-up does not extend to one day). While no tight relation is visible, there is a trend of increasing optical luminosity with increasing prompt energy release. This is confirmed by a linear fit (in log-log space), using a Monte Carlo analysis to account for the asymmetric errors. The dashed line shows the best fit, while the dotted line marks the 3σ error region. Several special GRBs are marked”. Middle panel: “ $L_{X,11}$ vs. $E_{\gamma,\text{prompt}}$ for SGRBs (blue) and LGRBs (grey) from Berger (2014). Open symbols for SGRBs indicate events without a known z , for which a fiducial value of $z = 0.75$ is assumed. The dashed blue and red lines are the best-fit power law relations to the trends for SGRBs and LGRBs, respectively, while the dotted black line is the expected relation based on the afterglow-synchrotron model with $v_r > v_c$ and $p = 2.4$ ($\log L_{X,11} \sim 1.1 \times \log E_{\gamma,\text{prompt}}$). The inset shows the distribution of the ratio $\log(L_{X,11} \times (11\text{ h})^{1.3}/E_{\gamma,\text{prompt}}^{1.1})$, for the full samples (thick lines) and for the region where SGRBs and LGRBs have equal $E_{\gamma,\text{prompt}}$ values (thin lines). The lower level of $L_{X,11}$ relative to $E_{\gamma,\text{prompt}}$ for SGRBs is evident from these various comparisons”. Right panel: same as in the middle panel, “but for the isotropic-equivalent afterglow optical luminosity at a rest frame time of 7 h ($L_{0,7}$), still from Berger (2014). The dotted black line is the expected relation based on the afterglow model for $v_m < v_0 < v_c$ and $p = 2.4$ ($\log L_{0,7} \sim 1.35 \times \log E_{\gamma,\text{prompt}}$). The inset shows the distribution of the ratio $\log(L_{0,7} \times (7\text{ h})^{1.05}/E_{\gamma,\text{prompt}}^{1.35})$, for the full samples (thick lines) and for the region where SGRBs and LGRBs have equal $E_{\gamma,\text{prompt}}$ values (thin lines). The lower level of $L_{0,7}$ relative to $E_{\gamma,\text{prompt}}$ for SGRBs is evident from these various comparisons”. (For interpretation of the references to colour in this figure legend, the reader is referred to the web version of this article.)

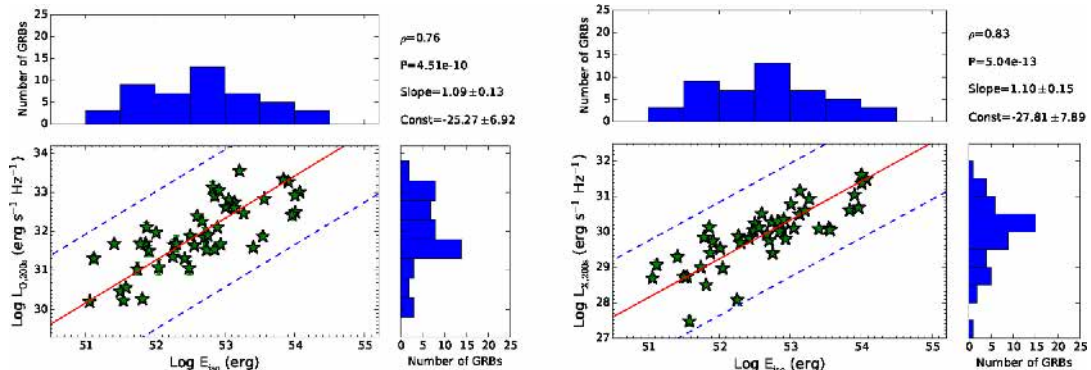


Fig. 21. Left panel: $\log L_{0,200s} - \log E_{\gamma,\text{prompt}}$ (E_{iso} in the picture) relation from Oates et al. (2015). Right panel: $\log L_{X,200s} - \log E_{\gamma,\text{prompt}}$ (E_{iso} in the picture) relation from Oates et al. (2015).

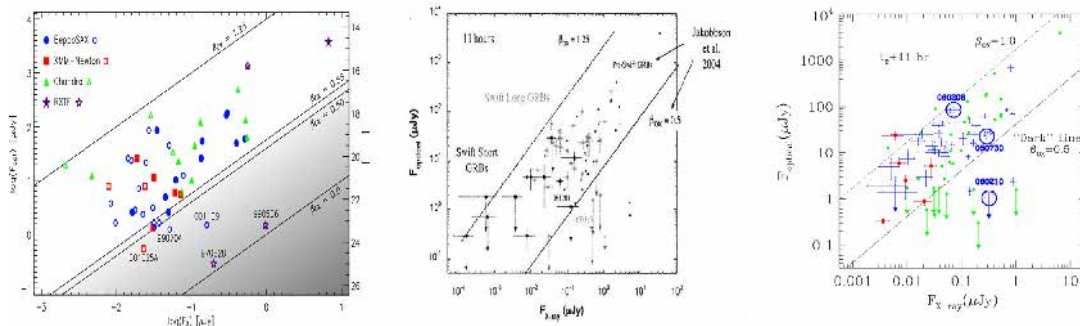


Fig. 22. Left panel: $\log F_{0,11} - \log F_{X,11}$ (F_{opt} and F_X respectively in the plot) distribution for the data set from Jakobsson et al. (2004). Filled symbols show optical detections while open symbols represent upper limits. Lines of constant $\beta_{\text{ox},a}$ are displayed with the corresponding value. Dark bursts are those which have $\beta_{\text{ox},a} < 0.5$. Middle panel: $F_{X,11} - F_{0,11}$ relation for Swift SGRBs and LGRBs from Gehrels (2007). Comparison is made to pre-Swift GRBs and to lines of optical to X-ray spectral index from Jakobsson et al. (2004). The grey points indicate LGRBs, the black points represent SGRBs and the small black points without error bars are the pre-Swift GRBs. Right panel: $F_{0,11} - F_{X,11}$ relation for Swift SGRBs (shown in red) and LGRBs (shown in blue) from Gehrels et al. (2008). The three circled bursts are those for which $z > 3.9$. The pre-Swift GRBs taken from Jakobsson et al. (2004) are presented in green. Also the dark burst separation line $\beta_{\text{ox},a} = 0.5$ (Jakobsson et al., 2004) and a line showing $\beta_{\text{ox},a} = 1.0$ are represented. (For interpretation of the references to colour in this figure legend, the reader is referred to the web version of this article.)

Table 6

Summary of the relations in this section. The first column represents the relation in log scale, the second one the authors, and the third one the number of GRBs in the used sample. Afterwards, the fourth and fifth columns are the slope and normalization of the relation and the last two columns are the correlation coefficient and the chance probability, P.

Correlations	Author	N	Slope	Norm	Corr.coeff.	P
$F_{X,1d} - S_{\gamma,prompt}$	Berger (2007)	16	$1.01^{+0.09}_{-0.09}$		0.86	5.3×10^{-5}
$F_{X,11} - S_{\gamma,prompt}$	Gehrels et al. (2008)	111	$0.63^{+0.04}_{-0.04}$	$2.11^{+0.21}_{-0.21}$	0.53	4×10^{-9}
	Gehrels et al. (2008)	10	$0.36^{+0.17}_{-0.17}$	$0.06^{+1.07}_{-1.07}$	0.35	0.31
$F_{0,11} - E_{\gamma,prompt}$	Nysewander et al. (2009)	421	~ 1			
$F_{0,11} - E_{\gamma,prompt}$	Nysewander et al. (2009)	37	~ 1			
$F_{X,11} - E_{\gamma,prompt}$	Nysewander et al. (2009)	421	~ 1			
$F_{X,11} - E_{\gamma,prompt}$	Nysewander et al. (2009)	37	~ 1			
$F_{0,a} - E_{\gamma,prompt}$	Panaiteescu&Vestrand (2011)	37	1.67		0.75	$10^{-7.3}$
$L_{X,1d} - E_{\gamma,prompt}$	Berger (2007)	13	$1.13^{+0.16}_{-0.16}$	$43.43^{+0.20}_{-0.20}$	0.94	3.2×10^{-6}
$L_{0,peak} - E_{\gamma,prompt}$	Liang et al. (2010)	32	$1.40^{+0.08}_{-0.08}$	$0.83^{+0.15}_{-0.15}$	0.87	10^{-4}
$L_{0,1d} - E_{\gamma,prompt}$	Kann et al. (2010)	76	0.36			
$L_{X,a} - E_{\gamma,prompt}$	Dainotti et al. (2011b)	62	$0.52^{+0.07}_{-0.06}$	$28.03^{+2.98}_{-2.97}$	0.43	1.4×10^{-5}
	Dainotti et al. (2011b)	8	$0.49^{+0.21}_{-0.16}$	$29.82^{+7.11}_{-7.82}$	0.83	3.2×10^{-2}
$L_{0,7} - E_{\gamma,prompt}$	D'Avanzo et al. (2012)	58	~ 1			≈ 0.70
	Margutti et al. (2013)	297	~ 1			≈ 0.70
$L_{X,11} - E_{\gamma,prompt}$	Berger (2014)	73	0.72	44.75		
	Berger (2014)	70	0.83	43.93		
$L_{0,7} - E_{\gamma,prompt}$	Berger (2014)	73	0.73	43.70		
	Berger (2014)	70	0.74	42.84		
$L_{X,200s} - E_{\gamma,prompt}$	Oates et al. (2015)	48	$1.10^{+0.15}_{-0.15}$	$-27.81^{+7.89}_{-7.89}$	0.83	5.04×10^{-13}
$L_{0,200s} - E_{\gamma,prompt}$	Oates et al. (2015)	48	$1.09^{+0.13}_{-0.13}$	$-25.27^{+6.92}_{-6.92}$	0.76	4.51×10^{-10}

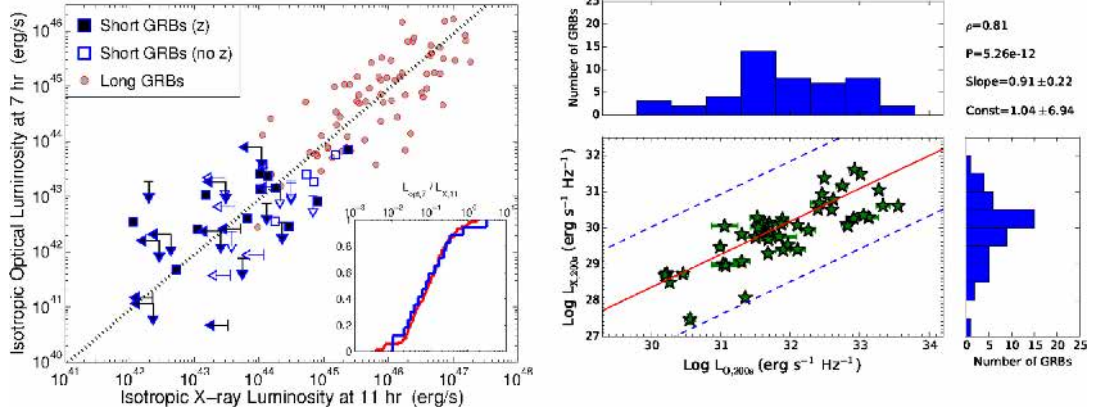


Fig. 23. Left panel: “ $L_{0,7}$ vs. $L_{X,11}$ from Berger (2014). The dotted black line marks a linear relation, expected for $v_X \sim v_c$. The inset shows the distribution of the ratio $L_{0,7}/L_{X,11}$, indicating that both SGRBs and LGRBs exhibit a similar ratio, and that in general $L_{0,7}/L_{X,11} \sim 1$, indicative of $v_X \sim v_c$ for SGRBs”. Right panel: “ $\log L_{0,200s}$ vs. $\log L_{X,200s}$ from Oates et al. (2015). The red solid line represents the best fit regression and the blue dashed line represents 3 times the RMS deviation. In the top right corner, it is given ρ and P and it is provided the best-fit slope and constant determined by linear regression”. (For interpretation of the references to colour in this figure legend, the reader is referred to the web version of this article.)

Table 7

Summary of the relations in this section. The first column represents the relation in log scale, the second one the authors, and the third one the number of GRBs in the used sample. Afterwards, the fourth and fifth columns are the slope and normalization of the relation and the last two columns are the correlation coefficient and the chance probability, P.

Correlations	Author	N	Slope	Norm	Corr.coeff.	P
$F_{X,11} - F_{0,11}$	Gehrels et al. (2008)	6	0.14 ± 0.45	0.72 ± 0.94	0.06	0.68
		37	0.38 ± 0.03	1.62 ± 0.04	0.44	0.006
$L_{X,11} - L_{0,7}$	Berger (2014)	70	0.08			
		73	0.08			
$L_{X,200s} - L_{0,200s}$	Oates et al. (2015)	48	0.91 ± 0.22	1.04 ± 6.94	0.81	5.26×10^{-12}

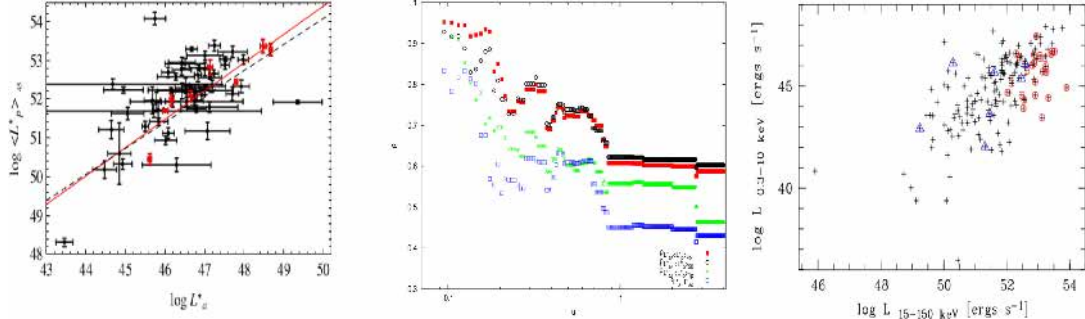


Fig. 24. Left panel: $\log L_{X,a}$ vs. $\log < L_{\gamma,iso} >_{45}$ relation ($\log L_{X,a}^*$ and $\log L_{\gamma,iso}^*$, respectively) for the E4 data set from Dainotti et al. (2011b), with the fitted relation dashed line in black. The red line is fitted to the 8 lowest error (red) points of the E0095 subset. Middle panel: correlation coefficients ρ for $\log L_{X,a} - \log < L_{\gamma,iso} >_{45}$ (red squares), $\log L_{X,a} - \log < L_{\gamma,iso} >_{90}$ (black circles), $\log L_{X,a} - \log < L_{\gamma,iso} >_{T_{X,p}}$ (green asterisks) and $\log L_{X,a} - \log E_{\gamma,prompt}$ (blue squares) relations, obtained using the LGRB subset with the maximum $u = \sigma_E$ from Dainotti et al. (2011b). Right panel: Luminosity in the 0.3–10 keV XRT band ($L_{X,a}$) vs. luminosity in the 15–150 keV BAT band ($L_{\gamma,iso}$) from Grupe et al. (2013). Short bursts are represented by triangles and high-redshift ($z > 3.5$) bursts by circles. (For interpretation of the references to colour in this figure legend, the reader is referred to the web version of this article.)

(the time at the end of the prompt emission within the W07 model). Furthermore, the E4 (defined in Table 1) subsample of 62 LGRBs with known z from a sample of 77 Swift LGRBs and the E0095 subsample of 8 GRBs with smooth light curves were used, see black and red points in the left panel of Fig. 24.

Therefore, it has been shown that the GRB subsample with the strongest correlation coefficient for the LT relation also implies the tightest prompt-afterglow relations. This subsample can be used as a standard one for astrophysical and cosmological studies.

In the middle panel of Fig. 24, the correlation coefficients ρ are shown for the following distributions: $(\log < L_{\gamma,iso} >_{45}, \log < L_{\gamma,iso} >_{90}, \log < L_{\gamma,iso} >_{T_{X,p}}, \log E_{\gamma,prompt}) - \log L_{X,a}$, represented by different colors, namely red, black, green and blue respectively.

No significant relations for the IC bursts have been found out. However, the paucity of the data does not allow a definitive statement. From this analysis, it is clear that the inclusion of the IC GRB class does not strengthen the existing relations.

In general, this study pointed out that the plateau phase results connected to the inner engine. In addition, also relations between $\log L_{X,a}$ and several other prompt emission parameters were analyzed, including $\log E_{\gamma,peak}$ and the variability, $\log V$. As a result, relevant relations are found between these quantities, except for the variability parameter, see Table 8.

Finally, as shown in Table 8, only a very small relation-shape exists between $\log L_{X,a}^* - \log E_{\gamma,prompt}$ with $\rho = -0.19$. Also Grupe et al. (2013) claimed the existence of relations between $\log < L_{\gamma,iso} >_{90}$ and $\log L_{X,a}$ (see the right panel of Fig. 24) and between $\log < L_{\gamma,iso} >_{90}$ and $\log T_{X,a}^*$ using a sample of 232 GRBs. The latter can be derived straightforwardly from the $\log T_{X,a}^* - \log E_{\gamma,prompt}$ relation, being $\log < L_{\gamma,iso} >_{90}$ computed as $\log(E_{\gamma,prompt}/T_{90})$.

4.5. The $L_{X,peak} - L_X(T_a)$ relation

Dainotti et al. (2015b) further investigated the prompt-afterglow relations presenting an updated analysis of 123 Swift BAT+XRT light curves of LGRBs with known z and afterglow plateau phase. The relation between the peak luminosity of the prompt phase in the X-ray, $\log L_{X,peak}$, and $\log L_{X,a}$ can be written as follows:

$$\log L_{X,a} = A + B \times \log L_{X,peak}, \quad (12)$$

with $A = -14.67 \pm 3.46$, $B = 1.21^{+0.14}_{-0.13}$ and with $\rho = 0.79$ and $P < 0.05$, see the left panel of Fig. 25. In the literature $L_{X,peak}$ is

denoted as:

$$L_{X,peak} = 4\pi \times D_L(z, \Omega_M, h)^2 \times F_{X,peak} \times K. \quad (13)$$

The relation $\log L_{\gamma,iso} - \log L_{X,a}$ (Dainotti et al., 2011b) for the same GRB sample presented a correlation coefficient, $\rho = 0.60$, smaller than the one of the $\log L_{X,peak} - \log L_{X,a}$ relation, see Section 4.4. This implied that a better definition of the luminosity or energy parameters improves ρ by 24%. In the left panel of Fig. 25 $\log L_{X,peak}$ is calculated directly from the peak flux in X-ray, $F_{X,peak}$, considering a broken or a simple power law as the best fit of the spectral model. Thus, the error propagation due to time and energy is not involved, differently from the earlier considered luminosities. In addition, Dainotti et al. (2015b) preferred the $\log L_{X,peak} - \log L_{X,a}$ to the relations presented in Dainotti et al. (2011b), namely the $(\log E_{\gamma,prompt}, \log E_{\gamma,peak}) - \log L_{X,a}$, due to the fact that $\log E_{\gamma,prompt}$ and $\log E_{\gamma,peak}$ can undergo double bias truncation due to high and low energy detector threshold. Instead, this problem does not appear for $\log L_{X,peak}$ (Lloyd and Petrosian, 1999). Furthermore, to show that the $\log L_{X,peak} - \log L_{X,a}$ relation is robust, the redshift dependence induced by the distance luminosity was eliminated employing fluxes rather than luminosities. A relation between $\log F_{X,a}$ and $\log F_{X,peak}$ was obtained with $\rho = 0.63$, see the right panel of Fig. 25.

However, for further details about a quantitative analysis of the selection effects see Section 5.

Finally, Dainotti et al. (2015b) showed that the LT relation has a different slope, at more than 2σ , from the one of the prompt phase relation between the time since ejection of the pulse and the respective luminosity, $\log L_{X,f} - \log T_{X,f}^*$ (Willingale et al., 2010), see the left panel of Fig. 26. This difference also implied a discrepancy in the distributions of the energy and time, see the right panel of Fig. 26. The interpretation of this discrepancy between the slopes opens a new perspective in the theoretical understanding of these observational facts, see the next section for details.

As a further step, Dainotti et al. (2016a) analyzed this relation adding as a third parameter $T_{X,a}$ with a sample of 122 LGRBs (without XRFs and GRBs associated to SNe). They found a tight relation:

$$\begin{aligned} \log L_{X,a} = & (15.69 \pm 3.8) + (0.67 \pm 0.07) \\ & \times \log L_{X,peak} - (0.80 \pm 0.07) \log T_{X,a}, \end{aligned} \quad (14)$$

with $\rho = 0.93$, $P \leq 2.2 \times 10^{-16}$, and $\sigma_{int} = 0.44 \pm 0.03$. Additionally, the scatter could be further reduced considering the subsample of 40 LGRBs having light curves with good data

Table 8

Correlation coefficients ρ , the respective relation fit line parameters (a, b), and the correlation coefficient r with the respective random occurrence probability P , for the considered prompt- afterglow and prompt-prompt distributions in log scale from Dainotti et al. (2011b).

Correlations	E4		E0095	
	ρ	(b, a)	ρ	(b, a)
$L_{X,a} - < L_{\gamma,iso} >_{45}$	0.59 0.62	$(0.67^{+0.14}_{-0.15}, 20.58^{+5.66}_{-6.73})$ 7.7×10^{-8}	0.95 0.90	$(0.73^{+0.16}_{-0.11}, 17.90^{+5.29}_{-6.0})$ 2.3×10^{-3}
$L_{X,a} - < L_{\gamma,iso} >_{90}$	0.60 0.62	$(0.63^{+0.15}_{-0.16}, 22.05^{+7.14}_{-7.31})$ 7.7×10^{-8}	0.93 0.94	$(0.84^{+0.11}_{-0.12}, 11.86^{+3.43}_{-3.44})$ 2.7×10^{-3}
$L_{X,a} - < L_{\gamma,iso} >_{T_{X,p}}$	0.46 0.56	$(0.73^{+0.09}_{-0.14}, 16.61^{+4.35}_{-4.35})$ 2.21×10^{-6}	0.95 0.90	$(0.93^{+0.20}_{-0.23}, 7.70^{+3.47}_{-3.46})$ 2.3×10^{-3}
$L_{X,a} - E_{\gamma,prompt}$	0.43 0.52	$(0.52^{+0.07}_{-0.06}, 28.03^{+2.98}_{-2.97})$ 1.4×10^{-5}	0.83 0.75	$(0.49^{+0.21}_{-0.16}, 29.82^{+7.11}_{-7.82})$ 3.2×10^{-2}
$T_{X,a}^* - E_{\gamma,prompt}$	-0.19 -0.21	$(-0.49^{+0.09}_{-0.08}, 54.51^{+0.37}_{-0.30})$ 1.0×10^{-1}	-0.81 -0.69	$(-0.96^{+0.21}_{-0.22}, 54.67^{+0.69}_{-0.69})$ 5.8×10^{-2}
$L_{X,a} - E_{\gamma,peak}$	0.54 0.51	$(1.06^{+0.53}_{-0.23}, 43.88^{+0.61}_{-1.00})$ 2.2×10^{-5}	0.74 0.80	$(1.5^{+0.65}_{-0.94}, 43.10^{+2.53}_{-2.26})$ 1.7×10^{-2}
$T_{X,a}^* - E_{\gamma,peak}$	-0.36 -0.35	$(-0.66^{+0.20}_{-0.29}, 4.96^{+0.81}_{-0.80})$ 5.2×10^{-3}	-0.74 -0.77	$(-1.40^{+0.66}_{-0.65}, 7.04^{+1.79}_{-1.77})$ 2.5×10^{-2}
$< L_{\gamma,iso} >_{45} - E_{\gamma,peak}$	0.81 0.67	$(1.14^{+0.22}_{-0.25}, 49.27^{+0.61}_{-0.66})$ 2.6×10^{-9}	0.76 0.92	$(1.45^{+0.26}_{-0.54}, 48.48^{+1.05}_{-1.04})$ 1.2×10^{-3}

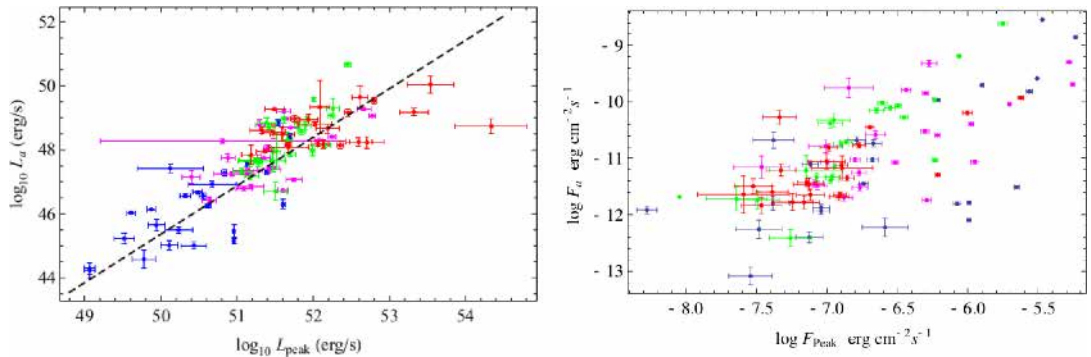


Fig. 25. Left panel: “GRB distributions in redshift bins on the $\log L_{X,a} - \log L_{X,peak}$ plane from Dainotti et al. (2015b), where $\log L_{X,peak}$ is computed using the approach used in the Second BAT Catalogue. The sample is split into 4 different equipopulated redshift bins: $z \leq 0.84$ (blue), $0.84 \leq z < 1.8$ (magenta), $1.8 \leq z < 2.9$ (green) and $z \geq 2.9$ (red). The dashed line is the fitting relation line”. Right panel: “GRB distributions in redshift bins on the $\log F_a - \log f_{X,peak}$ plane from Dainotti et al. (2015b), where $\log f_{X,peak}$ is computed following the approach used in the Second BAT Catalogue. The sample is split into 4 different equipopulated redshift bins: $z \leq 0.84$ (blue), $0.84 \leq z < 1.8$ (magenta), $1.8 \leq z < 2.9$ (green) and $z \geq 2.9$ (red)”. (For interpretation of the references to colour in this figure legend, the reader is referred to the web version of this article.)

coverage and flat plateaus:

$$\log L_{X,a} = (15.75 \pm 5.3) + (0.67 \pm 0.1) \times \log L_{X,peak} - (0.77 \pm 0.1) \log T_{X,a}, \quad (15)$$

with $\rho = 0.90$, $P = 4.41 \times 10^{-15}$, and $\sigma_{int} = 0.27 \pm 0.04$. These results may suggest the use of this plane as a “fundamental” plane for GRBs and for further cosmological studies.

4.5.1. Physical interpretation of the $L_X(T_a) - L_{\gamma,iso}$ and the $L_{X,peak} - L_X(T_a)$ relations

In Dainotti et al. (2015b), the two distinct slopes of the luminosity-duration and the energy-duration distributions of prompt and plateau pulses could reveal that these two are different characteristics of the radiation: the former may be generated by internal shocks and the latter by the external shocks. Indeed, if the plateau is produced by synchrotron radiation from the external shock, then all the pulses have analogous physical conditions (e.g.

the power law index of the electron distribution). In addition, the prompt-afterglow connections were analyzed in order to better explain the existing physical models of GRB emission predicting the $\log L_{X,a} - \log L_{\gamma,iso}$ and the $\log L_{X,peak} - \log L_{X,a}$ relations together with the LT one in the prompt and afterglow phases. They claimed that the model better explaining these relationships is the one by Hascoët et al. (2014). In this work they considered two scenarios: one in the standard FS model assuming a modification of the microphysics parameters to decrease the efficiency at initial stages of the GRB evolution; in the latter the early afterglow stems from a long-lived RS in the FS scenario. In the FS scenario a wind external medium is assumed together with a microphysics parameter $\epsilon_e \propto n^{-v}$, the amount of the internal energy going into electrons (or positrons), where n is the density medium. In the case of $v \approx 1$ is possible to reproduce a flat plateau. Thus, even operating on just one parameter can lead to the formation of a plateau that also reproduces the $\log L_{X,a} - \log L_{\gamma,iso}$ and the

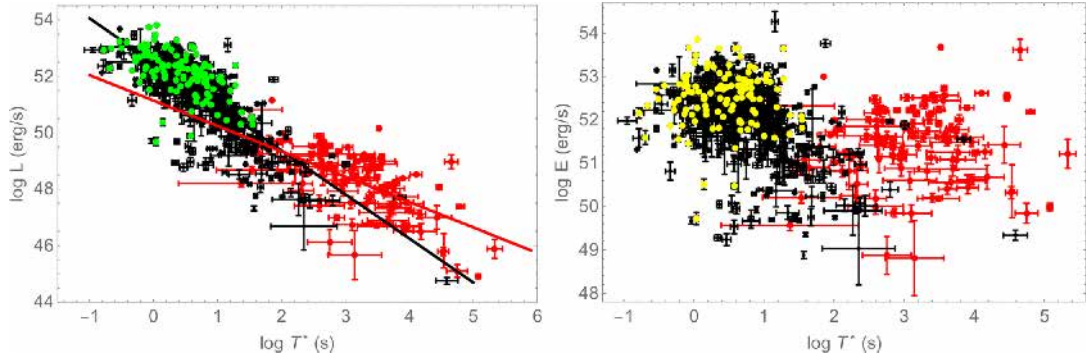


Fig. 26. Left panel: $\log L - \log T^*$ relation for all the pulses in the prompt (black symbols) and in the afterglow (red symbols) emissions from Dainotti et al. (2015b). $\log L$ is the same as $\log L_{X,f}$ for the prompt emission pulses, while indicates $\log L_{X,a}$ for the afterglow emission pulses, and, the time $\log T^*$ indicates $\log T_{X,f}^*$ for the prompt emission pulses and $\log T_{X,a}^*$ for the afterglow phase. The green points show the maximum luminosity prompt emission pulses ($\log T_{\text{max}}$, $\log L_{\text{max}}$). Right panel: $\log E$ vs. $\log T^*$ relation for all the pulses in the prompt (black symbols) and in the afterglow (red symbols) emissions from Dainotti et al. (2015b). $\log E$ represents $\log E_{X,f}$ for the prompt emission pulses, while it represents $\log E_{X,\text{plateau}}$ for the afterglow emission pulses, and the time $\log T^*$ indicates $\log T_{X,f}^*$ for the prompt emission pulses and $\log T_{X,a}^*$ for the afterglow phase. The yellow points display the maximum energy prompt emission pulses ($\log T_{\text{max}}$, $\log E_{\text{max}}$). (For interpretation of the references to colour in this figure legend, the reader is referred to the web version of this article.)

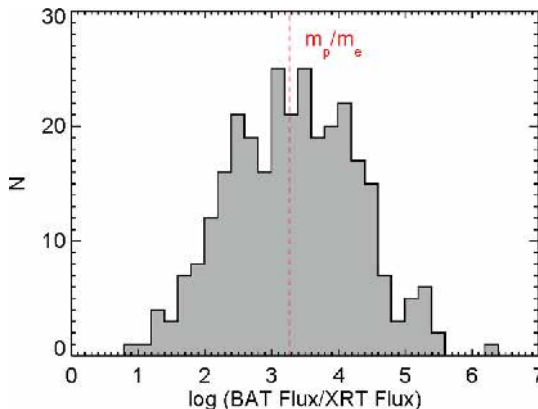


Fig. 27. The histogram of the BAT to XRT flux ratio for a number of Swift GRBs from Kazanas et al. (2015). The distribution shows clearly a preferred value for this ratio of order $\sim 10^3 - 10^4$. The vertical line shows also the proton to electron mass ratio m_p/m_e .

$\log L_{X,\text{peak}} - \log L_{X,a}$ relations. Alternatively, in the RS scenario, in order to obtain the observed prompt-afterglow relationships, the typical Γ of the ejecta should rise with the burst energy.

In addition, Ruffini et al. (2014) pointed out that the induced gravitational collapse paradigm can recover the $\log L_{X,a} - \log L_{\gamma,\text{iso}}$ and the $\log L_{X,\text{peak}} - \log L_{X,a}$ relations. This model considers the very energetic ($10^{52} - 10^{54}$ erg) LGRBs for which the SNe has been seen. The light curves were built assuming for the external medium either a radial structure for the wind (Guida et al., 2008; Bernardini et al., 2006,2007; Caiò et al., 2009) or a partition of the shell (Dainotti et al., 2007), therefore well matching the afterglow plateau and the prompt emission.

Recently, Kazanas et al. (2015) within the context of the Supercritical Pile Model claimed that they can reproduce the $\log L_{X,a} - \log L_{\gamma,\text{iso}}$ and the $\log L_{X,\text{peak}} - \log L_{X,a}$ relations, because the ratio, R , between the luminosities appears consistent with the one between the mean prompt energy flux from BAT and the

afterglow plateau fluxes detected by XRT. In particular, $R \approx 2000$ is close to the proton to electron mass ratio, see Fig. 27.

Indeed, this is a new challenge for theoretical modeling that would need to consider, simultaneously, the several prompt-afterglow connections in order to better reproduce the phenomenology of the relations from a statistical point of view.

4.6. The $L_{O,\text{peak}}^F - T_{O,\text{peak}}^F$ relation and its physical interpretation

Liang et al. (2010) studied the relation between the width of the light curve flares, w , and $T_{O,\text{peak}}$ of the flares, denoted with the index F, using a sample of 32 Swift GRBs, see the left panel of Fig. 28. This relation reads as follows:

$$\log w^F = (0.05 \pm 0.27) + (1.16 \pm 0.10) \times \log T_{O,\text{peak}}^F, \quad (16)$$

with $\rho = 0.94$.

Later, Li et al. (2012) found the same relation as Liang et al. (2010), but with smaller values of normalization and slope, using 24 flares from 19 single-pulse GRBs observed with CGRO/BATSE,⁶ see the right panel of Fig. 28. However, for these 19 GRBs only in 14 GRBs a flare activity is distinctly visible. The relationship was given by:

$$\log w^F = -0.32 + 1.01 \times \log T_{O,\text{peak}}^F. \quad (17)$$

They claimed that earlier flares are brighter and narrower than later ones. They compared the $w^F - T_{O,\text{peak}}^F$ distribution for the X-ray flares detected by Swift/XRT with the one for the optical flares in the R band. As a conclusion, they seemed to have a similar behavior (Chincarini et al., 2007; Margutti et al., 2010), see the right panel of Fig. 28.

Furthermore, in the rest frame band, they found a relation between the $L_{O,\text{peak}}$ of the flares in the R energy in units of 10^{48} erg s⁻¹ and $T_{O,\text{peak}}^*$ of the flares using 19 GRBs, see Fig. 29. Both prompt pulses and X-ray and optical flares are correlated and

⁶ Among the instruments of the Compton Gamma Ray Observatory (CGRO) satellite, running from 1991 to 2001, the Burst and Transient Source Experiment (BATSE) played a fundamental role in the measurements of GRB spectral features in the range from 20 keV to 8 MeV. Bursts were typically detected at rates of roughly one per day over the 9-year CGRO mission within a time interval ranging from ~ 0.1 s up to about 100 s. Therefore, this satellite enabled careful analysis of the spectral properties of the GRB prompt emission.

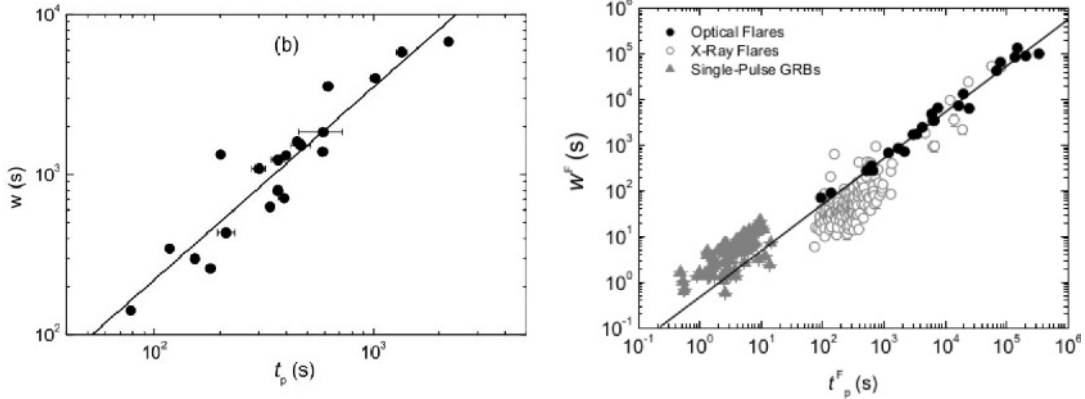


Fig. 28. Left panel: $\log w^F - \log T_{O,peak}^F$ distribution from Liang et al. (2010). Right panel: $\log w^F - \log T_{O,peak}^F$ distribution from Li et al. (2012). In both panels lines represent the best fit.

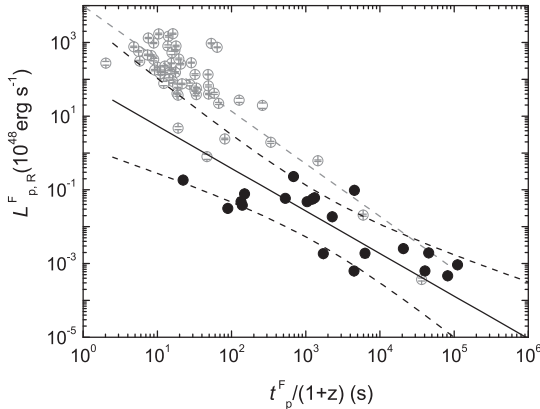


Fig. 29. $\log L_{p,R}^F - \log T_{O,peak}^F$ relation from Li et al. (2012). Lines represent the best fits, black dots indicate optical flares, and the grey circles with errors show X-ray flares associated with the optical flares.

present a visible temporal evolution, as seen in Fig. 29. This relation is given by:

$$\log L_{p,peak}^F = (1.89 \pm 0.52) - (1.15 \pm 0.15) \times \log T_{O,peak}^F, \quad (18)$$

with $\rho = 0.85$ and $P < 10^{-4}$. $T_{O,peak}^F$ spans from \sim tens of seconds to $\sim 10^6$ s, instead the $L_{p,peak}^F$ varies from 10^{43} to 10^{49} erg s^{-1} , with an average value of 10^{46} erg s^{-1} . In addition, considering only the most luminous GRBs, they found that $T_{O,peak}^F$ was strongly anti-correlated to $E_{\gamma,prompt}$ in the 1– 10^4 keV energy band:

$$\log T_{O,peak}^{*F} = (5.38 \pm 0.30) - (0.78 \pm 0.09) \times \log E_{\gamma,prompt}/10^{50}, \quad (19)$$

with $\rho = 0.92$. These outcomes revealed that the GRB flares in the optical wavelength with higher $E_{\gamma,prompt}$ peak earlier and are much more luminous. In Table 9 a summary of the relations described in this section is displayed.

As regards the physical interpretation of the $L_{p,peak}^F - T_{O,peak}^F$ relationship, Li et al. (2012) found that the flares are separated components superimposed to the afterglow phase. The coupling be-

tween $L_{p,peak}^F$ and $T_{O,peak}^F$ suggested that the prompt γ -ray and late optical flare emission may arise from the same mechanism, namely from a central engine that can periodically eject a number of shells during the emission. Impacts of these shells could create internal shocks or magnetic turbulent reconnections, which would emerge from the variability (Kobayashi et al., 1997; Zhang and Yan, 2011). Fenimore et al. (1995) revealed no relevant pattern in the width and intensity distributions using gamma ray data only. In addition, the usual tendency of the $w^F - T_{O,peak}^F$ relation cannot be due to hydrodynamical diffusion of the shells emitted at recent times, but it is necessary that the central engine radiates thicker and fainter shells at late stages (Maxham and Zhang, 2009). This could be explained as flares generated by clumps, such that the diffusion during the accretion mechanism would extend the accretion duration onto the BH (Perna et al., 2006; Proga and Zhang, 2006).

5. Selection effects

Selection effects are distortions or biases that usually occur when the sample observed is not representative of the “true” population itself. This kind of biases usually affects GRB relations. Efron and Petrosian (1992), Lloyd and Petrosian (1999), Dainotti et al. (2013a; 2015a) and Petrosian et al. (2013) emphasized that when dealing with a multivariate data set, it is imperative to determine first the true relations among the variables, not those introduced by the observational selection effects, before obtaining the individual distributions of the variables themselves. This study is needed for claiming the existence of the intrinsic relations. A relation can be called intrinsic only if it is carefully tested and corrected for these biases.

The selection effects present in the relations discussed above are mostly due to the dependence of the parameters on the redshift, like in the case of the time and the luminosity evolution, or due to the threshold of the detector used.

In this section, we describe several different methods to deal with selection biases.

In Section 5.1, we discuss the redshift induced relation through a qualitative method, while in Section 5.2 we present a more quantitative approach through the EP method. In Section 5.3, we describe how to obtain the intrinsic relations corrected by selection biases, and in Section 5.4 we report the selection effects for the optical and X-ray luminosities. Lastly, in Section 5.5 we

Table 9

Summary of the relations in this section. The first column represents the relation in log scale, the second one the authors, the third one the number of GRBs in the used sample, and the fourth and the fifth columns are the slope and normalization of the relation. The last two columns are the correlation coefficient and the chance probability, P.

Correlations	Author	N	Slope	Norm	Corr.coeff.	P
$w^F - T_{O,peak}^F$	Liang et al. (2010)	32	$1.16^{+0.10}_{-0.10}$	$0.05^{+0.27}_{-0.27}$	0.94	$< 10^{-4}$
$L_{O,peak}^F - T_{O,peak}^F$	Li et al. (2012)	19	1.01	-0.32		
$T_{O,peak}^F - E_{\gamma, prompt}$	Li et al. (2012)	19	$-1.15^{+0.15}_{-0.15}$	$1.89^{+0.52}_{-0.52}$	0.85	$< 10^{-4}$
$T_{O,peak}^F - E_{\gamma, prompt}$	Li et al. (2012)	19	$-0.78^{+0.09}_{-0.09}$	$5.38^{+0.40}_{-0.30}$	0.92	$< 10^{-4}$

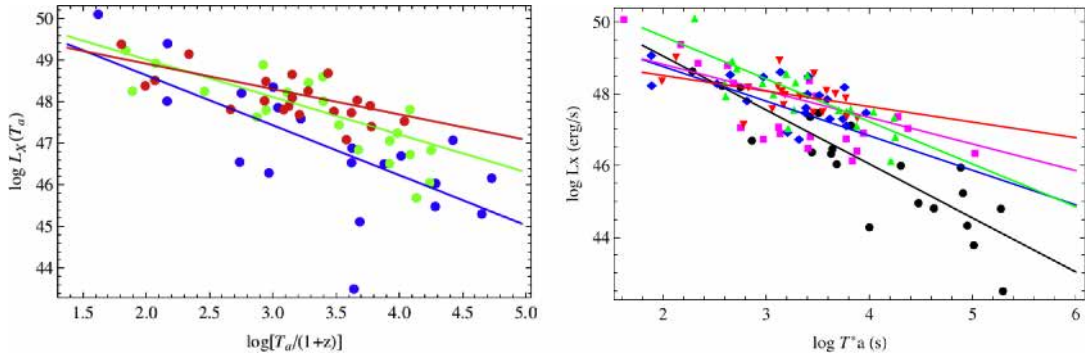


Fig. 30. Left panel: “ $\log L_{X,a} - \log T_{X,a}^*$ relation divided in the three redshift bins $Z1 = (0.08, 1.56)$, $Z2 = (1.71, 3.08)$ and $Z3 = (3.21, 8.26)$ from Dainotti et al. (2011a). With the blue points it is represented the Z1 sample, with the green ones the Z2 sample and with the red points the Z3 sample. The respective fitted lines are in the same colors”. Right panel: “ $\log L_{X,a} - \log T_{X,a}^*$ distribution from Dainotti et al. (2013a) for the sample of 101 GRB afterglows divided in 5 equipopulated redshift bins shown by different colors: black for $z < 0.89$, magenta for $0.89 \leq z \leq 1.68$, blue for $1.68 < z \leq 2.45$, green $2.45 < z \leq 3.45$, red for $z \geq 3.45$. Solid lines show the fitted relations”. (For interpretation of the references to colour in this figure legend, the reader is referred to the web version of this article.)

show the evaluation of the intrinsic relation through Monte Carlo simulations.

5.1. Redshift induced relations

An important source of possible selection effects is the dependence of the variables on the redshift. To this end, Dainotti et al. (2011a) investigated the redshift evolution of the parameters of the LT relation, because a change of the relation slope has been observed when comparing several analyses (Dainotti et al., 2008, 2010). Namely, in the first paper, it was found $b = -0.74^{+0.20}_{-0.19}$ and in the latter $b = -1.06^{+0.27}_{-0.28}$. Therefore, it became crucial to understand the reason of this change, even if the two slopes are still comparable at the $1-\sigma$ level. The distribution of the 62 LGRBs in the sample is not uniform within the range $(z_{min}, z_{max}) = (0.08, 8.26)$ with few data points at large redshifts. Even if this sample is sparse, it was important to investigate whether the calibration coefficients (a, b, σ_{int}) were in agreement within the error bars over this large redshift interval, see the left panel of Fig. 30.

For this reason, the data set was separated in three redshift bins with the same number of elements, $Z1 = (0.08, 1.56)$, $Z2 = (1.71, 3.08)$ and $Z3 = (3.21, 8.26)$ presented as blue, green and red points respectively in the left panel of Fig. 30. The results are presented in Table 10.

The correlation coefficient ρ was found quite high in each redshift bins, supporting the independence of the LT relation on z . The slopes b for bins Z1 and Z2 are comparable within the 68% CL, while the slopes in bins Z1 and Z3 only within the 95% CL, see Table 10. On the contrary, the normalization a is comparable in all the bins. From this analysis, it is not possible to confirm that the LT relation is shallower for larger z GRBs, due to the low number of data points and the presence of high σ_E GRBs. Finally, bigger

Table 10

Results of the calibration procedure for GRBs divided in three equally populated redshift bins with $(z_{min}, z_{max}) = (0.08, 1.56)$, $(1.71, 3.08)$, $(3.21, 8.26)$ for bins Z1, Z2, Z3 from Dainotti et al. (2011a). The subscript bf displays the best fit values, while the $median$ subscript shows the median values.

Id	ρ	$(b, a, \sigma_{int})_{bf}$	b_{median}	$(\sigma_{int})_{median}$
Z1	-0.69	$(-1.20, 51.04, 0.98)$	$-1.08^{+0.27}_{-0.30}$	$1.01^{+0.20}_{-0.16}$
Z2	-0.83	$(-0.90, 50.82, 0.43)$	$-0.86^{+0.18}_{-0.16}$	$0.45^{+0.09}_{-0.08}$
Z3	-0.63	$(-0.61, 50.14, 0.26)$	$-0.58^{+0.14}_{-0.15}$	$0.26^{+0.07}_{-0.06}$

samples with small σ_E values and a more uniform z binning are required to overcome this problem.

For this reason, Dainotti et al. (2013a) performed a similar analysis, but with a larger sample consisting of 101 GRBs. Specifically, this updated sample was split in 5 redshift ranges with the same number of elements, thus having 20 GRBs in each subgroup, represented in the right panel of Fig. 30 by different colors: black for $z < 0.89$, magenta for $0.89 \leq z \leq 1.68$, blue for $1.68 < z \leq 2.45$, green for $2.45 < z \leq 3.45$ and red for $z \geq 3.45$. The fitted lines for each redshift bin are also shown in the same colour code. The distribution of the subsamples presented different power law slopes when the whole sample was divided into bins. The objects in the different bins exhibited some separation into different regions of the LT plane. Moreover, the slope of the relation for each redshift bin versus the averaged redshift range has also been presented, see the left panel of Fig. 31.

In addition, in Dainotti et al. (2015a), the updated sample of 176 GRBs was divided into 5 redshift bins consisting of about 35 GRBs for each group, as shown in the right panel of Fig. 31. A small evolution in z has been confirmed with the following linear function $b(z) = 0.10z - 1.38$.

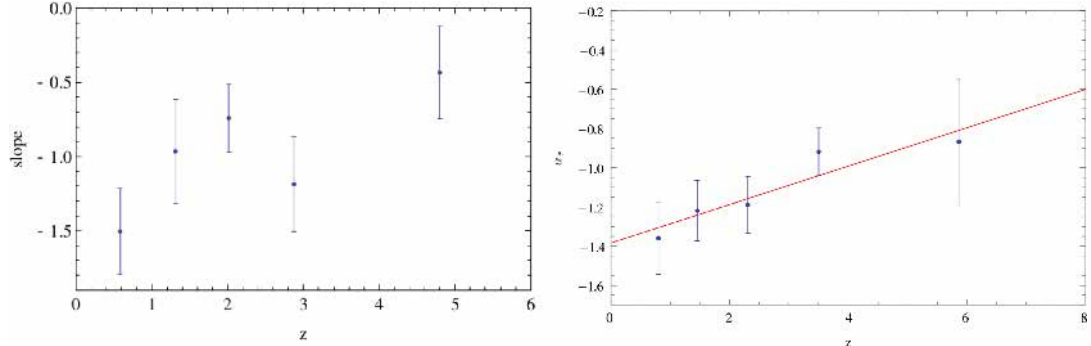


Fig. 31. Left panel: “the variation of b (and its error range) with the mean value of the redshift bins from Dainotti et al. (2013a)”. Right panel: “ α_τ , which is equivalent to the slope b , vs z using a linear function $\alpha_\tau = 0.10z - 1.38$ from Dainotti et al. (2015a)”.

Regarding the $\log L_{X,peak} - \log L_{X,a}$ relation, Dainotti et al. (2015b) showed that it is not produced by the dependence on the redshift of its variables. To estimate the redshift evolution, the sample was separated into 4 redshift bins as shown in the left panel of Fig. 25. The GRB distribution in each bin is not grouped or constrained within a specific region, therefore indicating no strong redshift evolution. For $\log L_{X,a}$ it was found that there was negligible redshift evolution of the afterglow X-ray luminosity (Dainotti et al., 2013a), while for $\log L_{X,peak}$ has been demonstrated that there is significant redshift evolution (Yonetoku et al., 2004; Petrosian et al., 2013; Dainotti et al., 2015b). For more details, see Sections 5.2.1 and 5.2.2.

5.2. Redshift induced relations through Efron and Petrosian method

For a quantitative study of the redshift evolution, which is the dependence of the variables on the redshift, we here refer to the EP method which is specifically designed to overcome the biases resulting from incomplete data. The Efron & Petrosian technique, applied to GRBs (Petrosian et al., 2009; Lloyd and Petrosian, 1999; Lloyd et al., 2000), allows to compute the intrinsic slope of the relation by creating new bias-free observables, called local variables and denoted with the symbol $'$. For these quantities, the redshift evolution and the selection effects due to instrumental thresholds are removed. The EP method uses a modification of the Kendall tau test⁷ τ to compute the best fit values of the parameters which represent the luminosity and time evolutionary functions. For details about the definition of τ see Efron and Petrosian (1992).

5.2.1. Luminosity evolution

The relation between luminosity and z is called luminosity evolution. We discuss the luminosity evolution for both prompt and plateau phases. Before applying the EP method to the plateau phase, the limiting plateau flux, F_{lim} , which gives the minimum observed luminosity for a given z needs to be parameterized. The XRT sensitivity, $F_{lim,XRT} = 10^{-14}$ erg cm $^{-2}$ s $^{-1}$, is not high enough to represent the truncation of the data set. Hence, as claimed by Cannizzo et al. (2011), a better choice for the flux threshold is 10 $^{-12}$ erg cm $^{-2}$ s $^{-1}$. Several threshold fluxes were analyzed (Dainotti et al., 2013a), finally $F_{lim,XRT} = 1.5 \times 10^{-12}$ erg cm $^{-2}$ s $^{-1}$, which leaves 90 out of 101 GRBs, was selected (see the left panel of Fig. 32). Regarding instead the prompt limiting flux,

Dainotti et al. (2015b) chose a BAT flux limit $F_{lim,BAT} = 4 \times 10^{-8}$ erg cm $^{-2}$ s $^{-1}$, which also allows 90% of GRBs in the sample, see the right panel of Fig. 32.

In Dainotti et al. (2013a), the relation function, $g(z)$, is defined when determining the evolution of $L_{X,a}$ so that the local variable $L'_{X,a} \equiv L_{X,a}/g(z)$ is not dependent anymore from z . The evolutionary function is parameterized by a simple relation function:

$$g(z) = (1+z)^{k_{L_{X,a}}}. \quad (20)$$

More complex evolution functions lead to comparable results, see Dainotti et al. (2013a, 2015b).

With this modified version of τ , the value of $k_{L_{X,a}}$ for which $\tau_{L_{X,a}} = 0$ is the one that best represents the luminosity evolution at the 1 σ level. $k_{L_{X,a}} = -0.05^{+0.35}_{-0.55}$ means that this evolution is negligible, see the left panel of Fig. 33. In the same panel, this distribution is also plotted for a smaller sample of 47 GRBs (green dotted line) in common with the previous one of 77 LGRBs presented in Dainotti et al. (2011a).

The results of the afterglow luminosity evolution among the two samples are compatible at 2 σ . Instead, regarding the study of the evolution of $L_{X,peak}$, the simple relation function (see Eq. 20) was compared to a more complex function (Dainotti et al., 2015b) given by:

$$g(z) = \frac{Z^{k_L}(1+Z^{k_{cr}})}{Z^{k_L} + Z^{k_{cr}}}, \quad (21)$$

where $Z = 1+z$ and $Z_{cr} = 3.5$. A relevant luminosity evolution was obtained in the prompt, $k_{L_{X,peak}} = 2.13^{+0.33}_{-0.37}$, using the simple relation, while $k_{L_{X,peak}} = 3.09^{+0.40}_{-0.35}$ for the more complex function, see the middle and right panels of Fig. 33 respectively. The results of the prompt luminosity evolution among the two different functions are compatible at 2 σ .

5.2.2. Time Evolution

Similarly to the treatment of the luminosity evolution, one has also to determine the limit of the plateau end time, $T_{X,a,lim}^* = 242/(1+z)$ s (Dainotti et al., 2013a), and of the prompt peak time $T_{X,prompt,lim}^* = 1.74/(1+z)$ s (Dainotti et al., 2015b), see the left and right panels of Fig. 34 and Fig. 35 respectively.

To determine the evolution of $T_{X,a}^*$, so that the de-evolved variable $T'_{X,a} \equiv T_{X,a}^*/f(z)$ is not correlated with z , the relation function $f(z)$ (Dainotti et al., 2013a) was specified:

$$f(z) = (1+z)^{k_{T_{X,a}^*}}. \quad (22)$$

⁷ The Kendall τ is a non-parametric statistical test used to measure the association between two measured quantities. It is a measure of rank relation: the similarity of the orderings of the data when ranked by each of the quantities.

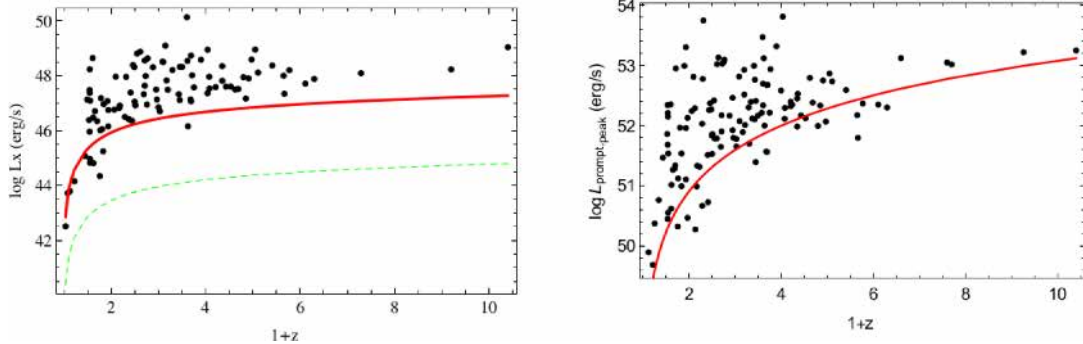


Fig. 32. Left panel: “the bivariate distribution of $\log L_{X,a}$ and z with two different flux limits from Dainotti et al. (2013a). The instrumental XRT flux limit, $1.0 \times 10^{-14} \text{ erg cm}^{-2} \text{ s}^{-1}$ (dashed green line), is too low to be representative of the flux limit, $1.5 \times 10^{-12} \text{ erg cm}^{-2} \text{ s}^{-1}$ (solid red line) represents better the limit of the sample”. Right panel: “the bivariate distribution of $\log L_{X,\text{peak}}$ and z with the flux limit assuming the K correction $K = 1$ from Dainotti et al. (2015b). The BAT flux limit, $4.0 \times 10^{-8} \text{ erg cm}^{-2} \text{ s}^{-1}$ (solid red line), better represents the limit of the sample”. (For interpretation of the references to colour in this figure legend, the reader is referred to the web version of this article.)

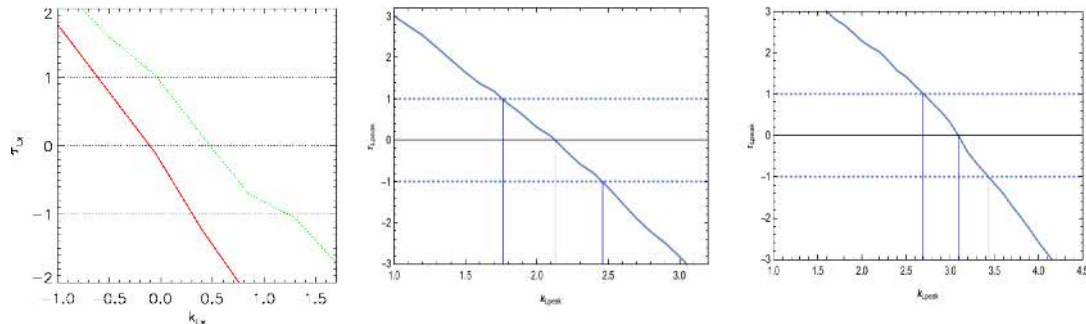


Fig. 33. Left panel: τ vs. $k_{Lx,a}$ from Dainotti et al. (2013a). The red line indicates the full sample, while the green dotted line indicates the sample of 47 GRBs in common with the 77 LGRBs in Dainotti et al. (2011a). Middle panel: τ vs. $k_{Lx,\text{peak}}$, using the Eq. 20, from Dainotti et al. (2015b). Right panel: τ vs. $k_{Lx,\text{peak}}$, using the Eq. 21, from Dainotti et al. (2015b). (For interpretation of the references to colour in this figure legend, the reader is referred to the web version of this article.)

The values of $k_{T_{X,a}^*}$ for which $\tau_{T_{X,a}^*} = 0$ is the one that best matches the plateau end time evolution at the 1σ uncertainty. $\tau_{T_{X,a}^*}$ versus $k_{T_{X,a}^*}$ distribution shows a consistent evolution in $T_{X,a}^*$, as seen in the left panel of Fig. 36, namely $k_{T_{X,a}^*} = -0.85^{+0.30}_{-0.30}$. In the same panel this distribution is also displayed for a smaller sample of 47 GRBs (green dotted line) in common with the previous one of 77 GRBs presented in Dainotti et al. (2011a). The results of the afterglow time evolution among the two samples are compatible at 1.5σ .

Regarding the prompt time evolution, a more complex function was also used in addition to the simple relation function (Dainotti et al., 2015b):

$$f(z) = \frac{Z^{k_t^*}(1 + Z_{cr}^{k_t^*})}{Z^{k_t^*} + Z_{cr}^{k_t^*}}, \quad (23)$$

where $Z = 1 + z$ and $Z_{cr} = 3.5$.

As a conclusion, a not relevant time evolution in the prompt was found for both the simple function, $k_{T_{X,\text{prompt}}^*} = -0.62^{+0.38}_{-0.38}$, and for the more complex one $k_{T_{X,\text{prompt}}^*} = -0.17^{+0.24}_{-0.27}$, see the middle and right panels of Fig. 36 respectively. The results of the prompt time evolution among the two different functions are compatible at 1σ .

5.3. Evaluation of the intrinsic slope

The last step to determine if a relation is intrinsic is to evaluate its “true” slope. To this end, the EP method was used in the local time ($T'_{X,a}$) and luminosity ($L'_{X,a}$) space obtaining an intrinsic slope for the LT relation $b_{int} = 1/\alpha = -1.07^{+0.09}_{-0.14}$. The significance of this relation is at 12σ level. It can be derived directly from the left panel of Fig. 37 (Dainotti et al., 2013a), because if there was no relation it would have been that $\tau = 0$ for $b_{int} = 0$ at 1σ .

Instead, regarding the evaluation of the intrinsic slope in the $\log L_{X,\text{peak}} - \log L_{X,a}$ relation, Dainotti et al. (2015b) used a different method, namely the partial correlation coefficient. This is the degree of association between two random variables calculated as a function of b_{int} in the following way:

$$r_{L'_{X,\text{peak}}, L'_{X,a}, D_L} = \frac{r_{L'_{X,\text{peak}}, L'_{X,a}} - r_{L'_{X,\text{peak}}, D_L} * r_{L'_{X,a}, D_L}}{(1 - r_{L'_{X,\text{peak}}, D_L}^2) * (1 - r_{L'_{X,a}, D_L}^2)}, \quad (24)$$

where $\log L'_{X,a} = L'_{X,a}$ and $\log L'_{X,\text{peak}} = L'_{X,\text{peak}}$.

As displayed in the right panel of Fig. 37, the relation is highly significant when $b_{int} = 1.14^{+0.83}_{-0.32}$, which is at 1σ of the observed slope.

In addition, following an analysis similar to the one of Butler et al. (2010), Dainotti et al. (2015a) simulated a sample for which biases on both time and luminosity are considered. Partic-

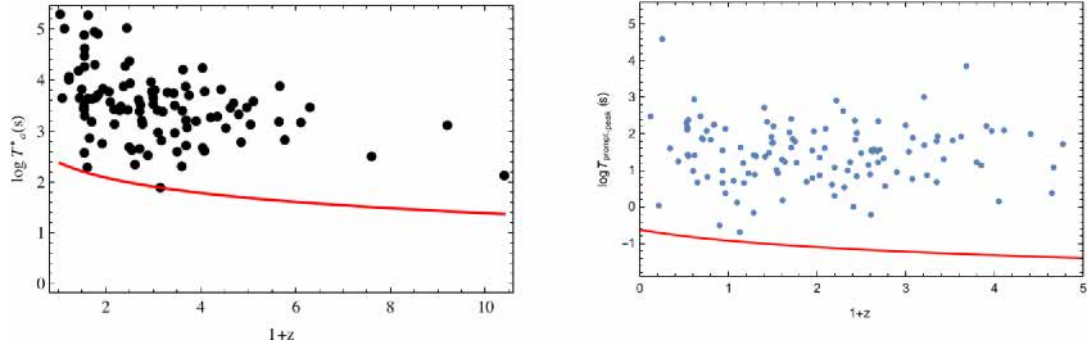


Fig. 34. Left panel: “the bivariate distribution of the rest frame time $\log T_{X,a}^*$ and z from Dainotti et al. (2013a). The red line is the limiting rest frame time, $\log(T_{X,a,lim}/(1+z))$ where the chosen limiting value of the observed end-time of the plateau in the sample is $T_{X,a,lim} = 242$ s”. Right panel: “the bivariate distribution of the rest frame time $\log T_{X,prompt}^*$ and z from Dainotti et al. (2015b), where with $\log T_{X,prompt}^*$ they denoted the sum of the peak pulses width of each single pulse in each GRB. The chosen limiting value of the observed pulse width in the sample is $\log T_{X,prompt,lim} = 0.24$ s. The red line is the limiting rest frame time, $\log(T_{X,prompt,lim}/(1+z))$ ”. (For interpretation of the references to colour in this figure legend, the reader is referred to the web version of this article.)

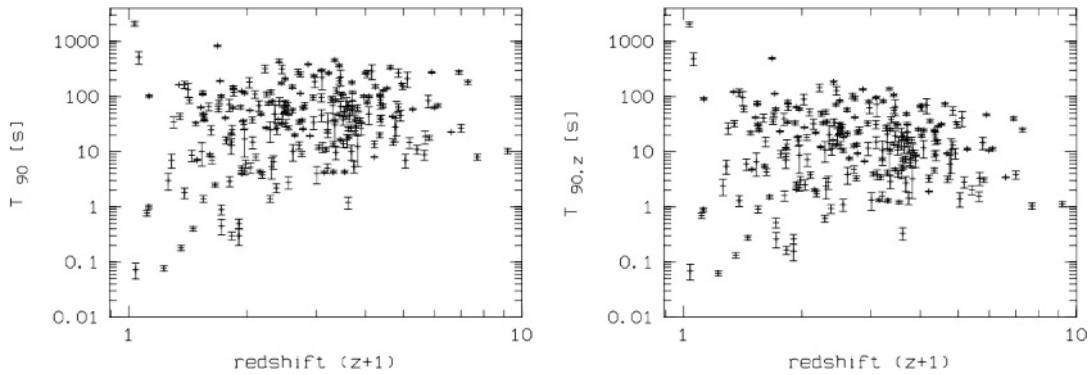


Fig. 35. Distributions between redshift and the observed (left panel) and rest-frame (right panel) T_{90} in the BAT energy range from Grupe et al. (2013).

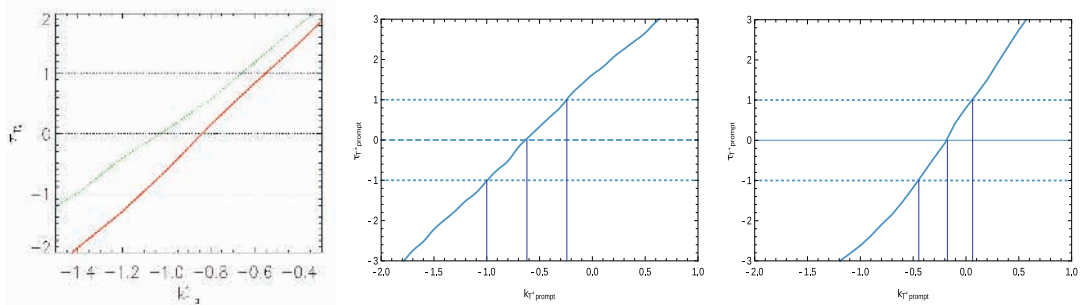


Fig. 36. Left panel: τ vs. $k_{T_X^*}$ from Dainotti et al. (2013a). The red line indicates the full sample, while the green dotted line indicates the 47 GRBs in common with the sample presented in Dainotti et al. (2011a). Middle panel: τ vs. $k_{T_{X,prompt}}^*$, using the eq. 22, from Dainotti et al. (2015b). Right panel: τ vs. $k_{T_{X,prompt}}^*$, using the eq. 23, from Dainotti et al. (2015b). (For interpretation of the references to colour in this figure legend, the reader is referred to the web version of this article.)

ularly, they assumed the biases to be roughly the same whichever monotonic efficiency function for the luminosity detection is taken. This method presented how an unknown efficiency function could affect the slope of any relation and the GRB density rate. Then, biases in slope or normalization caused by the truncations were analyzed. This gave distinct fit values that allow for studying the scatter of the relation and its selection effects. This analysis

has shown, together with the one in Dainotti et al. (2013a), that the LT relation can be corrected by selection effects and therefore can be used in principle as redshift estimator (see Section 6) and as a valuable cosmological tool (see Section 7). As regards other relations, D’Avanzo et al. (2012) for the $L_{X,a} - E_{Y,prompt}$ relation, Oates et al. (2015) for the $L_{0,200s} - \alpha_{0,>200s}$ relation, and Racusin et al. (2016) for the $L_{X,200s} - \alpha_{X,>200s}$ relation, also used the

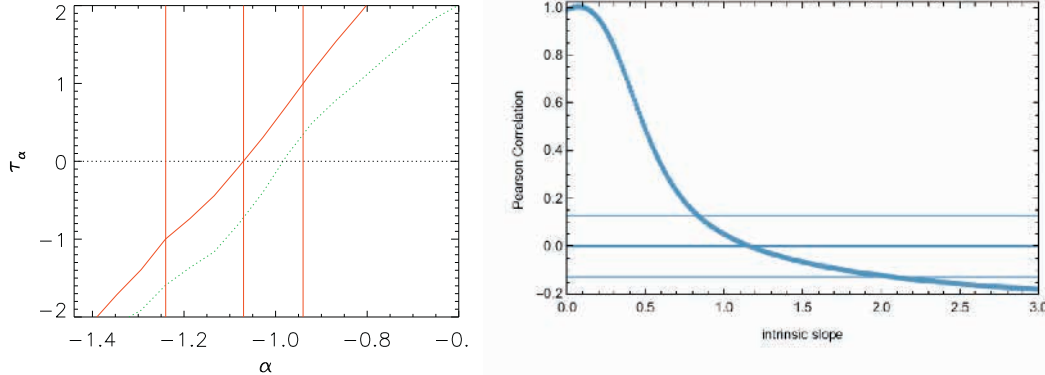


Fig. 37. Left panel: τ vs. b_{int} (indicated with α in the picture) from Dainotti et al. (2013a). Right panel: r vs. b_{int} from Dainotti et al. (2015b) with the best value where $\log L_{X,peak}$ and $\log L_{X,a}$ are strongly correlated (the central thick line). The two thinner lines indicate the 0.05% probability that the sample is drawn by chance.

partial correlation coefficient method to show that the redshift dependence does not induce these relations.

5.4. Selection effects for the optical and X-ray luminosities

In this section we discuss the selection effects due to the limiting optical and X-ray luminosities relevant for the relations mentioned above. Nardini et al. (2008b) investigated if the observed luminosity distribution can be the result of selection effects by studying the optically dark afterglows. By simulating the $\log L_{0,12}$, z , host galaxy dust absorption, A_V^{host} , and telescope limiting magnitude for each of the 30000 GRBs, the observed optical luminosity distribution was contrasted to the simulated one. From this simulated distribution regarding the intrinsic one, it is necessary to take only GRBs with a flux which is larger than the threshold flux of the associated detector. This corresponds with a lower luminosity truncation, which is around $\log L_{0,12} \approx 31.2$ ($\text{erg s}^{-1} \text{Hz}^{-1}$). Therefore, the fact that we do not observe GRBs with such a luminosity puts a limit to the luminosity function.

They also checked statistically the presence of a low luminosity category of events which are at 3.6σ off the central value of the distribution. They pointed out that if the absorption is chromatic, the observed luminosity distribution does not match with any unimodal one. If many GRBs are absorbed by "grey" achromatic dust, then a unimodal luminosity distribution can be obtained. In summary, dark bursts could belong to an optically subluminous group or to a category of bursts for which a high achromatic absorption is present.

As regards the evaluation of the selection effects of $L_{0,peak}$, the biases in the detection of $F_{0,peak}$ need to be considered. As found from Panaiteescu and Vestrand (2008), for a typical optical afterglow spectrum ($F_{0,a} \propto T_{0,a}^{-1}$), variations in the observer offset angle induce a $\log F_{0,peak} - \log T_{0,peak}$ anti-relation that is flatter than what is measured. In fact, an observational selection effect could steepen the slope of the anti-relation between $\log F_{0,peak}$ and $\log T_{0,peak}$.

In addition, SGRBs observed by Swift seem to be fluence-limited, while LGRBs detected with the same telescope are flux-limited (Gehrels et al., 2008) due to the instrument trigger.

Nysewander et al. (2009) pointed out that the ratio $F_{0,11}/F_{X,11}$ may be influenced by absorption of photons in the host galaxy. Furthermore, they showed that $F_{X,11}$ should be precise, because the LGRBs observed in the XRT passband do not present X-ray

column absorptions, differently from the majority of LGRBs. The computed optical absorption of LGRB afterglows indicates smaller column densities (N_H) than in the X-ray, with optical absorptions (A_V) about one-tenth to one magnitude (Schady et al., 2007; Cenko et al., 2009). Regarding the SGRBs, they have more luminous optical emission relative to the X-ray than what is assumed by the standard model. Later, Kann et al. (2010) claimed that the grouping of the optical luminosity at the time of 1 day, $L_{0,1d}$, is less remarkable than the one described by Liang and Zhang (2006a) and Nardini et al. (2006) for GRBs observed by Swift. This suggested that the grouping pointed out in pre-Swift data can be due to selection effects only. Finally, Berger (2014) claimed that the optical afterglow detection can influence the luminosity distribution towards places with larger densities medium.

5.5. Selection effects in the $L_{0,200s} - \alpha_{0,>200s}$ relation

Oates et al. (2012) ensured that a high S/N light curve, covering both early and late times, can be constructed from the UVOT multi-filter observations using the criteria from Oates et al. (2009). If the faintest optical/UV afterglows decay more slowly than the brightest ones, then at late time the luminosity distribution is less dispersed and the correlation coefficient of the $\log L_{0,200s} - \alpha_{0,>200s}$ relation must become smaller and/or negligible. Indeed, both of these effects were observed in their sample. Furthermore, the $\log L_{0,200s} - \alpha_{0,>200s}$ relation may arise, by chance, from the way in which the sample is chosen. Thus, to verify if this is not the case, they computed Monte Carlo simulations. Among the 10^6 trials, 34 have a correlation coefficient indicating a more significant relation than the original one. This points out that, at 4.2σ confidence, the $\log L_{0,200s} - \alpha_{0,>200s}$ relation is not caused by the selection criteria nor does it happen by chance, and thus it is intrinsic.

6. Redshift estimator

As we have pointed out in the introduction, the study of GRBs as possible distance estimators is relevant, since for many of them z is unknown. Therefore, having a relation which is able to infer the distance from known quantities observed independently of z would allow a better investigation of the GRB population. Moreover, in the cases in which z is uncertain, the estimator can give hints on the upper and lower limits of the distance at which the GRB is placed. Some examples of redshift estimators for the

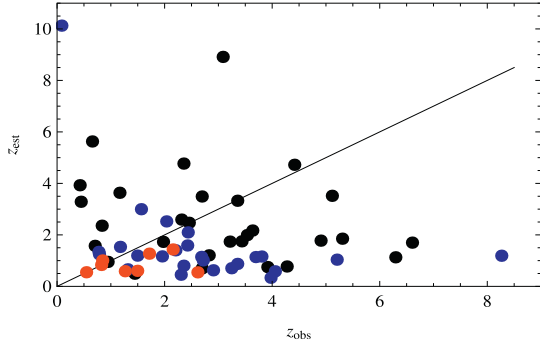


Fig. 38. $z_{\text{obs}} - z_{\text{est}}$ distribution for the 62 LGRBs divided in three σ_E ranges from Dainotti et al. (2011a): $\sigma_E \leq 0.095$ is represented by red points, $0.095 \leq \sigma_E \leq 0.3$ is represented by blue points, $0.3 \leq \sigma_E \leq 4$ is represented by black points. (For interpretation of the references to colour in this figure legend, the reader is referred to the web version of this article.)

prompt relations (Atteia, 2003; Yonetoku et al., 2004; Tsutsui et al., 2013) have been reported. In these papers, a method is developed for inverting GRB luminosity relations in respect to the redshift to have an expression of the distance as a function of z . The methodology used for the prompt emission relations can be then applied also to the afterglow or prompt-afterglow phase relations.

In this respect, Dainotti et al. (2011a) investigated the LT relation as a redshift estimator. From this relation, the best fit parameters of the slope and normalization are derived, while parameters such as $\log F_{X,a}$, $\log T_{X,a}$ and $\beta_{X,a}$ are known, because they are measured. Therefore, the LT relation can be inverted to obtain an estimate of z as it has been done for the prompt relations by Yonetoku et al. (2004). With this intention, let us return to the Eq. 2 and write it in another form:

$$\begin{aligned} \log L_{X,a} &= \log(4\pi F_{X,a}) + 2\log D_L(z, \Omega_M, h) - (1 - \beta_{X,a})\log(1+z) \\ &= \log(4\pi F_{X,a}) + (1 + \beta_{X,a})\log(1+z) + 2\log r(z) + 2\log(c/H_0) \\ &= a\log\left(\frac{T_{X,a}}{1+z}\right) + b \end{aligned} \quad (25)$$

where $r(z) = D_L(z, \Omega_M, h) \times (H_0/c)$. Solving respect to z , it was obtained:

$$(1 + \beta_{X,a} + a)\log(1+z) + 2\log r(z) = a\log T_{X,a} + b - \log(4\pi F_{X,a}) - 2\log(c/H_0). \quad (26)$$

The numerical solution of this equation may encounter some problems that must be taken into account: ($\log T_{X,a}$, $\log F_{X,a}$, $\beta_{X,a}$) and the LT calibration parameters (a , b) are influenced by their own errors. Furthermore, the errors on (a , b) are not symmetric and σ_{int} is summed to the total error in a nonlinear way. For details about possible solutions on how to consider the errors see Dainotti et al. (2011a). The above solution was employed for the E4 and the E0095 samples, pointing out that the LT relation can still not be considered as a precise redshift estimator, see Fig. 38. Assuming $\Delta z = z_{\text{obs}} - z_{\text{est}}$, where z_{obs} and z_{est} are the observed and the estimated redshifts respectively, it has been shown that $\sim 20\%$ of GRBs in the E4 sample ($0.3 \leq \sigma_E \leq 4$, and blue, $0.095 \leq \sigma_E \leq 0.3$, points in Fig. 38) has $|\Delta z/\sigma(z_{\text{est}})| \leq 1$. While for the E0095 subsample 28% has $|\Delta z/\sigma(z_{\text{est}})| \leq 1$, red dots in Fig. 38. The percentage of successful solutions rises to $\sim 53\%$ ($\sim 57\%$) for the E4 (E0095) sample if $|\Delta z/\sigma(z_{\text{est}})| \leq 3$ is considered. The comparison of the results for both the E4 and E0095 samples is proof that σ_E has no strong influence on the redshift estimate. The reason why the redshift indicator has not yet given successful results depends

on the intrinsic scatter of the LT relation. Thus, it is useful to check whether better results can be achieved by increasing the data sample size. For this reason, an E0095 subsample was simulated creating $(\log T_{X,a}, \beta_{X,a}, z)$ values from a distribution similar to the observed one for the E4 sample. Then, $\log L_{X,a}$ was selected from a Gaussian distribution with mean value obtained by the LT relation and with $\sigma_{\text{Gauss}} = \sigma_{\text{int}}$. These values were employed to compute $\log F_{X,a}$ and to reproduce the noise for all the quantities so that the relative errors resembled the observations. Then, using Markov chains as input to the redshift estimate formula, it is concluded that only enlarging the sample is not an appropriate methodology to increase the success of the LT relation as a redshift estimator.

In fact, with $N \simeq 50$, the number of GRBs with $|\Delta z/\sigma(z_{\text{est}})| \leq 1$ first rises to $\sim 34\%$ and then diminish to $\sim 20\%$ for $N \simeq 200$, while $\langle \Delta z/z_{\text{obs}} \rangle \simeq -17\%$ for both $N \simeq 50$ and $N \simeq 200$. The fact that enlarging the sample does not improve the result could be expected. Indeed, a bigger sample conducts to tighter constraints on the $(a, b, \sigma_{\text{int}})$ values, but does not affect σ_{int} which is the principal cause of inconsistencies between the observed and the estimated z .

Therefore, an alternative way was explored: σ_{int} was decreased and the best fit (a, b) parameters of the E0095 subsample were chosen. In fact, fixing $\sigma_{\text{int}} = 0.10$ gives $f(|\Delta z/z_{\text{obs}}| \leq 1) \simeq 66\%$. These outcomes suggested that the LT relation could be employed as a redshift estimator only in the case that a subsample of GRBs could be determined with $\sigma_{\text{int}} = 0.10 - 0.20$. If such a sample is achievable is not clear yet due to the paucity of the E0095 subsample. In fact, it is difficult to find out some useful indicators that can help to define GRBs close to the best fit line of the LT relation. To obtain ~ 50 GRBs to calibrate the LT relation with $\sigma_{\text{int}} \sim 0.20$ it has been estimated that a sample of ~ 600 GRBs with observed $(\log T_{X,a}, \log F_{X,a}, \beta_{X,a}, z)$ values is needed. However, even if this is a challenging goal, it may be possible to find out properties of GRB afterglows which enable us to reduce the σ_{int} of the LT relation with a much smaller sample. Finally, an interesting feature would be to correct for the selection effects all the physical quantities of the relations mentioned above. In this manner, it would be possible to average them in order to create a more precise redshift estimator.

7. Cosmology

The study of the Hubble Diagram (HD), namely the distribution of the distance modulus $\mu(z)^8$ versus z of SNe Ia, opened the way to the investigation of the nature of DE. As it is known from the literature, $\mu(z)$ is proportional to the logarithm of the luminosity distance $D_L(z, \Omega_M, h)$ through the following equation:

$$\mu(z) = 25 + 5 \times \log D_L(z, \Omega_M, h). \quad (27)$$

In addition, $D_L(z, \Omega_M, h)$ is related to different DE EoSs.

7.1. The problem of the calibration

One of the most important issues presented in the use of GRB relations for cosmological studies is the so-called circularity problem. Namely, a cosmological model needs to be assumed to compute $D_L(z, \Omega_M, h)$. This is due to the fact that local GRBs are not available apart from the case of GRB 980425. Indeed, this kind of GRBs would be observed at $z < 0.01$ and their measure would be independent of a particular cosmological setting. This issue could be overcome in three ways: (a) through the calibration of these relations by several low z GRBs (in fact, at $z \leq 0.1$ the luminosity distance is not sensitive to the balance of Ω_M and Ω_Λ for a given H_0 , where H_0 is between 65 and 72); (b) through

⁸ The difference between the apparent magnitude m , ideally corrected from the effects of interstellar absorption, and the absolute magnitude M of an astronomical object.

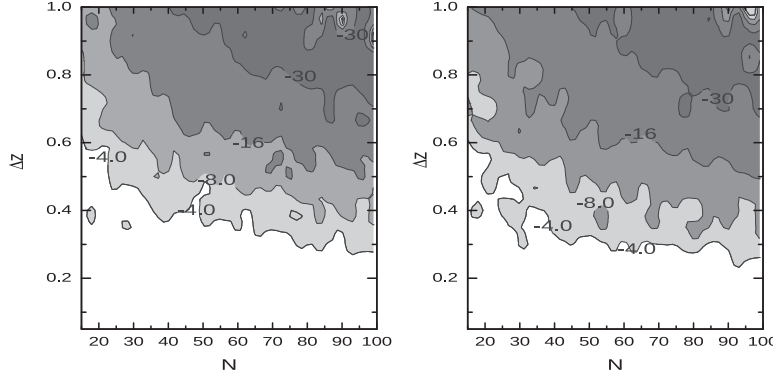


Fig. 39. “Distribution of $\log P$ in the $(N, \Delta z)$ plane from Liang and Zhang (2006a). The grey contours mark the areas where the dependencies of b_1 and b_2 on Ω_M are statistically significant ($P < 10^{-4}$). The white region is suitable for the calibration purpose”.

a solid theoretical model in order to explain the observed 2D relations. Namely, this would fix their slopes and normalizations independently of cosmology, but this task still has to be achieved; (c) through the calibration of the standard candles using GRBs in a narrow redshift range (Δz) near a fiducial redshift, z_c . We here describe some examples on how to overcome the problem of circularity using prompt relations.

The treatment of this problem will be the same once we consider afterglow or prompt-afterglow relations. Liang and Zhang (2006a) suggested a new GRB luminosity indicator, $E_{\gamma,iso} = aE_{\gamma,peak}^{b_1}T_{0,a}^{b_2}$, different from the previous GRB luminosity indicators that are generally written in the form of $L = a \prod_i x_i^{b_i}$, where a is the normalization, x_i is the i th observable, and b_i is its corresponding power law index. It was demonstrated that while a relies on the cosmological parameters, this is not the case for b_1 and b_2 until Δz is sufficiently little, see Fig. 39. The choice of Δz for a given GRB sample could be evaluated depending on its dimension and the errors on the variables. The most suitable approach would be to assemble GRBs within a small redshift range around a central z_c ($z_c \sim 1$ or $z_c \sim 2$), because the GRB z distribution peaks in this interval (see also Wang et al. 2011; 2015).

In addition, also Ghirlanda et al. (2006) defined the luminosity indicator $E_{\gamma,peak} = a \times E_{\gamma,cor}^b$ using the $\log E_{\gamma,peak} - \log E_{\gamma,cor}$ relation (Ghirlanda et al., 2004), where

$$E_{\gamma,cor} = (1 - \cos \theta_{jet}) \times 4\pi \times D_L^2(z, \Omega_M, h) \times S_{\gamma,prompt}/(1+z)^2 \quad (28)$$

is the energy corrected for the beaming factor and θ_{jet} is the opening angle of the jet. They calculated the minimum number of GRBs (N), within Δz around a certain z_c , needed to calibrate the relation, considering a sample of 19 GRBs detected mostly by Beppo-SAX and Swift. Particularly, they fitted the relation for each value of Ω_M and Ω_A using a set of N GRBs distributed in the interval Δz (centered around z_c). If the variation of the slope, b , is less than 1% the relation is assumed calibrated. N , Δz and z_c are free parameters. They checked several z_c and distinct z dispersions $\Delta z \in (0.05, 0.5)$ by Monte Carlo simulations. At every z the smaller the N the bigger the variation of the slope, Δb (for the same Δz), because the relation is more scattered. On the other hand, for greater z_c a tinier Δz is necessary to maintain Δb in its little state. Finally, they found that 12 GRBs with $z \in (0.9, 1.1)$ can be sufficient to calibrate the slope of the $\log E_{\gamma,peak} - \log E_{\gamma,cor}$ relation. Instead, at $z_c = 2$ a narrower redshift bin is needed, for example $z \in (1.95, 2.05)$.

However, this method might become unsuccessful, because the sample size of the observed GRBs is not sufficiently big. Another method for a model-independent calibration may be obtained employing SNe Ia as distance indicators. This method is based on the assumption that a GRB at redshift z must have the same distance modulus $\mu(z)$ of a SNe Ia at the same redshift. In this way, GRBs should be considered as complementary to SNe Ia at very high z , thus allowing for the construction of a very long distance ladder. Therefore, interpolating the SNe Ia HD provides the value of $\mu(z)$ for a subsample of GRBs with $z \leq 1.4$, which can be employed for the calibration of the 2D relations (Kodama et al., 2008; Liang et al., 2008; Wei and Zhang, 2009). This value is given by the formula:

$$\begin{aligned} \mu(z) &= 25 + (5/2)(\log y - k) \\ &= 25 + (5/2)(a + b \log x - k), \end{aligned} \quad (29)$$

where $y = kD_L^2(z, \Omega_M, h)$ is a given quantity with k a redshift independent constant, and a and b are the relation parameters. Presuming that this calibration is redshift independent, the HD at higher z can be constructed using the calibrated relations for the other GRBs in the data set.

Finally, Li and Hjorth (2014) analyzed the light curves of 8 LGRBs associated with SNe finding a relation between the peak magnitude and the decline rate at 5, 10 and 15 days as in SNe Ia. However, from the comparison with the well-known relation for SNe Ia (Phillips, 1993), it was pointed out that these two objects have two different progenitors. More importantly, this discovery allowed to use GRBs associated with SNe as possible standard candles. In addition, Cano (2014) investigated the optical light curves of 8 LGRBs associated with SNe discovering evidence of a relation between their luminosity and the width of the GRB light curves relative to the template of the well-known SN 1998bw. This result also confirmed the possibility of using GRBs associated with SNe as standard candles.

7.2. Applications of GRB afterglow relations

In this section, we describe some applications to cosmology only for the LT relation, because this is the only afterglow relation that has been used so far as a cosmological probe. However, the method is very general and it can be employed for all the other relations presented in the review. The idea to use afterglow GRBs phase as cosmological rulers was proposed for the first time in 2009, when the LT relation was used to derive a new HD (Cardone et al., 2009; 2010).

More specifically, Cardone et al. (2009) revised the data set used in Schaefer (2007) appending the LT relation. They used a Bayesian fitting method, similar to that used in Firmani et al. (2006) for the $\log E_{\gamma,peak} - \log E_{\gamma,cor}$ relation, to calibrate the different GRB relations known at that time assuming a fiducial Λ CDM model compatible with the data provided by the Wilkinson Microwave Anisotropy Probe, WMAP5.

A new HD including 83 objects was obtained (69 from Schaefer (2007) plus 14 new GRBs obtained by the LT relation) computing the mean performed over six relations ($\log E_{\gamma,cor} - \log E_{\gamma,peak}$, $\log L_{\gamma,iso} - \log V$, with V the variability which measures the difference between the observed light curve and a smoothed version of that light curve, $\log L_{X,a} - \log T_{X,a}^*$, $\log L_{\gamma,iso} - \log \tau_{lag}$, with τ_{lag} the difference in arrival time to the observer of the high energy photons and low energy photons, $\log L_{\gamma,iso} - \log \tau_{RT}$, with τ_{RT} the shortest time over which the light curve increases by the 50% of the peak flux of the pulse, and $\log L_{\gamma,iso} - \log E_{\gamma,peak}$).

To elude the circularity problem, local regression was run to calculate $\mu(z)$ from the newest SNe Ia sample containing 307 SNe Ia in the range $0.015 \leq z \leq 1.55$. Indeed, the GRB relations mentioned before were calibrated while considering only GRBs with $z \leq 1.4$ in order to cover the same redshift range spanned by the SNe Ia data. This SNe Ia sample is the input for the local regression estimate of $\mu(z)$.

The basic idea of the local regression analysis consists of several stages described in Cardone et al. (2009). To find out which are the optimal parameters of this procedure, a large sample of simulations was carried out. They set the value of the model parameters (Ω_M, w_0, w_a, h) , with w_0 and w_a given by the coefficient of the DE EoS $w(z) = w_0 + w_a z(1+z)^{-1}$ (Schaefer, 2007), in the ranges $0.15 \leq \Omega_M \leq 0.45$, $-1.5 \leq w_0 \leq -0.5$, $-2.0 \leq w_a \leq 2.0$ and $0.60 \leq h \leq 0.80$. For each z value, $\mu(z_i)$ was selected from a Gaussian distribution centered on the predicted value and with $\sigma_{int} = 0.15$, consistent with the σ_{int} of the SNe Ia absolute magnitude. This way, a mock catalogue with the same z and error distribution of the SNe sample was built. Each $\mu(z)$ value derived from this procedure is compared to the input one. The local regression method correctly produces the underlying $\mu(z)$ at each z from the SNe Ia sample, whichever is the cosmological model.

Furthermore, comparing their HD to the one derived by Schaefer (2007), referred as the Schaefer HD, they have updated the Schaefer HD in three ways, namely updating the Λ CDM model parameters, using a Bayesian fitting procedure and adding the LT relation. To analyze the influence of these changes, the sample of 69 GRBs adopted by Schaefer (2007) was also used and the distance moduli were computed with the new calibration, but without considering the LT relation. It was found that μ_{new}/μ_{old} is close to 1 within 5%. Thus, this calibration procedure has not modified the results.

In conclusion, it was pointed out that the $\mu(z)$ for each of the GRBs in common to Schaefer (2007) and Dainotti et al. (2008) samples is compatible with the one computed using the set of Schaefer (2007) relations. Therefore, no systematic bias is added by also considering the LT relation. On the other hand, the addition of the LT relation to the pre-existing ones not only decreases the errors on $\mu(z)$ by ~14%, but also expands the data set from 69 to 83 GRBs.

While Cardone et al. (2009) added the LT relation to a set of other 5 known prompt emission relations, Cardone et al. (2010) used instead the LT relation alone (66 LGRBs) or in combination with other cosmological tools in order to find some constraints on the cosmological parameters at large z . The GRBs were divided in E0095 and E4 samples, indicating that the introduction of the LT relation alone also provides constraints compatible with previous outcomes, since the HD spans over a large redshift range (0.033, 8.2).

Furthermore, considering three different cosmological models, namely the Λ CDM, the CPL (Chevallier and Polarski, 2001) and the quintessence (QCDM), it was discovered that the Λ CDM model is preferred. To better show the impact of GRBs, the fit was repeated only with other probes, such as SNe Ia or Baryon acoustic Oscillations, excluding the GRBs. The addition of GRBs does not significantly narrow the parameters confidence ranges, but GRBs drive the constraints on w_a to 0. This result indicates that the consideration of a big sample of E0095 GRBs may lead to a constant EoS DE model.

In addition, we may note that, different from what was done in the literature at the time of their publication, the HD for the E0095 and E4 samples is the only GRB HD built with a single relation in the afterglow containing a statistically significant sample.

Furthermore, the LT relation does not request the mix of several relations to rise the number of GRBs with a known $\mu(z)$. In fact, each relation is influenced by its own biases and intrinsic scatter; therefore, using all of them in the same HD can affect the evaluation of the cosmological parameters. The σ_{int} of the LT relation may be considerably decreased if only the E0095 subsample is analyzed. However, considering the whole sample of 66 LGRBs, Cardone et al. (2010) constrained Ω_M and H_0 obtaining values compatible with the ones presented in the literature.

This analysis clearly claimed that the LT relation can be considered for building a GRB HD without adding any bias in the study of the cosmological parameters. Equivalent findings were achieved considering E0095 GRBs even if they are just 12% of the whole sample. Therefore, a further investigation of E0095 GRBs can boost their use as standard sample for studying the DE mystery.

As a further development, Dainotti et al. (2013b) pointed out to what extent a separation of 5σ above and below the intrinsic value, $b_{int} = -1.07^{+0.09}_{-0.14}$, of the slope of the LT relation can influence the cosmological results.

For this study, a simulated data set of 101 GRBs obtained through a Monte Carlo simulation was collected assuming $b = -1.52$, $\sigma_{int} = 0.93$ (larger than the scatter computed from the original data set, namely $\sigma_{int} = 0.66$), and the fiducial Λ CDM flat cosmological model with $\Omega_M = 0.291$ and $H_0 = 71 \text{ Km s}^{-1} \text{ Mpc}^{-1}$. They investigated how much the scatter in the cosmological parameters can be diminished if, instead of the total sample (hereafter Full), a highly luminous subsample (hereafter High Luminosity) is considered, constrained by the condition that $\log L_{X,a} \geq 48.7$. The choice of this selection cut at a given luminosity is explained in Dainotti et al. (2013a), who showed that the local luminosity function is similar to the observed luminosity one for $\log L_{X,a} \geq 48$.

The methodology is similar to what has been done by Amati et al. (2008) for the $\log E_{\gamma,peak} - \log E_{\gamma,iso}$ relation, namely the fit has been performed varying simultaneously both the calibration parameters, $p_{GRB} = (a, b, \sigma_{int})$, and the cosmological parameters, $p_c = (\Omega_M, \Omega_\Lambda, w_0, w_a, h)$, each time for a given model in order to correctly take this issue into account.

In order to have stronger limits on the cosmological parameters two samples were added to the data set, the $H(z)$ sample ($H(z) = H_0 \times \sqrt{\Omega_M(1+z)^3 + \Omega_k(1+z)^2 + \Omega_\Lambda}$) over the redshift range $0.10 \leq z \leq 1.75$ (Stern et al., 2010) and the Union 2.1 SNe Ia sample containing 580 objects over the redshift range $0.015 \leq z \leq 1.414$ (Suzuki et al., 2012).

A Markov Chain Monte Carlo (MCMC) method was used, running three parallel chains and applying the Gelman-Rubin test⁹ in order to analyze the convergence for an assumed cosmological model characterized by a given set of cosmological parameters p_c to be determined.

⁹ The Gelman-Rubin diagnostics relies on parallel chains to test whether they all converge to the same posterior distribution.

From this statistical analysis results regarding the Full GRB sample, b , a and σ_{int} of the LT relation are independent of the chosen cosmological model and the presence of the SNe Ia and $H(z)$ data in the sample. In addition, even if a 5σ scatter in b_{int} is assumed, the results for the Full sample are in agreement with earlier outcomes (Dainotti et al., 2008; 2011a) where exclusively flat models were assumed.

On the other hand, due to the wide errors on the simulated data, the cosmological parameters are not emerging in the calibration procedure. However, the signature of the cosmology will appear considering a greater data set with low errors on ($\log T_{X,a}$, $\log L_{X,a}$).

Furthermore, for the Full sample, it was studied how much the deviation from the b_{int} of the LT relation influences the cosmological parameters. To analyze this problem, a model parameterized in terms of the present day values of Ω_M , Ω_Λ and H_0 was considered.

Although h is comparable with the values from both the local distance estimators (Riess et al., 2009) and CMBR data (Komatsu et al., 2011), the median values for (Ω_M , Ω_Λ) are broader if compared to a fiducial $\Omega_M \sim 0.27$ recovered in earlier works (Davis et al., 2007). For this reason, considering for the Full sample, a distinct b_{int} will lead to a disagreement of 13% with the best value of the Ω_M parameter (see the upper panels of Fig. 40). Even if the median values of the fit for the sample that also has SNe Ia and $H(z)$ data do not conduct towards flat models, a spatially flat Universe accords with, for example, the WMAP7 cosmological parameters within 95% giving $\Omega_k = -0.080^{+0.071}_{-0.093}$. This difference can be deduced, because in this case it is not possible to distinguish among flat and not flat models and this distinction is still not possible when SNe Ia data are present in the fit. Thus, constraining the model to be spatially flat, but shaping the DE EoS with $w(z)$, leads to a couple (w_0 , w_a) completely different irrespective of whether SNe Ia and $H(z)$ data are considered or not in the sample. Regarding instead the High Luminosity subsample, the limits on the calibration parameters mostly do not depend on either the used cosmological model or if SNe Ia and $H(z)$ data are considered in the sample. Furthermore, for the High Luminosity subsample it is shown that adding the SNe Ia and $H(z)$ data does not ameliorate the constraints on the calibration parameters.

Finally, the Full sample outcomes are comparable to those of the flat cosmological model for the SNe Ia sample, while the High Luminosity subsample diverges by 5% in the value of H_0 as computed in Petersen et al. (2010), and the scatter in Ω_M is underestimated by 13%, see the bottom panels of Fig. 40. In conclusion, an optimal procedure is to consider a High luminosity subsample provided by a cut exactly at $\log L_{X,a} = 48$; otherwise, the luminosity and time evolutions should be added in the computation of the cosmological parameters.

Later, another application of GRBs to cosmology is presented in Postnikov et al. (2014) where the DE EoS was analyzed as a function of z without assuming any a priori $w(z)$ functional form.

To build a GRB (μ , z) diagram, 580 SNe Ia from the Union 2.1 compendium (Suzuki et al., 2012) were used together with 54 LGRBs in the overlapping redshift ($z \leq 1.4$ see the left panel of Fig. 41) region between GRBs and SNe Ia. In addition, a standard $w = -1$ cosmological model was assumed.

One order of magnitude expansion in redshift interval is supplied by the GRB data set considering the correlation coefficients obtained for the SNe Ia. This detail allows for the enlargement of the cosmological model out to $z = 8.2$. In fact, a relation was found given by:

$$\log L_{X,a} = 53.27^{+0.54}_{-0.48} - 1.51^{+0.26}_{-0.27} \times \log T_{X,a}^*, \quad (30)$$

with $\rho = -0.74$ and $P = 10^{-18}$.

Postnikov et al. (2014) used a Bayesian statistical analysis, similarly to Firmani et al. (2006) and Cardone et al. (2010), in

which the hypothesis is related to a particular $w(z)$ function with the selection of H_0 and the present DE density parameter, $\Omega_{\Lambda 0}$. The assumption of isotropy for the cosmological model, reliable limits on the EoS and also a fixed value for $w(z)$ in the $z \leq 0.01$ redshift interval were employed. In addition, a huge number of randomly chosen $w(z)$ models were used.

To test the procedure, their pattern is verified through the simulated data sets obtained from several input cosmological models with relative errors and z distribution equal to the real data. Through this procedure, employing the LT relation, a data set of GRBs detected by the Swift satellite, with z from 0.033 to 9.44, was adopted (see inset in the right panel of Fig. 41). Thus, it is possible to investigate the history of the Universe out to $z \approx 10$. (However, an additional analysis would be beneficial if we would consider the sample without the GRB at $z = 9.4$. We note that indeed in Cardone et al. (2010) a sample of canonical GRBs was used in which this burst has not been included).

In order to do that, they simulated 2000 constant EoSs uniformly spaced between $-4 \leq w_\Lambda \leq 2$, with w_Λ the DE EoS. Beginning from SNe Ia data sample, a precise solution was found to be in agreement with the cosmological constant and a small confidence interval, $w = -0.99 \pm 0.2$, see the right panel of Fig. 41. Furthermore, it is shown that assuming also that the BAO limits do not differ from the solution of the EoS, but it considerably decreases the confidence interval ($w = -0.99 \pm 0.06$). In fact, the insertion of the BAO notably constrained the confidence region of the solutions, especially for the present DE density parameter, giving $\Omega_{\Lambda 0} = 0.723 \pm 0.025$.

As a further step, the $w(z)$ model which leads to the best evaluation of $D_L(z, \Omega_M, h)$, z of the SNe Ia sample and the BAO constraints needs to be selected. The confidence region of the allowed $w(z)$ curves is significantly constrained taking into account also the BAO data.

Afterwards, also considering that GRB data should constrain the cosmological parameters, apart from obtaining one order of magnitude expansion in the redshift range, it was extremely difficult to constrain the high z $w(z)$ functional form, considered the paucity of points over a broad redshift interval and the error bars related to these data. This is visible in the left panel of Fig. 42, where a simulated GRB data set having the same z distribution and error bars as the real data, but with assumed $w = -1$ Universe, is provided. It is noted that only strong $w(z)$ fluctuations are not allowed. Then, decreasing the errors by a factor of 4 led to more intriguing high z DE constraints, see the right panel of Fig. 42.

In addition, the small number of elements in the SNe Ia overlapping region indicated broad error bars on the GRB correlation coefficients. Meanwhile, the broad error bars for high z GRBs generated a very flat probability distribution (represented by the uniform black shading area in the left panel of Fig. 42) for the several EoSs checked. Therefore, there will be great interest for the $1 < z < 4$ region of the GRB HD as soon as the GRB data set is enlarged and the quality of data is upgraded.

8. Summary and discussion

From the analysis of the relations mentioned in previous sections, it is visible that:

1. The accretion model (Cannizzo and Gehrels, 2009; Cannizzo et al., 2011) and the magnetar model (Usov, 1992; Dall'Osso et al., 2011; Rowlinson and O'Brien, 2012) seem to give the best explanation of the Dainotti relation (giving best fit slopes $-3/2$ and -1 respectively). The magnetar model seems to be favored compared to the accretion one, because the intrinsic slope computed in Dainotti et al. (2013a) is exactly $-1.07^{+0.14}_{-0.9}$.

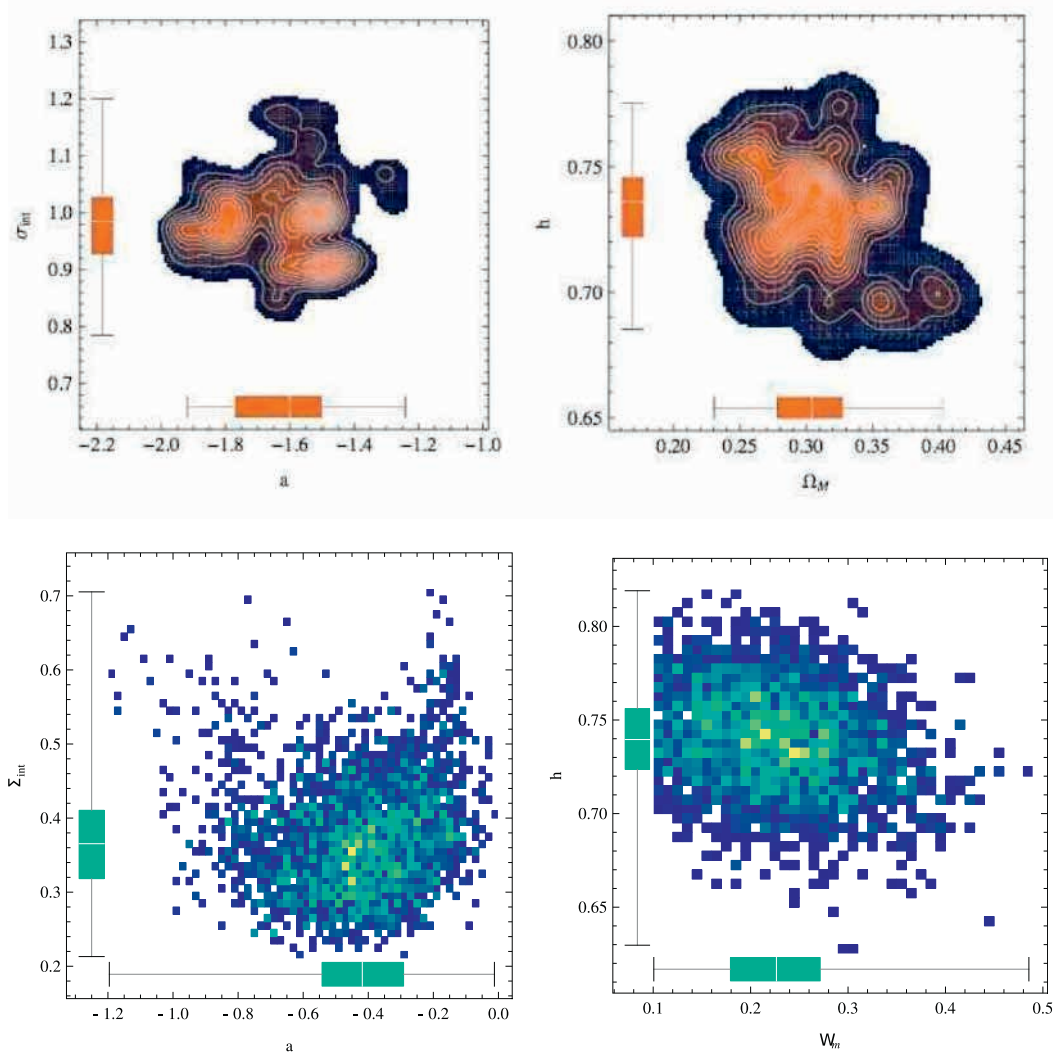


Fig. 40. Upper left panel: “regions of confidence for the marginalized likelihood function $\mathcal{L}(b, \sigma)$ from Dainotti et al. (2013b), obtained marginalizing over a and the cosmological parameters using the Full sample. The bright brown regions indicate the 1σ (full zone) and 2σ (bright grey) regions of confidence respectively. On the axes are plotted the box-and-whisker diagrams relatively to the b and σ_{int} parameters: the bottom and top of the diagrams are the 25th and 75th percentile (the lower and upper quartiles, respectively), and the band near the middle of the box is the 50th percentile (the median)”. Upper right panel: “regions of confidence for the marginalized likelihood function $\mathcal{L}(b, h)$, obtained using the Full sample, from Dainotti et al. (2013b)”. Bottom left panel: “regions of confidence for the marginalized likelihood function $\mathcal{L}(b, \sigma)$ from Dainotti et al. (2013b), obtained marginalizing over a and the cosmological parameters for the High Luminosity sample. The bright brown regions indicate the 1σ (full zone) and 2σ (bright grey) regions of confidence respectively. On the axes are plotted the box-and-whisker diagrams relatively to the b and σ_{int} parameters: the bottom and top of the diagrams are the 25th and 75th percentile (the lower and upper quartiles, respectively), and the band near the middle of the box is the 50th percentile (the median)”. Bottom right panel: “regions of confidence for the marginalized likelihood function $\mathcal{L}(\Omega_M, h)$, obtained using the High Luminosity sample, from Dainotti et al. (2013b)”.

2. A more complex jet structure is needed for interpreting the $\log L_{0,200s} - \alpha_{0,200s}$ relation (Oates et al. 2012). Indeed, Oates et al. (2012) showed that the standard afterglow model cannot explain this relation, especially taking into account the closure relations (Sari et al., 1998), which relate temporal decay and spectral indices. Therefore, in order to interpret their results, they claimed either the presence of some features of

the central engine which dominate the energy release or that the observations were made by observers at different angular distances from the source’s axis. Dainotti et al. (2013a) pointed out a similarity between the $\log L_{0,200s} - \alpha_{0,200s}$ relation and the $L_X - T_a$ relation, making worthy of investigating the possibility of a single physical mechanism inducing both of them.

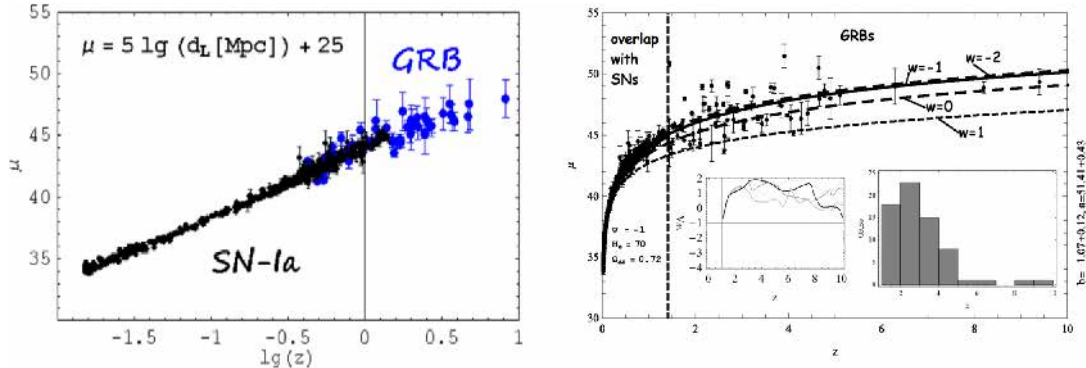


Fig. 41. Left panel: “ $(z_i, \mu_i \pm \Delta\mu_i)$ for SNe Ia from Postnikov et al. (2014). GRBs are inferred from the relation assuming a flat $w = -1$ cosmology and stand out only from their larger error bars, no discontinuity is evident, implying a first order consistency of a $w = -1$ model out to very high z . The SNe Ia data were taken from the Union 2.1 compendium (Suzuki et al., 2012)”. Right panel: “distance ladder from Postnikov et al. (2014). GRBs in the SNe Ia overlap redshift range, where cosmology is well constrained, are used to calculate the GRB intrinsic correlation coefficient. This relation is then used to calculate $D_L(z, \Omega_M, h)$ for high z GRBs from their X-ray afterglow luminosity curves. Standard constant w solutions are shown for reference. Vertical dashed line marks farthest SNe Ia event. Inset to the right shows a histogram of the GRB sample distribution in z . Inset to the left shows resulting most probable EoS, together with a small sample of models probed, confidence intervals are so large, that only extreme variations with respect to $w = -1$ can be excluded”.

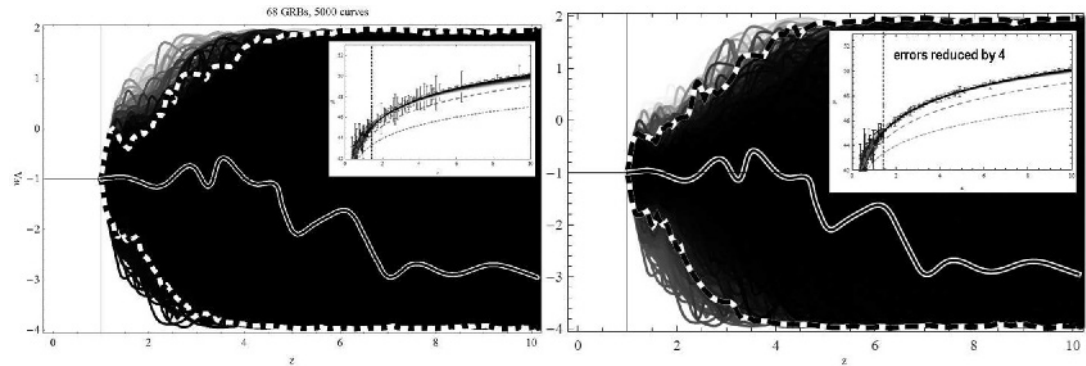


Fig. 42. “Tree of $w(z > 1)$ curves inferred from synthetic GRB samples constructed for $w(z) = -1$ cosmologies in Postnikov et al. (2014), showing to what extent correlated GRB errors constrain EoS at high z ($z > 1$). In the left side plot GRB errors taken from actual data are used, while in the right side plot GRB errors reduced by a factor of 4 are considered”.

3. In the external shock model the $L_X(T_a) - L_{\gamma,iso}$ and the $L_{X,peak} - L_X(T_a)$ relations cannot lead to a net distinction among constant or wind type density media, but they are able to exclude so far the thin shell models and to favor the thick shell ones. Among the models that very well describe the $L_X(T_a) - L_{\gamma,iso}$ and the $L_{X,peak} - L_X(T_a)$ relations there is the one by Hascoët et al. (2014). They investigated the standard FS model with a wind external medium and a microphysics parameter $\epsilon_e \propto n^{-v}$, and they found out that for values $v \approx 1$ is possible to reproduce a flat plateau phase, and consequently the relations mentioned above. This shows how important the study of correlations especially with the aim of discriminating among models.
4. In regard to the prompt-afterglow relations, mentioned in Section 4, involving the energies and the luminosities for the prompt and the afterglow phases, it is pointed out that they help to interpret the connection between these two GRB phases. For example, Racusin et al. (2011) pointed out that the fraction of kinetic energy transferred from the prompt phase to the afterglow one, for BAT-detected GRBs, is around 10%, in agreement with the analysis by Zhang et al. (2007a). However, from the investigation of these relations, the synchrotron radia-

tion process seems to not explain completely the observations, and also the scatter present in these relations is significant. Therefore, further analysis will be useful.

5. The study of the $L_{O,peak}^F - T_{O,peak}^F$ relation sheds light on the nature of the flares in the GRB light curves. From the analysis carried on by Li et al. (2012), it was found out that the flares are additional and distinct components of the afterglow phase. They also claimed that a periodically-emitting energy central engine can explain the optical and γ -ray flares in the afterglow phase.
6. One of the greatest issues that may undermine the GRB relations as model discriminators and as cosmological tools are selection bias and the evolution with the redshift of the physical quantities involved in these relations. An example of selection biases is given by Dainotti et al. (2013a), who used the Efron and Petrosian (1992) method to deal with the redshift evolution of the X-ray luminosity and the time, to evaluate the intrinsic $L_X - T_a^*$ relation. Furthermore, Dainotti et al. (2015a) assumed an unknown efficiency function for the detector and investigated the biases due to the detector's threshold and how they affect the X-ray luminosity and the time measurements. The methods described can be also useful to deal with

the selection effects for the optical luminosity and in the $\log L_{\text{O},2005} - \alpha_{\text{O},>2005}$ relation and any other relation.

7. Regarding the use of correlations as cosmological tools, we still have to further reduce the scatter of the GRB measurements and the dispersion of the relations themselves to allow GRBs to be complementary with the measurement of SNe Ia. Indeed, the redshift evolution effect and the threshold of the detector can generate relevant selection biases on the physical quantities which however we know how to treat analytically with robust statistical techniques as we have shown in several sections. Nevertheless, more precise calibration methods, with the help of other cosmological objects, and more space missions dedicated to detect faint GRBs and GRBs at high redshift (for example the future SVOM mission) can shed new light on the use of GRBs as cosmological tools. Lastly, other open questions are concerned with how much cosmological parameters can reduce their degeneracy adding GRBs into the set of cosmological standard candles. For example, different results of the value of w can lead to scenarios which can be compatible with a non-flat cosmological model.

9. Conclusions

In this work, we have summarized the bivariate relations among the GRB afterglow parameters and their characteristics in order to discuss their intrinsic nature and the possibility to use them as standardizable candles. It has been shown with different methodologies that some of the relations presented are intrinsic. However, the intrinsic slope has been determined only for a few relations. For the other relations, we are not aware of their intrinsic slopes and consequently how far the use of the observed relations can influence the evaluation of the theoretical models and the “best” cosmological settings (Dainotti et al., 2013b). Therefore, the estimate of the intrinsic relations is crucial for the determination of the most plausible model that can explain the plateau phase and the afterglow emission.

In fact, though there are several theoretical interpretations describing each relation, as we have shown, in many cases, more than one is viable. This result indicates that the emission processes that rule the GRBs still have to be further investigated. To this end, it is necessary to use the intrinsic relations and not the observed ones affected by selection biases to test the theoretical models. Moreover, the pure afterglow relations have the advantage of not presenting the double truncation in the flux limit, thus facilitating the correction for selection effects and their use as redshift estimators and cosmological tools.

A very challenging future step would be to use the corrected relations as a reliable redshift estimator and to determine a further estimate of H_0 , Ω_Λ and w . In particular, it is advisable to use all the afterglow relations which are not yet employed for cosmological studies as new probes, after they are corrected for selection biases, in order to reduce the intrinsic scatter as it has been done in Schaefer (2007) for the prompt relations.

Acknowledgments

This work made use of data supplied by the UK Swift Science Data Centre at the University of Leicester. We thank S. Capozziello for fruitful comments. M.G.D is grateful to the Marie Curie Program, because the research leading to these results has received funding from the European Union Seventh FrameWork Program (FP7-2007/2013) under grant agreement N 626267. R.D.V. is grateful to the Polish National Science Centre through the grant DEC-2012/04/A/ST9/00083.

References

- Amati, L., Della Valle, M., 2013. Measuring cosmological parameters with gamma ray bursts. *Int. J. Mod. Phys. D* 22, 30028. doi:[10.1142/S0218271813300280](https://doi.org/10.1142/S0218271813300280).
- Amati, L., Della Valle, M., Frontera, F., Malesani, D., Guidorzi, C., Montanari, E., Pian, E., 2007. On the consistency of peculiar GRBs 060218 and 060614 with the $E_{\text{p},i} - E_{\text{iso}}$ correlation. *ASA* 463, 913–919. doi:[10.1051/0004-6361:20065994](https://doi.org/10.1051/0004-6361:20065994).
- Amati, L., Frontera, F., Tavani, M., in’t Zand, J.J.M., Antonelli, A., Costa, E., Feroci, M., Guidorzi, C., Heise, J., Masetti, N., Montanari, E., Nicastro, L., Palazzi, E., Pian, E., Piro, L., Sofitta, P., 2002. Intrinsic spectra and energetics of BeppoSAX Gamma-Ray Bursts with known redshifts. *A&A* 390, 81–89. doi:[10.1051/0004-6361:20020722](https://doi.org/10.1051/0004-6361:20020722).
- Amati, L., Guidorzi, C., Frontera, F., Della Valle, M., Finelli, F., Landi, R., Montanari, E., 2008. Measuring the cosmological parameters with the $E_{\text{p},i} - E_{\text{iso}}$ correlation of gamma-ray bursts. *MNRAS* 391, 577–584. doi:[10.1111/j.1365-2966.2008.13943.x](https://doi.org/10.1111/j.1365-2966.2008.13943.x).
- Atteia, J.-L., 2003. A simple empirical redshift indicator for gamma-ray bursts. *A&A* 407, L1–L4. doi:[10.1051/0004-6361:20030958](https://doi.org/10.1051/0004-6361:20030958).
- Berger, E., 2007. The prompt gamma-ray and afterglow energies of short-duration gamma-ray bursts. *ApJ* 670, 1254–1259. doi:[10.1086/522195](https://doi.org/10.1086/522195).
- Berger, E., 2014. Short-duration gamma-ray bursts. *ARA&A* 52, 43–105. doi:[10.1146/annurev-astro-081913-035926](https://doi.org/10.1146/annurev-astro-081913-035926).
- Bernardini, M.G., Bianco, C.L., Caito, L., Chardonnet, P., Corsi, A., Dainotti, M.G., Fraschetti, F., Guida, R., Ruffini, R., Xue, S.S., 2006. GRB970228 as a prototype for short GRBs with afterglow. *Nuovo Cimento B Serie 121*, 1439–1440. doi:[10.1393/nccb2007-10283-0](https://doi.org/10.1393/nccb2007-10283-0).
- Bernardini, M.G., Bianco, C.L., Caito, L., Dainotti, M.G., Guida, R., Ruffini, R., 2007. GRB 970228 and a class of GRBs with an initial spikelike emission. *A&A* 474, L13–L16. doi:[10.1051/0004-6361:20078300](https://doi.org/10.1051/0004-6361:20078300).
- Bernardini, M.G., Margutti, R., Mao, J., Zaninoni, E., Chincarini, G., 2012. The X-ray light curve of gamma-ray bursts: clues to the central engine. *A&A* 539, A3. doi:[10.1051/0004-6361/201117895](https://doi.org/10.1051/0004-6361/201117895).
- Bernardini, M.G., Margutti, R., Zaninoni, E., Chincarini, G., 2012. A universal scaling for short and long gamma-ray bursts: $E_{\text{X, iso}} - E_{\text{iso}} - E_{\text{pk}}$. *MNRAS* 425, 1199–1204. doi:[10.1111/j.1365-2966.2012.21487.x](https://doi.org/10.1111/j.1365-2966.2012.21487.x).
- Betoule, M., Kessler, R., Guy, J., Mosher, J., Hardin, D., Biswas, R., Astier, P., El-Hage, P., Konig, M., Kuhlmann, S., Marriner, J., Pain, R., Regnault, N., Balland, C., Bassett, B.A., Brown, P.J., Campbell, H., Carlberg, R.G., Cellier-Holzem, F., Cinabro, D., Conley, A., D’Andrea, C.B., DePoy, D.L., Doi, M., Ellis, R.S., Fabro, S., Filippenko, A.V., Foley, R.J., Frieman, J.A., Fouchez, D., Galbany, L., Goobar, A., Gupta, R.R., Hill, G.J., Hlozek, R., Hogan, C.J., Hook, I.M., Howell, D.A., Jha, S.W., Le Guillou, L., Leloudas, G., Lidman, C., Marshall, J.L., Möller, A., Mourão, A.M., Neveu, J., Nichol, R., Olmstead, M.D., Palanque-Delabrouille, N., Perlmutter, S., Prieto, J.L., Pritchett, C.J., Rich mond, M., Riess, A.G., Ruhlmann-Kleider, V., Sako, M., Schahmaneche, K., Schneider, D.P., Smith, M., Sollerman, J., Sullivan, M., Walton, N.A., Wheeler, C.J., 2014. Improved cosmological constraints from a joint analysis of the SDSS-II and SNLS supernova samples. *A&A* 568, A22. doi:[10.1051/0004-6361/201423413](https://doi.org/10.1051/0004-6361/201423413).
- Bloom, J.S., Fraaij, D.A., Sari, R., 2001. The prompt energy release of gamma-ray bursts using a cosmological k-correction. *AJ* 121, 2879–2888. doi:[10.1086/321093](https://doi.org/10.1086/321093).
- Boér, M., Gendre, B., 2000. Evidences for two gamma-ray burst afterglow emission regimes. *A&A* 361, L21–L24.
- Butler, N.R., Bloom, J.S., Poznanski, D., 2010. The cosmic rate, luminosity function, and intrinsic correlations of long gamma-ray bursts. *ApJ* 711, 495–516. doi:[10.1088/0004-637X/711/1/495](https://doi.org/10.1088/0004-637X/711/1/495).
- Caito, L., Bernardini, M.G., Bianco, C.L., Dainotti, M.G., Guida, R., Ruffini, R., 2009. GRB060614: a “fake” short GRB from a merging binary system. *A&A* 498, 501–507. doi:[10.1051/0004-6361/200810676](https://doi.org/10.1051/0004-6361/200810676).
- Calzino, J., Davis, T., 2017. The need for accurate redshifts in supernova cosmology. *J. Cosmol. Astropart. Phys.* 1, 038. doi:[10.1088/1475-7516/2017/01/038](https://doi.org/10.1088/1475-7516/2017/01/038).
- Cannizzo, J.K., Gehrels, N., 2009. A new paradigm for gamma-ray bursts: long-term accretion rate modulation by an external accretion disk. *ApJ* 700, 1047–1058. doi:[10.1088/0004-637X/700/2/1047](https://doi.org/10.1088/0004-637X/700/2/1047).
- Cannizzo, J.K., Troja, E., Gehrels, N., 2011. Fall-back disks in long and short gamma-ray bursts. *ApJ* 734, 35. doi:[10.1088/0004-637X/734/1/35](https://doi.org/10.1088/0004-637X/734/1/35).
- Cano, Z., 2014. Gamma-ray burst supernovae as standardizable candles. *ApJ* 794, 121. doi:[10.1088/0004-637X/794/2/121](https://doi.org/10.1088/0004-637X/794/2/121).
- Cardone, V.F., Capozziello, S., Dainotti, M.G., 2009. An updated gamma-ray bursts Hubble diagram. *MNRAS* 400, 775–790. doi:[10.1111/j.1365-2966.2009.15456.x](https://doi.org/10.1111/j.1365-2966.2009.15456.x).
- Cardone, V.F., Dainotti, M.G., Capozziello, S., Willingale, R., 2010. Constraining cosmological parameters by gamma-ray burst X-ray afterglow light curves. *MNRAS* 408, 1181–1186. doi:[10.1111/j.1365-2966.2010.17197.x](https://doi.org/10.1111/j.1365-2966.2010.17197.x).
- Senko, S.B., Kelemen, J., Harrison, F.A., Fox, D.B., Kulkarni, S.R., Kasliwal, M.M., Ofek, E.O., Rau, A., Gal-Yam, A., Fraaij, D.A., Moon, D.-S., 2009. Dark bursts in the swift era: the palomar 60 inch-swift early optical afterglow catalog. *ApJ* 693, 1484–1493. doi:[10.1088/0004-637X/693/2/1484](https://doi.org/10.1088/0004-637X/693/2/1484).
- Chevallier, M., Polarski, D., 2001. Accelerating universes with scaling dark matter. *Int. J. Mod. Phys. D* 10, 213–223. doi:[10.1142/S0218271801000822](https://doi.org/10.1142/S0218271801000822).
- Chincarini, G., Moretti, A., Romano, P., Falcone, A.D., Morris, D., Racusin, J., Campana, S., Covino, S., Guidorzi, C., Tagliaferri, G., Burrows, D.N., Pagan, C., Stroh, M., Grupe, D., Capalbi, M., Cusumano, G., Gehrels, N., Giommi, P., La Parola, V., Mangano, V., Mineo, T., Nousek, J.A., O’Brien, P.T., Page, K.L., Perri, M., Troja, E., Willingale, R., Zhang, B., 2007. The first survey of X-ray flares from gamma-ray bursts observed by swift: temporal properties and morphology. *ApJ* 671, 1903–1920. doi:[10.1086/521591](https://doi.org/10.1086/521591).

- Cucchiara, A., Levan, A.J., Fox, D.B., Tanvir, N.R., Ukwatta, T.N., Berger, E., Krühler, T., Küpcü Yoldaş, A., Wu, X.F., Toma, K., Greiner, J., Olivares, F.E., Rowlinson, A., Amati, L., Sakamoto, T., Roth, K., Stephens, A., Fritz, A., Fynbo, J.P.U., Hjorth, J., Malesani, D., Jakobsson, P., Wiersema, K., O'Brien, P.T., Soderberg, A.M., Foley, R.J., Fruchter, A.S., Rhoads, J., Rutledge, R.E., Schmidt, B.P., Dopita, M.A., Podsiadlowski, P., Willingale, R., Wolf, C., Kulkarni, S.R., D'Avanzo, P., 2011. A Photometric Redshift of $z \sim 9.4$ for GRB 090429B. *ApJ* 736, 7. doi:10.1088/0004-637X/736/1/7.
- D'Agostini, G., 2005. Fits, and especially linear fits, with errors on both axes, extra variance of the data points and other complications. ArXiv Physics e-prints.
- Dai, Z.G., Lu, T., 1998. Gamma-ray burst afterglows and evolution of postburst fireballs with energy injection from strongly magnetic millisecond pulsars. *A&A* 333, L87–L90.
- Dainotti, M., Del Vecchio, R., Tarnopolski, M., 2016a. Gamma ray burst prompt correlations. ArXiv e-prints.
- Dainotti, M., Petrosian, V., Willingale, R., O'Brien, P., Ostrowski, M., Nagataki, S., 2015. Luminosity-time and luminosity-luminosity correlations for GRB prompt and afterglow plateau emissions. *MNRAS* 451, 3898–3908. doi:10.1093/mnras/stv1229.
- Dainotti, M.G., Bernardini, M.G., Bianco, C.L., Catto, L., Guida, R., Ruffini, R., 2007. GRB 060218 and GRBs associated with supernovae Ib/c. *A&A* 471, L29–L32. doi:10.1051/0004-6361:20078068.
- Dainotti, M.G., Cardone, V.F., Capozziello, S., 2008. A time-luminosity correlation for γ -ray bursts in the X-rays. *MNRAS* 391, L79–L83. doi:10.1111/j.1745-3933.2008.00560.x.
- Dainotti, M.G., Cardone, V.F., Piedipalumbo, E., Capozziello, S., 2013. Slope evolution of GRB correlations and cosmology. *MNRAS* 436, 82–88. doi:10.1093/mnras/stt1516.
- Dainotti, M.G., Del Vecchio, R., Nagataki, S., Capozziello, S., 2015. Selection effects in gamma-ray burst correlations: consequences on the ratio between gamma-ray burst and star formation rates. *ApJ* 800, 31. doi:10.1088/0004-637X/800/1/31.
- Dainotti, M.G., Fabrizio Cardone, V., Capozziello, S., Ostrowski, M., Willingale, R., 2011. Study of possible systematics in the L_x-T_x correlation of gamma-ray bursts. *ApJ* 730, 135. doi:10.1088/0004-637X/730/2/135.
- Dainotti, M.G., Nagataki, S., Maeda, K., Postnikov, S., Pian, E., 2016b. A study of gamma ray bursts with afterglow plateau phases associated with supernovae. ArXiv e-prints.
- Dainotti, M.G., Ostrowski, M., Willingale, R., 2011. Towards a standard gamma-ray burst: tight correlations between the prompt and the afterglow plateau phase emission. *MNRAS* 418, 2202–2206. doi:10.1111/j.1365-2966.2011.19433.x.
- Dainotti, M.G., Petrosian, V., Singal, J., Ostrowski, M., 2013. Determination of the intrinsic luminosity time correlation in the X-ray afterglows of gamma-ray bursts. *ApJ* 774, 157. doi:10.1088/0004-637X/774/2/157.
- Dainotti, M.G., Postnikov, S., Hernandez, X., Ostrowski, M., 2016. A fundamental plane for long gamma-ray bursts with X-ray plateaus. *ApJ* 825, L20. doi:10.3847/2041-8205/825/2/L20.
- Dainotti, M.G., Willingale, R., Capozziello, S., Fabrizio Cardone, V., Ostrowski, M., 2010. Discovery of a tight correlation for gamma-ray burst afterglows with "Canonical" Light Curves. *ApJ* 722, L215–L219. doi:10.1088/2041-8205/722/2/L215.
- Dall'Osso, S., Stratta, G., Guetta, D., Covino, S., De Cesare, G., Stella, L., 2011. Gamma-ray bursts afterglows with energy injection from a spinning down neutron star. *A&A* 526, A121. doi:10.1051/0004-6361/201014168.
- D'Avanzo, P., Salvaterra, R., Sbarufatti, B., Nava, L., Melandri, A., Bernardini, M.G., Campana, S., Covino, S., Fugazza, D., Ghirlanda, G., Ghisellini, G., Parola, V.L., Perri, M., Vergani, S.D., Tagliaferri, G., 2012. A complete sample of bright Swift Gamma-ray bursts: X-ray afterglow luminosity and its correlation with the prompt emission. *MNRAS* 425, 506–513. doi:10.1111/j.1365-2966.2012.21489.x.
- Davis, T.M., Mörtzell, E., Sollerman, J., Becker, A.C., Blondin, S., Challis, P., Cicchetti, A., Filippenko, A.V., Foley, R.J., Garnavich, P.M., Jha, S., Kruščić, K., Kirshner, R.P., Leibundgut, B., Li, W., Matheson, T., Miknaitis, G., Pignata, G., Rest, A., Riess, A.G., Schmidt, B.P., Smith, R.C., Spyromilio, J., Stubbs, C.W., Sunzucht, N.B., Tonry, J.L., Wood-Vasey, W.M., Zenteno, A., 2007. Scrutinizing exotic cosmological models using ESSENCE supernova data combined with other cosmological probes. *ApJ* 666, 716–725. doi:10.1086/519988.
- Del Vecchio, R., Giovanna Dainotti, M., Ostrowski, M., 2016. Study of GRB light-curve decay indices in the afterglow phase. *ApJ* 828, 36. doi:10.3847/0004-637X/828/1/36.
- Duffell, P.C., MacFadyen, A.I., 2015. From engine to afterglow: collapsars naturally produce top-heavy jets and early-time plateaus in gamma-ray burst afterglows. *ApJ* 806, 205. doi:10.1088/0004-637X/806/2/205.
- Efron, B., Petrosian, V., 1992. A simple test of independence for truncated data with applications to redshift surveys. *ApJ* 399, 345–352. doi:10.1086/171931.
- Fenimore, E.E., in 't Zand, J.J.M., Norris, J.P., Bonnell, J.T., Nemiroff, R.J., 1995. Gamma-ray burst peak duration as a function of energy. *ApJ* 448, L101. doi:10.1086/309603.
- Firmani, C., Ghisellini, G., Avila-Reese, V., Ghirlanda, G., 2006. Discovery of a tight correlation among the prompt emission properties of long gamma-ray bursts. *MNRAS* 370, 185–197. doi:10.1111/j.1365-2966.2006.10445.x.
- Gehrels, N., 2007. Short GRB Prompt and Afterglow Correlations. Gehrels, N., Barthelmy, S.D., Burrows, D.N., Cannizzo, J.K., Chincarini, G., Fenimore, E., Kouveliotou, C., O'Brien, P., Palmer, D.M., Racusin, J., Roming, P.W.A., Sakamoto, T., Tueller, J., Wijers, R.A.M.J., Zhang, B., 2008. Correlations of prompt and afterglow emission in swift long and short gamma-ray bursts. *ApJ* 689, 1161–1172. doi:10.1086/592766.
- Ghirlanda, G., 2009. Advances on GRB as cosmological tools. In: Giobbi, G., Torname, A., Raimondo, G., Limongi, M., Antonelli, L.A., Menci, N., Brocato, E. (Eds.), American Institute of Physics Conference Series. In: American Institute of Physics Conference Series, 1111, pp. 579–586. doi:10.1063/1.3141613.
- Ghirlanda, G., Ghisellini, G., Firmani, C., 2006. Gamma-ray bursts as standard candles to constrain the cosmological parameters. *New J. Phys.* 8, 123. doi:10.1088/1367-2630/8/7/123.
- Ghirlanda, G., Ghisellini, G., Lazzati, D., 2004. The collimation-corrected gamma-ray burst energies correlate with the peak energy of their vF_ν spectrum. *ApJ* 616, 331–338. doi:10.1086/424913.
- Ghisellini, G., Nardini, M., Ghirlanda, G., Celotti, A., 2009. A unifying view of gamma-ray burst afterglows. *MNRAS* 393, 253–271. doi:10.1111/j.1365-2966.2008.14214.x.
- Gompertz, B.P., O'Brien, P.T., Wynn, G.A., Rowlinson, A., 2013. Can magnetar spin-down power extended emission in some short GRBs? *MNRAS* 431, 1745–1751. doi:10.1093/mnras/stt293.
- Grupe, D., Nousek, J.A., Veres, P., Zhang, B.-B., Gehrels, N., 2013. Evidence for new relations between gamma-ray burst prompt and X-ray afterglow emission from 9 years of swift. *ApJS* 209, 20. doi:10.1088/0067-0049/209/2/20.
- Guida, R., Bernardini, M.G., Bianco, C.L., Catto, L., Dainotti, M.G., Ruffini, R., 2008. The Amati relation in the "fireshell" model. *A&A* 487, L37–L40. doi:10.1051/0004-6361:200810338.
- Hascoët, R., Daigne, F., Mochkovitch, R., 2014. The prompt-early afterglow connection in gamma-ray bursts: implications for the early afterglow physics. *MNRAS* 442, 20–27. doi:10.1093/mnras/stu750.
- Heise, J., Zand, J.I., Kippen, R.M., Woods, P.M., 2001. X-ray flashes and X-ray rich gamma ray bursts. In: Costa, E., Frontera, F., Hjorth, J. (Eds.), Gamma-ray Bursts in the Afterglow Era, p. 16. doi:10.1007/10853853_4.
- Ito, H., Nagataki, S., Matsumoto, J., Lee, S.-H., Tolstov, A., Mao, J., Dainotti, M., Mizuta, A., 2014. Spectral and polarization properties of photospheric emission from stratified jets. *ApJ* 789, 159. doi:10.1088/0004-637X/789/2/159.
- Jakobsson, P., Hjorth, J., Fynbo, J.P.U., Watson, D., Pedersen, K., Björnsson, G., Gorosabel, J., 2004. Swift identification of dark gamma-ray bursts. *ApJ* 617, L21–L24. doi:10.1086/427089.
- Kaneko, Y., Ramirez-Ruiz, E., Granot, J., Kouveliotou, C., Woosley, S.E., Patel, S.K., Rol, E., in 't Zand, J.J.M., van der Horst, A.J., Wijers, R.A.M.J., Strom, R., 2007. Prompt and afterglow emission properties of gamma-ray bursts with spectroscopically identified supernovae. *ApJ* 654, 385–402. doi:10.1086/508324.
- Kann, D.A., Klose, S., Zhang, B., Malesani, D., Nakar, E., Pozanenko, A., Wilson, A.C., Butler, N.R., Jakobsson, P., Schulze, S., Andreveit, M., Antonelli, L.A., Bikmaev, I.F., Biryukov, V., Böttcher, M., Burenin, R.A., Castro Cerón, J.M., Castro-Tirado, A.J., Chincarini, G., Cobb, B.E., Covino, S., D'Avanzo, P., D'Elia, V., Della Valle, M., de Ugarte Postigo, A., Efimov, Y., Ferriero, P., Fugazza, D., Fynbo, J.P.U., Gálfalvi, M., Grindahl, F., Görögsabel, J., Gupta, S., Guzily, S., Hafizov, B., Hjorth, J., Holljem, K., Ibrahimov, M., Im, M., Israel, G.L., Jelinek, M., Jensen, B.L., Karimov, R., Khamitov, I.M., Kızılığlu, Ü., Klunko, E., Kubánek, P., Kutyrév, A.S., Laursen, P., Levan, A.J., Mannucci, F., Martin, C.M., Meschedyakov, A., Mirabal, N., Norris, J.P., Ovaldsen, J.-E., Paraficz, D., Pavlenko, E., Piranomonte, S., Rossi, A., Rumyantsev, V., Salinas, R., Sergeev, A., Sharapov, D., Sollerman, J., Stecklum, B., Stella, L., Tagliaferri, G., Tanvir, N.R., Telting, J., Testa, V., Updike, A.C., Volnova, A., Watson, D., Wiersema, K., Xu, D., 2010. The afterglows of swift-era gamma-ray bursts. I. Comparing pre-swift and swift-era long/soft (Type II) GRB optical afterglows. *ApJ* 720, 1513–1558. doi:10.1088/0004-637X/720/2/1513.
- Kazanas, D., Racusin, J. L., Sultana, J., Mastichiadis, A., 2015. The statistics of the prompt-to-afterglow GRB flux ratios and the supercritical pile GRB model. ArXiv e-prints.
- Kippen, R.M., Woods, P.M., Heise, J., Zand, J.I., Preece, R.D., Briggs, M.S., 2001. BATSE observations of fast X-ray transients detected by BeppoSAX-WFC. In: Costa, E., Frontera, F., Hjorth, J. (Eds.), Gamma-ray Bursts in the Afterglow Era, p. 22. doi:10.1007/10853853_5.
- Klebesadel, R.W., Strong, I.B., Olson, R.A., 1973. Observations of gamma-ray bursts of cosmic origin. *ApJ* 182, L85. doi:10.1086/181225.
- Kobayashi, S., Piran, T., Sarai, R., 1997. Can internal shocks produce the variability in gamma-ray bursts? *ApJ* 490, 92. doi:10.1086/512791.
- Kodama, Y., Yonetoku, D., Murakami, T., Tanabe, S., Tsutsui, R., Nakamura, T., 2008. Gamma-ray burst bursts in $18 < z < 5.6$ suggest that the time variation of the dark energy is small. *MNRAS* 391, L1–L4. doi:10.1111/j.1365-2963.2008.05058.x.
- Komatsu, E., Smith, K.M., Dunkley, J., Bennett, C.L., Gold, B., Hinshaw, G., Jarosik, N., Larson, D., Nolta, M.R., Page, L., Spergel, D.N., Halpern, M., Hill, R.S., Kogut, A., Limon, M., Meyer, S.S., Odegard, N., Tucker, G.S., Weiland, J.L., Wollack, E., Wright, E.L., 2011. Seven-year Wilkinson microwave anisotropy probe (WMAP) observations: cosmological interpretation. *ApJS* 192, 18. doi:10.1088/0067-0049/192/2/18.
- Kouveliotou, C., Meegan, C.A., Fishman, G.J., Bhat, N.P., Briggs, M.S., Koshtut, T.M., Paciesas, W.S., Pendleton, G.N., 1993. Identification of two classes of gamma-ray bursts. *ApJ* 413, L101–L104. doi:10.1086/186969.
- Kumar, P., Narayan, R., Johnson, J.L., 2008. Properties of gamma-ray burst progenitor stars. *Science* 321, 376. doi:10.1126/science.1159003.
- Leventis, K., Wijers, R.A.M.J., van der Horst, A.J., 2014. The plateau phase of gamma-ray burst afterglows in the thick-shell scenario. *MNRAS* 437, 2448–2460. doi:10.1093/mnras/stt2055.
- Li, L., Liang, E.-W., Tang, Q.-W., Chen, J.-M., Xi, S.-Q., Lü, H.-J., Gao, H., Zhang, B., Zhang, J., Yi, S.-X., Lu, R.-J., Lü, L.-Z., Wei, J.-Y., 2012. A comprehensive study of gamma-ray burst optical emission. I. Flares and early shallow-decay component. *ApJ* 758, 27. doi:10.1088/0004-637X/758/1/27.

- Li, X., Hjorth, J., 2014. Light Curve Properties of Supernovae Associated With Gamma-ray Bursts. ArXiv e-prints.
- Liang, E., Zhang, B., 2006. Calibration of gamma-ray burst luminosity indicators. MNRAS 369, L37–L41. doi:10.1111/j.1745-3933.2006.00169.x.
- Liang, E., Zhang, B., 2006. Identification of two categories of optically bright gamma-ray bursts. ApJ 638, L67–L70. doi:10.1086/501049.
- Liang, E.-W., Yi, S.-X., Zhang, J., Lü, H.-J., Zhang, B.-B., Zhang, B., 2010. Constraining gamma-ray burst initial Lorentz factor with the afterglow onset feature and discovery of a tight $\Gamma_{\text{0-E}}^{\gamma}$ correlation. ApJ 725, 2209–2224. doi:10.1088/0004-637X/725/2/2209.
- Liang, E.-W., Zhang, B.-B., Zhang, B., 2007. A comprehensive analysis of swift XRT Data. II. Divers physical origins of the shallow decay segment. ApJ 670, 565–583. doi:10.1086/521870.
- Liang, N., Xiao, W.K., Liu, Y., Zhang, S.N., 2008. A cosmology-independent calibration of gamma-ray burst luminosity relations and the Hubble diagram. ApJ 685, 354–360. doi:10.1086/590903.
- Lindner, C.C., Milisavljević, M., Couch, S.M., Kumar, P., 2010. Collapsar accretion and the gamma-ray burst X-ray light curve. ApJ 713, 800–815. doi:10.1088/0004-637X/713/2/800.
- Lloyd, N.M., Petrosian, V., 1999. Distribution of spectral characteristics and the cosmological evolution of gamma-ray bursts. ApJ 511, 550–561. doi:10.1086/306719.
- Lloyd, N.M., Petrosian, V., Peebles, R.D., 2000. Synchrotron emission as the source of GRB spectra. Part II: observations. In: Kippen, R.M., Mallozzi, R.S., Fishman, G.J. (Eds.), Gamma-ray Bursts, 5th Huntsville Symposium. In: American Institute of Physics Conference Series, 526, pp. 155–159. doi:10.1063/1.1361525.
- Lü, H.-J., Zhang, B., 2014. A test of the millisecond magnetar central engine model of gamma-ray bursts with swift data. ApJ 785, 74. doi:10.1088/0004-637X/785/1/74.
- Lyons, N., O'Brien, P.T., Zhang, B., Willingale, R., Troja, E., Starling, R.L.C., 2010. Can X-ray emission powered by a spinning-down magnetar explain some gamma-ray burst light-curve features? MNRAS 402, 705–712. doi:10.1111/j.1365-2966.2009.15538.x.
- Mangano, V., Sbarufatti, B., Stratta, G., 2012. Extending the plateau luminosity-duration anticorrelation. Memorie della Società Astronomica Italiana Supplementi 21, 143.
- Margutti, R., Guidorzi, C., Chincarini, G., Bernardini, M.G., Genet, F., Mao, J., Pasotti, F., 2010. Lag-luminosity relation in γ -ray burst X-ray flares: a direct link to the prompt emission. MNRAS 406, 2149–2167. doi:10.1111/j.1365-2966.2010.16824.x.
- Margutti, R., Zaninoni, E., Bernardini, M.G., Chincarini, G., Pasotti, F., Guidorzi, C., Angelini, L., Burrows, D.N., Capalbi, M., Evans, P.A., Gehrels, N., Kennea, J., Mangano, V., Moretti, A., Nousek, J., Osborne, J.P., Page, K.L., Perri, M., Racusin, J., Romano, P., Sbarufatti, B., Stafford, S., Stamatisos, M., 2013. The prompt-afterglow connection in gamma-ray bursts: a comprehensive statistical analysis of Swift X-ray light curves. MNRAS 428, 729–742. doi:10.1093/mnras/sts066.
- Maxham, A., Zhang, B., 2009. Modeling gamma-ray burst X-ray flares within the internal shock model. ApJ 707, 1623–1633. doi:10.1088/0004-637X/707/2/1623.
- Mazets, E.P., Golatenetskii, S.V., Ilyinskii, V.N., Panov, V.N., Aptekar, R.L., Guryan, Y.A., Proskura, M.P., Sokolov, I.A., Sokolova, Z.Y., Khartonova, T.V., Dyatchkov, A.V., Khavenson, N.G., 1981. Catalog of cosmic gamma-ray bursts from the KONUS experiment data. ApSS 80, 85–117. doi:10.1007/BF00649141.
- Melandri, A., Covino, S., Rogantini, D., Salvaterra, R., Sbarufatti, B., Bernardini, M.G., Campana, S., D'Avanzo, P., D'Elia, V., Fugazza, D., Ghirlanda, G., Ghisellini, G., Nava, L., Vergani, S.D., Tagliaferri, G., 2014. Optical and X-ray rest-frame light curves of the BAT6 sample. A&A 565, A72. doi:10.1051/0004-6361/201323361.
- Melandri, A., Mundell, C.G., Kobayashi, S., Guidorzi, C., Gomboc, A., Steele, I.A., Smith, R.J., Bersier, D., Mottram, C.J., Carter, D., Bode, M.F., O'Brien, P.T., Tanvir, N.R., Rol, E., Chapman, R., 2008. The early-time optical properties of gamma-ray burst afterglows. ApJ 686, 1209–1230. doi:10.1086/502796.
- Mészáros, P., 1998. Theoretical models of gamma-ray bursts. In: Meegan, C.A., Preece, R.D., Kosuth, T.M. (Eds.), Gamma-Ray Bursts, 4th Huntsville Symposium. In: American Institute of Physics Conference Series, 428, pp. 647–656. doi:10.1063/1.155394.
- Mészáros, P., 2006. Gamma-ray bursts. Rep. Prog. Phys. 69, 2259–2321. doi:10.1088/0034-4885/69/8/R01.
- Metzger, B.D., Giannios, D., Thompson, T.A., Bucciantini, N., Quataert, E., 2011. The protomagnetar model for gamma-ray bursts. MNRAS 413, 2031–2056. doi:10.1111/j.1365-2966.2011.18280.x.
- Nardini, M., Ghisellini, G., Ghirlanda, G., 2008a. Optical afterglow luminosities in the Swift epoch: confirming clustering and bimodality. MNRAS 386, L87–L91. doi:10.1111/j.1745-3933.2008.00467.x.
- Nardini, M., Ghisellini, G., Ghirlanda, G., 2008b. Optical afterglows of gamma-ray bursts: a bimodal distribution? MNRAS 383, 1049–1057. doi:10.1111/j.1365-2966.2007.12588.x.
- Nardini, M., Ghisellini, G., Ghirlanda, G., Tavecchio, F., Firmani, C., Lazzati, D., 2006. Clustering of the optical-afterglow luminosities of long gamma-ray bursts. A&A 451, 821–833. doi:10.1051/0004-6361:20054085.
- Norris, J.P., Bonnell, J.T., 2006. Short gamma-ray bursts with extended emission. ApJ 643, 266–275. doi:10.1086/502796.
- Nousek, J.A., Kouveliotou, C., Grupe, D., Page, K.L., Granot, J., Ramirez-Ruiz, E., Patel, S.K., Burrows, D.N., Mangano, V., Barthelmy, S., Beardmore, A.P., Campana, S., Capalbi, M., Chincarini, G., Cusumano, G., Falcone, A.D., Gehrels, N., Giommi, P., Goad, M.R., Godet, O., Hurkett, C.P., Kennea, J.A., Moretti, A., O'Brien, P.T., Osborne, J.P., Romano, P., Tagliaferri, G., Wells, A.A., 2006. Evidence for a canonical gamma-ray burst afterglow light curve in the swift XRT data. ApJ 642, 389–400. doi:10.1086/500724.
- Nysewander, M., Fruchter, A.S., Pe'er, A., 2009. A comparison of the afterglows of short- and long-duration gamma-ray bursts. ApJ 701, 824–836. doi:10.1088/0004-637X/701/1/1824.
- Oates, S.R., Page, M.J., De Pasquale, M., Schady, P., Breeveld, A.A., Holland, S.T., Kuin, N.P.M., Marshall, F.E., 2012. A correlation between the intrinsic brightness and average decay rate of Swift/UVOT gamma-ray burst optical/ultraviolet light curves. MNRAS 426, L86–L90. doi:10.1111/j.1745-3933.2012.01331.x.
- Oates, S.R., Page, M.J., Schady, P., de Pasquale, M., Koch, T.S., Breeveld, A.A., Brown, P.J., Chester, M.M., Holland, S.T., Hoversten, E.A., Kuin, N.P.M., Marshall, F.E., Roming, P.W.A., Still, M., vanden Berk, D.E., Zane, S., Nousek, J.A., 2009. A statistical study of gamma-ray burst afterglows measured by the Swift Ultraviolet Optical Telescope. MNRAS 395, 490–503. doi:10.1111/j.1365-2966.2009.14544.x.
- Oates, S.R., Racusin, J.L., De Pasquale, M., Page, M.J., Castro-Tirado, A.J., Gorosabel, J., Smith, P.J., Breeveld, A.A., Kuin, N.P.M., 2015. Exploring the canonical behaviour of long gamma-ray bursts using an intrinsic multiwavelength afterglow correlation. MNRAS 453, 4121–4135. doi:10.1093/mnras/stv1956.
- O'Brien, P.T., Willingale, R., Osborne, J., Goad, M.R., Page, K.L., Vaughan, S., Rol, E., Beardmore, A., Godet, O., Hurkett, C.P., Wells, A., Zhang, B., Kobayashi, S., Burrows, D.N., Nousek, J.A., Kennea, J.A., Falcone, A., Grupe, D., Gehrels, N., Barthelmy, S., Cannizzo, J., Cummings, J., Hill, J.E., Krimm, H., Chincarini, G., Tagliaferri, G., Campana, S., Moretti, A., Giommi, P., Perri, M., Mangano, V., LaParola, V., 2006. The early X-ray emission from GRBs. ApJ 647, 1213–1237. doi:10.1086/505457.
- Panaiteescu, A., Vestrand, W.T., 2008. Taxonomy of gamma-ray burst optical light curves: identification of a salient class of early afterglows. MNRAS 387, 497–504. doi:10.1111/j.1365-2966.2008.13231.x.
- Panaiteescu, A., Vestrand, W.T., 2011. Optical afterglows of gamma-ray bursts: peaks, plateaus and possibilities. MNRAS 414, 3537–3546. doi:10.1111/j.1365-2966.2011.18653.x.
- Perlmutter, S., Aldering, G., della Valle, M., Deustua, S., Ellis, R.S., Fabbro, S., Fruchter, A., Goldhaber, G., Groom, D.E., Hook, I.M., Kim, A.G., Kim, M.Y., Knop, R.A., Lidman, C., McMahon, R.G., Nugent, P., Pain, R., Panagia, N., Pennypacker, C.R., Ruiz-Lapuente, P., Schafer, B., Walton, N., 1998. Discovery of a supernova explosion at half the age of the universe. Nature 391, 51. doi:10.1038/34124.
- Perna, R., Armitage, P.J., Zhang, B., 2006. Flares in long and short gamma-ray bursts: a common origin in a hyperaccreting accretion disk. ApJ 636, L29–L32. doi:10.1086/499775.
- Petersen, J.H., Holst, K.K., Budtz-Jørgensen, E., 2010. Correcting a statistical artifact in the estimation of the Hubble constant based on type Ia supernovae results in a change in estimate of 1.2%. ApJ 723, 966–968. doi:10.1088/0004-637X/723/1/966.
- Petrosian, V., Bouvier, A., Ryde, F., 2009. Gamma-ray bursts as cosmological tools. ArXiv e-prints.
- Petrosian, V., Singal, J., Stawarz, L., 2013. Luminosity correlations, luminosity evolutions, and radio loudness of agns from multiwavelength observations. In: Multi-wavelength AGN Surveys and Studies. Vol. 9 of Proceedings of the International Astronomical Union 172–172 doi:10.1017/S174392131400369X.
- Phillips, M.M., 1993. The absolute magnitudes of Type IA supernovae. ApJ 413, L105–L108. doi:10.1086/186970.
- Planck Collaboration, Ade, P.A.R., Aghanim, N., Arnaud, M., Ashdown, M., Aumont, J., Baccigalupi, C., Banday, A.J., Barreiro, R.B., Bartlett, J.G., et al., 2016. Planck 2015 results. XIII. Cosmological parameters. A&A 594, A13. doi:10.1051/0004-6361/201525830.
- Postnikov, S., Dainotti, M.G., Hernandez, X., Capozziello, S., 2014. Nonparametric study of the evolution of the cosmological equation of state with SN_{IA}, BAO, and High-redshift GRBs. ApJ 783, 126. doi:10.1088/0004-637X/783/2/126.
- Proga, D., Zhang, B., 2006. The late time evolution of gamma-ray bursts: ending hyperaccretion and producing flares. MNRAS 370, L61–L65. doi:10.1111/j.1745-3933.2006.00189.x.
- Racusin, J.L., Oates, S.R., de Pasquale, M., Kocevski, D., 2016. A correlation between the intrinsic brightness and average decay rate of gamma-ray burst X-ray afterglow light curves. ApJ 826, 45. doi:10.3847/0004-637X/826/1/45.
- Racusin, J.L., Oates, S.R., Schady, P., Burrows, D.N., de Pasquale, M., Donato, D., Gehrels, N., Koch, S., McEvney, J., Piran, T., Roming, P., Sakamoto, T., Swenson, C., Troja, E., Vasileiou, V., Virgili, F., Wanderman, D., Zhang, B., 2011. Fermi and swift gamma-ray burst afterglow population studies. ApJ 738, 138. doi:10.1088/0004-637X/738/2/138.
- Rea, N., Guillou, M., Pons, J. A., Perna, R., Dainotti, M. G., Miralles, J. A., Torres, D. F., 2015. Constraining the GRB-magnetar model by means of the Galactic pulsar population. ArXiv e-prints.
- Rees, M.J., Mészáros, P., 1998. Refreshed shocks and afterglow longevity in gamma-ray bursts. ApJ 496, L1–L4. doi:10.1086/311244.

- Riess, A.G., Filippenko, A.V., Challis, P., Clocchiatti, A., Diercks, A., Garnavich, P.M., Gilliland, R.L., Hogan, C.J., Jha, S., Kirshner, R.P., Leibundgut, B., Phillips, M.M., Reiss, D., Schmidt, B.P., Schommer, R.A., Smith, R.C., Spyromilio, J., Stubbs, C., Suntzeff, N.B., Tonry, J., 1998. Observational evidence from supernovae for an accelerating universe and a cosmological constant. *AJ* 116, 1009–1038. doi:[10.1086/300499](https://doi.org/10.1086/300499).
- Riess, A.G., Macri, L., Casertano, S., Sosey, M., Lampeitl, H., Ferguson, H.C., Filippenko, A.V., Jha, S.W., Li, W., Chornock, R., Sarkar, D., 2009. A redetermination of the Hubble constant with the Hubble space telescope from a differential distance ladder. *ApJ* 699, 539–563. doi:[10.1088/0004-637X/699/1/539](https://doi.org/10.1088/0004-637X/699/1/539).
- Rodney, S.A., Riess, A.G., Scolnic, D.M., Jones, D.O., Hemmati, S., Molino, A., McCully, C., Mobasher, B., Strolger, L.-G., Graur, O., Hayden, B., Casertano, S., 2015. Two SNe Ia at redshift 2: improved classification and redshift determination with medium-band infrared imaging. *AJ* 150, 156. doi:[10.1088/0004-6256/150/5/156](https://doi.org/10.1088/0004-6256/150/5/156).
- Rowlinson, A., Gompertz, B.P., Dainotti, M., O'Brien, P.T., Wijers, R.A.M.J., van der Horst, A.J., 2014. Constraining properties of GRB magnetar central engines using the observed plateau luminosity and duration correlation. *MNRAS* 443, 1779–1787. doi:[10.1093/mnras/stu1277](https://doi.org/10.1093/mnras/stu1277).
- Rowlinson, A., O'Brien, P., 2012. Energy injection in short GRBs and the role of magnetars. In: *Gamma-Ray Bursts 2012 Conference (GRB 2012)*.
- Rowlinson, A., O'Brien, P.T., Metzger, B.D., Tanvir, N.R., Levan, A.J., 2013. Signatures of magnetar central engines in short GRB light curves. *MNRAS* 430, 1061–1087. doi:[10.1093/mnras/sts683](https://doi.org/10.1093/mnras/sts683).
- Ruffini, R., Muccino, M., Bianco, C.L., Enderli, M., Izzo, L., Kovacevic, M., Penacchioni, A.V., Pisani, G.B., Rueda, J.A., Wang, Y., 2014. On binary-driven hypernovae and their nested late X-ray emission. *A&A* 565, L10. doi:[10.1051/0004-6361/201423812](https://doi.org/10.1051/0004-6361/201423812).
- Sakamoto, T., Barthelmy, S.D., Barbier, L., Cummings, J.R., Fenimore, E.E., Gehrels, N., Hullinger, D., Krimm, H.A., Markwardt, C.B., Palmer, D.M., Parsons, A.M., Sato, G., Stamatikos, M., Tueller, J., Ukwatta, T.N., Zhang, B., 2008. The first swift BAT gamma-ray burst catalog. *ApJS* 175, 179–190. doi:[10.1086/523646](https://doi.org/10.1086/523646).
- Sakamoto, T., Hill, J.E., Yamazaki, R., Angelini, L., Krimm, H.A., Sato, G., Swindell, S., Takami, K., Osborne, J.P., 2007. Evidence of exponential decay emission in the swift gamma-ray bursts. *ApJ* 669, 1115–1129. doi:[10.1086/521640](https://doi.org/10.1086/521640).
- Sari, R., Mészáros, P., 2000. Impulsive and varying injection in gamma-ray burst afterglows. *ApJ* 535, L33–L37. doi:[10.1086/312689](https://doi.org/10.1086/312689).
- Sari, R., Piran, T., Narayan, R., 1998. Spectra and light curves of gamma-ray burst afterglows. *ApJ* 497, L17–L20. doi:[10.1086/312690](https://doi.org/10.1086/312690).
- Schady, P., Mason, K.O., Page, M.J., de Pasquale, M., Morris, D.C., Romano, P., Roming, P.W.A., Immel, S., vanden Berk, D.E., 2007. Dust and gas in the local environments of gamma-ray bursts. *MNRAS* 377, 273–284. doi:[10.1111/j.1365-2966.2007.11592.x](https://doi.org/10.1111/j.1365-2966.2007.11592.x).
- Schaefer, B.E., 2007. The Hubble diagram to redshift > 6 from 69 gamma-ray bursts. *ApJ* 660, 16–46. doi:[10.1086/511742](https://doi.org/10.1086/511742).
- Stern, D., Jimenez, R., Verde, L., Stanford, S.A., Kamionkowski, M., 2010. Cosmic chronometers: constraining the equation of state of dark energy. II. A spectroscopic catalog of red galaxies in galaxy clusters. *ApJS* 188, 280–289. doi:[10.1088/0067-0049/188/1/280](https://doi.org/10.1088/0067-0049/188/1/280).
- Sultana, J., Kazanas, D., Fukumura, K., 2012. Luminosity correlations for gamma-ray bursts and implications for their prompt and afterglow emission mechanisms. *ApJ* 758, 32. doi:[10.1088/0004-637X/758/1/32](https://doi.org/10.1088/0004-637X/758/1/32).
- Sultana, J., Kazanas, D., Mastichiadis, A., 2013. The supercritical pile gamma-ray burst model: the GRB afterglow steep decline and plateau phase. *ApJ* 779, 16. doi:[10.1088/0004-637X/779/1/16](https://doi.org/10.1088/0004-637X/779/1/16).
- Suzuki, N., Rubin, D., Lidman, C., Aldering, G., Amanullah, R., Barbary, K., Barrientos, L.F., Botyanszki, J., Brodwin, M., Connolly, N., Dawson, K.S., Dey, A., Doi, M., Donahue, M., Deustua, S., Eisenhardt, P., Ellingson, E., Faccioli, L., Fadeyev, V., Fakhouri, H.K., Fruchter, A.S., Gilbank, D.G., Gladders, M.D., Goldhaber, G., Gonzalez, A.H., Goobar, A., Gude, A., Hattori, T., Hoekstra, H., Hsiao, E., Huang, X., Ihara, Y., Jee, M.J., Johnston, D., Kashikawa, N., Koester, B., Konishi, K., Kowalski, M., Linder, E.V., Lubin, L., Melbourne, J., Meyers, J., Morokuma, T., Munsch, F., Mullis, C., Oda, T., Panagia, N., Perlmutter, S., Postman, M., Pritchard, T., Rhodes, J., Ripoché, P., Rosati, P., Schlegel, D.J., Spadafora, A., Stanford, S.A., Stanishev, V., Stern, D., Strovink, M., Takanashi, N., Tokita, K., Wagner, M., Wang, L., Yasuda, N., Yee, H.K.C., Supernova Cosmology Project, T., 2012. The Hubble space telescope cluster supernova survey. V. Improving the dark-energy constraints above $z > 1$ and building an early-type-hosted supernova sample. *ApJ* 746, 85. doi:[10.1088/0004-637X/746/1/85](https://doi.org/10.1088/0004-637X/746/1/85).
- Troja, E., Cusumano, G., O'Brien, P.T., Zhang, B., Sbarufatti, B., Mangano, V., Willingale, R., Chincarini, G., Osborne, J.P., Marshall, F.E., Burrows, D.N., Campana, S., Gehrels, N., Guidorzi, C., Krimm, H.A., La Parola, V., Liang, E.W., Mineo, T., Moretti, A., Page, K.L., Romano, P., Tagliaferri, G., Zhang, B.B., Page, M.J., Schady, P., 2007. Swift observations of GRB 07010: an extraordinary X-ray afterglow powered by the central engine. *ApJ* 665, 599–607. doi:[10.1086/519450](https://doi.org/10.1086/519450).
- Tsutsui, R., Yonetoku, D., Nakamura, T., Takahashi, K., Moribara, Y., 2013. Possible existence of the E_p - L_p and E_p - E_{iso} correlations for short gamma-ray bursts with a factor 5–100 dimmer than those for long gamma-ray bursts. *MNRAS* 431, 1398–1404. doi:[10.1093/mnras/stt262](https://doi.org/10.1093/mnras/stt262).
- Urata, Y., Yamazaki, R., Sakamoto, T., Huang, K., Zheng, W., Sato, G., Aoki, T., Deng, J., Ioka, K., Ip, W., Kawabata, K.S., Lee, Y., Liping, X., Mito, H., Miyata, T., Nakada, Y., Ohshii, T., Qiu, Y., Soyano, T., Tarusawa, K., Tashiro, M., Uemura, M., Wei, J., Yamashita, T., 2007. Testing the external-shock model of gamma-ray bursts using the late-time simultaneous optical and X-ray afterglows. *ApJ* 668, L95–L98. doi:[10.1086/522930](https://doi.org/10.1086/522930).
- Usov, V.V., 1992. Millisecond pulsars with extremely strong magnetic fields as a cosmological source of gamma-ray bursts. *Nature* 357, 472–474. doi:[10.1038/35722a0](https://doi.org/10.1038/35722a0).
- van Eerten, H., 2014. Self-similar relativistic blast waves with energy injection. *MNRAS* 442, 3495–3510. doi:[10.1093/mnras/stu1205](https://doi.org/10.1093/mnras/stu1205).
- van Eerten, H.J., 2014. Gamma-ray burst afterglow plateau break time-luminosity correlations favour thick shell models over thin shell models. *MNRAS* 445, 2414–2423. doi:[10.1093/mnras/stu1921](https://doi.org/10.1093/mnras/stu1921).
- Wang, F.Y., Dai, Z.G., Liang, E.W., 2015. Gamma-ray burst cosmology. *New Astron. Rev.* 67, 1–17. doi:[10.1016/j.newar.2015.03.001](https://doi.org/10.1016/j.newar.2015.03.001).
- Wang, F.-Y., Qi, S., Dai, Z.-G., 2011. The updated luminosity correlations of gamma-ray bursts and cosmological implications. *MNRAS* 415, 3423–3433. doi:[10.1111/j.1365-2966.2011.18961.x](https://doi.org/10.1111/j.1365-2966.2011.18961.x).
- Wei, H., Zhang, S.-N., 2009. Reconstructing the cosmic expansion history up to redshift $z=6.29$ with the calibrated gamma-ray bursts. *Eur. Phys. J. C* 63, 139–147. doi:[10.1140/epjc/s10052-009-1086-z](https://doi.org/10.1140/epjc/s10052-009-1086-z).
- Weinberg, D.H., Mortonson, M.J., Eisenstein, D.J., Hirata, C., Riess, A.G., Rozo, E., 2013. Observational probes of cosmic acceleration. *Phys. Rep.* 530, 87–255. doi:[10.1016/j.physrep.2013.05.001](https://doi.org/10.1016/j.physrep.2013.05.001).
- Wijers, R.A.M.J., Rees, M.J., Mészáros, P., 1997. Shocked by GRB 970228: the afterglow of a cosmological fireball. *MNRAS* 288, L51–L56.
- Willingale, R., Genet, F., Granot, J., O'Brien, P.T., 2010. The spectral-temporal properties of the prompt pulses and rapid decay phase of gamma-ray bursts. *MNRAS* 403, 1296–1316. doi:[10.1111/j.1365-2966.2009.16187.x](https://doi.org/10.1111/j.1365-2966.2009.16187.x).
- Willingale, R., O'Brien, P.T., Osborne, J.P., Godet, O., Page, K.L., Goad, M.R., Burrows, D.N., Zhang, B., Bol, E., Gehrels, N., Chincarini, G., 2007. Testing the standard fireball model of gamma-ray bursts using late X-ray afterglows measured by swift. *ApJ* 662, 1093–1110. doi:[10.1086/517989](https://doi.org/10.1086/517989).
- Yamazaki, R., 2009. Prior emission model for X-ray plateau phase of gamma-ray burst afterglows. *ApJ* 690, L118–L121. doi:[10.1088/0004-637X/690/2/L118](https://doi.org/10.1088/0004-637X/690/2/L118).
- Yi, S. X., Dai, Z. G., Wu, X. F., Wang, F. Y., 2014. X-ray afterglow plateaus of long gamma-ray bursts: further evidence for millisecond magnetars. *ArXiv e-prints*.
- Yonetoku, D., Murakami, T., Nakamura, T., Yamazaki, R., Inoue, A.K., Ioka, K., 2004. Gamma-ray burst formation rate inferred from the spectral peak energy-peak luminosity relation. *ApJ* 609, 935–951. doi:[10.1086/421285](https://doi.org/10.1086/421285).
- Zaninoni, E., Bernardini, M.G., Margutti, R., Oates, S., Chincarini, G., 2013. Gamma-ray burst optical light-curve zoo: comparison with X-ray observations. *A&A* 557, A12. doi:[10.1051/0004-6361/201321221](https://doi.org/10.1051/0004-6361/201321221).
- Zhang, B., Kobayashi, S., 2005. Gamma-ray burst early afterglows: reverse shock emission from an arbitrarily magnetized ejecta. *ApJ* 628, 315–334. doi:[10.1086/492787](https://doi.org/10.1086/492787).
- Zhang, B., Liang, E., Page, K.L., Grupe, D., Zhang, B.-B., Barthelmy, S.D., Burrows, D.N., Campana, S., Chincarini, G., Gehrels, N., Kobayashi, S., Mészáros, P., Moretti, A., Nousek, J.A., O'Brien, P.T., Osborne, J.P., Roming, P.W.A., Sakamoto, T., Schady, P., Willingale, R., 2007. GRB radiative efficiencies derived from the swift data: GRBs versus XRFs, long versus short. *ApJ* 655, 989–1001. doi:[10.1086/510110](https://doi.org/10.1086/510110).
- Zhang, B., Mészáros, P., 2001. Gamma-ray burst afterglow with continuous energy injection: signature of a highly magnetized millisecond pulsar. *ApJ* 552, L35–L38. doi:[10.1086/320255](https://doi.org/10.1086/320255).
- Zhang, B., Yan, H., 2011. The internal-collision-induced magnetic reconnection and turbulence (ICMART) model of gamma-ray bursts. *ApJ* 726, 90. doi:[10.1088/0004-637X/726/2/90](https://doi.org/10.1088/0004-637X/726/2/90).
- Zhang, B.-B., Liang, E.-W., Zhang, B., 2007. A comprehensive analysis of swift XRT data. I. Apparent spectral evolution of gamma-ray burst X-ray tails. *ApJ* 666, 1002–1011. doi:[10.1086/519548](https://doi.org/10.1086/519548).

THE ASTROPHYSICAL JOURNAL, 800:31 (12pp), 2015 February 10
 © 2015. The American Astronomical Society. All rights reserved.

doi:10.1088/0004-637X/800/1/31

SELECTION EFFECTS IN GAMMA-RAY BURST CORRELATIONS: CONSEQUENCES ON THE RATIO BETWEEN GAMMA-RAY BURST AND STAR FORMATION RATES

M. G. DAINOTTI^{1,2,3}, R. DEL VECCHIO³, N. SHIGEHIRO¹, AND S. CAPOZZIELLO^{4,5,6}

¹ Astrophysical Big Bang Laboratory, Riken, 2-1 Hirosawa, Wako, Saitama 351-0198, Japan; maria.dainotti@riken.jp

² Physics Department, Stanford University, Via Pueblo Mall 382, Stanford, CA, USA; mdainott@stanford.edu

³ Observatorium Astronomiczne, Uniwersytet Jagielloński, ul. Orla 171, 31-501 Kraków, Poland;

delvecchio@obserwatorium.uj.edu.pl, mariagiavannadainotti@yahoo.it

⁴ Dipartimento di Fisica, Università di Napoli “Federico II,” Compl. Univ. di Monte S. Angelo, Edificio G, Via Cinthia,

I-80126 Napoli, Italy; capozziello@na.infn.it

⁵ INFN Sez. di Napoli, Complesso Universitario di Monte S. Angelo, Via Cinthia, Edificio N, I-80126 Napoli, Italy

⁶ Gran Sasso Science Institute (INFN), viale F. Crispi 7, I-67100 L’Aquila, Italy

Received 2014 May 23; accepted 2014 December 9; published 2015 February 5

ABSTRACT

Gamma-ray bursts (GRBs) visible up to very high redshift have become attractive targets as potential new distance indicators. It is still not clear whether the relations proposed so far originate from an unknown GRB physics or result from selection effects. We investigate this issue in the case of the $L_X-T_a^*$ (hereafter LT) correlation between the X-ray luminosity $L_X(T_a)$ at the end of the plateau phase, T_a , and the rest-frame time T_a^* . We devise a general method to build mock data sets starting from a GRB world model and taking into account selection effects on both time and luminosity. This method shows how not knowing the efficiency function could influence the evaluation of the intrinsic slope of any correlation and the GRB density rate. We investigate biases (small offsets in slope or normalization) that would occur in the LT relation as a result of truncations, possibly present in the intrinsic distributions of L_X and T_a^* . We compare these results with the ones in Dainotti et al. showing that in both cases the intrinsic slope of the LT correlation is ≈ -1.0 . This method is general and therefore relevant for investigating whether or not any other GRB correlation is generated by the biases themselves. Moreover, because the farthest GRBs and star-forming galaxies probe the reionization epoch, we evaluate the redshift-dependent ratio $\Psi(z) = (1+z)^\alpha$ of the GRB rate to the star formation rate. We found a modest evolution $-0.2 \leq \alpha \leq 0.5$ consistent with a *Swift* GRB afterglow plateau in the redshift range $0.99 < z < 9.4$.

Key words: gamma-ray burst: general – methods: data analysis – radiation mechanisms: non-thermal – stars: statistics

1. INTRODUCTION

Gamma-ray bursts (GRBs) are the farthest sources, seen up to redshift $z = 9.46$ (Cucchiara et al. 2011), and if emitting isotropically they are also the most powerful (with $E_{\text{iso}} \leq 10^{54} \text{ erg s}^{-1}$) objects in the universe. Notwithstanding the variety of their peculiarities, some common features may be identified by looking at their light curves. A crucial breakthrough in this area has been the observation of GRBs by the *Swift* satellite, launched in 2004. With the instruments on board, the Burst Alert Telescope (15–150 keV), the X-Ray Telescope (0.3–10 keV), and the Ultra-Violet/Optical Telescope (170–650 nm), *Swift* provides a rapid follow-up of the afterglows in several wavelengths with better coverage than previous missions. *Swift* observations have revealed a more complex behavior of the light curve afterglow (O’Brien et al. 2006; Sakamoto et al. 2007) that can be divided into two, three, and even more segments in the afterglows. The second segment, when it is flat, is called plateau emission. A significant step forward in determining common features in the afterglow light curves was made by fitting them with an analytical expression (Willingale et al. 2007, hereafter W07). This provides the opportunity to look for universal features that could provide a redshift-independent measure of the distance from the GRB, as in studies of correlations between the GRB isotropic energy and peak photon energy of the νF_ν spectrum, $E_{\text{iso}} - E_{\text{peak}}$, (Lloyd & Petrosian 1999; Amati et al. 2009), the beamed total energy $E_\gamma - E_{\text{peak}}$ (Ghirlanda et al. 2004; Ghirlanda et al. 2006), the luminosity-variability (L-V)

(Norris et al. 2000; Fenimore & Ramirez-Ruiz 2000), $L-E_{\text{peak}}$ (Yonetoku et al. 2004), and luminosity- τ lag (Schaefer 2003).

Dainotti et al. (2008, 2010), using the W07 phenomenological law for the light curves of long GRBs, discovered a formal anti-correlation between the X-ray luminosity at the end of the plateau L_X and the rest-frame plateau end-time, $T_a^* = T_a^{\text{obs}} / (1+z)$, where T_a^* is in seconds and L_X is in erg s^{-1} . The normalization and the slope parameters a and b are constants obtained by the D’Agostini fitting method (D’Agostini 2005). Dainotti et al. (2011a) attempted to use the $L_X-T_a^*$ (LT) correlation as a possible redshift estimator, but the paucity of the data and the scatter prevented them from obtaining a definite conclusion, at least for a sample of 62 GRBs. In addition, a further step to better understand the role of the plateau emission has been made with the discovery of new significant correlations between L_X , and the mean luminosities of the prompt emission, $\langle L_{\gamma, \text{prompt}} \rangle$ (Dainotti et al. 2011b)). The LT anticorrelation is also a useful test for theoretical models such as the accretion models, (Cannizzo & Gehrels 2009; Cannizzo et al. 2011), the magnetar models (Dall’Osso et al. 2011; Bernardini et al. 2012; Bernardini 2012; Rowlinson et al. 2010; Rowlinson et al. 2013; Rowlinson et al. 2014), the prior emission model (Yamazaki 2009), the unified GRB and active galactic nucleus (AGN) model (Nemmen et al. 2012), and the fireshell model (Izzo et al. 2013). Moreover, Hascoet et al. (2014) and Van Eerten (2014b) consider both the LT and the $L_X-\langle L_{\gamma, \text{prompt}} \rangle$ correlation to discriminate among several models proposed for the origin of the plateau. In Leventis et al. (2014) and Van Eerten (2014a), a smooth

THE ASTROPHYSICAL JOURNAL, 800:31 (12pp), 2015 February 10

DAINOTTI ET AL.

energy injection through the reverse shock has been presented as a plausible explanation for the origin of the LT correlation. Furthermore, other authors were also able to reproduce and use the LT correlation to extend it in the optical band (Ghisellini et al. 2009), to extrapolate it into correlations of the prompt emission (Sultana et al. 2012), and to use the same methodology to build an analogous correlation in the prompt (Qi & Lu 2012). Finally, it has been applied as a cosmological tool (Cardone et al. 2009, 2010; Dainotti et al. 2013a; Postnikov et al. 2014). The impacts of detector thresholds on cosmological standard candles have also been considered (Shahmoradi & Nemiroff 2009; Petrosian et al. 1998; Petrosian 1999, 2002; Cabrera et al. 2007). However, because of large dispersion (Butler et al. 2010; Yu et al. 2009) and the absence of good calibration, none of these correlations allow the use of GRBs as good standard candles, as has been done, e.g., with Type Ia supernovae. An important statistical technique to study selection effects for treating data truncation in GRB correlations is the Efron & Petrosian (1992) method. Another way to study the same problem in GRB correlations, derived by modeling the high-energy properties of GRBs, has been reported in Butler et al. (2010). In the latter paper, it has been shown that well-known examples of these correlations have common features indicative of strong contamination by selection effects. We compare this procedure with the method introduced by Efron & Petrosian (1992) and applied it to the LT correlation (Dainotti et al. 2013b). The paper is organized as follows: Section 2 introduces the relation between the GRB rate (RGRB) and the star formation rate (SFR), Section 2.1 is dedicated to the analysis of a GRB scaling relation; in particular, we consider the LT correlation as an example, but the procedure described can be adopted for any other correlation. In Section 3 we describe how to build the GRB samples. In Section 4 we analyze the redshift evolution of the slope and normalization of the LT correlation. In Section 5 we study the selection effects related to simulated samples assuming different normalization and slope values. Then, in Section 6 we draw conclusions on the intrinsic slope of the LT correlation and on the evaluation of the redshift-dependent ratio between the RGRB and the SFR.

2. THE RELATION BETWEEN GRB RATE AND SFR

In order to understand the relation between GRBs and star formation, it is often assumed that the RGRB is proportional to the SFR, and the predicted distribution of the GRB redshift is compared to the observed distribution (Totani 1997; Mao & Mo 1998; Wijers et al. 1998; Porciani & Madau 2001; Natarajan et al. 2005; Jakobsson et al. 2006; Daigne & Mochkovitch 2007; Le & Dermer 2007; Coward 2007; Mao 2010). However, this relationship is not an easy task to handle because some studies show that GRBs do not seem to trace star formation in an unbiased manner (Lloyd & Petrosian 1999). Namely, the ratio between the RGRB and the SFR (RGRB/SFR) significantly increases with redshift (Kistler et al. 2008; Yuksel & Kistler 2007). This means that GRBs are more frequent for a given star formation rate density at earlier times. In fact, while observations consistently show that the comoving rate density of star formation is nearly constant in the interval $1 \leq z \leq 4$ (Hopkins & Beacom 2006), the comoving rate density of GRBs appears to be evolving distinctly. In our approach we explicitly take into consideration this issue when we fit the observed RGRB with the model. Selection effects involved in a GRB sample are of two kinds: GRB detection and localization, and the redshift determination through spectroscopy and photometry of the GRB afterglow or the host galaxy. These problems have

been objects of extensive study in the literature (Bloom 2003; Fiore et al. 2007; Guetta & Della Valle 2007). Moreover, the *Swift* trigger is very complex and the sensitivity of the detector is very difficult to parameterize exactly (Band 2006), but in this case, not dealing with prompt peak energy, we do not have to take into consideration the double truncation present in the data (Lloyd & Petrosian 1999). In the case of the plateau it is easier, since an effective luminosity threshold appears to be present in the data, which can be approximated by a 0.3–10 keV energy flux limit $F_{\text{lim}} \equiv 2 \times 10^{12} \text{ erg cm}^{-2} \text{ s}^{-1}$ (Dainotti et al. 2013b). The luminosity threshold is then $L_{\text{lim}} = 4\pi D_L^2(z, \Omega_M, H_0)F_{\text{lim}}$, where D_L is the luminosity distance to the burst. Throughout the paper, we assume a flat universe with $\Omega_M = 0.28$, $\Omega_\lambda = 0.72$, and $H_0 = 70 \text{ km s}^{-1} \text{ Mpc}^{-1}$. In our approach below several models are considered and then the one that best matches the RGRB with the SFR has been chosen.

2.1. GRB World Model

We derive a model capable of reproducing the observed *Swift* RGRB as a function of redshift, luminosity, and time of the plateau emission.

Rest-frame time and luminosity at the end of the GRB plateau emission show strong correlations as discovered by Dainotti et al. (2008) and later updated by Dainotti et al. (2010, 2011a, 2011b, 2013b). Therefore, all these quantities must be considered in deriving reliable rates. We characterize the RGRB as a product of terms involving the redshift z of the bursts, the isotropic equivalent luminosity release (0.3–10 keV) L_X , and the duration T_a^* .

Let us assume that a scaling relation exists so that the luminosity $L_X(T_a)$ for a GRB with timescale T_a^* at redshift z is given by

$$\lambda = \alpha_0 + \alpha_\tau \tau + \alpha_\zeta \zeta \quad (1)$$

where we have introduced the compact notation

$$\begin{cases} \lambda = \log L_X(T_a) \\ \tau = \log [T_a^*/(1+z)] \\ \zeta = \log (1+z). \end{cases} \quad (2)$$

and the term ζ accounts for redshift evolution. The luminosity is normalized by the unit of 1 erg s^{-1} and the time by the unit of 1 s, so that non-dimensional quantities are considered. All the observables in this model are computed in the rest frame because we are testing the role played by selection effects in the rest frame, the LT correlation rest frame being corrected. Independently, on the physical interpretation of this relation (in fact, there are several models that can reproduce it as we have mentioned in the Introduction), we can nevertheless expect GRBs to follow Equation (1) with a scatter of σ_λ . Moreover, the zero point α_0 may be known only up to a given uncertainty σ_α . Following the approach of Butler et al. (2010), applied for prompt correlations, we assume that λ can be approximated by a Gaussian distribution with mean λ_0 , expressed in Equation (1), and the variance σ_{int} is the intrinsic scatter of the correlation. We also write the probability that a GRB with given (τ, ζ) values has a luminosity λ as follows:

$$P_\lambda(\lambda, \tau, \zeta) \propto \exp \left[-\frac{1}{2} \left[\frac{\lambda - (\alpha_0 + \alpha_\tau \tau + \alpha_\zeta \zeta)}{\sigma_{\text{int}}} \right]^2 \right] \quad (3)$$

where $\sigma_{\text{int}}^2 = \sigma_\lambda^2 + \sigma_\alpha^2$, σ_α is the uncertainty of the α_0 value, and σ_λ is the uncertainty on the luminosity value.

THE ASTROPHYSICAL JOURNAL, 800:31 (12pp), 2015 February 10

DAINOTTI ET AL.

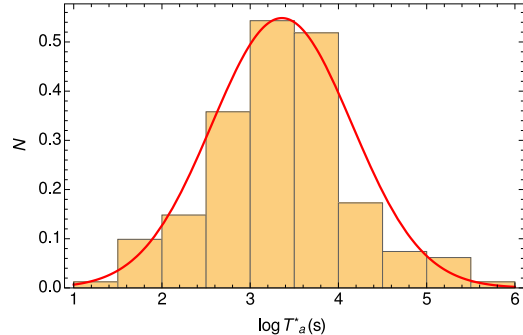


Figure 1. Probability density distribution of T_a^* , the rest frame end time of the plateau, for GRBs observed from 2005 January until 2014 July, analyzed following the Dainotti et al. (2013b) approach with a superimposed best fit of the Gaussian distribution.

The approximation of a Gaussian distribution both for luminosity and time is motivated by the goodness of the fit, which gives a probability of $P = 0.46$ and $P = 0.61$, respectively, see Figure 1 and 2. We note that the mean (indicated with $\langle \rangle$) $\langle T_a \rangle = 3.35$ (s) with a variance $\sigma_{T_a} = 0.77$ (s) and $\langle L_X \rangle = 48.04$ (erg s^{-1}) with a variance $\sigma_{L_X} = 1.37$ (erg s^{-1}) are represented, respectively, in Figures 1 and 2.

In order to obtain the number of GRBs with a given luminosity λ , we need to integrate over the distributions of τ and ζ . We will assume, for simplicity, that τ follows a truncated Gaussian law.

$$P_\tau(\tau) \propto \begin{cases} \exp[-\frac{1}{2}(\frac{\tau-\tau_0}{\sigma_{\tau}})^2] & \tau_L < \tau < \tau_U \\ 0 & \tau \leq \tau_L \text{ or } \tau \geq \tau_U \end{cases} \quad (4)$$

where τ_L and τ_U respectively indicate the lower limit and upper limit of the observed τ distribution and τ_0 is the mean value of this distribution. The limits of τ are taken from an updated sample of T_a^* composed of 176 GRB afterglows, with firm redshift determination, from 2005 January until 2014 July. The analysis follows the criteria adopted in Dainotti et al. (2013b).

If we assume that the GRBs trace the cosmic SFR, we can model their redshift distribution following Butler et al. (2010):

$$P_z(z) \propto \frac{\dot{\rho}_*(z) dV}{1+z dz} \quad (5)$$

where $\dot{\rho}_*(z)$ is the comoving RGRB density, V is the universal volume, and the factor $(1+z)$ accounts for the cosmic time dilatation and

$$\frac{dV}{dz} \propto \frac{r^2(z)}{E(z)} \quad (6)$$

with $r(z)$ being the comoving distance and $E(z) = H(z)/H_0$ being the Hubble parameter normalized to its present-day value.

Collecting the different terms, we can finally write the true, detector-independent event \mathcal{N} differential rate, for z , $\log T_a^*$, and $\log L_X$:

$$\frac{d\mathcal{N}}{d\lambda d\tau dz} \propto \Psi(z) P_\lambda(\lambda, \tau, \zeta) P_\tau(\tau) P_z(z). \quad (7)$$

We note here that we have introduced the term of the evolution in redshift, $\Psi(z) = (1+z)^\alpha$, following the approach of Lloyd & Petrosian (1999); Dermer (2007), and Robertson & Ellis (2012). In Dermer (2007), assuming that the emission properties of

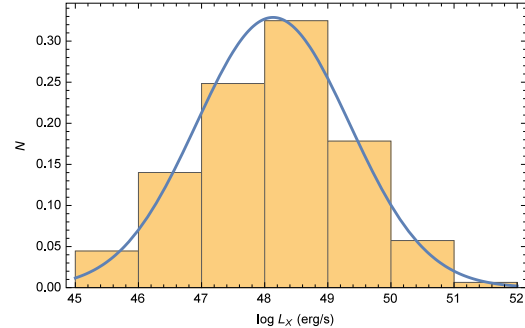


Figure 2. Probability density distribution of $L_X(T_a)$ at the end of the plateau for GRBs observed from 2005 January until 2014 July, analyzed following the Dainotti et al. (2013b) approach with a superimposed best fit of the Gaussian distribution.

GRBs do not change with time, they find that the *Swift* data can only be fitted if the comoving rate density of GRB sources exhibits positive evolution to $z > 3\text{--}5$. In our approach, we introduce evolution starting from $z \geq 0.99$.

Therefore, using the above expression for P_τ , we find that the number of GRBs with luminosity in the range $(\lambda, \lambda + d\lambda)$ and redshift between z and $z + dz$ is

$$\frac{d\mathcal{N}}{d\lambda dz} \propto \Psi(z) \frac{\dot{\rho}_*(z) (dV/dz)}{1+z} \frac{\mathcal{F}_{\tau_U} - \mathcal{F}_{\tau_L}}{\sqrt{8\pi\sigma_\tau^2}} \times \exp\left[-\frac{1}{2}\left[\frac{\lambda - (\alpha_0 + \alpha_\tau\tau + \alpha_\zeta\zeta)}{\sqrt{\sigma_{\text{int}}^2}}\right]^2\right] \quad (8)$$

where \mathcal{F}_{τ_U} and \mathcal{F}_{τ_L} are the respective error functions⁷ of the lower and upper limits of the time distribution. Note that Equation (8) is defined up to an overall normalization constant, which can be solved by imposing that the integral of $d\mathcal{N}/d\lambda dz$ over (λ, z) gives the total number of observed GRBs. Actually, this is not known since we do not observe all GRBs but only those passing a given set of selection criteria. However, we will only be interested in the fraction of GRBs in a cell in the two-dimensional (2D) (λ, z) space so that we do not need this quantity.

We are aware that we do not map out the true LT relation, given selection effects and the observed LT relation. Doing this would require modeling the selection of the GRB sample itself (using the gamma-ray threshold) and also seeking to understand the tie between the GRB flux and the afterglow L_X . However, the relation between the flux and L_X has already been studied by Dainotti et al. (2013b) and was reported briefly in the previous section above. Here we compute the new limit related to the updated sample, as shown in the middle panel of Figure 3.

3. SIMULATING THE GRB SAMPLES

The RGRB given by Equation (8) has been derived by implicitly assuming that all the GRBs can be detected notwithstanding their observable properties. This is actually not the case. As an

⁷ We remind the reader that the usual definition of the error function is

$$\text{erf}(x) = \frac{2}{\sqrt{\pi}} \int_0^x e^{-t^2} dt. \quad (9)$$

THE ASTROPHYSICAL JOURNAL, 800:31 (12pp), 2015 February 10

DAINOTTI ET AL.

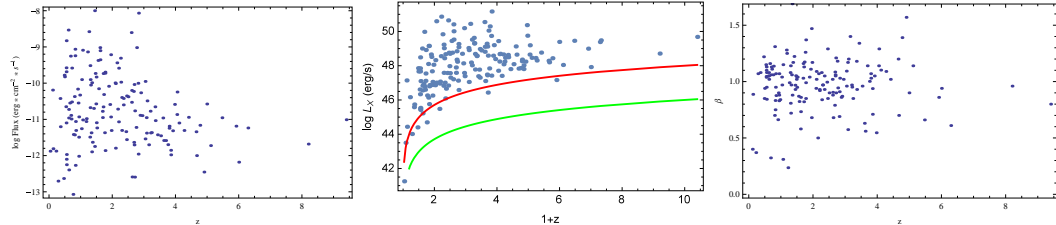


Figure 3. Flux at the end of the plateau phase, $\log T_d$, (left panel) and the spectral index, β , (right panel) as a function of redshift. The limiting luminosity, $\log L_X$ vs. $1+z$, shows (middle panel) two lines, one for the limiting flux, $F_{\text{Swift,lim}} = 10^{-14} \text{ erg cm}^{-2} \text{s}^{-1}$, and the other one is the most suitable for a plateau duration of 10^4 s, which is $2 \times 10^{-12} \text{ erg cm}^{-2} \text{s}^{-1}$.

example, we will consider hereafter the LT correlation, although the formalism and the method we will develop can be easily extended to whatever scaling law. For the LT case, there are two possible selection effects. First, each detector has an efficiency that is not the same for all the luminosities. Only GRBs with $\lambda > \lambda_L$, where λ_L is the lowest detectable luminosity for a given instrument, can be detected while all the GRBs with λ larger than a threshold luminosity λ_U will be found.

Moreover, it is likely that the efficiency of the detector is not constant, but is rather a function of the luminosity. We will therefore introduce an efficiency function $\mathcal{E}_\lambda(\lambda)$ whose functional expression is not known in advance, but can only take values in the range of (0,1). A second selection effect is related to the time duration of the GRB. Indeed, in order to be included in the sample used to calibrate the LT correlation, the GRB afterglow has to be measured over a sufficiently long timescale to make it possible to fit the data and extract the relevant quantities. If τ is too small (as shown in Dainotti et al. 2013b; the minimum rest-frame time is 14 s), few points will be available for the fit, while, on the contrary, large τ values will give rise to afterglow light curves, which could be well sampled by the data. Again, we can parameterize these effects by introducing a second efficiency function $\mathcal{E}_\tau(\tau)$ so that the final observable rate is the following:

$$\frac{dN_{\text{obs}}}{d\lambda dz} \propto \frac{dN}{d\lambda dz} \times \mathcal{E}_\lambda(\lambda) \mathcal{E}_\tau(\tau). \quad (10)$$

We point out that our formulation, which takes into account the efficiency functions $\mathcal{E}_\lambda(\lambda)$ and $\mathcal{E}_\tau(\tau)$ in the final observed RGRB, is similar to the approach by Robertson & Ellis (2012) in Equation (1), in which the additional factor K is presented. K is equivalent to our $\mathcal{E}_\lambda(\lambda)$ and $\mathcal{E}_\tau(\tau)$.

It is worth noting that Equation (10) is actually still a simplified description. Indeed, it is in principle possible that other selection effects take place involving observable quantities not considered here, as for example β and the redshift. However, these parameters enter into the determination of λ so that one can (at least in a first-order approximation) convert selection cuts on them in a single efficiency function, depending only on λ (for the dependence of the flux on the redshift, see the left panel of Figure 3). However, as we can see from Figure 3 β is constant with redshift, and there is no correlation between those two quantities; in fact, the Spearman correlation coefficient is $\rho = -0.062$. Nevertheless, Equation (10) provides a reasonably accurate description of the observable RGRB.

In order to evaluate Equation (10), there are different quantities to determine. First, we need to set the scaling coefficients ($\alpha_0, \alpha_\tau, \alpha_\zeta$) and the intrinsic scatter σ_{int} . Second, the mean and

variance of the τ distribution (τ_0, σ_τ) has to be given. Finally, an expression for the cosmic SFR $\dot{\rho}_*(z)$ has to be assigned. None of these quantities is actually available. In principle, one could assume an SFR law and fit for the model parameters to a large enough GRB sample with measured (λ, τ, ζ) values. To this end, one should know the selection function $\mathcal{E}_\lambda(\lambda) \mathcal{E}_\tau(\tau)$, which is not the case. Studies of how light curves would appear to a gamma-ray detector here on Earth have been performed (Kocevski & Petrosian 2013). In this paper the prompt emission pulses are investigated and the conclusion is that even a perfect detector that observes over a limited energy range would not faithfully measure the expected time dilation effects on a GRB pulse as a function of redshift.

Nevertheless, here we study detector threshold effects on afterglow properties. Our aim is to investigate how the ignorance of the efficiency function biases the estimate of the correlation coefficients. We can therefore rely on simulated samples based on a realistic intrinsic rate. We proceed as schematically outlined below.

1. We assume that the available data represent reasonably well the intrinsic τ distribution so that we can infer (τ_0, σ_τ) from the data themselves. We set $\tau_{L,U} = \tau_0 \pm 5\sigma_\tau$, thus symmetrically cutting the Gaussian distribution at its extreme ends.
2. Based on the shape of the cosmic SFR (Hopkins & Beacom 2006), we assume a broken power law for the comoving RGRB density:

$$\dot{\rho}_*(z) \propto \begin{cases} (1+z)^{g_0} & z \leq z_0 \\ (1+z)^{g_1} & z_0 \leq z \leq z_1 \\ (1+z)^{g_2} & z \geq z_1 \end{cases} \quad (11)$$

where the relative normalizations are set so that $\dot{\rho}_*(z)$ is continuous at $z_0 = 0.97$ and $z_1 = (0.97, 4.50)$, $(g_0, g_1, g_2) = (3.4, -0.3, -8.0)$. Moreover, besides Equation (11), we employed other shapes of the SFR (Li 2008, Robertson & Ellis 2012; Kistler et al. 2013) to obtain the observed RGRB density. The one used by (Li 2008) is

$$\dot{\rho}(z) = a + b \times \text{Log}(1+z). \quad (12)$$

The a and b parameters are

$$(a, b) = \begin{cases} (-1.70, 3.30) & z \leq 0.993 \\ (-0.727, 0.0549) & 0.993 \leq z \leq 3.80 \\ (2.35, -4.46) & z \geq 3.80 \end{cases} \quad (13)$$

Robertson & Ellis (2012) defined the SFR as

$$\dot{\rho}(z) = \frac{a + b(z/c)^f}{1 + (z/c)^d} + g, \quad (14)$$

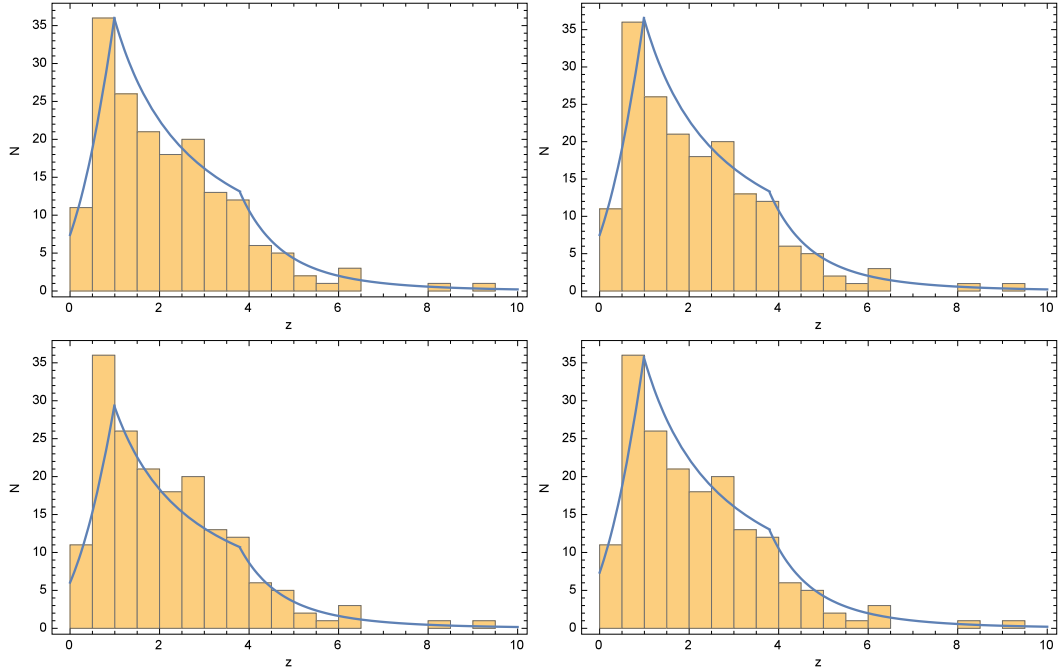


Figure 4. RGRB density using the method of Li (2008) and the observed RGRB density obtained by the linear efficiency functions (upper panel) and the polynomial efficiency function (lower panel) with the redshift distribution of our data sample.

where they have $a = 0.009 M_{\odot} \text{yr}^{-1} \text{Mpc}^{-3}$, $b = 0.27 M_{\odot} \text{yr}^{-1} \text{Mpc}^{-3}$, $c = 3.7$, $d = 7.4$, and $g = 10^{-3} M_{\odot} \text{yr}^{-1} \text{Mpc}^{-3}$.

Instead, Kistler et al. (2013) defined the SFR as

$$\dot{\rho}(z) = \dot{\rho}_0 \times \left[(1+z)^{a\psi} + \left(\frac{1+z}{B} \right)^{b\psi} + \left(\frac{1+z}{C} \right)^{c\psi} \right]^{\frac{1}{\psi}}, \quad (15)$$

with slopes of $a = 3.4$, $b = -0.3$, and $c = -2.5$, and breaks at $z_1 = 1$ and $z_2 = 4$ corresponding to $B = (1+z_1)^{1-\frac{a}{b}} \sim 5160$ and $C = (1+z_1)^{\frac{(b-a)}{c}} \times (1+z_2)^{\frac{(1-b)}{c}} \sim 11.5$, respectively, and $\psi = -10$.

Finally, we compare the fitted functions obtained with these four methods with our data distribution. The most reliable fit for our parameters is the SFR used by Li (2008); see Figure 4 where the best fit among linear (upper panel) and polynomial (lower panel) $\epsilon(\lambda)$ functions are considered. Moreover, we adopted the constraints for the redshift-dependent ratio between SFR and RGRB adopted by Robertson & Ellis (2012). In this paper a modest evolution (e.g., $\Psi(z) \approx (1+z)^\alpha$ with $-0.2 \leq \alpha \leq 1.5$, where the peak probability occurs for $\alpha \approx 0.5$) is consistent with the long GRB prompt data ($P \approx 0.9$). These values can be explained if GRBs occur primarily in low-metallicity galaxies that are proportionally more numerous at earlier times. We note that in our approach we assumed no evolution at low redshift for $z \leq 0.99$ consistently with the posterior probability in Robertson & Ellis (2012) in which no evolution is possible at the 2σ level. However, because a constant

Table 1
Efficiency Function Parameters for the Power-law \mathcal{E}_{λ} and no cut on τ , i.e., $\mathcal{E}_{\tau} = 1$.

Id	λ_L	λ_U	\mathcal{E}_{λ}	$P_{\text{GRB},\text{rate}}$
PL1	44.34	50.86	1.25	$\leq 10^{-4}$
PL2	43.64	49.87	2.99	0.003
PL3	43.77	50.74	1.65	0.53
PL4	44.77	49.59	2.04	0.001
PL5	44.14	50.83	0.23	0.54

Notes. $P_{\text{GRB},\text{rate}}$ is the goodness of fit between our data and the observed RGRB density and thus how well the data fit the observed GRB density rate. To compute the probability, we compute the χ^2 test, which performs a statistical hypothesis test in which the sampling distribution of the test statistic is a χ^2 distribution when the null hypothesis is true, in order to determine whether or not there is a significant difference between the expected frequencies and the observed frequencies.

$\Psi(z)$ is also ruled out (Robertson & Ellis 2012), we fit the normalization parameters and the evolution factors, obtaining $\Psi(z) \approx (1+z)^{-0.2}$ for $0.993 \leq z \leq 3.8$ and $\Psi(z) \approx (1+z)^{0.5}$ for $z \geq 3.8$. These values of the evolution are compatible with Robertson & Ellis (2012). Regarding the observed RGRB, we obtained that the best efficiency functions are possible both for two polynomial and two linear functions, as we show in Figure 4. Tables 1 and 2 show the probability that the density rate matches the afterglow plateau RGRB, assuming those efficiency functions.

- For given $(\alpha_0, \alpha_{\tau}, \alpha_{\zeta}, \sigma_{\text{int}})$ values, we divide the 2D space (λ, z) in \mathcal{M} cells and, for each cell, compute the fraction of

THE ASTROPHYSICAL JOURNAL, 800:31 (12pp), 2015 February 10

DAINOTTI ET AL.

Table 2

Same as Table 1 but for the Polynomial Functions

Id	λ_L	λ_U	\mathcal{E}_1	\mathcal{E}_2	\mathcal{E}_3	\mathcal{E}_4	$P_{\text{GRB,rate}}$
PoL1	44.90	49.14	0.46	0.01	0.24	0.80	0.54
PoL2	41.10	50.23	0.60	0.95	0.05	0.53	$\leq 10^{-4}$
PoL3	43.57	49.09	0.71	0.79	0.07	0.34	0.019
PoL4	44.37	49.52	0.51	0.03	0.46	0.78	0.15
PoL5	43.03	50.06	0.79	0.36	0.63	0.40	0.001

Note. $P_{\text{GRB,rate}}$ is the goodness of fit between our data and the observed RGRB density.

GRBs in it:

$$f_{\text{sim}}(\lambda_i, z_i) = \frac{\int_{\lambda_i - \Delta\lambda}^{\lambda_i + \Delta\lambda} d\lambda \int_{z_i - \Delta z}^{z_i + \Delta z} dz \frac{dN}{dz}}{\int_{\lambda_{\min}}^{\lambda_{\max}} d\lambda \int_{z_{\min}}^{z_{\max}} dz \frac{dN}{dz}} \quad (16)$$

where we set

$$(\lambda_{\min}, \lambda_{\max}) = (42.0, 52.0), (z_{\min}, z_{\max}) = (0, 10). \quad (17)$$

We find it more efficient to change the variable from z to ζ when dividing the 2D space in 10×10 square cells.

4. For each given cell, we generate $\mathcal{N}_{ij} = f_{\text{sim}}(\lambda_i, \zeta_j) \times \mathcal{N}_{\text{sim}}$ GRBs (with \mathcal{N}_{sim} the total number of objects to simulate) by randomly sampling (λ, ζ) within the cell boundaries and computing τ by solving Equation (1).
5. To take into account the selection effects, for each GRB we generate two random numbers (u_τ, u_λ) , uniformly sampling the range $(0, 1)$, and only retain the GRB if $u_\tau \leq \mathcal{E}_\tau(\tau)$ and $u_\lambda \leq \mathcal{E}_\lambda(\lambda)$. Note that, as a consequence of this cut, the final number \mathcal{N}_{obs} of observed GRBs is smaller than the input one \mathcal{N}_{sim} .
6. Finally, for each one of the \mathcal{N}_{obs} selected GRBs, we generate new $(\tau_{\text{obs}}, \lambda_{\text{obs}})$ values, extracting from Gaussian distributions centered on the simulated (τ, λ) values and with a 1% variance. We also assign to each GRB an error set in such a way as to be similar to what is actually obtained for GRBs with comparable (τ, λ) values.

The above procedure allows us to build a simulated GRB sample taking into account both the intrinsic properties of any scaling relation and the selection effects induced by the instrumental setup. Moreover, we have referred to an actual GRB sample in order to set both the limits on τ , ζ , and λ , and the typical measurement errors. Therefore, we can rely on these simulated samples to investigate the impact of selection effects on the recovered slope and intrinsic scatter of the given correlation. To this end, the last ingredient we need is a functional expression for the efficiency functions. Since these are largely unknown, we are forced to make some arbitrary guess. Therefore, we consider two different cases. First, we assume that there is no selection on τ , i.e., we set $\mathcal{E}_\tau = 1$. Two functional expressions are then used for \mathcal{E}_λ , namely a power law:

$$\mathcal{E}_\lambda(\lambda) = \begin{cases} 0 & \lambda < \lambda_L \\ (\frac{\lambda - \lambda_L}{\lambda_U - \lambda_L})^{\mathcal{E}_\lambda} & \lambda_L \leq \lambda \leq \lambda_U \\ 1 & \lambda > \lambda_U \end{cases} \quad (18)$$

and a fourth-order polynomial, i.e.,

$$\mathcal{E}_\lambda(\lambda) = \begin{cases} 0 & \lambda < \lambda_L \\ \frac{\mathcal{E}_1 \tilde{\lambda} + \mathcal{E}_2 \tilde{\lambda}^2 + \mathcal{E}_3 \tilde{\lambda}^3 + \mathcal{E}_4 \tilde{\lambda}^4}{\mathcal{E}_1 + \mathcal{E}_2 + \mathcal{E}_3 + \mathcal{E}_4} & \lambda_L \leq \lambda \leq \lambda_U \\ 1 & \lambda > \lambda_U \end{cases} \quad (19)$$

with $\tilde{\lambda} = (\lambda - \lambda_L)/(\lambda_U - \lambda_L)$. We try different arbitrary choices for the parameters entering both expressions of \mathcal{E}_λ in order to investigate to what extent the results depend on the exact choice of the efficiency function; see Figure 5. In a second step, we abandon the assumption $\mathcal{E}_\tau = 1$, to assume for it the same functional expression used for \mathcal{E}_λ , with the same choices for the parameters, but with different upper and lower limits depending on τ_U and τ_L ; see Figure 6.

4. REDSHIFT EVOLUTION ON THE NORMALIZATION AND SLOPE PARAMETERS

As we have already mentioned in the previous paragraph the polynomial and the linear model for the $\epsilon(\lambda)$ are unknown, and therefore assumptions need to be made. We chose these forms because both the normalization and the slope of the LT correlation depend on the redshift either with a polynomial or with a simple power law. Therefore, these choices for the selection functions take into account this redshift dependence. Namely, we consider a model redshift dependence because of the corresponding dependence of both luminosity and time. This has been already shown in Dainotti et al. (2013b) and is also shown in the middle panel of Figure 3 for the updated data sample. To study the behavior of the redshift evolution we plot the slope and the normalization values versus the redshift. These are obtained from the average values for the data set divided into 5 bins (see Figure 7) and into 12 bins (see Figure 8). As we can see from both Figures 7 and 8 that the normalization parameter α_0 decreases as the redshift increases, while the slope parameter α_τ shows the opposite trend. Goodness of fit is given by the probability $P = 0.79$ for the data set divided into 5 bins and $P = 0.87$ for the one divided into 12 bins for the linear case, while for the polynomial model it is $P = 0.99$ and $P = 0.94$ for the data set divided in 5 and 12 bins, respectively. These results show that both polynomial and linear fits are possible.

5. IMPACT OF SELECTION EFFECTS

The simulated samples generated as described above are input into the same Bayesian fitting procedure we use with real data. For each input $(\alpha_\tau, \alpha_\zeta, \alpha_0, \sigma_{\text{int}})$ parameter, we simulate a ~ 50 GRB sample setting $\mathcal{N}_{\text{sim}} = 200$, while the number of observed GRBs depends on the efficiency function used. We fit these samples assuming no redshift evolution in Equation (1), i.e., forcing $\alpha_\zeta = 0$ into the fit so that, for each simulated sample, the fitting procedure returns both the best fit and the median and 68% confidence range of the parameters $(\alpha_\tau, \alpha_0, \sigma_{\text{int}})$. In order to investigate whether or not the selection effects impact the recovery of the input scaling laws, we fit linear relations of the form:

$$x_f = \alpha x_{\text{inp}} + b \quad (20)$$

where x_{inp} is the input value and x_f can be either the best fit (denoted as x_{bf}) or the median x_{fit} value. When fitting the above linear relation, we use the χ^2 minimization for x_{bf} , while a weighted fit is performed for x_{fit} with weights $\omega_i = 1/\sigma_i^2$ where σ_i is the symmetrized 1σ error. Note that the label i here runs over the simulations performed for each given efficiency function.

5.1. No Redshift Evolution

Here, we consider input models with $\alpha_\zeta = 0$, i.e., no redshift evolution of the scaling law (1). It is worth noting that such an assumption is actually well motivated since it has

THE ASTROPHYSICAL JOURNAL, 800:31 (12pp), 2015 February 10

DAINOTTI ET AL.

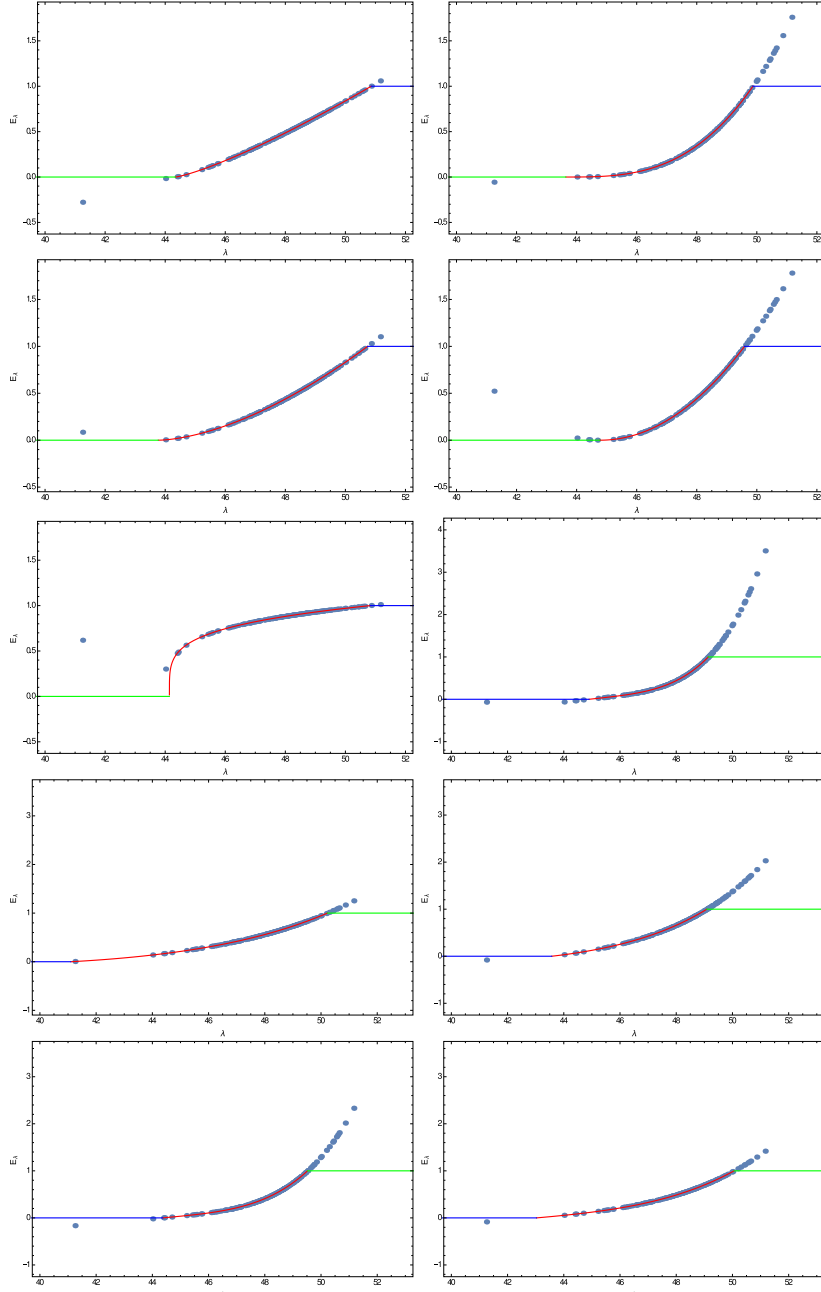


Figure 5. First five panels represent examples of the efficiency function for the linear case vs. luminosities of the GRBs, λ , in our data sample, while the last five panels represent the efficiency functions for the fourth-order polynomial. The linear functions as well as the polynomial ones are computed according to Equation (18) and Equation (19).

THE ASTROPHYSICAL JOURNAL, 800:31 (12pp), 2015 February 10

DAINOTTI ET AL.

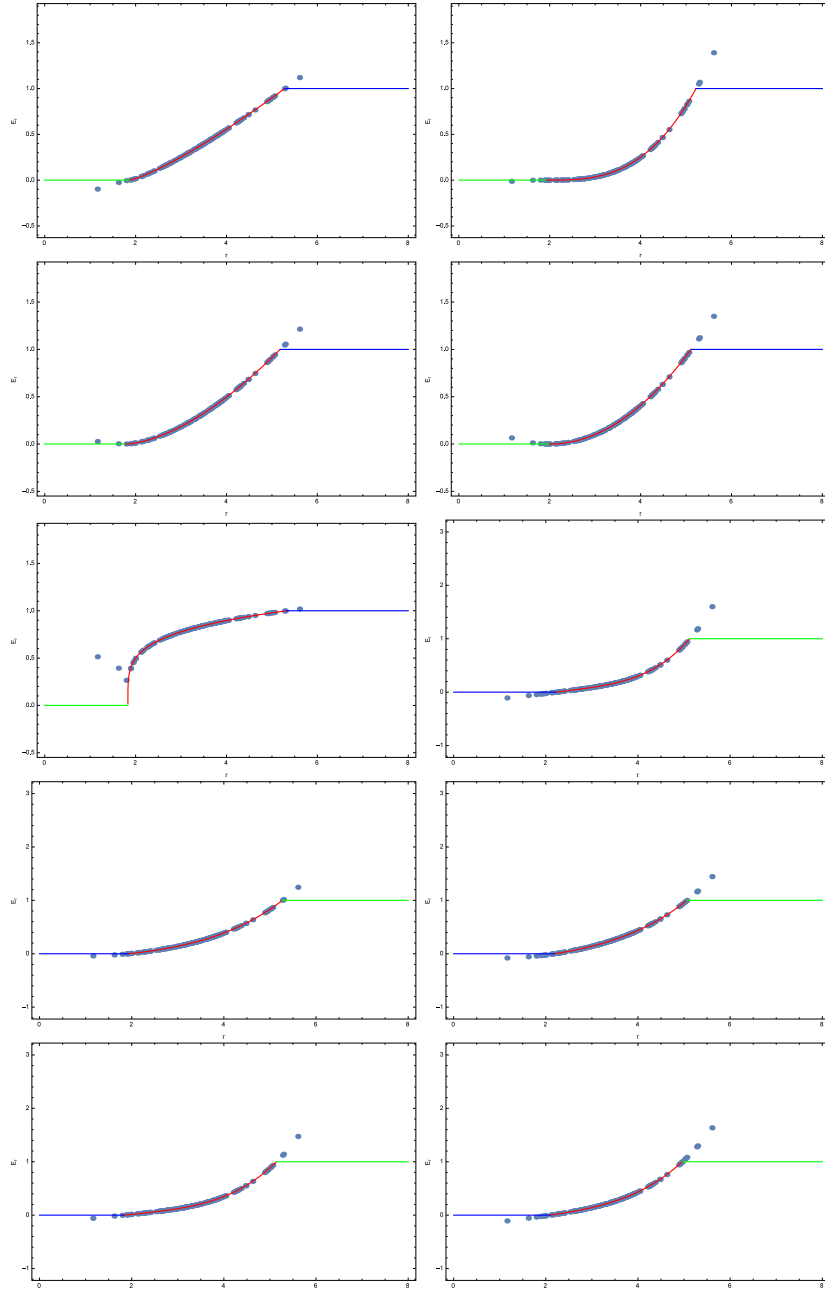


Figure 6. First five panels represent examples of the efficiency function for the linear case vs. the time, τ of the GRBs in our data sample, while the last five panels represent the efficiency functions for the fourth-order polynomial. The linear functions as well as the polynomial ones are computed according to Equation (18) and Equation (19).

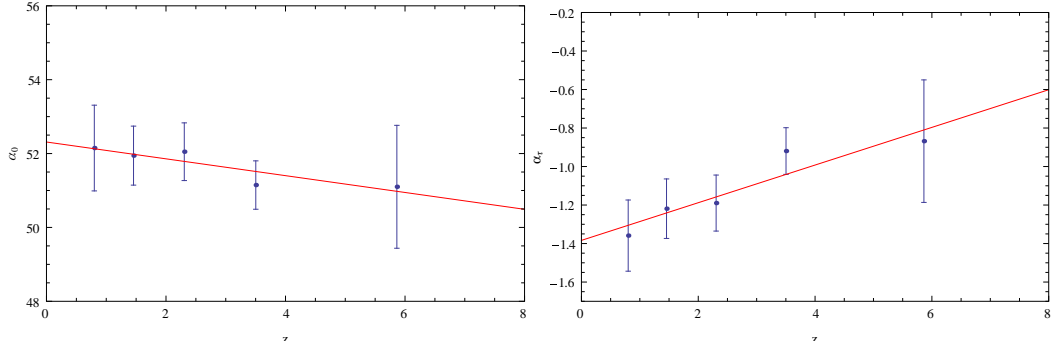


Figure 7. α_τ and normalization α_0 using a linear function $\alpha_0 = -0.22x + 52.31$ (left panel) and $\alpha_\tau = 0.10x - 1.38$ (right panel).

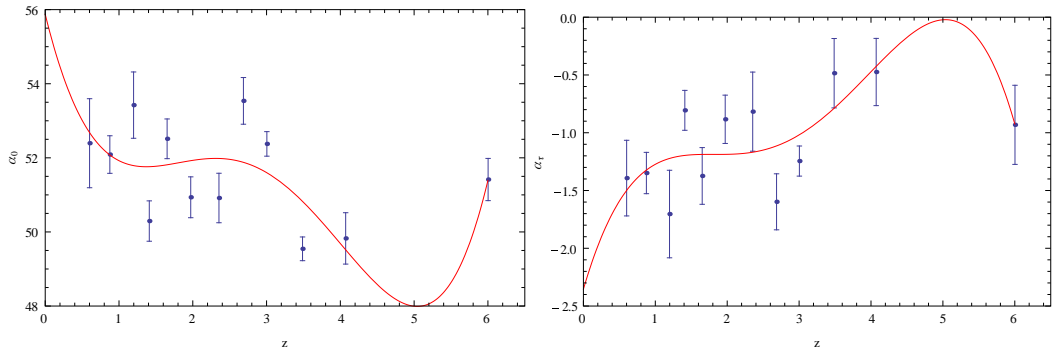


Figure 8. α_τ and normalization α_0 using a polynomial function $\alpha_0 = 55.87 - 8.13x + 5.53x^2 - 1.48x^3 + 0.13x^4$ (left panel) and $\alpha_\tau = -2.35 + 2.13x - 1.39x^2 + 0.37x^3 - 0.03x^4$ (right panel).

been demonstrated in Dainotti et al. (2013b) that luminosity is almost unaffected by redshift evolution, while time undergoes redshift evolution for high redshift only. From our point of view, however, this case allows us to directly quantify the impact of the efficiency functions on the recovery of the scaling correlation parameters, since any deviation will only be due to the selection effects and not due to any attempt of compensating the missed evolution with z .

5.1.1. No Selection on τ ($\mathcal{E}_\tau = 1$)

We start by considering the idealized case of no selection of τ , i.e., we force $\mathcal{E}_\tau = 1$, and set the \mathcal{E}_λ parameters as listed in Tables 1 and 2 for the power-law and polynomial expressions, respectively. As an example, Figure 9 shows the results for the efficiency function, while Table 3 summarizes the (a, b) coefficients of the linear fit between the input and recovered quantities. The closer a is to 1, the less the parameter is biased, while $b \neq 0$ should not be taken as evidence for bias. This result is in perfect agreement with the intrinsic correlation slope, which is $-1.07^{+0.09}_{-0.14}$ (Dainotti et al. 2013b), when we consider the selection functions that return values of a closer to 1 as the best choices. If Equation (20) is fulfilled, we can estimate the relative bias:

$$\frac{\Delta x}{x} = \frac{x_{\text{inp}} - x_f}{x_{\text{inp}}} = 1 - a - \frac{b}{x_{\text{inp}}}, \quad (21)$$

so that we can accept $b \neq 0$ if x_{inp} is much larger than b . This is indeed the case for $x_{\text{inp}} = \alpha_0$, which takes typical values (~ 50) that are much larger than the b ones in Table 3.

From the proximity between solid and dashed lines, which respectively represent the best-fit line and the no-bias line when $x_{\text{inp}} = x_f$, in the corresponding panels of Figure 9, we see that, for the power-law efficiency function (and no cut on τ), both the slope and the zero point of the scaling relation are correctly recovered. The reason why is that the relative bias is negligibly small, notwithstanding the values of the parameters setting \mathcal{E}_λ . This is particularly true if one relies on the median values as estimates since they are typically consistent with the no-bias line within less than 2σ .

The above results have been obtained considering a power-law \mathcal{E}_λ so that it is worth investigating whether or not they critically depend on this assumption. We have therefore repeated the analysis for the polynomial \mathcal{E}_λ models in Table 2, obtaining the results in Table 4. A comparison with the values in Table 4 shows that the (a, b) coefficients are similar so that one could preliminarily conclude that the shape of the efficiency function does not play a major role in the determination of the bias. Actually, although the functional expressions are different, both the power-law and the polynomial selection functions are qualitatively similar with \mathcal{E}_λ increasing with λ over a comparable range. Although such a behavior is likely common to any reasonable \mathcal{E}_λ , we can not exclude a priori that non-monotonic selection functions do actually exist. What the results would be

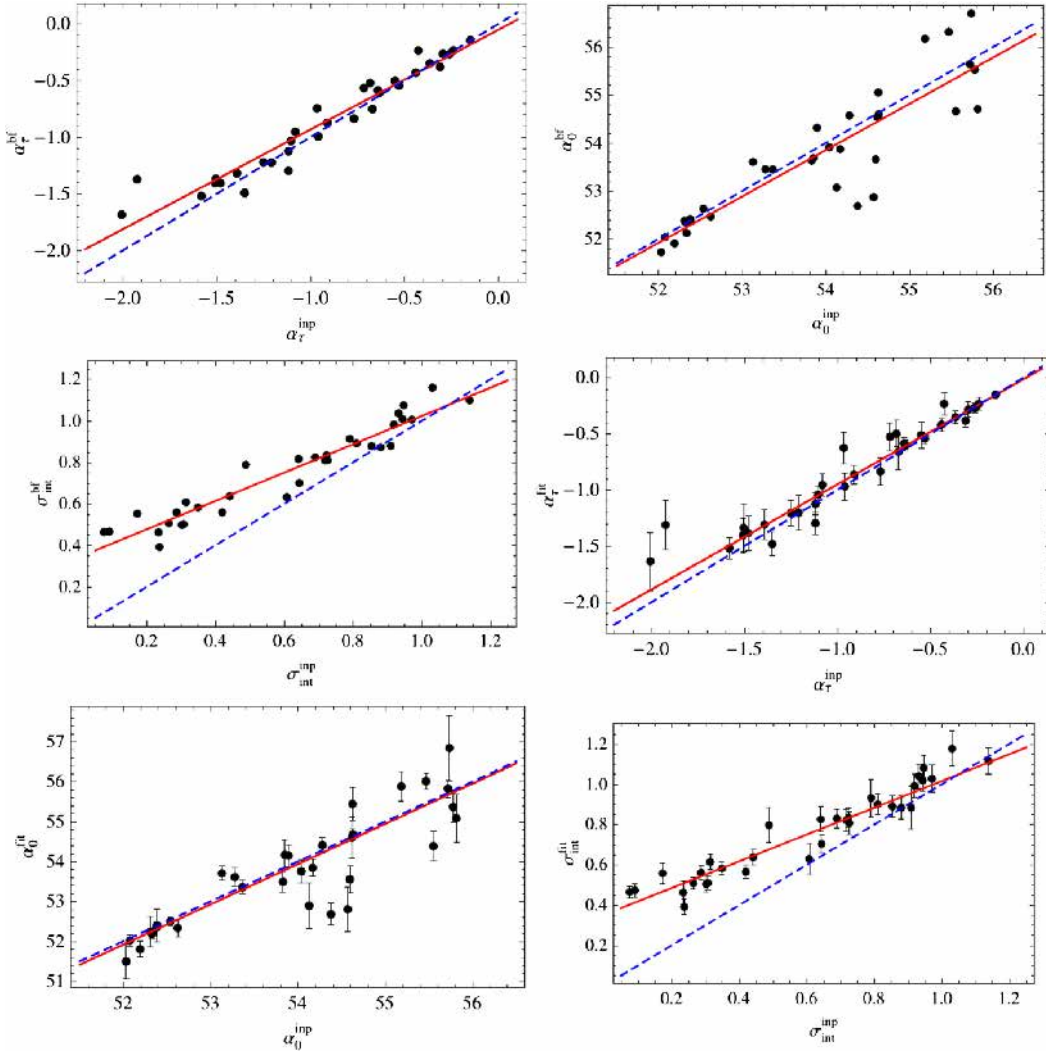


Figure 9. Fitted vs. input (α_{τ} , α_0 , σ_{int}) parameters obtained with the power-law function. The first three panels refer to the best-fit values, while the other three show the median values with the 1σ error bars. The solid red line is the best-fit line, while blue dashed is the no-bias line when $x_{\text{inp}} = x_f$.

Table 3
Slope a and Zero Point b of the Fitted versus Input Parameters for Both the Best-fit and Median Values (Labeled with Subscripts bf and fit, Respectively)

Id	$(a, b)_{bf}^{\tau}$	$(a, b)_{\text{fit}}^{\tau}$	$(a, b)_{bf}^{\alpha_0}$	$(a, b)_{\text{fit}}^{\alpha_0}$	$(a, b)_{bf}^{\sigma}$	$(a, b)_{\text{fit}}^{\sigma}$	Δ_x/x
PL1	(0.953, 0.010)	(0.959, 0.013)	(0.928, 3.688)	(1.000, -0.073)	(0.593, 0.354)	(0.616, 0.355)	0.004
PL2	(0.914, -0.008)	(0.873, -0.024)	(1.013, -0.836)	(0.989, 0.292)	(0.689, 0.299)	(0.643, 0.341)	0.002
PL3	(0.880, -0.052)	(0.937, -0.013)	(0.965, 1.729)	(1.008, -0.513)	(0.683, 0.340)	(0.664, 0.352)	0.003
PL4	(0.946, 0.024)	(0.964, 0.024)	(0.995, -0.076)	(1.086, -4.905)	(0.614, 0.364)	(0.585, 0.380)	0.006
PL5	(0.916, -0.030)	(0.962, 0.004)	(1.033, -2.067)	(0.828, 9.095)	(0.716, 0.333)	(0.679, 0.356)	0.005

Notes. The upper script denotes the parameter fitted with τ , α_0 , and σ referring to α_{τ} , α_0 , and σ_{int} , respectively. Δ_x/x is the bias for each efficiency function considered.

Table 4
Same as Table 3 but for the Polynomial \mathcal{E}_λ Model

Id	$(a, b)_{bf}^\tau$	$(a, b)_{fit}^\tau$	$(a, b)_{bf}^{\alpha_0}$	$(a, b)_{fit}^{\alpha_0}$	$(a, b)_{bf}^{\sigma}$	$(a, b)_{fit}^{\sigma}$	Δ_x/x
PoL1	(0.950, 0.020)	(0.928, 0.011)	(1.099, -5.545)	(1.178, -9.935)	(0.647, 0.350)	(0.673, 0.349)	0.004
PoL2	(1.095, 0.128)	(1.075, 0.105)	(1.030, -1.662)	(1.023, -1.278)	(0.681, 0.337)	(0.625, 0.372)	0.0008
PoL3	(0.984, 0.063)	(0.936, 0.015)	(0.711, 15.258)	(0.988, 0.376)	(0.741, 0.289)	(0.685, 0.336)	0.007
PoL4	(0.870, -0.025)	(0.969, 0.052)	(0.730, 14.103)	(0.734, 13.872)	(0.630, 0.351)	(0.582, 0.381)	0.009
PoL5	(1.004, 0.069)	(0.972, 0.030)	(0.963, 11.772)	(1.002, -0.374)	(0.581, 0.384)	(0.549, 0.402)	0.18

Table 5
Same as Table 3 but for the Selection Cuts on both (τ, λ) and Power-law \mathcal{E}_x Functions

Id	$(a, b)_{bf}^\tau$	$(a, b)_{fit}^\tau$	$(a, b)_{bf}^{\alpha_0}$	$(a, b)_{fit}^{\alpha_0}$	$(a, b)_{bf}^{\sigma}$	$(a, b)_{fit}^{\sigma}$	Δ_x/x
PLTa1	(0.842, -0.080)	(0.920, -0.016)	(1.099, -5.615)	(1.064, -3.650)	(0.615, 0.363)	(0.585, 0.387)	0.04
PLTa2	(0.972, -0.016)	(0.963, -0.027)	(1.112, -5.980)	(1.148, -7.746)	(0.720, 0.306)	(0.674, 0.335)	0.005
PLTa3	(0.960, -0.025)	(0.974, -0.005)	(0.985, 0.791)	(1.022, -1.228)	(0.725, 0.329)	(0.690, 0.345)	0.004
PLTa4	(0.877, -0.021)	(0.933, -0.005)	(1.005, -0.611)	(0.959, 2.196)	(0.702, 0.304)	(0.644, 0.345)	0.09
PLTa5	(0.860, -0.056)	(0.901, -0.026)	(0.911, 4.592)	(0.838, 8.655)	(0.687, 0.338)	(0.613, 0.382)	0.06
PLTa6	(0.904, -0.010)	(0.919, -0.003)	(0.734, 14.060)	(0.397, 32.119)	(0.678, 0.326)	(0.680, 0.330)	0.08
PLTa7	(0.915, -0.044)	(0.998, 0.035)	(1.119, -6.577)	(1.119, -6.474)	(0.736, 0.311)	(0.722, 0.327)	0.02
PLTa8	(0.967, -0.003)	(0.961, -0.017)	(1.027, -1.485)	(1.178, -9.515)	(0.731, 0.287)	(0.705, 0.313)	0.03
PLTa9	(0.933, -0.005)	(0.904, -0.031)	(1.026, -1.530)	(0.804, 10.289)	(0.641, 0.357)	(0.670, 0.352)	0.06
PLTa10	(1.040, 0.056)	(0.997, 0.028)	(0.753, 13.308)	(0.822, 9.345)	(0.736, 0.329)	(0.713, 0.344)	0.04

in such a case is not clear so that we prefer to be cautious and conclude that the bias is roughly the same whichever monotonic $\mathcal{E}_\lambda(\lambda)$ function is used, but not for all the possible \mathcal{E}_λ functions. For the non-monotonic shape of the selection function, see Stern et al. (2001), in which an assumed detection efficiency function, defined as the ratio of the number of detected test bursts to the number of test bursts applied to the data versus the expected peak count rate, is given by

$$E(c_e) = 0.70 \times \left[1 - \exp \left[- \left(\frac{c_e}{c_{e,0}} \right)^2 \right] \right]^v, \quad (22)$$

where $c_{e,0} = 0.097$ counts $\text{s}^{-1} \text{cm}^{-2}$ and $v = 2.34$ are two constants. However, quoting from Stern et al. (2001), the best possible efficiency quality has still not yet been achieved because in fact the detection efficiency depends on the peak count rate rather than on the time-integrated signal.

5.1.2. Selection Cuts on Both τ and λ

We now consider the case where the total selection function may be factorized as $\mathcal{E}(\tau, \lambda) = \mathcal{E}_\tau(\tau)\mathcal{E}_\lambda(\lambda)$ with both $\mathcal{E}_\tau(x)$ functions being given by power-law or fourth-order polynomial expressions. We consider 10 different arbitrary choices for both cases. Note that we have to increase \mathcal{N}_{sim} to 300 in order to have $\mathcal{N}_{\text{obs}} = 80\text{--}100$ as for the models discussed in the previous subsection.

Table 5 gives the (a,b) coefficients for the different models considered. A comparison with Table 3 shows that, on average, the bias on the parameters is roughly the same with the median values giving smaller deviations and significant bias on σ_{int} only. A more detailed analysis, however, shows that, in the $\mathcal{E}_\tau = 1$ case, biases larger than 5% are of the order of 10%. Namely, from Table 3 and 4 we show that the relative biases, Δ_x/x , both in the linear and the polynomial case, give very small values from 0.2% to 0.9%, with the only exception of 1 polynomial function, in which the bias is 18%, thus giving a $P = 10\%$ of having larger bias than 5%. If we consider selection cuts on both τ and λ we notice in Table 5 that the number of the bias

whose value is greater than 5% is four, thus increasing their probability of occurring ($P \sim 40\%$). This can be qualitatively explained by noting that a cut on λ only removes the points in the luminosity axis, thus possibly shifting the best-fit relation, but not changing the slope. On the contrary, removing points also along the horizontal τ axis can change the slope α_τ too and hence also affects $(\alpha_0, \sigma_{\text{int}})$ because of the correlation among these parameters and α_τ . Similar results are obtained when both \mathcal{E}_λ functions are modeled with fourth-order polynomials, so we will not discuss this case here. We stress that when Δ_x/x is larger than 6%, the slope of the correlation is farther from -1.0 compared to cases in which $\Delta_x/x \leq 0.06$. In fact, in the first case the slope values range from 0.86 to 0.91; see the functions PLTa4 and PLTa6 in Table 5. These values are not compatible in 1 σ with the claimed intrinsic slope of the correlation, $-1.07^{+0.09}_{-0.14}$. If we consider, instead, the lowest Δ_x/x , then we obtain ranges of $a = (0.94, 0.99)$, thus showing full compatibility in 1 σ with the intrinsic slope. In this way we have quantitatively confirmed the existence of the $L_X - T_a^*$ correlation with the same intrinsic slope as in Dainotti et al. (2013b) if appropriate selection functions are chosen.

6. CONCLUSIONS

Here we built a general method to evaluate selection effects for GRB correlations, not knowing a priori the efficiency function of the detector used. We have tested this method on the LT correlation. We chose a set of GRBs and assumed Gaussian distributions for the variables involved, for luminosity and time, and also a particular shape for the RGRB density. We simulated a mock sample of data in order to consider the selection effects of the detectors. As we can see in Section 3, assuming the correct observed RGRB density shape was not an easy task. In fact, we explored different methods (Li 2008; Robertson & Ellis 2012; Kistler et al. 2013; Hopkins & Beacom 2006) that use several SFR shapes to understand which one best matches the afterglow plateau data distribution, including the selection functions; see Figure 4. The most reliable fit for the GRB plateau data is the SFR used by Li (2008), while the

THE ASTROPHYSICAL JOURNAL, 800:31 (12pp), 2015 February 10

DAINOTTI ET AL.

best efficiency functions for $\epsilon(\lambda)$ that match the GRB density rate can be both two polynomial and two linear functions; see Figure 4. Tables 1 and 2 show the probability that the density rate fits the afterglow plateau RGRB assuming those efficiency functions. However, we assumed that there could be selection effects for both luminosity and time. In particular, the bias is roughly the same whichever monotonic efficiency function for the luminosity detection \mathcal{E}_λ is taken. In Tables 3 and 4 we show that the relative biases, Δ_x/x , both in the linear and the polynomial cases, give very small values from 0.2% to 0.9%, with the only exception being the 1 polynomial function, in which the bias is 18%, thus giving $P = 10\%$ of having a larger bias than 5%. If we consider selection cuts on both τ and λ , we notice in Table 5 that the number with bias whose value is greater than 5% is four, thus increasing the probability of having such biases ($P \sim 40\%$). In addition, we studied selection effects in the LT correlation assuming also a combination of the luminosity and time detection efficiency functions. Different values for the parameters of the efficiency functions in the detectors are taken into account as described in Section 5. This gives distinct fit values that are inserted into Equation (20) and allow us to study the scattering of the correlation and its selection effects. We have quantitatively confirmed the existence of the $L_X - T_a^*$ correlation with the same intrinsic slope as in Dainotti et al. (2013b) if appropriate selection functions are chosen. In particular, when Δ_x/x is larger than 6%, the slope of the correlation is farther from -1.0 compared to cases in which $\frac{\Delta_x}{x} \leq 0.06$. The lowest Δ_x/x leads to ranges of $a = (0.94, 0.99)$, thus showing full compatibility in σ with the intrinsic slope. Finally, the fact that the correlation is not generated by the biases themselves is a significant and further step toward considering a set of GRBs as standard candles and its possible and useful application as a cosmological tool.

This work made use of data supplied by the UK Swift Science Data Centre at the University of Leicester. We are particularly grateful to V. F. Cardone for the initial contribution to this work. M.G.D. and S.N. are grateful to the iTHES Group discussions at Riken. M.D. is grateful to the support from the JSPS Foundation (No. 25.03786). N.S. is grateful to JSPS (No.24.02022, No.25.03018, No.25610056, No.26287056) & MEXT(No.26105521), and R.D.V. is grateful to 2012/04/A/ST9/00083.

REFERENCES

- Amati, L., Frontera, F., & Guidorzi, C. 2009, *A&A*, **508**, 173
 Band, D. L. 2006, *ApJ*, **644**, 378
 Bernardini, M. G. 2012, *MNRAS*, **425**, 1199
 Bernardini, M. G., Margutti, R., Mao, J., Zaninoni, E., & Chincarini, G. 2012, *A&A*, **539**, A3
 Bloom, J. S. 2003, *ApJ*, **125**, 2865
 Butler, N. R., Bloom, J. S., & Poznanski, D. 2010, *ApJ*, **711**, 495
 Cabrera, J. I., Firmani, C., Avila-Reese, V., et al. 2007, *MNRAS*, **382**, 342
 Cannizzo, J. K., & Gehrels, N. 2009, *ApJ*, **700**, 1047
 Cannizzo, J. K., Troja, E., & Gehrels, N. 2011, *ApJ*, **734**, 35
 Cardone, V. F., Capozziello, S., & Dainotti, M. G. 2009, *MNRAS*, **400**, 775
 Cardone, V. F., Dainotti, M. G., Capozziello, S., & Willingale, R. 2010, *MNRAS*, **408**, 1181
 Coward, D. 2007, *NewAR*, **51**, 539
 Cucchiara, A., Levan, A. J., Fox, D. B., et al. 2011, *ApJ*, **736**, 7
 D'Agostini, G. 2005, arXiv:physics/0511182
 Daigne, F., & Mochkovitch, R. 2007, *A&A*, **465**, 1
 Dainotti, M. G., Cardone, V. F., & Capozziello, S. 2008, *MNRAS*, **391**, L79
 Dainotti, M. G., Cardone, V. F., Piedipalumbo, E., & Capozziello, S. 2013a, *MNRAS*, **436**, 82
 Dainotti, M. G., Fabrizio Cardone, V., Capozziello, S., Ostrowski, M., & Willingale, R. 2011a, *ApJ*, **730**, 135
 Dainotti, M. G., Petrosian, V., Singal, J., & Ostrowski, M. 2013b, *ApJ*, **774**, 157
 Dainotti, M. G., Ostrowski, M., & Willingale, R. 2011b, *MNRAS*, **418**, 2202
 Dainotti, M. G., Willingale, R., Capozziello, S., Fabrizio Cardone, V., & Ostrowski, M. 2010, *ApJL*, **722**, L215
 Dall'Osso, S., Stratta, G., Guetta, D., et al. 2011, *A&A*, **526A**, 121
 Dermer, C. D. 2007, *ApJ*, **664**, 384
 Efron, B., & Petrosian, V. 1992, *ApJ*, **399**, 345
 Fenimore, E. E., & Ramirez-Ruiz, E. 2000, *ApJ*, **539**, 712
 Fiore, F., Guetta, D., Piranomonte, S., DeLia, V., & Antonelli, L. A. 2007, *A&A*, **470**, 515
 Ghirlanda, G., Ghisellini, G., & Lazzati, D. 2004, *ApJ*, **616**, 331
 Ghirlanda, G., Ghisellini, G., & Firmani, C. 2006, *NuPh*, **8**, 123
 Ghisellini, G., Nardini, M., Ghirlanda, G., & Celotti, A. 2009, *MNRAS*, **393**, 253
 Guetta, D., & Della Valle, M. 2007, *ApJL*, **657**, L73
 Hascoet, R., Daigne, F., & Mochkovitch, R. 2014, *MNRAS*, **442**, 20
 Hopkins, A. M., & Beacom, J. F. 2006, *ApJ*, **651**, 142
 Izzo, L., Pisani, G. B., Muccino, M., et al. 2013, in Gamma-Ray Bursts: 15 years of GRB Afterglows, ed. J. Castro-Tirado, J. Gosabel, & I. H. Park (EAS Publ. Ser. 61; Les Ulis: EDP Sciences), 595
 Jakobsson, P., Levan, A., Fynbo, J. P. U., et al. 2006, *A&A*, **447**, 897
 Kistler, M. D., Yuksel, H., Beacom, J. F., & Stanek, K. Z. 2008, *ApJL*, **673**, L119
 Kistler, M. D., Yuksel, H., & Hopkins, A. M. 2013, arXiv:1305.1630
 Kocevski, D., & Petrosian, V. 2013, *ApJ*, **765**, 116
 Le, T., & Dermer, C. D. 2007, *ApJ*, **661**, 394
 Leventis, K., Wijers, R. A. M. J., & van der Horst, A. J. 2014, *MNRAS*, **437**, 2448
 Li, L.-X. 2008, *MNRAS*, **388**, 1487
 Lloyd, N. M., & Petrosian, V. 1999, *ApJ*, **511**, 550
 Mao, J. 2010, *ApJ*, **717**, 140
 Mao, S., & Mo, H. J. 1998, *A&A*, **339**, L1
 Natarajan, P., Albanna, B., Hjorth, J., et al. 2005, *MNRAS*, **364**, L8
 Nemmen, R. S., Georganopoulos, M., Guiriec, S., et al. 2012, *Sci*, **338**, 1445
 Norris, J. P., Marani, G. F., & Bonnell, J. T. 2000, *ApJ*, **534**, 248
 O'Brien, P. T., Willingale, R., Osborne, J., et al. 2006, *ApJ*, **647**, 1213
 Petrosian, V., Maloney, A., & Efron, B. 1998, *BAAS*, **30**, 831
 Petrosian, V. 2002, in ASP Conf. Proc. 284, AGN Surveys, ed. R. F. Green, E. Y. Khachikian, & D. B. Sanders (San Francisco, CA: ASP), 389
 Petrosian, V. 1999, in Proc. IAU Symp. 194, Active Galactic Nuclei and Related Phenomena, ed. Y. Terzian, E. Khachikian, & D. Weedman (San Francisco, CA: ASP), 105
 Porciani, C., & Madau, P. 2001, *ApJ*, **548**, 522
 Postnikov, S., Dainotti, M. G., Hernandez, X., & Capozziello, S. 2014, *ApJ*, **783**, 126
 Qi, S., & Lu, T. 2012, *ApJ*, **749**, 99
 Robertson, B. E., & Ellis, R. S. 2012, *ApJ*, **744**, 95R
 Rowlinson, A., Gompertz, B. P., Dainotti, M., et al. 2014, *MNRAS*, **443**, 1779
 Rowlinson, A., O'Brien, P. T., Metzger, B. D., Tanvir, N. R., & Levan, A. J. 2013, *MNRAS*, **430**, 1061
 Rowlinson, A., O'Brien, P. T., Tanvir, N. R., et al. 2010, *MNRAS*, **409**, 531
 Sakamoto, T., Hill, J. E., Yamazaki, R., et al. 2007, *ApJ*, **669**, 1115
 Schaefer, B. E. 2003, *ApJL*, **583**, L67
 Shahmoradi, A., & Nemiroff, R. 2009, *BAAS*, **42**, 228
 Stern, B. E., Tikhomirova, Y., Kompaneets, D., Svensson, R., & Poutanen, J. 2001, *ApJ*, **563**, 80
 Sultana, J., Kazanas, D., & Fukumura, K. 2012, *ApJ*, **758**, 32
 Totani, T. 1997, *ApJL*, **486**, L71
 Van Eerten, H. J. 2014a, *MNRAS*, **442**, 3495
 Van Eerten, H. J. 2014b, *MNRAS*, **445**, 2414
 Wijers, R. A. M. J., Bloom, J. S., Bagla, J. S., & Natarajan, P. 1998, *MNRAS*, **294**, L13
 Willingale, R., O'Brien, P. T., Osborne, J. P., et al. 2007, *ApJ*, **662**, 1093
 Yamazaki, R. 2009, *ApJL*, **690**, L118
 Yonetoku, D., Murakami, T., Nakamura, T., et al. 2004, *ApJ*, **609**, 935
 Yu, B., Qi, S., & Lu, T. 2009, *ApJL*, **705**, L15
 Yuksel, H., & Kistler, M. D. 2007, *PhRvD*, **75**, 083004



STUDY OF GRB LIGHT-CURVE DECAY INDICES IN THE AFTERGLOW PHASE

ROBERTA DEL VECCHIO¹, MARIA GIOVANNA DAINOTTI^{1,2,3}, AND MICHAŁ OSTROWSKI¹¹ Astronomical Observatory, Jagiellonian University, ul. Orla 171, 30-244 Kraków, Poland;² roberta@oa.uj.edu.pl (RDV), mdainott@stanford.edu (MGD), michał.ostrowski@uj.edu.pl (MO)³ Physics Department, Stanford University, Via Pueblo Mall 382, Stanford, CA, USA

3 INAF-Istituto di Astrofisica Spaziale e Fisica cosmica, Via Gobetti 101, I-40129, Bologna, Italy

Received 2015 October 5; revised 2016 June 12; accepted 2016 July 1; published 2016 August 26

ABSTRACT

In this work, we study the distribution of temporal power-law decay indices, α , in the gamma-ray burst (GRB) afterglow phase, fitted for 176 GRBs (139 long GRBs, 12 short GRBs with *extended emission*, and 25 X-ray flashes) with known redshifts. These indices are compared with the temporal decay index, α_w , derived with the light-curve fitting using the Willingale et al. model. This model fitting yields similar distributions of α_w to the fitted α , but for individual bursts a difference can be significant. Analysis of (α, L_a) distribution, where L_a is the characteristic luminosity at the end of the plateau, reveals only a weak correlation of these quantities. However, we discovered a significant regular trend when studying GRB α values along the Dainotti et al. correlation between L_a and the end time of the plateau emission in the rest frame, T_a^* , hereafter LT correlation. We note a systematic variation of the α parameter distribution with luminosity for any selected T_a^* . We analyze this systematics with respect to the fitted LT correlation line, expecting that the presented trend may allow us to constrain the GRB physical models. We also attempted to use the derived correlation of $\alpha(T_a)$ versus $L_a(T_a)$ to diminish the luminosity scatter related to the variations of α along the LT distribution, a step forward in the effort of standardizing GRBs. A proposed toy model accounting for this systematics applied to the analyzed GRB distribution results in a slight increase of the LT correlation coefficient.

Key words: distance scale – gamma-ray burst: general

Supporting material: figure set, machine-readable table

1. INTRODUCTION

Gamma-ray bursts (GRBs) with their powerful emission processes are observed up to high redshifts, $z > 9$ (Cucchiara et al. 2001). A significant progress in studying GRB observations has been the advent of the *Swift* satellite (Gehrels et al. 2004), which has revealed a more complex behavior of the light curves (Nousek et al. 2006; O’Brien et al. 2006; Zhang et al. 2006; Sakamoto et al. 2007) than in the past. There are several emission models proposed in the literature providing predictions for characteristic GRB light-curve features. Well known is the model of Mészáros (1998, 2006) and Meszaros & Rees (1999), consisting of jet internal shocks generating the GRB prompt phase emission and external shocks of the GRB expanding fireball generating the afterglow emission.

In the present paper, we study distributions of the GRB afterglow parameters versus light-curve temporal decay indices α , for the power-law decay observed in the afterglow phase, with the X-ray luminosity L_a . We analyze an extended sample of 176 GRBs with known redshifts observed by *Swift* from 2005 January to 2014 July. In the presented analysis, we use the LT correlation (Dainotti et al. 2008), updated in Dainotti et al. (2010, 2011a, 2013b, 2015b), between the derived characteristic afterglow plateau luminosity, L_a , and time, T_a^* (an index * indicates the GRB rest frame quantity). An attempt to study similar afterglow properties was presented by Gendre et al. (2008). They analyzed the “late” light-curve properties at the time of one day after the burst to reveal the existence of grouping the GRB luminosities into two groups, which also differ in their redshift distributions. In their study they noted relations among some GRB parameters, in particular, a non-trivial distribution of X-ray spectral indices versus the light-curve temporal decay indices, but no dependence of these

indices on the GRB luminosity. In addition, prompt-afterglow correlations have been studied by Dainotti et al. (2015a, 2011b), Margutti et al. (2013), and Grupe et al. (2013).

Importance of the present study results also from the fact that the afterglow LT correlation has already been the object of theoretical modeling either via accretion (Kumar et al. 2008; Cannizzo & Gehrels 2009; Lindner et al. 2010; Cannizzo et al. 2011), via a magnetar model (Bernardini et al. 2011; Dall’Osso et al. 2011; Rowlinson & O’Brien 2012; Rowlinson et al. 2013, 2014; Rea et al. 2015) or via energy injection (Sultana et al. 2013; Leventis et al. 2014; van Eerten 2014a, 2014b), and there were attempts to apply it as a cosmological tool (Cardone et al. 2009, 2010; Dainotti et al. 2013a; Postnikov et al. 2014). Here, we extend the LT correlation study looking into its possible dependence on the additional physical parameter α characterizing the afterglow light curve.

Below, in Section 2, we introduce the data set analyzed in this study. In Section 3, we describe the performed observational data analysis and the derived distributions of decay indices α . The analysis reveals a weak correlation for α and L_a , but a significant systematic trend along the correlated (L_a, T_a^*) distribution. In Section 4, we present our final discussion and conclusions. We shortly consider the physical interpretation of the α distribution. Then, we perform a preliminary exploration of a new possibility of using GRBs as cosmological standard candles, illustrated with a proposed toy model involving scaling GRB afterglow luminosity to the selected standard α_0 .

The fitted slopes and normalization parameters of the correlations presented in this paper are derived using the D’Agostini (2005) method. The Λ CDM cosmology applied here uses the parameters $H_0 = 71 \text{ km s}^{-1} \text{ Mpc}^{-1}$, $\Omega_\Lambda = 0.73$, and $\Omega_M = 0.27$.

THE ASTROPHYSICAL JOURNAL, 828:36 (6pp), 2016 September 1

DEL VECCHIO, DAINOTTI, & OSTROWSKI

Table 1
GRB Afterglow Decay Index Fits

GRB	α	σ_α	T1 (s)	T2 (s)	Type
050315	1.26	0.05	4.80	5.87	L
050318	1.28	0.04	3.50	4.50	L
050319	1.53	0.09	4.50	5.73	L(XRF)
050401	1.35	0.07	3.70	5.74	L
050416A	0.91	0.02	3.60	6.38	L(XRF)

Note. T1 and T2 are the logarithms of the start and ending times of the fit. The types are L = Long, S = short, and XRF = X-ray flashes.

(This table is available in its entirety in machine-readable form.)

2. DATA SAMPLE

Below, we analyze the distribution of afterglow light-curve decay indices, α , for the data set of 176 GRBs with known redshifts, observed by *Swift* from 2005 January to 2014 July. Within this sample, we consider separately subsamples of 139 long GRBs, 25 X-Ray Flashes (XRFs)⁴, and 12 short GRBs with extended emission. The sample of 164 long GRBs and XRFs is also considered together as a single sample.

As described in Dainotti et al. (2013b), all the analyzed light curves were fitted using an analytic functional form proposed by Willingale et al. (2007). The considered sample was chosen from all *Swift* GRBs with known redshifts by selecting only those events that allowed a reliable afterglow fitting. The fits provided physical parameters for the GRB afterglows, including their characteristic luminosities and time, L_a and T_a^* , at the end of the afterglow plateau phase, and the power-law temporal decay index, α_w , for the afterglow decaying phase.⁵ The fitted indices α_w are influenced by the requirement of the best global light-curve fitting for the considered analytic model. Therefore, we decided to apply a different procedure for the derivation of the temporal decay index α to be used in the following analysis, intended to provide a more accurate fit of the light-curve power-law decay part immediately after the plateau. In each GRB, we selected the afterglow light-curve section with a power law and we performed the χ^2 fitting of α in such a range, as presented in figure set 1 for all GRBs showing the performed fits and providing the fitting parameters in Table 1. We compared these parameters with those by Evans et al. (2009) and the ones quoted in the *Swift* Burst Analyzer (http://www.swift.ac.uk/burst_analyser/), having nearly the same α values in the majority of cases. However, significant differences are also found in individual cases due to the different time ranges considered for the fits.

The applied procedure allowed us to remove all clear deviations of the power-law from the fitting due to flares and non-uniformities in the observational data. In the case of a break in the decaying part of the light curve, a value of α was fitted to the brighter/earlier part of the light curve. We have to note that in some rare cases it was impossible to decide if the first part of the light curve can be considered the decaying part,

⁴ XRFs are bursts of high energy emission similar to long GRBs, but with a spectral peak energy one order of magnitude smaller than in the long GRBs and with fluence greater in the X-rays than in the gamma-ray band. Sometimes XRFs are considered to be misaligned long GRBs (Ioka & Nakamura 2001; Yamazaki et al. 2002) and this is why we also analyze both of these samples together.

⁵ These data are available upon request from M.G. Dainotti.

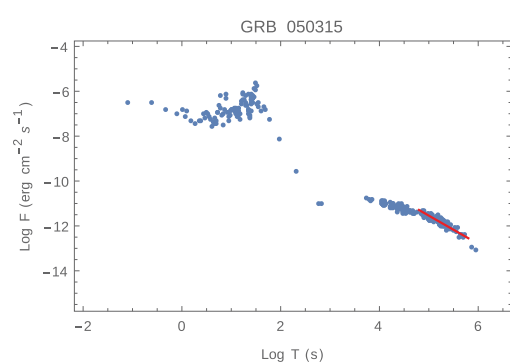


Figure 1. GRB 050315: $\alpha = 1.26$. Our fits are indicated by the red line and the time range for the fit is available in Table 1.
(The complete figure set (172 images) is available.)

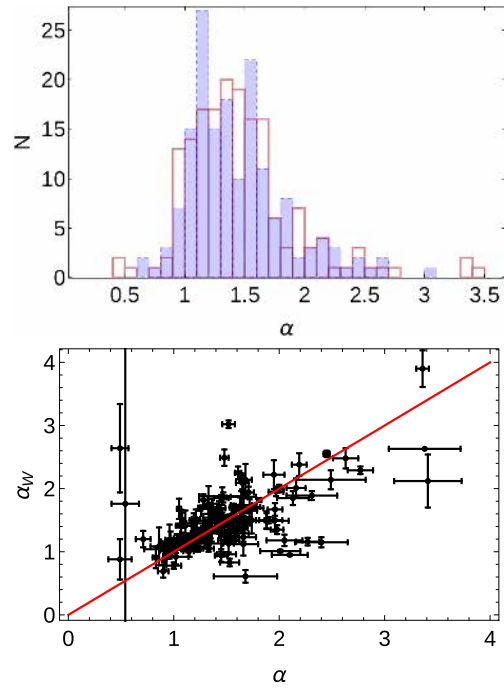


Figure 2. Comparison of the derived indices α and α_w . Upper panel: histograms of fitted α (solid red line) and α_w (shaded area). Bottom panel: the α_w vs. α distribution. The red line $\alpha = \alpha_w$ is provided for reference.

or still a steep plateau phase, and the presented fits can be disputed. We decided to use all derived data in the analysis and correlations studied in this paper, leaving the possibility of some particular data selection and/or rejecting some events from the analysis to the future study.

Comparison of the α and α_w distributions in Figure 2 shows that both measured decay indices have similar distributions, but differences for individual fitted values can be

THE ASTROPHYSICAL JOURNAL, 828:36 (6pp), 2016 September 1

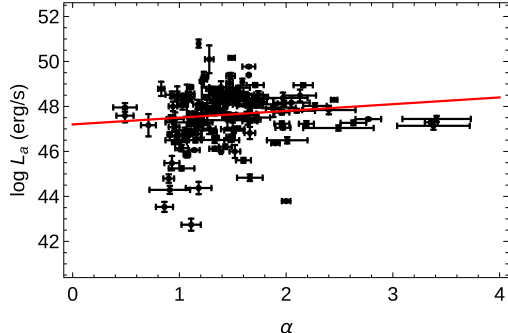


Figure 3. Distribution of $\log L_a$ vs. α for the long GRBs+XRFs subsample. The line presents a fitted weak correlation.

significant. The parameters of the Gaussian fits for both presented distributions are a mean value $\mu(\alpha) = 1.40$ with standard deviation $\sigma(\alpha) = 0.46$ for our power-law fitting compared to $\mu(\alpha_W) = 1.45$ and $\sigma(\alpha_W) = 0.45$ for the Willingale model fitting. The P -value of the T-test between these two distributions is 0.89, indicating no statistically significant differences between the two distributions.

3. ANALYSIS OF THE AFTERGLOW DECAY LIGHT CURVES

By adopting the analyzed subsample of long GRBs+XRFs, systematic trends in the $(\log L_a, \alpha)$ distribution can be studied. As presented in Figure 3, there is an indication that these quantities are (weakly) correlated. However, the scatter of points around the correlation line is substantial and the derived Spearman (1904) correlation coefficient $\rho = 0.17$ is small. The fitted correlation line is $\log L_a = 0.30 \alpha + 47.20$, showing that on average faster light-curve decay seems to occur for GRBs with higher luminosities. However, here we stress again that the trend is weak in this highly scattered distribution. The same analysis using the long GRBs subsample only leads to a slightly weaker correlation with $\rho = 0.14$ and $P = 10^{-4}$.

It should be noted that the large scatter of the GRB luminosity distribution cannot be due only to the fitting method used for its derivation. Significant contribution to this scatter must result from the very nature of the GRB sources, possibly modified by the explosion geometry.

In an attempt to evaluate the trend in Figure 3, we decided to compare distributions of α plotted for three luminosity ranges with equal numbers of GRBs: a low luminosity range $-\log L_a < 47.25$, a medium range $47.25 < \log L_a < 48.2$, and a high range $\log L_a > 48.2$. Normalized cumulative distribution function CDF ($CDF(x) \equiv \sum_0^x (1/N)$, where summing includes all GRBs with $\alpha < x$ and N is the number of GRBs in the considered sample) approximates the cumulative probability function in the α space. In Figure 4, we present these functions in the three analyzed luminosity ranges for the whole GRB sample, as well as for long GRBs, short GRBs, and XRF subsamples. Comparison of the red and blue CDF distributions presented in Figure 4 convincingly (maybe less convincingly for the short subsample) supports the existence of the $(\log L_a, \alpha)$ correlation. The same systematics for all analyzed GRB samples with lower luminosity events show the tendency to slower light-curve decay. The most luminous

DEL VECCHIO, DAINOTTI, & OSTROWSKI

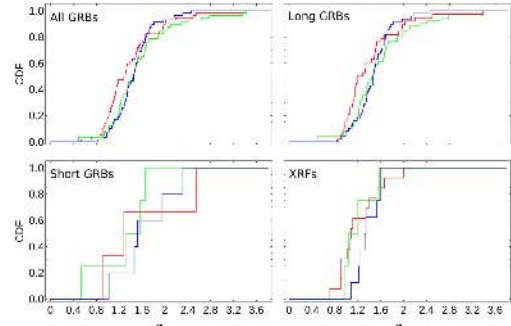


Figure 4. Normalized cumulative distribution functions, CDF, vs. α for the analyzed GRB subsamples in three considered luminosity ranges: $\log L_a < 47.25$ (red), $47.25 < \log L_a < 48.2$ (green), and $\log L_a > 48.2$ (blue).

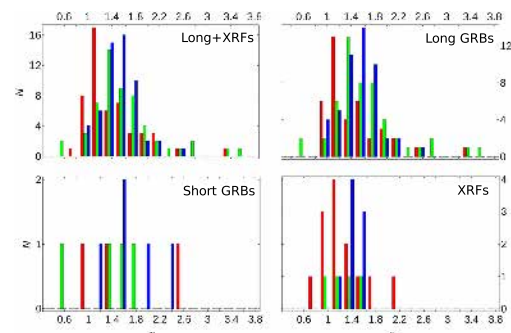


Figure 5. GRB distributions of α for the analyzed subsamples in three considered luminosity ranges: $\log L_a < 47.25$ (red), $47.25 < \log L_a < 48.2$ (green), and $\log L_a > 48.2$ (blue). In each $\Delta\alpha$ bin, the data for the different luminosity ranges are plotted as (shifted within the considered bin) separate color bars.

GRBs (blue lines) seem to grow faster to unity with their smaller α scatter. This result is also confirmed by the Kolmogorov-Smirnov (KS) test. The test applied for low (red line) and high (blue line) luminosity GRB distributions along the α coordinate (Figure 5) shows that it is highly unlikely, with $P = 0.01$, that both distributions are drawn randomly from the same population. As regards the XRFs and short GRBs subsamples, the available number of elements is too low for establishing reliable statistical results; however, the distributions of brighter GRBs seem to show the same tendency to be centered at higher α values than the dimmer ones.

There is no well understood universal recipe for differentiating the physical properties of the GRB source from observational data yet, but the existence of $\log L_a$ versus $\log T_a^*$ correlation reflects the presence of approximately uniformly varying properties of GRB progenitor in the plateau phase. If these properties would be the GRB progenitor mass and/or its angular momentum, then different external medium profiles could be expected around the exploding massive star, where the afterglow related shock propagates. Therefore, it may be expected to detect more clear dependence between the afterglow luminosity and the α index for GRBs analyzed

THE ASTROPHYSICAL JOURNAL, 828:36 (6pp), 2016 September 1

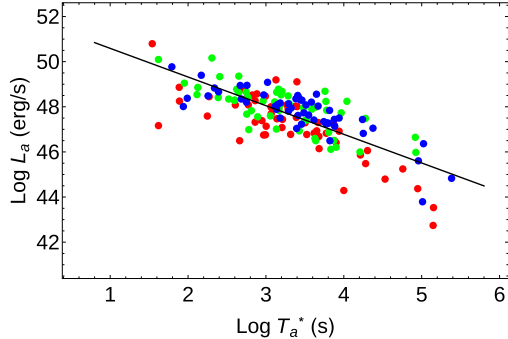


Figure 6. Distribution of the long GRBs+XRFs subsample on the $(\log L_a, \log T_a^*)$ plane for the three selected α subsamples: $0.53 < \alpha < 1.23$ (red), $1.23 < \alpha < 1.54$ (green) and $1.54 < \alpha < 3.41$ (blue). The black line represents the LT correlation line fitted for all presented GRBs.

within a limited range of T_a^* . To proceed, in analogy to the above analysis for selected luminosity ranges, we study relative distributions of GRB subsamples along the LT distribution in three ranges of the decay index: the “slowly” decaying light curves with $0.53 < \alpha < 1.23$, the “intermediate” ones with $1.23 < \alpha < 1.54$, and the “fast” decaying light curves with $1.54 < \alpha < 3.41$. With such a selection, each subsample has the same size.

Inspection of Figure 6, presenting the considered long GRBs+XRFs α -subsamples distributed along the LT correlation line, clearly reveals separation among these distributions. This behavior is also visible in the normalized cumulative distribution functions plotted in Figure 7. In particular, in Figure 7, the considered samples (all GRBs, long GRBs and long GRBs+XRFs) are presented with respect to the ratio of the GRB afterglow luminosity $L_a(T_a^*)$ to the respective luminosity $L_{LT}(T_a^*)$ at the fitted correlation line: in the logarithmic scale $\log(L_a/L_{LT}) = \log L_a - \log L_{LT}$. A significant trend between the relative luminosity, $\log(L_a/L_{LT})$, and α is visible in Figure 8, leading, e.g., to negligible KS probability, $P = 1.4 \times 10^{-6}$, that the low and high α subsamples are randomly drawn from a single GRB population.

In Figure 9, we present the distribution of $\log(L_a/L_{LT})$ versus the α index for the long GRBs+XRFs subsample. A linear fit for this distribution is

$$\log L_a - \log L_{LT} = (0.49 \pm 0.17)\alpha - (0.70 \pm 0.25), \quad (1)$$

with Spearman correlation coefficient $\rho = 0.36$, and the probability for random occurrence $P = 10^{-10}$. Using the long GRB subsample only, the correlation has a slightly smaller slope (0.42) with $\rho = 0.36$ and $P = 7.7 \times 10^{-10}$. This correlation shows the observed tendency—with respect to the LT correlation line—for higher afterglow luminosity to have steeper light-curve decay.

To better evaluate the errors of the parameters fitted for the analyzed GRB sample, we decided to perform an additional statistical analysis using the Monte Carlo modeling of the data with $3 \cdot 10^4$ simulations in each case. For each GRB, we consider parameters L_a , T_a^* , and α to have Gaussian distributions around the fitted values, with the distribution width given by the respective 1σ uncertainty. Then, we randomly selected from the considered GRB sample—using a

DEL VECCHIO, DAINOTTI, & OSTROWSKI

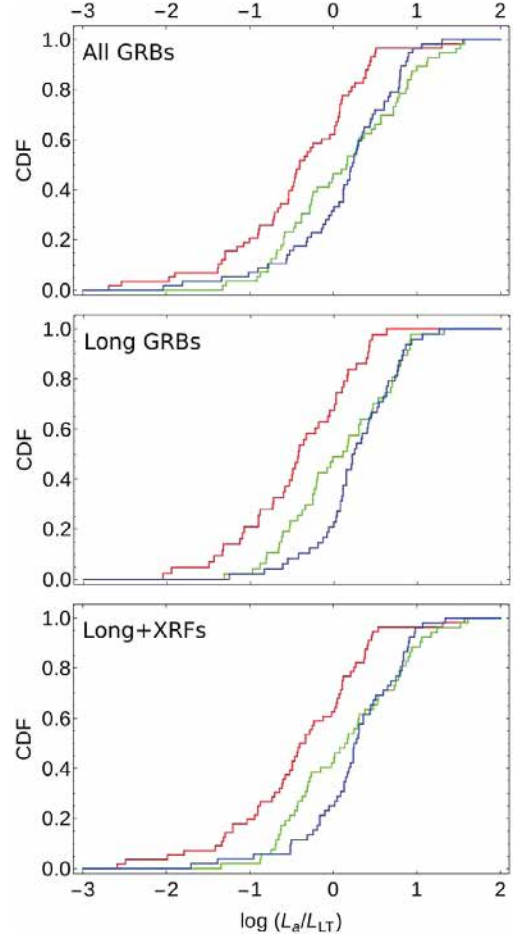


Figure 7. Normalized cumulative distributions function CDF vs. $\log(L_a/L_{LT})$ for the analyzed GRB subsamples in three considered α ranges: $0.53 < \alpha < 1.23$ (red), $1.23 < \alpha < 1.54$ (green), and $1.54 < \alpha < 3.41$ (blue).

bootstrap procedure—the samples to be analyzed, where each GRB parameter was drawn from the respective Gaussian distribution. For each randomly created data sample, we derived the correlation coefficient and the correlation slope by fitting the respective correlation $\log(L_a/L_{LT})$ versus α . As presented in the upper panels of Figure 10, the simulations fully confirm the reality of the derived correlation. We find that within the measurement errors the existing correlation coefficient should be approximately between $0.2 < \rho < 0.5$ (mean value 0.35) and the fitted $\log(L_a/L_{LT})$ versus α correlation should have an inclination of $0.3 < a < 0.5$ (mean value 0.41), in agreement with the fitted errors in Equation (1).

Using similar simulations as above, the possibility of randomly obtaining the studied $\log(L_a/L_{LT})$ versus α correlation can also be independently be checked if no systematic relation of α in respect to L_a and T_a^* exists. We performed such an analysis by randomly drawing samples using the procedure

THE ASTROPHYSICAL JOURNAL, 828:36 (6pp), 2016 September 1

DEL VECCHIO, DAINOTTI, & OSTROWSKI

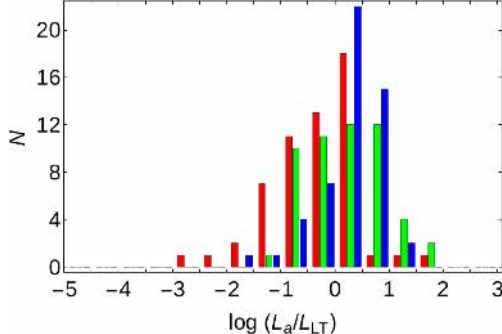


Figure 8. Distributions of $\log(L_a/L_{LT})$ for the long GRBs+XRFs subsamples, for the three α ranges: $0.53 < \alpha < 1.23$ (red), $1.23 < \alpha < 1.54$ (green), and $1.54 < \alpha < 3.41$ (blue).

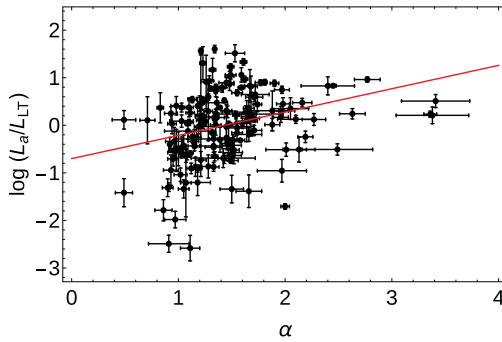


Figure 9. Distribution of the long GRBs+XRFs subsample on the $(\alpha, \log(L_a/L_{LT}))$ plane. The red line presents the fitted correlation (See Equation (1)).

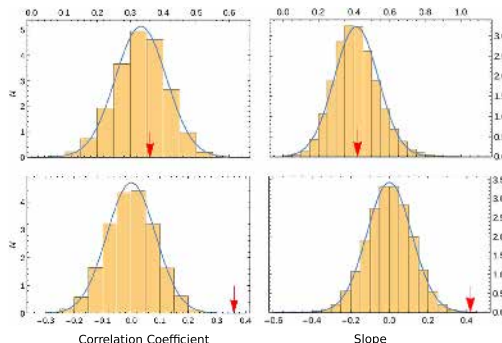


Figure 10. Results of the Monte Carlo simulations for the long subsample: the normalized distributions of the correlation coefficient ρ and the slope a of the $\log(L_a/L_{LT})$ vs. α correlation for bootstrapped simulations including random data scatter within the measurement error ranges (upper panels) and the analogous distributions with the α parameters separately randomly drawn from the sample (lower panels). The red arrows indicate the values obtained in the above analysis of the original data.

above, again within the bootstrap scheme, but with separately drawing pairs of parameters L_a and T_a^* from the GRB sample, and the α values from the sample of these values for the considered GRBs. Such a procedure removes any correlation between α and other GRB parameters in the sample and shows that the possibility of randomly obtaining the correlation coefficient found in the real data is negligible (Figure 10, lower panels).

4. FINAL DISCUSSION AND CONCLUSIONS

Analysis of the fitted afterglow power-law temporal decay indices for the subsample of long GRBs+XRFs reveals a weak trend toward a steeper decay phase for higher afterglow luminosity L_a . The trend turns into a significant correlation if we consider GRB afterglow luminosity scaled to the one expected from the fitted LT correlation, for a given GRB afterglow plateau end time T_a^* . As different T_a^* values result from varying properties of the GRB sources, the present analysis can be used to get new insight into the physical nature of such sources.

4.1. Theoretical Models

It is worth noting the attempts in the literature to provide a physical interpretation of the $\log L_a$ versus α relation. We can refer to such a model presented by Hascoet et al. (2014; see also Genet et al. 2007) in order to relate the considered α parameter to the microphysics of the reverse shock emission. In the model of Hascoet et al., the energy deposition rate, \dot{E}_T , in the GRB afterglow, varied in time “ t ” with a power-law dependence on the Lorentz gamma factor, $\Gamma(t)$:

$$\dot{E}_T(\Gamma(t)) = \begin{cases} \dot{E}_* \left(\frac{\Gamma(t)}{\Gamma_*} \right)^{-q} & \text{for } \Gamma(t) > \Gamma_* \\ \dot{E}_* \left(\frac{\Gamma(t)}{\Gamma_*} \right)^{q'} & \text{for } \Gamma(t) < \Gamma_* \end{cases}, \quad (2)$$

where the energy scale \dot{E}_* is determined by the total energy injected in the afterglow phase; q and q' are the power-law indices for the time dependence of the energy injection rate. In this model, the q parameter constrains the shape of the plateau phase, while q' carries information about the light-curve temporal decay index after the plateau. The characteristic value of Γ_* sets the duration of the plateau. With the assumed power-law radial distribution of the medium surrounding the GRB progenitor, the Lorentz factor evolves as

$$\Gamma(t) = \Gamma_* \left(\frac{t}{T_a^*} \right)^{-\gamma}, \quad (3)$$

where, e.g., $\gamma = 3/8$ for a uniform medium and $\gamma = 1/4$ for a stellar wind. Hascoet et al. derived the light-curve temporal decay indices before (α_1) and after (α_2) the break at the end of the plateau phase as

$$\begin{cases} \alpha_1 = \gamma q - 1 \\ \alpha_2 = -\gamma q' - 1 \end{cases}, \quad (4)$$

so that the flat plateau phase should be present for $q \approx 1/\gamma$, i.e., close to $q = 8/3$ in the uniform medium and $q = 4$ in the wind case. In the presented example, Hascoet et al. (2014) considered the temporal decay index after the plateau

THE ASTROPHYSICAL JOURNAL, 828:36 (6pp), 2016 September 1

$\alpha_2 = -1.5$, leading to $q' = 1/(2\gamma)$ and the parameters of the central engine energy deposition in the late afterglow stage $q' = 4/3$ and 2, for the uniform medium and the wind case, respectively. It should be noted that this example uses the α_2 value very close to the mean value of our distribution, $\alpha_{\text{mean}} = 1.4 \pm 0.3$, as visible in the upper panel of Figure 2.

We should remark here that the observed large scatter in the α distribution seems to be difficult to be explained only by variations of the source radial density profile, influencing the shock propagation. Therefore, we consider the present discussion only as an example of the study based on the α parameter measurements.

4.2. GRB Standardization

As the second aspect of the present study, we consider a possible usage of the measured afterglow light curve α for physically differentiating the observed GRBs. For example, the revealed $\log(L_a/L_{\text{LT}})$ versus α correlation can be used to search for the procedure, which could enable the standardization of GRBs and eventually reveal a new cosmological standard candle. As an *illustrative toy model*, for such an approach, we introduce a procedure for GRBs resembling the one used for the standardization of SN Ia light curves by using the so-called Phillips relation between the peak magnitude and the “stretching parameter” (Phillips 1993). In an attempt to scale GRBs with different temporal decay indices α to the standard source properties, we define the standard GRB as the one characterized by the value of the temporal decay index $\alpha_0 = 1.4$, approximately the mean value of the distribution presented in Figure 2. Furthermore, we postulate that the expected “standardized” GRB luminosity, $L_{a,0}$, can be derived using its measured decay index α and by scaling it to α_0 using Equation (1):

$$\log L_{a,0} = \log L_a + 0.49 (\alpha_0 - \alpha). \quad (5)$$

This procedure applied for all the events in the analyzed subsample of long GRBs+XRFs results in only a slight increase in the LT correlation coefficient absolute value, from $\rho = -0.72$ for the original ($\log L_a$, $\log T_a^*$) data to $\rho_0 = -0.76$ for the modified distribution ($\log L_{a,0}$, $\log T_a^*$). When using the long GRB subsample only the increase in the correlation coefficient is even smaller. This increase in the correlation coefficient is obtained by the fits for quite different shapes of the afterglow light curves and thus different quality of available GRB parameters L_a , T_a^* , and α . More detailed analysis of this standardization procedure, with careful consideration of the afterglow light curves for the selected events, is in progress now.

This work made use of data supplied by the UK Swift Science Data Centre at the University of Leicester. The work of R.D.V. and M.O. was supported by the Polish National Science Centre through the grant DEC-2012/04/A/ST9/00083. M.G.D. is grateful to the Marie Curie Program, because the research leading to these results has received funding from

DEL VECCHIO, DAINOTTI, & OSTROWSKI

the European Union Seventh FrameWork Program (FP7-2007/2013) under grant agreement N 626267. We thank the anonymous referee for helpful comments and suggestions.

REFERENCES

- Bernardini, M. G., Margutti, R., Chincarini, G., Guidorzi, C., & Mao, J. 2011, *A&A*, **526**, A27
 Cannizzo, J. K., & Gehrels, N. 2009, *ApJ*, **700**, 1047
 Cannizzo, J. K., Troja, E., & Gehrels, N. 2011, *ApJ*, **734**, 35
 Cardone, V. F., Capozziello, S., & Dainotti, M. G. 2009, *MNRAS*, **400**, 775
 Cardone, V. F., Dainotti, M. G., Capozziello, S., & Willingale, R. 2010, *MNRAS*, **408**, 1181
 Cucchiara, A., Levan, A. J., Fox, D. B., et al. 2001, *ApJ*, **736**, 7
 Dainotti, M., Petrosian, V., Willingale, R., et al. 2015a, *MNRAS*, **451**, 3898
 Dainotti, M. G., Cardone, V. F., & Capozziello, S. 2008, *MNRAS*, **391**, L79
 Dainotti, M. G., Cardone, V. F., Capozziello, S., Ostrowski, M., & Willingale, R. 2011a, *ApJ*, **730**, 135
 Dainotti, M. G., Cardone, V. F., Piedipalumbo, E., & Capozziello, S. 2013a, *MNRAS*, **436**, 82
 Dainotti, M. G., Del Vecchio, R., Nagataki, S., & Capozziello, S. 2015b, *ApJ*, **800**, 31
 Dainotti, M. G., Ostrowski, M., & Willingale, R. 2011b, *MNRAS*, **418**, 2202
 Dainotti, M. G., Petrosian, V., Singal, J., & Ostrowski, M. 2013b, *ApJ*, **774**, 157
 Dainotti, M. G., Willingale, R., Capozziello, S., Cardone, V. F., & Ostrowski, M. 2010, *ApJL*, **722**, L215
 Dall’Osso, S., Stratta, G., Guetta, D., et al. 2011, *A&A*, **526**, A121
 D’Agostini, G. 2005, arXiv:physics/0511182
 Evans, P. A., Beardmore, A. P., Page, K. L., et al. 2009, *MNRAS*, **397**, 1177
 Gehrels, N., Chincarini, G., Giommi, P., et al. 2004, *ApJ*, **611**, 1005
 Gendre, B., Galli, A., & Boér, M. 2008, *ApJ*, **683**, 620
 Genet, F., Daigne, F., & Mochkovitch, R. 2007, *MNRAS*, **381**, 732
 Grupe, D., Nousek, J. A., Veres, P., Zhang, B. B., & Gehrels, N. 2013, *ApJS*, **209**, 20
 Hascoet, R., Daigne, F., & Mochkovitch, R. 2014, *MNRAS*, **442**, 20
 Ioka, K., & Nakamura, T. 2001, *ApJL*, **554**, L163
 Kumar, P., Narayan, R., & Johnson, J. L. 2008, *Sci*, **321**, 376
 Leventis, K., Wijers, R. A. M. J., & van der Horst, A. J. 2014, *MNRAS*, **437**, 2448
 Lindner, C. C., Milosavljević, M., Couch, S. M., & Kumar, P. 2010, *ApJ*, **713**, 800
 Margutti, R., Zaninoni, E., Bernardini, M. G., et al. 2013, *MNRAS*, **428**, 729
 Mészáros, P. 1998, in AIP Conf. Ser. 428, Gamma-Ray Bursts IV, ed. C. A. Meegan, T. M. Koshut, & R. D. Preece (Melville, NY: AIP), 647
 Mészáros, P. 2006, *RPPh*, **69**, 2259
 Meszaros, P., & Rees, M. J. 1999, *MNRAS*, **306**, L39
 Nousek, J., Kouveliotou, C., Grupe, D., et al. 2006, *ApJ*, **642**, 389
 O’Brien, P. T., Willingale, R., Osborne, J., et al. 2006, *ApJ*, **647**, 1213
 Phillips, M. M. 1993, *ApJL*, **413**, L105
 Postnikov, S., Dainotti, M. G., Hernandez, X., & Capozziello, S. 2014, *ApJ*, **783**, 126
 Rea, N., Gullón, M., Pons, J. A., et al. 2015, *ApJ*, **813**, 92
 Rowlinson, A., Gompertz, B. P., Dainotti, M. G., et al. 2014, *MNRAS*, **443**, 1779
 Rowlinson, A., & O’Brien, P. 2012, in Proc. of the Gamma-Ray Bursts 2012 Conference, History and Future Instrumentation (Trieste: SISSA), **120**
 Rowlinson, A., O’Brien, P. T., Metzger, B. D., Tanvir, N. R., & Levan, A. J. 2013, *MNRAS*, **430**, 1061
 Sakamoto, T., Hill, J., Yamazaki, R., et al. 2007, *ApJ*, **669**, 1115
 Spearman, C. 1904, *Amer. J. Psychol.*, **15**, 72
 Sultana, J., Kazanas, D., & Mastichiadis, A. 2013, *ApJ*, **779**, 16
 van Eerten, H. 2014a, *MNRAS*, **442**, 3495
 van Eerten, H. J. 2014b, *MNRAS*, **445**, 2414
 Willingale, R., O’Brien, P. T., Osborne, J. P., et al. 2007, *ApJ*, **662**, 1093
 Yamazaki, R., Ioka, K., & Nakamura, T. 2002, *ApJL*, **571**, L31
 Zhang, B., Fan, Y. Z., Dyks, J., et al. 2006, *ApJ*, **642**, 354